Introduction to $k-$ Horadam hybrid numbers

Nayil Kilic

Dept. of Mathematics and Science Education
Hasan Ali Yucel Education Faculty
Istanbul University-Cerrahpasa
Istanbul, Turkey
Corresponding author: nayilkilic@gmail.com

Abstract

In this paper, we consider the $k-$ Horadam hybrid numbers and investigate some of their properties. We also give some applications related to the $k-$ Horadam hybrid numbers in matrices.

Keywords: Complex numbers; fibonacci and lucas numbers; generating functions; hyperbolic numbers; recurrences.

1. Introduction

Let k be any positive real number and $h(k)$ and $g(k)$ are scaler value polynomials. For $m \geq 0$ and $h^2(k) + 4g(k) > 0$ the generalized $k-$ Horadam sequence $\{H_{k,m}\}_{m \in \mathbb{N}}$ is described by

$$H_{k,m+2} = h(k)H_{k,m+1} + g(k)H_{k,m} \tag{1}$$

with initial conditions $H_{k,0} = w$, $H_{k,1} = z$.

The solutions of the equation $y^2 - h(k)y - g(k) = 0$ associated with the recurrence relation (1) are

$$\lambda = \frac{h(k) + \sqrt{h^2(k) + 4g(k)}}{2} \quad and$$
$$\gamma = \frac{h(k) - \sqrt{h^2(k) + 4g(k)}}{2}. \tag{2}$$

Note that:

$$\lambda + \gamma = h(k), \quad \lambda - \gamma = \sqrt{h^2(k) + 4g(k)}, \quad \lambda\gamma = -g(k). \tag{3}$$

So the Binet formula for the $k-$ Horadam sequence is given by

$$H_{k,m} = \frac{N\lambda^m - K\gamma^m}{\lambda - \gamma}, \tag{4}$$
$$where \quad N = z - w\gamma, \quad K = z - w\lambda.$$

$k-$ Horadam sequence is a generalization of some sequences such as the Fibonacci, Lucas, Pell, Pell-Lucas, Jacobsthal, $k-$ Fibonacci and $k-$ Lucas sequences. These sequences have applications in algebra, number theory and geometry. Hence, these sequences have been studied by a number of researchers; see for examples: (Horadam, 1965; Koshy, 2001; Koshy, 2018; Kilic, 2019a; Kilic, 2019b; Kilic, 2019c; Akkus & Kizilaslan, 2019; Yazlik & Taskara, 2012).

Remark 1.1. *Some particular cases of (1) are ;*

• *If $h(k) = k$, $g(k) = 1$, $w = 0$ and $z = 1$ then we get the $k-$ Fibonacci sequence;*

$$F_{k,m+2} = kF_{k,m+1} + F_{k,m}, \quad F_{k,0} = 0, F_{k,1} = 1.$$

• *If $h(k) = k$, $g(k) = 1$, $w = 2$ and $z = k$ then we have the $k-$ Lucas sequence;*

$$L_{k,m+2} = kL_{k,m+1} + L_{k,m}, \quad L_{k,0} = 2 \quad L_{k,1} = k.$$

• *If $h(k) = 2$, $g(k) = k$, $w = 0$ and $z = 1$ then we obtain the $k-$ Pell sequence;*

$$P_{k,m+2} = 2P_{k,m+1} + kP_{k,m}, \quad P_{k,0} = 0 \quad P_{k,1} = 1.$$

• *If $h(k) = p$, $g(k) = q$, then we find the Horadam sequence;*

$$H_{m+2} = pH_{m+1} + qH_m, \quad H_0 = w \quad H_1 = z.$$

• *If $h(k) = 1$, $g(k) = 1$, $w = 0$ and $z = 1$ then we get the Fibonacci sequence;*

$$F_{m+2} = F_{m+1} + F_m, \quad F_0 = 0 \quad F_1 = 1.$$

• *If $h(k) = 2$, $g(k) = 1$, $w = 1$ and $z = 1$ then we have the Pell-Lucas sequence;*

$$PL_{m+2} = 2PL_{m+1} + PL_m, \quad PL_0 = 1 \quad PL_1 = 1.$$

The set $\mathbb{T}$, defined below, represents the set of hybrid numbers;

$$\mathbb{T} = \{t_1 + t_2i + t_3\varepsilon + t_4\mathbf{h} | t_1, t_2, t_3, t_4 \in \mathbb{R}; i^2 = -1, \varepsilon^2 = 0, \mathbf{h}^2 = 1, i\mathbf{h} = -\mathbf{h}i = \varepsilon + i\}. \quad (5)$$

Addition and subtraction of hybrid numbers are done by adding and subtracting corresponding terms. The product of any two hybrid numbers, using the expression (5), can be defined as in Szynal-Liana (2018) (see Table 1).

The conjugate of a hybrid number $P = t_1 + t_2i + t_3\varepsilon + t_4\mathbf{h}$ is defined by

$$\overline{P} = t_1 - t_2i - t_3\varepsilon - t_4\mathbf{h}. \quad (6)$$

The nth Horadam hybrid numbers $\widetilde{hH_n}$ is described as

$$\widetilde{hH_n} = H_n + iH_{n+1} + \varepsilon H_{n+2} + H_{n+3}\mathbf{h}. \quad (7)$$

where H_n is the nth Horadam number and $i, \varepsilon, \mathbf{h}$ denote hybrid units.

Hybrid numbers and hybrid polynomials have been studied by several researchers; (Szynal-Liana, 2018) introduced Horadam hybrid numbers and found some results about them. In 2019, Szynal-Liana & Włoch, studied Fibonacci and Lucas hybrinomials. The authors (Liana *et al.*, 2019) introduced Pell hybrid numbers and investigated some of their properties. Kizilates (2020) studied the $q-$ Fibonacci hybrid numbers. Kilic, (2019a) considered split $k-$ Jacobsthal and $k-$ Jacobsthal Lucas quaternions and obtained some properties of them. Also, Kilic studied Horadam octonions and dual Horadam octonions (Kilic, 2019b, 2019c).

Now, we introduce the $k-$Horadam hybrid numbers and investigate some of their properties. We also give some applications related to the $k-$ Horadam hybrid numbers in matrices.

2. $k-$ **Horadam hybrid numbers**

For $m > 0$, the $k-$ Horadam hybrid numbers are defined by

$$\widetilde{h}H_{k,m} = H_{k,m} + iH_{k,m+1} + \varepsilon H_{k,m+2} + H_{k,m+3}\mathbf{h} \tag{8}$$

where $H_{k,m}$ is the mth $k-$ Horadam number and $i, \varepsilon, \mathbf{h}$ are hybrid units.

Theorem 2.1. *Let $s \geq 2$ be an integer. Then*

$$\widetilde{h}H_{k,s} = h(k)\widetilde{h}H_{k,s-1} + g(k)\widetilde{h}H_{k,s-2} \tag{9}$$

with $\widetilde{h}H_{k,0} = w + iz + \varepsilon[h(k)z + g(k)w] + \mathbf{h}[h^2(k)z + h(k)g(k)w + g(k)z]$ and $\widetilde{h}H_{k,1} = z + i[h(k)z + g(k)w] + \varepsilon[h^2(k)z + h(k)g(k)w + g(k)z] + \mathbf{h}[h^3(k)z + h^2(k)g(k)w + 2h(k)g(k)z + g^2(k)w]$.

Proof. If $s = 2$ then, we get

$$h(k)\widetilde{h}H_{k,1} + g(k)\widetilde{h}H_{k,0}$$
$$= h(k)\{z + i[h(k)z + g(k)w] + \varepsilon[h^2(k)z + h(k)g(k)w + g(k)z] + \mathbf{h}[h^3(k)z + h^2(k)g(k)w$$
$$+ 2h(k)g(k)z + g^2(k)w]\} + g(k)\{w + iz + \varepsilon[h(k)z + g(k)w] + \mathbf{h}[h^2(k)z + h(k)g(k)w$$
$$+ g(k)z]\}$$
$$= h(k)z + g(k)w + i[h^2(k)z + h(k)g(k)w + g(k)z] + \varepsilon[h^3(k)z + h^2(k)g(k)w + 2h(k)g(k)z$$
$$+ g^2(k)w] + \mathbf{h}[h^4(k)z + h^3(k)g(k)w + 3h^2(k)g(k)z + 2h(k)g^2(k)w + g^2(k)z]$$
$$= H_{k,2} + iH_{k,3} + \varepsilon H_{k,4} + \mathbf{h}H_{k,5}$$
$$= \widetilde{h}H_{k,2}.$$

If $s \geq 3$ then using (1), we obtain

$$\widetilde{h}H_{k,s}$$
$$= H_{k,s} + iH_{k,s+1} + \varepsilon H_{k,s+2} + \mathbf{h}H_{k,s+3}$$
$$= h(k)H_{k,s-1} + g(k)H_{k,s-2} + i[h(k)H_{k,s} + g(k)H_{k,s-1}] + \varepsilon[h(k)H_{k,s+1} + g(k)H_{k,s}]$$
$$+ \mathbf{h}[h(k)H_{k,s+2} + g(k)H_{k,s+1}]$$
$$= h(k)[H_{k,s-1} + iH_{k,s} + \varepsilon H_{k,s+1} + \mathbf{h}H_{k,s+2}] + g(k)[H_{k,s-2} + iH_{k,s-1} + \varepsilon H_{k,s} + \mathbf{h}H_{k,s+1}]$$
$$= h(k)\widetilde{h}H_{k,s-1} + g(k)\widetilde{h}H_{k,s-2}$$

which completes the proof.

Theorem 2.2. *(Binet Formula) For $m \geq 0$, the Binet formula for $k-$Horadam hybrid numbers is*

$$\widetilde{h}H_{k,m} = \frac{N\lambda^m\hat{\lambda} - K\gamma^m\hat{\gamma}}{\lambda - \gamma} \tag{10}$$

where $N = z - w\gamma, \quad K = z - w\lambda, \quad \hat{\lambda} = 1 + i\lambda + \varepsilon\lambda^2 + \mathbf{h}\lambda^3$ and $\hat{\gamma} = 1 + i\gamma + \varepsilon\gamma^2 + \mathbf{h}\gamma^3$.

Proof. Using (8) and (4), we can write the following expression

$$\widetilde{h}H_{k,m}$$
$$= H_{k,m} + iH_{k,m+1} + \varepsilon H_{k,m+2} + \mathbf{h}H_{k,m+3}$$
$$= [\frac{N\lambda^m - K\gamma^m}{\lambda - \gamma}] + i[\frac{N\lambda^{m+1} - K\gamma^{m+1}}{\lambda - \gamma}] + \varepsilon[\frac{N\lambda^{m+2} - K\gamma^{m+2}}{\lambda - \gamma}] + \mathbf{h}[\frac{N\lambda^{m+3} - K\gamma^{m+3}}{\lambda - \gamma}]$$
$$= \frac{N\lambda^m}{\lambda - \gamma}[1 + i\lambda + \varepsilon\lambda^2 + \mathbf{h}\lambda^3] - \frac{K\gamma^m}{\lambda - \gamma}[1 + i\gamma + \varepsilon\gamma^2 + \mathbf{h}\gamma^3]$$
$$= \frac{N\lambda^m\hat{\lambda} - K\gamma^m\hat{\gamma}}{\lambda - \gamma}.$$

Remark 2.3. *For $h(k) = k$, $g(k) = 1$, $w = 0$ and $z = 1$, we obtain $\lambda = \frac{k+\sqrt{k^2+4}}{2}$, $\gamma = \frac{k-\sqrt{k^2+4}}{2}$, $N = 1$, $K = 1$ and the Binet formula for the $k−$ Fibonacci hybrid number $FH_{k,m}$ has the form*

$$FH_{k,m}$$
$$= \frac{1}{\sqrt{k^2+4}}\left\{\left(\frac{k+\sqrt{k^2+4}}{2}\right)^m\left[1 + (\frac{k+\sqrt{k^2+4}}{2})i + (\frac{k+\sqrt{k^2+4}}{2})^2\varepsilon + (\frac{k+\sqrt{k^2+4}}{2})^3\mathbf{h}\right]\right.$$
$$\left. - \left(\frac{k-\sqrt{k^2+4}}{2}\right)^m\left[1 + (\frac{k-\sqrt{k^2+4}}{2})i + (\frac{k-\sqrt{k^2+4}}{2})^2\varepsilon + (\frac{k-\sqrt{k^2+4}}{2})^3\mathbf{h}\right]\right\}.$$

Remark 2.4. *For $h(k) = k$, $g(k) = 1$, $w = 2$ and $z = k$, we obtain $\lambda = \frac{k+\sqrt{k^2+4}}{2}$, $\gamma = \frac{k-\sqrt{k^2+4}}{2}$, $N = \sqrt{k^2+4}$, $K = -\sqrt{k^2+4}$ and the Binet formula for the $k−$ Lucas hybrid number $LH_{k,m}$ has the form*

$$LH_{k,m}$$
$$= \left(\frac{k+\sqrt{k^2+4}}{2}\right)^m\left[1 + (\frac{k+\sqrt{k^2+4}}{2})i + (\frac{k+\sqrt{k^2+4}}{2})^2\varepsilon + (\frac{k+\sqrt{k^2+4}}{2})^3\mathbf{h}\right]$$
$$+ \left(\frac{k-\sqrt{k^2+4}}{2}\right)^m\left[1 + (\frac{k-\sqrt{k^2+4}}{2})i + (\frac{k-\sqrt{k^2+4}}{2})^2\varepsilon + (\frac{k-\sqrt{k^2+4}}{2})^3\mathbf{h}\right].$$

Lemma 2.5. *Let $m \geq 1$ be an integer. Then*

$$\widetilde{h}H_{k,m}\overline{\widetilde{h}H_{k,m}} = \frac{1}{h^2(k)+4g(k)}\left\{N^2\lambda^{2m}[1 + \lambda^2 - 2\lambda^3 - \lambda^6] - 2NK(-g(k))^m[1 - g(k)\right.$$
$$\left. + g(k)h(k) + g^3(k)] + K^2\gamma^{2m}[1 + \gamma^2 - 2\gamma^3 - \gamma^6]\right\}.$$

Proof. From (10), we have

$$\widetilde{h}H_{k,m}\overline{\widetilde{h}H_{k,m}} = \left[\frac{N\lambda^m\hat{\lambda} - K\gamma^m\hat{\gamma}}{\lambda-\gamma}\right]\overline{\left[\frac{N\lambda^m\hat{\lambda} - K\gamma^m\hat{\gamma}}{\lambda-\gamma}\right]}$$

By Eq. (3) and some elementary calculations we have

$$\widetilde{h}H_{k,m}\overline{\widetilde{h}H_{k,m}} = \frac{1}{h^2(k)+4g(k)}\left\{N^2\lambda^{2m}[1 + \lambda^2 - 2\lambda^3 - \lambda^6] - 2NK(-g(k))^m[1 - g(k)\right.$$
$$\left. + g(k)h(k) + g^3(k)] + K^2\gamma^{2m}[1 + \gamma^2 - 2\gamma^3 - \gamma^6]\right\}.$$

Theorem 2.6. *The generating function for the $k−$ Horadam hybrid number sequence $\{\widetilde{h}H_{k,m}\}$ is*

$$\sum_{m=0}^{\infty} \widetilde{h}H_{k,m}t^m = \frac{\widetilde{h}H_{k,0} + t[\widetilde{h}H_{k,1} - h(k)\widetilde{h}H_{k,0}]}{1 - h(k)t - g(k)t^2}. \tag{11}$$

Proof. Let $A(t) = \sum_{m=0}^{\infty} \widetilde{h}H_{k,m}t^m$. Then

$$A(t) = \widetilde{h}H_{k,0} + \widetilde{h}H_{k,1}t + \widetilde{h}H_{k,2}t^2 + ... \tag{12}$$

Multiply (12) on both sides by $-h(k)t$ and then $-g(k)t^2$ we have

$$-h(k)tA(t) = -h(k)t\widetilde{h}H_{k,0} - h(k)t^2\widetilde{h}H_{k,1} - h(k)t^3\widetilde{h}H_{k,2} - ... \tag{13}$$

$$-g(k)t^2 A(t) = -g(k)t^2 \widetilde{h}H_{k,0} - g(k)t^3 \widetilde{h}H_{k,1} - g(k)t^4 \widetilde{h}H_{k,2} - \ldots \tag{14}$$

By adding (12), (13) and (14), we have

$$A(t) = \frac{\widetilde{h}H_{k,0} + t[\widetilde{h}H_{k,1} - h(k)\widetilde{h}H_{k,0}]}{1 - h(k)t - g(k)t^2}.$$

Theorem 2.7. *Let* $m \geq 1$ *be an integer. Then*

$$\sum_{l=1}^{m} \widetilde{h}H_{k,l} = \frac{1}{1 - h(k) - g(k)}[\widetilde{h}H_{k,1} + g(k)\widetilde{h}H_{k,0} - \widetilde{h}H_{k,m+1} - g(k)\widetilde{h}H_{k,m}].$$

Proof. By using the Binet formula of the $k-$ Horadam hybrid numbers, we find that

$$\sum_{l=1}^{m} \widetilde{h}H_{k,l} = \sum_{l=1}^{m} \frac{N\lambda^l \widehat{\lambda} - K\gamma^l \widehat{\gamma}}{\lambda - \gamma}$$

$$= \frac{N\widehat{\lambda}}{\lambda - \gamma}\Big[\frac{\lambda - \lambda^{m+1}}{1 - \lambda}\Big] - \frac{K\widehat{\gamma}}{\lambda - \gamma}\Big[\frac{\gamma - \gamma^{m+1}}{1 - \gamma}\Big]$$

By Eqs. (3), (10) and some elementary calculation, we obtain

$$\sum_{l=1}^{m} \widetilde{h}H_{k,l} = \frac{1}{1 - h(k) - g(k)}[\widetilde{h}H_{k,1} + g(k)\widetilde{h}H_{k,0} - \widetilde{h}H_{k,m+1} - g(k)\widetilde{h}H_{k,m}].$$

The results in following theorem can be obtained by Theorem 2.2, Eq.(3) and convenient routine operations.

Theorem 2.8. *For* $m \geq 1$*, the following identities hold:*
(i) $\sum\limits_{i=1}^{m} \widetilde{h}H_{k,2i} = \frac{\widetilde{h}H_{k,2} - g^2(k)\widetilde{h}H_{k,0} - \widetilde{h}H_{k,2m+2} + g^2(k)\widetilde{h}H_{k,2m}}{1 - h^2(k) - 2g(k) + g^2(k)},$
(ii) $\sum\limits_{i=1}^{m} \widetilde{h}H_{k,2i+1} = \frac{\widetilde{h}H_{k,3} - g^2(k)\widetilde{h}H_{k,1} - \widetilde{h}H_{k,2m+3} + g^2(k)\widetilde{h}H_{k,2m+1}}{1 - h^2(k) - 2g(k) + g^2(k)}.$

Theorem 2.9. *The exponential generating function for the* $k-$ *Horadam hybrid number* $\widetilde{h}H_{k,l}$ *is*

$$\sum_{l=0}^{\infty} \widetilde{h}H_{k,l}\frac{t^l}{l!} = \frac{N\widehat{\lambda}e^{\lambda t} - K\widehat{\gamma}e^{\gamma t}}{\lambda - \gamma}.$$

Proof. By considering Theorem (2.2) we have

$$\sum_{l=0}^{\infty} \widetilde{h}H_{k,l}\frac{t^l}{l!} = \frac{N\widehat{\lambda}}{\lambda - \gamma}\sum_{l=0}^{\infty}\frac{\lambda^l t^l}{l!} - \frac{K\widehat{\gamma}}{\lambda - \gamma}\sum_{l=0}^{\infty}\frac{\gamma^l t^l}{l!}$$

$$= \frac{N\widehat{\lambda}e^{\lambda t} - K\widehat{\gamma}e^{\gamma t}}{\lambda - \gamma}.$$

Corollary 2.10. *The Poisson generating functions for the* $k-$ *Horadam hybrid numbers are*

$$\sum_{i=0}^{\infty} \frac{\widetilde{h}H_i t^i e^{-t}}{i!} = \frac{N\hat{\lambda}e^{\lambda t} - K\hat{\gamma}e^{\gamma t}}{e^t(\lambda - \gamma)}.$$

Proof. By Theorem 2.2, we have

$$\sum_{i=0}^{\infty} \frac{\widetilde{h}H_i t^i e^{-t}}{i!} = \sum_{i=0}^{\infty} \left(\frac{N\lambda^i\hat{\lambda} - K\gamma^i\hat{\gamma}}{\lambda - \gamma}\right)\frac{t^i e^{-t}}{i!}$$

$$= \frac{N\hat{\lambda}}{\lambda - \gamma}e^{-t}\sum_{i=0}^{\infty}\frac{\lambda^i t^i}{i!} - \frac{K\hat{\gamma}}{\lambda - \gamma}e^{-t}\sum_{i=0}^{\infty}\frac{\gamma^i t^i}{i!}$$

$$= \frac{N\hat{\lambda}e^{\lambda t} - K\hat{\gamma}e^{\gamma t}}{e^t(\lambda - \gamma)}.$$

Theorem 2.11. *For $q > p \geq 0$, we have*

$$\sum_{l=0}^{m}\widetilde{h}H_{k,pl+q} = \frac{(-g(k))^p[\widetilde{h}H_{k,mp+q} - \widetilde{h}H_{k,q-p}]}{(-g(k))^p - \lambda^p - \gamma^p + 1} + \frac{-\widetilde{h}H_{k,mp+p+q} + \widetilde{h}H_{k,q}}{(-g(k))^p - \lambda^p - \gamma^p + 1}.$$

Proof. From Theorem 2.2, we have

$$\sum_{l=0}^{m}\widetilde{h}H_{k,pl+q} = \widetilde{h}H_{k,q} + \widetilde{h}H_{k,q+p} + ... + \widetilde{h}H_{k,q+mp}$$

$$= \frac{N\lambda^q\hat{\lambda} - K\gamma^q\hat{\gamma}}{\lambda - \gamma} + \frac{N\lambda^{p+q}\hat{\lambda} - K\gamma^{p+q}\hat{\gamma}}{\lambda - \gamma} + ... + \frac{N\lambda^{mp+q}\hat{\lambda} - K\gamma^{mp+q}\hat{\gamma}}{\lambda - \gamma}$$

$$= \frac{1}{\lambda - \gamma}\left\{\frac{N\hat{\lambda}\lambda^q[\lambda^{mp+p}\gamma^p - \lambda^{mp+p} - \gamma^p + 1]}{\lambda^p\gamma^p - \lambda^p - \gamma^p + 1} - \frac{K\hat{\gamma}\gamma^q[\gamma^{mp+p}\lambda^p - \gamma^{mp+p} - \lambda^p + 1]}{\lambda^p\gamma^p - \lambda^p - \gamma^p + 1}\right\}$$

$$= \frac{1}{(-g(k))^p - \lambda^p - \gamma^p + 1}\left\{[\frac{N\hat{\lambda}\lambda^{mp+p+q}\gamma^p - K\hat{\gamma}\gamma^{mp+p+q}\lambda^p}{\lambda - \gamma}] - [\frac{N\hat{\lambda}\lambda^{mp+p+q} - K\hat{\gamma}\gamma^{mp+p+q}}{\lambda - \gamma}]\right.$$

$$\left. - [\frac{N\hat{\lambda}\lambda^q\gamma^p - K\hat{\gamma}\gamma^q\lambda^p}{\lambda - \gamma}] + [\frac{N\hat{\lambda}\lambda^q - K\hat{\gamma}\gamma^q}{\lambda - \gamma}]\right\}$$

$$= \frac{(-g(k))^p[\widetilde{h}H_{k,mp+q} - \widetilde{h}H_{k,q-p}]}{(-g(k))^p - \lambda^p - \gamma^p + 1} + \frac{-\widetilde{h}H_{k,mp+p+q} + \widetilde{h}H_{k,q}}{(-g(k))^p - \lambda^p - \gamma^p + 1}.$$

Theorem 2.12. *(Catalan Identity) For $m, r \in \mathbb{Z}^+$ such that $m \geq r$. Then*

$$\widetilde{h}H_{k,m+r}\widetilde{h}H_{k,m-r} - (\widetilde{h}H_{k,m})^2 = \frac{NK(-g(k))^m}{h^2(k) + 4g(k)}\left\{\hat{\lambda}\hat{\gamma}[1 - \frac{\lambda^r}{\gamma^r}] + \hat{\gamma}\hat{\lambda}[1 - \frac{\gamma^r}{\lambda^r}]\right\}. \qquad (15)$$

Proof. By using Theorem 2.2, we obtain;

$$\widetilde{h}H_{k,m+r}\widetilde{h}H_{k,m-r} - (\widetilde{h}H_{k,m})^2$$

$$= [\frac{N\lambda^{m+r}\hat{\lambda} - K\gamma^{m+r}\hat{\gamma}}{\lambda - \gamma}][\frac{N\lambda^{m-r}\hat{\lambda} - K\gamma^{m-r}\hat{\gamma}}{\lambda - \gamma}] - [\frac{N\lambda^m\hat{\lambda} - K\gamma^m\hat{\gamma}}{\lambda - \gamma}]^2$$

$$= \frac{NK}{(\lambda - \gamma)^2}[\hat{\lambda}\hat{\gamma}(\lambda^m\gamma^m - \lambda^{r+m}\gamma^{m-r}) + \hat{\gamma}\hat{\lambda}(\lambda^m\gamma^m - \lambda^{m-r}\gamma^{m+r})].$$

After some elementary calculations, we obtain

$$\widetilde{h}H_{k,m+r}\widetilde{h}H_{k,m-r} - (\widetilde{h}H_{k,m})^2 = \frac{NK(-g(k))^m}{h^2(k) + 4g(k)}\left\{\hat{\lambda}\hat{\gamma}[1 - \frac{\lambda^r}{\gamma^r}] + \hat{\gamma}\hat{\lambda}[1 - \frac{\gamma^r}{\lambda^r}]\right\}.$$

For $r = 1$ in the Catalan identity, we get the Cassini identity for $k-$ Horadam hybrid numbers in the next Theorem.

Theorem 2.13. *(Cassini Identity) Let $m \geq 1$ be an integer. Then*

$$\widetilde{h}H_{k,m+1}\widetilde{h}H_{k,m-1} - (\widetilde{h}H_{k,m})^2 = \frac{NK(-g(k))^m}{h^2(k) + 4g(k)}\left\{ \hat{\lambda}\hat{\gamma}[1 - \frac{\lambda}{\gamma}] + \hat{\gamma}\hat{\lambda}[1 - \frac{\gamma}{\lambda}] \right\}.$$

Theorem 2.14. *(d'Ocagne Identity) For $m \in \mathbb{Z}^+$ and $n \in \mathbb{N}$ such that $m > n + 1$. Then*

$$\widetilde{h}H_{k,m}\widetilde{h}H_{k,n+1} - \widetilde{h}H_{k,m+1}\widetilde{h}H_{k,n} = \frac{NK(-g(k))^n}{\sqrt{h^2(k) + 4g(k)}}[\lambda^{m-n}\hat{\lambda}\hat{\gamma} - \gamma^{m-n}\hat{\gamma}\hat{\lambda}].$$

Proof. From Theorem 2.2 and Eq.(3), we have

$$\widetilde{h}H_{k,m}\widetilde{h}H_{k,n+1} - \widetilde{h}H_{k,m+1}\widetilde{h}H_{k,n}$$

$$= [\frac{N\lambda^m\hat{\lambda} - K\gamma^m\hat{\gamma}}{\lambda - \gamma}][\frac{N\lambda^{n+1}\hat{\lambda} - K\gamma^{n+1}\hat{\gamma}}{\lambda - \gamma}] - [\frac{N\lambda^{m+1}\hat{\lambda} - K\gamma^{m+1}\hat{\gamma}}{\lambda - \gamma}][\frac{N\lambda^n\hat{\lambda} - K\gamma^n\hat{\gamma}}{\lambda - \gamma}]$$

$$= \frac{NK}{(\lambda - \gamma)^2}\left\{ \hat{\lambda}\hat{\gamma}[-\lambda^m\gamma^{n+1} + \lambda^{m+1}\gamma^n] + \hat{\gamma}\hat{\lambda}[\lambda^n\gamma^{m+1} - \lambda^{n+1}\gamma^m] \right\}$$

$$= \frac{NK(-g(k))^n}{\sqrt{h^2(k) + 4g(k)}}[\lambda^{m-n}\hat{\lambda}\hat{\gamma} - \gamma^{m-n}\hat{\gamma}\hat{\lambda}].$$

3. Matrix representations of k-Horadam hybrid numbers

Now, we will give the matrix representation of $k-$ Horadam hybrid numbers. Also we obtain a formula for $k-$ Horadam hybrid numbers $\widetilde{h}H_{k,m}$, in terms of tridiagonal determinant, by using the same kind of approach that was used in (Catarino, 2016; Kizilates et al., 2019).

Theorem 3.1. *Let $u \geq 0$ be an integer. Then*

$$\begin{bmatrix} \widetilde{h}H_{k,u+2} & \widetilde{h}H_{k,u+1} \\ \widetilde{h}H_{k,u+1} & \widetilde{h}H_{k,u} \end{bmatrix} = \begin{bmatrix} \widetilde{h}H_{k,2} & \widetilde{h}H_{k,1} \\ \widetilde{h}H_{k,1} & \widetilde{h}H_{k,0} \end{bmatrix} \times \begin{bmatrix} h(k) & 1 \\ g(k) & 0 \end{bmatrix}^u \tag{16}$$

Proof. We use the induction method to prove this theorem. If $u = 0$, then the result is obvious. Assume the expression is satisfied for $u \geq 0$

$$\begin{bmatrix} \widetilde{h}H_{k,u+2} & \widetilde{h}H_{k,u+1} \\ \widetilde{h}H_{k,u+1} & \widetilde{h}H_{k,u} \end{bmatrix} = \begin{bmatrix} \widetilde{h}H_{k,2} & \widetilde{h}H_{k,1} \\ \widetilde{h}H_{k,1} & \widetilde{h}H_{k,0} \end{bmatrix} \times \begin{bmatrix} h(k) & 1 \\ g(k) & 0 \end{bmatrix}^u.$$

We next prove that

$$\begin{bmatrix} \widetilde{h}H_{k,u+3} & \widetilde{h}H_{k,u+2} \\ \widetilde{h}H_{k,u+2} & \widetilde{h}H_{k,u+1} \end{bmatrix} = \begin{bmatrix} \widetilde{h}H_{k,2} & \widetilde{h}H_{k,1} \\ \widetilde{h}H_{k,1} & \widetilde{h}H_{k,0} \end{bmatrix} \times \begin{bmatrix} h(k) & 1 \\ g(k) & 0 \end{bmatrix}^{u+1} \tag{17}$$

We consider the right-hand side of (17)

$$\begin{bmatrix} \widetilde{h}H_{k,2} & \widetilde{h}H_{k,1} \\ \widetilde{h}H_{k,1} & \widetilde{h}H_{k,0} \end{bmatrix} \times \begin{bmatrix} h(k) & 1 \\ g(k) & 0 \end{bmatrix}^{u+1} = \left\{ \begin{bmatrix} \widetilde{h}H_{k,2} & \widetilde{h}H_{k,1} \\ \widetilde{h}H_{k,1} & \widetilde{h}H_{k,0} \end{bmatrix} \times \begin{bmatrix} h(k) & 1 \\ g(k) & 0 \end{bmatrix}^u \right\} \times \begin{bmatrix} h(k) & 1 \\ g(k) & 0 \end{bmatrix}$$

From Eq.(9) and induction hypothesis, we have

$$\left\{ \begin{bmatrix} \widetilde{\hbar H}_{k,2} & \widetilde{\hbar H}_{k,1} \\ \widetilde{\hbar H}_{k,1} & \widetilde{\hbar H}_{k,0} \end{bmatrix} \times \begin{bmatrix} h(k) & 1 \\ g(k) & 0 \end{bmatrix}^u \right\} \times \begin{bmatrix} h(k) & 1 \\ g(k) & 0 \end{bmatrix}$$

$$= \begin{bmatrix} \widetilde{\hbar H}_{k,u+2} & \widetilde{\hbar H}_{k,u+1} \\ \widetilde{\hbar H}_{k,u+1} & \widetilde{\hbar H}_{k,u} \end{bmatrix} \times \begin{bmatrix} h(k) & 1 \\ g(k) & 0 \end{bmatrix}$$

$$= \begin{bmatrix} \widetilde{\hbar H}_{k,u+3} & \widetilde{\hbar H}_{k,u+2} \\ \widetilde{\hbar H}_{k,u+2} & \widetilde{\hbar H}_{k,u+1} \end{bmatrix}$$

Thus the proof is completed.

Using Theorem 2.1 and Eq. (16), the following remarks can be given;

Remark 3.2. *For $h(k) = k$, $g(k) = 1$, $w = 0$ and $z = 1$ in Eq.(16) and Theorem 2.1 , we have the matrix representation of $k-$ Fibonacci hybrid numbers as follows;*

$$\begin{bmatrix} \widetilde{\hbar FH}_{k,u+2} & \widetilde{\hbar FH}_{k,u+1} \\ \widetilde{\hbar FH}_{k,u+1} & \widetilde{\hbar FH}_{k,u} \end{bmatrix} = \begin{bmatrix} \widetilde{\hbar FH}_{k,2} & \widetilde{\hbar FH}_{k,1} \\ \widetilde{\hbar FH}_{k,1} & \widetilde{\hbar FH}_{k,0} \end{bmatrix} \times \begin{bmatrix} k & 1 \\ 1 & 0 \end{bmatrix}^u$$

Remark 3.3. *For $h(k) = k$, $g(k) = 1$, $w = 2$ and $z = k$ in Eq.(16) and Theorem 2.1 , we have the matrix representation of $k-$ Lucas hybrid numbers as follows;*

$$\begin{bmatrix} \widetilde{\hbar LH}_{k,u+2} & \widetilde{\hbar LH}_{k,u+1} \\ \widetilde{\hbar LH}_{k,u+1} & \widetilde{\hbar LH}_{k,u} \end{bmatrix} = \begin{bmatrix} \widetilde{\hbar LH}_{k,2} & \widetilde{\hbar LH}_{k,1} \\ \widetilde{\hbar LH}_{k,1} & \widetilde{\hbar LH}_{k,0} \end{bmatrix} \times \begin{bmatrix} k & 1 \\ 1 & 0 \end{bmatrix}^u$$

The nth terms of $k-$ Horadam hybrid number can be easily obtained by calculating the determinant of the tridiagonal matrix A_{n-1}.

Using Eq.(9) the following propositions can be easily proved.

Proposition 3.4. *The $n \times n$ tridiagonal matrices*

$$A_n = \begin{pmatrix} a & b & & & & & \\ c & d & 1 & & & & \\ & c & d & 1 & & & \\ & & & \ddots & \ddots & \ddots & \\ & & & & c & d & 1 \\ & & & & & c & d \end{pmatrix}$$

satisfy $\det A_n = \widetilde{\hbar H}_{n+1}$, where $a = \widetilde{\hbar H}_{k,2}, b = \widetilde{\hbar H}_{k,1}, c = -g(k)$ and $d = h(k)$.

$k-$ Horadam hybrid number can be obtained using another tridiagonal matrix.

Proposition 3.5. *For $m \geq 1$, we have*

$$\widetilde{\hbar H}_{k,m} =$$

$$\begin{vmatrix} b & a & 0 & 0 & \dots & 0 & 0 \\ -1 & 0 & c & 0 & \dots & 0 & 0 \\ 0 & -1 & d & c & \dots & 0 & 0 \\ \vdots & \vdots & \vdots & \ddots & \ddots & \vdots & \vdots \\ 0 & 0 & 0 & 0 & \dots & d & c \\ 0 & 0 & 0 & 0 & \dots & -1 & d \end{vmatrix}_{m \times m}$$

where $a = \widetilde{\hbar H}_{k,2}, b = \widetilde{\hbar H}_{k,1}, c = g(k)$ and $d = h(k)$.

References

Akkus, I. & **Kizilaslan, G. (2019)**. Quaternions: Quantum calculus approach with applications. Kuwait J. Sci., 46(4), 1–13.

Catarino, P. (2016). A note on certain matrices with $h(x)$ Fibonacci quaternion polynomials. J. Differ. Equ. Appl. , 22, 343–351.

Horadam, A. F. (1965). Basic properties of a certain generalized sequence of numbers. The Fibonacci Quarterly, 3, 161–176.

Kilic, N. (2019a). On split $k-$ Jacobsthal and $k-$ Jacobsthal Lucas quaternions. Ars Combinatoria, 142, 129–139.

Kilic, N. (2019b). On dual Horadam octonions. Notes on Number Theory and Discrete Mathematics, 25(1), 137—149.

Kilic, N. (2019c). On Horadam octonions. Utilitas Mathematica, 113, 229–241.

Kizilates, C. (2020). A new generalization of Fibonacci hybrid and Lucas hybrid numbers. Chaos, Solutions and Fractals, 130, 1–5.

Kizilates, C. , Catarino, P. & **Tuglu, N. (2019)**. On the Bicomplex Generalized Tribonacci Quaternions. Mathematics, 7(1), 1–8.

Koshy, T. (2001). Fibonacci and Lucas Numbers with Applications. Pure and Applied Mathematics; Wiley-Interscience: New York, NY, USA. [CrossRef].

Koshy, T. (2018). Fibonacci and Lucas Numbers with Applications,   2nd ed. Pure and Applied Mathematics: John Wiley and Sons, Inc.: Hoboken, NJ, USA, Volume 1.

Liana, M., Szynal-Liana, A. & **Włoch, I. (2019)**. On Pell hybrinomials. Miskolc Mathematical Notes , 20(2), 1051–1062.

Szynal-Liana, A. (2018). The Horadam hybrid numbers. Discussiones Mathematicae. General Algebra and Application , 38(1), 91–98.

Szynal-Liana, A. & **Włoch, I.(2019)**. Introduction to Fibonacci and Lucas hybrinomials. Complex Variables and Elliptic Equations, 1–12.

Yazlik, Y. & **Taskara, N. (2012)**. A note on generalized $k-$ Horadam sequence. Computers and Mathematics with Applications, 63, 36–41.

New characterizations of k-normal and k-EP matrices

ZhiMei Fu[1], KeZheng Zuo[2,*], Yang Chen[3]

Dept. of Mathematics
Hubei Normal University, China
*Corresponding author: xiangzuo28@163.com

Abstract

In this paper, some new characterizations of k-normal and k-EP matrices are obtained using the core-EP decomposition. We obtain several equivalent conditions for a matrix A to be k-normal and k-EP in terms of certain generalized inverses.

Keywords: Core-EP decomposition; generalized inverses; k-core EP matrices; k-EP matrices; k-normal matrices.

1. Introduction

The concepts of the classes of k-normal matrices and k-EP matrices were introduced by Malik *et al.* in (Malik *et al.*, 2016) where the authors studied characterizations and properties of both k-normal and k-EP matrices using the Hartwing-Spindelböck decomposition. More properties of these two types of matrices have been given in (Ferreyra *et al.*, 2018; Wang *et al.*, 2019). Inspired by the previous work, the intention of this paper is to discuss both classes and their further properties and characterizations using some generalized inverses.

The classical Moore-Penrose inverse(Penrose *et al.*, 1955) and Drazin inverse(Drazin *et al.*, 1958) were defined in the fifties and have been thoroughly studied since then. On the other hand, some generalized inverses such as core inverse(Baksalary *et al.*, 2010), core EP inverse(**?**), DMP inverse(Malik *et al.*, 2014), WG inverse(Wang *et al.*, 2018), etc., were introduced in the last decade. Nowadays, they attract the attention of many researchers.

Let $\mathbb{C}^{m \times n}$ be the set of all $m \times n$ complex matrices and $\mathbb{Z}^+$ denotes the set of all positive integers. The symbols $\mathcal{R}(A), \mathcal{N}(A), A^*, r(A)$ and I_n will denote the range space, null space, conjugate transpose, rank of $A \in \mathbb{C}^{m \times n}$ and the identity matrix of order n. $\mathrm{Ind}(A)$ means the index of $A \in \mathbb{C}^{n \times n}$. Let $\mathbb{C}_k^{n \times n}$ be the set consisting of $n \times n$ complex matrices with index k.

For convenience, throughout the paper we will use the following notations: $\mathbb{C}_n^{k-\mathrm{N}}$, $\mathbb{C}_n^{k,\text{⊕}}$ and $\mathbb{C}_n^{k-\mathrm{EP}}$ will denote the subsets of $\mathbb{C}^{n \times n}$ consisting of k-normal, k-core EP and k-EP matrices, respectively, i.e.,

$$\mathbb{C}_n^{k-\mathrm{N}} = \{A \mid A \in \mathbb{C}^{n \times n}, A^k A^* = A^* A^k\};$$

$$\mathbb{C}_n^{k,\text{⊕}} = \{A \mid A \in \mathbb{C}_k^{n \times n}, A^k A^{\text{⊕}} = A^{\text{⊕}} A^k\}$$
$$= \{A \mid A \in \mathbb{C}_k^{n \times n}, A^k \in \mathbb{C}_n^{\mathrm{EP}}\};$$

$$\mathbb{C}_n^{k-\mathrm{EP}} = \{A \mid A \in \mathbb{C}_k^{n \times n}, A^k A^\dagger = A^\dagger A^k\}.$$

The structure of this article is as follows: In the Section 2, we discuss several sufficient and necessary conditions for the class of k-normal matrices in terms of generalized inverses. The Section 3 is devoted to the characterizations of the sets $\mathbb{C}_n^{k,\text{⊕}}$ and $\mathbb{C}_n^{k-\mathrm{EP}}$.

2. Properties of the k-normal matrices

In this section, we will consider the class of k-normal matrices in terms of some generalized inverses.

In the following lemma, we will present the core-EP decomposition, which was given by Wang in (Wang *et al.*, 2016).

Lemma 2.1 (Wang *et al.*, 2016)(*core-EP decomposition*) *Let $A \in \mathbb{C}_k^{n \times n}$. Then A can be represented as*

$$A = U \begin{bmatrix} T & S \\ 0 & N \end{bmatrix} U^*, \tag{1}$$

where $T \in \mathbb{C}^{t \times t}$ is nonsingular and $t = r(T) = r(A^k)$, N is nilpotent with index k, and $U \in \mathbb{C}^{n \times n}$ is unitary.

Moreover, the representation of A given by (1) *is unique (Wang et al., 2016, Theorem 2.4). Furthermore, in that case the core-EP inverse of A is given by*

$$A^{\scriptsize\textcircled{\dagger}} = U \begin{bmatrix} T^{-1} & 0 \\ 0 & 0 \end{bmatrix} U^*. \tag{2}$$

Next we will introduce the following notations, that will be used throughout this paper.

Let $A \in \mathbb{C}_k^{n \times n}$ be given by (1). Then

$$\triangle = [TT^* + S(I_{n-t} - N^\dagger N)S^*]^{-1};$$

$$\widetilde{T} = \sum_{j=0}^{k-1} T^j S N^{k-1-j};$$

$$T_q = \sum_{j=0}^{q-1} T^j S N^{q-1-j} (q \in \mathbb{Z}^+).$$

Lemma 2.2 *Let $A \in \mathbb{C}_k^{n \times n}$ be given by* (1). *Then (Ferreyra et al., 2018; Wang et al., 2018):*

$$A^\dagger = U \begin{bmatrix} T^*\triangle & -T^*\triangle SN^\dagger \\ (I_{n-t} - N^\dagger N)S^*\triangle & N^\dagger - (I_{n-t} - N^\dagger N)S^*\triangle SN^\dagger \end{bmatrix} U^*; \tag{3}$$

$$A^D = U \begin{bmatrix} T^{-1} & (T^{k+1})^{-1}\widetilde{T} \\ 0 & 0 \end{bmatrix} U^*; \tag{4}$$

$$A^{D,\dagger} = U \begin{bmatrix} T^{-1} & (T^{k+1})^{-1}\widetilde{T}NN^\dagger \\ 0 & 0 \end{bmatrix} U^*; \tag{5}$$

$$A^{\dagger,D} = U \begin{bmatrix} T^*\triangle & T^*\triangle T^{-k}\widetilde{T} \\ (I_{n-t} - N^\dagger N)S^*\triangle & (I_{n-t} - N^\dagger N)S^*\triangle T^{-k}\widetilde{T} \end{bmatrix} U^*; \tag{6}$$

$$A^{\scriptsize\textcircled{W}} = U \begin{bmatrix} T^{-1} & T^{-2}S \\ 0 & 0 \end{bmatrix} U^*. \tag{7}$$

According to (1) and (3), we have

$$AA^\dagger = U \begin{bmatrix} I_t & 0 \\ 0 & NN^\dagger \end{bmatrix} U^*, \tag{8}$$

$$A^\dagger A = U \begin{bmatrix} T^*\triangle T & T^*\triangle S(I_{n-t} - N^\dagger N) \\ (I_{n-t} - N^\dagger N)S^*\triangle T & N^\dagger N + (I_{n-t} - N^\dagger N)S^*\triangle S(I_{n-t} - N^\dagger N) \end{bmatrix} U^*. \tag{9}$$

Lemma 2.3 *Let $A \in \mathbb{C}_k^{n \times n}$ be given by (1). Then $A \in \mathbb{C}_n^{k-N}$ if and only if $T^k T^* = T^* T^k$ and $S = 0$.*

   Proof. Using (1), we have

$$A^k = U \begin{bmatrix} T^k & \widetilde{T} \\ 0 & 0 \end{bmatrix} U^*. \tag{10}$$

Now it is easy to check that $A \in \mathbb{C}_n^{k-N}$ if and only if $T^k T^* = T^* T^k$ and $S = 0$.

Lemma 2.4 *Let $A \in \mathbb{C}_k^{n \times n}$ be given by (1) and $q \in \mathbb{Z}^+$. Then $T_q = 0$ if and only if $S = 0$. In particular, $\widetilde{T} = 0$ if and only if $S = 0$.*

   Proof. The proof is similar to (Wang *et al.*, 2019), Theorem 2.3.

Lemma 2.5 *(Sylvester et al., 1884) Let $A \in \mathbb{C}^{p \times p}$ and $B \in \mathbb{C}^{q \times q}$ have no common eigenvalues. Then $AY - YB = 0$ has a unique solution $Y = 0$, where $Y \in \mathbb{C}^{p \times q}$.*

Theorem 2.6 *Let $A \in \mathbb{C}_k^{n \times n}$ be given by (1) and $q \in \mathbb{Z}^+$. Then the following conditions are equivalent:*

   (a) $A \in \mathbb{C}_n^{k-N}$;

   (b) $A^{k+1} A^\dagger A^* = A^* A^{k+1} A^\dagger$;

   (c) $A^* A^\dagger A^{k+1} = A^\dagger A^{k+1} A^*$;

   (d) $A^* A^{k+q} = A^k A^* A^q$;

   (e) $A^{k+q} A^* = A^q A^* A^k$.

Proof. That (a) implies all other items (b), (c), (d) and (e) follow directly by Lemma 2.3.

   $(b) \Rightarrow (a)$. It follows from (1), (3) and (10) that $T^k T^* = T^* T^k$ and $S = 0$. Hence by Lemma 2.3, we have that (a) holds.

   $(c) \Rightarrow (a)$. By taking the conjugate transpose of $A^* A^\dagger A^{k+1} = A^\dagger A^{k+1} A^*$ and applying item (b) we get that $A \in \mathbb{C}_n^{k-N}$.

   $(d) \Rightarrow (a)$. Since $A^* A^{k+q} = A^k A^* A^q$, it follows from (1) and (10) that $T^k T^* = T^* T^k$ and $S = 0$. Hence by Lemma 2.3, we have that (a) holds.

   $(e) \Rightarrow (a)$. By taking the conjugate transpose of $A^{k+q} A^* = A^q A^* A^k$ and applying point $(d) \Rightarrow (a)$, we can deduce $A \in \mathbb{C}_n^{k-N}$.

   Next we will present 10 conditions involving A^*, X, A and their powers to assure that $A \in \mathbb{C}_n^{k-N}$, where $X \in \{A^{\circledT}, A^D, A^{D,\dagger}, A^{\dagger,D}, A^{\circledW}\}$.

Theorem 2.7 *Let $A \in \mathbb{C}_k^{n \times n}$ be given by (1) and $X \in \{A^{\circledT}, A^D, A^{D,\dagger}, A^{\dagger,D}, A^{\circledW}\}$. The following assertions are equivalent:*

   (a) $A \in \mathbb{C}_n^{k-N}$;

   (b) $A(A^*)^k X = (A^*)^k$;

   (c) $X(A^*)^k A = (A^*)^k$;

   (d) $(A^*)^k A X = A(A^*)^k X$;

   (e) $(A^*)^k X A = A(A^*)^k X$;

   (f) $A^* A^k X = A^k A^* X$;

   (g) $A^* A^{k+1} X = X A^{k+1} A^*$;

   (h) $A^* A^{k+1} X = A^{k+1} X A^*$;

(i) $A^*XA^{k+1} = XA^{k+1}A^*$;

(j) $A^*XA^{k+1} = A^{k+1}XA^*$;

(k) $A^*AX^{k+1} = AX^{k+1}A^*$.

Proof. From (2), (4), (5), (6) and (7), that (a) implies all items $(b) - (k)$ can be directly verified by Lemma 2.3.

On the converse, we have to prove that each of conditions $(b) - (k)$ implies that $T^kT^* = T^*T^k$ and $S = 0$.

$(b) \Rightarrow (a)$. Assume that $A(A^*)^k A^{\dagger,D} = (A^*)^k$. From (6) and (10), we obtain that

(i) $(T(T^k)^* + S\widetilde{T}^*)T^*\triangle = (T^k)^*$;

(ii) $(T(T^k)^* + S\widetilde{T}^*)T^*\triangle T^{-k}\widetilde{T} = 0$;

(iii) $N\widetilde{T}^*T^*\triangle = \widetilde{T}^*$;

(iv) $N\widetilde{T}^*T^*\triangle T^{-k}\widetilde{T} = 0$.

From (iii) we have that $H\widetilde{T} - \widetilde{T}N^* = 0$, where $H = (\triangle^*T)^{-1}$. Notice that H is invertible and N^* is nilpotent, hence H and N^* have no common eigenvalues. By Lemma 2.5, we get that $\widetilde{T} = 0$, which implies $S = 0$. Now we obtain $T^kT^* = T^*T^k$ by (i). The other cases follow similarly.

$(c) \Rightarrow (a)$. Let $\widetilde{X} \in \{A^{\textcircled{\dagger}}, A^D, A^{D,\dagger}, A^{\textcircled{W}}\}$. From $\widetilde{X}(A^*)^kA = (A^*)^k$, using (2), (4), (5), (7) and (10), it can be easily verified that $T^*T^k = T^*T^k$ and $S = 0$. If $A^{\dagger,D}(A^*)^kA = (A^*)^k$, then it follows from (6), (10) and Lemma 2.4 that $T^*T^k = T^*T^k$ and $S = 0$.

$(d) \Rightarrow (a)$ and $(e) \Rightarrow (a)$. These proofs are similar to the proof of the part $(b) \Rightarrow (a)$.

$(f) \Rightarrow (a)$. By (2), (4), (5), (6), (7) and (10), it follows from $A^*A^kX = A^kA^*X$ that $T^*T^k = T^*T^k$ and $S = 0$.

$(g) \Rightarrow (a)$. Let $\widetilde{X} \in \{A^{\textcircled{\dagger}}, A^D, A^{D,\dagger}, A^{\textcircled{W}}\}$. If $A^*A^{k+1}\widetilde{X} = \widetilde{X}A^{k+1}A^*$, then we get $T^*T^k = T^*T^k$ and $S = 0$ by (2), (4), (5), (7) and (10). In the case when $A^*A^{k+1}A^{\dagger,D} = A^{\dagger,D}A^{k+1}A^*$, the proof is similar to that for $(b) \Rightarrow (a)$.

$(h) \Rightarrow (a)$. If $A^*A^{k+1}X = A^{k+1}XA^*$, then it follows from (2), (4), (5), (6), (7) and (10) that $T^*T^k = T^*T^k$ and $S = 0$.

$(i) \Rightarrow (a)$, $(j) \Rightarrow (a)$ and $(k) \Rightarrow (a)$. These are all similar to the proof of $(g) \Rightarrow (a)$.

3. More properties of the k-core EP and k-EP matrices

In the section, we discuss the necessary and sufficient conditions to satisfy a matrix A such that $A \in \mathbb{C}_n^{k,\textcircled{\dagger}}$ and $A \in \mathbb{C}_n^{k-\text{EP}}$ using some generalized inverses.

Lemma 3.1 (Ferreyra *et al.*, 2018) *Let $A \in \mathbb{C}_k^{n \times n}$ be given by (1). Then $A \in \mathbb{C}_n^{k,\textcircled{\dagger}}$ if and only if $\widetilde{T} = 0$.*

We recall that the class of k-core EP matrices are defined by satisfying $A^kA^{\textcircled{\dagger}} = A^{\textcircled{\dagger}}A^k$ (Ferreyra *et al.*, 2018), which is equivalent with $A^k(A^k)^{\dagger} = (A^k)^{\dagger}A^k$ (in short, $A^k \in \mathbb{C}_n^{EP}$). Next, we will give a new sufficient and necessary condition for A such that $A \in \mathbb{C}_n^{k,\textcircled{\dagger}}$.

Theorem 3.2 *Let $A \in \mathbb{C}_k^{n \times n}$ be given by (1) and $q \in \mathbb{Z}^+$. Then $A \in \mathbb{C}_n^{k,\textcircled{\dagger}}$ if and only if $A^q(A^k)^{\dagger} = (A^k)^{\dagger}A^q$.*

Proof. It follows from (Ferreyra *et al.*, 2018) that

$$(A^k)^{\dagger} = U \begin{bmatrix} (T^k)^*(T^k(T^k)^* + \widetilde{T}\widetilde{T}^*)^{-1} & 0 \\ \widetilde{T}^*(T^k(T^k)^* + \widetilde{T}\widetilde{T}^*)^{-1} & 0 \end{bmatrix} U^*. \tag{11}$$

From $A^q(A^k)^{\dagger} = (A^k)^{\dagger}A^q$ and $(T^k)^*(T^k(T^k)^* + \widetilde{T}\widetilde{T}^*)^{-1}$ is invertible, we obtain $\widetilde{T} = 0$, we now have $A \in \mathbb{C}_n^{k,\textcircled{\dagger}}$ by Lemma 3.1.

Conversely, if $A \in \mathbb{C}_n^{k,\textcircled{\dagger}}$, it is simple to show that $A^q(A^k)^{\dagger} = (A^k)^{\dagger}A^q$ by Lemma 3.1.

Next we will consider different characterizations of $A \in \mathbb{C}_n^{k,\textcircled{\dagger}}$ using several generalized inverses.

Theorem 3.3 *Let $A \in \mathbb{C}_k^{n \times n}$ be given by (1) and $X \in \{A^{\textcircled{\dagger}}, A^D, A^{D,\dagger}, A^{\dagger,D}, A^{\textcircled{W}}\}$. The following are equivalent:*

(a) $A \in \mathbb{C}_n^{k,\textcircled{\dagger}}$;

(b) $(A^*)^k X A = (A^*)^k$;

(c) $AX(A^*)^k = (A^*)^k$;

(d) $(A^*)^k A X = AX(A^*)^k$;

(e) $(A^*)^k X A = XA(A^*)^k$;

(f) $(A^*)^k A X = XA(A^*)^k$;

(g) $(A^*)^k X A = AX(A^*)^k$.

Proof. The proofs of $(a) \Leftrightarrow (b)$ and $(a) \Leftrightarrow (c)$ follow directly by (2), (4), (5), (6) and (7).

$(a) \Rightarrow (d)$. If $A \in \mathbb{C}_n^{k,\textcircled{\dagger}}$, it is not difficult to verify that $(A^*)^k AX = AX(A^*)^k$ by Lemma 3.1.

$(d) \Rightarrow (a)$. By (2), (4), (5), (6), (7) and Lemma 3.1, we can deduce that $A \in \mathbb{C}_n^{k,\textcircled{\dagger}}$.

The proofs of $(a) \Rightarrow (e)$, $(a) \Rightarrow (f)$ and $(a) \Rightarrow (g)$ are similar to the proof of $(a) \Rightarrow (d)$.

The proofs of $(e) \Rightarrow (a)$, $(f) \Rightarrow (g)$ and $(g) \Rightarrow (a)$ are similar to the proof of $(d) \Rightarrow (a)$.

In (Ferreyra *et al.*, 2018), the authors presented some equivalent conditions for $A^k A^\dagger = A^\dagger A^k$. Inspired by this work, we will present several new characterizations of the class of k-EP matrices.

Lemma 3.4 *Let $A \in \mathbb{C}_k^{n \times n}$ be given by (1) and $p \geq k$. The following are equivalent:*

(a) $A \in \mathbb{C}_n^{k-EP}$;

(b) (Ferreyra *et al.*, 2018) $S = SN^\dagger N$ and $\widetilde{T} = \widetilde{T}NN^\dagger$;

(c) $A^{p+1}A^\dagger = A^\dagger A^{p+1}$.

Proof. The proof follows directly by (1), (3) and (10).

Theorem 3.5 *Let $A \in \mathbb{C}_k^{n \times n}$ be given by (1) and $p, q \geq k$. The following are equivalent:*

(a) $A \in \mathbb{C}_n^{k-EP}$;

(b) $AA^\dagger(A^*)^p = (A^*)^p A^\dagger A$;

(c) $A^{p+1}A^\dagger = A^p$ and $A^\dagger A^{q+1} = A^q$;

(d) $A^{p+1}A^\dagger + A^\dagger A^{q+1} = A^p + A^q$.

Proof. $(a) \Rightarrow (b)$. It follows from Lemma 3.4 that $A^{p+1}A^\dagger = A^\dagger A^{p+1}$, then by taking the conjugate transpose of $A^{p+1}A^\dagger = A^\dagger A^{p+1}$, we obtain $AA^\dagger(A^*)^p = (A^*)^p A^\dagger A$.

$(b) \Rightarrow (c)$. By taking the conjugate transpose of $AA^\dagger(A^*)^p = (A^*)^p A^\dagger A$, we get that $A^{p+1}A^\dagger = A^\dagger A^{p+1}$. Then, by Lemma 3.4, we obtain that $A \in \mathbb{C}_n^{k-EP}$. Furthermore, we can directly check $A^{p+1}A^\dagger = A^p$ and $A^\dagger A^{q+1} = A^q$ by condition (b) of Lemma 3.4.

$(c) \Rightarrow (d)$. It is evident.

$(d) \Rightarrow (a)$. Premultplying and postmultiplying the condition $A^{p+1}A^\dagger + A^\dagger A^{q+1} = A^p + A^q$ by A, we get $A^{p+2}A^\dagger = A^{p+1}$ and $A^\dagger A^{q+2} = A^{q+1}$, respectively, which imply $A \in \mathbb{C}_n^{k-EP}$.

In the next result, we will show certain necessary and sufficient conditions for a matrix A such that $A \in \mathbb{C}_n^{k-\text{EP}}$ using MP and Drazin inverse.

Theorem 3.6 *Let $A \in \mathbb{C}_k^{n \times n}$ be given by (1) and $q \in \mathbb{Z}^+$. The following are equivalent:*

(a) $A \in \mathbb{C}_n^{k-EP}$;

(b) $A^q (A^D)^k A^\dagger = A^\dagger A^q (A^D)^k$;

(c) $A^\dagger A^2 (A^D)^k A^\dagger = (A^D)^k$;

(d) $(A^D)^k A^\dagger = A^\dagger (A^D)^k$.

Proof. $(b) \Leftrightarrow (a)$. By (1) and (4), we get that $A^q (A^D)^k A^\dagger = A^\dagger A^q (A^D)^k$ is equivalent with $S = SN^\dagger N$ and $\widetilde{T} = \widetilde{T} N N^\dagger$, i.e., $A \in \mathbb{C}_n^{k-\text{EP}}$.

The proofs of $(c) \Leftrightarrow (a)$ and $(d) \Leftrightarrow (a)$ follow as the proof of the part $(b) \Leftrightarrow (a)$.

4. Funding

References

Baksalary, O. M., & Treakler, G. (2010). Core inverse of matrices. Linear and Multilinear Algebra, 58, 681-697.

Drazin, M. P. (1958). Pseudo-inverses in associative rings and semigroups. American Mathematical Monthly, 65(7), 506-514.

Ferreyra, D. E., Levis, F. E., & Thome, N. (2018). Revisiting the core-EP inverse and its extension to rectangular matrices. Quaestiones Mathematicae, 41, 1-17.

Ferreyra, D. E., Levis, F. E., & Thome, N. (2018). Characterizations of k-commutative egualities for some outer generalized inverse. Linear and Multilinear Algebra, 68(1), 177-192.

Malik, S. B., Rueda, L., & Thome, N. (2016). The class of m-EP and m-normal matrices. Linear and Multilinear Algebra, 64(11), 2119-2132.

Malik, S. B., Rueda, L., & Thome, N. (2014). On a new generalized inverse for matrices of an arbitrary index. Applied Mathematics and Computation, 226,575-580.

Penrose, R. A. (1955). A generalized inverse for matrices. Mathematical Proceedings of the Cambridge Philosophical Society, 51(03), 406-413.

Sylvester, J. J. (1884). Sur l'equation en matrices $px = xq$. Comptes Rendus de l'Acad*é*mie des Sciences de Paris, 99, 67-71.

Wang, H. X. (2016). Core-EP decomposition and its applications. Linear Algebra and its Applicatians, 508, 289-300.

Wang, H. X., & Chen, J. L. (2018). Weak group inverse. Open Mathematics, 16(1), 1218-1232.

Wang, H. X., & Liu, X. J. (2019). The weak group matrix. Aequationes Mathematicae, 93(6), 1261-1273.

On some variations of dominating identification in graphs

Muhammad Fazil[1], Iffat Fida Hussain[2], Ateqa Akbar[2], Usman Ali[2,*]

[1]*Dept. of Basic Sciences and Humanities, Bahauddin Zakariya University, Multan 60800, Pakistan*

[2]*CASPAM, Bahauddin Zakariya University, Multan 60800, Pakistan*

Corresponding author: uali@bzu.edu.pk

Abstract

In this study, we introduce the locating-dominating value and the location-domination polynomial of graphs and location-domination polynomials of some families of graphs were identified. Locating-dominating set of graph G is defined as the dominating set which locates all the vertices of G. And, location-domination number G is the minimum cardinality of a locating-dominating set in G.

Keywords: Lexicographic product; locating-dominating set; location-domination number; location-domination polynomial; locating-dominating value

1. Introduction

Let G be a simple undirected graph. If every pair of vertices in G has a path between them, then G is said to be a *connected graph*, else, G is *disconnected*. *Neighborhood* of vertex v of G is set $N(v) = \{u \in V(G) : u \text{ is adjacent to } v\}$. The number of elements in $N(v)$ is the *degree* of v, denoted by $d_G(v)$. A vertex v with $d_G(v) = 0$ is an *isolated vertex*. If every vertex of connected graph G has two neighbors, then G is called a *cycle*. The *girth* of a graph G is the number of edges in its shortest cycle. If two distinct vertices u and v of G have the property that $N(u) - \{v\} = N(v) - \{u\}$, then u and v are called *twin vertices* (or simply twins) in G. A set $T \subseteq V(G)$ is said to be a *twin-set* in G if every two elements of T are twin vertices of G. The *complement* of G, denoted by $\overline{G}$, has the same vertex set as G and x is adjacent to y in $\overline{G}$ if and only if x is not adjacent to y in G. For a graph G, if $V(H) \subseteq V(G)$ and $E(H) \subseteq E(G)$, then H is called a *subgraph* of G. A non empty subset H of a connected graph G is called an *induced subgraph* of G, if H contains all the edges $uv \in E(G)$ with $u, v \in V(H)$. The *component* is the maximal connected subgraph of G.

A set $D \subseteq V(G)$ is called *dominating* if for every vertex $u \in V(G) \setminus D$, $N(u) \bigcap D \neq \phi$. A set L_d of vertices of a graph G is called a *locating-dominating set* if, for every two distinct vertices $u, v \in V(G) - L_d$, $\phi \neq N(u) \bigcap L_d \neq N(v) \bigcap L_d \neq \phi$. The *location-domination number* of a graph G, denoted by $LD(G)$, is the minimum cardinality of a locating-dominating set of G. Caceres *et al.* (2013), showed that each locating-dominating set is both locating and dominating set. However, the converse is not true in general.

The initial application of locating-dominating sets was fault-diagnosis in maintenance of multiprocessor systems (Karpovsky, Chakrabarty & Levitin, 1998). The purpose of fault detection is to test the system and locate faulty processors. Locating-dominating sets have since been extended and applied. The decision problem for locating-dominating sets for directed graphs has been shown to be an NP-complete problem (Charon, Hudry & Lobstein, 2002).

Balbuena *et al.* (2015), studied the locating-dominating sets of graphs containing no triangle. They also gave upper bound on the smallest size of such sets in term of the order of the graphs. Blidia *et al.* (2007), have worked on the location-domination number of trees. The study revealed upper and

lower bounds of a tree graph of order greater than or equal to 3, in terms of leaves and support vertices. And classify all the graphs satisfying the upper bound. Fazil *et al.* (2016) worked on the locationg-dominating sets in hyper graph. Mphako-Banda & Ncambalala, 2019; Alaeiyan *et al.,* 2014; Imran *et al.,* 2014; Bertrand *et al.,* 2004; Honkala *et al.,* 2004; Charon *et al.,* 2003; Slater, 2002; Slater, 1988; Colbourn *et al.,* 1987; Finbow & Hartnell, 1987; Fall & Slater, 1984 came up with helpful results.

2. Location-domination polynomials and Locating-dominating values

In this section, we introduce two new graph invariants, ie., the location-domination polynomial of a graph and the locating-dominating value of a vertex of a graph.

Initially recall some results on the location-domination number to proceed.

Proposition 2.1 *(Murtaza, 2020). Suppose that u, v are twins in a connected graph G and L_d is a locating-dominating set of G. Then either u or v is in L_d. Moreover, if $u \in L_d$ and $v \notin L_d$, then $(L_d - \{u\}) \cup \{v\}$ is a locating-dominating set of G.*

Remark 2.2 *(Murtaza, 2020). Let $T \subseteq V(G)$ be a twin-set of order $k \geq 2$. Then every locating-dominating set L_d of G contains at least $k - 1$ vertices of T.*

Lemma 2.3 *(Balbuena, 2015). Let G be a graph of girth at least 5, and let C be a dominating set of G. Let $X = \{x \in V(G) \setminus C : |N(x) \bigcap C| = 1\}$, then C is a locating-dominating set of G if and only if there is an injective function $f : X \to C$ such that $f(x) \in C \bigcap N(x)$ for all $x \in X$.*

Akbari *et al.* (2010), introduced the concept of domination polynomial of G. This family is related to all the dominating sets of G. Birkhoff (1912), introduced the concept of chromatic polynomial of G, which is related to all the color classes of G. Heilmann & Lieb (1972) came up with the concept of matching polynomial which corresponds to all the edges of G. Gutman & Harary (1983) introduced the concept for the independent polynomial of G, which corresponds to all the independent sets of G. Salman *et al.* introduced the concept for the resolving polynomial of G which corresponds to all the resolving sets of G. Javaid *et al.* (2018) proposed the concept of fixing polynomial of the graph, defines the fixing sets of G. In this paper, we studied the location-domination polynomial of the graph which corresponds to all the locating-dominating sets of G.

For a graph G of order n and location-domination number $LD(G)$, the location-domination polynomial $LD(G, x)$ is a generating polynomial for the locating-dominating sequence $(l_{LD(G)}, l_{LD(G)+1}, \ldots, l_n)$ which helps in counting all the locating-dominating sets of cardinality j; $LD(G) \leq j \leq n$, for G. j-set is the subset of the vertices of the graph G of cardinality j. Let $\mathcal{L}(G, j)$ denote the family of all the locating-dominating sets of G which are j-sets. Let $l_j = |\mathcal{L}(G, j)|$.

Definition 2.4 $LD(G, x) = \sum\limits_{j=LD(G)}^{n} l_j x^j$, *is defined as location-domination polynomial of G. Where, $l_j = 0$ iff $j = LD(G) = 0$ or $j < LD(G)$.*

Some properties related to location-domination polynomial $LD(G, x)$ of graph G are listed below.

Properties 2.5 (1) $l_{|G|} = 1$ *and* $l_{|G|-1} = |G|$.
    (2) $LD(G, x)$ *is monic.*
    (3) *Since* $l_i = 0$ *for* $j = LD(G) = 0$ *or* $j < LD(G)$, *so* $LD(G, x)$ *has no constant term.*
    (4) *Each value of the locating-dominating sequence* $(l_{LD(G)}, l_{LD(G)+1}, \ldots, l_n)$ *is non-zero.*
    (5) *For any* $a, á \in [0, \infty)$ *such that* $a < á$, $LD(G, a) < LD(G, á)$. *It concludes that* $LD(G, x)$ *is strictly increasing function on* $[0, \infty)$.
    (6) *If* G_1 *is any subgraph of a graph* G, *then* $deg(LD(G, x)) \geq deg(LD(G_1, x))$.

Proposition 2.6 *Let G be a graph with t components $G_1, G_2, ..., G_t$, then $LD(G, x) = \prod\limits_{i=1}^{t} LD(G_i, x)$.*

Proof. Since all the components are disjoint, the locating-dominating sets of each component are disjoint with other components. This implies that any locating-dominating set L_d of cardinality say r, where $LD(G) \leq r \leq |G|$, there must exist t disjoint locating-dominating sets one from each $G_i, 1 \leq i \leq t$, such that L_d is the union of these t locating-dominating sets. Thus, the coefficient of x^r in both polynomials $LD(G, x)$ and $\prod_{i=1}^{t} LD(G_i, x)$ is the same. Hence the polynomials are identical and completes the proof.

Proposition 2.7 *Let G be the graph of order $n \geq 2$ with $t \geq 2$ isolated vertices. If $LD(G, x)$ is the location-domination polynomial of G, then $t = n - l_{n-1}$.*

Proof. Suppose $A = \{x \in V(G) : d_G(x) = 0\}$ and $|A| = t$. Then for any vertex $u \in V(G) \setminus A$, the set $V(G) \setminus \{u\}$ is a locating-dominating set of G. Also, for any locating-dominating set B and any vertex $v \in A$, $B \setminus \{v\}$ is not a locating-dominating set of G. Accordingly, the result follows.

Proposition 2.8 *Let G be a graph of order $n \geq 2$ with $t \geq 2$ isolated vertices and G_1 be a graph induced by the set $V(G) \setminus A$, A is the set of isolated vertices (if $n = 2$, $t = 2$, then G_1 is not a graph). Then $LD(G_1, x) = \frac{LD(G,x)}{x^t}$.*

Proof. Let G_2 be a graph induced by A. Since G_1 is a subgraph induced by $V(G) \setminus A$, so $LD(G_1, x) = \sum_{i=LD(G_1)}^{m} l_i x^i$, $m = |V(G) \setminus A|$. Because A has at least two isolated vertices, G_2 must have two components. Thus, G_1 and G_2 have at least three components. Applying Proposition 2.6, we have $LD(G, x) = LD(G_1, x)x^t$, and then $LD(G_1, x) = \frac{LD(G,x)}{x^t}$.

Corollary 2.9 *Let G be a graph of order $n \geq 2$ with $t \geq 2$ isolated vertices and G_1 be its subgraph induced by the set $V(G) \setminus A$, A is the set of $t \geq 2$ isolated vertices. If $LD(G, x) = \sum_{i=LD(G)}^{n} l_i x^i$ and $LD(G_1, x) = \sum_{j=LD(G_1)}^{n-t} l_j x^j$ are location-domination polynomials of G and G_1, respectively. Then $t = \deg(LD(G, x)) - \deg(LD(G_1, x))$.*

Consider the set G^* which contains all locating-dominating sets of cardinality $LD(G)$, then $|G^*| = l_{LD(G)}$. The definition of locating-dominating value of each vertex of G as follows: for each vertex $v \in V(G)$, the *locating-dominating value*, $LDV(v)$, is the total number of the elements of G^* for which v belongs.

Proposition 2.10 *Let G be a graph, then*
    (1) $\sum_{v \in V(G)} LDV(v) = |G^*| \cdot LD(G)$.
    (2) *If u and v are twin vertices in G, then $LDV(u) = LDV(v)$.*
    (3) *If G has $t \geq 2$ components $G_1, G_2, ..., G_t$, then $|G^*| = \prod_{i=1}^{t} |G_i^*|$. Further, for $v \in V(G)$,*
$LDV(v) = LDV(G_i(v)) \prod_{j=1 j \neq i}^{t} |G_j^*|$.

3. Location-domination polynomials and Locating-dominating values of some families of graphs

This section considers location-domination polynomials of various graph families, such as the complete multipartite graphs, Petersen graph and lexicographic product of cycle graph of order $n_1 \geq 3$ with $n_2 \geq 2$ isolated vertices.

Let G be a complete multipartite graph and $P_1, P_2, P_3, ..., P_q$ be its q-partites. It is clear that each partite is a twin set. Also, for any $u \in P_{q_1}$ and any $v \in P_{q_2}, q_1 \neq q_2, N(u) \neq N(v)$. Thus, $LD(G) = \sum_{j=1}^{q} |P_j| - q$

We prove the following theorem for $|P_j| = n_j$, $1 \le j \le q$, which describes the location-domination polynomial of the complete multipartite graph.

Theorem 3.1 *Let* $G = K_{n_1,n_2,n_3,...,n_q}$ *be the complete multipartite graph with* $n_1 \ge n_2 \ge n_3 \ge .... \ge n_q$, *then for each* $n_j \ge 2$, $LD(G,x) = x^{|G|} + \sum\limits_{i=1}^{q} [\sum\limits_{1=j_1<j_2<...<j_i}^{q} (n_{j_1} n_{j_2} \ldots n_{j_i}) x^{|G|-i}]$.

Proof. Since each partite P_j with $|P_j| = n_j$, $1 \le j \le q$, is in fact a twin set, therefore every minimal locating-dominating set of $G = K_{n_1,n_2,n_3,...,n_q}$ contains all but one vertex from each P_j. Applying Properties 2.5(1), we have $l_{|G|} = 1$, $l_{|G|-1} = |G|$, and for $l_{|G|-i}$, $2 \le i \le LD(G)$, we choose all vertices of G except i vertices with one vertex from each P_j. It is possible to do this in exactly $\sum\limits_{1=j_1<j_2<...<j_i}^{q} n_{j_1} n_{j_2} \ldots n_{j_i}$. This proves the result.

From Theorem 3.1, there are $\prod\limits_{j=1}^{q} n_j$ locating-dominating sets of minimum cardinality, and each locating-dominating set must contain all but one vertex from each partite, so we have the following corollary:

Corollary 3.2 *Let* $G = K_{n_1,n_2,n_3,...,n_q}$ *be the complete multipartite graph with* $n_1 \ge n_2 \ge n_3 \ge .... \ge n_q$ *and each* $n_j \ge 2$, *then for any* $v \in V(G)$, *there is a partite* P_k, $1 \le k \le q$ *such that* $LDV(v) = \prod\limits_{j=1 j\ne k}^{q} n_j(n_k - 1)$.

The Petersen graph $G = P(5,2)$ is the graph with the vertex set $V(G) = \{u_1, u_2, u_3, u_4, u_5, v_1, v_2, v_3, v_4, v_5\}$, and the edge set $E(G) = \{u_i u_{(i+1)mod5}, v_i v_{(i+1)mod5}, u_i v_{(i+j)mod5}, 1 \le i \le 5, j = i - 1\}$, with $u_0 = u_5$ and $v_0 = v_5$.

The following theorem points to the Petersen graph's location-domination number.

Theorem 3.3 *(Balbuena, 2015) Let* $G = P(5,2)$ *be the Petersen graph, then* $LD(G) = 4$.

Following proposition gives the location-domination polynomial of Petersen graph.

Proposition 3.4 *Let* $G = P(5,2)$, *then* $LD(G,x) = x^{10} + 10x^9 + 45x^8 + 120x^7 + 200x^6 + 192x^5 + 65x^4$.

Proof. Since the girth of Petersen graph $G = P(5,2)$ is 5. A dominating set D is also a locating if it does not have two vertices that are each uniquely dominated by one vertex. Let V denotes the vertex set of Petersen graph, D dominating set and $E = V \setminus D$. Here are the cases for E.

1. When $|E| = 0, 1, 2, or\ 3$, then D is a dominating set because no vertex of E is isolated from the set D. By Lemma 2.3, D is also a locating set, so $l_j = \binom{10}{j}$, for $j = 7, 8, 9, 10$.

2. When $|E| = 4$, then there exist 10 possibilities to choose E with 1 vertex isolated from D, so there exist $\binom{10}{4} - 10 = 200$ dominating sets of size 6. All of them are also locating, and $l_6 = 200$.

3. When $|E| = 5$, then there exist $10 * 6$ possibilities to choose E with 1 vertex isolated from D, so there exist $\binom{10}{5} - 60 = 192$ dominating sets of size 5. All of them are also locating, and $l_5 = 192$.

4. When $|E| = 6$, then there exist $10 * 12$ possibilities to choose E with 1 vertex isolated from D, and 15 possibilities to choose E with 2 vertices isolated from D. So there exist $\binom{10}{6} - 120 - 15 = 75$ dominating sets of size 4. A dominating set D is not locating if there exists a vertex $v \in D$ with two adjacent vertices u and w such that $N[u] \bigcup N[w] \setminus \{v\} \subset V \setminus D$. In this case set E contains another 4 vertices different from u and w. Vertices of D induce a star $K_{1,3}$. There are 10 ways to pick this star, so there are 10 different sets of dominating characteristics not located in the Petersen graph. 65 of the remaining dominating sets are also locating and $l_4 = 65$.

Consequently, $LD(G, x) = x^{10} + 10x^9 + 45x^8 + 120x^7 + 200x^6 + 192x^5 + 65x^4$.

Definition 3.5 *Lexicographic product between the graphs G and $\acute{G}$, denoted by $G[\acute{G}]$, is the graph with vertex set $V(G) \times V(\acute{G}) = \{(u, v) : u \in V(G), v \in V(\acute{G})\}$ and (u_1, v_1) is adjacent to (u_2, v_2) if $u_1 = u_2$ and v_1 is adjacent to v_2, or u_1 is adjacent to u_2.*

Here is the result for a graph G which is the lexicographic product of a cycle graph with n_1 nodes and the complement of a complete graph with n_2 nodes.

Theorem 3.6 *Let G be the graph $C_{n_1}[\overline{K_{n_2}}]$ with $n_1 \geq 3$ and $n_2 \geq 2$, then*

$$LD(G) = \begin{cases} n_1(n_2 - 1) & \text{when } n_1 \neq 4, \\ n_1(n_2 - 1) + 2 & \text{when } n_1 = 4. \end{cases}$$

Proof. Let $V(G) = \{(u_i, v_j); 1 \leq i \leq n_1, 1 \leq j \leq n_2\}$, where $u_i \in V(C_{n_1})$ and $v_j \in V(\overline{K_{n_2}})$. Then for each i, where $1 \leq i \leq n_1$, the set $T_i = \bigcup_{j=1}^{n_2} \{(u_i, v_j)\}$ is a twin set. Since there are n_1 twin sets and each twin set is of cardinality n_2. Thus, every locating-dominating set of the minimum cardinality contains at least $n_1(n_2 - 1)$ vertices, and hence $LD(G) \leq n_1(n_2 - 1)$.

Consider the set $L_d = \bigcup_{i=1}^{n_1} \bigcup_{j=1}^{n_2-1} \{(u_i, v_j)\}$. Then for each i, $1 \leq i \leq n_1$ and $j = n_2$,

$$N(u_i, v_j) \bigcap L_d = \bigcup_{k_1=1(k_1 \neq i)}^{n_1} \bigcup_{k_2=1}^{n_2-1} \{(u_{k_1}, v_{k_2})\}.$$

This implies that all the remaining vertices $(u_i, v_j) \notin L_d$, $1 \leq i \leq n_1$ and $j = n_2$, have different non-empty neighborhoods in L_d. Thus, the set L_d is a locating-dominating set of cardinality $n_1(n_2 - 1)$. Hence, $LD(G) = n_1(n_2 - 1)$ for $n_1 \geq 3$, $n_1 \neq 4$ and $n_2 \geq 2$.

Further, for $n_1 = 4$ and $n_2 \geq 2$, the set $L_d^* = \bigcup_{i=1}^{n_1} \bigcup_{j=1}^{n_2-1} \{(u_i, v_j)\}$ does not form a locating-dominating set because $N(u_i, v_{n_2}) = N(u_j, v_{n_2}), 1 \leq i \leq 2, j = i+2$. However, the set $L_d^* \bigcup_{i=1}^{2} \{(u_i, v_{n_2})\}$ is a locating-dominating set of the minimum cardinality. Thus, for $n_1 = 4$ and $n_2 \geq 2$, $LD(G) = n_1(n_2 - 1) + 2$.

Theorem 3.7 *Let $G = C_{n_1}[\overline{K_{n_2}}]$, then for $n_1 \neq 4 \geq 3$, $n_2 \geq 2$,*

$$LD(G, x) = \sum_{j=0}^{n_1} \binom{n_1}{j} n_2^{n_1-j} x^{n_1(n_2-1)+j}.$$

And, for $n_1 = 4$, $n_2 \geq 2$,

$$LD(G, x) = x^{4n_2} + 4n_2 x^{4n_2-1} + 4n_2^2 x^{4n_2-2}.$$

Proof. Note that there are n_1 twin-sets of cardinality n_2 in G. From these n_1 twin-sets, we can choose k twin-sets from which we will choose all the n_2 vertices, and this can be done in $\binom{n_1}{k}$ different ways. From the remaining $n_1 - k$ twin-sets, we can choose $n_2 - 1$ vertices out of n_2 vertices, which can be done in $n_2^{n_1-k}$ ways. This implies that

$$LD(G, x) = \sum_{j=0}^{n_1} \binom{n_1}{j} n_2^{n_1-j} x^{n_1(n_2-1)+j}.$$

Now, for $n_1 = 4$ and $n_2 \geq 2$, $LD(G) = n_1(n_2 - 1) + 2$, so $l_{4n_2} = 1$ and $l_{4n_2-1} = 4n_2$. In this case, we notice that $V(G) = T_1 \bigcup T_2$, where $T_1 = \bigcup_{j=1}^{n_2} \{(u_1, v_j), (u_3, v_j)\}$ and $T_2 = \bigcup_{j=1}^{n_2} \{(u_2, v_j), (u_4, v_j)\}$ are the twin sets. Since $|T_1| = |T_2| = 2n_2$, therefore $l_{4n_2-2} = 4n_2^2$, and hence, the result holds.

From Theorem 3.7, we have the following corollary:

Corollary 3.8 *Let* $G = C_{n_1}[\overline{K_{n_2}}]$, $n_1 \geq 3$, $n_2 \geq 2$, *and* $T_1, T_2,...,T_t$ *are the twin sets of* G *such that* $V(G) = \bigcup\limits_{i=1}^{t} T_i$, *then for any* $v \in T_k, 1 \leq k \leq t$, $LDV(v) = \prod\limits_{\substack{i=1 \\ i \neq k}}^{t} |T_i|(|T_k| - 1)$.

4. Conclusion

The location-domination polynomial of a graph is a new concept within graph theory. This article introduces the location-domination polynomial of a graph G and discusses its properties. Additionally, location-dominating value has also been introduced. Our research also computed the location-domination numbers and polynomials of several families of graphs.

References

Akbari, Alikhani, S. & **Peng, Y. (2010).** Characterization of graphs using domination polynomials. Europ. J. of Combin., 31: 1714-1724.

Alaeiyan, M., Gilani, A., Mojarad, R. & **Asadpour, J. (2014).** Omega and related polynomials of polyomino chains of 4 k-cycles. Kuwait J. Sci., 41: 85-92.

Balbuena, C., Foucaud, F, & **Hansberg, F. (2015).** Locating-dominating sets and identifying codes in graphs of girth at least 5. Elect. J. Combin., 22.

Bertrand, N., Charon, I,. Hudry O. & **Lobstein, A. (2004).** Identifying and locating- dominating codes on chains and cycles. Europ. J. Combin., 25: 969-987.

Birkhoff, G. D. (1912). A determinant formula for the number of ways of coloring a map. The Annals of Maths., 14: 42-46.

Blidia, M., Chellali, M., Maffray, F. & **Moncel, J. (2007).** Location-domination and identifying codes in trees. Aust. J. Combin., 39: 219-232.

Caceres, J., Hernando, C., Mora, M., Pelayo, I. M. & **Puertas, M. L. (2013).** Locating dominating codes. Appl. Math. Comput., 220: 38-45.

Charon, I., Hudry, O. & **Lobstein, A. (2002).** Identifying and locating-dominating codes; NP-completeness results for directed graphs. IEEE Trans. Inform. Theory, 48: 2192-2200.

Charon, I., Hudry, O. & **Lobstein, A. (2003).** Minimizing the size of an identify- ing or locating-dominating code in a graph is NP-hard. Theor. Comput. Sci., 290: 2109-2120.

Colbourn, C. J., Slater, P. J. & **Stewart, L. K. (1987).** Locating-dominating sets in series parallel networks. Congr. Numer., 56: 135-162.

Fazil, M., Javaid, I., Salman, M. & **Ali, U. (2016).** Locating-dominating sets in hypergraphs. Period. Math. Hung., 24.

Finbow, A. & **Hartnell, B. L. (1987).** On locating-dominating sets and well-covered graphs. Congr. Numer., 56: 135-162.

Foucaud, F. & **Henning, M. A. (2016).** Locating-total dominating sets in twin-free graphs: a conjecture. Elect. J. Combin., 23.

Gutman, I. & **Harary, F. (1983).** Generalizations of the matching polynomial. Util. Math., 24: 97-106.

Heilmann, O. J. & **Lieb, E. H. (1972).** Theory of monomer-dimer systems. Commun. Math. Phy., 25: 190-232.

Honkala, I., Laihonen, T. & **Ranto, S. (2004).** On locating-dominating codes in binary hamming spaces. Disc. Math. Theor. Comput. Sci., 6: 265-282.

Imran, M., Baig, A. Q. & **Shafiq, M. K. (2014).** On metric dimension of generalized Petersen graphs $P(n, 3)$. Ars Combin., 17: 113-130.

Javaid, I., Fazil, M., Ali, U. & **Salman, M. (2018).** On some parameters related to fixing sets in graphs. J. Prime Research in Math., 14: 1-12 .

Karpovsky, M. G., Chakrabarty, K. & **Levitin, L. B. (1998).** On a new class of codes for identifying vertices in graphs. IEEE Transactions on Information Theory, 44: 599-611.

Khuller, S., Raghavachari, B. & **Rosenfeld, A. (1996).** Landmarks in graphs. Disc. Appl. Math., 70: 217—229.

Mphako-Banda, E. & **Ncambalala, T. (2019).** Hosoya polynomial of the subdivided join. Kuwait J. Sci., 46: 7-12.

Murtaza, M., Javaid, I. & **Fazil, M. (2020).** Locating-dominating sets and identifying codes of a graph associated to a finite vector space. Ukrainian Mathematical Journal, 72: 952-959.

Rall, D. F. & **Slater, P. J. (1984).** On location-domination numbers for certian classes of graphs. Congr. Numer., 45: 97-106.

Salman, M., Chaudhry, M. A. & **Javaid, I.** The resolving polynomial of graph, Submitted.

Slater, P. J. (1988). Dominating and reference sets in a graph. J. Math. Phy. Sci., 22: 445-455.

Slater, P. J. (2002). Fault-tolerant locating-dominating sets. Disc. Math., 249: 179-189.

An easy construction of generalized neighbor designs in minimal circular blocks

Muhammad Nadeem, Muhammad Rasheed, M. H. Tahir, Khadija Noreen,
Sajid Hussain*, Rashid Ahmed

Dept. of Statistics, The Islamia University of Bahawalpur, Pakistan
Corresponding author: sajidhussain060917@gmail.com

Abstract

Neighbor designs (NDs) are used in the experiments where neighbor effects may arise. Neighbor designs neutralize these effects and are, therefore, considered to be robust against neighbor effects. Minimal neighbor designs are always most economical among the neighbor designs and are, therefore, preferred by the experimenters. Method of cyclic shifts provides these designs in circular blocks only for odd v (number of treatments). For v even, minimal circular generalized neighbor designs in which only $\frac{v}{2}$ unordered pairs of distinct treatments that do not appear as neighbors will be the better alternate to the minimal neighbor designs. In this article, such minimal generalized neighbor designs are constructed in circular blocks for v even.

Keywords: Direct effects; minimal circular blocks; neighbor designs; neighbor effects; robust to neighbor effects.

1. Introduction

Neighbor designs (NDs) are used in the experiments where neighbor effects may arise. Neighbor designs neutralize these effects and are, therefore, considered to be robust against neighbor effects. Minimal neighbor designs are always most economical among the neighbor designs and are, therefore, preferred by the experimenters. Tomar *et al.* (2005) suggested that competition among neighboring units becomes a source of bias and treatments comparisons are not much affected by neighbor effects with the use of neighbor balanced designs (NBDs). If each treatment appears exactly once with all other treatments as neighbor then design is minimal neighbor balanced. If every treatment occurs equal number of times, say λ' as neighbor of every other treatment, design is called neighbor balanced, here λ' is positive integer. If $\lambda' = 1$ then it is minimal NBD. If each treatment appears either (i) $\lambda'_1 = 1$ and $\lambda'_2 = 0$, or (ii) $\lambda'_1 = 1$ and $\lambda'_2 = 2$ times with other treatments as neighbor (left or right) then designs are called minimal generalized neighbor designs (GNDs).

Rees (1967) finds application of minimal NBDs in serology for virus research. In experiments of agriculture, horticulture, and forestry, neighbor effects arise due to plots' nature, plots' layout, pest infections from neighboring plots, etc. Minimal NBDs are available in literature to neutralize neighbor effects economically for v odd. For v even, our proposed minimal circular GNDs (MCGNDs) will reduce the bias due to neighbor effects economically and efficiently. Williams (1952) constructed NBDs in linear blocks. Rees (1967) used neighbor designs in virus research using circular blocks. Rees (1967) constructed neighbor designs also for $k \leq v$. Hwang (1973) constructed NBDs for some cases of v odd. Cheng (1983) constructed neighbor designs for block size (k) equal to v. NBDs reduce bias due to neighbor effects, see Azais (1987), Langton (1987), Azais *et al.* (1993) and Kunert (2000). Iqbal *et al.* (2009) constructed some series of NBDs through method of cyclic shifts. Akhtar *et al.* (2010) and Ahmed & Akhtar (2011) presented NBDs for $k = 5$ and 6 respectively. Shehzad *et al.* (2011a)

constructed minimal circular blocks neighbor designs for some limited cases. Misra *et al.* (1991) relaxed the conditions of balance property up to some extent and constructed GNDs. GNDs will be minimal GN_2-designs if λ' may take only two values (i) $\lambda_1' = 1$ and $\lambda_2' = 0$, or (ii) $\lambda_1' = 1$ and $\lambda_2' = 2$. Nutan (2007) and Kedia & Misra (2008) constructed some classes of circular GNDs (CGNDs) in which some are GN_2-designs. Ahmed *et al.* (2009), Zafaryab *et al.* (2010), Shehzad *et al.* (2011b) and Iqbal *et al.* (2012) presented MCGNDs for some limited cases. In this article, MCGNDs are obtained for v even in equal and unequal block sizes. In our proposed designs, $\frac{v}{2}$ pairs of treatments do not appear as neighbors.

This article is organized as: Method of cyclic shifts is described in Section 2, along with the conditions for existence of MCGNDs. Efficiency measure is described in Section 3. MCGNDs are obtained for $m \equiv 0 \pmod 4$ in Section 4 and for $m \equiv 3 \pmod 4$ in Section 5. Discussion and conclusion are given in Section 6.

2. Method of cyclic shifts

Iqbal (1991) introduced method of cyclic shifts which is simplified here for minimal CNBDs and minimal CGNDs.

Let $S_j = [q_{j1}, q_{j2}, \cdots, q_{j(k-1)}]$ be i sets, $j = 1, 2, \cdots, i$, $1 \le q_{ju} \le v - 1$ and $u = 1, 2, \cdots, k - 1$.

- If each of $1, 2, \cdots, v - 1$ appears exactly once in S^* then designs will be minimal CNBD.

- If each of $1, 2, \cdots, v - 1$ appears either (a) 1 and 0, or (b) 1 and 2 in S^* then designs will be minimal CGND.

Here S^* contains:

(i) Each element of all sets S_j.

(ii) Sum (mod v) of all elements in each set S_j.

(iii) Complements of all elements in (i) and (ii), here complement of a being $v - a$.

In this article, we deal with the construction of MCGNDs in which $\frac{v}{2}$ unordered pairs will not appear as neighbors. To construct minimal CGNDs for $v = 2ik_1 + 2k_2 + 2k_3 + \cdots + 2k_h + 2$, using Rule I, proceed as.

- If sum of A is divisible by v then it will produce required MCGNDs, here A = $[1, 2, \cdots, m]$. For this, one or more elements can be replaced with their complements, here $2m = v - 2$.

- Divide resultant A in i classes of k_1 size , one class each of $k_2, k_3, \cdots$, and k_h sizes in such a way that sum of each class is divisible by v.

- Required sets of shifts will be obtained by deleting one element (any) from each class.

Example 2.1

$S = [1, 2, 3]$ provides minimal CGND for $v = 10$ and $k = 4$.

Proof: $S^* = [1, 2, 3, 6, 9, 8, 7, 4]$ which contains each of $1, 2, \cdots, 9$ once but 5 does not appear. Hence $S = [1, 2, 3]$ provides minimal CGND in blocks of size 4. Blocks of the design are generated as follows from the given set(s) of shifts.

Each set requires v blocks. Assign to each block 0 to $v - 1$ as first unit element. Add 1 (mod v) to first unit elements for second unit elements. Then add 2 (mod v) to second unit values and so on, see Table 1.

Example 2.2

Table 1. Blocks obtained from S = [1, 2, 3]

				Blocks					
1	**2**	**3**	**4**	**5**	**6**	**7**	**8**	**9**	**10**
0	1	2	3	4	5	6	7	8	9
1	2	3	4	5	6	7	8	9	0
3	4	5	6	7	8	9	0	1	2
6	7	8	9	0	1	2	3	4	5

$S_1 = [3,4,7]$, $S_2 = [1,5]$ produce following MCGND for $v = 16$, $k_1 = 4$ and $k_2 = 3$.

Proof: $S^* = [3,4,7,14,1,5,6,13,12,9,2,15,11,10]$, Here each of $1, 2, \cdots, 15$ appears once except 8 which does not appear. Hence S_1 and S_2 generate MCGND for $v = 16$, $k_1 = 4$, $k_2 = 3$.

Table 2 and 3 jointly present MCGND for $v = 16$, $k_1 = 4$, $k_2 = 3$. In this design, unordered pairs (0,8), (1,9), (2,10), (3,11), (4,12), (5,13), (6,14), (7,15) do not appear as neighbors. Hence we save $[16(15) - 16(7)] = 53.33\%$ experimental units at the cost of losing $[\frac{8}{120} \times 100\%] = 6.67\%$ neighbor balance.

Table 2. Blocks obtained from $S_1 = [3, 4, 7]$

							Blocks								
1	**2**	**3**	**4**	**5**	**6**	**7**	**8**	**9**	**10**	**11**	**12**	**13**	**14**	**15**	**16**
0	1	2	3	4	5	6	7	8	9	10	11	12	13	14	15
3	4	5	6	7	8	9	10	11	12	13	14	15	0	1	2
7	8	9	10	11	12	13	14	15	0	1	2	3	4	5	6
14	15	0	1	2	3	4	5	6	7	8	9	10	11	12	13

Table 3. Blocks obtained from $S_2 = [1, 5]$

							Blocks								
17	**18**	**19**	**20**	**21**	**22**	**23**	**24**	**25**	**26**	**27**	**28**	**29**	**30**	**31**	**32**
0	1	2	3	4	5	6	7	8	9	10	11	12	13	14	15
1	2	3	4	5	6	7	8	9	10	11	12	13	14	15	0
6	7	8	9	10	11	12	13	14	15	0	1	2	3	4	5

3. Efficiency of neighbor effects

The model repeatedly discussed for residual effects in literature is the traditional model given by,

$$y_{ijk} = \mu + \tau_{d(k,j)} + \gamma_{d(k-1,j)} + \pi_k + \xi_{ij} + \varepsilon_{ijk}, \tag{1}$$

The efficiency factor for neighbor effect is the harmonic mean of non-zero Eigen values of their respective information matrix, see James & Wilkinson (1971) and Pearce *et al.* (1974). Design with high value of E_n is considered efficient to estimate neighbor effects. Our proposed designs possess high values of E_n, therefore, these are suitable for this purpose.

Example 3.1

[2,3,4,5,7,13], [1,6,8,9,10], [11,12,14,15,16] produce MCGND for $v = 34$, $k_1 = 6$ and $k_2 = 5$ with $E_n = 0.90$.

4. Minimal CGNDs for $m \equiv 3 \pmod 4$

Here, MCGNDs are obtained for $m \equiv 3 \pmod 4$ with $m = \frac{v-2}{2}$.

Theorem 4.1

If $m \equiv 3 \pmod 4$, sets obtained from A = $[1, 2, \cdots, \frac{(3m-1)}{4}, \frac{(3m+7)}{4}, \frac{(3m+11)}{4}, \cdots, m, \frac{5(m+1)}{4}]$ will produce MCGNDs for:

- $v = 2ik + 2$.

- $v = 2ik_1 + 2u_1k_2 + 2$.

- $v = 2ik_1 + 2u_1k_2 + 2u_2k_3 + 2$ and so on.

Proof: Let
$$
\begin{aligned}
S &= 1 + 2 + \cdots + \frac{(3m-1)}{4} + \frac{(3m+7)}{4} + \frac{(3m+11)}{4} + \cdots + m + \frac{5(m+1)}{4} \\
&= 1 + 2 + \cdots + \frac{(3m-1)}{4} + \frac{(3m+3)}{4} + \frac{(3m+7)}{4} + \frac{(3m+11)}{4} + \cdots + m + \frac{5(m+1)}{4} - \frac{(3m+3)}{4} \\
&= [1 + 2 + \cdots + m] + \frac{(2m+2)}{4} \\
&= \frac{m(m+1)}{2} + \frac{2(m+1)}{4} \\
&= \frac{2(m+1)(m+1)}{4}, \quad \text{Since} \quad v = 2(m+1) \\
&= \frac{v(m+1)}{4}.
\end{aligned}
$$
$\frac{(m+1)}{4}$ will be integer for $m \equiv 3 \pmod 4$.

S $(\bmod\ v) \equiv 0$ if $\frac{(m+1)}{4}$ is integer. Hence proved.

4.1 MCGNDs in equal block sizes when $m \equiv 3 \pmod 4$

For the following cases, minimal CGNDs can be constructed in equal block sizes using i sets derived from theorem 4.1.

(i) $v = 2ik + 2$, $k = 5, 9, 13, \cdots$, $i = 3, 7, 11, \cdots$

(ii) $v = 2ik + 2$, $k = 7, 11, \cdots$, $i = 1, 5, 9, \cdots$

Example 4.1

Following sets generate minimal CGND for $v = 32$ and $k = 5$ with $E_n = 0.92$.
$S_1 = [4,6,10,11]$, $S_2 = [5,7,8,9]$, $S_3 = [13,14,15,20]$

4.2 MCGNDs in two different block sizes when $m \equiv 3 \pmod 4$, through i sets for k_1 and one for k_2

For the following cases, MCGNDs can be obtained in two different block sizes from i sets for k_1 and one set for k_2 derived from theorem 4.1.

(i) $v = 2k_1(i + 1)$, $k_1 = 4l = k_2 + 1$, i & l integers.

(ii) $v = 2k_1(i + 1)$, $k_1 = 4l + 2 = k_2 + 1$, i odd.

(iii) $v = 2k_1(i + 1)$, $k_1 \text{ (odd)} = k_2 + 1 > 3$, $i \equiv 3 \pmod 4$.

(iv) $v = 2k_1(i + 1) - 2$, $k_1 \equiv 1 \pmod 4 = k_2 + 2$, $i \equiv 0 \pmod 4$.

(v) $v = 2k_1(i + 1) - 2$, $k_1 \equiv 3 \pmod 4 = k_2 + 2$, $i \equiv 2 \pmod 4$.

(vi) $v = 2ik_1 + 8$, $k_1 = 4l$, $k_2 = 3$, i & l integers and $m \equiv 3 \pmod 4$.

(vii) $v = 2ik_1 + 8$, $k_1 = 4l + 2$, $k_2 = 3$, i even.

(viii) $v = 2ik_1 + 8$, k_1 (odd) > 3, $k_2 = 3$, $i \equiv 0 \pmod 4$.

(ix) $v = 2ik_1 + 10$, $k_1 \equiv 1 \pmod 4$, $k_2 = 4$, $i \equiv 3 \pmod 4$.

(x) $v = 2ik_1 + 10$, $k_1 \equiv 3 \pmod 4$, $k_2 = 4$, $i \equiv 1 \pmod 4$.

(xi) $v = 2ik_1 + 12$, $k_1 = 4l + 2$, $k_2 = 5$, and i odd.

(xii) $v = 2ik_1 + 12$, $k_1 = 4l + 2$, k_1 (odd) > 5, $k_2 = 5$, $i \equiv 2 \pmod 4$ and $m \equiv 3 \pmod 4$.

Example 4.2

Following sets generate MCGND for $v = 16$, $k_1 = 4$, $k_2 = 3$ with $E_n = 0.85$.

$$S_1 = [2,3,10], \qquad S_2 = [5,4]$$

4.3 MCGNDs in two different block sizes when $m \equiv 3 \pmod 4$, through i sets for k_1 and two for k_2

For the following cases, MCGNDs can be obtained in two different block sizes using i sets for k_1, two for k_2 derived from theorem 4.1.

(i) $v = 2k_1(i + 2) - 2$, $k_1 = 5, 9, \cdots$, $k_1 = k_2 + 1$, $i = 3, 7, 11, \cdots$

(ii) $v = 2k_1(i + 2) - 2$, $k_1 = 7, 11, \cdots$, $k_1 = k_2 + 1$, $i = 1, 5, 9, \cdots$

(iii) $v = 2k_1(i + 2) - 6$, $k_1 = 5, 9, \cdots$, $k_1 = k_2 + 2$, $i = 1, 5, 9, \cdots$

(iv) $v = 2k_1(i + 2) - 6$, $k_1 = 7, 11, \cdots$, $k_1 = k_2 + 2$, $i = 3, 7, 11, \cdots$

(v) $v = 2k_1(i + 2) - 10$, $k_1 = 5, 9, \cdots$, $k_1 = k_2 + 3$, $i = 3, 7, 11, \cdots$

(vi) $v = 2k_1(i + 2) - 10$, $k_1 = 7, 11, \cdots$, $k_1 = k_2 + 3$, $i = 1, 5, 9, \cdots$

Example 4.3

Following sets generate minimal CGND for $v = 40$, $k_1 = 7$ and $k_2 = 6$ with $E_n = 0.93$.
$S_1 = [3,4,5,6,7,14]$, $S_2 = [10,11,12,13,25]$, $S_3 = [8,16,17,18,19]$

4.4 MCGNDs in three different block sizes when $m \equiv 3 \pmod 4$, through i sets for k_1 and one set for k_2, one for k_3

For the following cases, MCGNDs can be obtained in three different block sizes from i sets for k_1, one set for k_2, one for k_3 derived from theorem 4.1.

(i) $v = 2k_1(i + 2) - 4$, $k_1 = 4l + 2 = k_2 + 1$, $k_3 = k_1 - 2$, i odd.

(ii) $v = 2k_1(i + 2) - 4$, $k_1 = k_2 + 1 > 3$, $k_3 = k_1 - 2$, $i \equiv 0 \pmod 4$.

(iii) $v = 2k_1(i + 2) - 4$, $k_1 \equiv 1 \pmod 4 = k_2 + 1$, $k_3 = k_1 - 3$, $i \equiv 1 \pmod 4$.

(iv) $v = 2k_1(i + 2) - 6$, $k_1 \equiv 3 \pmod 4 = k_2 + 1$, $k_3 = k_1 - 3$, $i \equiv 3 \pmod 4$.

(v) $v = 2k_1(i + 2) - 8$, $k_1 = 4l$, $l > 1$, $k_2 = k_1 - 2$, $k_3 = k_1 - 3$, i, l integer and $m \equiv 3 \pmod 4$.

(vi) $v = 2k_1(i + 2) - 8$, $k_1 = 4l + 2$, $k_2 = k_1 - 2$, $k_3 = k_1 - 3$, i even, l integer, $m \equiv 3 \pmod 4$.

(vii) $v = 2k_1(i + 2) - 8$, $k_1 > 5$, $k_2 = k_1 - 2$, $k_3 = k_1 - 3$, $i \equiv 2 \pmod 4$.

(viii) $v = 2k_1(i + 1) + 6$, $k_1 \equiv 1 \pmod 4 = k_2 + 1$, $k_3 = 3$, $i \equiv 0 \pmod 4$.

(ix) $v = 2k_1(i + 1) + 6$, $k_1 \equiv 3 \pmod 4 = k_2 + 1$, $k_3 = 3$, $i \equiv 2 \pmod 4$.

(x) $v = 2k_1(i + 1) + 8$, $k_1 = 4l = k_2 + 1$, $l > 1$, $k_3 = 4$.

(xi) $v = 2k_1(i + 1) + 8$, $k_1 = 4l + 2 = k_2 + 1$, $k_3 = 4$, i odd.

(xii) $v = 2k_1(i + 1) + 8$, $k_1 = k_2 + 1 > 5$, $k_3 = 4$, $i \equiv 3 \pmod 4$.

(xiii) $v = 2k_1(i + 1) + 10$, $k_1 \equiv 1 \pmod 4 = k_2 + 1$, $k_3 = 5$, $i \equiv 3 \pmod 4$.

(xiv) $v = 2k_1(i + 1) + 10$, $k_1 \equiv 3 \pmod 4 = k_2 + 1$, $k_3 = 5$, $i \equiv 0 \pmod 4$.

(xv) $v = 2k_1(i + 1) + 4$, $k_1 = 4l + 2$, $l > 1$, $k_2 = k_1 - 2$, $k_3 = 3$, i even, $m \equiv 3 \pmod 4$.

(xvi) $v = 2k_1(i + 1) + 4$, $k_1 > 5$, $k_2 = k_1 - 2$, $k_3 = 3$, $i \equiv 1 \pmod 4$.

(xvii) $v = 2k_1(i + 1) + 6$, $k_1 \equiv 1 \pmod 4 = k_2 + 2$, $k_3 = 4$, $i \equiv 0 \pmod 4$.

(xviii) $v = 2k_1(i + 1) + 6$, $k_1 \equiv 3 \pmod 4 = k_2 + 2$, $k_3 = 4$, $i \equiv 2 \pmod 4$.

(xix) $v = 2k_1(i + 1) + 8$, $k_1 = 4l$, $l > 2$, $k_2 = k_1 - 2$, $k_3 = 5$, i integer and $m \pmod 4 \equiv 0$.

(xx) $v = 2k_1(i + 1) + 8$, $k_1 = 4l + 2 = k_2 + 2$, $k_3 = 5$, i odd.

(xxi) $v = 2k_1(i + 1) + 8$, $k_1 > 5$, $k_2 = k_1 - 2$, $k_3 = 5$, $i \equiv 3 \pmod 4$.

(xxii) $v = 2k_1(i + 1) + 2$, $k_1 \equiv 1 \pmod 4$, $k_2 = k_1 - 3$, $k_3 = 3$, $i \equiv 2 \pmod 4$.

(xxiii) $v = 2k_1(i + 1) + 2$, $k_1 \equiv 3 \pmod 4$, $k_2 = k_1 - 3$, $k_3 = 3$, $i \equiv 0 \pmod 4$.

(xxiv) $v = 2k_1(i + 1) + 4$, $k_1 = 4l + 2 = k_2 + 3$, $k_3 = 4$, i even.

(xxv) $v = 2k_1(i + 1) + 4$, $k_1 > 5$, $k_2 = k_1 - 3$, $k_3 = 4$, $i \equiv 1 \pmod 4$.

(xxvi) $v = 2k_1(i + 1) + 6$, $k_1 \equiv 1 \pmod 4 = k_2 + 3$, $k_3 = 5$, $i \equiv 2 \pmod 4$.

Example 4.4

Following sets generate minimal CGND for $v = 32$, $k_1 = 6$, $k_2 = 5$ and $k_3 = 4$ with $E_n = 0.92$.
S_1 = [9,11,13,14,15], S_2 = [6,7,8,10], S_3 = [4,5,20]

4.5 MCGNDs in three different block sizes when $m \equiv 3 \pmod 4$, through i sets for k_1, one set for k_2, two for k_3

For the following cases, MCGNDs can be obtained in blocks of three different sizes through i sets for k_1, one set for k_2, two for k_3 derived from theorem 4.1.

(i) $v = 2k_1(i + 3) - 8$, $k_1 = 4l = k_2 + 1$, $k_3 = k_1 - 2$.

(ii) $v = 2k_1(i + 3) - 8$, $k_1 = 4l + 2 = k_2 + 1$, $k_3 = k_1 - 2$, i odd.

(iii) $v = 2k_1(i + 3) - 8$, k_1 (odd) > 3, $k_2 = k_1 - 1$, $k_3 = k_1 - 2$, $i \equiv 1 \pmod 4$.

(iv) $v = 2k_1(i + 3) - 12$, $k_1 = 4l + 2 = k_2 + 1$, $k_3 = k_1 - 3$, i even.

(v) $v = 2k_1(i + 3) - 12$, k_1 (odd) > 3, $k_1 = k_2 + 1$, $k_3 = k_1 - 3$, $i \equiv 3 \pmod 4$.

Example 4.5

Following sets generate minimal CGND for $v = 32$, $k_1 = 5$, $k_2 = 4$ and $k_3 = 3$ with $E_n = 0.85$.
S_1 = [3,5,9,14], S_2 = [7,8,11], S_3 = [10,20], S_4 = [13,15]

5. Minimal CGNDs for $m \equiv 0 \pmod 4$

Here, MCGNDs are generated for $m \pmod 4 \equiv 0$, where $m = \frac{v-2}{2}$.

Theorem 5.1

If $m \equiv 0 \pmod 4$, sets obtained from B = $[1, 2, \cdots, m]$ will produce proposed MCGNDs for:

- $v = 2ik + 2$.

- $v = 2ik_1 + 2u_1k_2 + 2$.

- $v = 2ik_1 + 2u_1k_2 + 2u_2k_3 + 2$, and so on.

Proof: Let
$$S = 1 + 2 + \cdots + m$$
$$= \frac{(m+1)m}{2}$$
$$= \frac{2(m+1)m}{4} = v.\frac{m}{4} \quad \text{Since} \quad v = 2(m+1)$$
$\frac{m}{4}$ will be integer for m $\equiv 0 \pmod 4$.
S $\pmod v \equiv 0$ if $\frac{m}{4}$ is integer. Hence proved.

5.1 MCGNDs in equal block sizes when $m \equiv 0 \pmod 4$

For the following cases, minimal CGNDs can be constructed in equal block sizes using i sets derived from theorem 5.1

(i) $v = 2ik + 2$, $k = 4l$, i, l integer and $m \equiv 0 \pmod 4$.

(ii) $v = 2ik + 2$, $k = 4l + 2$, i even, l integer and $m \equiv 0 \pmod 4$.

(iii) $v = 2ik + 2$, k (odd) > 3, $i \equiv 0 \pmod 4$ and $m \equiv 0 \pmod 4$.

Example 5.1

Following sets generate minimal CGND for $v = 18$ and $k = 4$ with $E_n = 0.88$.
S_1 = [3, 4, 5], S_2 = [1, 2, 7]

5.2 MCGNDs in two different block sizes when $m \equiv 0 \pmod 4$ through i sets for k_1 and one for k_2

For the following cases, minimal CGNDs can be constructed in two different block sizes from i sets for k_1 and one for k_2 derived from theorem 5.1.

(i) $v = 2k_1(i + 1)$, $k_1 \equiv 1 \pmod 4 = k_2 + 1$, $i \equiv 0 \pmod 4$.

(ii) $v = 2k_1(i + 1)$, $k_1 \equiv 3 \pmod 4 = k_2 + 1$, $i \equiv 2 \pmod 4$.

(iii) $v = 2k_1(i + 1) - 2$, $k_1 = 4l + 2 = k_2 + 2$, i even, l integer.

(iv) $v = 2k_1(i + 1) - 2$, $k_2 = k_1 - 2$, k_1 (odd) > 3, $i \equiv 1 \pmod 4$.

(v) $v = 2ik_1 + 8$, $k_1 \equiv 1 \pmod 4$, $k_2 = 3$, $i \equiv 1 \pmod 4$.

(vi) $v = 2ik_1 + 8$, $k_1 \equiv 3 \pmod 4$, $k_2 = 3$, $i \equiv 3 \pmod 4$.

(vii) $v = 2ik_1 + 10$, $k_1 = 4l$, $l > 1$, $k_2 = 4$, i integer.

(viii) $v = 2ik_1 + 10$, $k_1 = 4l + 2$, $k_2 = 4$, i even.

(ix) $v = 2ik_1 + 10$, k_1 (odd) > 3, $k_2 = 4$, $i \equiv 0 \pmod 4$.

(x) $v = 2ik_1 + 12$, $k_1 \equiv 1$ (mod 4), $k_2 = 5$, $i \equiv 3$ (mod 4).

(xi) $v = 2ik_1 + 12$, $k_1 \equiv 3$ (mod 4), $k_2 = 5$, $i \equiv 1$ (mod 4).

Example 5.2

Following sets generate MCGND for $v = 18$, $k_1 = 5$, $k_2 = 3$ with $E_n = 0.88$.

$$S_1 = [2,4,5,6], \qquad S_2 = [7,8]$$

5.3 MCGNDs in two different block sizes when $m \equiv 0$ (mod 4), through i sets for k_1 and two for k_2

For the following cases, minimal CGNDs can be constructed in two different block sizes from i sets for k_1, two for k_2 derived from theorem 5.1.

(i) $v = 2k_1(i + 2) - 2$, $k_1 = 4l + 2 = k_2 + 1$, i odd.

(ii) $v = 2k_1(i + 2) - 6$, $k_1 = 4l = k_2 + 2$, i & $l > 1$.

(iii) $v = 2k_1(i + 2) - 6$, $k_1 = 4l + 2 = k_2 + 2$, i even.

(iv) $v = 2k_1(i + 2) - 6$, $k_2 = k_1 - 2$, k_1 (odd) > 3, $i \equiv 2$ (mod 4).

(v) $v = 2k_1(i + 2) - 10$, $k_2 = k_1 - 3$, $k_1 = 4l + 2$, i odd.

(vi) $v = 2k_1(i + 2) - 10$, $k_2 = k_1 - 3$, k_1 (odd) > 3, $i \equiv 0$ (mod 4).

Example 5.3

Following sets generate MCGND for $v = 34$, $k_1 = 6$ and $k_2 = 5$ with $E_n = 0.90$.
$S_1 = [3,5,6,7,11]$, $S_2 = [4,8,9,12]$, $S_3 = [13,14,15,16]$

5.4 MCGNDs in three different block sizes when $m \equiv 0$ (mod 4), through i sets for k_1, one set for k_2 and one for k_3

For the following cases, MCGNDs can be obtained in blocks of three different sizes from i sets for k_1, one set for k_2, one for k_3 derived from theorem 5.1.

(i) $v = 2k_1(i + 2) - 4$, $k_1 \equiv 1$ (mod 4)$= k_2 + 1$, $k_3 = k_1 - 2$, $i \equiv 1$ (mod 4).

(ii) $v = 2k_1(i + 2) - 4$, $k_1 \equiv 3$ (mod 4)$= k_2 + 1$, $k_3 = k_1 - 2$, $i \equiv 3$ (mod 4).

(iii) $v = 2k_1(i + 2) - 6$, $k_1 = 4l$, $l > 4$, $k_2 = k_1 - 1$ & $k_3 = k_1 - 3$, i, l integer.

(iv) $v = 2k_1(i + 2) - 6$, $k_1 = k_2 + 1 = 4l + 2$, $k_3 = k_1 - 3$, i even.

(v) $v = 2k_1(i + 2) - 6$, $k_1 > 5$, $k_2 = k_1 - 1$ & $k_3 = k_1 - 3$, $i \equiv 2$ (mod 4).

(vi) $v = 2k_1(i + 2) - 8$, k_1 (mod 4) $\equiv 1$, $k_2 = k_1 - 2$, $k_3 = k_1 - 3$, $i \equiv 3$ (mod 4).

(vii) $v = 2k_1(i + 2) - 8$, k_1 (mod 4) $\equiv 3$, $k_2 = k_1 - 2$, $k_3 = k_1 - 3$, $i \equiv 1$ (mod 4).

(viii) $v = 2k_1(i + 2) + 6$, $k_1 = 4l + 2 = k_2 + 1$, $l > 1$, $k_3 = 3$, i even.

(ix) $v = 2k_1(i + 2) + 6$, $k_1 = k_2 + 1 > 5$, $k_3 = 3$, $i \equiv 1$ (mod 4).

(x) $v = 2k_1(i + 1) + 8$, $k_1 \equiv 1$ (mod 4)$= k_2 + 1$, $k_3 = 4$, $i \equiv 3$ (mod 4).

(xi) $v = 2k_1(i + 1) + 8$, $k_1 \equiv 3$ (mod 4)$= k_2 + 1$, $k_3 = 4$, $i \equiv 2$ (mod 4).

(xii) $v = 2k_1(i+1) + 10$, $k_1 = 4l$, $l > 1$, $k_2 = k_1 - 1$, $k_3 = 5$, i integer.

(xiii) $v = 2k_1(i+1) + 10$, $k_1 = k_2 + 1 = 4l + 2$, $k_3 = 5$, i odd.

(xiv) $v = 2k_1(i+1) + 10$, $k_1 = k_2 + 1 > 5$, $k_3 = 5$, $i \equiv 3 \pmod 4$.

(xv) $v = 2k_1(i+1) + 4$, $k_1 \equiv 1 \pmod 4$, $k_2 = k_1 - 2$, $k_3 = 3$, $i \equiv 2 \pmod 4$.

(xvi) $v = 2k_1(i+1) + 4$, $k_1 \equiv 3 \pmod 4$, $k_2 = k_1 - 2$, $k_3 = 3$, $i \equiv 2 \pmod 4$.

(xvii) $v = 2k_1(i+1) + 6$, $k_1 = k_2 + 2 = 4l + 2$, $k_3 = 4$, i even.

(xviii) $v = 2k_1(i+1) + 6$, $k_1 > 7$, $k_2 = k_1 - 2$, $k_3 = 4$, $i \equiv 1 \pmod 4$.

(xix) $v = 2k_1(i+1) + 8$, $k_1 \equiv 1 \pmod 4$, $k_2 = k_1 - 2$, $k_3 = 5$, $i \equiv 0 \pmod 4$.

(xx) $v = 2k_1(i+1) + 8$, $k_1 \equiv 3 \pmod 4$, $k_2 = k_1 - 2$, $k_3 = 5$, $i \equiv 2 \pmod 4$.

(xxi) $v = 2k_1(i+1) + 2$, $k_1 = 4l$, $l > 1$, $k_2 = k_1 - 3$, $k_3 = 3$, i integer.

(xxii) $v = 2k_1(i+1) + 2$, $k_1 = 4l + 2$, $l > 1$, $k_2 = k_1 - 3$, $k_3 = 3$, i odd.

(xxiii) $v = 2k_1(i+1) + 2$, $k_1 > 5$, $k_2 = k_1 - 3$, $k_3 = 3$, $i \equiv 3 \pmod 4$.

(xxiv) $v = 2k_1(i+1) + 4$, $k_1 \equiv 1 \pmod 4$, $k_2 = k_1 - 3$, $k_3 = 4$, $i \equiv 2 \pmod 4$.

(xxv) $v = 2k_1(i+1) + 4$, $k_1 \equiv 3 \pmod 4$, $k_2 = k_1 - 3$, $k_3 = 4$, $i \equiv 0 \pmod 4$.

(xxvi) $v = 2k_1(i+1) + 6$, $k_1 = 4l + 2 = k_2 + 3 > 5$, $k_3 = 5$, i even, l integer.

(xxvii) $v = 2k_1(i+1) + 6$, $k_1 > 5$, $k_2 = k_1 - 3$, $k_3 = 5$, $i \equiv 2 \pmod 4$.

Example 5.4

Following sets generate minimal CGND for $v = 26$, $k_1 = 5$, $k_2 = 4$ and $k_3 = 3$ with $E_n = 0.87$.
$S_1 = [3,5,7,9]$, $S_2 = [4,10,11]$, $S_3 = [8,12]$

5.5 MCGNDs in three different block sizes when $m \equiv 0 \pmod 4$, from i sets for k_1, one set for k_2 and two for k_3

For the following cases, MCGNDs can be obtained in blocks of three different sizes through i sets for k_1, one set for k_2 and two for k_3, derived from theorem 5.1.

(i) $v = 2k_1(i+3) - 8$, $k_1 \equiv 1 \pmod 4 = k_2 + 1$, $k_3 = k_1 - 2$, $i \equiv 2 \pmod 4$.

(ii) $v = 2k_1(i+3) - 8$, $k_1 \equiv 3 \pmod 4 = k_2 + 1$, $k_3 = k_1 - 2$, $i \equiv 0 \pmod 4$.

(iii) $v = 2k_1(i+3) - 12$, $k_1 \equiv 3 \pmod 4 = k_2 + 1$, $k_3 = k_1 - 3$, $i \equiv 2 \pmod 4$.

(iv) $v = 2k_1(i+3) - 14$, k_1 (odd) > 3, $k_2 = k_1 - 2$, $k_3 = k_1 - 3$, $i \equiv 1 \pmod 4$.

Example 5.5

Following sets generate minimal CGND for $v = 42$, $k_1 = 5$, $k_2 = 4$ and $k_3 = 3$ with $E_n = 0.88$.
$S_1 = [3,4,14,20]$, $S_2 = [7,8,9,12]$, $S_3 = [10,13,17]$, $S_4 = [15,16]$, $S_5 = [18,19]$

6. Discussion and conclusion

Neighbor effects may arise in experiments of serology for virus research and in agriculture experiments, due to nature of plots, etc. In the presence of neighbor effects, misleading conclusions may be drawn in the variety competition experiments. Minimal NBDs are available in literature to neutralize these effects economically for v odd.

To overcome this problem for v even, complete solution is given in this article to construct proposed MCGNDs. For v even, our proposed designs have been proved efficient mathematically and logically to reduce the bias due to neighbor effects, therefore, practitioners are recommended to implement these designs in their experiments where neighbor effects may arise. With the collaboration of practitioners in future research, author(s) will apply these designs on their relevant experiments and then give numerical results for further recommendations.

References

Ahmed, R., Akhtar, M., & **Tahir, M. H. (2009)**. Economical generalized neighbor designs of use in Serology. *Computational Statistics and Data Analysis*, **53**, 4584-4589.

Ahmed, R., & **Akhtar, M. (2011)**. Designs balanced for neighbor effects in circular blocks of size six. *Journal of Statistical Planning and Inference*, **141**, 687-691.

Akhtar, M., Ahmed, R., & **Yasmin, F. (2010)**. A catalogue of nearest neighbor balanced-designs in circular blocks of size five. *Pakistan Journal of Statistics*, **26**(2), 397-405.

Azais, J. M. (1987). Design of experiments for studying intergenotypic competition. *Journal of the Royal Statistical Society: Series B*, **49**, 334-345.

Azais, J. M., Bailey, R. A., & **Monod, H. (1993)**. A catalogue of efficient neighbor designs with border plots. *Biometrics*, **49**(4), 1252-61.

Cheng, C. S. (1983). Construction of optimal balanced incomplete block designs for correlated observations. *Annals of Statistics*, **11**, 240-246.

Hwang, F. K. (1973). Constructions for some classes of neighbor designs. *Annals of Statistics*, **1**(4), 786–790.

Iqbal, I. (1991). Construction of experimental design using cyclic shifts, Ph.D. Thesis, University of Kent at Canterbury, U. K.

Iqbal, I., Tahir, M. H., & **Ghazali, S. S. A. (2009)**. Circular neighbor-balanced designs using cyclic shifts. *Science in China Series A: Mathematics*, **52**(10), 2243–2256.

Iqbal, I., Tahir, M. H., Aggarwal, M. L., Ghazali, S. S. A., & **Ahmed, I. (2012)**. Generalized neighbor designs with block size 3. *Journal of Statistical Planning and Inference*, **142**, 626-632.

James, A. T., & **Wilkinson, G. N. (1971)**. Factorization of the residual operator and canonical decomposition of non-orthogonal factors in the analysis of variance. *Biometrika*, **58**, 258-294.

Kedia, R. G., & **Misra, B. L. (2008)**. On construction of generalized neighbor design of use in serology. *Statistics and Probability Letters*, **18**, 254-256.

Kunert, J. (2000). Randomization of neighbour balanced designs. *Biometrical Journal*, **42**(1), 111-118.

Langton, S. (1987). Avoiding edge effects in agroforestry experiments: The use of neighbour-balanced designs and guard areas. *Agroforestry Systems*, **12**, 173-185.

Misra, B. L., Bhagwandas, & **Nutan S. M. (1991)**. Families of neighbor designs and their analysis. *Communications in Statistics-Simulation and Computation*, **20**, 427-436.

Nutan, S. M. (2007). Families of proper generalized neighbor designs. *Journal of Statistical Planning and Inference*, **137**, 1681–1686.

Pearce, S. C., Calinski, T., & **Marshall,T. F. D. C. (1974)**. The basic contrasts of an experimental design with special reference to the analysis of data. *Biometrika*, **61**(3),449–60.

Rees, D. H. (1967). Some designs of use in serology. *Biometrics*, **23**, 779-791.

Shehzad, F., Zafaryab, M., & **Ahmed, R. (2011a)**. Minimal neighbor designs in circular blocks of unequal sizes. *Journal of Statistical Planning and Inference*, **141**, 3681-3685.

Shehzad, F., Zafaryab, M., & **Ahmed, R. (2011b)**. Some series of proper generalized neighbor designs. *Journal of Statistical Planning and Inference*, **141**, 3808-3818.

Tomar, J. S., Jaggi, S., & **Varghese, C. (2005)**. On totally balanced block designs for competition effects. *Journal of Applied Statistics*, **32**(1), 87-97.

Williams, R. M. (1952). Experimental designs for serially correlated observations. *Biometrika*, **39**, 151-167.

Zafaryab, M., Shehzad, F., & **Ahmed, R. (2010)**. Proper generalized neighbor designs in circular blocks. *Journal of Statistical Planning and Inference*, **140**, 3498-3504.

A novel deep neural network for hidden target detection in images

Rabeb Hendaoui *, Vasif Nabiyev

Dept. of Computer Engineering, Karadeniz Technical University, Turkey
*Corresponding author: rabeb@ktu.edu.tr

Abstract

The significant similarity between the hidden target and the background makes it difficult to find camouflaged people, such as warriors in warfare, or even camouflaged objects in natural environments. Hence, it is hard to ascertain these concealed targets. To address this issue, a novel deep neural network is proposed in this paper that produces an estimated mask within the hidden target for an input image. Our approach consists of two phases: hidden target segmentation and hidden target identification. For the first phase, we propose the Multilevel Attention Network (MA-Net), which generates the camouflaged target mask based on a Multi-Attention Module (MAM) that helps distinguish the hidden people from the background. Later on, the concealed target will be highlighted in the second phase. Experimental results on the camouflaged people dataset demonstrate that our proposed method can achieve state-of-the-art performance for hidden target detection.

Keywords: Concealed people; hidden target; neural network; target identification; target segmentation

1. Introduction

Computer vision applications have been well explored in the literature. In particular, many notable object detection methods (He *et al.*, 2017; Redmon *et al.*, 2016) have already been studied by various researchers.

At times, objects conceal their signatures and generate disguises in their surrounding environment. The presence of camouflage makes the identification of objects more difficult. Camouflage is the capacity of the prey to hide from predators by adjusting their pattern, texture, and coloration according to the background. This phenomenon was adopted by human beings and broadly utilized on the battlefield. Human vision systems cannot sufficiently recognize a hidden target. Certain animals have distinct biological capabilities that conceal them in their surroundings. The visual characteristics of a disguised object (like color/texture) resemble the background, making detecting procedures complicated. Hence, a camouflaged target cannot be identified by state-of-the-art methods for object detection. Consequently, the study of hidden target detection in the sector is required.

Owing to the complexity of the issue, less work has been suggested to detect camouflaged people. Existing studies (Pan *et al.*, 2011; Song & Geng, 2010; Bhajantri & Nagabhushan, 2006; Galun *et al.*, 2003; Tankus & Yeshurun, 2001) investigated the matter with low-level features. Generally, these methods use texture, brightness, color, and edge features to distinguish objects from backgrounds. Disguised target detection is not fully explored; most research is concerned with detecting the foreground region despite some parts of its texture being similar to that of the background. These techniques rely on hand-crafted characteristics and are effective in a limited number of situations where images have an essential and non-uniform backdrop. Additionally, their effectiveness in detecting and segmenting camouflage is poor when the foreground and background have a high degree of resemblance. Recently, a new camouflaged people detection has been proposed via a dense deconvolution network (Zheng *et al.*, 2018). The authors introduced a dense deconvolution network to fuse the extracted features in deep CNN. Then super-pixel

segmentation was applied in detection optimization. Within this context, using high-level features, we propose a new hidden target detection and demonstrate through experiments that it outperforms the state-of-the-art methods.

In summary, we present the following contributions: 1) We adopt an inception module to enhance the ability to excavate the interior of visual features and focus on feature representation, 2) We design a multi attention module that can compensate for the loss of perceptual details, emphasize hidden targets, and better identify small-scale disguised objects, 3) We evaluate our model and compare it with state-of-the-art methods. Results show that our approach performs favorably over all the others.

This paper proceeds as follows: Section 2 introduces the proposed framework. Section 3 outlines the experiments. In Section 4, we discuss the study's limitations. Lastly, we reach conclusions.

2. Proposed method

Hidden target detection is a fundamentally difficult task because the camouflage strategy works by misleading the observer's visual perceptual system. A substantial amount of visual perception information is necessary to remove the uncertainties produced by the substantial inherent similarities between the target and the background. As seen in the natural environment, predators and prey animals use camouflage to conceal their location and prevent bringing attention to themselves, making it harder to find them. Based on this observation, we were inspired to detect the disguised target through an attention mechanism to bring attentiveness and pay attention to the target. In the first phase, we aim at segmenting the hidden target where we implement an inception module to enhance the feature representation. Then we introduce a Multi-Attention Module to improve the detection of the ambiguous hidden target further from the background and generate finer details. In the second phase, we identify the concealed target based on the predicted mask.

In this section, we explain our proposed approach for hidden target detection. As shown in Figure 1, our method involves two steps: hidden target segmentation and hidden target extraction.
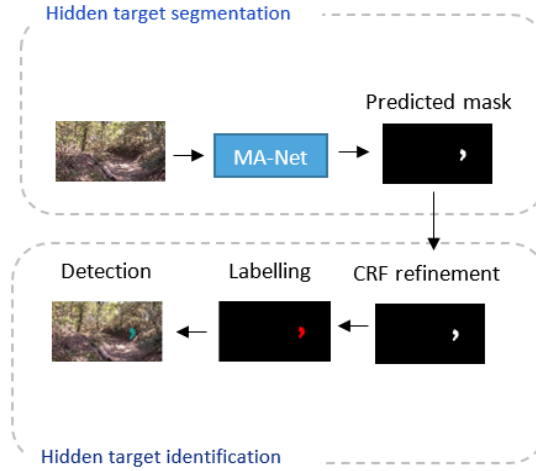
Fig. 1. Our overall framework for hidden target detection.

2.1 Hidden target segmentation

As shown in Figure 2, we propose the MA-Net model for hidden target segmentation. First, we extract features in a bottom-up way from the input images based on the ResNet (He *et al.*, 2016) backbone network. Then features are enhanced based on an inception module with multi-scale receptive fields. Furthermore, we fuse generated feature maps with multilevel semantic information in a top-down way. Finally, we employ the MAM for every level, and we combine the findings of the predictions from all layers for an outcome.
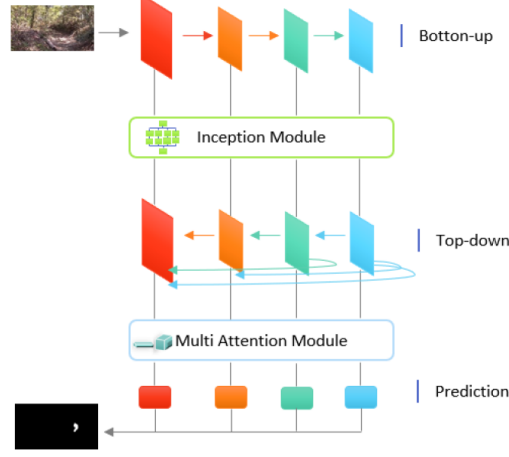
Fig. 2. The architecture of our proposed MA-Net Network.

2.1.1 CNN feature extraction and enhancement

To extract features from multiple levels, we employ ResNet (He *et al.*, 2016) as the backbone because of its fast convergence compared to VGG (Simonyan & Zisserman, 2015). ResNet-101 consists of 101 convolutional layers with five convolutional blocks, an average pooling layer, and one fully connected layer. We made some changes to it in order to adapt it to our camouflage target prediction task. First, the fully connected layers, which are built explicitly for classification tasks, are removed. The number of parameters is also considerably reduced as a result of this. Second, because the final feature map size of the original ResNet is 32 times less than the input, if we directly upsample on it, the results will be too coarse. To overcome this, in levels 4 and 5, we utilize dilated convolution (Chen *et al.*, 2016) which allows us to keep the same receptive field without lowering the size of the feature map or adding any additional parameters. As a result, the feature map size at these two levels is only eight times less than the input. The extracted features from different levels are fed into an inception module to enhance feature representation by extracting multi-scale receptive field features. As shown in Figure 3, the designed
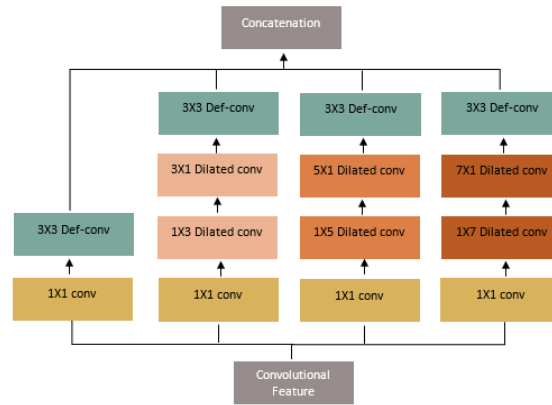
Fig. 3. Our inception module.

module consists of 4 branches with a 1 × 1 convolution at the beginning to reduce the number of channels. The outputted features from three branches go through 1 × y dilated convolution and then through y × 1 dilated convolution with a rate equal to 3. Here, y= 3, 5, and 7. In order to localize small and irregular objects, a deformable convolution (Dai *et al.*, 2017) layer is added at the end of each branch. The features from all branches will be concatenated, go through 1 × 1 convolution, and have a residual connection with input features for faster optimization. To encode more contextual information, we densely connect the features in a top-down way. High-level feature maps are reused multiple times to add more contextual

information to low levels.

2.1.2 Feature refinement and prediction

As in the natural environment, animals utilize camouflage to not draw attention to themselves; thereby, it is difficult to find them. Based on this fact, we constructed a MAM to better detect the disguised target from the background and create more delicate features to draw attention to this hidden target. Our suggested MAM highlights essential features in the image by disregarding less critical information. As illustrated in Figure 4, initially, a Pyramid Pooling Module (Zhao *et al.*, 2017) is applied to the
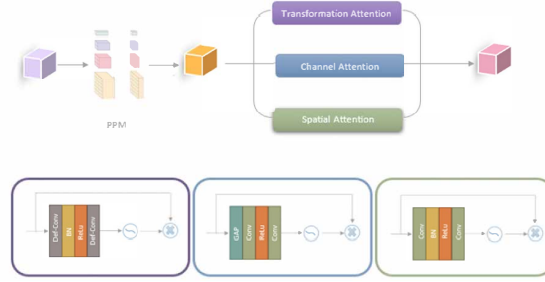
Fig. 4. Multi Attention Module.

input feature, and the output feature is used as an input feature for the MAM. This latter consists of three attention blocks: the Transformation attention block, the Channel Attention Block, and the Spatial Attention Block. The first block attempts to represent feature transformations by using deformable convolution (Dai *et al.*, 2017). It can improve the network's attention to foreground areas. The feature map is processed by a 3 × 3 deformable convolutional layer, followed by a normalization layer, ReLu, and a second 3 × 3 deformed convolutional layer. The channel attention block highlights the camouflaged target and reduces the inaccuracies caused by duplicated channel features. The feature map is re-allocated using two 1 × 1 convolutions and a global pooling operation. This global attention map explicitly makes the positions of the hidden objects known on feature maps. The spatial attention block attempts to investigate where to concentrate on a feature map more. The spatial attention module is used as a complement to the channel attention module to produce efficient features. Finally, the refined features from all the blocks are concatenated into a final attention map.

2.2 Hidden target identification

In order to make the extracted camouflaged objects more accurate, we use the Dense CRF (Krähenbühl & Koltun, 2011) method to refine the camouflaged target contours. A conditional random field (CRF) is a probabilistic graph modeled by a Gibbs distribution as follows:

$$P\left(X \mid Q\right) = \frac{1}{Z\left(Q\right)} \exp\left(-E\left(X \mid Q\right)\right) \tag{1}$$

where Q is the global observation (image), $Z\left(Q\right)$ is the normalization factor, and E(X) denotes the Gibbs energy. In Dense CRF, the energy function is defined as:

$$E\left(X\right) = i\sum \psi_u\left(x_i\right) + i < j\sum \psi_p(x_i, x_j) \tag{2}$$

where x_i and x_j denote the vertices of CRF, ψ_u is the unary potential, and ψ_p is the pairwise potential. The unary potential is calculated based on the predicted segmentation map while the pairwise potential $\psi_p\left(x_i\right)$ is given by:

$$\psi_p\left(x_i, x_j\right) = \mu\left(x_i, x_j\right) m\sum w^{(m)} k^{(m)}(f_i, f_j) \tag{3}$$

where $\mu\left(x_i, x_j\right) = 1$ if $x_i \neq x_j$ and equal to 0 otherwise. f_i and f_j are feature vectors. Specifically, the kernel k is defined as:

$$w_1 \exp\left(\frac{-|p_i - p_j|^2}{2\sigma_\alpha^2} - \frac{|q_i - q_j|^2}{2\sigma_\beta^2}\right) + w_2 \exp\left(-\frac{|p_i - p_j|^2}{2\sigma_\gamma^2}\right) \tag{4}$$

where p_i, indicate the pixel's location, q_i, q_j the pixel's spectral features. σ_α, σ_β, and σ_γ are three key hyper-parameters controlling the degree of connectivity and similarity.

After the camouflaged map is refined, the connected components are decided to identify each object in the image. The corresponding bounding box for each connected component is then computed. Figure 5 demonstrates the final target detection results of our proposed approach.

Fig. 5. Some examples of target detection results of our proposed approach. Image (row 1), GT (row 2), labeled image from our segmentation mask (row 3), and final detection (row 4).

3. Experiments

3.1 Dataset

To evaluate our method, we used the camouflaged people dataset (Zheng *et al.*, 2018). It contains 1000 images of size 480×854, including camouflaged people with ten different kinds of camouflage patterns like Arid Fleck, Desert, and different scenes like woodlands and snowfields. From the dataset,

Fig. 6. A few examples from the Camouflaged People Dataset with corresponding ground truth labels.

80% of images are randomly selected for training, and the remaining 20% are used for testing. We apply data augmentation to the selected training images. Mirror reflection and rotation techniques were used.

3.2 Implementation Details

Our model is implemented based on the Caffe framework (Jia *et al.*, 2014), using GPU Nvidia GTX 1080. A stochastic gradient descent optimization (SGD) algorithm was used for training with a momentum value of 0.9 and a weight decay of 0.0005. We set the base learning rate to 1e-10 with a mini-batch size of one. After $20K$ iterations, we stopped the training.

3.3 Evaluation Metrics

In our experiments, we use the following evaluation metrics: Mean Absolute Error (MAE) (Perazzi *et al.*, 2012) , F-Measure (Achanta *et al.*, 2009), E-measure (Fan *et al.*, 2018) and Structure Measure (S-Measure) (Fan *et al.*, 2017), which are explained below.

MAE: is a metric to directly calculate the average absolute error between the prediction maps S and the corresponding ground truth maps G. The formula is as follows:

$$MAE = \frac{1}{H \times W} Wx = 1\sum Hy = 1\sum |S(x,y) - G(x,y)| \tag{5}$$

where W and H are the width and height of the input image. In general, a lower MAE indicates a better result.

F-measure: is defined as the weighted harmonic mean of recall and precision metrics, with an anon negative weight of β. The F-measure is defined as:

$$F_\beta = \frac{(1 + \beta^2)\ Precision \times Recall}{\beta^2 Precision + Recall} \tag{6}$$

where we set β^2 to a fixed value of 0.3 as suggested in (Achanta *et al.*, 2009) to emphasize precision over recall. Note that, unlike MAE, a higher F_β indicates a better performance.

E-measure: is a perceptual-inspired criterion and is defined as:

$$E = \frac{1}{H \times W} Wx = 1\sum Hy = 1\sum \phi_{FM}(x, y) \tag{7}$$

in which ϕ_{FM} is an enhanced alignment matrix. The greater the E Score, the better the performance.

S-measure: is to measure the structural similarity between the predicted map and the ground-truth map.

$$S_\alpha = (1 - \alpha)S_o + \alpha S_r \tag{8}$$

in which S_r indicates the region-aware structural similarity and S_o denotes the object-aware structural similarity. As suggested in (Fan *et al.*, 2017) , we set $\alpha = 0.5$. Note that the higher the S-measure score, the better the model performs. The significantly larger the S-score, the better the model is.

3.4 Ablation Study

To investigate the impact of the different modules in our method, we conducted an ablation study. The experiment selects ResNet-101 as the baseline (B). Then we add the Inception Module (IM), Transformation Attention Module (TAM), Chanel Attention Module (CAM), and Spatial Attention Module (SAM) into the network in turn. As shown in Table 1, with the addition of modules, the test performance gradually improves. All these modules boost the model performance. When these modules are combined, we can get the best results. It demonstrates that all components are necessary for the proposed framework.

Table 1. Component analysis. Note that a lower MAE and higher F, S, and E correspond to better results.

Settings	MAE	F	E	S
B	0.01	0.847	0.954	0.922
B + IM	0.008	0.853	0.967	0.930
B + IM + TAM	0.006	0.854	0.969	0.933
B + IM + TAM + CAM	0.005	0.856	0.972	0.934
B+ IM + TAM + CAM + SAM	0.004	0.859	0.974	0.937

3.5 Baseline Models

We select deep learning baseline models according to different categories such as edge, FCN, and high-resolution-based techniques. The chosen models are as follows:
- HDFN (Zhang *et al.*, 2019) utilizes a densely hierarchical feature fusion network that predicts the most critical area and segments the associated objects.
- AFNet (Feng *et al.*, 2019) predicts salient objects with entire structures and exquisite boundaries.
- HRSOD (Zeng *et al.*, 2019) leverages global semantic information and local high-resolution details to detect salient objects accurately in high-resolution images.
- SFCN (Zhang *et al.*, 2018) uses asymmetrical FCN to learn complementary visual features under the guidance of lossless feature reflection.

- Amulet (Zhang *et al.*, 2017) aggregates multi-level features into multiple resolutions.
- UCF (Zhang *et al.*, 2017) uses an encoder-decoder architecture to produce finer-resolution predictions. It learns uncertainty through a reformulated dropout in the decoder and avoids artifacts using a hybrid up-sampling scheme.

3.6 Comparison

We compared our model to DDCN (Zheng *et al.*, 2018), a technique for detecting camouflaged people, as well as to other state-of-the-art deep learning detection approaches, including Amulet (Zhang *et al.*, 2017), UCF (Zhang *et al.*, 2017), SFCN (Zhang *et al.*, 2018), HDFN (Zhang *et al.*, 2019), HRSOD (Zeng *et al.*, 2019) and AFNet (Feng *et al.*, 2019). Table 2 shows the comparison results of all methods on the four evaluation metrics. Obviously, our method outperforms competing approaches with a large margin across all the evaluation metrics, which demonstrates the superiority of the proposed model. Compared with the state-of-the-art method DDCN, our method improves F-measure and E-measure by 3.9% and 3.2%, respectively. Also, our model significantly lowers the MAE scores. This indicates that our model is more convinced of the predicted target regions and provides more accurate mask maps. S-measure, the most recent evaluation measure, has been used to emphasize the deficiencies of traditional evaluation metrics. When mask maps are evaluated, conventional metrics use pixels, which provide inadequate overall structural information. In the present study, our model still maintains the outstanding S-measure performance with an improvement of 6.5%. All quantitative results show that our model yields improved performance.

Table 2. Quantitative results on camouflaged people dataset. The best two scores are shown in red and blue colors, respectively.

Model	F	MAE	E	S
Amulet	0.349	0.081	0.587	0.630
UCF	0.254	0.168	0.497	0.589
SFCN	0.303	0.130	0.528	0.617
HDFN	0.313	0.140	0.534	0.618
HRSOD	0.489	0.018	0.741	0.690
AFNet	0.451	0.020	0.715	0.728
DDCN	0.820	0.007	0.942	0.872
Ours	0.859	0.004	0.974	0.937

In order to more intuitively illustrate the advantages of the proposed method, we visualize the prediction results of our network with DDCN in different scenarios. As shown in Figure 7, we observe that the proposed method highlights the hidden target completer and is more precise compared to DDCN. It excels in dealing with various challenging scenarios, different scales, and postures of people (rows 1 and 3), small objects (row3), occlusion (rows 2 and 4), and also accurately locating hidden targets (rows 5 and 6). From this comparison, the segmentation maps produced by our method are sharper and more accurate. Our model consistently outperforms DDCN. This can also illustrate the effectiveness of the proposed approach.

4. Discussion

It is noteworthy that disguised target detection is more complicated than salient object detection. The goal of salient object predictors is to identify and segment prominent features in images. To segment salient objects, we just need to focus on detecting such remarkable and discriminative areas. On the other hand, hidden targets fuse too much with their surroundings. It becomes even more difficult to discriminate between them from the background. The boundaries of the concealed target are therefore challenging to detect.
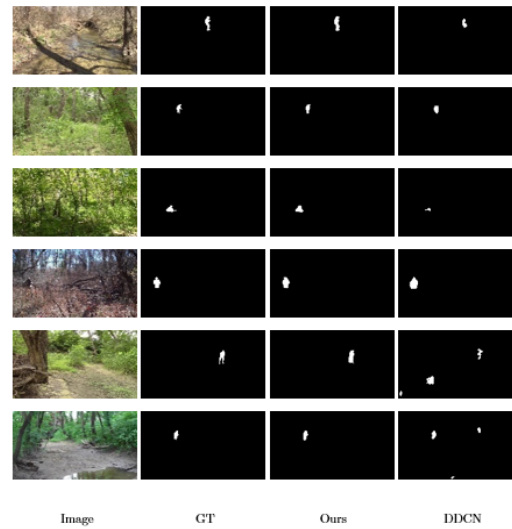
Fig. 7. Qualitative visual comparison of segmentation masks of our proposed model and DDCN.

There are two significant limitations in this study that could be addressed in future research. First, the study focused on evaluating the model on a single dataset. This is because the problem of hidden target detection is not well explored in the literature. The lack of diverse datasets remains the main issue. Thus, to promote advancements in hidden target detection and its evaluation, we aim to build a new, more challenging dataset for future work. Second, through the experimental evaluation and visual observation of the segmentation results, we found that not all the mask results of the images are satisfactory, and the segmentation results of some scenes are still deficient. Therefore, in future work, we plan to enhance the network for better detection.

5. Conclusion

In this paper, we have proposed a novel hidden target detection network that segments and effectively identifies the concealed target for accurate detection. Our model first extracts and enhances the features via enlarging receptive fields with different kernels. Then the multi-attention module is used to differentiate the disguised target from the background even more. Finally, based on the predicted mask result, the hidden target is identified. Experiments on the camouflaged people dataset demonstrate that our model is an effective detection model and outperforms state-of-the-art methods both qualitatively and quantitatively.

References

Achanta, R., Hemami, S., Estrada, F. & **Susstrunk, S. (2009).** Frequency-tuned salient region detection. In: Conference on Computer Vision and Pattern Recognition,1597–1604.

Bhajantri, N.U. & **Nagabhushan, P. (2006).** Camouflage Defect Identification: A Novel Approach. In Proc. International Conference on Information Technology, 145-148.

Chen, L., Papandreou, G., Kokkinos, I., Murphy, K. & **Yuille, A.L. (2016).** Deeplab: Semantic image segmentation with deep convolutional nets, atrous convolution, and fully connected CRFs. IEEE Transactions on Pattern Analysis and Machine Intelligence.

Dai, J., Qi, H., Xiong Y. ,Li Y. , Zhang, G., Hu, H. & **Wei, Y. (2017).** Deformable convolutional networks. International Conference on Computer Vision.

Fan, D.-P.,Cheng, M.-M., Liu, Y., Li, T. & **Borji, A. (2017).** Structure-measure: a new way to evaluate foreground maps. IEEE International Conference on Computer Vision, 4558–4567.

Fan, D.-P., Gong, C., Cao, Y., Ren, B., Cheng, M.-M. & Borji, A. (2018). Enhanced-alignment measure for binary foreground map evaluation. Proceedings of the Twenty-Ninth International Joint Conference on Artificial Intelligence, 698–704.

Feng M., Lu H. & Ding, E. (2019). Attentive feedback network for boundary-aware salient object detection. IEEE Conference on Computer Vision and Pattern Recognition, 1623–1632.

Galun, M., Sharon, E., Basri, R. & **Brandt A. (2003).** Texture segmentation by multiscale aggregation of filter responses and shape elements. International Conference on Computer Vision, 716–723.

He, k., Gkioxari, G., Dollár, P. & **Girshick, R. B. (2017).** Mask R-CNN. IEEE International Conference on Computer Vision (ICCV).

He, K., Zhang, X., Ren, S. & **Sun, J. (2016).** Deep residual learning for image recognition. IEEE Conference on Computer Vision and Pattern Recognition, 770–778.

Jia, Y., Shelhamer, E., Donahue, J., Karayev, S., Long, J., Girshick, R., Guadarrama,S. & **Darrell, T.(2014).** Caffe: Convolutional architecture for fast feature embedding. ACM international conference on Multimedia, 675–678.

Krähenbühl, P. & **Koltun,V. (2011).** Efficient inference in fully connected crfs with gaussian edge potentials. Advances in neural information processing systems, 109–117.

Pan,Y., Chen,Y., Fu, Q., Zhang, P. & **Xu, X. (2011).** Study on the camouflaged target detection method based on 3d convexity. Mod. Appl. Sci. 5 (152).

Perazzi, F., Krähenbühl, P., Pritch, Y. & **Hornung, A. (2012).** Saliency filters: Contrast based filtering for salient region detection. IEEE conference on computer vision and pattern recognition, 733–740.

Redmon, J., Divvala, S., Girshick R. & **Farhadi, A. (2016).** You Only Look Once: Unified, Real-Time Object Detection. IEEE Conference on Computer Vision and Pattern Recognition (CVPR).

Simonyan, K. & **Zisserman, A. (2015).** Very deep convolutional networks for large-scale image recognition. International Conference on Learning Representations.

Song, L. & **Geng, W. (2010).** A New Camouflage Texture Evaluation Method Based on WSSIM and Nature Image Features. In Proc. International Conference on Multimedia Technology, 1-4.

Tankus, A. & **Yeshurun, Y. (2001).** Convexity-Based Visual Camouflage Breaking. Computer Vision and Image Understanding, 82(3),208-237.

Zeng, Y., Zhang, P., Zhang, J., Lin, Z. & **Lu, H. (2019).** Towards High-Resolution Salient Object Detection. IEEE International Conference Computer Vision, 7234–7243.

Zhang, P., Liu, W.,Lei, Y. & **Lu, H. (2019).** Hyperfusion-Net: Hyper-densely reflective feature fusion for salient object detection. Pattern Recognition, 521-533.

Zhang, P., Liu, W., Lu, H. & **Shen, C. (2018).** Salient object detection by lossless feature reflection. International Joint Conference on Artificial Intelligence, 1–8.

Zhang, P., Wang, D., Lu, H., Wang, H. & **Ruan, X. (2017).** Amulet: Aggregating Multi-Level Convolutional Features for Salient Object Detection. IEEE International Conference on Computer Vision.

Zhang, P., Wang, D., Lu, H., Wang, H. & **Yin, B. (2017).** Learning Uncertain Convolutional Features for Accurate Saliency Detection. IEEE International Conference on Computer Vision.

Zhao, H., Shi, J., Qi, X., Wang, X. & **Jia, J.(2017).** Pyramid scene parsing network. IEEE Conference on Computer Vision and Pattern Recognition, 2881–2890.

Zheng, Y., Zhang, X., Wang, F., Cao, T. & **Sun, M. (2018).** Detection of People with Camouflage Pattern Via Dense Deconvolution Network. IEEE Signal Processing Letters, 14(8), 29-33.

Prognostics-aware multi-robot route planning to extend the lifetime

Uğur Yayan[1,*], Ahmet Yazıcı[2], İnci Sarıçiçek[3]

[1]*Dept. of Software Engineering, Eskisehir Osmangazi University, Eskisehir, Turkey*
[2]*Dept. of Computer Engineering, Eskisehir Osmangazi University, Eskisehir, Turkey*
[3]*Dept. of Industrial Engineering, Eskisehir Osmangazi University, Eskisehir, Turkey*
*Corresponding author: ugur.yayan@ogu.edu.tr

Abstract

In the transition to Industry 4.0, manufacturing systems need more intelligent devices that are capable of automation. Prognostic-aware robotic systems are one of the key components of automation in manufacturing. Furthermore, prognostics-aware route planning is essential for the success of multi-robot teams during long-term and uninterrupted operations, while also extending robot lifetime and reducing maintenance costs. In this study, a Prognostics-aware Multi-Robot Route Planning (P-MRRP) algorithm is proposed for extending the lifetime of the robot team. In the P-MRRP algorithm, first, routes are obtained from the Route Set Construction algorithm, and the most reliable set of routes is selected by calculating the Probability of Route Completion (PoRC) according to the reliability of the robot team. The proposed algorithm also considers the effect of load on robots during the route. In this study, the reliability of the robot is updated considering the travelled distances and loads of the robot between pickup and delivery nodes. The results of the P-MRRP algorithm are compared with the results of classical MRRP, which reveals that the lifetime of a mobile robot team can be extended using the P-MRRP algorithm.

Keywords: Lifetime extension; performance evaluation; prognostics-aware multi-robot route planning; reliability; remaining useful life.

1. Introduction

Autonomous robots are useful instruments that can overcome the physical inadequacies of humans and perform monotonous and high-precision repetitive manufacturing tasks in smart factories (Kapanoglu *et al.,* 2012). Smart factories will require more autonomous capabilities with the progress of Industry 4.0 (Oztemel & Gursev, 2020). Long-term repetitive operations performed by a team of autonomous robots require further development of automation capabilities in intelligent manufacturing systems (Villani *et al.,* 2018). Factory level autonomy with robot health management is necessary for intelligent manufacturing with almost no human intervention, which provides reduced maintenance costs, enhanced safety for humans, uninterrupted operations and more (Hossain & Muhammad, 2016). Enhanced autonomy can be achieved by considering the reliability (i.e., remaining useful life) (Kishorilal & Mukhopadhyay, 2018) of the autonomous robots during route planning. Reliability is an important metric for reducing the risk of failures for the team of robots.

The Prognostics-aware Multi-Robot Route Planning (P-MRRP) algorithm can be used to increase the lifetime of the mobile robot teams by considering reliability. Prognostics-aware planning aims to integrate the prognostics health information and the knowledge about the future operating conditions into the process of selecting subsequent actions for the system. Prognostics information can be used to predict the reliability of the system, and thus, promote the efficiency and lifetime of autonomous

operations (Shah *et al.,* 2020). Estimation of the reliability has been conducted to suppress the possible faults of robotic systems and increase their success (Hossain & Muhammad, 2016).

In the literature, there are a few route planning studies for single mobile robotic systems that focus on increasing the lifetime or health management of the system. Mimlitz *et al.* (Mimlitz *et al.,* 2016) present a Goal-Oriented, Risk Attitude-Driven Reward Optimization (GORADRO) method that increases lifetime efficiency. GORADRO uses the local area and internal prognostics and health management (PHM) information to determine system health and potential localized risks for planning routes. LeSage and Longoria (LeSage & Longoria, 2015) measure the single mission feasibility for the mobile robotic system and present a sequential method for forecasting the mission feasibility for the mobile robotic system operating in risky environments. The method makes use of the marginal predictions required to permit Bayesian correlation estimation and improved process characterization. On the other hand, newly developed robots utilize health diagnostics for detecting possible faults inside the robot. In one study (Balaban *et al.,* 2013), a mobile robot platform is developed specifically for testing in failure scenarios. Different failure modes are examined for electrical, mechanical, and power subsystems of the mobile robot. In addition to the mobile robot, a software simulator has been developed for the validation of Prognostics-enabled Decision-making (PDM) algorithms. In another study (Sweet *et al.,* 2014), the hardware platform is designed to inject the predefined failure modes to the mobile robot's electrical power subsystem. The PDM algorithms were adapted to the hardware platform, including the development of a new route planner that replans the route based on faults in the mobile robot.

The previous studies typically consider a single-robot planning problem. However, a multi-robot route planning system appears to be more effective and adaptive to accomplish various complex tasks (Arai *et al.,* 2002). There are a few studies regarding the performance of the system that is required for the given mission. One study presents the Active Mission Success Estimation algorithm, which estimates real-time risks during a space mission by functional modelling and risk analysis techniques based on PHM information (Short *et al.,* 2018). The ASME algorithm provides a quick and effective estimation of current mission success, and projections of possible total mission success based on potential decisions. Another report proposes a method for developing safety indicators for the missions of Autonomous Marine Systems (AMS) (Thieme & Utne, 2017). The results of safety indicators reflect safety in the AMS mission and can help in planning. Additionally, a mission execution decision-making approach is proposed based on the correlation between mission requirements and the health of the system (Geng *et al.,* 2016). This approach transforms the inherent health into mission health and conducts correlation analysis, which provides quantitative implications for decision-making during the given mission. However, there is no study that measures the performance of the robot team for the given mission. In a study among the first few articles on MRRP considering the reliability of the robot team, the Route Set Construction (RSC) and Route Set Analysis (RAS) algorithms are proposed (Yayan & Yazici, 2019). The RSC algorithm is responsible for constructing route sets, and the RAS algorithm analyses route sets while considering the reliability and PoRC for each route set. Although the effect of the robot reliabilities on planned routes are shown, route planning and lifetime analysis are not given for extending the lifetime.

In the current study, a Prognostics-aware Multi-Robot Route Planning (P-MRRP) algorithm is proposed for increasing the number of completed tasks during the lifetime of the robot team. In route planning of the robot team, the Vehicle Routing Problem with Backhauls (VRPB) (Deif & Bodin, 1984, Koç & Laporte, 2018), which is one of the most common problems for in-plant logistics of autonomous vehicles, is considered. Routes are obtained using the Simulated Annealing (SA) algorithm (Van Laarhoven & Aarts, 1987) for the minimum distance objective function and minimum energy objective function. Furthermore, routes are generated for various load combinations of robots in the team. Thus, the proposed P-MRRP algorithm is analysed considering the effect of load. Moreover, the Prognostics-aware Lifetime Analysis (PLA) algorithm is proposed to analyse the lifetime extension of P-MRRP and classical MRRP algorithm for both the loaded and unloaded cases. The PoRC is calculated for each route on the route set, and the most reliable route set is selected. The hazard rate of components and the initial reliability of the robots are used in PoRC calculations. The results showed that the number

of routes during the lifetime of the robot team is increased using the proposed P-MRRP algorithm. To the best of our knowledge, there are no previous reports that utilize prognostics-aware MRRP to increase the lifetime of a robot team by considering the loads of robots during tasks.

Definitions and preliminary descriptions are given in the following section. The P-MRRP algorithm is introduced in the third section, and the test results are given in the fourth section. The last section includes the conclusion and future works.

2. Definitions and preliminaries

The lifetime of the robot team may be increased if the team can know the health status of each robot and make task assignment decisions accordingly. Thus, it is necessary to consider the effects of reliability on the decision-making results in sustainable autonomous operations for the robot team (Fudzin & Majid, 2015). System Health Management (SHM) of a robot depends on prognostics technology and can be supported by diagnostics and health-based planning for a fully autonomous system. In the context of SHM, the end-of-life, availability, and reliability of systems and components can be predicted (Okoh *et al.,* 2014).

Prognostics are the data that forecast when a component or system doesn't satisfy desired operations. Using this prognostics knowledge, the system can make more appropriate decisions, like changing the component before it fails, prolonging component life by load reduction or task switching, and optimally plan or replan a route. In this study, the reliability is used for informing the P-MRRP problem. The PoRC is calculated considering the reliability value of each robot in the team.

Reliability is the probability that a piece of equipment operating under specified conditions can perform satisfactorily for a given period (Dhillon, 2015). The reliability takes values between 0 and 1. Reliability models involve descriptions of how the hazard rate changes over time. The exponential distribution model, with only one unknown parameter, is the simplest and most common model. Additionally, the exponential model exhibits a constant failure rate property. Due to this property, the exponential model is the perfect model for most of the components and systems that are used. Therefore, in this study, an exponential distribution alias bathtub curve is used as a reliability model for analysis. The bathtub curve has three distinct regions such as the infant mortality, useful life, and wear-out phases. There are formulations required in the analysis of a robotic system's reliability, which are shown below.

Mobile robots have many critical modules and components, including communication, sensor, battery, and mobility components. These components are used for the reliability estimation of mobile robots. The reliability of the whole system is analysed with its components. First, all components' reliabilities are calculated separately. Then, the reliability of the system is calculated as a combination of all components' reliability. For the calculation of reliability G and hazard rate of components, the usage time of components t and system architecture (series or parallel) must be known. It is assumed that the whole robot has a series configuration and constant hazard rate ht (failure/hour) according to the reliability model, which is based on the bathtub curve model for unloaded cases.

Equation (1) and (2) for $G_k(t)$, $k=1...m$ shows how a robot reliability is calculated in the series configuration. The reliability of a robot in a robot team can be calculated using the following Equation (1). In Equation (1), t denotes usage time, and λ denotes the hazard rate of the robot, which is equal to the summation of the hazard rates of each component.

$$G_k(t) = e^{-\lambda t} \tag{1}$$

The hazard rate of a robot with multiple components can be calculated according to Equation (2).

$$\lambda = \sum_{q=1}^{c} \lambda_q \tag{2}$$

Notably, it is assumed that each component in a robot is assumed to be in a series configuration. On the other hand, if there are multiple robots in a team, then the reliability of a robot team can be calculated using Equation (3).

$$G_s(t) = G_1(t)G_2(t).....G_c(t) = \prod_{q=1}^{c} G_k(t) \tag{3}$$

$G_s(t)$ denotes robot team reliability, which is equal to the product of each robot's reliabilities in Equation (3). In this study, reliability is updated using Equation (4).

$$G_{s\_new} = G_{s\_old}e^{-\lambda t} \tag{4}$$

G_{s_new} denotes updated reliability, G_{s_old} denotes the reliability of previous situation, and the rest of the formula is necessary to calculate new reliability values G_{s_new} according to the usage time t and hazard rate λ.

Moreover, we are dealing with the mobility component of the mobile robot and we are calculating the reliability of the robot using the hazard rate of the mobility component. The hazard rate depends on several conditions, and one of them is the load on the bearing in the mobility component. In this study, we analyse the effects of load on the reliability of the mobility component by estimating the reliability of the bearings (Medjaher *et al.,* 2012). Bearings are the most critical sub-component of the mobility system in the mobile robot. In this study, the customized hazard rate is used for estimating the reliability of the bearing in the robot's mobility module. Although the reliability estimation of the bearing with a constant initial hazard rate is assumed for robots in every route analysis, the hazard rate changes according to the load and returns to the initial value. The relationship between the hazard rate and the load is shown in Equation (5). In this study, the robot's utilize ball bearings. In the literature, when ball bearings are used, the power should be selected as "3" in Equation (5) (Shanker & Kumar, 2020):

$$\lambda_{load} = \lambda_0 (\frac{P}{P_0})^3 \tag{5}$$

In Equation (5), λ_0 denotes the initial hazard rate, and λ_{load} denotes the hazard rate that occurs when the robot is loaded. *P* indicates the load carried by the robot, and P_0 indicates the robot's load capacity. Equations (5) and (6) are used for analysing the load effect on the robot's reliability.

$$G_{s\_new} = G_{s\_old}e^{-\lambda_{load}t} \tag{6}$$

In Equation (7), G_s and d_{total} are the reliability of robot team and total distance traversed by the robot team for a given route, respectively. In this study, the time is assumed to be proportional to the travelled distance. The PoRC for all tasks $PoRC_s$ for the robot team is calculated using Equation (7).

$$PoRC_s = G_{s\_new}{}^{d_{total}} \tag{7}$$

Reliability of robotic systems can be analysed in terms of the components of the systems. According to the literature, Equation (1) can be used for the calculation of the hazard rate of any robot or component, and then the robot's reliability can be calculated using Equation (2). The reliability of the robot team can be calculated using Equation (3). Overall, the reliability of the robot team can be updated using Equation (4). If the effect of carrying a load is considered, then the reliability of the robot team could be updated using Equations (5) and (6). Equation (7) can be used for the calculation of PoRC for any given mission.

3. Proposed Prognostics-aware multi-robot route planning algorithm

In the factories, the transportation of all materials, parts, and finished products by robots are usually repeated actions. Transportation of empty vehicles is called deadheading, and the corresponding distance is denoted by deadhead distances (meters), which can be translated to an increase in cost. To reduce the deadheading, after delivery activities, the vehicle visits the pickup points and picks up finished products at these points to transport them to the depot. This process is called backhauling (Dolgui & Proth, 2010). For this type of repetitive task, P-MRRP becomes particularly useful. Although there are various studies in this area, reliability-based multi-robot route planning is not considered in the literature, as mentioned before. The proposed P-MRRP algorithm focuses on extending the lifetime of the robot

team by considering the reliability and loads of the robots. In this study, the reliability of the robot is updated considering both the travelled distances for the assigned route and the load of the robot between pickup and delivery nodes. Moreover, the lifetime extension of the robot team can be analysed using the proposed PLA algorithm. In the following subsections, the proposed P-MRRP algorithm and its sub-algorithms are discussed. The route planning algorithm (SA) is used to construct the route sets for pickup and delivery (P/D) problems. The PLA is used to analyse the lifetime of the robot team while considering the PoRC value.

3.1 Proposed prognostics-aware multi-robot route planning algorithm

P-MRRP algorithm is proposed to increase the number of completed tasks during the lifetime of the robot team. P-MRRP algorithm could be used with any route planning algorithm and could help to solve any vehicle routing problem considering the lifetime extension of the robot team. In this case study, the SA algorithm is used for RSC as given in Section 3.2. Steps of the P-MRRP algorithm are given in Algorithm 1.

It is assumed that the robots know positions of nodes x_i, y_i, $i=1,\ldots,n$, required time to complete task at nodes $t_i, i = 1,\ldots,n$, weight of loads at nodes w_i, $i=1,\ldots,n$, relative distances d_{ij} between nodes, and connections of the nodes. And robot positions x_k, y_k, $k=1,\ldots,m$, initial reliability G_k, $k=1,\ldots,m$ of each robot, hazard rates of components λ_q, $q=1...c$, nominal load capacity P_k, $k=1...m$, nominal speed S_k, $k=1...m$, virtual capacity V_{k_cap} have been known in advance. E_{ij} indicates consumption of energy for the travelling from node i to node j, and E_i, $for\ i=1,\ldots,n$, indicates required energy in performing its task at the specified node. Robots R_k, $k=1,\ldots,m$ have limited capacity of E_{k_cap}, $k=1,\ldots,m$, according to route plannig algorithm for constructing all the possible route combinations of robot team and case study environment.

Algorithm 1. Prognostics-aware Multi-Robot Route Planning (P-MRRP) Algorithm.

Initialization Phase:
Step 1;Get all the information about environment and robots n, (x_i, y_i), d_{ij}, t_i, w_i, E_i; *for $i \neq j$ and $i, j = 1, \ldots, n, m$*, (x_k, y_k), E_{k_cap}; *for $k = 1, \ldots, m$*, ΔV_{cap}, update distance matrix D,
Step 2;Run route planner algorithm for the robot team using pre-determined virtual capacities $V_{k\_cap} \in V_{cap}$ *for $k = 1, \ldots, m$*, and save each constructed tour R_{k_tour} and total traversed distances d_{k_total} to the route set H.

Main Phase:
Step 1;Set $r = 1$
Step 2;Get initial reliability of robots G_k *for $k = 1, \ldots, m$*, hazard rates of components belong to robots λ_q, *for $q = 1...c$*
Step 3;Calculate $PoRC_s(r)$ using Equation (7). Note that the reliability of the robots is updated using Equation (4) or (6) at each node of their tour.
Step 4;IF $r < p^m$ set $r = r + 1$ GOTO Step – 2 ELSE GOTO Step – 5
Step 5;Find the most reliable route set index $R_{k\_tour} = H(\widehat{r},:)$

In the initialization phase of the P-MRRP algorithm, a route set H is constructed for the given problem environment. To realize this, in the first step of the algorithm, the traversed distances d_{ij} and required energies E_{ij} for the robots between all pairs of nodes are calculated. In the second step, a virtual capacity set V_{cap} is determined considering the objective functions of the route planning algorithm that is given in the next subsection. Note that, the user may also consider workload balancing issues for selecting V_{cap} for each of the robots in the team. For this study, the SA algorithm is used to find route sets considering all possible variations of robots regarding the V_{cap}.

In the P-MRRP algorithm, the most reliable route set is selected among route set H. In the second step of the main part, the initial reliability G_k values of robots and hazard rates of components λ_l belong to robots are obtained. Note that, these values are kept the same for every route set of H. Then, $PoRC_s$ value is calculated for the system using Equation (7). In this step, a variable reliability and hazard rate are

used to calculate reliability for a given route. For a given robot, after completing a sub-route (i.e., arrived at a node of the route) the robot's initial hazard rate λ_l, $l = 1 \dots c$ and reliability values G_k are updated using Equation (4) or (6), and these values are used for the remaining sub-route of the main route. In Equation (6), the value of reliability is updated also considering carried load if it exists. Therefore, these approaches not only consider travelling issues but also carried a load. The algorithm repeats $PoRC_s(r)$ calculation until $r := p^m$. In the last step of the P-MRRP algorithm the most reliable route set is selected considering the values of $PoRC_s$. The P-MRRP algorithm can be used to determine the most reliable route set for a given robot team.

To analyse the effect of the algorithm on the lifetime extension following the PLA algorithm is proposed in Section 3.3.

3.2 Route planning algorithm

P/D problems are common problems of in-plant transportation. VRPBs where all deliveries have to be made for each route before the first pickup is one of the possible variants considered in intralogistics (Koç & Laporte, 2018). The VRPB was introduced by Deif and Bodin (Deif & Bodin, 1984). VRPBs increase efficiency by limiting the number of meters that is driven with an empty vehicle after all deliveries have been made should be balanced with preceding pickups on every route (Goetschalckx, 2011). Routing of robots and scheduling of P/D tasks are established using a metaheuristic algorithm, the SA algorithm. The conventional routing and scheduling problem is known as a combinational optimization problem, which is an NP-hard problem and cannot be solved by existing exact algorithms in a reasonable time. Therefore, metaheuristic algorithms are generally used to solve these kinds of problems (Sarıçiçek *et al.,* 2022). The SA algorithm is one of them. It is widely used and its performance is proven in the literature (Wu & Chen, 2003).

In our industrial environment (Figure 1), there are 12 workstations which have P/D points. Robots take the parts from the raw material warehouse (depot 1) to the workstations, which request P/D tasks. They also take the products or semi-products from the pickup points and deliver them to the finished products warehouse (depot 2).
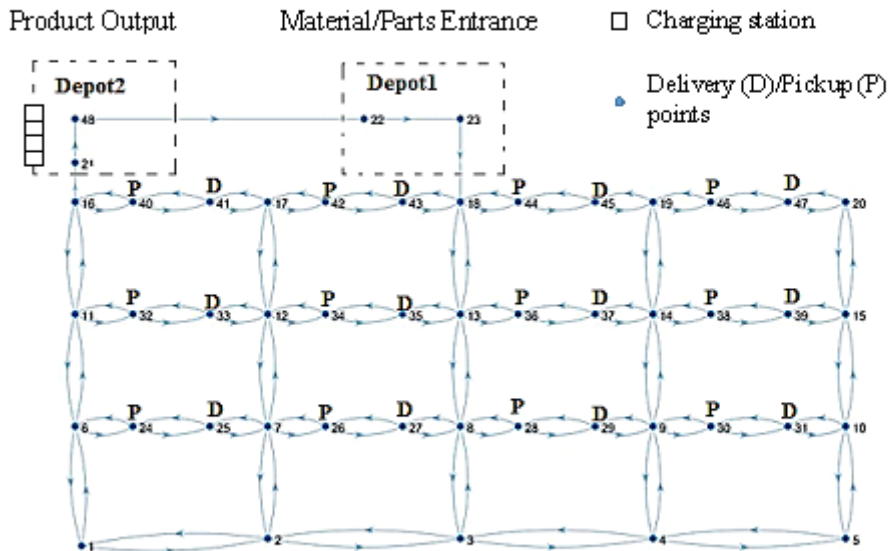
Fig. 1. The graph of the factory environment

Table 1. An example of the P/D task list.

Number of Items	P/D Point number	Type of the task (P/D)	Item	Weight (kg)
1 Item	25	Delivery	C	20
1 Item	27	Delivery	E	20
1 Item	29	Delivery	E	20
1 Item	31	Delivery	D	20
...	...	...	...	...
1 Item	30	Pickup	F	20
1 Item	32	Pickup	D	20
1 Item	34	Pickup	E	20
1 Item	36	Pickup	A	20
...	...	...	...	...

Table 2. Details of the Example Route Plan

Robot (Virtual Capacity (kg))	Robot 1 (40)	Robot 2 (40)	Robot 3 (80)	Robot 4 (80)
	Point (Weight)	Point (Weight)	Point (Weight)	Point (Weight)
Delivery tasks	43 (20)	35 (20)	25 (20)	45 (20)
	41 (20)	33 (20)	27 (20)	37 (20)
	-	-	29 (20)	39 (20)
	-	-	31 (20)	47 (20)
Pickup tasks	42 (20)	34 (20)	30 (20)	46 (20)
	40 (20)	32 (20)	28 (20)	38 (20)
	-	-	26 (20)	36 (20)
	-	-	24 (20)	44 (20)

The P/D requests for workstations are listed in Table 1. The task scheduling and route planning are established using a path planning algorithm.

In Figure 2, the number (-1) is a delimiter of the routes. According to the solution, the robot assigned to the first route leaves depot 1 and brings the requested part to points 43 and 41, then goes to points 42 and 40 to take the load/product and to bring them to the depot 2. The same process is implemented for route 2, 3 and 4. Each route is assigned to a robot in Figure 2. Therefore, four routes are assigned to four robots.

[43,41,42,40,-1,35,33,34,32,-1,25,27,29,31,30,28,26,24,-1,45,37,39,47,46,38,36,44]

Route 1   Route 2   Route 3   Route 4

Fig. 2. An example for route plan

In Table 2, the details of the example route plan are shown. Virtual capacity is used for generating all possible route sets of a given environment and the robot team. For example, in this plan, the virtual capacities for the loads of four robots are 40, 40, 80 and 80 kg. Furthermore, pickup and delivery tasks are given in Table 2.

In the route planning algorithm,

i, j: index for nodes,

k: index for robots,

d_{ij}: distance between node i and j,

ρ^*: energy spent when the robot is full-load,

ρ_0: energy spent when the robot is no-load,

Table 3. The comparison of costs for two solutions

	Minimum Distance Objective Function SA		
Robot #	Energy(kg*m)	Distance(m)	Time(s)
4	787840	4774	33.7
	Minimum Energy Objective Function SA		
Robot #	Energy(kg*m)	Distance(m)	Time(s)
4	785760	4898	34.9

RC: robot capacity,
decision variables
x_{ijk}: 1; robot k moves from node i to node j, 0; otherwise
and
y_{ijk}: load from node i to node j with robot k.
Objective functions for selecting routes are shown in Equations (8) and (9).
Objective function 1: Minimum distance;

$$Min\ z1 = \sum_{k \in K} \sum_{i \in V} \sum_{j \in V} (d_{ij} x_{ijk}) \tag{8}$$

Objective function 2: Minimum energy;

$$Min\ z2 = \sum_{k \in K} \sum_{i \in V} \sum_{j \in V} d_{ij} (\rho_0 x_{ijk} + \alpha y_{ijk}) \tag{9}$$

$$where\ \alpha = (\rho * -\rho 0)/RC \tag{10}$$

The first objective function in Equation (8) is necessary to minimize the total distance travelled. In Equation (9), minimization of energy depends on the transported load and the travelled distance between nodes. Based on the number of robots, their starting positions, and the P/D requests, the assignment of requests and appropriate routes for the robots are obtained to minimize the total energy consumed by robots. Objective functions directly affect the lifetime of the robot team by selecting the tasks for the robots. Thus, objective function selection is critically important in the lifetime of the robot team.

In Table 3, trade-offs between costs for the minimum distance objective function and the minimum energy objective function can be seen. The total distance travelled and total energy consumption are calculated as 4744 m and 787840 kg × m using the minimum distance model, respectively. On the other hand, the values are 4898 m and 785760 kg × m for the minimum energy model, respectively.

3.3 Prognostics-aware Lifetime Analysis (PLA) algorithm
The PLA algorithm can be used for long-term reliability analysis of a routing strategy with different performance measures. The steps of the algorithm are given in Algorithm 2.

Algorithm 2. Prognostics-aware Lifetime Analysis (PLA) Algorithm
Step 1. GET a user-specified threshold for PoRC ($PoRC_{th}$) value and robot reliability values
Step 2. RUN the P-MRRP algorithm or classical MRRP algorithm for the defined mission
Step 3. For the routes, calculate $PoRC_s$ and update robot reliability values
Step 4. IF $PoRC_s < PoRC_{th}$ terminate the algorithm otherwise GOTO Step − 2

In the first step of the PLA algorithm, a user-specific $PoRC_{th}$ value that defines termination condition, and actual robot reliability values, are obtained. In the second step, a route set is constructed using the determined performance measure. In this step, the P-MRRP algorithm or classical MRRP algorithm can be used. In the third step, the PoRC values are calculated for the robot team and the

Table 4. Test Setup Values

λ_l, for l = 1...c	$5.07e^{-004}$
S_k, for k = 1...m	4.32 km/h
P_k, for k = 1...m	200 kg
$PoRC_{th}$	0.1

reliability values are updated considering the nature of the mission (i.e., travelled times, carried loads). If $PoRC_s < PoRC_{th}$, then the algorithm recalls the MRRP algorithms, otherwise it terminates. Thus, the PLA algorithm can be used to assign the number of sequential missions for a given environment and robot team. In this way, the lifetime extension characteristics of any MRRP algorithm, including P-MRRP, can be determined.

4. Test results

The proposed approach is tested in the simulation environment in Figure 2, which includes 48 nodes. Figure 3 gives the configuration space in the GAZEBOSim environment. Initially, all the robots are assumed to be at node 21 of depot 2 (Figure 3).
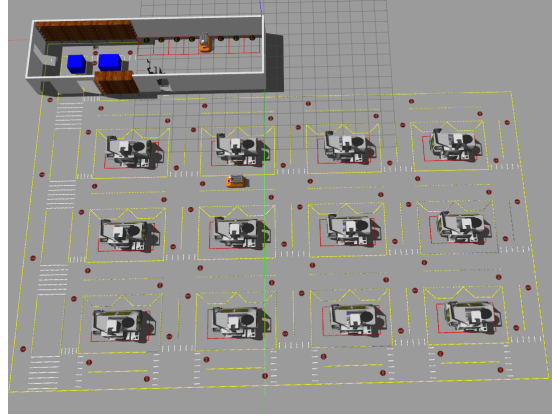
Fig. 3. Gazebo simulation case study environment

The hazard rates of the robot components λ_l, l = 1...c, nominal speed of robots S_k, k = 1...m, nominal load capacity of robots P_k, k = 1...m, and user-specified threshold value for $PoRC_{th}$ are given in Table 4. Initially, all parameters of the robots in the team are assumed to be identical to each other. In this study, the autonomous mobile robot's (IMTGD, 2021) datasheet is used as a base while configuring the test setup values.

Tests are conducted with a specially developed GUI, which is shown in Figure 4. In this GUI, the number of robots in the team, load case selection, PoRC or reliability threshold type and value can be selected. Via the GUI, the user can select the threshold type as reliability or PoRC. This means that the algorithm will stop after reaching the threshold for the reliability or PoRC value of the robot team. After reaching the threshold value, the algorithm creates a report that contains the number of completed tasks during the lifetime of the robot team. Furthermore, robots in the robot team can be configured according to the initial hazard rate value, initial reliability value, robot maximum speed value and nominal capacity value for each robot.
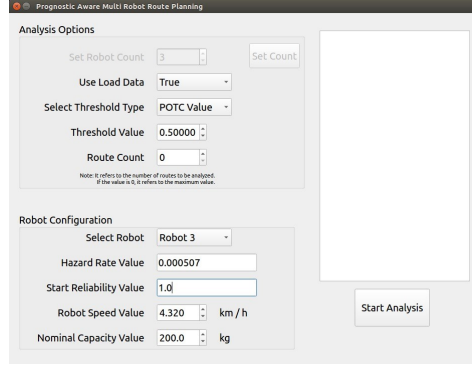
Fig. 4. P-MRRP test GUI

The reliability of a robot team is highly related to the number of completed tasks during the operation time. The P-MRRP algorithm chooses routes for the robot team according to the PoRC values. After that, the proposed PLA algorithm is applied for the lifetime analysis of the robot team using the P-MRRP algorithm. In this algorithm, the PoRC values are calculated, and the reliability values are updated considering the nature of the mission (i.e., travelled times, carried loads) for the robot team. The PLA algorithm continues to recall the MRRP algorithm as long as $PoRC_s < PoRC_{th}$, otherwise it terminates. In the analysis, it is assumed that the user-specific value of $PoRC_{th}$ that defines the termination condition is set to 0.1.

Furthermore, routes are obtained using two different objective functions. The energy minimization or the distance minimization objective function is selected for creating route sets. The lifetime analysis results of the proposed P-MRRP algorithm and classical MRRP are compared in terms of both load and unload cases, and energy and distance-based objective functions. Notably, the classical MRRP-based route sets are not changed in the lifetime of the robot team, i.e., the shortest distance route does not change. Besides that, these route sets are created for 3, 4 and 6 robot team combinations. In the following, firstly, MRRP with minimum distance objective function studies are analysed. Later, MRRP with minimum energy objective function studies are given. Lastly, MRRP with prognostics-aware algorithm results are compared among themselves, and the results are commented on.

4.1 MRRP with minimum distance objective function

First, the analysis is conducted for the route set of MRRP with minimum distance objective function. In this analysis, it's assumed that robots are homogeneous and have the same reliability value $G_k = 1.0$ $k = 1, \ldots, m$ and the loaded and unloaded cases are considered and configurations are given in Table 4. A comparison among the conducted tests are given in Table 5. In Table 5, the number of completed tasks during the lifetime of the robot team is given according to robot team combination, load case and objective function of route planning. The PLA comparison of the P-MRRP and classical MRRP for different robot team combinations (3, 4, 6 robots) is realized. Unloaded and loaded cases of MRRP with distance objective function-based route set are given in Figure (5a) and Figure (5b) respectively. As demonstrated in Table 5 and Figure 5, the robot team with the P-MRRP algorithm has completed more tasks than classical MRRP algorithms with minimum distance-based MRRP during the lifetime of the robot team.

Table 5. Lifetime Analysis for MRRP with Minimum Distance Objective Function

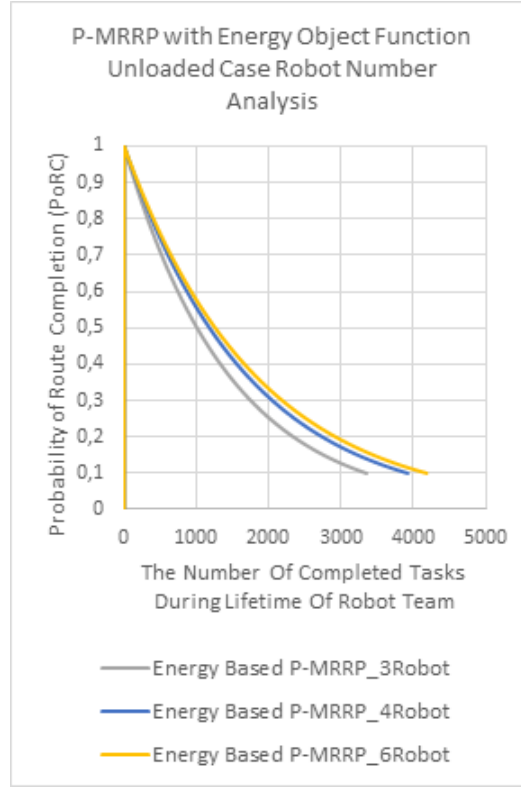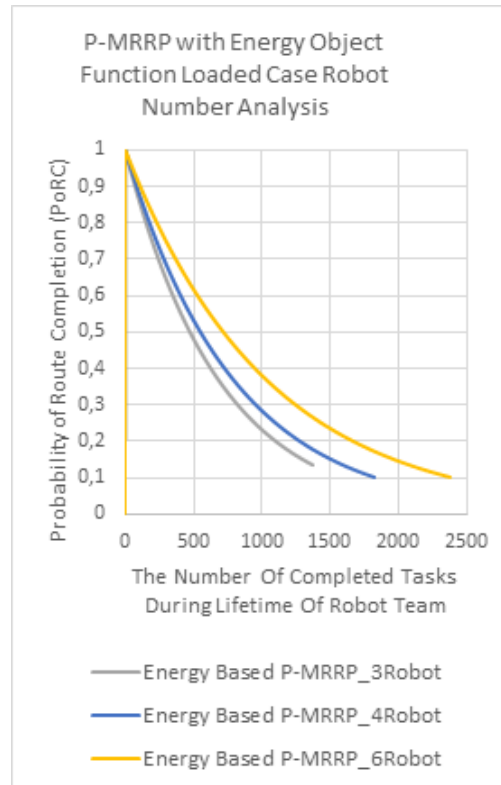| Load Case	Robot Team	Objective function of Route planning	The num of comp. tasks during lifetime of robot team
Loaded	3 Robots	Distance based P-MRRP	1367
		Minimum Distance Based MRRP	1204
	4 Robots	Distance based P-MRRP	1836
		Minimum Distance Based MRRP	1244
	6 Robots	Distance based P-MRRP	2332
		Minimum Distance Based MRRP	1634
Unloaded	3 Robots	Distance based P-MRRP	3302
		Minimum Distance Based MRRP	2836
	4 Robots	Distance based P-MRRP	3899
		Minimum Distance Based MRRP	2882
	6 Robots	Distance based P-MRRP	4192
		Minimum Distance Based MRRP	3236
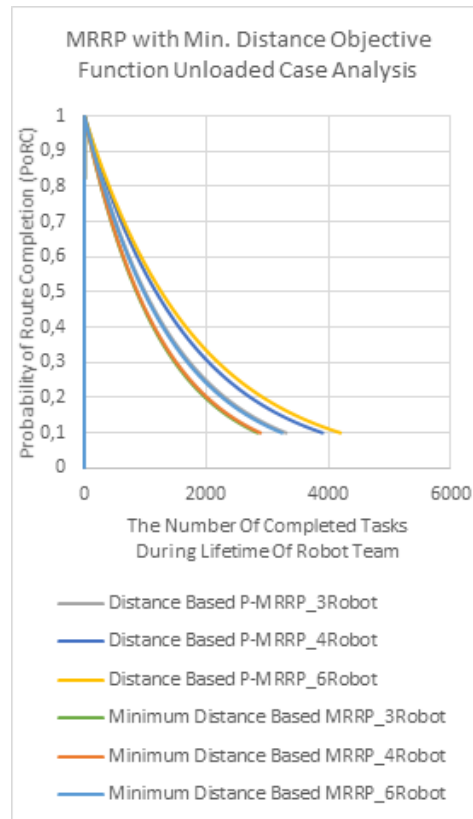
(a)Unloaded
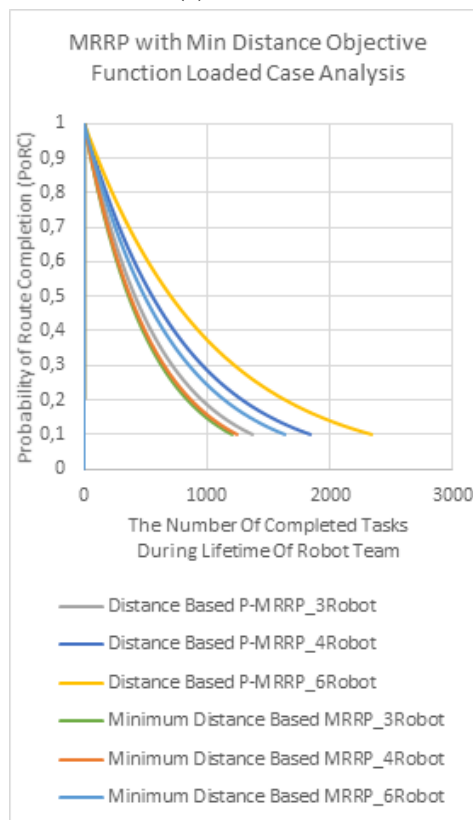
(b)Loaded

Fig. 5. Lifetime analysis for MRRP with minimum distance objective function
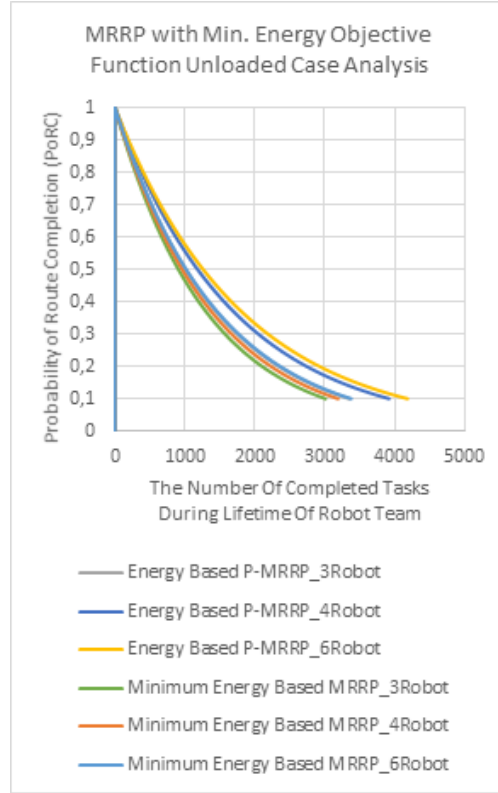
(a)Unloaded
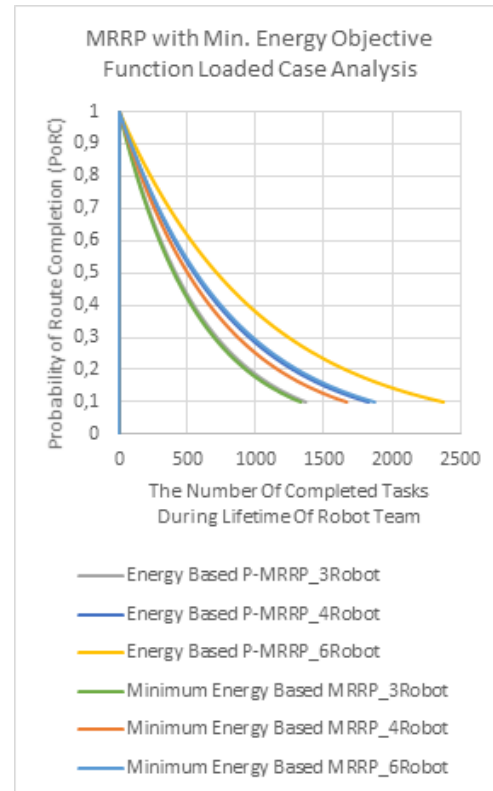
(b)Loaded

Fig. 6. Lifetime analysis for MRRP with minimum energy objective function

In Figure 5 (a) and (b), the load effect can be seen clearly. In the loaded case, the completed tasks of

Table 6. Lifetime Analysis for MRRP with Minimum Energy Objective Function

Load Case	Robot Team	Objective function of Route planning	The num of comp. tasks during lifetime of robot team
Loaded	3 Robots	Energy based P-MRRP	1563
		Minimum Energy Based MRRP	1331
	4 Robots	Energy based P-MRRP	1826
		Minimum Energy Based MRRP	1667
	6 Robots	Energy based P-MRRP	2375
		Minimum Energy Based MRRP	1871
Unloaded	3 Robots	Energy based P-MRRP	3349
		Minimum Energy Based MRRP	3010
	4 Robots	Energy based P-MRRP	3920
		Minimum Energy Based MRRP	3189
	6 Robots	Energy based P-MRRP	4182
		Minimum Energy Based MRRP	3380

the robot team are approximately half of the unloaded case without distinction of robot team combination. Moreover, as shown in Figure 5 (a) and (b), as the number of robots in the robot team increases, the number of completed tasks during the lifetime also increases.

4.2 MRRP with minimum energy objective function

Second, analysis is conducted for the route set of MRRP with energy objective function. In this analysis, all configurations and test scenarios are the same as in Section 4.1. In Table 6, lifetime analysis results of MRRP with minimum energy objective function are given.

The comparison of Tables 5 and 6 show that the MRRP algorithm with minimum energy objective function completes slightly more than the MRRP algorithm with minimum distance-based objective function. This means that MRRP with the minimum energy objective function route set is more suitable for lifetime extension than MRRP with the minimum distance objective function route set.

When the unloaded case is compared with that loaded one in Figure 6, the load effect in the number of completed tasks during the lifetime of the robot team could be seen. Besides, the number of robots in the team is another crucial factor in extending the lifetime of the robot team.

4.3 MRRP with the Prognostics-aware algorithm

P-MRRP algorithm results are analysed depending on the number of robots in the team. In Tables 5 and 6, P-MRRP algorithm test results for a different number of robots can be analysed.

The lifetime of the robot team is extended when the number of robots is increased in the P-MRRP algorithm for the loaded and unloaded cases. For example, the difference between three robots and four robots in terms of the number of completed tasks is approximately 500 tasks for the loaded case and 600 tasks for the unloaded case. The situation is roughly the same for a four-robot team and six-robot team, with 500 tasks for the loaded case and 300 tasks for the unloaded case.

From Table 6, the P-MRRP algorithm analysis with energy objective function route set is shown. The lifetime is extended according to the number of robots in the team.
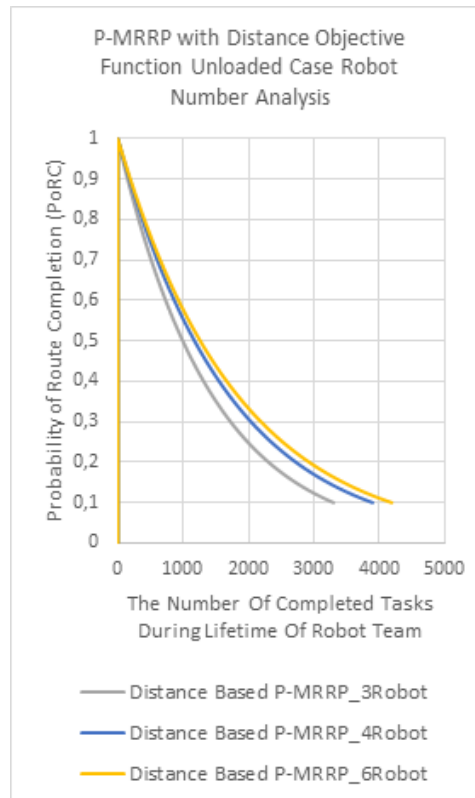
(a)Unloaded
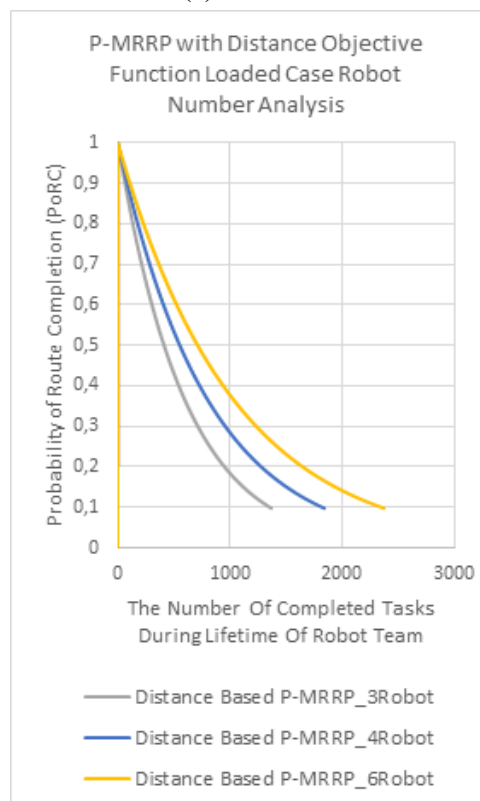
(b)Loaded

Fig. 7. Robot Number Analysis for P-MRRP with Minimum Distance Objective Function

(a)Unloaded

(b)Loaded

Fig. 8. Robot Number Analysis for P-MRRP with Energy Objective Function

In Figure 8, comparing the unloaded case with the loaded one, the number of completed tasks during the lifetime of the robot team is approximately similar to the minimum energy objective function-based

route set test results (see Figure 7). However, the minimum energy objective function-based route set has a higher number of completed tasks than the minimum distance objective function-based route set cases. On the other hand, the route planning strategy is very important for the robot team when loaded and unloaded cases are compared, and the load effect is clearly seen for the lifetime of the robot team. Significantly, the experiments show that the P-MRRP algorithm is capable of extending the lifetime of the system.

5. Conclusion

In Industry 4.0 era, long-term repetitive operations are an important application of autonomous multi-robot teams in manufacturing facilities. The transportation of parts to the workstations from the depot and transportation of the finished products to the depot are repetitive tasks that affect the lifetime of autonomous robots. The lifetime of the robot team is increased if the team can know the reliability values of each robot in the team and plan routes accordingly. In this study, a P-MRRP algorithm is proposed for extending the lifetime of the robot team. Using reliability-based route planning enables long-term autonomous operations of the robot team. Moreover, the P-MRRP algorithm can consider the carried loads of robots in the environment, and the PLA algorithm results show the extension of robot lifetime by comparing P-MRRP with the classical MRRP (specifically, their minimum distance and energy objective functions) in loaded and unloaded scenarios. The proposed P-MRRP algorithm outperforms the classical MRRP algorithm, especially in the loaded case. The P-MRRP algorithm can be used for lifetime planning, reduction of the maintenance cost, sustaining autonomy and more. Therefore, it is preferable for fully autonomous systems considering long-term strategic planning. In the future, the reliability analysis of robots will be extended to include other components such as communication, sensors, batteries and electronics. Furthermore, the optimum number of robots could be estimated with the P-MRRP algorithm for the given test environments.

References

Arai, T., Pagello, E., & **Parker, L. E. (2002).** Advances in multi-robot systems. IEEE Transactions on robotics and automation, 18(5), (pp. 655-661).

Balaban, E., Narasimhan, S., Daigle, M., Roychoudhury, I., Sweet, A., Bond, C., & **Gorospe, G. (2013** Development of a mobile robot test platform and methods for validation of prognostics-enabled decision-making algorithms. International journal of prognostics and health management, 4(1), 87, (pp. 1-19).

Deif I. & **Bodin L.D., (1984).** Extension of the Clarke and Wright algorithm for solving the vehicle routing problem with backhauling, In: Proceedings of the Bab-son conference on software uses in transportation and logistics management, Bab- son Park, MA.

Dhillon, B. S. (2015). Robot system reliability and safety: A modern approach. CRC press.

Dolgui, A., & **Proth, J. M. (2010).** Supply chain engineering: useful methods and techniques. Book from springer science & business media.1-535

Fudzin, A. F., & **Majid, M. A. A. (2015).** Reliability and availability analysis for robot subsystem in automotive assembly plant: A case study. In IOP conference series: Materials science and engineering, 100(1), (pp. 012022).

Geng, J., Lv, C., Zhou, D., & **Wang, Z. (2016).** A mission execution decision making methodology based on mission-health interrelationship analysis. Computers & industrial engineering, 95, (pp. 97-110).

Goetschalckx M., (2011). Supply chain engineering, international series in operations research& management science, Springer, NewYork.

Hossain, M. S. & **Muhammad, G. (2016).** Cloud-assisted industrial internet of things (iiot)—enabled framework for health monitoring. Computer networks, 101, (pp.192–202).

Inovasyon Muhendislik Ltd. Sti. (IMTGD), (2021). Autonomous transport vehicle (inota), https://www.inovasyonmuhendislik.com /en/products/inota, Access Date: 09.09.2021

Kapanoglu M., Alikalfa M., Ozkan M., Yazıcı A., & **Parlaktuna O. (2012).** A pattern-based genetic algorithm for multi-robot coverage path planning minimizing completion time. Journal of intelligent manufacturing, 23(4), (pp. 1035-1045).

Kishorilal, D. B., & **Mukhopadhyay, A. K. (2018).** Reliability investigation of diesel engines used in dumpers by the bayesian approach, Kuwait journal of science, 45(4), (pp. 15- 25)

Koc¸ Ç . & **Laporte G., (2018).** Vehicle routing with backhauls: Review and research perspectives, Computers and operations research, 91 (pp. 79–91).

LeSage, J. R., & **Longoria, R. G. (2015).** Mission feasibility assessment for mobile robotic systems operating in stochastic environments, Journal of dynamic systems, measurement, and control, 137(3), (pp. 1-11).

Mimlitz, Z., Short, A., & **Van Bossuyt, D. L. (2016).** Toward risk-informed operation of autonomous vehicles to increase resilience in unknown and dangerous environments, In ASME 2016 international design engineering technical conferences and computers and information in engineering conference, American society of mechanical engineers digital collection. (pp. 1-10)

Medjaher, K., Tobon-Mejia, D. A., & **Zerhouni, N. (2012).** Remaining useful life estimation of critical components with application to bearings. IEEE transactions on reliability, 61(2), (pp.292-302).

Okoh, C., Roy, R., Mehnen, J., & **Redding, L. (2014).** Overview of remaining useful life prediction techniques in through-life engineering services. Procedia CIRP, 16, (pp.158-163).

Oztemel E. & **Gursev S., (2020).** Literature review of Industry 4.0 and related technologies, Journal of intelligent manufacturing, 31, (pp. 127–182).

Sarıçiçek I˙., Bozkurt Keser S., Cibi A., Ö zdemir T. & **Yazıcı A., (2022).** Energy efficient routing and task scheduling for autonomous transport vehicles in intra logistics, Kuwait journal of science, 49(1).

Shah, S. I. H., Nawaz, R., Ahmad, S., & **Arshad, M. (2020).** Sustainability assessment of modern urban transport and its role in emission reduction of greenhouse gases: A case study of lahore metro bus, Kuwait journal of science, 47(2), (pp. 68-81).

Shanker S. & **Kumar S., (2020).** Reliability prediction of deep groove ball bearings of rotary actuator, International journal of machine tools and maintenance engineering, 1(1), (pp. 15-19).

Short, A. R., Hodge, R. D., Van Bossuyt, D. L., & **DuPont, B. (2018).** Active mission success estimation through functional modeling. Research in engineering design, 29(4), (pp. 565-588).

Sweet, A., Gorospe, G., Daigle, M., Celaya, J. R., Balaban, E., Roychoudhury, I., & **Narasimhan, S. (2014)** Demonstration of prognostics-enabled decision-making algorithms on a hardware mobile robot test platform, SGT Inc. Moffett field US. (pp. 1-9).

Thieme, C. A., & **Utne, I. B. (2017).** Safety performance monitoring of autonomous marine systems. Reliability engineering & system safety, 159, (pp. 264-275).

Van Laarhoven, P. J., & **Aarts, E. H. (1987).** Simulated annealing: Theory and applications, Springer, Dordrecht, (pp. 7-15).

Villani, V., Pini, F., Leani, F., & **Secchi, C. (2018).** Survey on human–robot collaboration in industrial settings: Safety, intuitive interfaces and applications. Mechatronics, 55, (pp. 248-266).

Wu T-H., & **Chen J. F., (2003).** Solving vehicle routing problem with backhauls, Journal of the chinese institute of industrial engineers, 20(6), (pp. 651-665).

Yayan, U., & **Yazici, A. (2019).** Reliability-Based Multi-Robot Route Planning. International journal of robotics and automation, 34(3), (pp. 1-7).

Analysis of field-free region formed by parametric positioning of a magnet pair for targeted magnetic hyperthermia

Serhat Küçükdermenci[1, *]

[1]*Dept. of Electrical and Electronics Engineering, Balikesir University, Balikesir, Turkey*
[*]Corresponding author: kucukdermenci@balikesir.edu.tr

Abstract

One of the challenges in using magnetic fluid hyperthermia in practical applications is the limited control of magnetic nanoparticle oscillations. In this study, we investigated how the form and location of a static magnetic field-free region can be modified by the symmetrical and asymmetrical positioning of a magnet pair. The gradient patterns in the workspace were estimated using a finite element method simulation. On an experiment platform, measurements were taken using a point probe. It has been demonstrated that parametric changes in distance and angle allow changing of the form and location of the field-free region. Field-free regions can shrink and have shapes similar to a line or point. The focus of the field-free region can be directed to various parts of the target object. The mapping of gradient patterns formed by a magnet pair for the use of targeted magnetic fluid hyperthermia is described for the first time in this paper. Furthermore, the findings highlight the significance of the fit between the target objects and the created gradient models.

Keywords: Cancer treatments; field-free region; gradient pattern; magnetic fluid hyperthermia; permanent magnet.

1. Introduction

Magnetic fluid hyperthermia (MFH) is a medical procedure in which cancerous cells are brought to a temperature between 42-46 °C with magnetic nanoparticles (MNPs) (Deatsch & Evans, 2014). When MNPs are exposed to an alternating magnetic field (AMF), the magnetic energy is converted into heat energy with the oscillating movement. Cancerous cells lose their effectiveness with the high temperature in the environment. Inversely, healthy cells are more resistant to heat than cancer cells. The heat generating capacity of MNPs is defined as the specific absorption rate (SAR) and it is expressed by Equation 1.

$$SAR = c\frac{V_s}{m_{MNP}} \times \frac{dT}{dt}$$

(1)

Here, c is the specific heat capacity of the medium, V_S is the volume of the sample, m_{MNP} is the mass of the MNPs, and dT/dt is the time derivative of the temperature difference.

The heat production of MNPs by the AMF effect is explained by the relaxation losses. The deflection motion of MNP moments is defined as Neel relaxation. In Brownian relaxation, MNPs interact with the medium fluid and make a mechanical motion. The Neel and Brownian characteristic relaxation times are expressed as τ_N and τ_B, respectively. The effective relaxation time (τ_{eff}) is given by Equation 2.

$$\tau_{eff} = (\tau_B . \tau_N)/(\tau_B + \tau_N) \qquad (2)$$

One of the models describing the volumetric power density emitted by MNPs exposed to AMF is the Rosensweig model and it is expressed by Equation 3.

$$P = \pi \mu_0 \chi_0 H_{ac}^2 f \frac{\omega \tau}{1+(\omega \tau)^2} [W/m^3] \qquad (3)$$

Here, χ_0 is magnetic susceptibility, H_{ac} and f are AMF amplitude and frequency, τ is effective relaxation time and ω is angular frequency, respectively.

The typical problem in MFH applications is the difficulty of localizing the heat to the tumor without damaging the healthy tissues. Because there is a tendency for MNPs to migrate from the tumor site to healthy tissues during MFH tests. There are theoretical and experiment studies (Dhavalikar & Rinaldi, 2016), (Cantillon-Murphy *et al.*, 2010) showing that MNP behaviors under the influence of AMF can be changed by adding static magnetic field (SMF). SMF sources are positioned such that the SMF vectors bend each other (see Figure 1) and field-free region (FFR) occurs in the workspace (WS). MNPs remaining in FFR can oscillate freely under the influence of AMF. MNPs in the SMF are either restricted or completely blocked.

Among the studies on MFH, Tasci *et al.* (Tasci *et al.*, 2009) showed that the MNP temperature rise can be controlled with their proposed method. The SMF source made with DC coils is positioned on both sides of the AMF generating coil in their study. Lu *et al.,*2020 used magnets to focus the heat on a specific area. This system is capable of performing magnetic particle imaging and MFH operations (Lu *et al.*, 2020). Ma *et al.* (Ma *et al.*, 2015) used Neodymium Iron Boron (NdFeB) magnets. It was reported that MNP samples remaining within the FFR effectively generate heat and the SAR value of MNPs is limited in the SMF. GP mapping has not been studied in detail in any of these studies. The mapping of GPs produced by a magnet pair (MP) for the use of targeted MFH is discussed for the first time in this study.
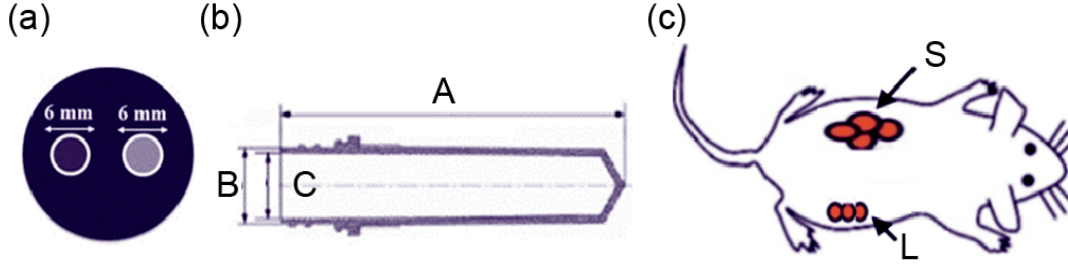
Fig. 1. Schematic representation of FFR.

2. Materials and methods

Literature comparison of WSs and target objects (TOs) are shown in Table 1. WSs are generally inner volume of helical shaped work-coil. Ferrofluid containing test tubes and regional tumor masses of small animals can be considered as the TO.

Table 1. Workspace and target object properties.

Properties of the WS	Properties of the TO	Ref.
Radius of the coil ≈ 5 cm, Cross-section area of WS ≈ 78.5 cm^2	One test-tube located in the center of the coil, the radius of the tube, r ≈ 0.5 cm, Target area ≈ 0.785 cm^2	(Bauer *et al.*, 2016)
Radius ≈2 cm, height ≈ 6 cm, Cross-section area of WS ≈ 24 cm^2	Spherical plastic cups, r ≈ 0.2 cm, target area ≈ 0.126 cm^2	(Tasci *et al.*, 2009)
Coil diameter = 3 cm	Two phantoms stay close to the heating region of the coil (20mm).	(Ma *et al.*, 2015)
Coil with a diameter = 3 cm,	Tube diameter = 8 mm, target area ≈ 0.502 cm^2	(Murase *et al.*, 2013)
Solenoid coil diameter = 4 cm, length = 10 cm. Cross-section area of WS ≈ 40 cm^2	Spherical core with a radius of 4.9 mm	(Zhao *et al.*, 2012)
90 mm diameter circle and a square of 56 x 56 mm^2 can be fitted into it.	TO can be small test tube array, long test tube or a small test animal	Proposed study

Small test tubes (see Figure 2a) or a long test tube containing MNP can be TO for in vitro tests. A long test tube may have a length of 47.5 mm and an outer diameter of 9.6 mm (labeled with letters *A* and *B* in Figure 2b). If it is placed horizontally, the FFR can be applied to some parts of the tube. If TO is the tumor mass in the small animal, it can be in the shape of line-like or point-like geometries as shown with the letters L and S (see Figure 2c).

Fig. 2. Schematic representation of TOs (a) small tube, (b) long tube, (c) test animal.

In bioelectromagnetic applications, either current fed electromagnets (Ristic-Djurovic *et al.*, 2018) or permanent magnets (Ren *et al.*, 2019) are preferred as SMF sources. However, coils need power supplies and sometimes chiller. This makes experiment setup more complex and expensive. NdFeB magnets produce stronger SMF compared to coils (Mahadi *et al.*, 2003). Experiment setups containing magnets are less complex and cost-effective than coils.

Due to the properties mentioned above it was decided to use the following materials and methods. NdFeB magnets were preferred in this study. NdFeB magnets with volume of $50 \times 10 \times 20$ mm^3 were used. N54 has relative magnet permeability and B_r of 1.05 T and 1.47 T, respectively. (d_1, d_2) are the distances from the center point of magnets to the origin and (θ_1, θ_2) are angles of magnets referencing the x-axis. Six cases were chosen to investigate effect of magnet positions on FFR (see Table 2).

Table 2. Magnet positions and angles.

(θ_1, θ_2) degrees	(d_1, d_2) mm	Case
(180, 0)	(-70, 70)	1
(180, 0)	(-60, 60)	2
(180, 0)	(-70, 60)	3
(180, 0)	(-80, 60)	4
(225, 45)	(-60, 60)	5
(197, -17)	(-60, 60)	6

2.1 Simulation medium

A multiphysics simulation software (COMSOL® Multiphysics, COMSOL AB, Stockholm, Sweden) was used for GP modeling. Simulation medium consists of source magnets and TO. The TO is a cylinder has a radius of 28 mm and a height of 56 mm as shown in Figure 3a. This cylinder could be a representative model for a work area. Test tube or a small animal can be placed in this space for in vitro or in vivo applications.

2.2 Experiment setup

3D-printed experiment setup consists of magnets, holders, arms and center platform (see Figure 3b). Magnets are placed inside the holders. The distances and angles can be changed gradually by

the help of arms. Holders, arms and center platform are connected together. Center platform keeps all system aligned, and its center room was used for measuring. This room is a 90 mm diameter circle and a square of 56×56 mm^2 can be fitted into it. WP and TO comparison can be found in Table 1. Technical drawings of each part and information of 3D printing process can be found as a file in supplementary materials.
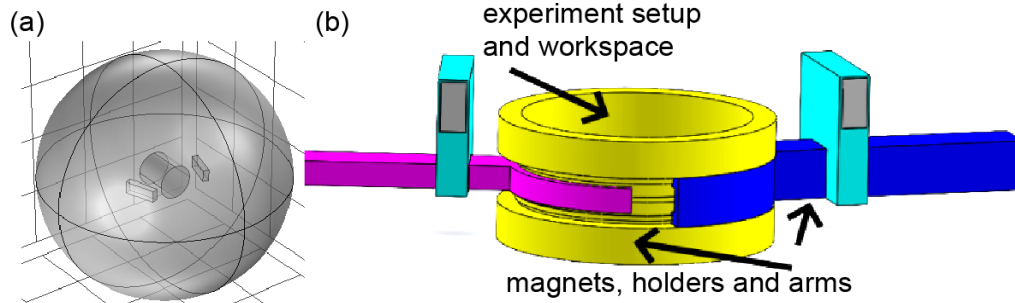
Fig. 3. (a) simulation medium, (b) experiment setup.

3. Results and discussion

3.1 Simulation results

Color maps and arrow representations of flux lines for different parametric values are shown in Figure 4 a-f, respectively.
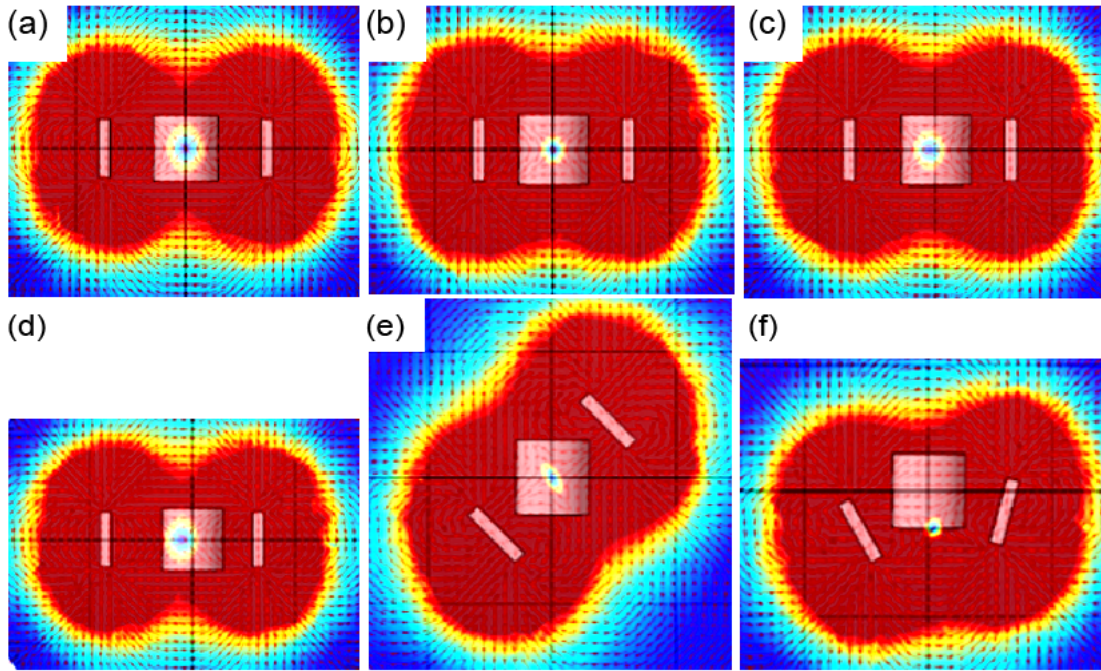
Fig. 4. GPs for (a) Case 1, (b) Case 2, (c) Case 3, (d) Case 4, (e) Case 5 and (f) Case 6.

For the linear symmetric cases (Case 1-2), it is found that the form of the FFR can shrink and focus in the center. For the linear asymmetric cases (Case 3-4), it is observed that FFR focus can be shifted and its form can be manipulated. FFR can be directed to different parts of the TO by using angular symmetric/asymmetric cases. From Case 5 to Case 6 the focus of FFR can be moved from the center point to the lower mid part of the TO. And its shape changes from a diagonal line form to a point-like form.

Conditions of MFH experiments in the literature vary widely. For example, AMF intensity can range from 0.8 to 115 kA/m (Vilas-Boas *et al.*, 2020). So the limit value of SMF can be selected as 20 G ($\approx$1.6 kA/m). Contour lines are drawn and areas below 20 G are accepted as FFR (see Figure 5). FFR (B $\leq$ 20 G) can be considered as ellipse. Semi-major axis a and semi-minor axis b of FFRs are measured. (a, b) are (2.15 , 1.45), (1.15, 0.9), (1.45, 1.05) and (2.15, 1.3) cm for Case 1-4, respectively. It is found that if magnets come closer symmetrically, FFR can be focused into a very small area. (a, b) are (1.3, 0.55) and (1, 0.75) cm for Case 5 and Case 6, respectively. And the FFR can be in the form of diagonal line-like or point-like form for these cases. The equation $A = \pi ab$ gives the area of the ellipse. Area calculations were done for all cases. Surface areas are 9.79, 3.25, 4.78, 8,78, 2.25 and 2.36 cm^2 for Case 1-6, respectively. These surface areas can be suitable for TOs like small test tubes, long test tube or small test animal.
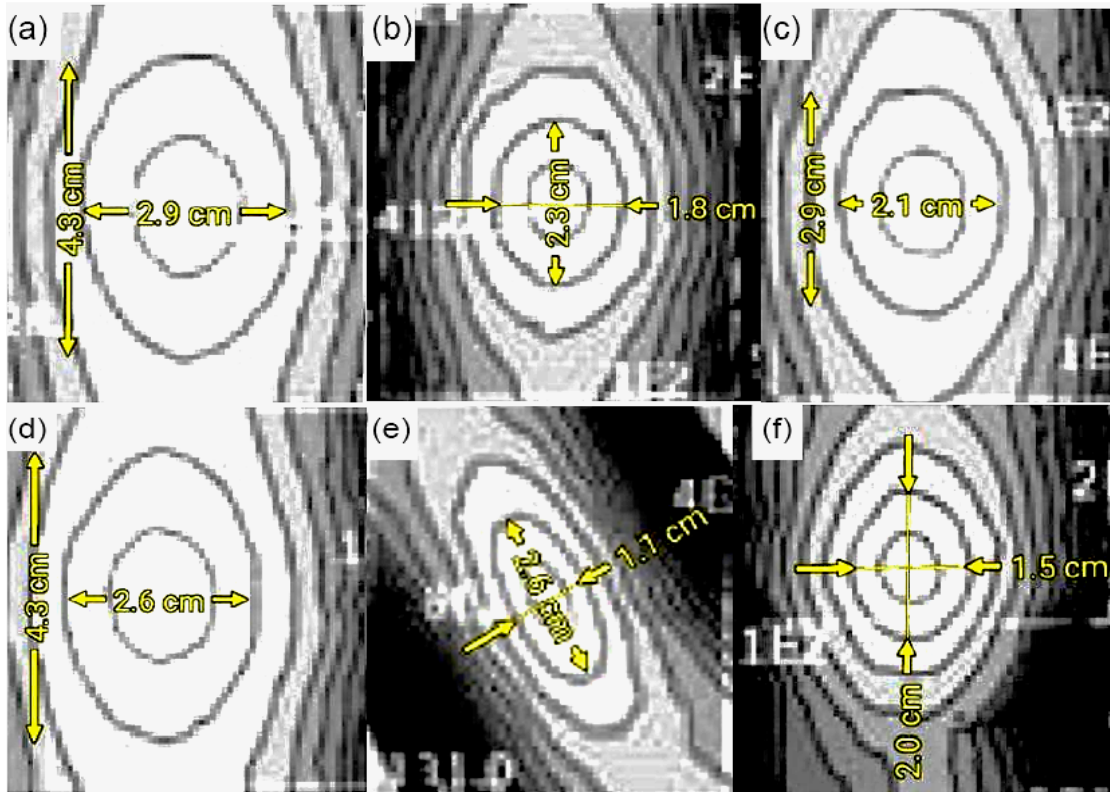
Fig. 5. Axis measurements of FFR for a) Case 1, b) Case 2, c) Case 3, d) Case 4, e) Case 5 and f) Case 6.

Total 49 measurement points were determined on the x and y axes with 8 mm intervals from -24 mm to 24 mm in WS (see Figure 6). Point probe measurements (PPMs) of SMF for simulation environment are generated for all cases. Related tables can be found as a file in the supplementary material.
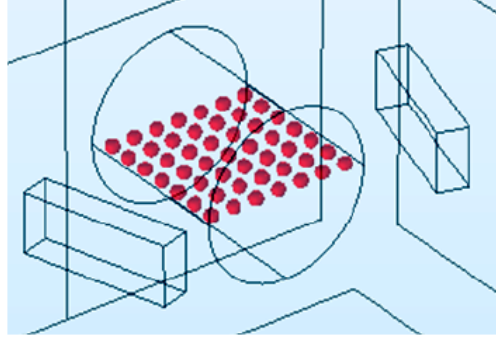
Fig. 6. Probe positions in the simulation setup.

3.2 Experiment setup results

PPMs were made at the same probe positions as in the simulation. Magnetic flux measurements in the x and y directions (B_x and B_y) were taken for all cases with WT10A commercial magnetic flux meter. The magnitude of vector B for every point was calculated by Equation 4.

$$B = \sqrt{B_x^2 + B_y^2}$$

(4)

Measurements were repeated four times in a row and the average values were transferred to Table 3. The number of points forming the FFR (red colored regions in Table 3, $B \leq 20$ G) are 5, 1, 2, 4, 1, and 1 for Case 1-6, respectively. It is seen that PPMs in the experiment setup also give information about the position and flux density levels of the FFRs.

Table 3. Point probe measurements.

B (G)		Case 1 x-axis prob position (mm)							Case 2 x-axis prob position (mm)							Case 3 x-axis prob position (mm)					
		-24	-16	-8	0	8	16	24	-24	-16	-8	0	8	16	24	-24	-16	-8	0	8	16	24
y axis probe	40	92	65	49	48	48	65	92	163	112	83	74	83	105	164	96	68	60	59	74	99	165
	30	82	57	42	33	39	55	87	142	99	66	54	65	86	151	79	59	43	48	60	84	149
	8	74	46	25	17	25	47	74	125	76	45	33	41	77	127	69	41	26	31	43	78	128
	0	71	42	19	2	18	43	76	125	68	36	3	35	68	133	72	37	11	17	46	79	137
	-8	74	50	27	17	30	43	73	130	79	44	32	47	70	129	70	43	28	30	50	79	132
	-16	84	61	38	34	41	59	82	144	102	66	56	63	97	138	82	61	46	46	60	98	141
	-24	94	64	54	46	48	63	92	165	106	84	72	82	108	161	94	70	61	61	75	105	160

B (G)		Case 4 x-axis prob position (mm)							Case 5 x-axis prob position (mm)							Case 6 x-axis prob position (mm)					
		-24	-16	-8	0	8	16	24	-24	-16	-8	0	8	16	24	-24	-16	-8	0	8	16	24
y axis probe	40	62	48	49	51	68	99	156	78	72	81	99	165	271	485	137	102	87	82	88	103	130
	30	49	36	37	44	61	87	146	86	72	55	68	119	185	321	158	119	94	91	94	113	153
	8	41	26	18	30	52	83	133	110	76	38	39	66	152	208	166	120	91	84	##	126	181
	0	40	14	7	26	47	79	141	165	97	49	6	49	110	164	170	109	86	82	86	122	180
	-8	43	27	18	31	53	80	137	217	146	74	34	38	74	108	163	100	68	57	67	103	176
	-16	51	37	36	41	60	96	138	324	202	120	69	53	67	89	173	92	46	27	49	94	166
	-24	61	49	48	54	71	105	162	458	281	167	95	72	72	83	182	91	44	16	42	91	170

3.3 Discussion

Small deviations of PPMs between simulation medium and experiment setup may have different reasons. Magnets are identical in simulation medium but in real life they may not be exactly the same. Commercial flux meter measurements were done with hand and probe alignments can't be perfect as in the simulation. Some gaps should be added to the 3D printed objects for assembly. For example, the magnet edges should be set to 10 and 20 mm, while the room edges in the holder should be set to 10.3 and 20.3 mm. The gaps were left for assembly and the 3D printouts could be different from the ideal dimensions in the technical drawing. This can lead to inevitable alignment and measurement differences (see supplementary material).

A brief literature comparison of MFH studies including SMF sources is presented in Table 4. It is seen that both DC current fed coils and magnets can be used as SMF sources. The opposite or same SMF poles can face each other. Topics like parametrization of linear distance and angle, major and minor axis measurements and area calculations of FFR, PPMs and GP mapping have not been studied in detail in any of these studies. This proposed study addresses these topics.

Table 4. Comparison of MFH studies.

Reference	SMF source / Flux direction	Parametrization of linear distance and angle	GP mapping	FFR measurements
(Bauer *et al.*, 2016)	Magnet Single magnet, MP / same dir.	-	-	-
(Tasci *et al.*, 2009)	DC fed coil A pair / opposite dir.	-	-	-
(Ma *et al.*, 2015)	Magnet A pair / opposite and same dir.	-	-	-
(Murase *et al.*, 2013)	DC fed coil A pair / same dir.	-	-	-
(Zhao *et al.*, 2012)	DC fed coil A pair / same dir.	-	-	-
Proposed study	Magnets A pair / opposite direction	The symmetrical and asymmetrical situations of distance and angle are examined.	PPMs are taken in WS for FFR investigations.	FFR major and minor axis mesurements and area calculations are done.

4. Conclusions

In this study, GP mapping produced by parametric position changes of a MP for using in targeted MFH tests was investigated for the first time. It is found that symmetric and asymmetric displacements of a MP can manipulate FFR form (changes its shape to surface, line and point like forms) and location (can be focused to center or edge of the TO). FFR structures were analyzed with color maps and arrow representations, axis measurements and area calculations from contour representations, PPMs and GP mappings. Considering cross-sectional region of TO and the WS quite suitable choices can be made for in vitro and in vivo MFH experiments among the GPs

mapped in this study. For in vitro tests, FFR can be applied to test tubes in periodic array or a long tube with horizontal positioning. For MFH test with small animals, FFR and target tissue overlap can be achieved by appropriate placement of the SMF source and/or TO. The utilized system in this study could be used in real scenario if the specific conditions of each experiment are taken into account.

The obtained results provide data for in vitro and in vivo MFH tests performed prior to clinical trials. With the help of GP mapping, suitable FFRs for different tumor geometries can be determined. The ability to ablate a tumor of any possible geometry by moving the FFR over the tumor is important for future studies. This highlights the importance of adapting the position and shape of the FFR in MFH applications. In the future, designs may be considered to focus FFR with highly sensitive robotic devices for each patient's unique individual conditions.

Supplementary material

The PPMs in simulation medium, technical drawings of each part and information of 3D printing process for experiment setup are available online at https://docs.google.com/document/d/1-ZgJM6A52fsg9gH_Kx6iLBgRIwojSAtX.

References

Bauer, L. M., Situ, S. F., Griswold, M. A., & Samia, A. C. S. (2016) High-performance iron oxide nanoparticles for magnetic particle imaging-guided hyperthermia (hMPI). Nanoscale, 8(**24**), 12162–12169.

Cantillon-Murphy, P., Wald, L. L., Zahn, M., & Adalsteinsson, E. (2010) Proposing magnetic nanoparticle hyperthermia in low-field MRI. Concepts in Magnetic Resonance Part A: Bridging Education and Research, 36(**1**), 36–47.

Deatsch, A. E., & Evans, B. A. (2014) Heating efficiency in magnetic nanoparticle hyperthermia. Journal of Magnetism and Magnetic Materials, 354, 163–172.

Dhavalikar, R., & Rinaldi, C. (2016) Theoretical predictions for spatially-focused heating of magnetic nanoparticles guided by magnetic particle imaging field gradients. Journal of Magnetism and Magnetic Materials, 419, 267–273.

Lu, Y., Rivera-Rodriguez, A., Tay, Z. W., Hensley, D., Fung, K. L. B., Colson, C., Saayujya, C., Huynh, Q., Kabuli, L., Fellows, B., Chandrasekharan, P., Rinaldi, C., & Conolly, S. (2020) Combining magnetic particle imaging and magnetic fluid hyperthermia for localized and image-guided treatment. International Journal of Hyperthermia, 37(**3**), 141–154.

Ma, M., Zhang, Y., Shen, X., Xie, J., Li, Y., & Gu, N. (2015) Targeted inductive heating of nanomagnets by a combination of alternating current (AC) and static magnetic fields. Nano Research, 8(**2**), 600–610.

Mahadi, W. N. L. W., Adi, S. R., & Nor, K. M. (2003) Application of the rare earth permanent magnet in linear generator driven by an internal combustion engine. National Power Engineering Conference, PECon 2003 - Proceedings, 256–261.

Murase, K., Takata, H., Takeuchi, Y., & Saito, S. (2013) Control of the temperature rise in magnetic hyperthermia with use of an external static magnetic field. Physica Medica, 29(**6**), 624–630.

Ren, Z. H., Mu, W. C., & Huang, S. Y. (2019) Design and Optimization of a Ring-Pair Permanent Magnet Array for Head Imaging in a Low-Field Portable MRI System. IEEE Transactions on Magnetics, 55(**1**), 1–8.

Ristic-Djurovic, J. L., Gajic, S. S., Ilic, A. Z., Romcevic, N., Djordjevich, D. M., De Luka, S. R., Trbovich, A. M., Jokic, V. S., & Cirkovic, S. (2018) Design and Optimization of Electromagnets for Biomedical Experiments With Static Magnetic and ELF Electromagnetic Fields. IEEE Transactions on Industrial Electronics, 65(**6**), 4991–5000.

Tasci, T. O., Vargel, I., Arat, A., Guzel, E., Korkusuz, P., & Atalar, E. (2009) Focused RF hyperthermia using magnetic fluids. Medical Physics, 36(**5**), 1906–1912.

Vilas-Boas, V., Carvalho, F., & Espiña, B. (2020) Magnetic hyperthermia for cancer treatment: Main parameters affecting the outcome of in vitro and in vivo studies. Molecules, 25(**12**).

Zhao, Q., Wang, L., Cheng, R., Mao, L., Arnold, R. D., Howerth, E. W., Chen, Z. G., & Platt, S. (2012) Magnetic nanoparticle-based hyperthermia for head & neck cancer in mouse models. Theranostics, 2(**1**), 113–121.

Broadband low-frequency sound absorption via a hexagonal acoustic metamaterial in the honeycomb structure

Fatma Nafaa Gaafer

Dept. of Science, College of Basic Education, Wasit University, Iraq
Corresponding author: fnafie@uowasit.edu.iq

Abstract

I constructed two models for achieving a perfect absorption acoustic metamaterial using a hexagonal honeycomb structure in the air with a change in folding number. The purpose of these models was to construct a hexagonal honeycomb metamaterial derived from Polydimethylsiloxane (PDMS) polymer. I carried out finite element simulations using COMSOL Multiphysics software to take theoretical measurements for our honeycomb structure and to show the influence of structural parameters in our models. Our simulations revealed that, depending upon the theoretical analysis, an acoustic metamaterial that supports resonance at 210 Hz for folding number n = 6 can be developed to construct a low-frequency sound-absorbing technology. I demonstrate that the dissipative loss effect can be controlled by folding number and high space utilization through adjusting the hexagonal dimensions to achieve perfect absorption. I also demonstrate the important effects of folding number, rotation angle, and structural parameters on improving acoustic absorption performance for honeycomb structural design. The results are of extraordinary correspondence at low frequency for achieving an ideal sound absorbing material.

Keywords: Acoustic focusing; acoustic metamaterial; hexagonal honeycomb structure; perfect absorber; sound insulation.

1. Introduction

Acoustic metamaterials (Mei *et al*., 2012) and metasurfaces (Ma *et al*., 2014) have attracted a great deal of work dedicated to designing new materials and structures of deep subwavelength thickness at work frequency in recent years. Acoustic metamaterials have been an important study topic in recent years. Acoustic cloaking, perfect absorbers (Ma *et al*., 2014), Sound concentration based on index lens gradient (Climente *et al*., 2010; Welter *et al*., 2011; Zhao *et al*., 2016), acoustic topological systems (Ni *et al*., 2015; Peano *et al*., 2015; Peng *et al*., 2016), and other applications have been developed. Furthermore, nonlinear acoustic metamaterials have recently received increased interest via research on acoustic diodes (Li *et al*., 2011; Liang *et al*., 2009), bifurcation-based acoustic switching and rectification (Boechler *et al*., 2011), nonlinear acoustic lenses (Donahue *et al*., 2014), and acoustic solitons (Achilleos *et al*., 2015). In other research, linear losses are attributed to low dissipation. However, nonlinear losses may quickly arise in acoustics, for example, due to geometrical discontinuities. Controlling sound waves on a subwavelength scale was challenging in acoustics due to the constraints of the mass law until the discovery of acoustic metamaterials (Li &

Chan, 2004; Li *et al*., 2016; Liu *et al*., 2000; Pennec *et al*., 2008; Yang *et al*., 2008). Artificially constructed acoustic metamaterials contradict the mass rule and exhibit several exceptional and uncommon acoustic characteristics such as negative refraction (Feng *et al*., 2005; Li *et al*., 2016; Mokhtari *et al*., 2019; Nemat-Nasser, 2019; Zhang & Liu, 2004; Zhu *et al*., 2014), acoustic focusing, and remarkable transmission, piquing the attention of many scientists and researchers (Liu *et al*., 2020; Songkaitiwong & Locharoenrat, 2020). In-room acoustics sound absorption is essential (e.g., reduction of noise). In recent decades, the following have been widely explored: Dark-acoustic metamaterials, including such porosity (Biot, 1962) structures (Lee *et al*., 2010; Ma *et al*., 2014), hybrid resonator membrane patterns (Jiang *et al*., 2017; Xiao *et al*., 2015; Zhao *et al*., 2020), metamaterials of plates (Badreddine *et al*., 2012), and resonators of the Helmholtz oscillation (Cai *et al*., 2014). The resonant structures supporting the increasing density of acoustics during resonant frequencies have been highly able to absorb sound (<500 Hz) at low frequency due to the non-trivial wave diffraction of conventional sound-absorber material plastic foam, fiberglass, and mineral wool (Allard & Atalla, 2009). As stated in earlier studies, space coiling may be used to build counterintuitive metamaterials. These metamaterials have a single negative/double negative zero indexes metamaterial and a very high index of refractive metamaterials. These extreme material characteristics are usually complex values in which the imaginary parts indicate the intrinsic loss or absorption of energy. Note that the zigzag or spiral patterns improve absorption by extending the length of the viscous limit. (Xie *et al*., 2020).

This paper investigates the acoustic metamaterial of a honeycomb structure with various designs that cause the optimal acoustic insulation and absorber design using hexagonal honeycomb structure. The use of finite element simulations via COMSOL Multiphysics software to calculate the absorption coefficient of the hexagonal honeycomb metamaterial. To improve the accuracy of the sound absorber. I proposed models by adjusting the internal parameters of the acoustic metamaterial.

2. Result and discussion

The low-frequency sound (<500Hz) attenuation by deep subwavelength thickness absorber (<5cm) is very interesting in noise control techniques. However, the high penetration of low-frequency sound and essential weakness dissipation of common materials has been challenging. The traditional materials for absorption of sound, such as porosity materials, have proved to be efficient in sound absorption at high frequency (>1000 Hz), but with low frequencies limits if the restricted thickness is imposing (Wu *et al*., 2019). As shown in Figures 1(a) and 1(b), the honeycomb structure has a dimension of length L = 188 mm, width w = 164 mm, height h = 80 mm and the hexagonal inscribed in a circle with that radius to be 30 mm, neck width w_1 = 10 mm and inner width w_2 = 8 mm. In theoretical design consisting of air and acoustic metamaterial Polydimethylsiloxane (PDMS) polymer. The air density is 1.21 Kg/m^3, and the Polydimethylsiloxane (PDMS) density is 995 Kg/m^3, while the corresponding sound velocity of the air is 343 m/s and sound velocity of the Polydimethylsiloxane (PDMS) is 1000 m/s. The metamaterials were placed in an aluminium tube with a square cross-section, as presented in Figure 1(c).
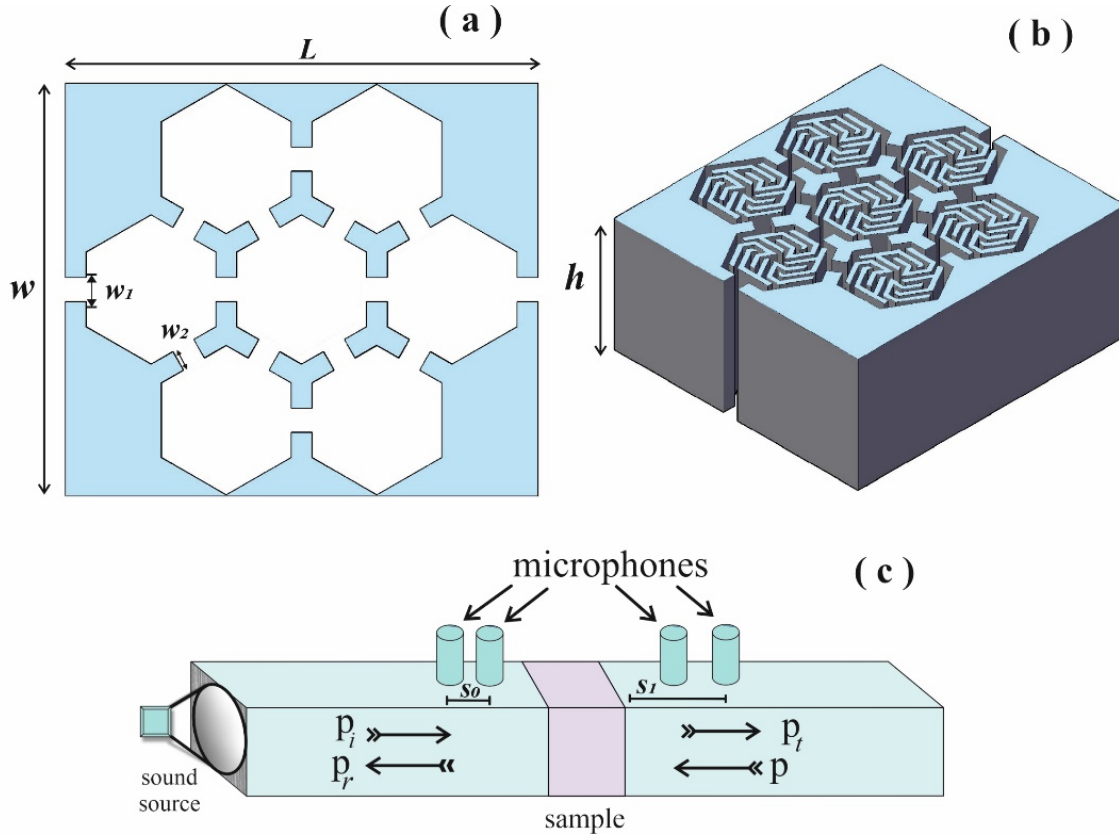
Fig. 1. (a) Schematic diagram of the hexagonal honeycomb structure dimensions without models. (b) Schematic diagram of the hexagonal honeycomb structure with the second model at n = 6. (c) The samples (honeycomb structure) were placed between two Aluminum tubes with a square cross-section, four microphones in the two-port technique, where p, p_t, p_i, p_r, and are the complex amplitudes of the transmitted, incident, and reflected plane waves, respectively.

I carefully designed two models of the absorber acoustic metamaterial of the honeycomb structure constructed based on the folding number, angle of rotation and geometric parameters of the metamaterial that were changed with high space utilization and moderate lateral dimension to match a hexagonal structure dimensions. Figures 2(a) and 2(b) show the schematics of the folding numbers from $n = 2$ to $n = 6$. The first model is denoted in Figure 2(a), where the folding number $n = 2$ at an angle of rotation by 180º. For the folding numbers $n = 3$ and 4, the inner shape is designed to be less by 75% at an angle of rotation by 120º, 90º, respectively. When the rotation angle by 72º and 60º, respectively, the internal parameters of the model are decreased by around 70% in the designed structure at folding numbers $n = 5$ and 6, as marked by the arrow in Figure 2(a). Figure 2(b) shows that the inner shape of the second model metamaterial is designed to match the outer hexagonal structure with narrow channels that take the form of hexagonal at the folding number $n = 2$, 3, and 6 with an angle rotation by 180º, and 120º, respectively. The internal channels hexagonal structure takes the form of a honeycomb lattice.
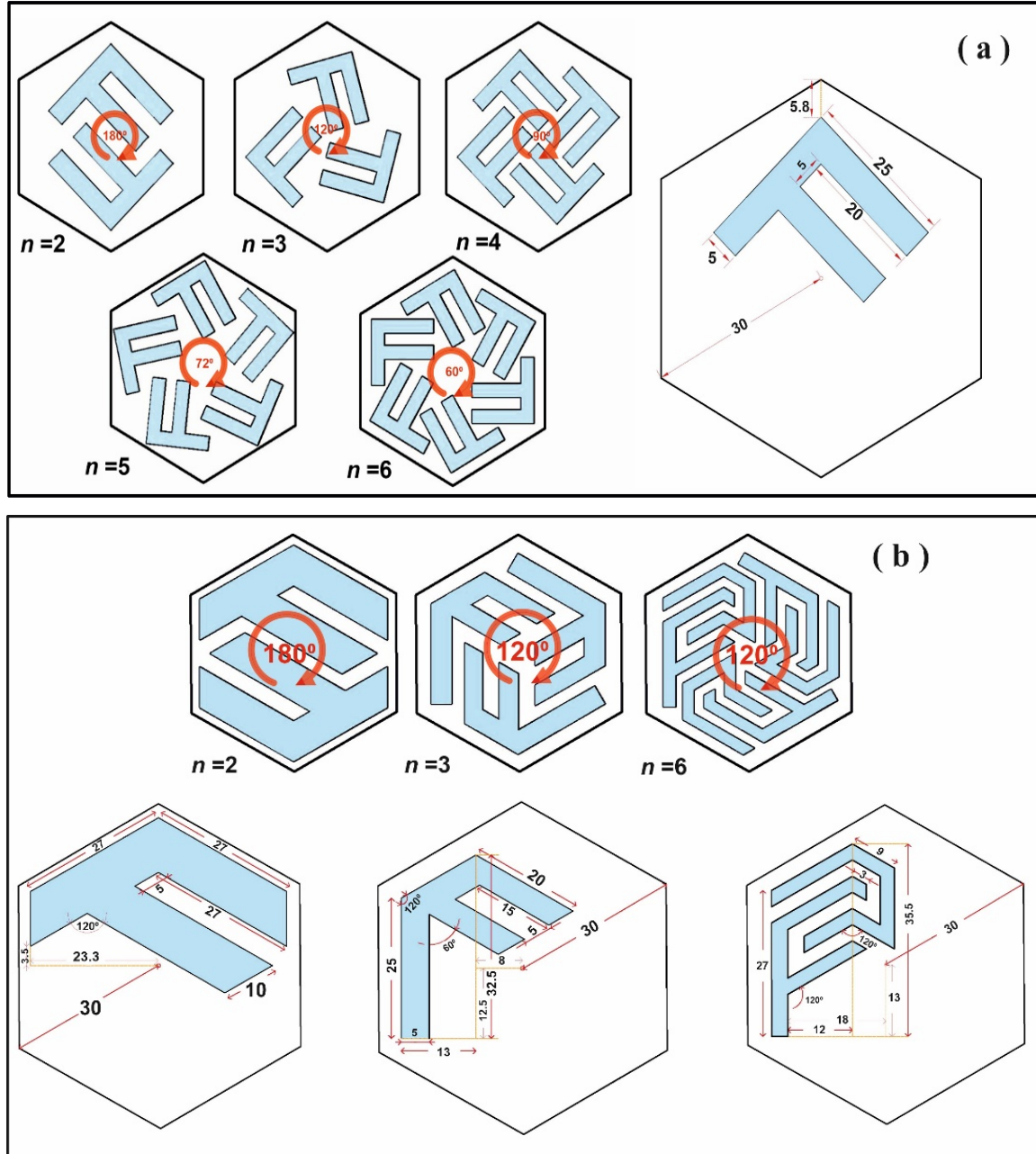
Fig. 2. (a) and (b) Schematic diagram, the hexagonal metamaterial structure with different folding numbers *n*, rotation angle, and geometric parameters.

I employ the COMSOL Multiphysics finite element solver to calculate the acoustic metamaterial simulation absorption coefficient as $A = 1 - |r|^2 - |t|^2$ with *r* and *t* representing the reflection and transmission coefficients, respectively. The microphones are placed symmetrically about the sample with the positions, as shown in Figure 1(c). The complex pressures at the measurement positions are then (Mahjoob *et al.*, 2009):

$$p_1 = p_i\, e^{ikb_1} + p_r\, e^{-ikb_1} \tag{1}$$

$$p_2 = p_i\, e^{ikb_2} + p_r\, e^{-ikb_2} \tag{2}$$

$$p_3 = p\, e^{ikb_3} + p_t\, e^{-ikb_3} \tag{3}$$

$$p_4 = p\, e^{ikb_4} + p_t\, e^{-ikb_4} \tag{4}$$

The four complex sound pressures can then be obtained from the measurements as

$$p_i = (p_1 \exp(jks_o) - p_2)\exp(-jks_1) \tag{5}$$

$$p_r = (p_2 - p_1 \exp(-jks_o))\exp(jks_1) \tag{6}$$

$$p = (p_4 \exp(jks_o) - p_3)\exp(-jks_1) \tag{7}$$

$$p_t = (p_3 - p_4 \exp(-jks_o))\exp(jks_1) \tag{8}$$

In formula $s_o = b_1 - b_2 = b_4 - b_3$ and $s_1 = b_1 = b_4$ since the microphones are symmetrically placed about the metamaterial slab. where p_t, p_r, and p_i are transmitted, reflected, and incident plane modes, respectively (Feng, 2013). From previous equations, the reflection ($r = p_r / p_i$), and transmission ($t = p_t / p_i$) coefficients are obtained as follows:

$$r = \frac{(p_2 - p_1 \exp(-iks_0))\exp(iks_1)}{(p_1 \exp(iks_0) - p_2)\exp(-iks_1)} \tag{9}$$

$$t = \frac{(p_3 - p_4 \exp(-jks_o))\exp(jks_1)}{(p_1 \exp(iks_0) - p_2)\exp(-iks_1)} \tag{10}$$

Where s_0 and s_1 are the distance between microphone and sample, respectively, k is the effective wave number for sound waves propagating inside the structure ($k = 2\pi f / c$, where f indicates the frequency in Hz, and c sound velocity of the air is 343 m/s).

If waves travel through the structure of a wave, energy trapped in the resonant element produces a perfect metamaterial absorber. In the first model, I would study the effect of a different folding number with inner shape dimensions of the honeycomb structure to achieve ideal sound absorption. The absorption performance of the absorber is tightly related to its inner meandering paths in the honeycomb structure. The results reveal high space utilization in hexagonal honeycomb structure led to a perfect absorber at the decreased rotation angle in the five cases, as shown in Figure 2(a). Figure 3(a) shows the effect geometric parameters of the absorber with three-folding numbers (n=2, 3, 4) at low-frequency of 209Hz, 242Hz, and 202Hz, respectively. It can be found that the absorption coefficient peak at 0.935, 0.722, and 0.95, respectively. It can be seen that the absorption coefficients peak moves to low frequency, the peak of sound absorption has been improved with the increase of the folding number, and the sound absorber performance of the honeycomb structure with $n = 4$ is better than that of the other two structures. Figures 3(b) and 3(c) compare the sound absorptions for the folding numbers between $n = 5$ and $n = 6$ with low-frequency. Figure 3(b) shows a high absorption peak at a lower frequency by 128.5Hz and 140 Hz

at 0.999 by adjusting the folding number $n = 5$. From Figure 3(c), the frequency of the sound absorption of the honeycomb structure is 114.5Hz and 124Hz at (0.95) of the absorption coefficient. I further compute the velocity fields in the absorber metamaterial to detect the physical mechanism of acoustic absorption in the structure. Figures 3(d)–3(j) show the simulated particle velocity fields at different frequencies of 209 Hz, 242 Hz, 202 Hz, 128.5Hz, 140 Hz, 114.5Hz and 124Hz, respectively, where the arrows mark the corresponding absorption coefficients in Figures 3(a), 3(b) and 3(c). From simulations, the local resonances play an essential role in the optimal sound absorber, which causes non-trivial relative motion in the viscous boundary layer through resonance-induced velocity fields (Ward *et al*., 2015).
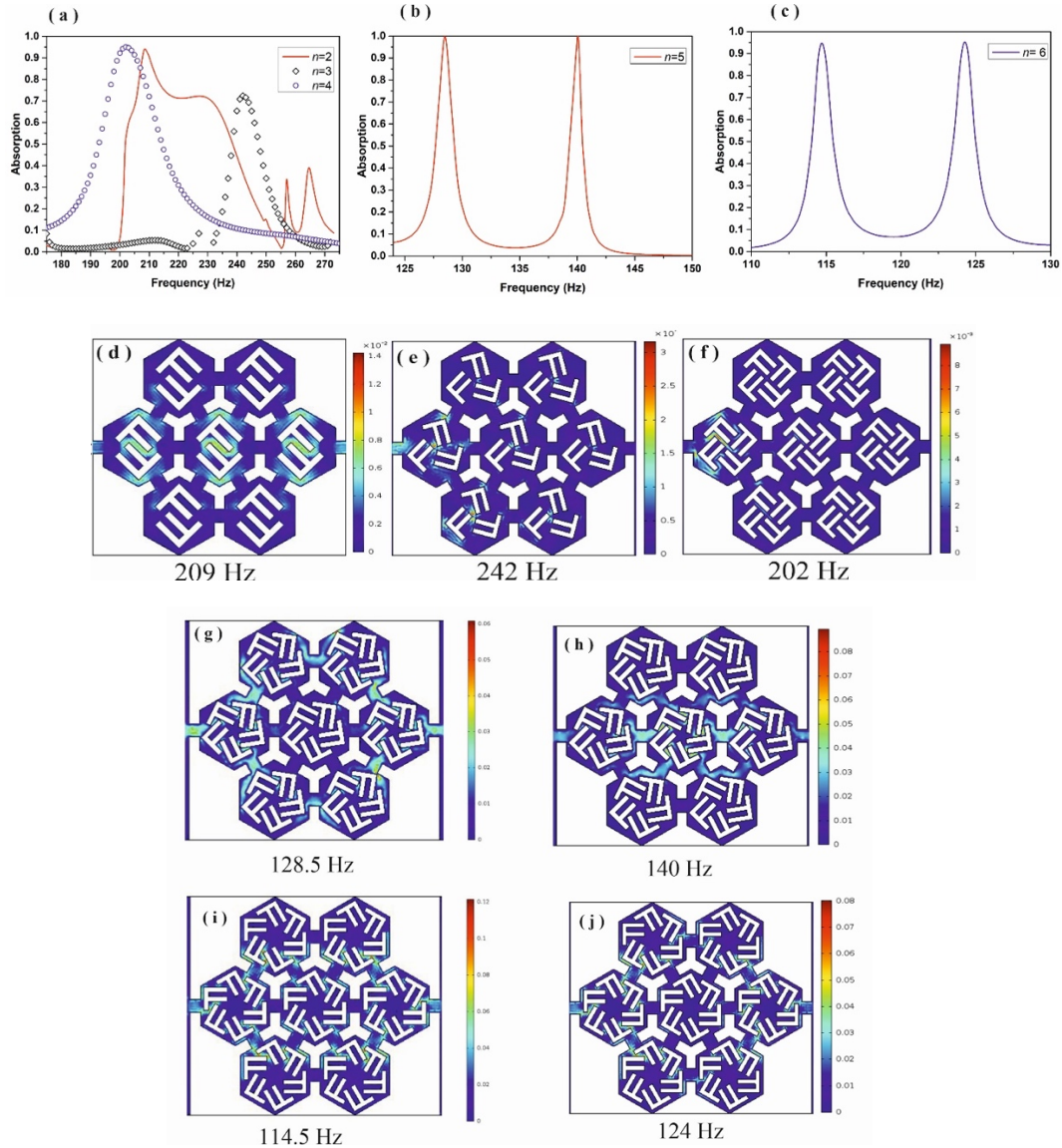
Fig. 3. (a), (b), and (c) Absorption coefficients as frequency function for acoustic metamaterial in the air at different folding numbers n = 2, 3, 4, 5 and 6. (d-j) Simulated particle velocity fields of sound at the frequencies of 209 Hz, 242 Hz, 202 Hz, 128.5Hz, 140 Hz, 114.5Hz, and 124Hz, respectively.

Figures 4(a), 4(b), and 4(c) show that the internal geometric parameters change with designs, as shown in Figure 2(b). Searching for the incident sound waves entering through to honeycomb metamaterial paves the way to achieve the perfect absorber at low-frequency. The incidence wave energy is lost mainly because of the increased friction between the wave and the internal shape of the channels. Therefore, an acoustic absorber low-frequency absorption mechanism converts sound energy resonance frequency into thermal energy. Figure 4(a) and 4(b) shows the absorption coefficient of the absorber. One can observe that the finite element simulation results are 210 Hz and 119.5 Hz at folding numbers ($n = 2, 3$) with an absorption peak of 0.982 and 0.81, respectively, and almost perfect absorption is obtained. Due to the severe air resonance in the wave structure, the absorption peak is generated, and after that, the sound energy is dissipated mainly by the loss of friction and viscous damping. The absorption coefficient set by n shows that the metamaterials enable to slow down the effective speed of acoustic waves due to path elongation through folded narrow channels. Unitary sound absorption is seen at 210 Hz for $n = 6$, i.e., absorption peaks are substantially increased at low frequencies while n increases, as shown in Figure 4(c). In Figure 4(d) - 4(f), I further show the particle velocity fields at the rotation angles of 180° and 120°, with the frequencies at 210 Hz, 119.5Hz, and 210 Hz, respectively. The results reveal that at the operating frequencies for the three cases, local resonances take place with non-trivial particle velocity fields observed at the rotation angles, leading to perfect sound absorption. It provides two critical guidelines for the application of acoustic metamaterial devices. Firstly, the maximum intensity of absorption is affected by n and also the internal geometric parameters. The other is that the effective length of the hexagonal structure of the internal channels primarily affects the optimum absorption.
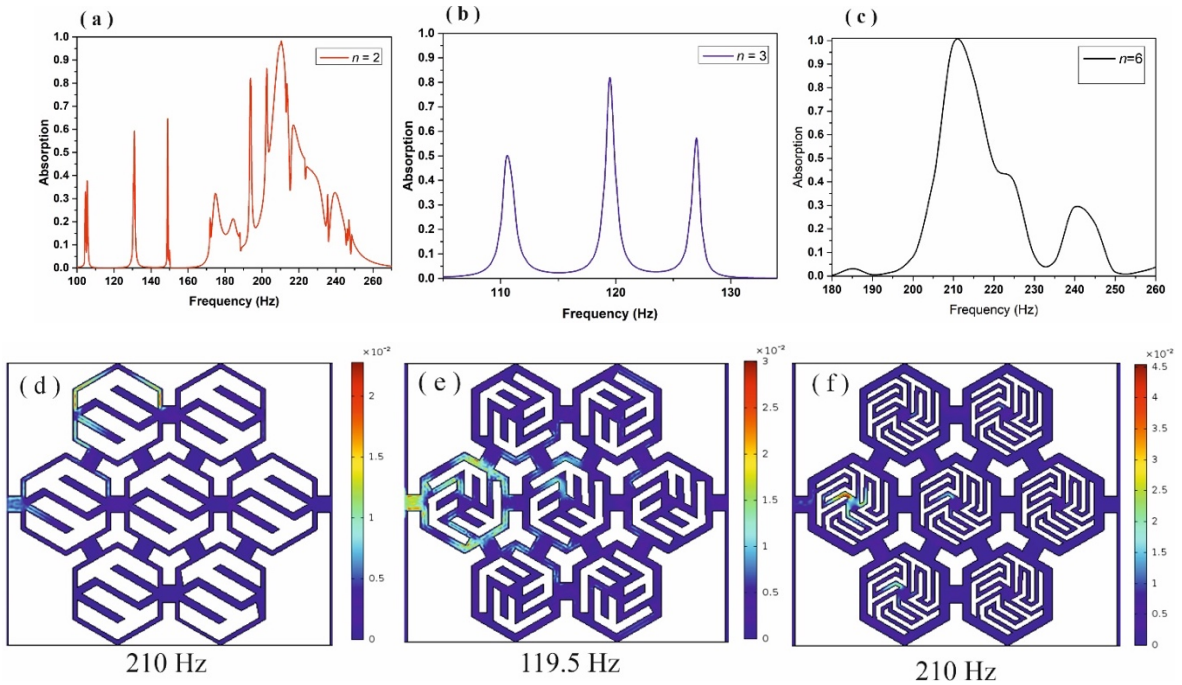
Fig. 4. (a), (b), and (c) Absorption coefficients as frequency function for acoustic metamaterial in the air at different folding numbers $n = 2, 3$, and 6. (d-f) Simulated particle velocity fields of sound at the frequencies of 210 Hz, 119.5 Hz, and 210Hz, respectively.

3. Conclusion

A finite element simulation of the acoustic metamaterial composed hexagonal honeycomb structure with different folding numbers *n* for two models are developed using multi-physics commercial software COMSOL. Therefore, metamaterial structures for satisfying the perfect absorption at low frequency in the air are designed. I focus on the concept of hexagonal honeycomb metamaterial with changes in shapes dimensions and folding numbers to match hexagonal structure dimensions. A theory of the perfect absorber of hexagonal honeycomb metamaterial is proposed. This feature was exploited for low-frequency acoustic absorbers, which play an essential role in sound absorption in honeycomb metamaterial containing the influence of structural parameters and effective length of the hexagonal structure of the internal channels that could be detected for achieving higher absorption. At the frequency of resonance 210 Hz, the effect of sound-absorbing in the second model material is reached 99%. The friction loss and viscous damping of sound energy contribute extremely to better performance related to the sound-absorbing of this metamaterial.

References

Achilleos, V., Richoux, O., Theocharis, G., & Frantzeskakis, D. J. (2015). Acoustic solitons in waveguides with Helmholtz resonators: Transmission line approach. Physical Review E - Statistical, Nonlinear, and Soft Matter Physics, 91(**2**).

Allard, J. F., & Atalla, N. (2009). Propagation of Sound in Porous Media: Modelling Sound Absorbing Materials. Propagation of Sound in Porous Media: Modelling Sound Absorbing Materials, 1–358. https://doi.org/10.1002/9780470747339

Badreddine Assouar, M., Senesi, M., Oudich, M., Ruzzene, M., & Hou, Z. (2012). Broadband plate-type acoustic metamaterial for low-frequency sound attenuation. Applied Physics Letters, 101(**17**). https://doi.org/10.1063/1.4764072

Biot, M. A. (1962). Generalized Theory of Acoustic Propagation in Porous Dissipative Media. The Journal of the Acoustical Society of America, 34(**9A**), 1254–1264.

Boechler, N., Theocharis, G., & Daraio, C. (2011). Bifurcation-based acoustic switching and rectification. Nature Materials, 10(**9**), 665–668. https://doi.org/10.1038/nmat3072

Cai, X., Guo, Q., Hu, G., & Yang, J. (2014). Ultrathin low-frequency sound absorbing panels based on coplanar spiral tubes or coplanar Helmholtz resonators. Applied Physics Letters, 105(**12**). https://doi.org/10.1063/1.4895617

Climente, A., Torrent, D., & Sánchez-Dehesa, J. (2010). Sound focusing by gradient index sonic lenses. Applied Physics Letters, 97(**10**). https://doi.org/10.1063/1.3488349

Donahue, C. M., Anzel, P. W. J., Bonanomi, L., Keller, T. A., & Daraio, C. (2014). Experimental realization of a nonlinear acoustic lens with a tunable focus. Applied Physics Letters, 104(**1**). https://doi.org/10.1063/1.4857635

Feng, Leping. (2013). Modified impedance tube measurements and energy dissipation inside absorptive materials. Applied Acoustics, 74(**12**), 1480–1485.

Feng, Liang, Liu, X. P., Chen, Y. Bin, Huang, Z. P., Mao, Y. W., Chen, Y. F., Zi, J., & Zhu, Y. Y. (2005). Negative refraction of acoustic waves in two-dimensional sonic crystals. Physical Review B - Condensed Matter and Materials Physics, 72(**3**).

Jiang, X., Li, Y., & Zhang, L. (2017). Thermoviscous effects on sound transmission through a metasurface of hybrid resonances. The Journal of the Acoustical Society of America, 141(**4**), EL363–EL368. https://doi.org/10.1121/1.4979682

Lee, S. H., Park, C. M., Seo, Y. M., Wang, Z. G., & Kim, C. K. (2010). Composite acoustic medium with simultaneously negative density and modulus. Physical Review Letters, 104(**5**). https://doi.org/10.1103/PhysRevLett.104.054301

Li, Jensen, & Chan, C. T. (2004). Double-negative acoustic metamaterial. Physical Review E - Statistical Physics, Plasmas, Fluids, and Related Interdisciplinary Topics, 70(**5**), 4. https://doi.org/10.1103/PhysRevE.70.055602

Li, Junfei, Zhou, X., Huang, G., & Hu, G. (2016). Acoustic metamaterials capable of both sound insulation and energy harvesting. Smart Materials and Structures, 25(**4**).

Li, X. F., Ni, X., Feng, L., Lu, M. H., He, C., & Chen, Y. F. (2011). Tunable unidirectional sound propagation through a sonic-crystal-based acoustic diode. Physical Review Letters, 106(**8**). https://doi.org/10.1103/PhysRevLett.106.084301

Liang, B., Yuan, B., & Cheng, J. C. (2009). Acoustic diode: Rectification of acoustic energy flux in one-dimensional systems. Physical Review Letters, 103(**10**).

Liu, Y., Xu, W., Chen, M., Yang, T., Wang, K., Huang, X., Jiang, H., & Wang, Y. (2020). Three-dimensional fractal structure with double negative and density-near-zero properties on a subwavelength scale. Materials and Design, 188. https://doi.org/10.1016/j.matdes.2020.108470

Liu, Z., Zhang, X., Mao, Y., Zhu, Y. Y., Yang, Z., Chan, C. T., & Sheng, P. (2000). Locally resonant sonic materials. Science, 289(**5485**), 1734–1736.

Ma , G., Yang, M., Xiao, S., Yang, Z., & Sheng, P. (2014). Acoustic metasurface with hybrid resonances. Nature Materials, 13(**9**), 873–878. https://doi.org/10.1038/nmat3994

Mahjoob, M. J., Mohammadi, N., & Malakooti, S. (2009). An investigation into the acoustic insulation of triple-layered panels containing Newtonian fluids: Theory and experiment. Applied Acoustics, 70(**1**), 165–171. https://doi.org/10.1016/j.apacoust.2007.12.002

Mei , J., Ma, G., Yang, M., Yang, Z., Wen, W., & Sheng, P. (2012). Dark acoustic metamaterials as super absorbers for low-frequency sound. Nature Communications, 3.

Mokhtari, A. A., Lu, Y., & Srivastava, A. (2019). On the emergence of negative effective density and modulus in 2-phase phononic crystals. Journal of the Mechanics and Physics of Solids, 126, 256–271. https://doi.org/10.1016/j.jmps.2019.02.016

Nemat-Nasser, S. (2019). Inherent negative refraction on acoustic branch of two dimensional phononic crystals. Mechanics of Materials, 132(**4**), 1–8.

Ni, X., He, C., Sun, X. C., Liu, X. P., Lu, M. H., Feng, L., & Chen, Y. F. (2015). Topologically protected one-way edge mode in networks of acoustic resonators with circulating air flow. New Journal of Physics, 17. https://doi.org/10.1088/1367-2630/17/5/053016

Peano, V., Brendel, C., Schmidt, M., & Marquardt, F. (2015). Topological phases of sound and light. Physical Review X, 5(**3**). https://doi.org/10.1103/PhysRevX.5.031011

Peng, Y. G., Qin, C. Z., Zhao, D. G., Shen, Y. X., Xu, X. Y., Bao, M., Jia, H., & Zhu, X. F. (2016). Experimental demonstration of anomalous Floquet topological insulator for sound. Nature Communications, 7. https://doi.org/10.1038/ncomms13368

Pennec, Y., Djafari-Rouhani, B., Larabi, H., Vasseur, J. O., & Hladky-Hennion, A. C. (2008). Low-frequency gaps in a phononic crystal constituted of cylindrical dots deposited on a thin homogeneous plate. Physical Review B - Condensed Matter and Materials Physics, 78(**10**).

Songkaitiwong, K., & Locharoenrat, K. (2020). Computational algorithm of high-intensity focused ultrasound beams in cancer tissue model for hyperthermia therapy. Kuwait Journal of Science, 47(**1**), 50–64.

Ward, G. P., Lovelock, R. K., Murray, A. R. J., Hibbins, A. P., Sambles, J. R., & Smith, J. D. (2015). Boundary-Layer Effects on Acoustic Transmission Through Narrow Slit Cavities. Physical Review Letters, 115(**4**). https://doi.org/10.1103/PhysRevLett.115.044302

Welter, J. T., Sathish, S., Christensen, D. E., Brodrick, P. G., Heebl, J. D., & Cherry, M. R. (2011). Focusing of longitudinal ultrasonic waves in air with an aperiodic flat lens. The Journal of the Acoustical Society of America, 130(**5**), 2789–2796. https://doi.org/10.1121/1.3640841

Wu, F., Xiao, Y., Yu, Di., Zhao, H., Wang, Y., & Wen, J. (2019). Low-frequency sound absorption of hybrid absorber based on micro-perforated panel and coiled-up channels. Applied Physics Letters, 114(**15**). https://doi.org/10.1063/1.5090355

Xiao, S., Ma, G., Li, Y., Yang, Z., & Sheng, P. (2015). Active control of membrane-type acoustic metamaterial by electric field. Applied Physics Letters, 106(**9**). https://doi.org/10.1063/1.4913999

Xie, S. H., Fang, X., Li, P. Q., Huang, S., Peng, Y. G., Shen, Y. X., Li, Y., & Zhu, X. F. (2020). Tunable Double-Band Perfect Absorbers via Acoustic Metasurfaces with Nesting Helical Tracks. Chinese Physics Letters, 37(**5**). https://doi.org/10.1088/0256-307X/37/5/054301

Yang, Z., Mei, J., Yang, M., Chan, N. H., & Sheng, P. (2008). Membrane-type acoustic metamaterial with negative dynamic mass. Physical Review Letters, 101(**20**).

Zhang, X., & Liu, Z. (2004). Negative refraction of acoustic waves in two-dimensional phononic crystals. Applied Physics Letters, 85(**2**), 341–343. https://doi.org/10.1063/1.1772854

Zhao, H., Wang, Y., Yu, D., Yang, H., Zhong, J., Wu, F., & Wen, J. (2020). A double porosity material for low frequency sound absorption. Composite Structures, 239.

Zhao, J., Bonello, B., & Boyko, O. (2016). Focusing of the lowest-order antisymmetric Lamb mode behind a gradient-index acoustic metalens with local resonators. Physical Review B, 93(**17**). https://doi.org/10.1103/PhysRevB.93.174306

Zhu, R., Liu, X. N., Hu, G. K., Sun, C. T., & Huang, G. L. (2014). Negative refraction of elastic waves at the deep-subwavelength scale in a single-phase metamaterial. Nature Communications, 5. https://doi.org/10.1038/ncomms6510

Engineering of Ultraviolet reflectors by varying alternate layers of Titania/Silica for harmful UV-protection

R.S. Dubey

Advanced Research Laboratory for Nanomaterials and Devices,
Dept. of Nanotechnology, Swarnandhra College of Engineering and Technology,
Narsapur (A.P.), Seetharampuram, India
Corresponding author: rag_pcw@yahoo.co.in

Abstract

This paper presents the engineering of ultraviolet (UV) reflectors made up of alternate layers of titania (TiO_2) and silica (SiO_2) by using the sol-gel spin coating method. The choice of these two materials is appropriate to realize the optical reflectors due to their large refractive index contrast. The formation of multilayer films of TiO_2 and SiO_2 are studied by field emission scanning electron microscopy (FESEM), while UV-vis spectroscopy measurement is performed to study the reflectance. By varying the number of TiO_2/SiO_2 stacks, we have achieved the maximum reflectance within the UV region at center wavelengths of 335 nm, 358 nm, and 367 nm corresponding to the 3-, 6-, and 9-stacks based reflectors. Finally, it is summarized that these reflectors prohibit the propagation of ultraviolet light, and therefore, promising for UV protection coating.

Keywords: Cross-section morphology; reflection; reflectors; thin films; UV Reflector.

1. Introduction

The solar spectrum is composed of ultraviolet (UV), visible (Vis), and infrared (IR) radiations. Out of these, UV radiation has adverse effects on human life, which causes sunburn, immune system, suntan, DNA damage, and ageing. Furthermore, UV exposure damages the human body, which often induces darker skin and macular degeneration in the eyes (Chalam *et al.,* 2021). It is, therefore, rather essential that human bodies are protected and safe from exposure to ultraviolet radiation. Reflectors are merely passive devices created by metal and dielectric layers. Nonetheless, due to their high maintenance and manufacturing costs, metal reflectors are of low interest. Thus, dielectric reflectors are the alternative to conventional metal reflectors and can be tailored for the interesting wavelength region. Such reflectors can be made by preparing alternate films of two different dielectric materials: zinc oxide, zirconium dioxide, hafnium dioxide, silicon dioxide, aluminum oxide, and titanium dioxide. The refractive index contrast of the corresponding materials is the primary consideration in manufacturing dielectric reflectors. The greater the refractive index contrast, the higher will be the reflectance window (Flannery *et al.,* 1979). Among the above-discussed dielectric materials, the combination of TiO_2/SiO_2 materials with their refractive index contrast 2.4/1.4 is the best choice for fabricating dielectric reflectors. Such reflectors can be produced using chemical vapor deposition, physical vapor deposition, angles of glancing, sol-gel-spin-coating, dip-coating, and spray pyrolysis methods (Jung *et. al.,* 2008; Kitano *et al.,* 2006; Singh *et al.,* 2015; Vincent *et al.,* 2007; Yuehui *et al.,* 2018; Abou-Helal *et al.,* 2002). One should carefully choose a suitable method for fabricating such dielectric reflectors to minimize the

production cost and the processing time. The sol-gel spin coating process is beneficial over other techniques due to its simple and easy control of process parameters (Subramanian *et al.,* 2008; Wu *et al.,* 2001; Zhang *et al.,* 2012). These reflectors can be adopted as a UV coating material for the glass windows of houses/buildings/offices for UV protection to human skin and the eyes. It is also beneficial to resist ultraviolet radiation during the biological process for protecting useful bacteria. These multilayer dielectric structures have other applications, such as complimentary metal-oxide-semiconductor (CMOS) devices, flame sensors, space communications, and rocket systems (Monroy *et al.,* 2003; Yonemaru *et al.,* 2002; Xie *et al.,* 2007). Various research groups have reported the fabrication and realization of UV reflectors. Plasma-CVD fabrication of SiO_2/Si_3N_4 reflector having 27 layers of SiO_2 and Si_3N_4 demonstrated maximum reflectance in the UV wavelength range (Dai *et. al.,* 2016). The preparation of dense multilayer reflectors based on HfO_2/SiO_2 films using the plasma-ion-assisted technique was reported to deal with ultraviolet light. The reflector based on 23 layers of HfO_2/SiO_2 endorsed the reflectance window in the ultraviolet region with the minimum optical loss (Torchio *et al.,* 2002). A report on the fabrication of a 22-layer-based ultraviolet reflector using the ion-assisted e-beam evaporation method is presented. They explored the performance of light-emitting diodes integrated with UV reflectors and showed better performance (Lin *et. al.,* 2015). An ultraviolet reflector composed of 26 layers of LaF_3 and MgF_2 prepared by thermal evaporation technique was employed for the far-ultraviolet radiation. They explored the application of fabricated reflectors for the wide-angle aurora imager (Wang *et al.,* 2018). Various multilayer structures based on 99, 55 and 35 layers of BaF_2 and LaF_3 fabricated by the e-beam evaporation technique were studied. The reflectance of these UV reflectors was noticed to be 96.5 %, 95.3 %, and 93.6 % based on samples 99-, 55- and 35-layers (Zukic *et al.,* 1991). Further, a dielectric reflector composed of 25 layers of LaF_3 and MgF_2 materials processed by the e-beam evaporation technique was explored. The author noticed an excellent optical property of the UV reflector and suggested its application in the Fabry-Perot interferometer (Malherbe *et al.,* 1974). Similarly, another group reported the preparation of an 8-layer based dielectric mirror composed of Al/MgF_2 films by using the electron-beam evaporation technique. This prepared structure endorsed the reflection of the UV-A spectrum. This experimental finding was compared with the simulated result and found in good agreement. Further, they suggested the application of the reflector in the Fabry-Perot interferometer (Spiller *et al.,* 174). A multilayer thin-film structure based on seven stacks of TiO_2/SiO_2 was fabricated by adopting the sol-gel spin coating technique. The prepared reflector is endorsed as much as 100% reflectance in the UV spectrum (Dubey *et al.,* 2017).

According to the above-reported literature, we have noticed that fabricated reflectors comprise many layers, which severely affects the fabrication cost and processing time of such reflectors. So, the development of low-cost reflectors is essential to save resources. In this paper, we report the engineering of UV reflectors by varying the number of TiO_2 and SiO_2 layers with the projection to reduce the fabrication cost and processing time. Section 2 presents the experimental approach, and the results are explored in section 3. Section 4 summarizes the work.

2. Experimental approach

The chemicals used in the synthesis process of TiO_2/SiO_2 gels do not require any extra further

purification. Tetra-butylorthotitanate (TBOT) and tetraethyl orthosilicate (TEOS) procured from Sigma-Aldrich were used as the precursors for fabricating the TiO_2 and SiO_2 thin films. For gel preparation, solvent 'ethanol' and catalyst 'acetic acid' was preferred. The gel of TiO_2 was synthesized using TBOT, ethanol, and acetic acid in the molar ratio of 1.2:20:1.7, respectively. Ethyl alcohol and acetic acid were thoroughly mixed under continuous magnetic stirring for 15 minutes. Later, precursor TBOT was added drop-by-drop under vigorous stirring. Further, stirring was maintained for a period of 3 hr. The asobtained TiO_2 gel was clear and transparent, which was left for 24 hr ageing. Similarly, SiO_2 gel was synthesized using TEOS, ethanol and, acetic acid in the molar ratio of 1.5:20:2.3, respectively. The gel was synthesized by slowly adding the precursor TEOS solution in the ethanol and acetic acid mixed solution under continuous stirring. The stirring process was continued for 4 hr to obtain a transparent gel. Finally, the solution was left for 24 hr ageing. After ageing, the solutions were found viscous enough and used for the film preparation on the cleaned glass substrates. The spin rate and spin duration were fixed to 2500 RPM for 30 sec. Multilayer structures of TiO_2/SiO_2 were deposited alternately by spin coating. After fabrication, each film of TiO_2 and SiO_2 was sintered at temperatures of 500 ^oC and 300 ^oC, respectively, for about 60 min. The spin coating process was repeated to fabricate the dielectric reflectors based on three, six, and nine alternate films. The fabricated multilayer structures were examined for surface and cross-section morphology using field-emission scanning electron microscopy (FESEM, ZEISS, Germany). The elements composition investigation was performed using energy-dispersive x-ray spectroscopy (EDS) attached to FESEM. The reflectance analyses were carried out using an ultraviolet-visible spectrophotometer (UV-vis, UV1800 Shimadzu, Japan).

3. Results and discussion

We have performed the FESEM measurement to analyze the surface and cross-section morphology. Figure 1 depicts the top-view and cross-sectional FESEM images, EDS, and reflectance spectra of three stack-based reflectors of TiO_2/SiO_2 thin films. Figure 1(a) and 1(b) show the top view of 3-stacks based TiO_2/SiO_2 reflector recorded at 1μm and 100 nm scale, respectively. We can observe the uniform coating of the top TiO_2 film. The average grain size of the top TiO_2 film was estimated to be 7.5 nm. The cross-section view of the reflector is shown in Figures 1(c) and 1(d) recorded at a scale of 1 μm and 200 nm, respectively. We can observe the formation of a multilayer structure consisting of periodically arranged $TiO_2/SiO_2/TiO_2/SiO_2/TiO_2/SiO_2$ films having thicknesses of 37.05 nm, 55.42 nm, 22.12 nm, 66.46 nm, 37.05 nm, and 103.5 nm, respectively in figure 1(d) recorded at a scale of 200 nm. EDS spectroscopy was performed to know the elemental composition in the multilayer structures. Figure 1(e) shows the presence of Ti, O, and Si peaks at 0.45keV, 0.5keV, and 1.7 keV, respectively. Reflectance spectra of 3-stacks-based SiO_2/TiO_2 reflector is plotted in the wavelength range from 300-400 nm, as shown in figure 1(f). The opening of a reflection band can be noticed with its reflectance of 76 % at the center wavelength of 335 nm. Further, we have engineered the reflector's fabrication to maximize the reflectance in a broad range of UV spectrum. With this, we have fabricated a 6-stacks-based TiO_2/SiO_2 reflector, as shown in figure 2. Compared to 3-stacks based TiO_2/SiO_2 reflector, uniform deposition of the films can be noticed as depicted in figure 2(a). FESEM image recorded at an increased scale as shown

in figure 2(b), which depicts similar grains with an average diameter of 6.5 nm. We can observe the layered structure of TiO_2 and SiO_2 in the cross-section FESEM image recorded at a scale of 1 μm, as shown in figure 2(c). In contrast, a closer look at the 6-stacks-based TiO_2/SiO_2 reflector shows distinct layers of TiO_2 and SiO_2 with slightly different morphology of individual layers.
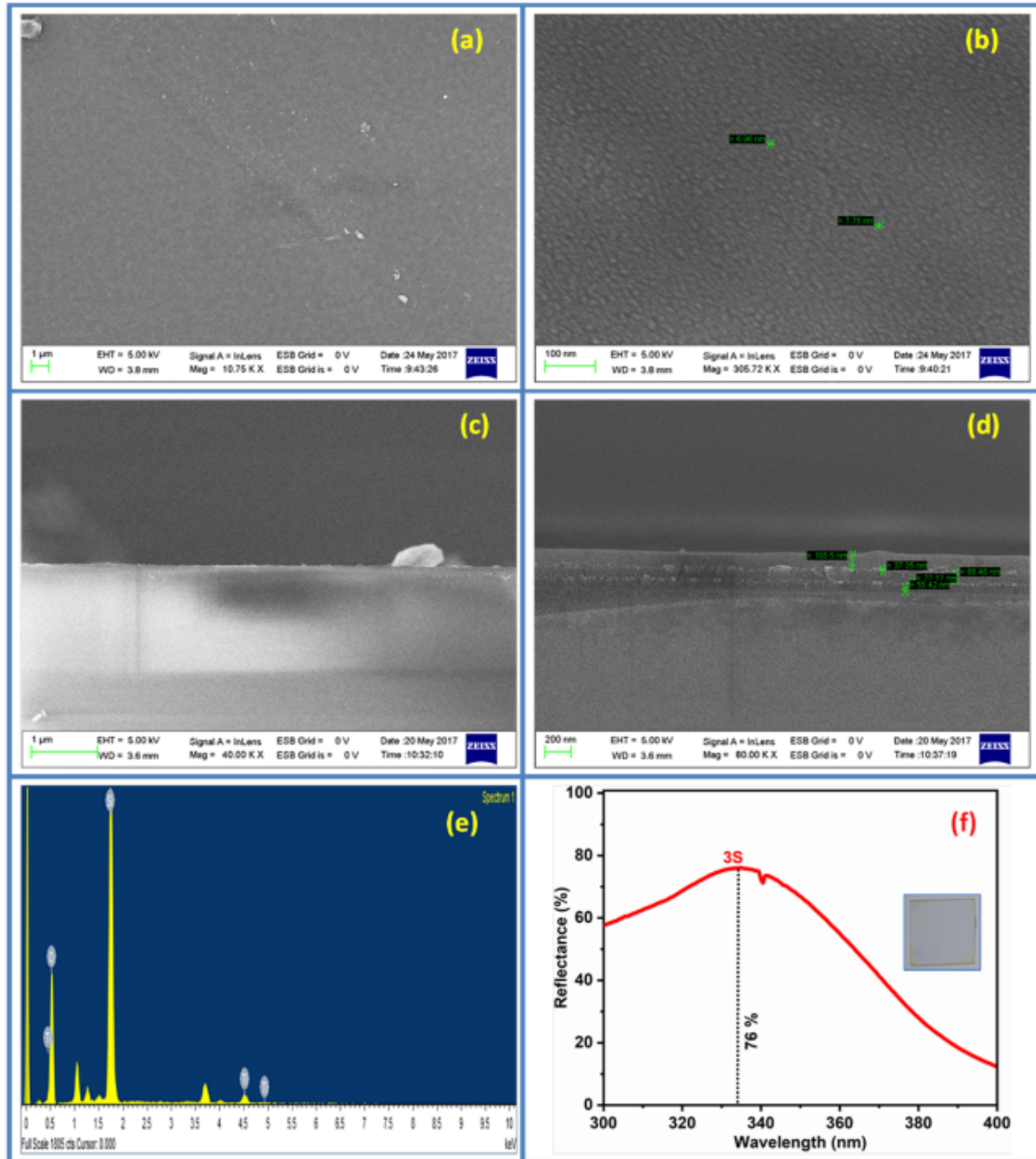

Fig. 1. FESEM top-view fig.(a)-fig.(b) recorded at the scale of 1μm and 100 nm, a crosssectional view fig.(c)-fig.(d) recorded at the scale of 1 μm and 200 nm, EDS spectra fig.(e) and reflectance spectra fig.(f) of 3-stacks TiO_2/SiO_2 reflector.

The calculated thicknesses of each TiO_2/SiO_2 film were 22/75.22, 19.17/75.22, 22.21/75.57, 35/82.63, 32.47/101.8, and 33.95/112.1 nm, respectively. As shown in figure 2e, EDS spectra show the peaks of Ti, O, and Si elements at energy 0.45 keV, 0.5 keV, and 1.7

keV, respectively. It is interesting to notice the reflectance spectra of 6-stacks-based TiO_2/SiO_2 reflectors compared to 3-stacks-based reflectors, as depicted in figure 2(f). By increasing the number of stacks, one can notice an enhancement in reflectance to 100 %. Further, we can also realize the broadening and shifting of the reflection band within the range of the UV spectrum. The center wavelength is noticed to be shifted to 358 nm instead of 335 nm for the case of 3-stacks based reflector, as observed previously and also found to coincide with the reported literature (Venkatesh *et al.*, 2020).
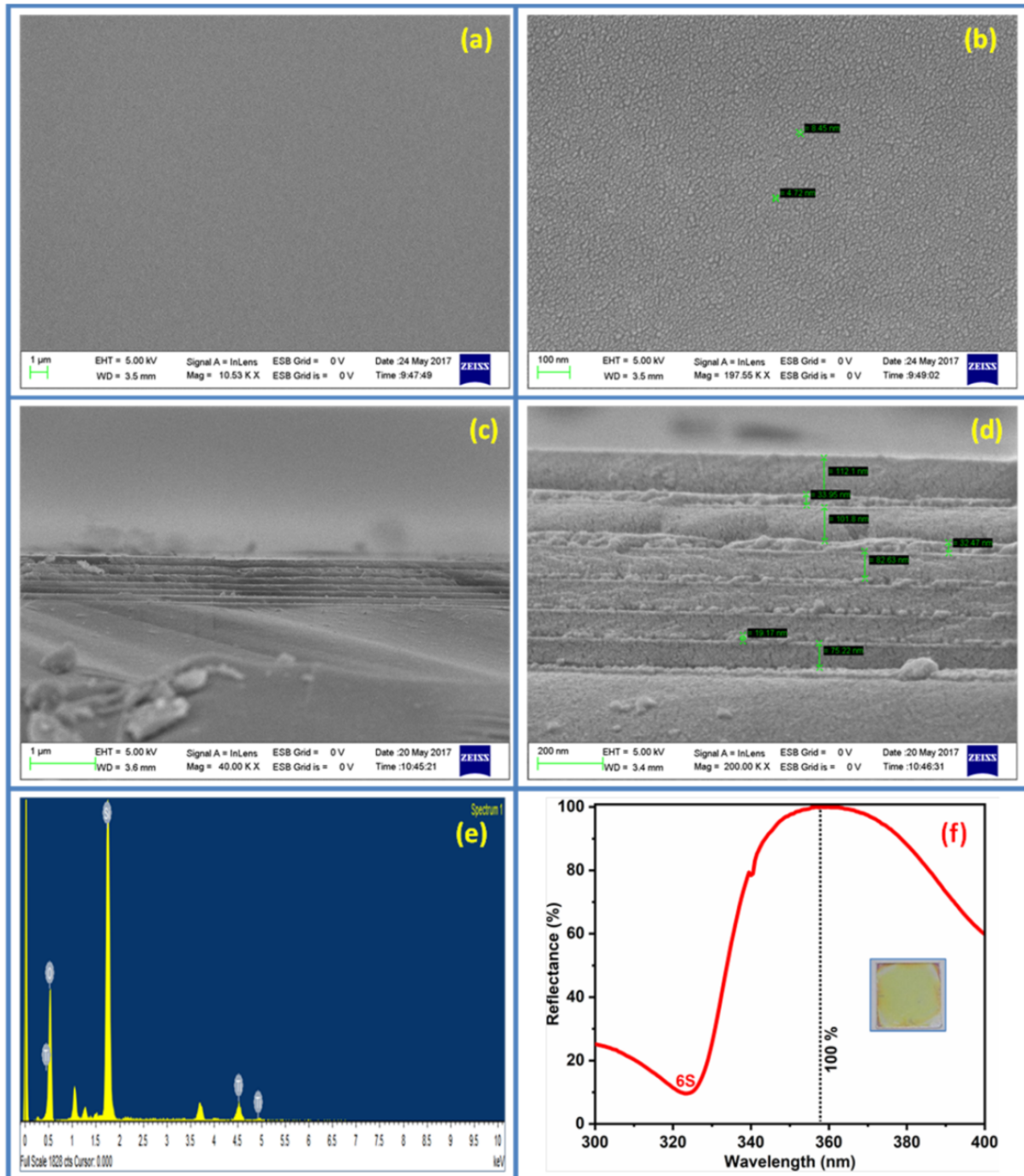
Fig. 2. FESEM top-view fig.(a)-fig.(b) recorded at the scale of 1µm and 100 nm, a crosssectional view fig.(c)-fig.(d) recorded at the scale of 1µm and 200 nm, EDS spectra fig.(e) and reflectance spectra fig.(f) of 6-stacks TiO_2/SiO_2 reflector.

It is interesting to notice the reflectance spectra of 6-stacks-based TiO2/SiO2 reflectors compared to 3-stacks-based reflectors, as depicted in figure 2(f). By increasing the number of stacks, one can notice an enhancement in reflectance to 100 %. Further, we can also realize the broadening and shifting of the reflection band within the range of the UV spectrum. The center wavelength is noticed to be shifted to 358 nm instead of 335 nm for the case of 3 stacks based reflector, as observed previously and also found to coincide with the reported literature (Venkatesh et al., 2020).

Finally, we have increased the number of stacks to 9, and the obtained results are shown in figure 3. The uniform deposition of the films is noticed as visible in figure 3(a), while figure 3(b) depicts the distribution of uniform grains with their average size of 4.5 nm.
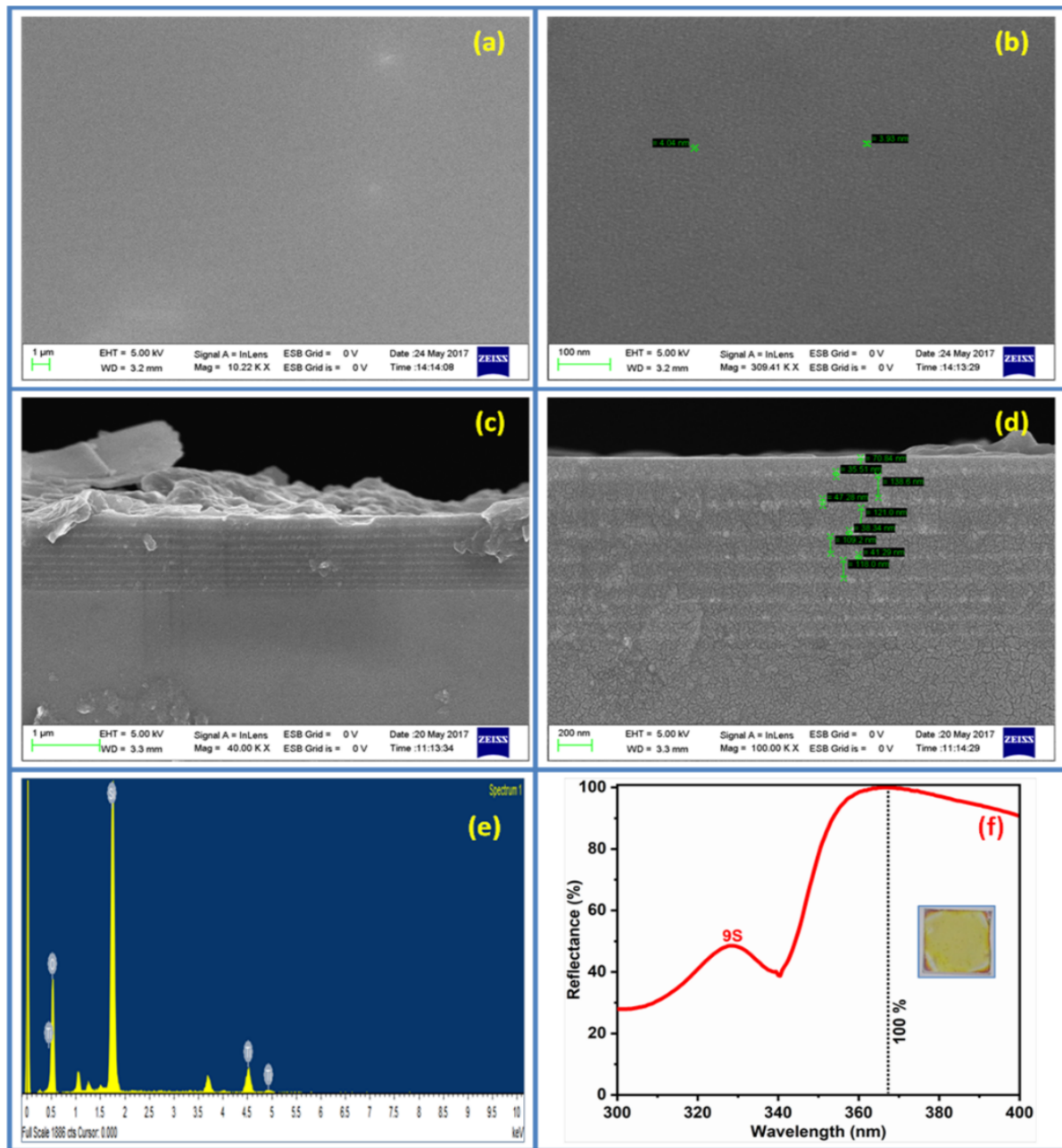
Fig. 3. FESEM top-view fig.(a)-fig.(b) recorded at the scale of 1 µm and 100 nm, a cross-sectional view fig.(c)-fig.(d) recorded at the scale of 1 µm and 200 nm, EDS spectra fig.(e) and reflectance spectra fig.(f) of 9-stacks TiO$_2$/SiO$_2$ reflector.

A cross-sectional multilayer structure view can be seen in figure 3(c), while figure 3(d) depicts the 18 layers of TiO_2/SiO_2. The thicknesses of 18 layers of TiO_2/SiO_2 films were 35.51/120, 47/100, 41/121, 41/118, 35/118, 41.29/ 109.2, 38.34/121, 47.26/138.6, and 35.51/70.84, respectively. The EDS spectrum is plotted in figure 3e, which shows the elemental composition of Ti, O, and Si at energy 0.45 keV, 0.5 keV, and 1.7 keV, respectively. A broader reflection window is observed for the case of a 9-stacks-based TiO_2/SiO_2 reflector, as depicted in figure 3(f). One can notice as much as 100% reflectance at the center wavelength of 367 nm. In addition, we can observe the presence of a small reflectance peak at a wavelength of 330 nm, which could be regarded as the interference of light due to the increased number of stacks compared to previous reflectors based on 3- and 6-stacks based. With the fabrication of TiO_2/SiO_2 reflectors by varying the number of stacks 3, 6, and 9 and one can observe corresponding shifting of their center wavelengths towards the higher values i.e., 335 nm, 358 nm, and 367 nm, and found in good agreement with the reported literature (Yuehui *et al.,* 2018). Notably, the 6 and 9-stacks-based reflectors evidence their 100 % reflectance with a broad reflection window.

4.   Conclusions

Using the sol-gel spin coating approach, various dielectric reflectors by varying the number of TiO2/SiO2 stacks were fabricated and studied. The surface morphology investigation of 3-, 6- and 9-stacks-based reflectors evidenced the deposition of uniform films. The FESEM cross section study demonstrated the fabrication of 6, 12, and 18 periodic layers of TiO2 and SiO2. The EDS spectrum confirmed the presence of elemental peaks of Ti, Si, and O in all three samples. The obtained reflectance values are 76 %, 100 %, and 100% corresponding to the TiO2/SiO2 reflectors based on 3-, 6-, and 9-stacks. The increased number of stacks yielded the maximum reflectance and resulted in the broadening of the reflection windows. In summary, the maximum reflectance was attained within the UV band at center wavelengths of 335 nm, 358 nm, and 367 nm corresponding to the 3-, 6-, and 9- stacks based reflectors. These reflectors are capable of prohibiting the propagation of a broad range of ultraviolet light, and therefore, they are promising as the UV protection coating of glass windows. Further, such reflectors are also beneficial in light-emitting diodes to maximize optical efficiency.

References

Abou-Helal M.O., Seeber W.T. (2002). Preparation of TiO_2 thin films by spray pyrolysis to be used as a photocatalyst, Appl. Surf. Sci. 195(1-4)**,** 53-62.

Chalam, K.V. (2011). Role of Ultraviolet Radiation in Age-Related Macular Degeneration, Eye contact lens. 37(4), 225-232.

Dai, J. (2016). Design and fabrication of UV band-pass filters based on SiO_2/Si_3N_4 dielectric distributed Bragg reflectors, Appl. Surf. Sci. 64, 886-891.

Dubey, R.S. & Ganesan V. (2017). Fabrication and Characterization of TiO$_2$/SiO$_2$ based Bragg Reflectors for Light Trapping Applications, Results Phys. **7**, 2271-2276.

Flannery, M. (1979). Nearly perfect multilayer dielectric reflectors: theory, Appl. Opt. 18(9), 1428-1435.

Jung, S.C. (2008). Photocatalytic activities and specific surface area of TiO$_2$ films prepared by CVD and sol-gel method, Korean J. Chem. Eng. 25(2), 364-367.

Kitano, M., Funatsu, K., Matsuoka, M., Ueshima, M., & Anpo, M. (2006). Preparation of nitrogen substituted TiO$_2$ thin film photocatalysts by the radio frequency magnetron sputtering deposition method and their photocatalytic reactivity under visible light irradiation, J. Phys. Chem. B. 110(50), 25266-25272.

Lin, NM., Shei, SC., & Chang, SJ. (2015). Design and Fabrication of a TiO$_2$/SiO$_2$ Dielectric Broadband and Wide-Angle Reflector and Its Application to GaN-Based Blue LEDs, IEEE J. Quantum Elect. 51 (7), 1-5.

Malherbe, A. (1974). Interference filters for the far ultraviolet, Appl.Opt. 13, 1275-1276.

Monroy, E., Omnes, F., & Calle (2003). Wide-bandgap semiconductor ultraviolet photodetectors, Semiconduct. Sci. Technol. 18(4), R33-R51.

Singh, D.P., Seung Hee Lee, II Yong Choi, & Jong Kyu Kim. (2015). Spatially graded TiO$_2$-SiO$_2$ Bragg reflector with rainbow-colored photonic bandgap, Opt. Express. 23(13), 17568-17575.

Spiller, E. (1974). Interference filters for the ultraviolet and the surface plasmon of aluminum, Appl. Opt. 13(6), 1209-1215.

Subramanian, M., Vijayalakshmi, S., Venkataraj, S., & Jayavel, R. (2008). Effect of cobalt doping on the structural and optical properties of TiO$_2$ films prepared by sol-gel process, Thin Solid Films. 516 (12), 3776-3782.

Torchio, P., Gatto, A., Alvisi, M., Albrand, G., Kaise, N., & Amra. C. (2002). High-reflectivity HfO$_2$/SiO$_2$ ultraviolet mirrors, Appl. Opt. 41(16), 3256-3261.

Venkatesh Yepuri, Dubey, R. S. & Brijesh Kumar. (2020). Fabrication and characterization of spectrally selective glazing dielectric multilayer structures, Nanosystems: Phys. Chem. Math. 11 (4), 488-492.

Venkatesh Yepuri, Dubey, R. S., & Brijesh Kumar. (2020). Rapid and economic fabrication approach of dielectric reflectors for energy harvesting applications, Sci. Rep. 10, 1-9.

Vincent, A., Babu, S., Brinley, E., Karakoti, A., Deshpande, & Seal, S. (2007). Role of catalyst on refractive index tunability of porous silica antireflective coatings by sol–gel technique, J. Phys. Chem. C. 111(23), 8291-8298.

Wang, X., Chen, B., & Yao, L. (2018). Design and Fabrication of Far-Ultraviolet Reflective Broadband Filter Based on Dielectric Materials, J. Appl.Spectrosc. 72(6), 943-946.

Wu. G., Wang, J., Shen, J., Yang, T., Zhang, Q., Zhou, B., Deng, Z., Fan, B., Zhou, D., & Zhang, F. (2001). A new method to control nano-porous structure of sol–gel-derived silica films and their properties, Mater. Res. Bull. 36(12), 2127-2139.

Xie, Z.L., Zhang, R., Xiu, X.Q., Han, P., Liu, B., Chen, L., Yu, H.Q., Jiang, R.L., Shi, Y., & Zheng Y.D. (2007). MOCVD growth and characteristics of high-quality AlGaN used in the DBR structure of ultraviolet detector, Acta Phys. Sin. Chem. Ed. 56(11), 6717-6721.

Yonemaru, M., Kikuchi, A., & Kishino, K. (2002). Improved Responsivity of AlGaN-Based Resonant Cavity-Enhanced UV Photodetectors Grown on Sapphire by RF-MBE, Phys. stat. sol. (a). 192(2), 292-295.

Yuehui, W., & Xing, Y. (2018). High-reflection optical thin films based on SiO_2/TiO_2 nanoparticles multilayers by dip coating, Micro Nano Lett. 13(9), 1349-1351.

Zhang, Y., Gao, F., Gao, L., Hou, L., & Jia, Y. (2012). Study of tri-layer antireflection coatings prepared by sol-gel method, J. Sol-Gel Sci. Technol. 62, 134-139.

Zukic, M., & Torr, G. (1991). Multiple reflectors as narrow-band and broadband vacuum ultraviolet filters, Appl. Opt. 31(10), 1588-1596.

Hydrothermal analysis of water-Al₂O₃ nanofluid flow through a sudden expansion channel with an intermediate step

Sandip Saha[1, *], Apurba Narayan Das[2]

[1] *Division of Mathematics, School of Advanced Sciences, Vellore Institute of Technology Chennai, Chennai-600127, Tamilnadu, India*
[2] *Dept. of Mathematics, Alipurduar University, Alipurduar-736121, West Bengal, India*
[*] *Corresponding author: sandip.tfgss@gmail.com*

Abstract

This work presents the dynamic behavior of the laminar hydrothermal flow of nanofluid through a sudden expansion channel with the variations in the normalized length, height, and pitch to width ratio of the intermediate step. The governing equations have been discretized using the finite volume method, and the SIMPLE algorithm has been applied to solve the system of algebraic equations. The effect of the variations in the Reynolds number (Re), normalized height (B/C), normalized length (A/C), and step pitch-width ratio (A/B) on the enhancement of heat transfer has been studied. For different values of A/C, A/B, and B/C, this work indicates that the average Nusselt number (Nu$_{avg}$), thermal resistance factor (R), and performance number (PN) increase with the increase in Re. In the case of the hydrothermal flow phenomena, the configuration associated with B/C provides better results than those associated with A/B and A/C. As an important outcome, we see that the presence of an intermediate step enhances the average Nusselt number and thermal resistance factor. This will become very much helpful for various realistic circumstances for triggering additional thermo-mechanical loads on the surface.

Keywords: Friction factor; intermediate step; laminar flow; performance number; thermal resistance factor.

1. Introduction

Transport of nanofluid flow and heat transfer phenomena through sudden expansion channels and rectangular channels have wide applications in different engineering appliances [Al-Ashhab (2019); Al-Hajri *et al.* (2020); Saha *et al.* (2020); Wei *et al.* (2020); AL-Jawary (2020); Saha *et al.* (2021a); Kiran *et al.* (2021); Saha *et al.* (2021b)]. Several authors have studied different characteristics of HT phenomena through various types of the channel in the presence of porous media [Joibary & Siavashi (2019); Norouzi *et al.* (2020); Rashidi *et al.* (2019)]. Generally, porous media is used in the channels to increase the rate of HT. Flow through a sudden expansion channel is a well-known phenomenon [Mostafavi & Meghdadi (2017)]. Many authors [Menouer *et al.* (2019)], experimentally and numerically, have shown that the increase in Re causes the existence of two or more flow separation zones at the lower and upper corner walls,

which causes a substantial heat loss [Galuppo & De (2017)]. Hilo *et al*. (2020) studied different properties of the hydrothermal phenomena of flow over a suddenly expanded channel. To enhance the rate of HT, many researchers [Rashidi *et al*. (2019); Boudiaf *et al*. (2020)] have investigated the hydrothermal phenomena using nanofluid and stated that the rate of HT can be enhanced using nanofluid instead of the base fluid. In a sudden expansion channel with porous suction, Terekhov & Terekhov (2017) discussed the flow separation region and stated that an increase in the strength of transverse mass flux shortens the separation region in suction and lengthens the same in blowing. Dyachenko *et al*. (2019) investigated the profiles of Δp in the separation zone forms after the expanded section of a suddenly expanded channel with vortex generators. They stated that the rate of HT increases with the enhancement of vortex lengths. Naphon (2007) experimentally investigated the different characteristics of heat transfer through a V-shaped sudden expansion channel. It is demonstrated that after the recirculation zone the mixing of the fluid in the boundary layer intensifies, which increases convective HT. In addition, he studied that the breaking of the thermal boundary layer could increase the rate of HT when the flow past the corrugated surfaces. Through various types of corrugated channels, Ajeel *et al.* (2019) studied the thermal enhancement of nanofluid flow phenomena. They concluded that the pressure drop and recirculation characteristics depend on the shape of the teeth. It has also been shown that the value of Nu_{avg} increases with the increase in Re. In an abruptly changed channel, Maghsoudi & Siavashi (2019) showed that the value of Nu_{avg} found in the case of a smooth channel increases by 8.3% for the presence of porous insert. In the presence of a porous floor segments in a sudden expansion channel, Abu-Hijleh, (2000) investigated the reattaching flow characteristics. They concluded that the value of Nu_{avg} found in the case of a smooth channel increases by 16% for the existence of porous media. Martin *et al*. (1998) numerically analyzed the hydrothermal phenomena through a sudden expansion channel with a porous medium. They concluded that thermal behavior enhances with the increase in the height of the porous medium.

In this work, we have studied the effect of the variations in A/B, B/C, and A/B on flow phenomena, and this will be helpful to form thermo-mechanical machines at low production costs. Nanofluid has better heat transfer enhancement compared to any base/Newtonian fluid for having a higher thermal conductivity of the nanoparticles and is used in many engineering equipment. From the above literature survey, it has been found that no work has been done on nanofluid flow and the rate of HT phenomena through sudden expansion channel with intermediate step. This provides us enough confidence to carry forward the current work. The present work is an extension of the studies of Ternik *et al*. (2006). They studied the flow phenomena of power-law fluids without considering HT phenomena and the effect of the intermediate step. In this work, we have investigated the water-Al₂O₃ nanofluid flow phenomena and HT characteristics including streamlines, F, Nu_{avg}, R, and PN with the variations of A/B, B/C, A/B, and Re in a two-dimensional sudden expansion channel with intermediate step.

2. Geometry of the problem

The flow geometry of the physical domains has been presented in the figures. 1(a-b), where the flow enters through the inlet with velocity, u_{in} at the temperature, T_{in}. Figure. 1(a) presents the flow geometry of the suddenly expanded channel and figure 1(b) presents the computational domain with an intermediate step. The flow is assumed viscous, incompressible, steady, single phase, laminar, and the particles have no inertia and the radiation of HT has been neglected. Constant heat flux has been assigned to the lower wall only, and other walls have been kept insulated.
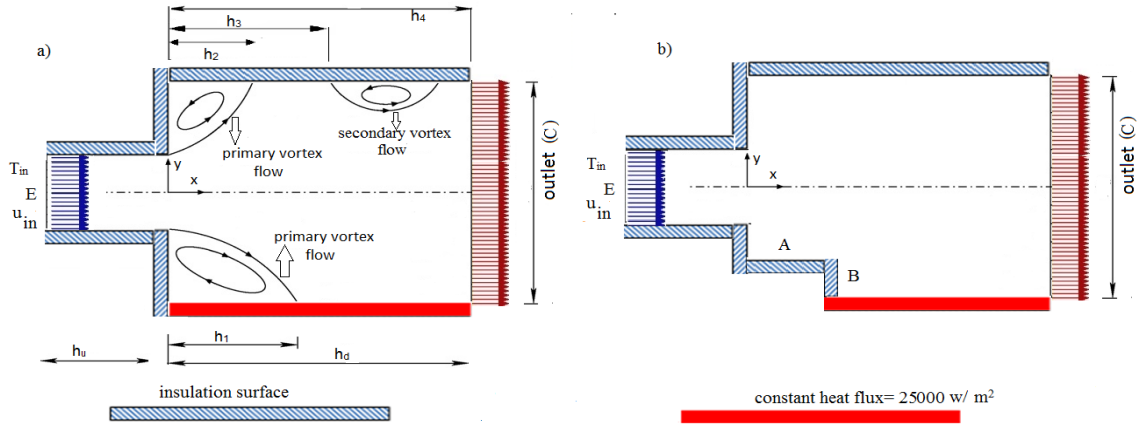
Fig. 1. Geometry without (a) intermediate step and with (b) intermediate step.

3. Formulation of the Problem

The following non-dimensional equations have been used to analyze the hydrothermal phenomena of fluid flow in the Cartesian coordinate system [Aminossadati *et al*. (2011); Akbari *et al*. (2015); Behnampour *et al*. (2017)].

Continuity equation:
$$\frac{\partial U}{\partial X} + \frac{\partial V}{\partial Y} = 0 \qquad (1)$$

The momentum of X equation:
$$U\frac{\partial U}{\partial X} + V\frac{\partial U}{\partial Y} = \frac{\mu_{nf}}{\rho_{nf}\vartheta_f}\frac{1}{Re}\left(\frac{\partial^2 U}{\partial X^2} + \frac{\partial^2 U}{\partial Y^2}\right) - \frac{\partial P}{\partial X} \qquad (2)$$

The momentum of Y equation:
$$n \quad U\frac{\partial V}{\partial X} + V\frac{\partial V}{\partial Y} = \frac{\mu_{nf}}{\rho_{nf}\vartheta_f}\frac{1}{Re}\left(\frac{\partial^2 V}{\partial X^2} + \frac{\partial^2 V}{\partial Y^2}\right) - \frac{\partial P}{\partial Y} \qquad (3)$$

Energy equation:
$$U\frac{\partial \theta}{\partial X} + V\frac{\partial \theta}{\partial Y} = \frac{\gamma_{nf}}{\gamma_f}\frac{1}{Re}\frac{1}{Pr}\left(\frac{\partial^2 \theta}{\partial X^2} + \frac{\partial^2 \theta}{\partial Y^2}\right). \qquad (4)$$

Where the following non-dimensional parameters have been used:

$$X = \frac{x}{E}, \ Y = \frac{y}{E}, \ \theta = \frac{T - T_{in}}{\Delta T}, \ \Delta T = \frac{25000 \ E}{k_f}, \ Re = \frac{\rho_f u_{in} E}{\mu_f}, \ U = \frac{u}{u_{in}}, \ V = \frac{v}{u_{in}}, \ Pr = \frac{\vartheta_f}{\gamma_f}, \ P = \frac{p}{\rho_{nf} u_{in}^2}.$$

3.1 Boundary conditions

At the inlet section: X = -2, -1.5< Y <1.5, U= 1, θ = 0, and at the outlet section: Outflow boundary conditions; $\frac{\partial U}{\partial X} = 0$, $\frac{\partial V}{\partial X} = 0$ and $\frac{\partial \theta}{\partial X} = 0$ have been imposed and finally, at the wall section: No slip ($U_X = 0$, $V_X = 0$) and no penetration ($U_Y = 0$, $V_Y = 0$) boundary conditions have been implemented at the walls and a constant heat flux has been applied at the lower wall but the other walls remain insulated ($\frac{\partial \theta}{\partial X} = 0$).

4. Characteristics of Nano fluid

The following equations have been used to calculate the ρ_{nf} and $(\rho C_p)_{nf}$ [Behnampour *et al.* (2017)].

$$\rho_{nf} = (1 - D)\rho_f + D\rho_s \tag{5}$$

$$(\rho C_p)_{nf} = (1 - D)(\rho C_p)_f + D(\rho C_p)_s \tag{6}$$

The following mean empirical correlation [Patel *et al.* (2005); Behnampour *et al.* (2017)] is used to evaluate the k_ef.

$$k_{ef} = k_f + k_f \frac{k_s D}{k_f \ (1-D)} [1 + 36000 \ Pe] \tag{7}$$

Thermo-physical properties of nanofluid have been taken from the studies of Corcione (2010) and Akbari *et al.* (2016).

5. Computational procedures, the test of grid and validation of the model

The computational fluid dynamics solver, Fluent [Soueid *et al.* (2020)] has been utilized for simulation and visualization purposes. FVM has been utilized to solve the governing equations (equation 1-equation 3) with the aid of a second-order upwind scheme. In addition, the SIMPLE algorithm [Corcione (2010); Akbari *et al.* (2015); Behnampour *et al.* (2017)] has been used to discretize the pressure-velocity coupling. The convergence criteria have been set as 10^{-6}, 10^{-6}, and 10^{-9} for continuity, momentum, and energy equations respectively.

The whole computation domain has been segregated into two parts (figure. 2). To study the effect of mesh size, three different mesh studies and grid tests have been performed at Re = 30, as illustrated in figure. 3. Figure. 3(a) presents the variation in the pressure coefficient along the x-axis with the variations in the length of the channel. It is clearly shown in figure. 3(a) that the mesh 2 can be taken for future analysis and from figure. 3(b), it is investigated that 91,260 cells are sufficient for further analysis. The code validation has been done with the studies of
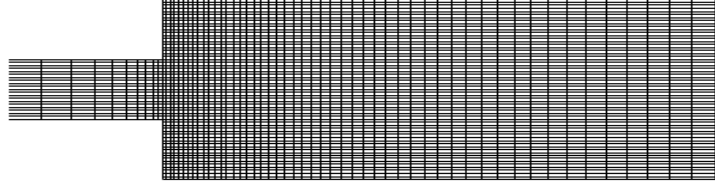
Fig. 2. Geometry of mesh.
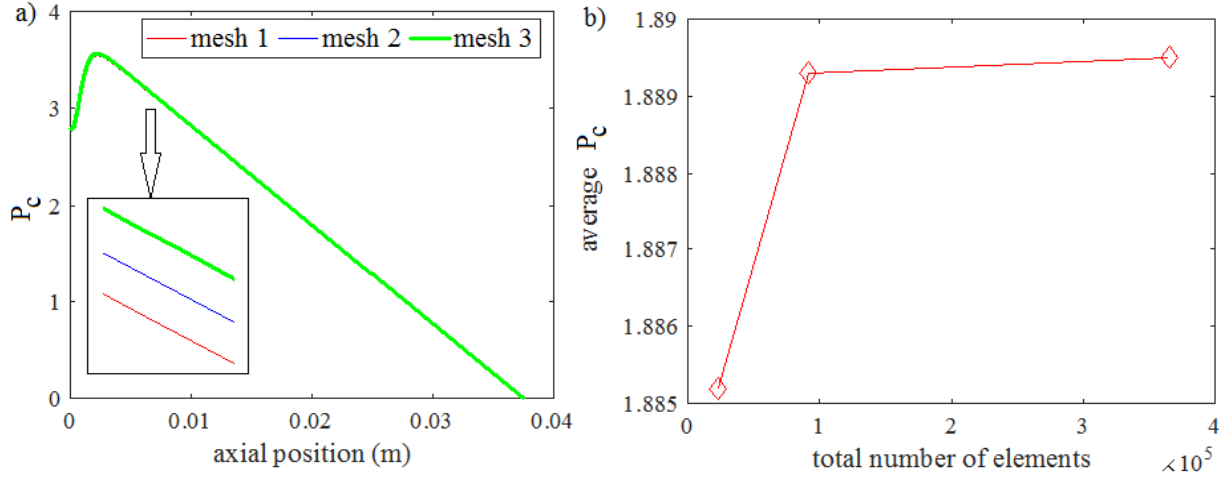
Fig. 3. Plots of (a) P$_c$ vs. axial position and (b) average P$_c$ vs. the total number of elements.
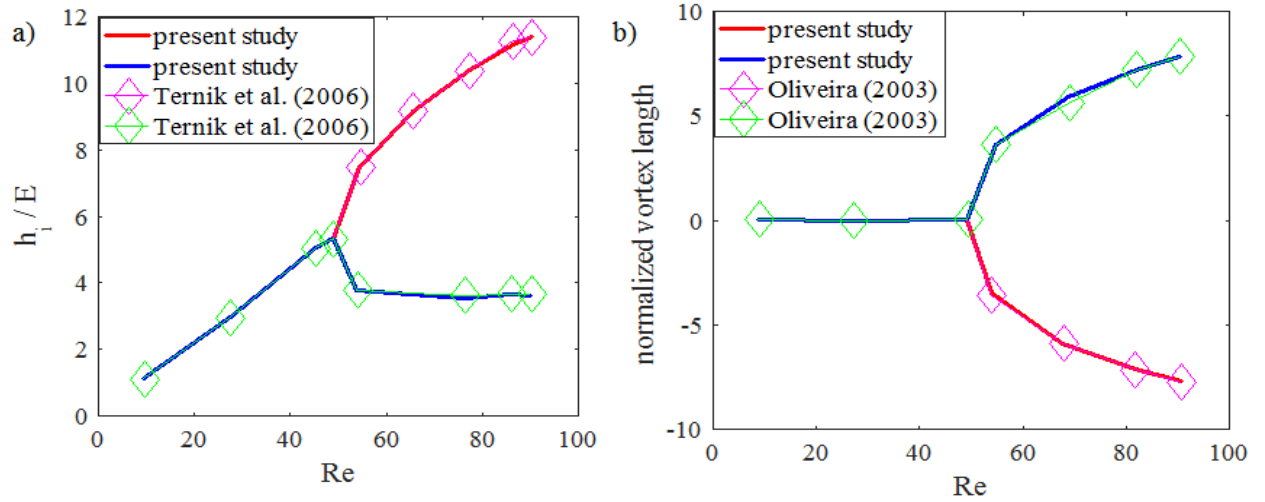

Fig. 4. Plots of (a) primary vortex length and (b) normalized vortex length *vs.* Re.

Oliveira (2003) and Ternik *et al.* (2006) by comparing the results of primary and normalized vortex lengths, and shows a good agreement with the present model, as can be seen in the figures. 4(a-b).

6. Results and discussions

This section describes the effect of various parameters, viz., Re, Nu_{avg}, PN, and different geometrical parameters of intermediate steps (A/B, B/C, and A/B) on the hydrothermal phenomena of flow.

6.1 Effect of B/C, A/C, and A/B on flow phenomena at D= 0%

The flow is separated from the lower corner of the suddenly expanded channel and creates a primary weak zone in the clockwise direction. At Re= 100, the profiles of velocity streamlines
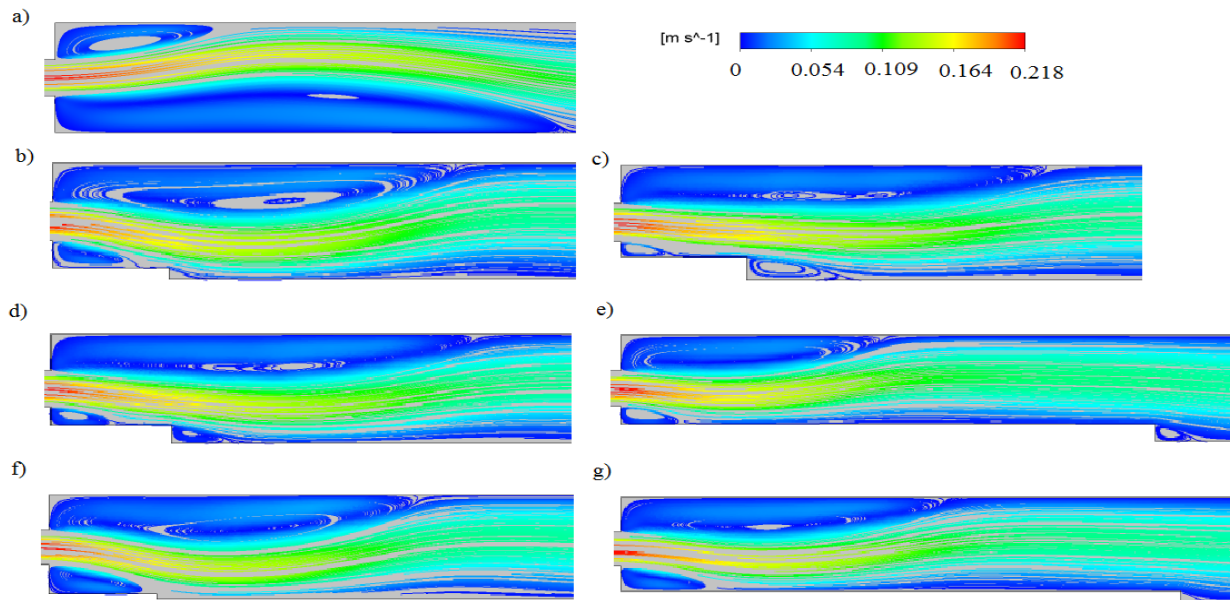
Fig. 5. Velocity streamlines for different configurations at Re = 100 and D = 0%.

have been shown in the absence of intermediate step, i.e., for A/B = 0, B/C = 0 and A/C = 0 (figure. 5a), and in the presence of intermediate steps, i.e., for A/C=0.05 (figure. 5b), A/C=0.2 (figure. 5c), B/C=1 (figure. 5d), B/C = 5 (figure. 5e), A/B = 5 (figure. 5f) and A/B = 30 (figure. 5g). It is observed that the presence of intermediate step at higher values of B/C, and A/C allow the fluid to flow smoothly, which causes the existence of weak zones after the intermediate step. In addition, the size of recirculation zones is found to depend on the configurations of intermediate step. Moreover, just after the step, a weak zone of small length appears and becomes stronger as the fluid passes the steps. Furthermore, the rate of heat transfer enhances due to the existence of a second weak zone, as a result, isotherms become denser. It has been investigated that with the increase in the value of B/C, the first weak zone disappears and the length of the second weak zone increases. It has also been observed that the second weak zone disappears as the value of A/B increases. In addition, the length of the flow reattachment point increases with the increase in Re.

6.2 Effect of Re and PN

Due to the adverse pressure gradient in the sudden expansion zone, it has been noted from figure. 5(a) that the weak zone appears at both the lower and upper walls. From the figure. 5, it has been observed that velocity streamlines become slightly sparse just after the sudden expansion and also found that as it proceeds towards the outlet section, it becomes scattered indicating that due to low velocity, heat transfer rate decreases. The permeability of the streamlines near the walls reduces and heat transmission increases. As a result, the thickness of the thermal and hydrodynamic boundary layer increases. As the step height increases, the length of the weak zone also increases, as a result, the rate of heat transfer enhances slightly. Moreover, as the value of A/C increases to some specific value, the length of the weak zone continuously reduces and the same lies completely within the step. This mechanism destabilizes the heat transfer by itself, but the heat transfer is usually improved by having higher thermal conductivity. The effects of Re, A/B, A/C, and A/B on Nu_{avg}, F have been shown in the figures. 6(a-e). In all the considered cases, it has been found that the increase in Re, B/C, A/C, and A/B causes an increase in Nu_{avg} [figures. 6(a-c)] and decrease in F (figures. 6(d-e)). The profile of F depends on the values of Δp. Due to the effect of viscous dissipation, Δp increases monotonically and causes enhancement of heat transfer. The value of Nu_{avg} attains its maximum at the zone surrounding the attachment point, and these points move the downstream with the increase in Re. Generally, the increased values of Re are correlated with the increased shear stress. At Re = 300 and D = 0%, it has been revealed that the value of Nu_{avg} enhances by 56% at B/C = 0.33 of that at B/C = 0. At Re= 300 and D=4%, it has also been studied that the value of Nu_{avg} reaches approximately 1.46 times at A/C = 15 of that at A/C = 1, and at A/B = 50, the value of Nu_{avg} increases up to 1.438 times of that at A/B = 10, as can be seen from the figures. 6(a-c). It has also been investigated that the plots of Nu_{avg}, and F become more pronounced with the increase in D%. At Re = 300, the figure. 7 shows the variation in R with D for different configurations of the intermediate step. The profile of R has been described as an efficient parameter of thermal enhancement. It is noted that the value of R increases with the increase in the values of B/C (figure. 7a), A/C (figure. 7b), and D%. The value of thermal enhancement factor starts to increase due to the enhancement in the cooling effect by reducing the wall temperature at the downstream section. Consequently, the boundary-layer thickness decreases. At Re = 300, B/C = 0.33 and D = 4%, it has been found that the value of R increases up to 1.2 times of that at D = 0%, while at A/C = 7, it becomes 1.12 times of that at D = 0%. Effects of different geometric parameters of intermediate steps on the performance number have been shown in the figures. 8(a-c). For the values of B/C, the boundary layer of the lower wall occupies a significant portion of the step, particularly at a low velocity. As the value of B/C increases, a large portion of the fluid tends to flow through the intermediate step. The use of a porous medium can prevent the sudden increase in Nu_{avg} at the reattachment point, which is unacceptable in many realistic contexts for triggering additional thermo-mechanical loads on the material surface. Moreover, the thickness of the step, rather than the porosity or permeability of the porous material, has a greater effect on the flow and heat transfer

characteristics. In all the considered cases, it has been noted that the performance number reaches greater than one, implying a greater thermal enhancement.
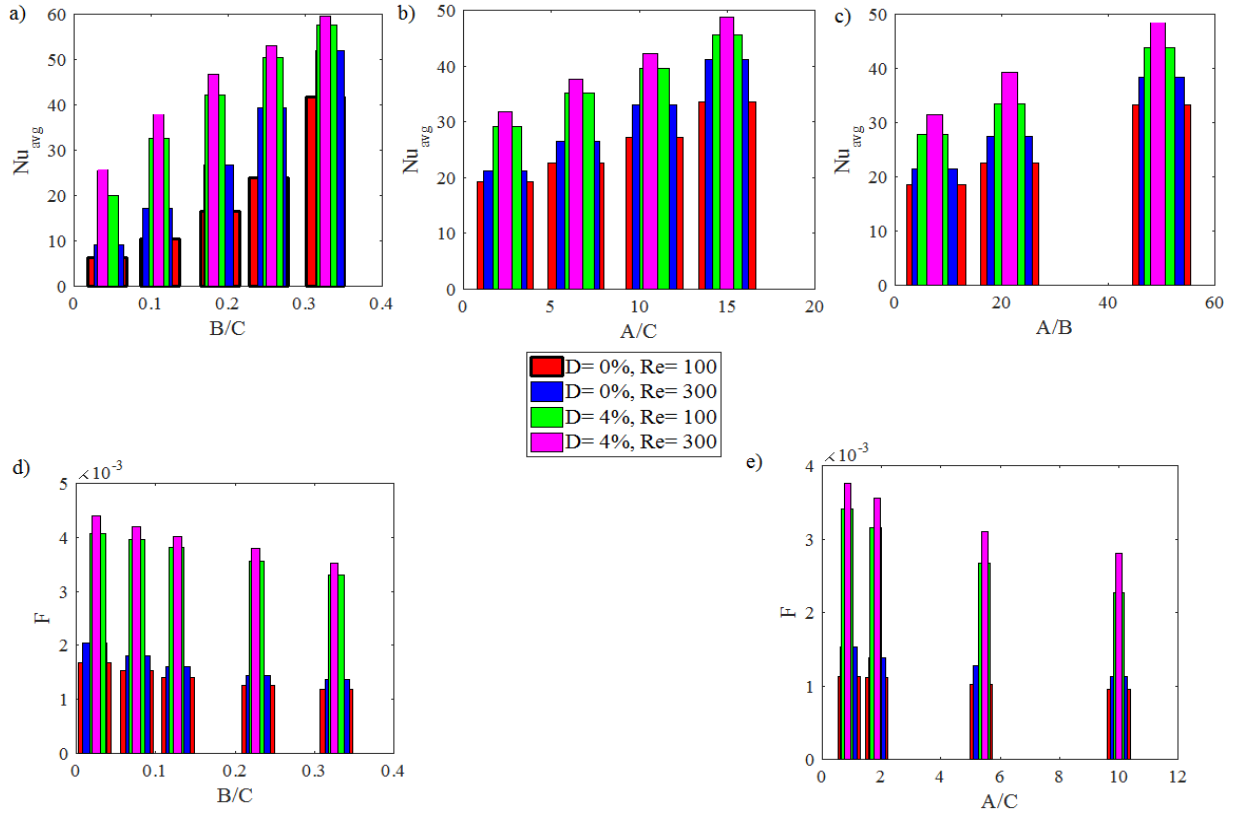

Fig. 6. Variations of (a-c) Nu_{avg} and (d-e) F at Re = 100, 300 for D= 0% and 4%.
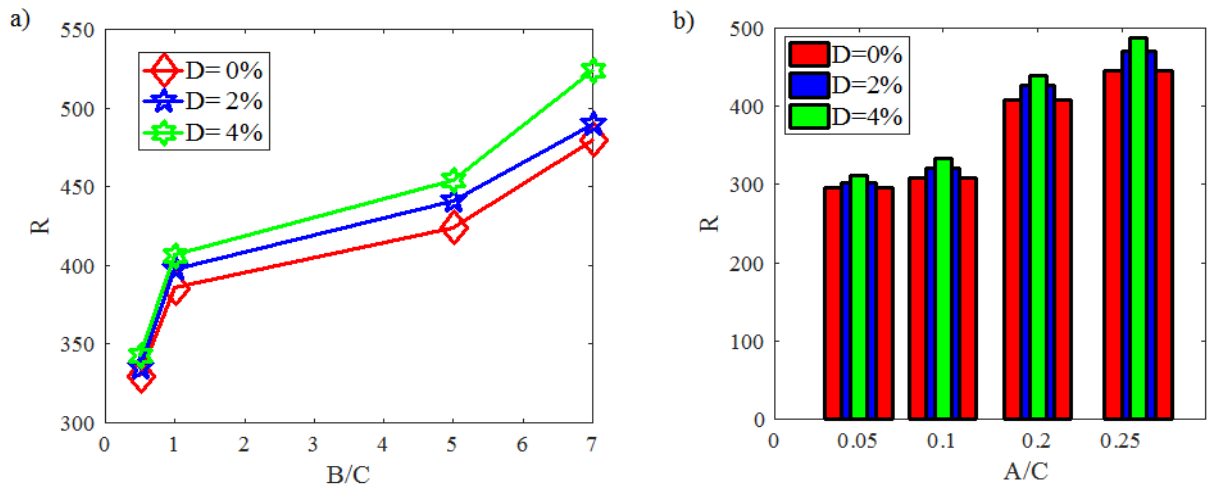

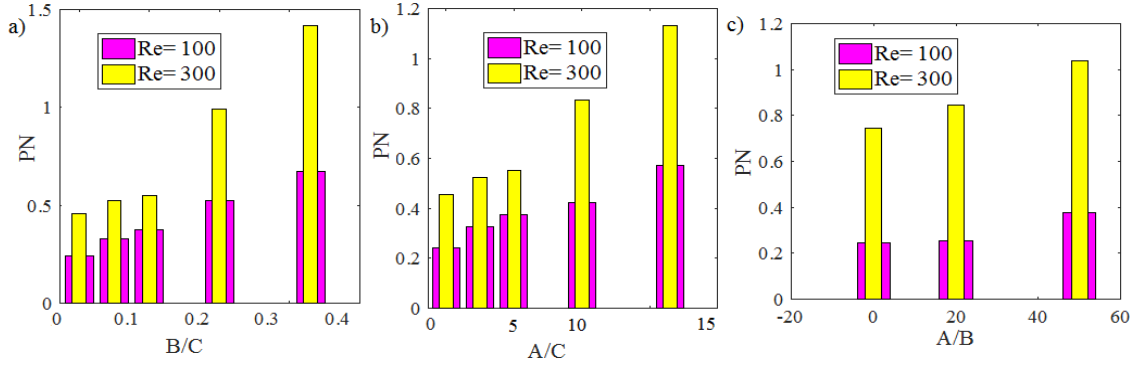**Fig. 7.** Variations of R for different configurations at various D.

Fig. 8. Bar diagrams of PN for different configurations at Re = 100 and 300 and D= 4%.

7. Conclusions

A numerical study has been performed to investigate the influence of intermediate step with limited length, height, and pitch-width ratio on the enhancement of heat transfer phenomena. The major findings of the present work are as follows:

(a)   Enhancement of heat transfer causes the enhancement in Re, percentage of volume fraction of nanoparticles, normalized step height, normalized step length, and pitch-width ratio. An increase in Re causes an increase in the average Nusselt number and performance number. In the case of thermal enhancement, the following configurations have been followed:

B/C (normalized height of intermediate step) > A/C (step pitch to width ratio) > A/B (normalized length of intermediate step).

(b)   A porous medium can prevent the sudden increase in Nu_{avg} at the reattachment point, which is unacceptable in many realistic contexts for triggering additional thermo-mechanical loads on the material surface.

(c)   To enhance the heat transfer, the use of a porous block or the use of bell surface in a thermo-mechanical model is too expensive, but the present study suggests that the presence of the intermediate step in a sudden expansion channel reduces the cost, which becomes very much helpful for the engineering communities related to flow phenomena.

References

Abu-Hijleh, B. A. (2000) Heat transfer from a 2D backward facing step with isotropic porous floor segments. Int J Heat Mass Transf, 43: 2727-2737.

Ajeel, R. K., Salim, W. S. & Hasnan, K. (2019) Thermal performance comparison of various corrugated channels using nanofluid: numerical study. Alex Eng J, 58: 865-877.

Akbari, A. O., Toghraie, D., Karimipor, A., Safaei, R. M., Goodarzi, M., Alipour, H. & Dahari, M. (2016) Investigation of rib's height effect on heat transfer and flow parameters of laminar water - Al_2O_3 nanofluid in a rib-microchannel. Applied Mathematics and Computations, 290: 135-153.

Akbari, O. A., Karimipour, A., Toghraie, D. Karimipour, A. (2015) Impact of ribs on flow parameters and laminar heat transfer of Water-Aluminum oxide nanofluid with different nanoparticle volume fractions in a three-dimensional rectangular microchannel. Adv Mech Eng, 7: 1-11.

AL-Ashhab, S. (2019) Asymptotic Behaviour and Existence of Similarity Solutions for a Boundary Layer Flow Problem. Kuwait Journal of Science, 46(2), 13-20.

AL-Hajri, S., Mahmood, S.M., Akbari, S., Abdulelah, H., Yekeen, N. & Saraih, N. (2020) Experimental investigation and development of correlation for static and dynamic polymer adsorption in porous media. J Pet Sci Eng, 189: 1058-1064.

AL-Jawary, M. (2020) Three iterative methods for solving Jeffery-Hamel flow problem. Kuwait Journal of Science, 47(1): 1-13.

Aminossadati, M. S., Raisi, A., & Ghasemi, B. (2011) Effects of magnetic field on nanofluid forced convection in a partially heated microchannel. Int. J. Non Linear Mech, 46: 1373-1382.

Behnampour, A., Akbari, O. A., Safaei, M. R., Ghavami, M., Marzban, A., Shabani, G. A. S., Zarringhalam, M. & Mashayekhi, R. (2017) Analysis of heat transfer and nanofluid fluid flow in microchannels with trapezoidal, rectangular and triangular shaped ribs. Phys E, 91: 15-31.

Boudiaf, A., Danane, F., Benkahla, Y.K., Berabou, W., Benzema, M. & Ouyahia, S. E. (2020) Heat transfer analysis of nanofluid flow through backward facing step. MATECWeb Conf, 307: 01-10.

Corcione, M. (2010) Heat transfer features of buoyancy-driven nanofluids inside rectangular enclosures differentially heated at the sidewalls. Int. J. Thermal Sci, 49(9): 1536-1546.

Dyachenko, A. Y., Zhdanov, V. L., Smulskii, Y. I. & Terekhov, V. I. (2019) Experimental investigation of heat transfers in the separation zone behind a backward-facing step in the presence of tabs. Thermophys Aero-mech, 26: 509-518.

Galuppo, W. C. & De, L. M. J. S. (2017) Turbulent heat transfers past a sudden expansion with a porous insert using a nonlinear model. Numer Heat Transf Part Appl, 71: 290-310.

Hilo, A. K., Abu, T. A. R., Acosta, I. A., Hameed, S. M. T. & Abdul, H. M. F. (2020) Effect of corrugated wall combined with backward-facing step channel on fluid flow and heat transfer. Energy, 190: 1162-1194.

Joibary, S. M. M. & Siavashi, M. (2019) Effect of Reynolds asymmetry and use of porous media in the counterfow double-pipe heat exchanger for passive heat transfer enhancement. J Therm Anal Calorim, 140: 1079-1093.

Kiran, S., Mani, S. & Sivanandam, S. (2021) Numerical study on conjugate convective thermal transport in an annular porous geometry. Kuwait Journal of Science, https://doi.org/10.48129/kjs.10789

Maghsoudi, P. & Siavashi, M. (2019) Application of nanofluid and optimization of pore size arrangement of heterogeneous porous media to enhance mixed convection inside a two-sided lid-driven cavity. J Therm Anal Calorim, 135: 947-961.

Martin, A. R., Saltiel, C. & Shyy, W. (1998) Heat transfer enhancement with porous inserts in recirculating flows. J Heat Transf, 120: 458-467.

Menouer, A., Chemloul, S. N. & Chaib, A. K. (2019) Steady Flow of Purely Viscous Shear-Thinning Fluids in a 1:3 Planar Gradual Expansion. Journal of Applied Fluid Mechanics, 12(3): 789-801.

Mostafavi, M. & Meghdadi, A. H. (2017) New Formulation for Prediction of Permeability of Nano Porous Structures using Lattice Botzmann Method. Journal of Applied Fluid Mechanics, 10(2): 639- 649.

Naphon, P. (2007) Heat transfer characteristics and pressure drop in channel with V corrugated upper and lower plates. Energy Convers Manag, 48: 1516-1524.

Norouzi, A. M., Siavashi, M. & Khaliji, O. M. (2020) Efficiency enhancement of the parabolic trough solar collector using the rotating absorber tube and nanoparticles. Renew Energy, 145: 569-584.

Patel, E. H., Sundararajan, T., Pradeep, T., Dasgupta, A., Dasgupta, N. & Das, K. S. (2005) A micro-convection model for thermal conductivity of nanofluids. Pramana- J. Phys, 65 (5): 863-869.

Oliveira, J. P. (2003) Asymmetric flows of viscoelastic fluids in symmetric planar expansion geometries. J. Non-Newtonian Fluid Mech, 114: 33-63.

Rashidi, S., Karimi, N., Mahian, O. & Abolfazli, E. J. (2019) A concise review on the role of nanoparticles upon the productivity of solar desalination systems. J Therm Anal Calorim, 135: 1145-1159.

Saha, S., Biswas, P. & Nath, S. (2020) Bifurcation phenomena for incompressible laminar flow in expansion channel to study Coanda effect. Journal of Interdisciplinary Mathematics, 23 (2): 493-502.

Saha, S., Biswas, P., Rout, S. & Das, N. A. (2021a) Convective heat transfer of laminar nano-fluids flow through a rectangular micro-channelwith different types of baffle-corrugation. International Journal for Computational Methods in Engineering Science & Mechanics, 22 (2): doi.org/10.1080/15502287.2021.1894509.

Saha, S., Rout, S. & Das, N. A. (2021b). Thermal enhancement and entropy generation of laminar water-Al2O3 nano-fluid flow through a sudden expansion channel with bell-shaped surface. International Journal of Fluid Mechanic Research, 48 (3): 65-78.

Soueid, A. A., Revil, A., Bolve, A., Steck, B., Vergniault, C. & Courivaud, J. R. (2020) Determination of the permeability of seepage flow paths in dams from self-potential measurements. Eng Geol, 268: 1055-1064.

Ternik, P., Marn, J. & Zunic, Z. (2006) Non-Newtonian Fluid Flow through a Planar Symmetric Expansion: Shear-thickening Fluids. Journal of Non-Newtonian Fluid Mechanics, 13: 136-148.

Terekhov, V. V. & Terekhov, V. I. (2017) Effect of surface permeability on the structure of a separated turbulent flow and heat transfer behind a backward-facing step. J Appl Mech Tech Phys. 58: 254-263.

Wei, B., Zhang, X., Liu, J., Xu, X., Pu, W. & Bai, M. (2020) Adsorptive behaviors of supercritical CO_2 in tight porous media and triggered chemical reactions with rock minerals during CO_2-EOR and sequestration. Chem Eng J, 381: 1225-1237.

Epitomizing mercury concentrations in incenses as a potential marker to respiratory ailments

Abdul Hadi E. Bu-Olayan*

Dept. of Chemistry, Kuwait University,
Safat-13060, State of Kuwait, Kuwait
* Corresponding author: abdul.buolayan@ku.edu.kw

Abstract

Recent years witnessed the use of incense in aromatherapy, religious festivals, warding negative vibes, and indoor air refreshers at home. Their consequences to respiratory ailments over a long period in relation to pollution from trace metals were least studied. The present study aimed to analyze the elemental mercury (Hg) concentrations directly and indirectly in different marketed incenses and validated their effect on respiratory ailments in residents. Sixteen common brands of incense of pollution interests from the local markets were analyzed using a direct mercury analyzer that measured samples from 0.0015ng/g onwards with precise and reproducible results. Subsequently, residents apportioned in six Governorate areas of environmental interest were provided with questionnaires and sought responses to the use of incenses and their health issues. Analysis revealed high Hg concentrations in the perfume-soaked incenses compared to the non-perfume-soaked incenses besides their significant site-wise variations. The questionnaire from 60 respondents who used 'Bokhour' often and were exposed to smoke for >8h showed mild to severe respiratory ailments in line with the indoor-outdoor air quality. Despite the beneficial effect of incenses described in the past, Hg concentration was observed high in the incense that caused varying respiratory ailments which were attributed to the native's selectivity, regional specificity, and recurrent uses of incenses. This study labeled Hg in incense as an additive bio-indicator to indoor pollution. Furthermore, restricting the burning of unmonitored locally available incense is recommended to prevent health issues and subsequent indoor pollution.

Keywords: Bokhour; frankincense; indoor pollution; Kuwait; mercury.

1. Introduction

The custom of burning incenses namely, the perfumed and non-perfumed scented wood ('Bokhour') and naturally available resin (Frankincense) is a customary practice of the residents of many countries. They are smoldered to disperse the aroma to their clothes and rooms besides, their use in aromatherapy and health rejuvenation (Ahmed *et al*., 2020; Mfarrej *et al*., 2020; Shen *et al*., 2017; El-Sayed *et al*., 2016; Ali *et al*., 2016; Wolter,2015). Evidence indicates the extraction of aromatic oils from the best *Boswellia sacra* resin of Salalah and Dhofar Valley of Oman added in 'Bokhour'. Incense materials are available in various forms and vary with personal choices, culture, and tradition. Direct burning of incense involved direct ignition by a flame or a heat source like charcoal and indirect burning of incense utilized electricity (Ahmad & Balkhyour, 2020). This

incense varies in the duration of its burning with the texture of the material. Finer ingredients tend to burn more rapidly, while coarse ground burns gradually as they have a less total surface area (Incense, 2018).

Many investigations (Lorena 2020; Geng *et al*., 2019; Al-Yasiry *et al*., 2016; Vudanna *et al*., 2016; Al-Hararasi *et al*., 2014; Zarshenas *et al*., 2013) observed these incenses (a) to alleviate stress and emotion, (b) boost and balance immune and hormone system, (c) anti-aging properties, (d) catalyze the secretion of digestive enzymes and, (e) decrease inflammation. Contrastingly, studies (Ahmed *et al*., 2020; Mfarrej *et al*., 2020; Tran *et al.,* 2020; Hussain *et al*., 2018; Seow & Lan 2016; Al-Busaidi *et al*., 2015; Jankowich & Rounds 2012; Orecchio 2011) showed the harmful effects of hazardous smoke that included organic compounds and heavy metals from such incenses causing respiratory ailments to humans. Interestingly, investigators (Abdu Alrasool *et al*., 2018; BuHamra *et al.,* 2018; Višić, *et al*., 2018; Tsiouri *et al*., 2015; Zhou *et al* 2015; Lui *et al*., 2016; Kumar *et al*., 2014) showed that the particulates (PM_{10}) in the incense smoke exceeded the standard values of tobacco smoke emission described by the statutory bodies besides, the synergism between the incense (Courtes *et al*., 2018; Wu *et al*., 2012), and lung cancer. Evidence (Courtes *et al*., 2018; Azevado *et al*., 2012; Amoatey *et al*., 2018) showed high mercury (Hg), concentrations with increasing temperature in the indoor environment indicating the possible elevation of respiratory ailments besides, mood swings, headache, and insomnia. Such health issues evinced further interest to persevere an in-depth study.

In the six Kuwait Governorates, the practice of burning 'Bokhour,' frankincense, incense stick, and the use of herbal aromatic oil are on the rise over a few decades. 'Bokhour' and Frankincense in the Kuwait market originate from the State of Oman, Saudi Arabia, Yemen, and the United Arab Emirates. Air contaminant standards were set by statutory bodies (Azevado *et al*., 2012). However, the local statutory bodies did not undertake any precautionary measures or standardized regulations to burn incense. Nonetheless, the effects of burning such incenses in Kuwait were least described (Wolter, 2015; Geng *et al*., 2019; Amoatey *et al*., 2018; OSHA, 2017; Yuan *et al*., 2020; Bahloul & Gevao,2014; Wu *et al*., 2012).

Based on the earlier findings, this novel study (2018-2020), fulfilled the lacunae on the possible pollution impact of Hg from various imported incenses distributed in the local markets of the six Kuwait Governorates by (a) directly analyzing the Hg in the perfumed and non-perfumed incenses, (b) perfecting the technology using a direct mercury analyzer, and (c) indirectly validating the responses to questionnaire from the residents in relation to the frequent use of incenses and their effect to respiratory ailments.

2. Materials and methods

2.1 Sample location

Three distinct markets each, from the six areas (Figure 1) of pollution importance (vicinity to thermal and coal plants, oil sector, small and large-scale industries, thickly populated residential area, waste treatment plants) was selected besides, the availability of the incense throughout the study period (2018-2019).
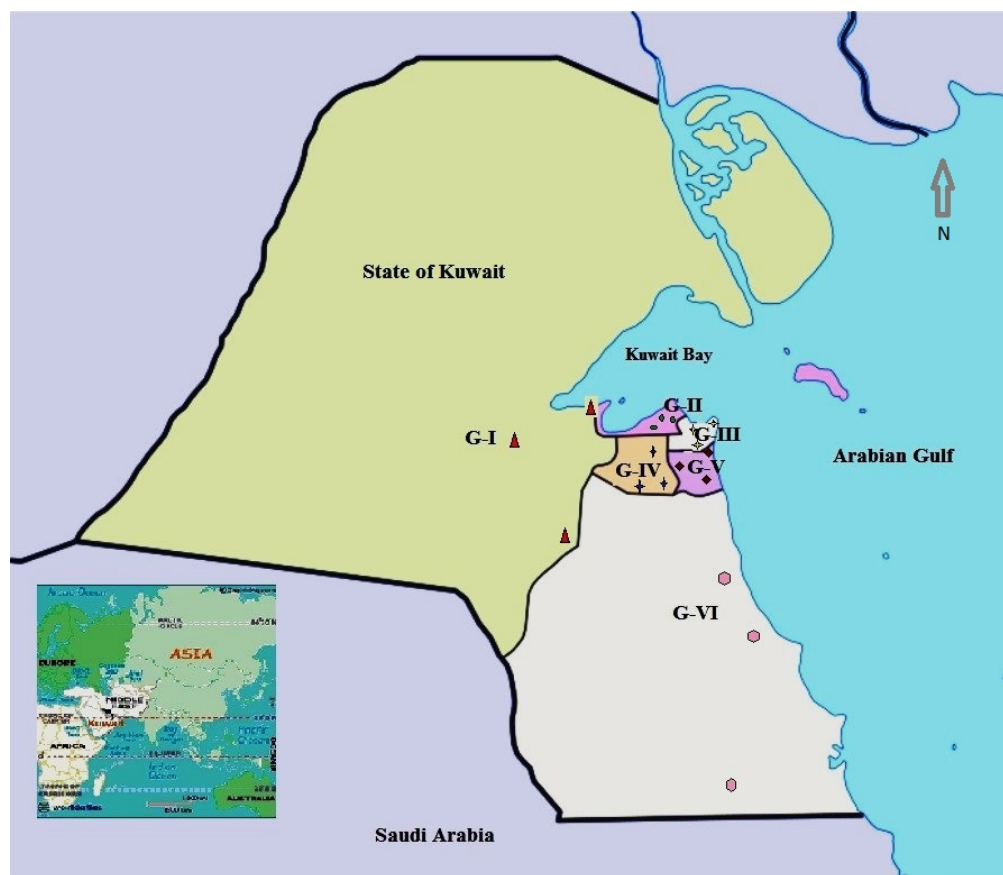
Fig. 1. Six Kuwait Governorates selected for sampling
G-I to GVI: Governorates: Al-Jahra, Al-Asimah, Al-Hawalli, Farwaniya, Mubarek Al-Kabeer, Al-Ahmedi

2.2 Sample analysis

Eight non-perfume-soaked incense samples (six Frankincense resin, two Oudh wood-*Aquilaria* species) and Eight 'Bokhour' (perfume soaked) samples collected separately in sterile plastic containers were analyzed in the laboratory. Replicates (5g) of vended incense samples collected from three areas were, dried in an oven (GallenKamp-II) at 45°C for 12h, powdered and sieved in a #18 mesh of 1.0mm size to enable the uniformity of the sample (WHO, 2012). The Direct Mercury analyzer (DMA-80, Milestone, Italy, Inc.) offered a lower detection limit value of 0.0015ng/g for a powdered samples (0.2 g) for Hg. Quality assurance followed using blanks, triplicate samples, controls, spikes and standard reference material [SRM 1575A: Pine needle from National Institute of Science and Technology (NIST), US]. Mercury with recovery (>95%) in the samples with that of the SRM confirmed the precision of the instrument, consistency, and reproducibility of the experiments (Ahmed *et al.,* 2020). Following OSHA (2017), questionnaire was distributed to ten residents from each Governorate areas and prior to the mutual consent of response and privacy by the residents and assessor, respectively. The questionnaire detailed the information on the respondent's inhabitation in the indoor environment, the size of the rooms, hours spent while burning the incenses, the type of direct or indirect burning and their general ailments.

3. Results

Classification of the eight non-perfumed incenses revealed high Hg concentrations in the Oudh wood of Somalia (0.23ng/g) and the least in Cambodia Bokhour wood (0.10ng/g) as well, the least Hg concentrations in frankincense from Dhofar-Oman. However, the high Hg concentrations in the perfumed incenses were observed in the Cambodia Bokhour wood chips (0.50ng/g) and the least in the Indonesian grey wood (0.14ng/g) chips (Figure 2). Analysis revealed the Hg concentrations >1.5 to 2.0 times more in the perfume-soaked Bokhour wood than in the non-perfumed incenses. Furthermore, the percentage of essential oil content indicated by the merchandiser was high in the perfumed incenses compared to the non-perfumed incenses (Figure 2). Statistically, the test of ANOVA validated their effect (Table 1). The wood chips soaked with high concentrations of aromatic oils or perfumed alcohol base for a longer period revealed high Hg contamination in the samples. This was validated by the statistical test of ANOVA (Table 1). The mean site-wise analysis showed high Hg concentrations in the sequence of GI >GIV >GVI >GII >GIII >GV and GI >GIV >GVI >GIII >GII >GV in the non-perfumed and perfumed incenses, respectively (Figures. 3a-3b).
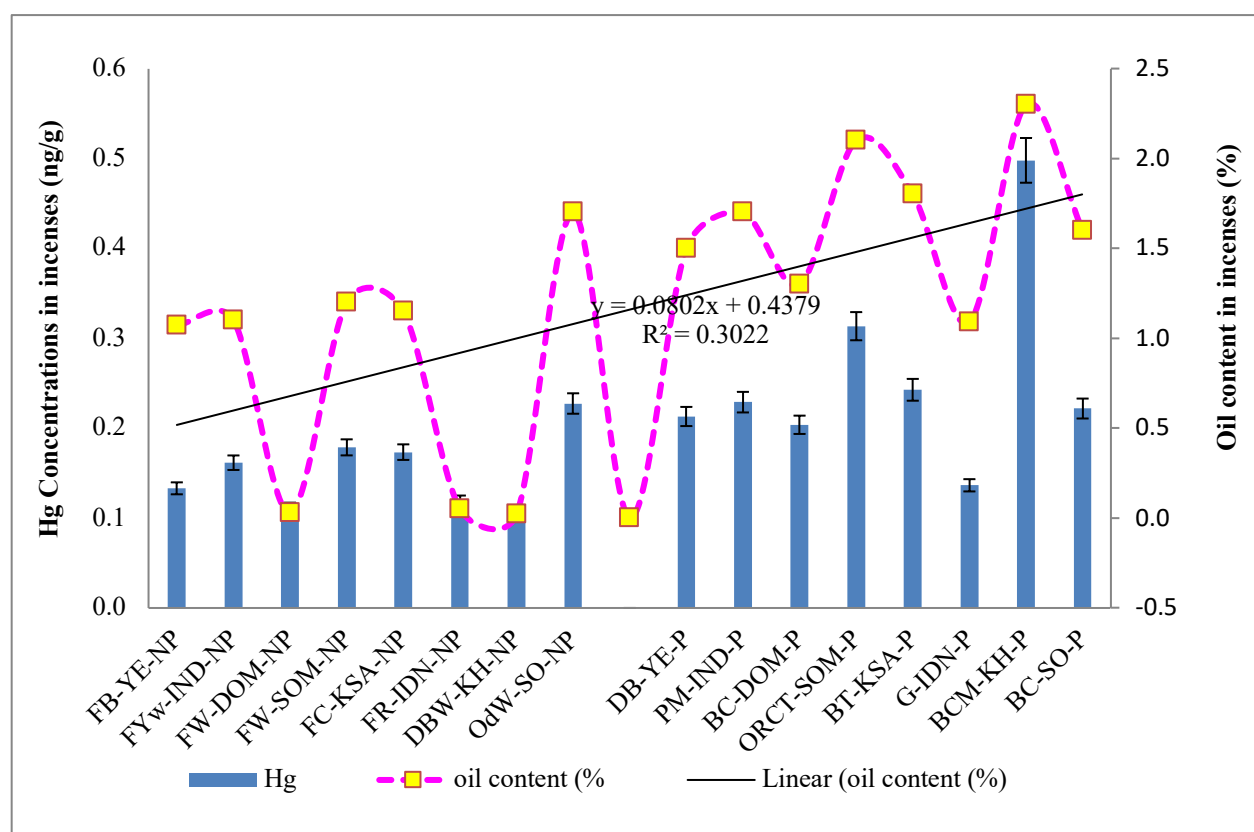
Fig. 2. Countries-wise mean Hg concentrations in the marketed non-perfumed and perfumed incenses

NP: non-perfumed; P: perfumed; IDN: Indonesia, YE: Yemen, SO: Somalia, IND: India, OM: Oman, KH: Cambodia, KSA: Saudi Arabia; G: grey wood, DB: black wood, BC: black cone, PM:powder mix, ORCT: Flower mix, BCM: brown chips, BT: black top; FB: frankincense , FYw: frankincense yellow; FWD: Dohar frankincense, FW: white incense; FC: coated incense coated; FR: red incense; DBW: brown wood, OdW: Oudh wood

Table 1. ANOVA test on the country-wise and site-wise non-perfumed and perfumed incenses

Summary	Count	Sum	Average	Variance		
FB-YE-NP	6	0.798	0.133	0.002		
FYw-IND-NP	6	0.969	0.161	0.006		
FWD-OM-NP	6	0.669	0.111	0.008		
FW-OM-NP	6	1.071	0.178	0.008		
FC-KSA-NP	6	1.040	0.173	0.017		
FR-IDN-NP	6	0.714	0.119	0.002		
DBW-KH-NP	6	0.616	0.102	0.006		
OdW-SO-NP	6	1.364	0.227	0.005		
G-IDN-P	6	0.818	0.136	0.006		
DB-YE-P	6	1.278	0.213	0.001		
BC-SO-P	6	1.331	0.221	0.003		
PM-IND-P	6	1.373	0.228	0.006		
ORCT-OM-P	6	1.880	0.313	0.044		
BCM-KH-P	6	2.987	0.497	0.060		
BC-OM-P	6	1.222	0.203	0.007		
BT-KSA-P	6	1.456	0.242	0.004		
GI	16	5.479	0.342	0.036		
GII	16	2.522	0.157	0.005		
GIII	16	2.571	0.160	0.009		
GIV	16	4.121	0.257	0.013		
GV	16	1.492	0.093	0.004		
GVI	16	3.406	0.212	0.010		
Source of Variation	SS	df	MS	F	P-value	F crit
Incenses	0.84	15	0.06	12.57*	0.0001	1.80
Sites	0.61	5	0.12	27.50*	0.0001	2.33
Error	0.34	75				
Total	1.79	95				

GI-GVI: Kuwait Governorates; NP: non-perfume incense, P: perfumed incense; F: frankincense, B:Bokhour; YE: Yemen, IND: India, OM: Oman, KSA: Kingdom of Saudi Arabia, IDN: Indonesia, KH: Cambodia, SO: Somalia; Yw: Yellow, W: Bokhour wood; D-OM: Dohfar Oman; C: coated wood; R: red Bokhour; DB: dark brown; OdW: Oudh wood; G: grey; BC: brown chips; PM: powder mix; SS: sum of squares, MS: mean square, F: calculated F ratio, F Crit: F critical table value; * significance P=0.0001
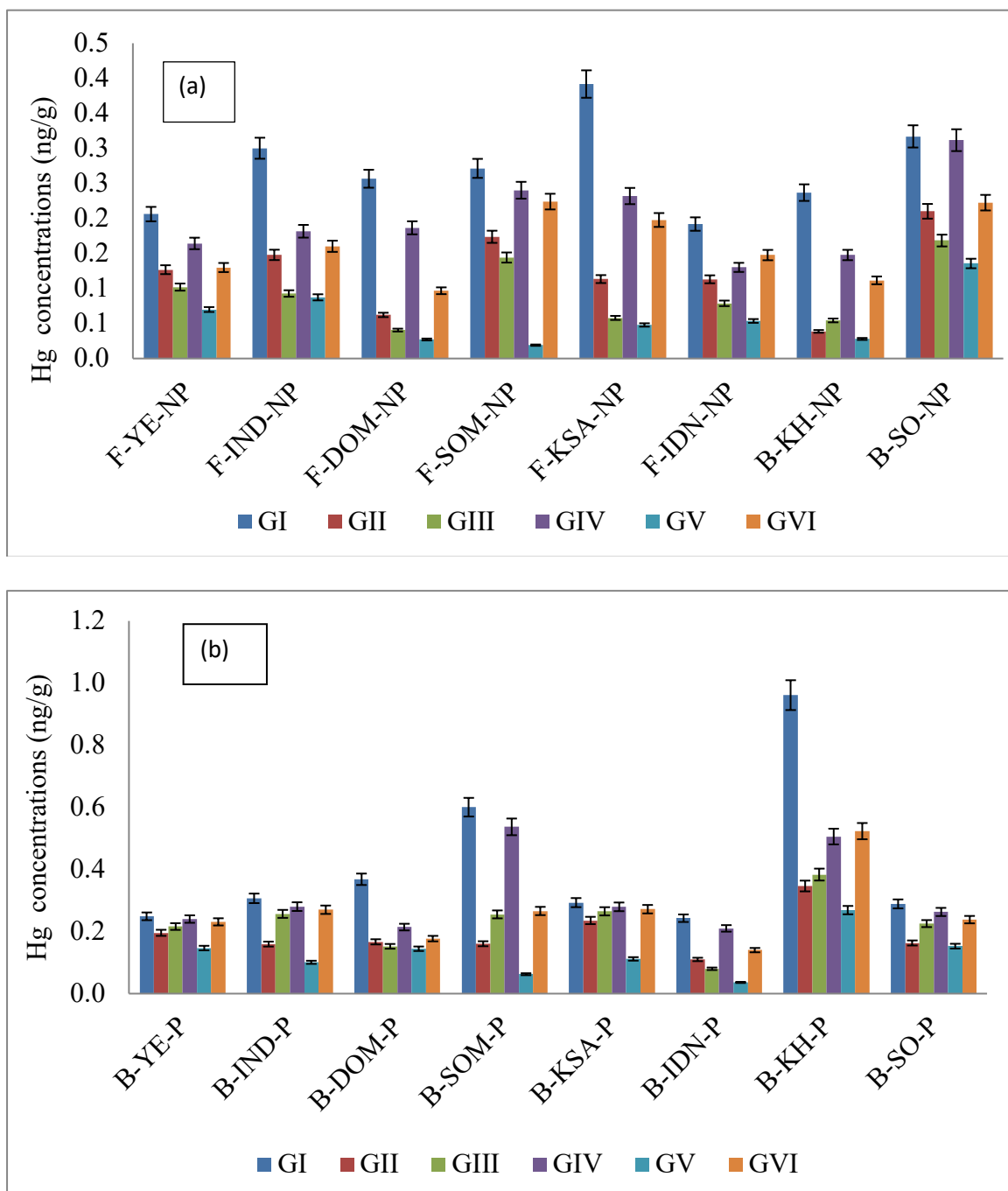
Fig. 3. (a) Spatial distributions of Hg concentrations in non-perfumed marketed incenses
GI-GVI: Kuwait Governorates; NP: non-perfume incense, F: frankincense, B: Bokhour; YE: Yemen, IND: India,
OM: Oman, KSA: Kingdom
of Saudi Arabia, IDN: Indonesia, KH: Cambodia, SO: Somalia
(b) Spatial distributions of Hg concentrations in perfumed marketed incenses
GI-GVI: Kuwait Governorates; P: perfumed incense; F: frankincense, B:Bokhour; YE: Yemen, IND: India, OM:
Oman, KSA: Kingdom of
Saudi Arabia, IDN: Indonesia, KH: Cambodia, SO: Somalia

The response to the questionnaire revealed a higher respiratory illness in Kuwait respondents subjected to the daily use of incenses smoldered in smaller-sized rooms than in larger-sized rooms. The incense burning on a charcoal base revealed high mercury concentration than when burnt on an electric burner or direct flame (Table 1). Furthermore, this study revealed dermatitis, Chronic Obstructive Pulmonary Disease (COPD-2), and Emphysema ailments in respondents regularly using (a) body sprays and cloth sprays and, (b) perfume soaked Bokhour or a combination of Bokhour mixture (e.g., Jasmine-Oudh-Musk aromatic flavor) especially when burnt on a charcoal burner. The responses to incenses smoldered in electric burners revealed respiratory ailments only with breathing difficulties (BD) and Chronic Obstructive Pulmonary Disease (COPD-1) and when residents were exposed for >6-8h in small rooms. Statistically, the test of ANOVA confirmed the significant difference between the Governorate-wise perfumed and non-perfumed incenses.

4. Discussion

Earlier studies witnessed the use of frankincense and 'Bokhour' in the Middle East countries (Vuddana *et al*., 2016; Wolter, 2015). Among the eight marketed non-perfumed incenses apportioned in Kuwait (Figure 1), the high Hg concentrations in the Oudh wood of Somalia attributes to: a) the absorption and translocation of pollutants through the various parts of the Oudh wood as well, in the resin of frankincense trees from the atmosphere, b) the contamination of Hg during the collection of wood and resin, storage and, c) species specificity and quality of the resin that retains Hg concentrations (Figure 2). These findings agreed with the earlier studies (Lorena 2020; Shen *et al*., 2017; Ali *et al*., 2016; Zarshenas *et al*., 2013). The low Hg concentrations in Cambodia Bokhour and in frankincense from Dhofar-Oman attributes to the contrary effect described with Oudh wood from Somalia. ANOVA tests revealed significant difference between the country-wise perfumed and non-perfumed incenses (Table 1). The increasing Hg concentrations by site-wise analysis in G1, G4 and G6 (Figures 3a-3b) in the marketed incenses could be attributed to a) incenses wood chips stored in exposed bags and sold in small quantity in loose packing b) low grade quality sold for economic viability besides, c) the influence of outdoor and indoor pollution composed of particulates, PAHS and Hg impurities that adds to the inhaler while burning these incenses. This agreed with the earlier findings (Višić, *et al*., 2018; El-Sayed *et al*., 2016; Orecchio, 2011). The high Hg concentrations in the perfumed Bokhour wood than in the non-perfumed incenses attributed to the influence of the additive external and internal contaminants in the perfumed incenses. Geng *et al*. (2019), Al-Yasiry and Kiczorowska (2016) and Tsiouri *et al*. (2015) revealed such additive pollutants in the incense with organic constituents. Furthermore, the high percentage of essential oil content attributed to the Bokhour soaked with perfume in correlation with the volume, duration and storage process of such perfumed incenses when compared to the absence of such attributes in the non-perfumed incenses (Figure 2). This was in line with the earlier studies of Al-Harrasi (2014). This study also revealed the Hg concentrations in these incenses exceeding the limits of statutory bodies (OSHA, 2017) thus, indicating the need to curb such hazards of burning such incenses.

The indirect assessment on the incenses smoldered in small-sized rooms causing respiratory illness in the respondents of Kuwait attributed to the regular use of incenses, the extent of suffocation and, dispersion of smoke containing these trace metals compared to such effects in the larger-sized rooms. This validates the earlier findings (Mfarrej *et al*., 2020; Yuan *et al*., 2020; Abdu alrasool *et al*., 2018; BuHamra *et al.,* 2018; Zhou *et al*., 2015; Kumar *et al*., 2014; Wu *et al*., 2012) revealing the detrimental respiratory illness in residents who inhaled incense smoke over a continuous and longer exposure period than the occasional cigarette smokers. The incense burning on a charcoal base revealed high mercury concentrations dispersion than other burners because charcoal attributed the addition of carbon, impurities and trace metals that resulted in respiratory illness, asthma and, cancer (Ahmad and Balkhyour, 2020; Hussain *et al*., 2018; Al-Harbi *et al*., 2016; Ali *et al*., 2016; Al-Busaidi *et al*., 2015). Furthermore, the cause of ailments as categorized earlier in this study attributes to the (a) daily use of perfumes, body sprays and cloth sprays, (b) when perfume (>5ml at 90-100% concentrations) was soaked in Bokhour either individually or in combinations, and (c) when such incenses were burnt regularly on a charcoal burner with more than 2-4h exposure period. Towards the lighter effect, the responses revealed the ailments from BD, intermittent cough and moderate Chronic COPD-1 because of occasional smoldering of incenses. Furthermore, the sites assessed for outdoor and indoor pollution revealed the synergistic effect of Hg causing respiratory illness that was in line with the effect of organic constituents observed earlier (Shen *et al*., 2017; El-Sayed *et al*., 2016; Seow & Lan, 2016; Bahloul & Gevao, 2014; Jankowich & Rounds, 2012). Thus, in an overall view, the present study recommends not to use low quality incenses continuously despite their aromatic and beneficial traditional purposes.

5. Conclusions

This study revealed the effect of Hg from different incenses to residents, inhabiting the indoor environment and, their detection from trace concentrations that was unheeded by other researcher for want of a precision instrument like the DMA-80. This instrument detected samples at trace Hg concentrations from 0.0015ng/g onward and yielded high precision consistent results over the earlier instruments. This study showed the raw incenses exceeding the permissible limits of Hg concentrations in the environment compared to the standards of statutory body. Interesting factors that were ignored by earlier investigators was observed during this study namely, the increasing Hg concentrations in incenses soaked with perfumed oil, burnt on a charcoal burner and in a limited area, and burnt in residences that had excess inmates (6 people/100sq.ft) against the locally prescribed standard space to inhabitants (2 people/100sq.ft). The indirect method of assessment validated the effect of different kinds of incenses and characteristic variables causing different intensity of respiratory ailments. Thus, this study suggests to substantially reduce: (a) the addition of perfumes and their combination at high concentrations in the preparation of 'Bokhour incenses, (b) incessant exposure to incenses during their preparation and while smoldering them and, (c) the inexhaustible use of incenses in habitat already subjected to indoor and outdoor pollutants that is in synergism to human ill-health.

ACKNOWLEDGEMENTS

References

Abdu alrasool, M., Al-Shanfari, B.H., Boujarwa, A., Al-Mukaim, A.I, Alkandery, O., *et al*. **(2018).** Exposure to environmental tobacco smoke and prevalence of atopic dermatitis among adolescents in Kuwait. Dermatology, 234**(5-6)**: 186-191.

Ahmad, I. & Balkhyour, M.A. (2020). Occupational exposure and respiratory health of workers at small scale industries. Saudi Journal of Biological Sciences, 27**(3)**: 985-990.

Amer Ahmed, S.B., , S., Hussein, A., Kampani, D.D., Al-Hasham, N., *et al*. **(2020).** Assessing the knowledge of environmental risk factors for cancer among the UAE population: A pilot study. International Journal of Environment and Research Public Health, 17**(9)**: 2984.

Al-Busaidi, N., Habibulla, Z., Bhatnagar, M., Al-Lawati, N. & Al-Mahrouqi, Y. (2015). The burden of asthma in Oman. Sultan Qaboos University Medical Journal, 15**(2)**: e184–e190.

Al-Harbi, S., Al-Harbi, A., Al-Khorayyef, A., Al-Qwaiee, M., Al-Shamarani, A., *et al*. **(2016).** Awareness regarding childhood asthma in Saudi Arabia. Annals of Thoracic Medicine, 11**(1)**:60–65.

Al-Harrasi, A., Ali L, Hussain, J., Rehman, N.U., Mehjabeen, Z., et al. (2014). Analgesic effects of crude extracts and fractions of Omani frankincense obtained from traditional medicinal plant *Boswellia sacra* on animal models. Asian Pacific Journal of Tropical Medicine, 7**(1)**: S485–S490.

Al-Yasiry, A.R.M. & Kiczorowska, B. (2016). Frankincense–therapeutic properties. Postepy Higieny i Medycyny Doswiadyczalnej (online), 70: 380-391.

Ali, N., Iqbal., Ismail, M.I., Khoder, M., Shamy, M., *et al*. **(2016).** Polycyclic aromatic hydrocarbons (PAHs) in indoor dust samples from cities of Jeddah and Kuwait: Levels, sources and non-dietary human exposure. The Science of the Total Environment, 573: 1607-1614.

Bahloul, M. & Gevao, B. (2014). Persistent organic pollutants in house dust in Kuwait. International Journal of Advanced Agriculture Environment Engineering (IJAAEE), 1**(1)**: 2349-1523.

BuHamra, S., Al-Kanderi N. & Al-Harbi, M. (2018). Parametric and non-parametric bootstrap: an analysis of indoor data from Kuwait. Kuwait Journal of Sciences, 45**(2)**:22-29.

El-Sayed, Y., Dalibalta, S., Gomes, I., Fernandes, N. & Alqtaishat, F. (2016). Chemical composition and potential health risks of raw Arabian incense (Bokhour). Journal of Saudi Chemical Society, 20: 465–473.

Geng, T.T., Jafar, T.H., Yuan, J.M. & Koh, W.P. (2019). Long-term incense use and the risk of end-stage renal disease among Chinese in Singapore: the Singapore Chinese health study. BMC Nephrology, 20**(1)**: 1-9.

Hussain, S.M., Farhana, S.A. & Alnasser, S.M. (2018). Time trends and regional variation in prevalence of asthma and associated factors in Saudi Arabia: A systematic review and meta-analysis. Bio Medical Research International, 2018: 1-9.

Incense (2018). New World Encyclopedia. Retrieved 06:56, November 29, 2021 from https://www.newworldencyclopedia.org/p/index.php?title=Incense&oldid=1009384.

Jankowich, M.D. & Rounds, S.I.S. (2012). Combined pulmonary fibrosis and emphysema syndrome: A Review. Chest, 141**(1)**: 222-231.

Kumar, R., Gupta, N., Kumar, D., Mavi, A.K., Singh, K., *et al*. **(2014).** Monitoring of indoor particulate matter during burning of mosquito coil, incense sticks and dhoop. Indian Journal of Allergy Asthma Immunology, 28**(2)**: 68-73.

Lorena, R.L.V. (2020). Effects of essential oils on central nervous system: Focus on mental health. Phytotherapy Research, 35**(2)**: 657-679.

Lui, K.H., Musa, B.A., Hang-Ho, S.S., Hsiao-Chi, C., Jun-Ji, C., *et al*. **(2016).** Characterization of chemical components and bioreactivity of fine particulate matter (PM2.5) during incense burning. Environmental Pollution, 213: 524–532.

Mfarrej, M.F.B., Qafisheh, N.A. & Bahloul, M.M. (2020). Investigation of indoor air quality inside houses from UAE. Air, Soil and Water Research, 13: 1–10.

Orecchio, S. (2011). Polycyclic aromatic hydrocarbons (PAHs) in indoor emission from decorative candles. Atmosphere Environment, 54**(10)**: 1888-1895.

OSHA (2017). Limits of air contaminants. Occupational Safety and Health Administration.

Seow, W.J. & Lan, Q. (2016). Domestic incense use and lung cancer in Asia: a review. Review of Environmental Health, 31**(1)**: 155-158.

Shen, H., Cheng-Mou, T., Chung-Shin, Y., Yi-Hsiu, J. & Ie, I.R. (2017). How incense and joss paper burning during the worship activities influences ambient mercury concentrations in indoor and outdoor environments of an Asian temple? Chemosphere, 167:530-540.

Tran, V. V., Park, D. & Lee, Y. C. (2020). Indoor air pollution, related human diseases, and recent trends in the control and improvement of indoor air quality. International Journal of Environmental Research and Public Health, 17**(8)**: 2927.

Tsiouri, V., Kakosimos, K.E. & Kumar, P. (2015). Concentrations, sources and exposure risks associated with particulate matter in the Middle East Area—a review. Air Quality Atmosphere Health, 8**(1)**: 67–80.

Višić, B., Kranjc, E., Pirker, L., Bačnik, U., Tavčar, G., *et al*. **(2018).** Incense powder and particle emission characteristics during and after burning incense in an unventilated room setting. Air Quality and Atmosphere Health, 11: 649–663.

Vuddana, P.R., Singh, S. & Velaga, S. (2016). Boswellic acid-medicinal use of an ancient herbal remedy. Journal of Herbal Medicine, 6**(4)**: 163-170.

WHO (2012). World Health Organization- International Agency for Research on Cancer (IARC). IARC Monographs on the evaluation of carcinogenic risks to humans.

Wolter, A.N. (2015). Gold, frankincense and myrrh, the healing gifts of the Magi. Deutsche Medizinische Wochenschrift, 140**(25)**: 1874.

Wu, C.L, Chao, C.Y.H., Sze-To, G.N., Wan, M.P. & Chan, T.C. (2012). Ultrafine particle emissions from cigarette smouldering, incense burning, vacuum cleaner motor operation and cooking. Indoor and Built Environment, 21**(6)**:782–796.

Yuan, Y., Alahmad, B., Kang, C.M., Al-Marri, F., Kommula, V., *et al.* **(2020).** Dust events and indoor air quality in residential homes in Kuwait. International Journal of Environment Research and Public Health, 17**(7):** 2433.

Zarshenas, M.M., Zargaran, A., Müller, J. & Mohagheghzadeh, A. (2013). Nasal drug delivery in traditional Persian medicine. Jundishapur Journal of Natural Pharmaceutical Products, 8**(3):** 144–148.

Zhou, R., AnQPan, X.W., Yang, B., Hu, J. & Wang, Y.H. (2015). Higher cytotoxicity and genotoxicity of burning incense than cigarette. Environmental Chemistry Letters, 13**(4)**: 465–471.

Selective adsorption of cationic dye utilizing poly (methacrylic acid-co-ethylene dimethacrylate) monolith from wastewater

Bessy D'Cruz, Mohamed O. Amin, Metwally Madkour, Entesar Al-Hetlani*

*Dept. of Chemistry, Faculty of Science, Kuwait University,
P.O. Box 5969, Safat, 13060, Kuwait*

Corresponding author: entesar.alhetlani@ku.edu.kw

Abstract

In this study, a poly (methacrylic acid-co-ethylene dimethacrylate (poly(MAA-co-EDMA)) monolith was prepared for the selective adsorption of acidic dye, namely, methylene blue (MB), from wastewater. The fabrication of the monolith was carried out via photoinitiation polymerization by irradiating a mixture of methacrylic acid (MAA), ethylene dimethacrylate (EDMA), porogenic solvents and an initiator. Batch adsorption assays were performed to examine the impact of monolithic dosage and initial dye concentration on the adsorption capacity and efficiency of the monolith towards MB dye molecules. This adsorption kinetic study revealed that MB adsorption on the monolith followed a pseudo-second-order model and equilibrium adsorption behavior was best modeled with the Langmuir adsorption isotherm, which indicated monolayer adsorption with a maximum adsorption capacity of 50.00 mg g^{-1}. Owing to the presence of negative binding sites on the monolithic surface, cationic MB molecules were selectively adsorbed in the MB/methyl orange (MO) mixture with an adsorption efficiency of 99.54% at equilibrium. Moreover, the MB-adsorbed monolith was regenerated up to four cycles, and the percentage removal efficiency of MB on the monolith dropped to 67.64 % after the fourth cycle. Finally, the monolith effectively adsorbed MB from the tap water in the presence of competing ions, and the maximum adsorptive capacity obtained was 47.62 mg g^{-1} with 84.5% adsorption efficiency. Hence, the poly(MAA-co-EDMA) monolith was found to be an adequate sorbent for the treatment of cationic dyes in the presence of other dyes and competing ions from wastewater.

Keywords: Acidic dye; adsorption; competitive sorption; methacrylate monoliths; wastewater

1. Introduction

Textile, leather, paper, plastic and other processing industries that utilize various dyes and pigments are major sources of water pollution. During the coloring process, it is estimated that 10-15% of the dyestuff is disposed into the aquatic environment; this is highly toxic and carcinogenic, even at trace-level concentrations. Dyes are highly colored and water-soluble materials; thus, they can reduce the amount of light penetrating the water. Subsequently, they have a derogatory impact on photosynthetic phenomena (B. Hameed & Ahmad, 2009). Therefore, dyes from wastewater should be removed or treated prior to their release into the environment to avoid serious health and environmental consequences (Parshetti, Parshetti, Kalyani, Doong & Govindwar, 2012).

Currently, several physical (D'Cruz, Madkour, Amin & Al-Hetlani, 2020), chemical (Al-Hetlani, Amin & Madkour, 2017) and biological (Bharti , 2019) approaches are employed to aid wastewater treatment. For example, coagulation/flocculation (Dotto, Fagundes-Klen, Veit, Palacio & Bergamasco, 2019), membrane filtration (Jiang *et al*., 2018), ozonation (Venkatesh, Venkatesh & Quaff, 2017) and biodegradation (B. B. Hameed & Ismail, 2018) are among the most commonly used methods in wastewater treatment. Although they are highly effective, they still suffer from some inherent limitations, e.g., some can be expensive and time consuming, require specialized equipment and generate secondary waste. Adsorption, in terms of promoting water purification, offers several advantages, such as the efficient adsorption of organic dyes using a variety of adsorbents organic, inorganic and hybrids (D'Cruz, Amin & Al-Hetlani, 2021; Thilagavathi, Arivoli & Vijayakumaran, 2015), and the ability to regenerate and reuse the adsorbents several times after the adsorption process (Astuti, Sulistyaningsih, Kusumastuti, Thomas & Kusnadi, 2019) using simple apparatuses. The level of adsorption efficiency is largely influenced by several factors, including the adsorbent properties and dosage as well as the adsorbate type, concentration and pH (Rajendran, Samuel, Amin, Al-Hetlani & Makhseed, 2020). Thus, it is imperative to optimize the experimental conditions to obtain a high adsorption efficiency.

A variety of organic, inorganic and hybrid adsorbents have been proposed for the adsorption of pollutants from wastewater. They display a range of properties, such as high porosity (Liu *et al*., 2021), hydrophobicity (Al-Hetlani, Amin, Bezzu & Carta, 2020), biocompatibility (Asadi, Eris & Azizian, 2018), surface chemistry (Islam *et al*., 2017) and others (Astuti *et al*., 2019), which can influence the adsorption process. Recently, organic polymers with controlled porosity, a large surface area and different functional groups have been the focus of many research studies (Shen *et al*., 2018). Such organic polymers have gained a lot of attention, and several organic polymers are already utilized as effective adsorbents to remove organic dyes from wastewater. For example, spirobifluorene polymers of intrinsic microporosity (PIMs) (Al-Hetlani, Amin, *et al*., 2020), porous organic polymers (POPs) (Al-Hetlani *et al*., 2021), hypercross linked porous polymers (Huang *et al*., 2018) and covalent organic frameworks (COFs) (Li, Yang, Qian, Zhao & Yan, 2019) have been successfully used for the adsorptive removal of organic dyes from wastewater. On one hand, despite their efficiency, the fabrication of these materials requires several steps and thorough purification of the final product. On the other hand, polymer monolithic materials (PMMs) are crosslinked co-polymers prepared via free-radical polymerization in a single step. They have been extensively utilized for chromatographic separation (F. Svec, E. C. Peters, D. Sýkora & J. M. J. Fréchet, 2000), solid-phase extraction (Fan, Feng, Zhang, Da & Zhang, 2005) and as solid supports for catalysis and other applications (Al-Hetlani, D'Cruz & Amin, 2020). PMMs are generated via thermal or photo-initiation in the presence of an initiator to generate free radicals, in the presence of a monomer to provide chemical functionality, a crosslinker to increase the mechanical strength of the polymer and porogenic solvents to control the porosity. They can be easily fabricated in large amounts (a few grams), and their functionality can be controlled with commercially available monomers; they have high pH stability, and most importantly, they are biocompatible (F. Svec, E. C. Peters, D. Sýkora & J. M. Fréchet, 2000).

In this work, we investigated the use of a poly (methacrylic acid-co-ethylenedimethacrylate) (poly(MAA-co-EDMA)) monolith for the adsorption of methylene blue (MB) dye from wastewater. To the best of our knowledge, these crosslinked co-polymers have not been previously employed for wastewater treatment applications. The polymer monolith was prepared using photo-initiation, and due to the abundance of the carboxylic acid groups in its skeleton which carry a negative charge, it was ideal for the selective adsorptive removal of cationic pollutants. The amount of poly(MAA-co-EDMA), the initial concentration of MB, the presence of competing ions from tap water, polymer selectivity towards anionic dye (methyl orange (MO) and reusability were investigated in this study.

2. Experimental

2.1 Materials and methods

Methacrylic acid (MAA), ethylene dimethacrylate (EDMA), 2,2-dimethoxy-2-phenylacetophenone (DAP), ethanol, toluene, 1-dodecanol, methylene blue (MB) and methyl orange (MO) were purchased from Sigma-Aldrich and were used as received. Throughout all experiments, double-distilled water was used.

2.2 Preparation of poly (MAA-co-EDMA) monolith

The fast and simple fabrication of methacrylic acid based monolith was adopted from (Al-Hetlani, D'Cruz, *et al*., 2020) and the pre-polymerization mixture was prepared by dissolving 0.237 mL of MAA, 1.998 mL of crosslinker EDMA and 0.023 g of initiator DAP in porogenic solvents, 1.45 mL of toluene and 4.35 mL of dodecanol. To obtain a homogeneous polymeric-mixture solution, this was sonicated for 20 minutes, followed by irradiation with a UV lamp ($\lambda = 365$ nm). To remove unreacted materials from the obtained polymer monolith, this was repeatedly washed with ethanol before being dried in an oven at 60 ºC overnight.

2.3 Adsorption of methylene blue from wastewater

The synthesized methacrylic acid based monolith was utilized in the adsorption batch assays. Variables affecting the monolithic absorption of MB, including the dose of the monolith, the initial dye concentration and contact time, were evaluated and optimized. All adsorption assays were conducted at room temperature using a 10 mL aqueous solution of MB and poly(MAA-co-EDMA) as the adsorbent, and the reaction mixture was sonicated for 20 min. Afterwards, the solution was filtered through a 0.45 µm GHP syringe filter to obtain clear filtrate; then, UV–Vis measurements at $\lambda_{max} = 663$ nm were performed to find the concentration of unadsorbed MB in the filtrate after adsorption. The percentage of dye removal (adsorption efficiency (%AE)) and the adsorption capacities of the adsorbent towards MB were calculated using the following equations:

$$\%AE = \frac{(C_o - C_t)}{C_o} \times 100 \tag{1}$$

$$q_{eq} = \frac{(C_0 - C_{eq})V}{m} \tag{2}$$

where C_o represents the initial MB concentration (mg L^{-1}); C_t and C_{eq} are the MB concentrations (mg L^{-1}) at time t and at equilibrium, respectively; V is the volume (L) of the MB solution; and m represents the mass of the adsorbent (g).

To investigate the adsorption selectivity of the monolith towards a mixture of organic dye molecules, 10 mg L^{-1} cationic MB and anionic MO mixture solution was chosen as the model initial concentration. The effectiveness of the monolith as an adsorbent for MB adsorption in tap water in the presence of competing ions was further examined with dye concentrations ranging from 10 to 50 mg L^{-1} under optimized adsorption conditions.

2.4 Regeneration of poly(MAA-co-EDMA)

To investigate the practical utility of the poly(MAA-co-EDMA) monolith as an adsorbent, adsorption–desorption experiments were conducted. The desorption experiment was studied with 25 mg of adsorbent and a constant initial MB concentration (10 mg L^{-1}) for a contact time of 20 min. The MB adsorbed monolith was collected via centrifugation, followed by washing five times with water and ethanol. Then, the adsorbent was dried at 80 °C overnight and reused for the next cycle. In this experiment, the adsorption–desorption cycle was repeated four times and the %AE was assessed in each cycle using equation.1.

3. Results and discussion

3.1 Adsorption experiments

The characterization of the fabricated monolith using several analytical techniques can be found in (Al-Hetlani, D'Cruz, *et al.*, 2020). The maximum MB %AE with the minimum amount of monolith dose played a key role in wastewater treatment. Hence, the effect of the adsorbent dose towards the MB dye removal was investigated with various amounts of the monolith, ranging from 5 to 15 mg, mixed with the 10 mL MB solution (10 mg L^{-1}), and UV–Vis measurements were carried out. As depicted in Figure 1a, it was found that the adsorption efficiency increased from 97.81 to 99.71% with an increment in the adsorbent dose from 5 to 8 mg mL^{-1}; thereafter, a slight change in adsorption efficiency was observed. This could be attributed to the existence of a large number of adsorption binding sites for adsorbent–adsorbate interactions with the increase in the adsorbent dosage. However, the adsorption capacity showed a reverse trend with the further increase in adsorbent dosage. At higher monolith dosages, there is a higher chance for the collision and aggregation of poly(MAA-co-EDMA), which can limit the availability of binding sites for the adsorption process to proceed (D'Cruz *et al.*, 2020). Therefore, 8 mg was chosen as the optimum adsorbent dosage to conduct the subsequent experiments.

In wastewater treatment, there is a direct relation between the adsorption efficiency and the initial MB concentration (Al-Ghouti & Al-Absi, 2020). Figure 1b shows the impact of the initial dye concentration on the %AE and the adsorption capacity of the monolith towards MB in the range from 5 to 50 mg L^{-1}. It was clear that, as the initial concentration of MB increased, the %AE increased up to 99.71% at 10 mg L^{-1}, and that at higher MB concentrations, the %AE decreased. However, the adsorption capacities of the monolith increased as the initial MB concentration increased. Due to this, the accessibility of the active sites on the poly(MAA-co-EDMA) monolith was high at the lower initial MB concentration, but the adsorption and mass transfer of MB were lowered at 5 mg L^{-1}, leading to a lower %AE. As the initial concentration of MB increased from 5 to 10 mg L^{-1}, the mass transfer resistance of dye molecules between water and adsorbent decreased, showing a higher %AE at 10 mg L^{-1}. Moreover, with the increase in the initial concentrations of MB above 10 mg L^{-1}, the saturation of the active adsorption sites on the adsorbent was observed, and consequently, the %AE decreased (Al-Ghouti & Al-Absi, 2020). Accordingly, 10 mg L^{-1} was selected as the initial concentration of MB for further studies.
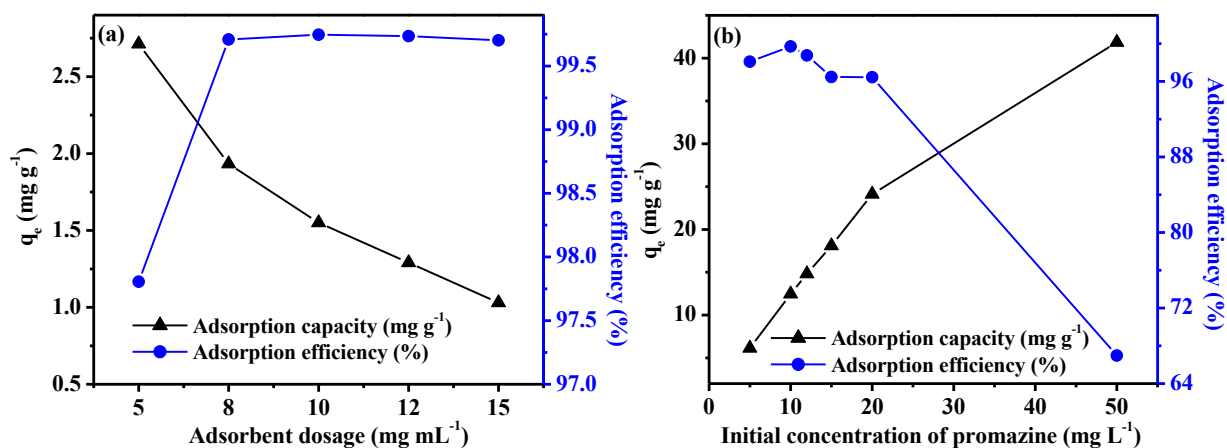
Fig. 1. Effects of (**a**) poly(MAA-co-EDMA) dosage (experimental conditions: C$_0$ = 10 mg L^{-1}; contact time = 20 min; total volume = 10 mL; 25 ºC) and (**b**) initial MB concentration (experimental conditions: adsorbent dosage = 8 mg; contact time = 20 min; total volume = 10 mL; 25 ºC) on adsorption efficiency and adsorption capacity.

3.2 Adsorption kinetics and isotherms studies

The effects of contact time between the monolith and dye molecules on the adsorption process were significant. Hence, the influence of contact time on the adsorption of MB onto the monolith was examined considering various time intervals under the optimum adsorption conditions, and the amount of MB adsorbed was calculated using equation 2. As depicted in Figure 2a, the adsorption capacity of the monolith was very high at the starting point of the adsorption process due to the presence of highly active vacant surface adsorption sites on the adsorbent, and with the increase in time, the saturation of the adsorption sites gradually occurred, followed by the state of

adsorption equilibrium, which was reached after 20 min. The amount of MB adsorbed, q_e, (exp, experimental) at equilibrium was found to be 12.47 mg g^{-1}.

In order to illustrate the adsorption mechanism behind MB adsorption onto the poly(MAA-co-EDMA) monolith, two conventional kinetic modelspseudo-first-order model and the pseudo-second-order model were employed (D'Cruz *et al.*, 2020). The suitability of the kinetic model was evaluated by comparing the correlation coefficients (R^2) or by comparing the amounts of MB adsorbed on the monolith estimated experimentally, q_e, (exp), and theoretically, q_e, (calc) (Sivaprakasam & Venugopal, 2019). The correlation coefficients (R^2) and q_e, (calc) obtained for the two models are reported in Table 1. It was clearly observed that the pseudo-second-order model was in good agreement with the experimental data calculated for the MB adsorption process on the binding sites of the monolith, as demonstrated in Figure 2b. Additionally, Langmuir and Freundlich models are well known to analyze the equilibrium adsorption isotherms data and simulate with the experimental data (D'Cruz *et al.*, 2020). Figure 3a illustrates the equilibrium adsorption of MB onto the poly(MAA-co-EDMA) monolith at different initial MB concentrations ranging from 10 to 50 mg L^{-1}. As can be seen, the adsorbent exhibited a maximum adsorption capacity of 50.00 mg g^{-1}. In addition, the equilibrium parameters of the isotherm models were calculated and are here listed in Table 1. The Langmuir adsorption isotherm model was better suited to describe the adsorption of MB on the active surface sites of the monolith, which could also be observed from the linear plot of the Langmuir adsorption isotherm displayed in Figure 3b. The Langmuir adsorption model assumes that the active adsorptive sites on the surface of a monolithic adsorbent are homogeneous in nature and that the adsorption process occurs uniformly within the adsorbent (monomolecular layer adsorption).
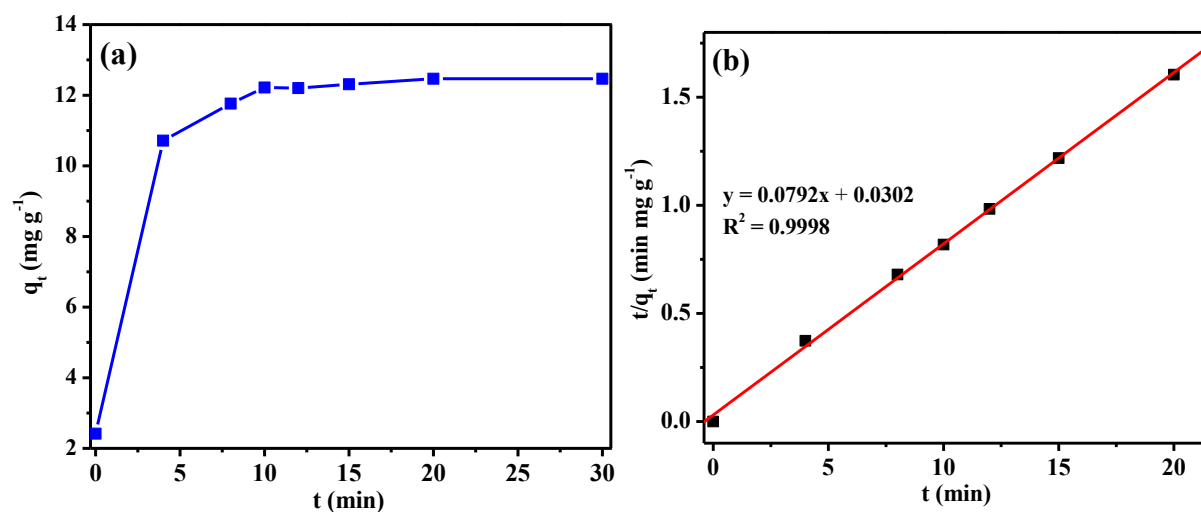
Fig. 2. (a) Influence of contact time on the adsorption capacity of poly(MAA-co-EDMA), towards MB. **(b)** Plot of pseudo-second-order kinetic model for the adsorption of MB onto poly(MAA-co-EDMA) (experimental conditions: initial concentration of MB = 10 mg L^{-1}; adsorbent dosage = 8 mg; 25 ºC).
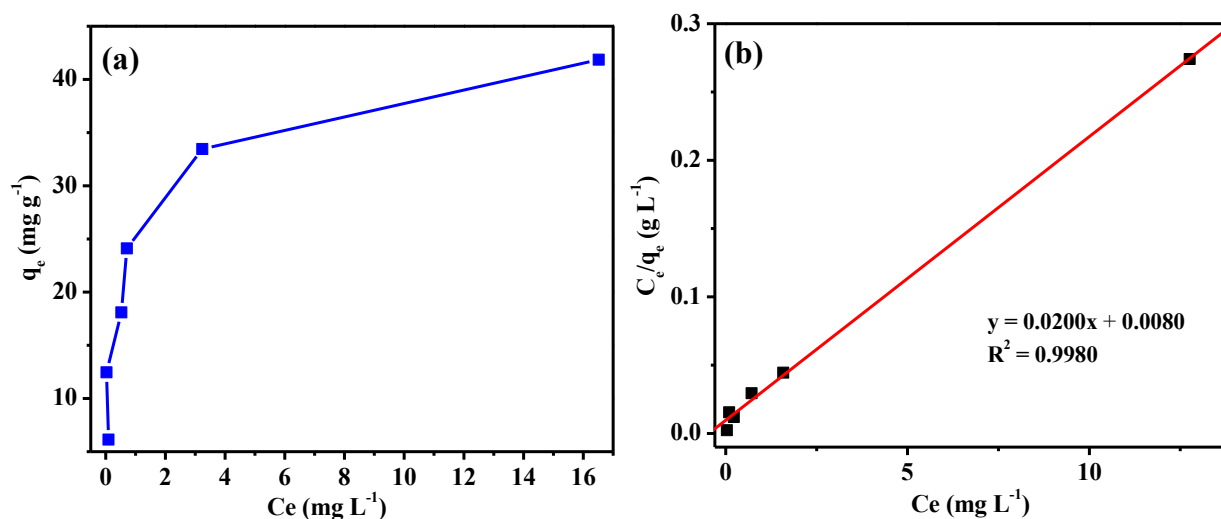

Fig. 3. (a) Adsorptionisotherm study of MB onto poly(MAA-co-EDMA). **(B)** Langmuir plot for MB adsorption onto poly(MAA-co-EDMA) (experimental conditions: adsorbent dosage = 8 mg; pH = 6.28; contact time = 20 min; 25ºC).

Table 1. Parameters of kinetic and isotherm adsorption models for MB adsorption onto the poly(MAA-co-EDMA) monolith.

Model	Parameters	Values
Pseudo-first-order model	k_1 (min^{-1})	0.2780
	q_e (mg g^{-1})	6.90
	R^2	0.9450
Pseudo-second-order model	k_2 (g mg^{-1} min^{-1})	0.2077
	q_e (mg g^{-1})	12.63
	R^2	0.9990
Langmuir isotherm model	K_L (L mg^{-1})	2.50
	q_m (mg g^{-1})	50.00
	R^2	0.9980
Freundlich isotherm model	K_F ((mg g^{-1}) (L mg^{-1})$^{1/n}$)	2.49 x 10^{-4}
	n	0.3962
	R^2	0.7360

The adsorption capacities towards MB of some adsorbents found in the literature are displayed in Table 2. Referring to the table, the adsorption capacity of poly(MAA-co-EDMA) towards MB was quite effective compared with other nanomaterials. This can be explained by the predominant negative charge on the surface of the polymer, which stimulated several electrostatic interactions between the adsorbent and the adsorbate (section 3.4).

Table 2. Adsorption capacity of other adsorbents for the removal of MB in aqueous solution.

Adsorbent	Conditions	%Of removal	Adsorption capacity (mg g^{-1})	Reference
FeFe$_2$O$_4$ magnetic nanomaterial	pH = 10; t = 80 min; C_0 = 100 ppm	35	42.35	(Dinh, Tran, Tran, & Nguyen, 2019)
Reduced graphene oxide	pH = 6.02; t = 30 min; C_0 = 100 ppm		121.95	(Arias Arias *et al.*, 2020; Dinh *et al.*, 2019)
Ag-Fe$_3$O$_4$-polydopamine	pH = 10; t = 26 hours	-	169.5	(Wu, Li, Yue, Zhang, & Huang, 2017)
Magnetic carboxyl functional nanoporous polymer	pH = 6.0; t = 30 min; C_0 = 15 ppm	90	57.74	(Su, Li, Han, & Liu, 2018)
g-C$_3$N$_4$ (Urea)	t = 50 min; C_0 = 0.5 ppm	-	2.51	(Zhu, Xia, Ho, & Yu, 2015)
CeO$_2$	pH = 9.0; MB t = 30 min; C_0 = 15 ppm	80.3	4.37	(Wei *et al.*, 2019)
Poly(MAA-co-EDMA	pH = 6.28; contact time = 20 min; 25 ºC; C_0 = 10 ppm	99.54	50	This work

3. 3 Effect of water type

To examine the effect of competing ions on the adsorption capacity and %AE of the fabricated monolith for the removal of cationic dye MB from tap water, a series of adsorption experiments were conducted utilizing MB concentrations ranging from 10 to 50 mg L^{-1} with the optimum amount of adsorbent. Inductively coupled plasma mass spectrometry (ICP-MS) was used to examine the ions and their corresponding concentrations present in tap water, and [Na$^+$] =13.90 mg L^{-1}, [K$^+$] = 0.28 mg L^{-1}, [Ca^{2+}] =21.62 mg L^{-1} and [Mg^{2+}] = 1.85 mg L^{-1} were detected. The adsorption capacity and adsorption efficiency of the poly(MAA-co-EDMA) monolith towards MB

adsorption from tap water are shown in Figure 4. Indeed, no significant differences were evident in the %AE of the monolith when DI water was employed. The maximum adsorption capacity obtained was 47.62 mg g^{-1}, with 84.5% adsorption efficiency. It was found that the coexisting ions had an insignificant effect on the adsorption process of MB onto the poly(MAA-co-EDMA) monolith from tap water.
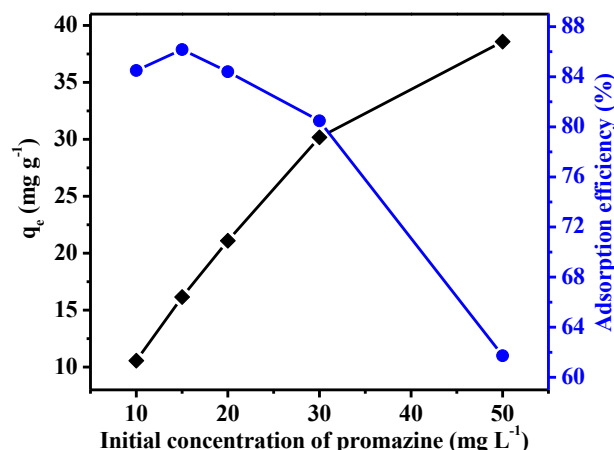

Fig. 4. Adsorption capacity and adsorption efficiency for the removal of MB from ordinary tap water samples using a poly(MAA-co-EDMA) monolith (experimental conditions: adsorbent dosage = 8 mg; initial concentrations of MB = 10-50 mg L^{-1}; contact time = 20 min; 25 ºC)

3.4 Selective adsorption and mechanism of MB from mixed dyes solution

To evaluate the selective adsorption property of the prepared monolith from a mixed dye solution, two kinds of dye molecules with different sizes and charges were used for the adsorption experiments (Pourzare, Farhadi, & Mansourpanah, 2018). Figure 5 presents the UV–Vis adsorption spectra for the adsorption of MB and MO from the MB/MO mixture onto the monolith under optimized conditions. The absorbance in the UV–Vis spectra of cationic MB declined within 25 min, indicating an enhanced adsorption property of the monolith towards MB dye molecules, while there was no adsorption of MO dye molecules from the mixture solution. The inset in Figure 5 represents photographs of the MB/MO mixture solution before and after the adsorption process that confirmed the presence of MO dye molecules after adsorption. Consequently, the adsorbent showed an excellent adsorption efficiency (99.54%) towards MB in the mixture after 20 min due to the surface charge property of the monolith. The measured initial solution pH of the MB/MO mixture was 6.28, and at this pH, the monolith possessed a negative zeta potential value of -17.10 mV (Al-Hetlani, D'Cruz, *et al.*, 2020); hence, the surface of the monolith was eminently negatively charged. Consequently, the selective capture of positively charged MB in the MB/MO mixture was due to the electrostatic attraction between negatively charged carboxylate ligands on the surface of the monolith and positively charged MB dye molecules, as shown in Figure 6a. The stability of the monolith adsorbent before and after MB adsorption was investigated using scanning

electron microscopy with energy-dispersive X-ray spectrometry (SEM-EDX). Based on the micrographs shown in Figure 6b and c, no differences in the surface morphologies of the monolith before and after MB adsorption were evident. However, the elemental analysis of the monolith after MB adsorption confirmed the presence of nitrogen and sulfur in addition to carbon and oxygen, which indicated the successful adsorption of MB molecules on the monolith. Hence, poly(MAA-co-EDMA) is a promising adsorbent for the selective removal and separation of MB in wastewater treatment.
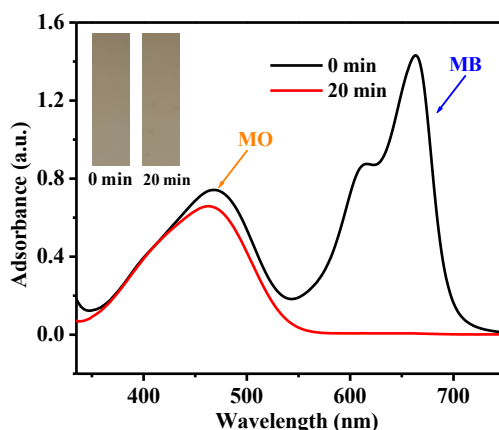
Fig. 5. UV–Vis adsorption spectra for the adsorption of MB and MO from the MB/MO mixture before and after adsorption onto the poly(MAA-co-EDMA) monolith (experimental conditions: adsorbent dosage = 8 mg; concentration of MB/MO mixture = 10 mg L^{-1}; pH = 6.28; contact time = 20 min). The corresponding photographs show the color change of the MB/MO mixture solution before and after adsorption.

Element	Mass%	Atom%
C	91.34	93.36
O	8.66	6.64

Element	Mass%	Atom%
C	78.95	82.54
N	8.92	7.99
O	11.99	9.41
S	0.15	0.06
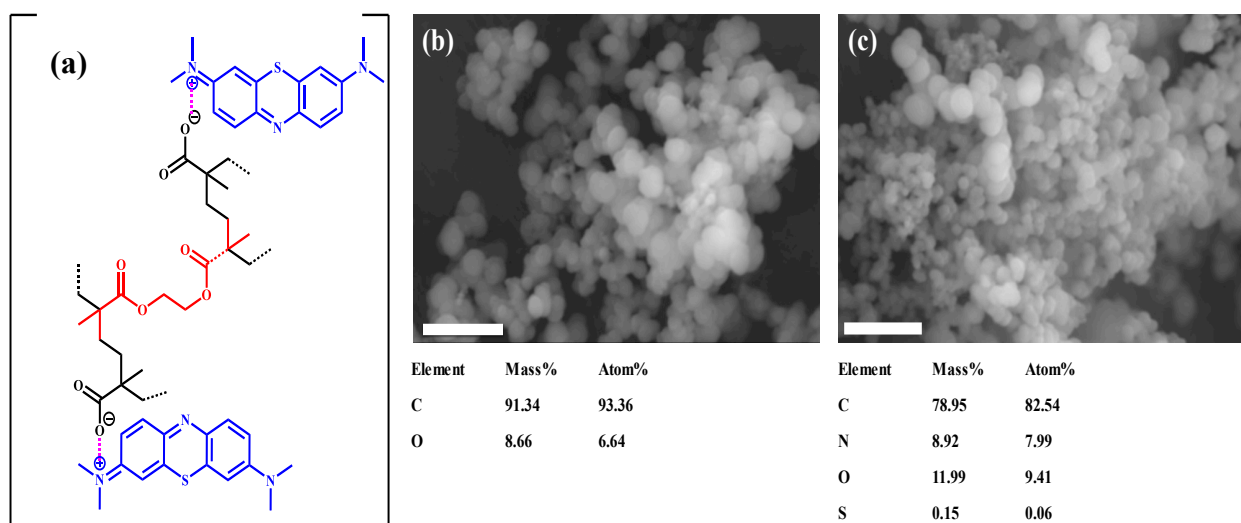
Fig. 6. (a) Adsorption mechanism of MB adsorption onto the poly(MAA-co-EDMA) monolith. **(b)** SEM-EDX analysis of the poly(MAA-co-EDMA) monolith before adsorption and **(c)** SEM-EDX analysis of the poly(MAA-co-EDMA) monolith after MB adsorption. Scale bar is 5 μm.

3.5. Desorption and reusability of poly(MAA-co-EDMA) monolith

The reusability of the used poly(MAA-co-EDMA) monolith was tested by performing four adsorption-desorption cycles of MB onto the adsorbent using ethanol and water as desorption eluents, and the results are shown in Figure 7. It was observed that the regenerated monolith could be used for two cycles without any remarkable decrease in the %AE, and after the sequence of two cycles, the %AE reduced from 97.97 to 77.13 %. Thus, the poly(MAA-co-EDMA) monolith could be employed for the removal of MB molecules from wastewater for up to four successive cycles.
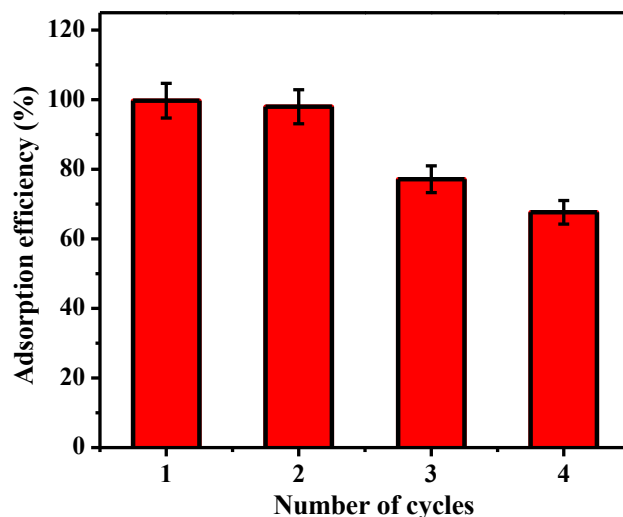
Fig. 7. The adsorption efficiency of the regenerated poly(MAA-co-EDMA) monolith for the removal of MB from wastewater after four adsorption-desorption cycles (conditions: initial MB concentration = 10 mg L^{-1}; adsorbent dosage = 8 mg; contact time = 20 min; 25 ºC).

4. Conclusion

For the first time, an organic-based monolith namely poly(MAA-co-EDMA) was employed for the selective adsorptive capture of MB from wastewater. The batch adsorption experiments were performed to examine the adsorption efficiency and capacity of the poly(MAA-co-EDMA) monolith, and under optimum conditions using 8 mg of the monolith and 10 mg mL^{-1} MB, the monolith exhibited an excellent adsorption efficiency of 99.71% towards MB. The kinetic adsorption model was described by the pseudo-second-order kinetic model, and the Langmuir adsorption isotherm described the equilibrium adsorption isotherm of MB adsorption over the monolith. Due to the high negative zeta potential of the monolith, the cationic dye molecules could rapidly and selectively adsorb onto the surface of the monolith via electrostatic attraction in aqueous solution in the presence of anionic MO dye. The adsorption process from the tap water confirmed that the poly(MAA-co-EDMA) monolith could be a potential adsorbent to selectively remove cationic dye molecules, which is very significant for environmental clean-up in the presence of competing ions. Finally, the monolith was successfully regenerated and reused for the removal of MB for four adsorption–desorption cycles.

ACKNOWLEDGMENTS

References

Al-Ghouti, Mohammad A. & Al-Absi, Rana S. (2020) Mechanistic understanding of the adsorption and thermodynamic aspects of cationic methylene blue dye onto cellulosic olive stones biomass from wastewater. Scientific Reports, 10(**1**), 1-18.

Al-Hetlani, Entesar, Amin, Mohamed O, Bezzu, C Grazia & Carta, Mariolino. (2020) Spirobifluorene-based polymers of intrinsic microporosity for the adsorption of methylene blue from wastewater: effect of surfactants. Royal Society open science, 7(**9**), 200741.

Al-Hetlani, Entesar, Amin, Mohamed O. & Madkour, Metwally. (2017) Detachable photocatalysts of anatase TiO_2 nanoparticles: Annulling surface charge for immediate photocatalyst separation. Applied Surface Science, 411, 355-362.

Al-Hetlani, Entesar, D'Cruz, Bessy. & Amin, Mohamed O. (2020) A 3D miniaturized solid-state chemiluminescence sensor based on ruthenium functionalized polymeric monolith for the detection of pharmaceutical drugs. Journal of Materials Science, 55(**27**), 13232-13243.

Al-Hetlani, Entesar, Rajendran, Narendran, BabuVelappan, Anand, Amin, Mohamed O, Ghazal, Basma. & Makhseed, Saad. (2021) Design and Synthesis of a Nanopolymer for CO_2 Capture and Wastewater Treatment. Industrial & Engineering Chemistry Research, 60, 8664−8676.

Arias Arias, Fabian, Guevara, Marco, Tene, Talia, Angamarca, Paola, Molina, Raul, Valarezo, Andrea, . . . Caputi, Lorenzo S. (2020) The adsorption of methylene blue on eco-friendly reduced graphene oxide. Nanomaterials, 10(**4**), 681.

Asadi, Safoura, Eris, Setareh & Azizian, Saeid. (2018) Alginate-Based Hydrogel Beads as a Biocompatible and Efficient Adsorbent for Dye Removal from Aqueous Solutions. ACS Omega, 3(**11**), 15140-15148.

Astuti, Widi, Sulistyaningsih, Triastuti, Kusumastuti, Ella, Thomas, Gui Yanny Ratna Sari & Kusnadi, Rizky Yogaswara. (2019) Thermal conversion of pineapple crown leaf waste to magnetized activated carbon for dye removal. Bioresource technology, 287, 121426.

Bharti, Vikash, Vikrant, Kumar, Goswami, Mandavi, Tiwari, Himanshu, Sonwani, Ravi Kumar, Lee, Jechan, . . . Kumar, Sunil. (2019) Biodegradation of methylene blue dye in a batch and continuous mode using biochar as packing media. Environmental research, 171, 356-364.

D'Cruz, Bessy, Madkour, Metwally, Amin, Mohamed O. & Al-Hetlani, Entesar. (2020) Efficient and recoverable magnetic AC-Fe3O4 nanocomposite for rapid removal of promazine from wastewater. Materials Chemistry and Physics, 240, 122109.

D'Cruz, Bessy, Amin, Mohamed O. & Al-Hetlani, Entesar. (2021) Polyoxometalate-Based Materials for the Removal of Contaminants from Wastewater: A Review. Industrial & Engineering Chemistry Research, 60(**30**), 10960-10977.

Dinh, Van-Phuc, Tran, Ngoc Quyen, Tran, Quang-Huy. & Nguyen, Trinh Duy. (2019) Facile synthesis of FeFe2O4 magnetic nanomaterial for removing methylene blue from aqueous solution. Progress in Natural Science: Materials International, 29(**6**), 648-654.

Dotto, Juliana, Fagundes-Klen, Marcia Regina, Veit, Marcia Teresinha, Palacio, Soraya Moreno. & Bergamasco, Rosangela. (2019) Performance of different coagulants in the coagulation/flocculation process of textile wastewater. Journal of Cleaner Production, 208, 656-665.

Fan, Yi, Feng, Yu-Qi, Zhang, Jian-Tao, Da, Shi-Lu. & Zhang, Min. (2005) Poly (methacrylic acid-ethylene glycol dimethacrylate) monolith in-tube solid phase microextraction coupled to high performance liquid chromatography and analysis of amphetamines in urine samples. Journal of Chromatography A, 1074(**1-2**), 9-16.

Hameed, Basma B. & Ismail, Zainab Z. (2018) Decolorization, biodegradation and detoxification of reactive red azo dye using non-adapted immobilized mixed cells. Biochemical Engineering Journal, 137, 71-77.

Hameed, BH. & Ahmad, AA. (2009) Batch adsorption of methylene blue from aqueous solution by garlic peel, an agricultural waste biomass. Journal of hazardous materials, 164(**2-3**), 870-875.

Huang, Yipeng, Ruan, Guihua, Ruan, Yuji, Zhang, Wenjuan, Li, Xianxian, Du, Fuyou, . . . Li, Jianping. (2018) Hypercrosslinked porous polymers hybridized with graphene oxide for water treatment: dye adsorption and degradation. RSC advances, 8(**24**), 13417-13422.

Islam, Md Tariqul, Hernandez, Cesar, Ahsan, Md Ariful, Pardo, Andrew, Wang, Huiyao & Noveron, Juan C. (2017) Sulfonated resorcinol-formaldehyde microspheres as high-capacity regenerable adsorbent for the removal of organic dyes from water. Journal of environmental chemical engineering, 5(**5**), 5270-5279.

Jiang, Mei, Ye, Kunfeng, Lin, Jiuyang, Zhang, Xinying, Ye, Wenyuan, Zhao, Shuaifei, & Van der Bruggen, Bart. (2018) Effective dye purification using tight ceramic ultrafiltration membrane. Journal of Membrane Science, **566**, 151-160.

Li, Yang, Yang, Cheng-Xiong, Qian, Hai-Long, Zhao, Xu & Yan, Xiu-Ping. (2019) Carboxyl-Functionalized Covalent Organic Frameworks for the Adsorption and Removal of Triphenylmethane Dyes. ACS Applied Nano Materials, 2(**11**), 7290-7298.

Liu, Xiaolu, Pang, Hongwei, Liu, Xuewei, Li, Qian, Zhang, Ning, Mao, Liang, . . . Wang, Xiangke. (2021) Orderly Porous Covalent Organic Frameworks-based Materials: Superior Adsorbents for Pollutants Removal from Aqueous Solutions. The Innovation, 2(**1**), 100076.

Parshetti, Ganesh Kashinath, Parshetti, Supriya, Kalyani, Dayanand C, Doong, Ruey-an & Govindwar, Sanjay P. (2012) Industrial dye decolorizing lignin peroxidase from Kocuria rosea MTCC 1532. Annals of microbiology, 62(**1**), 217-223.

Pourzare, Kolsoum, Farhadi, Saeed & Mansourpanah, Yaghoub. (2018) Anchoring H3PW12O40 on aminopropylsilanized spinel-type cobalt oxide (Co3O4-SiPrNH2/H3PW12O40): A novel nanohybrid adsorbent for removing cationic organic dye pollutants from aqueous solutions. Applied Organometallic Chemistry, 32(**5**), e4341.

Rajendran, Narendran, Samuel, Jacob, Amin, Mohamed O, Al-Hetlani, Entesar & Makhseed, Saad. (2020) Carbazole-tagged pyridinic microporous network polymer for CO2 storage and organic dye removal from aqueous solution. Environmental research, 182, 109001.

Shen, Xiaochen, Ma, Si, Xia, Hong, Shi, Zhan, Mu, Ying & Liu, Xiaoming. (2018) Cationic porous organic polymers as an excellent platform for highly efficient removal of pollutants from water. Journal of Materials Chemistry A, 6(**42**), 20653-20658.

Sivaprakasam, A & Venugopal, T. (2019) Modelling the removal of lead from synthetic contaminated water by activated carbon from biomass of Diplocyclos Palmatus by RSM. Global Nest Journal, 21(**3**), 319-327.

Su, Hongxin, Li, Weiwei, Han, Yide & Liu, Ningning. (2018) Magnetic carboxyl functional nanoporous polymer: synthesis, characterization and its application for methylene blue adsorption. Scientific Reports, 8(**1**), 1-8.

Svec, Frantisek, Peters, Eric C, Sýkora, David, & Fréchet, Jean MJ. (2000) Design of the monolithic polymers used in capillary electrochromatography columns. **Journal of Chromatography A,** 887(**1-2**), 3-29.

Svec, Frantisek, Peters, Eric C., Sýkora, David, & Fréchet, Jean M. J. (2000) Design of the monolithic polymers used in capillary electrochromatography columns. Journal of Chromatography A, 887(**1**), 3-29.

Thilagavathi, Muthaiyan, Arivoli, Shanmugam, & Vijayakumaran, Vaithilingam. (2015) Adsorption of malachite green from waste water using prosopis juliflora bark carbon. Kuwait Journal of Science, 42(**3**) 120-133.

Venkatesh, Smita, Venkatesh, Kumar, & Quaff, Abdur Rahman. (2017) Dye decomposition by combined ozonation and anaerobic treatment: Cost effective technology. Journal of applied research and technology, 15(**4**), 340-345.

Wei, Xiaoshu, Wang, Yi, Feng, Yuqian, Xie, Xiaomin, Li, Xiaofeng, & Yang, Sen. (2019) Different adsorption-degradation behavior of methylene blue and Congo red in nanoceria/H 2 O 2 system under alkaline conditions. Scientific Reports, 9(**1**), 1-10.

Wu, Maoling, Li, Yinying, Yue, Rui, Zhang, Xiaodan, & Huang, Yuming. (2017) Removal of silver nanoparticles by mussel-inspired Fe 3 O 4@ polydopamine core-shell microspheres and its use as efficient catalyst for methylene blue reduction. Scientific Reports, 7(**1**), 1-9.

Zhu, Bicheng, Xia, Pengfei, Ho, Wingkei, & Yu, Jiaguo. (2015) Isoelectric point and adsorption activity of porous g-C3N4. Applied Surface Science, 344, 188-195.

Synthesis and photocatalytic activity of TiO$_2$ on phenol degradation

Muhamad D. Permana[1], Atiek R. Noviyanti[1], Putri R. Lestari[2], Nobuhiro Kumada[2],
Diana R. Eddy[1, *], Iman Rahayu[1]

[1]Dept. of Chemistry, Faculty Mathematics and Natural Sciences,
Universitas Padjadjaran
Sumedang, West Java-45363, Indonesia
[2]Center for Crystal Science and Technology, University of Yamanashi
Kofu, Yamanashi 400-8511, Japan
[*]Corresponding author: diana.rahmawati@unpad.ac.id

Abstract

Photocatalysis is a process of accelerating reactions that are assisted by energy from light irradiation. Titanium dioxide (TiO$_2$) is one of the most widely developed photocatalysis materials, and is used because of its high catalytic activity, stability and very affordable. The most commonly used precursors of TiO$_2$ are titanium butoxide (TBOT) and titanium tetraisopropoxide (TTIP). These variations in precursor can lead to phase difference in the formation of TiO$_2$ crystals, which further improves its nature in the activity of photocatalysis. In this study, the sol-gel method was used to synthesize titanium dioxide nanoparticles from variations of TBOT and TTIP. Furthermore, the structure, crystallite size and band gap of TiO$_2$ were determined by X-ray diffraction (XRD) and UV-vis reflectance spectroscopy (DRS). Subsequently, TiO$_2$ photocatalytic activity was evaluated in phenol photodegradation as a contaminant model with UV irradiation. The results showed the structure synthesized from TBOT had a higher amount of anatase, higher crystallinity, smaller crystallite size, larger band gap, and better photocatalytic activity than those from TTIP. Furthermore, it was shown that TiO$_2$ from TBOT had an efficiency of 147% greater than TiO$_2$ P25 Degussa, while TiO$_2$ from TTIP had 66% efficiency compared to TiO$_2$ P25.

Keywords: Phenol; photo catalyst; TBOT; TiO$_2$; TTIP

1. Introduction

Phenols are toxic chemical compounds and they are slowly degraded in the environment to form different aromatic intermediates. In fact, most of them cause environmental hazards (Peiró *et al*., 2001). Nevertheless, this compound and its intermediates can be reduced by various methods, which include photocatalysis (Lestari *et al*., 2021), ozonation (Shahamat *et al*., 2014; Wei *et al*., 2020), adsorption (Miao *et al*., 2013; Zhang *et al*., 2016; Dehmani *et al*., 2020), biological (Pradeep *et al*., 2015), and Fenton methods (Gümüş & Akbal, 2016; Yazdanbakhsh *et al*., 2020). Although the most suitable and widely used method is photocatalysis due to its advantages of

efficient industrial waste degradation (Ameta & Ameta, 2016), affordability, and environmentally friendly (Chong *et al*., 2010).

Titanium dioxide (TiO_2) is an effective photocatalyst and it is applied in various fields such as environmental and energy, including self-cleaning surfaces (Tavares *et al*., 2014; Banerjee *et al*., 2015), air and water purification systems (Turkay & Kumbur, 2019; Mamaghani *et al*., 2020), sterilization (Junkar *et al*., 2016), and photoelectrochemical conversion (Wang *et al*., 2011; Nakata & Fujishima, 2012). The main advantages of this compound include high chemical stability under acidic and basic conditions, non-toxic, affordability, and is an environmentally safe oxidizer, making it potential for many photocatalytic applications (Eddy *et al*., 2018; Alkhayatt *et al*., 2021).

The TiO_2 is divided into 3 main phases namely anatase, rutile, and brookite (Haggerty *et al*., 2017). Generally, anatase has the best photocatalytic ability compared to others because it shows a deeper excited charge carrier in large part leading to a higher surface reaction (Luttrell *et al*., 2014). Heterophase of TiO_2 can effectively stimulate electron transfer from one phase to another which helps to increase its photocatalytic performance (Hu *et al*., 2018; Ding *et al*., 2020). For instance, the well-known TiO_2 P25 Degussa which consists of ~20% rutile and ~80% anatase, is an exceptionally good photocatalyst (Berger *et al*., 2005).

Most of this compound was synthesized using organometallic precursors such as titanium butoxide (TBOT) (Gan *et al*., 2018; Wang *et al*., 2018; Lendzion-Bieluń *et al*., 2020) and titanium tetraisopropoxide (TTIP) (Cenovar *et al*., 2012; Paunović *et al*., 2015). The inorganic alkoxide precursor is preferred because of its ability to hydrolyze easily to the oxide phase due to its exposure to water (Syoufian *et al*., 2007).

Behnajady *et al*. (2011) investigated the conditions of TiO_2 synthesis using TBOT and TTIP for photocatalysis on the removal of C.I. Acid Red27 (AR27). Niu *et al*. (2014) also reported the synthesis of nanoparticles of this compound by microwave radiation method under difference precursor between $TiCl_4$, $Ti(SO_4)_2$, and TBOT for photocatalytic degradation of methylene blue (MB).

Cenovar *et al*. (2012) reported that they have successfully synthesized TiO_2 using the sol-gel method from TTIP. The results showed anatase had a stable crystal structure within the temperature range of 250 - 650°C. Zhao *et al*. (2009) reported a tested and proven effective method to synthesize brookite TiO_2 which is using hydrothermal methods or reflux conditions from the TBOT precursor. The results showed crystal structure of pure anatase, pure brookite, and brookite/anatase mixtures were formed.

However, there has been no report showing comparison in the effect of TBOT and TTIP precursors on TiO_2 crystal properties and their activity on phenol degradation. In this study, the compound was synthesized by sol-gel method from organometallic TBOT and TTIP. The effect of these parameters was further investigated on the crystal phase, size, lattice parameters, band gap energy, and its photocatalytic activity in phenol degradation.

2. Materials and methods

2.1 Materials

The materials used in this study were ethanol (C_2H_5OH, 99%, Merck), phenol (C_6H_5OH, 99%, Merck), TiO_2 nanoparticles (P25 Degussa, 20% rutile and 80% anatase, Merck), titanium butoxide (TBOT, $Ti(OC_4H_9)_4$, 99%, Sigma Aldrich), and titanium tetraisopropoxide (TTIP, $Ti(OC_3H_7)_4$, 99%, Sigma Aldrich). All ingredients were used without treatment.

2.2 Synthesis of TiO_2

Ethanol 95 mL and 0.48 mL of distilled water were mixed together and stirred for 30 mins, then a TiO_2 precursor (1.5 mL TBOT or 2.0 mL TTIP) in 18 mL ethanol was injected into the mixture at a rate of 0.5 mL/min using a syringe pump. After injection, the temperature was raised to 85°C under reflux at a stirring speed of 900 rpm for 100 mins. Furthermore, the precipitate was isolated by centrifugation, washed with distilled water and ethanol, dried in vacuum, and calcined at 800°C for 2 hours in the air to obtain TiO_2 TBOT (representing TiO_2 synthesized from the precursor TBOT) and TiO_2 TTIP (representing TiO_2 synthesized from the precursor TTIP).

2.3 Characterization of TiO_2

X-ray diffraction (XRD) patterns were obtained on a Rigaku/MiniFlex 600, and then measured at room temperature with Cu Kα radiation (λ = 1.5418 Å). The scan ranged from 20 to 80 (2θ). Also, the crystallite size was determined by using the Debye-Scherrer equation (Eddy et al. 2020):

$$B = K\lambda / D \cos \qquad (1)$$

Where D is the crystal size, K is the Scherrer constant (0.9), λ is the wavelength of the X-ray radiation, B is the value of the peak FWHM (full width at half maximum), and θ is the angle of diffraction.

Crystallinity was calculated by comparing the crystalline peak (I_c) with the total (crystalline peak (I_c) and amorphous peak (I_a)).

$$\text{Crystallinity (\%)} = I_c / (I_c+I_a) \text{ x } 100\% \qquad (2)$$

A Jasco V-550 spectroscopy was used to record the UV-visible (UV-vis) spectra, and the analysis range was from 200 to 800 nm. The optical band gap energy (E_g) was obtained using the Tauc equation:

$$(\alpha h v)^{1/n} = A(h v - E_g) \qquad (3)$$

where α is the absorption coefficient, hv is photon energy, and A is the proportionality constant. Furthermore, the transition property is represented by n, where n = 2 for the indirect band gap allowed (Chowdhury et al. 2019).

2.4 Photocatalytic Analysis

Photocatalytic degradation was carried out with 50 mL of a 20 mg/L phenol solution with 15 mg catalyst, within a period of 60 mins under dark adsorption (no irradiation source). Subsequently, the mixture was stirred at 300 rpm for 2 hours under light irradiation (300 W Xe lamp, UV ray with wavelength <390 nm, PE300BUV) at a distance of 150 mm above the surface of the solution. Furthermore, the time was tested to determine the remaining phenol concentration using reverse-phase high-performance liquid chromatography (HPLC, Jasco Co-2065Plus), with UV detector (Jasco UV-2075Plus), C-18 column or Octadecyl Silica (ODS) as the stationary phase and a mixture of distilled water and methanol as the mobile phase. The HPLC used methanol:water (1:1) as eluent, with a column temperature of 40°C and a column flow rate of 1.00 mL/min (Lestari *et al.*, 2020).

The equation below was used to calculate the percentage of phenol adsorption and degradation:

$$\% \text{ Removing} = (C_i - C_t) / C_i \times 100\% \tag{4}$$

Where C_i is the initial phenol concentration and C_t is phenol concentration at time t.

The kinetics of photocatalysis were calculated using first and second-order models. The first-order kinetics were calculated (Eddy *et al.*, 2020):

$$\ln(C_t/C_i) = -k_1 t + b \tag{5}$$

Where, C_i denotes the initial phenol concentration (mg.L^{-1}), C_t is the phenol concentration (mg.L^{-1}) in solution at t mins, b denotes the constant, and k_1 (min^{-1}) is the first-order rate constant. Then a second-order kinetics model was calculated based on the rate obtained from square of the number of sites on the catalyst surface (Turki *et al.*, 2015). The equation after integration is obtained as:

$$1/C_t - 1/C_i = -k_2 t + b \tag{6}$$

Where, k_2 denotes the second-order rate constant (L.mol^{-1}.min^{-1}).

3. Result and discussion

3.1 Characterization of Photocatalyst

3.1.1 X-ray diffraction Analysis

The results of X-ray diffraction (XRD) analysis are shown in Figure 1. The XRD patterns of P25, TiO₂ TBOT, and TiO₂ TTIP showed similarity with the Inorganic Crystal Structure Database (ICSD) 98-017-2914 for anatase (tetragonal, space group $I4_1/amd$) and ICSD 98-016-7961 for

rutile (tetragonal, space group $P4_2/mmm$). The highest peak of P25 was attained at $2\theta = 25.27°$, while the highest peak of TiO_2 TBOT was observed at $2\theta = 25.25°$, and the highest peak of TiO_2 TTIP was at $2\theta = 27.38°$. Also, P25 and TiO_2 TBOT had the highest peaks in relation to the anatase at $2\theta = 25.30°$, while TiO_2 TTIP had the highest peaks in relation to rutile at $2\theta = 27.43°$.

   TiO_2 P25 Degussa crystals showed peak pattern at $2\theta = 25.3°$ (011), 37.8° (004), 48.0° (020), 53.9° (015), 55.0° (121), 62.7° (024), 68.8° (116), 70.3° (220), and 75.1° (125) in the crystalline plane of anatase. In addition, the peaks at 27.4° (110) and 36.1° (011) were obtained from the rutile phase plane. For TiO_2 TBOT, there were additional peaks at 41.23° (111) and 44.04° (120) which were considered to be from the rutile phase. This was also observed in TiO_2 TTIP at 41.23° (111), 44.04° (120), 54,31° (121), 56.62° (220), and 68.99° (031), and is considered to have been derived from the rutile phase.

Table 1. Percentage of anatase and rutile phase in photocatalysts.

Photocatalysts	Phase (%)	
	Anatase	Rutile
TiO_2 P25	85.7	14.3
TiO_2 TBOT	33.2	66.8
TiO_2 TTIP	0.9	99.1
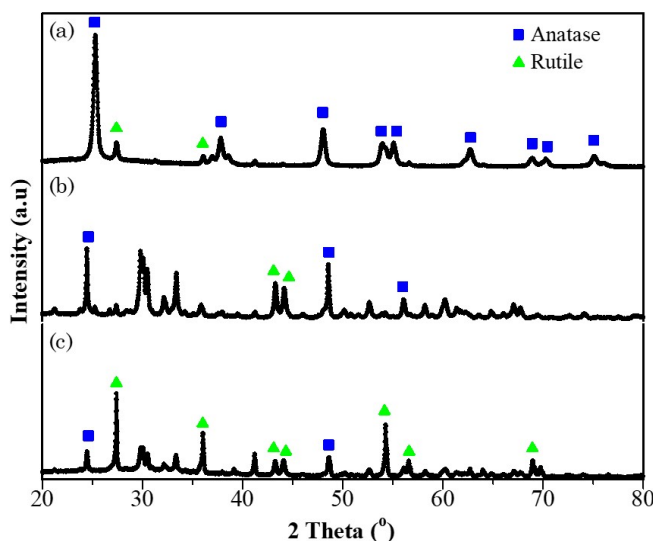
Fig. 1. XRD pattern of photocatalyst (a) P25, (b) TiO_2 TBOT, and (c) TiO_2 TTIP.

   A Rietveld refinement of the TiO_2 sample was performed from the XRD pattern. The percentage of TiO_2 phase is shown in Table 1. At the same calcination temperature (800°C), TiO_2 TBOT had a higher anatase percentage (33.2%) than TiO_2 TTIP (0.9%). This showed that different precursors require different energy to form its crystal lattice. These results can be compared to Behnajady *et al*. (2011) which stated that TiO_2 synthesized through the TBOT precursor produced a higher percentage of anatase than TiO_2 from TTIP.

Table 2 shows the crystallinity and crystallite size of photocatalysts. It shows that the synthesis from TBOT and TTIP precursors have a higher crystallinity than TiO_2 P25 Degussa. Meanwhile, high crystallinity is required in photocatalysis because of its ability to prevent the possibility of electron-hole recombination, in order to increase photocatalytic activity (Zheng *et al*. 2018). However, those from TBOT have higher crystallinity than those from TTIP which can support photocatalysis.

The crystallite size of the synthesized TiO_2 showed a larger size than Degussa TiO_2 P25 in anatase and rutile. This result was possible due to the sol-gel method which increased the crystallite size. However, those from the TBOT showed smaller size in anatase (75.28 nm) than those from the TTIP (81.44 nm). Also, in the rutile phase, TiO_2 from TBOT showed a larger size (73.37 nm) than TiO_2 from TTIP (52.23 nm).

Table 2. The crystallinity and crystallite size of photocatalysts.

Photocatalysts	Crystallinity (%)	Crystallite size (nm)	
		Anatase	Rutile
TiO_2 P25	46.01	32.84	22.59
TiO_2 TBOT	75.67	75.28	73.37
TiO_2 TTIP	60.57	81.44	52.23

Table 3. The crystal lattice parameters of photocatalysts.

Photocatalyst	Anatase			Rutile		
	$a=b$ (Å)	c (Å)	V(Å^3)	$a=b$ (Å)	c (Å)	V(Å^3)
ICSD 98-017-2914	3.78	9.51	136,27	-	-	-
ICSD 98-016-7961	-	-	-	4.59	2.96	62.47
TiO_2 P25	3.78	9.50	136.11	4.59	2.96	62.32
TiO_2 TBOT	3.78	9.50	135.89	4.59	2.96	62.38
TiO_2 TTIP	3.73	9.37	130.36	4.59	2.96	62.42

Table 4. The band gap of photocatalysts.

Photocatalysts	Wavelength (nm)	Band gap (eV)
TiO_2 P25	411.9	3.01
TiO_2 TBOT	414.7	2.99
TiO_2 TTIP	439.7	2.82

Table 3 shows the lattice parameters of TiO_2, and is seen that the synthesized substance has anatase crystals with a smaller lattice than TiO_2 P25 Degussa. Furthermore, those from the TTIP have smaller lattice than those from the TBOT with a crystal lattice volume of 135.8914 Å^3 for TiO_2 TBOT and 130.3639 Å^3 for TiO_2 TTIP. Whereas in rutile crystals, the synthesized substance showed a larger lattice than TiO_2 P25 Degussa. A comparison of the precursor

synthesis was also done, and it was observed that those of TTIP have larger lattice with a volume of 62.4220 $Å^3$ compared to TBOT, with a crystal lattice volume of 62.3819 $Å^3$. This shows that synthesizing this compound by sol-gel method can decrease the anatase crystal lattice and increase rutile. This effect occurs more in synthesis from TTIP precursors than those from TBOT.
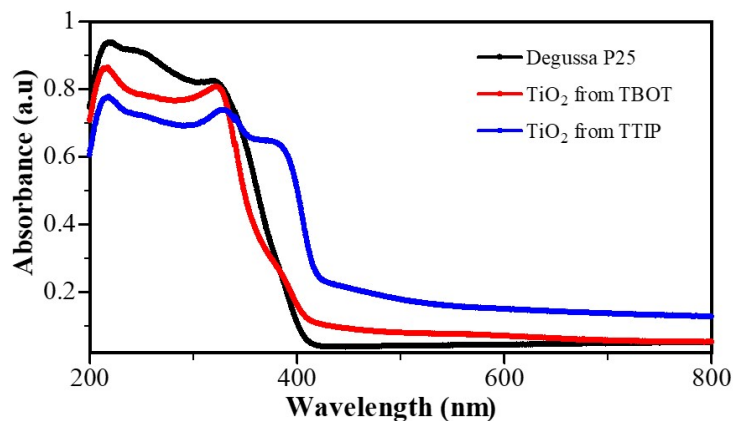

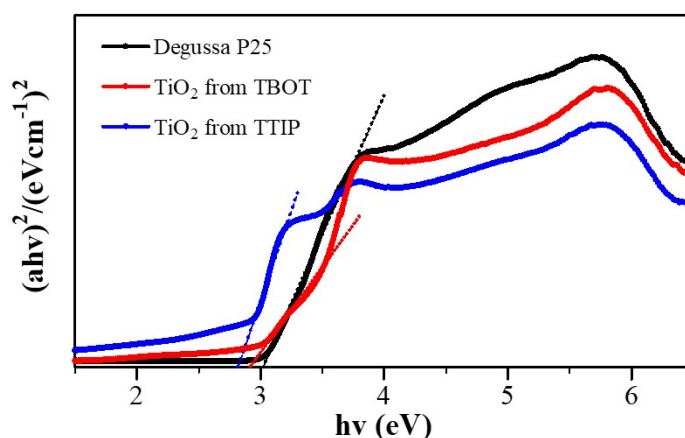**Fig. 2.** Photocatalysts absorbtion in range 200-800 nm.

Fig. 3. The band gap of a photocatalysts using Tauc equation.

3.1.2 UV-vis Spectroscopy Analysis

The UV-vis absorption spectrum is shown in Figure 2. TiO_2 P25 Degussa has clear ultraviolet light absorption characteristics and does not absorb visible light. However, those synthesized from the TTIP has absorption characteristics that extends from 350 nm to 413 nm, and attain its maximum absorption at 385 nm. The red shift of TiO_2 uptake from TBOT and TiO_2 from TTIP compared to TiO_2 P25 Degussa showed there was a decrease in the band gap for the synthesized TiO_2.

Band gap energy is calculated by plotting $(αhv)^2$ vs hv (Figure 3). The values for P25, TiO_2 from TBOT, and TiO_2 from TTIP are shown in Table 4. Therefore, it is seen that the synthesized TiO_2 causes a slight decrease in band gap than P25 Degussa. This is due to the formation of rutile phase, which is more dominant than anatase, where the standard anatase has a band gap of 3.2

eV and rutile has 3.0 eV (Luttrell *et al*. 2014). In addition, TiO_2 from TTIP has a smaller band gap value (2.82 eV) because it has a more rutile phase than TiO_2 from TBOT (2.99 eV). The values determined in this work are all smaller than those reported in other literatures.
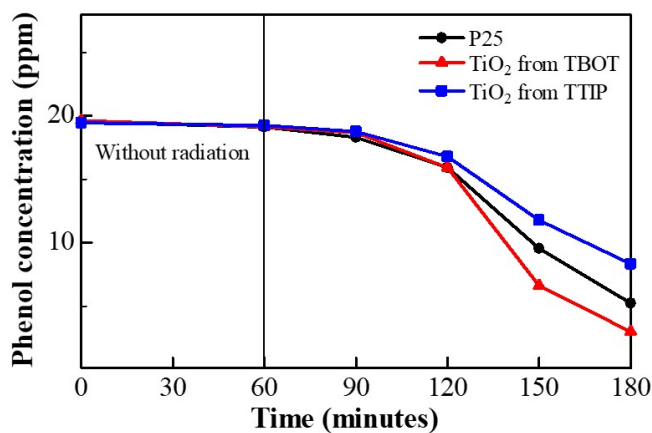
Fig. 4. Photocatalytic activity of catalyst on phenol. The experiment was conducted using 50 mL phenol solution 20 mg/L and 15 mg catalyst with 180 min treatment.

Table 5. The percentage efficiency of phenol adsorption and degradation.

Photocatalysts	Phenol adsorption (%)	Phenol degradation (%)
TiO₂ P25	2.04	71.15
TiO₂ TBOT	2.46	82.38
TiO₂ TTIP	1.04	56.14

Also, variations in the band gap value can be influenced by differences in the crystal lattice parameters. This causes changes of electron density in the crystal (Barajas-Aguilar *et al*., 2018), therefore, the band gap value can be changed.

3.2 Photocatalytic Activity

Experimental results of the photocatalytic degradation of phenol are shown in Figure 4. The activity of photocatalysts exposed to UV rays has better percentage degradation when compared to those not exposed. This showed photons from UV light have a positive effect on photocatalyst performance in phenol oxidation.

Table 5 shows the percentage adsorption and degradation of phenol by photocatalysts. It can be seen that TiO_2 from the TBOT had the largest percentage of adsorption (2.46%) which correlates with the largest percentage of degradation (82.38%). In contrast, those from TTIP have the lowest percentage of adsorption (1.04%) and degradation (56.14%) compared to TBOT and P25 Degussa after 2 hours of UV irradiation. This is because TiO_2 from TBOT has the highest crystallinity which reduces the occurrence of recombination (Zheng *et al*. 2018), while the smaller crystallite anatase size increases the photocatalytic ability. Furthermore, it had a greater

percentage of anatase (33.2%) than the other. The presence of this anatase-rutile heterophase enhances the formation of an electron synergistic effect, which effectively stimulates the transfer of electrons from one phase to another (Hu *et al*., 2018; Ding *et al*., 2020). Although its amount of anatase was too low (0.9%), therefore, this effect might not occur.

Table 6 shows the reaction of kinetic rate constant data based on the pseudo first and second-order models. It is seen that the pseudo first-order model gives a better R-value than the second. This implies that the photocatalytic reaction of phenol degradation fits it. Meanwhile, the highest k value is found in TiO_2 from the TBOT precursor in both models, namely with k_1 of 0.0159 min^{-1} in the first-order model and k_2 of 0.0017 $L.mol^{-1}.min^{-1}$ in the second. The k_1 value in the first is followed by Degussa TiO_2 P25 (0.0108 min^{-1}) and TiO_2 TTIP (0.0071 min^{-1}).

Table 6. The kinetic study of photocatalysts.

Sample	Pseudo first-order		Pseudo second-order	
	k_1	R^2	k_2	R^2
TiO_2 P25	0.0108	0.8663	0.0008	0.6651
TiO_2 TBOT	0.0159	0.8505	0.0017	0.6315
TiO_2 TTIP	0.0071	0.8859	0.0004	0.7243

The results showed the efficiency of phenol removal with TiO_2 from TBOT was 147% greater than TiO_2 P25 Degussa for the first-order model, while TiO_2 from TTIP had 66% efficiency compared to TiO_2 P25 Degussa.

4. Conclusions

In this study, the sol-gel method was used to synthesize titanium dioxide from variations of the TBOT and TTIP precursors and tested for photocatalytic activity on phenol. Results show that TBOT makes TiO_2 dominant with the anatase phase. Also, TiO_2 synthesized from TBOT has high crystallinity, small crystallite size, and higher band gap than TiO_2 from TTIP. In addition, TiO_2 synthesized from TBOT precursor has a higher photocatalytic activity than TiO_2 P25 Degussa with greater efficiency of 147%, while that from TTIP has an efficiency of 66%.

ACKNOWLEDGEMENTS

References

Alkhayatt, A.H.O., Hussain, S.A. & Muhammad, S.K. (2021) Hydrothermally growth of TiO_2 Nanorods, characterization and annealing temperature effect. Kuwait Journal of Science, **48**(3).

Ameta, R. & Ameta, S.C. (2016) Photocatalysis: principles and applications. CRC Press, Boca Raton.

Banerjee, S., Dionysiou, D.D. & Pillai, S.C. (2015) Self-cleaning applications of TiO$_2$ by photo-induced hydrophilicity and photocatalysis. Applied Catalysis B: Environmental, **176**: 396-428.

Barajas-Aguilar, A.H., Irwin, J.C., Garay-Tapia, A.M., Schwarz, T., Delgado, F.P., Brodersen, P.M., Prinja, R., Kherani, N. & Sandoval, S.J.J. (2018) Crystalline structure, electronic and lattice-dynamics properties of NbTe$_2$. Scientific Reports, **8**(1): 1-14.

Behnajady, M.A., Eskandarloo, H., Modirshahla, N. & Shokri, M. (2011) Investigation of the effect of sol–gel synthesis variables on structural and photocatalytic properties of TiO$_2$ nanoparticles. Desalination, **278**(1-3): 10-17

Berger, T., Sterrer, M., Diwald, O., Knözinger, E., Panayotov, D., Thompson, T.L. & Yates, J.T. (2005) Light-induced charge separation in anatase TiO$_2$ particles. The Journal of Physical Chemistry B, **109**(13): 6061-6068.

Cenovar, A., Paunovic, P., Grozdanov, A., Makreski, P. & Fidanccevska, E. (2012) Preparation of nano-crystalline TiO$_2$ by Sol-gel method using titanium tetraisopropoxide (TTIP) as a precursor. Advances in Natural Science: Theory & Applications. **1**(2): 133-142.

Chong, M.N., Jin, B., Chow, C.W. & Saint, C. (2010) Recent developments in photocatalytic water treatment technology: a review. Water research, **44**(10): 2997-3027.

Chowdhury, I.H., Roy, M., Kundu, S. & Naskar, M.K. (2019) TiO$_2$ hollow microspheres impregnated with biogenic gold nanoparticles for the efficient visible light-induced photodegradation of phenol. Journal of Physics and Chemistry of Solids, **129**: 329-339.

Dehmani, Y., Sellaoui, L., Alghamdi, Y., Lainé, J., Badawi, M., Amhoud, A., Bonilla-Petriciolet, A., Lamhasni, T. & Abouarnadasse, S. (2020) Kinetic, thermodynamic and mechanism study of the adsorption of phenol on Moroccan clay. Journal of Molecular Liquids, **312**: 113383.

Ding, L., Yang, S., Liang, Z., Qian, X., Chen, X., Cui, H. & Tian, J. (2020) TiO$_2$ nanobelts with anatase/rutile heterophase junctions for highly efficient photocatalytic overall water splitting. Journal of Colloid and Interface Science, **567**: 181-189.

Eddy, D.R., Anggraeni, A., Fauzia, R.P., Rahayu, I., Mutalib, A., Firdaus, M.L. & Bahti, H.H. (2018) Gadolinium-Mesoporous Silica as a Potential Magnetic Resonance Imaging Contrast Agents. Oriental Journal of Chemistry, **34**(5): 2603.

Eddy, D.R., Ishmah, S.N., Permana, M.D. & Firdaus, M.L. (2020) Synthesis of Titanium Dioxide/Silicon Dioxide from Beach Sand as Photocatalyst for Cr and Pb Remediation. Catalysts, **10**(11): 1248.

Gan, Y., Wei, Y., Xiong, J. & Cheng, G. (2018) Impact of post-processing modes of precursor on adsorption and photocatalytic capability of mesoporous TiO$_2$ nanocrystallite aggregates towards ciprofloxacin removal. Chemical Engineering Journal, **349**: 1-16.

Gümüş, D. & Akbal, F. (2016) Comparison of Fenton and electro-Fenton processes for oxidation of phenol. Process Safety and Environmental Protection, **103**: 252-258.

Haggerty, J.E., Schelhas, L.T., Kitchaev, D.A., Mangum, J.S., Garten, L.M., Sun, W., Stone, K.H., Perkins, J.D., Toney, M.F., Ceder, G. & Ginley, D.S. (2017) High-fraction brookite films from amorphous precursors. Scientific Reports, **7**(1): 1-11.

Hu, J., Zhang, S., Cao, Y., Wang, H., Yu, H. & Peng, F. (2018) Novel highly active anatase/rutile TiO_2 photocatalyst with hydrogenated heterophase interface structures for photoelectrochemical water splitting into hydrogen. ACS Sustainable Chemistry & Engineering, **6**(8): 10823-10832.

Junkar, I., Kulkarni, M., Drašler, B., Rugelj, N., Mazare, A., Flašker, A., Drobne, D., Humpolíček, P., Resnik, M., Schmuki, P. & Mozetič, M. (2016) Influence of various sterilization procedures on TiO_2 nanotubes used for biomedical devices. Bioelektrochemistry, **109**: 79-86.

Lendzion-Bieluń, Z., Wojciechowska, A., Grzechulska-Damszel, J., Narkiewicz, U., Śniadecki, Z. & Idzikowski, B. (2020) Effective processes of phenol degradation on Fe_3O_4–TiO_2 nanostructured magnetic photocatalyst. Journal of Physics and Chemistry of Solids, **136**: 109178.

Lestari, P.R., Takei, T. & Kumada, N. (2021) Novel $ZnTi/C_3N_4/Ag$ LDH heterojunction composite for efficient photocatalytic phenol degradation. Journal of Solid State Chemistry, **294**: 121858.

Lestari, P.R., Takei, T., Yanagida, S. & Kumada, N. (2020) Facile and controllable synthesis of Zn-Al layered double hydroxide/silver hybrid by exfoliation process and its plasmonic photocatalytic activity of phenol degradation. Materials Chemistry and Physics, **250**: 122988.

Luttrell, T., Halpegamage, S., Tao, J., Kramer, A., Sutter, E. & Batzill, M. (2014) Why is anatase a better photocatalyst than rutile? -Model studies on epitaxial TiO_2 films. Scientific Reports, **4**(1): 1-8.

Mamaghani, A.H., Haghighat, F. & Lee, C.S. (2020) Role of titanium dioxide (TiO_2) structural design/morphology in photocatalytic air purification. Applied Catalysis B: Environmental, **269**: 118735.

Miao, Q., Tang, Y., Xu, J., Liu, X., Xiao, L. & Chen, Q. (2013) Activated carbon prepared from soybean straw for phenol adsorption. Journal of the Taiwan Institute of Chemical Engineers, **44**(3): 458-465.

Nakata, K. & Fujishima, A. (2012) TiO_2 photocatalysis: Design and applications. Journal of Photochemistry and Photobiology C: Photochemistry Reviews, **13**(3): 169-189.

Niu, J., Yao, B., Peng, C., Zhang, W. & Chen, Y. (2014) Rapid microwave hydrothermal methods synthesis of TiO₂ photocatalysts using different sources of materials. Integrated Ferroelectrics, **152**(1): 163-173.

Paunović, P., Grozdanov, A., Češnovar, A., Makreski, P., Gentile, G., Ranguelov, B. & Fidančevska, E. (2015) Characterization of nanoscaled TiO₂ produced by simplified sol–gel method using organometallic precursor. Journal of Engineering Materials and Technology, **137**(2).

Peiro, A.M., Ayllón, J.A., Peral, J. & Doménech, X. (2001) TiO₂-photocatalyzed degradation of phenol and ortho-substituted phenolic compounds. Applied Catalysis B: Environmental, **30**(3-4): 359-373.

Pradeep, N.V., Anupama, S., Navya, K., Shalini, H.N., Idris, M. & Hampannavar, U.S. (2015) Biological removal of phenol from wastewaters: a mini review. Applied Water Science, **5**(2): 105-112.

Shahamat, Y.D., Farzadkia, M., Nasseri, S., Mahvi, A.H., Gholami, M. & Esrafili, A. (2014) Magnetic heterogeneous catalytic ozonation: a new removal method for phenol in industrial wastewater. Journal of Environmental Health Science and Engineering, **12**(1): 1-12.

Syoufian, A., Inoue, Y., Yada, M. & Nakashima, K. (2007) Preparation of submicrometer-sized titania hollow spheres by templating sulfonated polystyrene latex particles. Materials Letters, **61**(7): 1572-1575.

Tavares, M.T.S., Santos, A.S.F., Santos, I.M.G., Silva, M.R.S., Bomio, M.R.D., Longo, E., Paskocimas, C.A. & Motta, F.V. (2014) TiO₂/PDMS nanocomposites for use on self-cleaning surfaces. Surface and Coatings Technology, **239**: 16-19.

Turkay, G.K. & Kumbur, H. (2019) Investigation of amoxicillin removal from aqueous solution by Fenton and photocatalytic oxidation processes. Kuwait Journal of Science, **46**(2)**.**

Turki, A., Guillard, C., Dappozze, F., Ksibi, Z., Berhault, G. & Kochkar, H. (2015) Phenol photocatalytic degradation over anisotropic TiO₂ nanomaterials: Kinetic study, adsorption isotherms and formal mechanisms. Applied Catalysis B: Environmental, **163**: 404-414.

Wang, G., Wang, H., Ling, Y., Tang, Y., Yang, X., Fitzmorris, R.C., Wang, C., Zhang, J.Z. & Li, Y. (2011) Hydrogen-treated TiO₂ nanowire arrays for photoelectrochemical water splitting. Nano letters, **11**(7): 3026-3033.

Wang, X., Bai, L., Liu, H., Yu, X., Yin, Y. & Gao, C. (2018) A Unique Disintegration–Reassembly Route to Mesoporous Titania Nanocrystalline Hollow Spheres with Enhanced Photocatalytic Activity. Advanced Functional Materials, **28**(2): 1704208.

Wei, X., Shao, S., Ding, X., Jiao, W. & Liu, Y. (2020) Degradation of phenol with heterogeneous catalytic ozonation enhanced by high gravity technology. Journal of Cleaner Production, **248**: 119179.

Yazdanbakhsh, A., Aliyari, A., Sheikhmohammadi, A. & Aghayani, E. (2020) Application of the enhanced sono-photo-Fenton-like process in the presence of persulfate for the simultaneous removal of chromium and phenol from the aqueous solution. Journal of Water Process Engineering, **34**: 101080.

Zhang, D., Huo, P. & Liu, W. (2016) Behavior of phenol adsorption on thermal modified activated carbon. Chinese Journal of Chemical Engineering, **24**(4): 446-452.

Zhao, B., Chen, F., Huang, Q. & Zhang, J. (2009) Brookite TiO_2 nanoflowers. Chemical Communications, (34): 5115-5117.

Zheng, H., Svengren, H., Huang, Z., Yang, Z., Zou, X. & Johnsson, M. (2018) Hollow titania spheres loaded with noble metal nanoparticles for photocatalytic water oxidation. Microporous and Mesoporous Materials, **264**: 147-150.

Biosynthesis of iron oxide nanoparticles from dates, characterisation, and investigation of anticarcinogenic and antimicrobial properties

Kannan Kathiresan[1], Mani Ramakrishnan[2, 3,*]

[1]Kalasalingam School of Agriculture and Horticulture,
Kalasalingam Academy of Research and Education, Deemed-to-be University,
Krishnankoil– 626126, Srivilliputhur, Virudhunagar (Dt.), Tamil Nadu, India
[2]Faculty of Environmental Studies, Presidency College (Autonomous),
Bengaluru-560024, Karnataka, India
[3]Centre for Environmental Studies, School of Engineering, Presidency University,
Bengaluru - 560064, Karnataka, India
[*]Corresponding author: maniramiyer@yahoo.com

Abstract

Nanomaterial synthesis using natural biological systems, especially plant-based green synthesis, has displayed great excitement and interest. This study synthesised iron oxide nanomaterials from three different varieties of date palms obtained from Srivilliputhur, Tamil Nadu, India. The extract of date palms reduced ferric chloride in the solution and facilitated the formation of iron oxide nanomaterials. Phytochemical studies of the extracts obtained from all three varieties of date palms indicated the presence of phenols. The synthesised nanomaterials were characterised by UV-VIS spectroscopy, SEM, EDAX, XRD and FTIR methods. The ability of the synthesised nanomaterials to inhibit human microbial pathogens proliferation was tested in *Staphylococcus* sp. and *Bacillus* sp. by turbidity method and recorded the maximum antimicrobial property against *Bacillus* sp. in the iron nanomaterial synthesised from Sukhri date palm. The cytotoxic potential of the iron oxide nanomaterials against two human cancer cell lines (A-549 and MDA-MB-231) by MTT assay. The iron oxide nanomaterials from Sukhri date palm detected a substantial cytotoxicity response.

Keywords: Anticancer; antimicrobial; date palms; green synthesis; iron oxide nanomaterials.

1. Introduction

The demand for producing nontoxic, hygienic, eco-friendly solvents is growing. Hence, the synthesis of nanoparticles using biological systems and organisms has been given more importance (Das & Brar, 2013; Mahdavi *et al.,* 2013; David *et al.,* 2014; Kajani *et al.,* 2016; Muthu & Priya, 2017). The biological synthesis of nanoparticles is being exploited commercially to a more significant extent (Mahdavi *et al.,* 2013). Plant leaf and fruit extracts are used to synthesise iron oxide nanomaterials because of their nontoxic and ecofriendly nature and their benefits in pharma industries (Das *et al.,*2014). A plant's system has inorganic substances mostly found in nanoscale sizes (Raveendran *et al.,* 2003). The extracts from various plant parts produce biochemical nanoparticles of different sizes and compositions. Therefore, green synthesis of iron nanoparticles

obtained using plant parts such as leaf and fruit extracts are most feasible, and they need not require cell culture maintenance. Besides, nanoparticles' size, shape and dispersity are controlled effectively in plant cell extracts. (Ghorbanpour, 2015; Pansare *et al.,* 2016; Yadav *et al.,* 2017; Rivera-Rangel *et al.,* 2018). Bioreduction of metal ions occurs during the synthesis of nanoparticles from various plant parts. The constituents in plant cell extracts are vital for the reduction of iron ions, while water-soluble heterocyclic compounds are involved in the stabilisation of nanoparticles generated. Ferric chloride is also used to remove plant extracts (Senthil & Ramesh, 2012). Iron nanomaterials have exceptional antibacterial activity (Oladipo *et al.,* 2017; Rajan *et al.,* 2017). Moreover, the size of these iron oxide nanomaterials played a vital role in controlling their effects (Karthik *et al.,* 2016; Asiabani *et al.,* 2017; Lebaschi *et al*., 2017). Iron nanocrystals have also exhibited added effectiveness when equated to cisplatin in lysing HeLa cells (Gao *et al.,* 2007; Nadagouda *et al.,* 2008; Song *et al.,* 2010).

Date fruits from varieties such as Ambera, Sukhri and Khudri possess high nutritional value and are effective for healing diseases. These three varieties of date palms contain the following nutrients, viz., 5.33 g of carbohydrates, 0.3 g of fat, 0.6 g of dietary fibre, 4.5 g of sugar, 0.17 g of protein, 0.012 mg of Vitamin B 6 or pyridoxine, 0.07 mg of iron, 47 mg of potassium and 3 mg of magnesium. Besides these nutrients, they also possess substantial amounts of calcium, sulphur, manganese, copper and phosphorus. They have a high nutritional profile offering several health benefits. Date palms are a major source of fiber, iron, numerous nutrients, and antioxidants, providing health benefits from better digestion and a reduced risk of diseases. They are essential in treating several diseases due to their low glycemic index, fiber content, and antioxidants. They also promote brain health and bone health.

Moreover, they possess excellent antimicrobial activities (Al-orf *et al.,* 2012; Bouhlali *et al.,* 2015; Saafi *et al.,* 2011). Date palm varieties contain vitamins and numerous essential amino acids (Dash *et al.,* 2013). Phytochemicals found in the fruit of the date palm serve as potential metal reducing and stabilising agents (Philip, 2010). Fruits of date palms were chosen for the study because they are edible, most preferred dry fruits, and have better nutritive and therapeutic values. The synthesis of metal nanoparticles using plant extracts, inactivated plant parts, and fruit extracts is a modern alternative for their production. Recent research indicates that the major components of the dates exhibit antioxidant, antidiabetic, antimicrobial and anticancer activity. The present investigation aimed to develop a simple process to produce iron nanomaterials from date palms, their characterisation and evaluation of the potential of the nanomaterial in terms of antimicrobial and anticancer activity.

2. Materials and methods

2.1 Collection of date palm fruits and preparation of Extract

Three varieties of date palms, such as Ambera, Sukhri and Khudri, were obtained from various supermarkets such as RGN Nanayam supermarket, VRN Babu supermarket, and Alagapuri farm in Srivilliputhur, Tamil Nadu, India. These three varieties of date palms have been imported from Egypt and Saudi Arabia. First, the three varieties of date palms were dried in a hot air oven to

remove the moisture content. Then, 10 g of the three varieties of date palms, such as Ambera, Sukhri and Khudri, were boiled in 200 ml of distilled water until the volume was reduced to half, and thereby the extracts of date palms were prepared.

Fig. 1. Three varieties of date palms used in the study, A. Ambera, B. Sukhri. C. Khudri

2.2   Chemicals

The chemical Ferric chloride hexahydrate ($FeCl_3.6H_2O$, 98%) and the solvents used in the investigation were pure analytical grades purchased from Sigma Aldrich.

2.3   Synthesis of Iron oxide nanomaterials

It was synthesised using a modified protocol obtained from previous studies (Pattanayak *et al.,* 2013; Ramya *et al*., 2012; Li., 2007). First, 20 g of ferric chloride was added to 200 ml of ethanol, mixed well, and 200 ml of ether was added to the mixture. The mixture was then transferred to the extracts obtained from three varieties of date palms and placed on a magnetic stirrer, Lanphan ZNCL-BS model, at 150 rpm for 90 min. to ensure proper mixing of the particles. Reduction of ferric chloride to ferric oxide occurred, and the modification showed the synthesis of iron oxide nanomaterials in colour to reddish-brown. The solution was then filtered, and the filtrate was kept in a hot air oven at 60◦C to form a powder.

2.4   Characterisation of Iron oxide nanomaterials

The iron oxide nanomaterials synthesised were characterised by performing different spectroscopic and analytical techniques (Jahja *et al.,* 2018). After 24 hours of incubation, the nanoparticle reaction medium was centrifuged at 10,000 rpm for 15 min. Then, the supernatant was subjected to UV-VIS Perkin-Elmer Lambda 25 spectrophotometer studies. The size and shape of the nanomaterials were observed with a Scanning Electron Microscope (SEM)with a very thin layer of platinum (Pt) (BAL-TECSCD 005 sputter coater) to increase the sample surface contrast and avert charge buildup. SEM pictures were attained using a Zeiss LEO instrument (Model 1455VP).

The microstructure of iron oxide nanomaterials was analysed by X-ray diffraction (XRD), Philips PW 11/90 diffractometer with nickel filtered CuKα (l = 1.5405 Å). The X-ray diffractometer was fitted with a nickel foil filter having a thickness between 15 – 25 µm. Using the Debye-Scherrer equation, the iron oxide nanocrystals' average diameter (D) was measured from the broadening of the XRD peak intensity after Kα$_2$corrections.

Fourier Transformation Infra-Red (FTIR) spectroscopy examined the samples' dissimilarities in chemical groups. FTIR spectroscopy has been used as a technique for the investigation of the characteristic functional groups of iron oxides. The wavelength of light absorbed is characteristic of the chemical bond reflected in the annotated spectrum. Therefore, the chemical bonds in a molecule were calculated by interpreting the infrared absorption spectrum. The FTIR spectra of the samples were recorded with a Perkin Elmer Spectrophotometer (Model Perkin Elmer-1600 series) in the range of $400 - 4000$ cm^{-1} using the KBr pellet technique. FTIR studies were conducted on compressed pills prepared by mixing iron oxide powder with potassium bromide.

2.5 Phytochemical analysis of date palms

Phytochemical analysis of the three varieties of date palms was carried out. The procedure is as follows:

a) Terpenoids: sample extract (1 ml) + chloroform (2 ml) + concentrated H2 SO4. Reddish Brown colouration was found at the interface layer.

b) Flavonoids (AlCl$_3$): 1ml of extract + 1ml of 1% AlCl$_3$. The appearance of a light-yellow colour.

c) Phenols: Folin-Ciocalteau reagent + Sodium Carbonate + extract. The appearance of dark green colour.

d) Saponins (Lead Acetate test): 1ml of extract + 1% lead acetate. Formation of white precipitate.

e) Cardioglycans: 1ml of extract + 1ml of glacial acetic acid + FeCl$_3$ + Concentrated H$_2$SO$_4$.

f) Tannins: 1ml extract + 5ml distilled water + few drops of 5% neutral solution (5% FeCl$_3$ in 90% alcohol).

g) Alkaloids (Mayer's test): 2ml of extract + 2drops of Mayer's reagent. Formation of a creamy white precipitate.

2.6 Determination of the antimicrobial activity of Iron oxide nanomaterials

Turbidity examined the antimicrobial action of the synthesised nanomaterials against bacteria such as *Staphylococcus* and *Bacillus*. Broth cultures of *Staphylococcus* and *Bacillus* were transferred to the extracts of the three different samples of date palms containing iron oxide nanomaterials at different concentrations such as100µl, 250µl and 500µland. The turbidity was determined using a colourimeter. The positive control contained the culture with an antibiotic, whereas the negative control contained only the culture (Sudhama & M, 2019).

2.7 Determination of the anticancer activity of iron oxide nanomaterials

The synthesised iron oxide nanomaterials' anticancer properties were tested against two cell lines such as A-549 and MDA-MB-231 by 3-(4,5-dimethylthiazol-2-yl)-2,5-diphenyl tetrazolium bromide (MTT) assay. In addition, the anticancer potential of the iron oxide nanomaterials was compared with the standard drug, cisplatin (Sudhama, V. N. & M. Ramakrishnan, 2020).

3. Results and discussion

3.1 Biosynthesis of iron oxide nanomaterials

Biomaterials and biochemical compounds present in the date palm extract caused the conversion of iron precursor salts into iron oxide nanomaterials and served as stabilising agents. The appearance of reddish-brown colour in the extracts of date palms showed the formation and presence of iron oxide nanomaterials (Figure 2). The colour arises due to surface plasmon vibrations in the iron oxide nanomaterials.
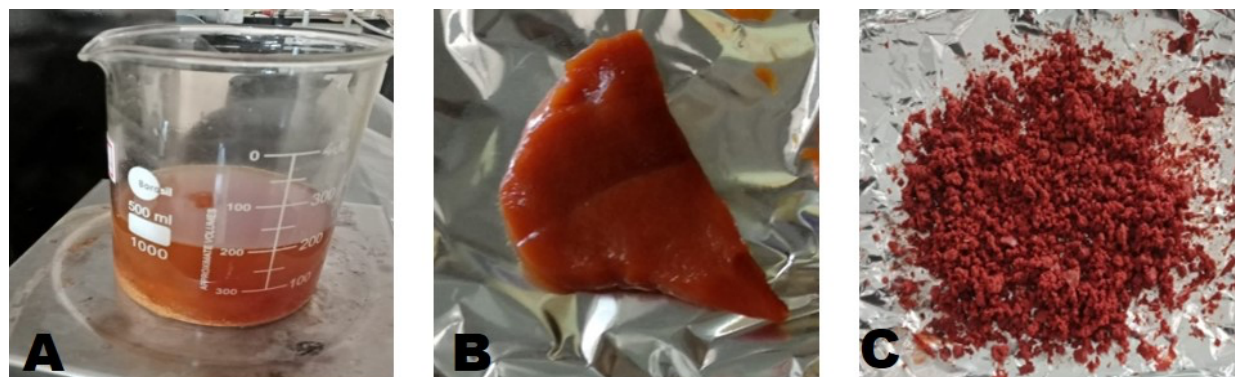

Fig.2. Process of synthesis of nanomaterials from date palms. A. Fe nanoparticle extraction. B. The paste obtained after filtration C. The powder obtained after drying

3.2 Characterisation of Iron oxide nanomaterials

The iron oxide nanomaterials have been subjected to UV-VIS spectrophotometric analysis. Absorption peaks were spotted at 270 nm and 390nm due to the iron metallic core hydrolysis products. Synthesis of nanomaterials from plant sources exhibits strong captivation of electromagnetic waves in the visible range due to their visual resonant stuff, called Surface Plasmon Resonance (SPR) due to excitation of surface plasmon vibrations. The frequency and width of the surface plasmon absorption depend on the size and shape of the metal nanomaterials and the dielectric constant of the metal itself and the surrounding medium. The absorption of visible radiations due to the excitation of SPR imparts various colours to the nanomaterials. As the nanomaterial size changes, the colour of the solution also changes (Breck, 2016). Hence, the UV-VIS absorption spectrum is quite sensitive to the formation of nanomaterials.

Table 1. Absorption spectra of Iron oxide nanomaterials in UV-VIS spectrophotometer

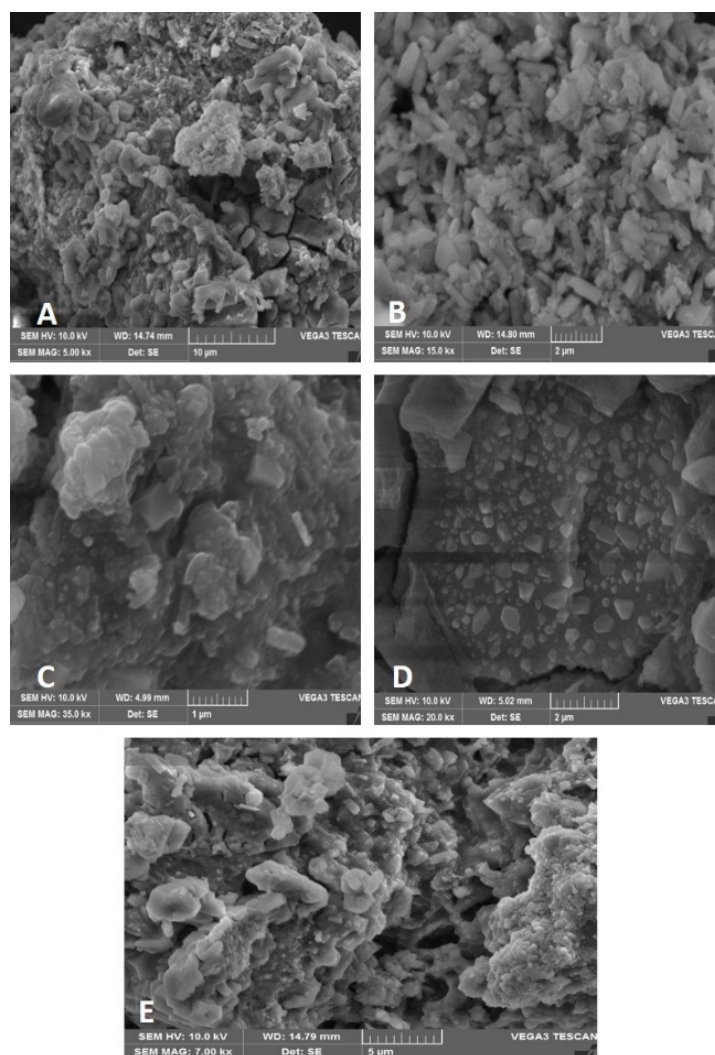| S.No.	Varieties of dates	Absorption spectra in UV-VIS Spectrophotometer	
		Lowest absorption peak (nm)	Highest absorption peak (nm)
1.	Ambera	275	398
2.	Sukhri	273	395
3.	Khudri	270	390

Fig 3. SEM micrographs of iron oxide nanomaterials synthesised from date palms.

The nanostructure of iron oxide nanomaterials was further investigated using SEM. The SEM micrographs obtained from the ready sample exhibited that iron oxide nanomaterials are sphere shaped and rod-shaped, clustered together and bear an overall rough morphology with aggregation in solution (Figure 3).

EDAX spectrum (Figure 4) shows the presence of compounds such as carbon, oxygen, sodium, potassium and chloride in the reaction mixture or the date palm extract other than iron oxide nanomaterials. The date palm extract recorded 17% iron and 44% oxygen in the total weight of Fe_2O_3NPs. This is based on the bremsstrahlung X-ray intensity as a function of energy. Potassium modifies the general form of the enzyme iota, revealing the suitable chemically active sites for reaction. It also defuses various organic anions and other compounds within the date fruits, serving to ease the optimum pH between 7.0 and 8.0, suitable for most enzyme reactions

eZAF Smart Quant Results		
Element	Weight %	Atomic %
C	28.96	41.03
O	44	46.8
Na	8.33	6.17
C	1.73	0.83
Fe	16.98	5.17
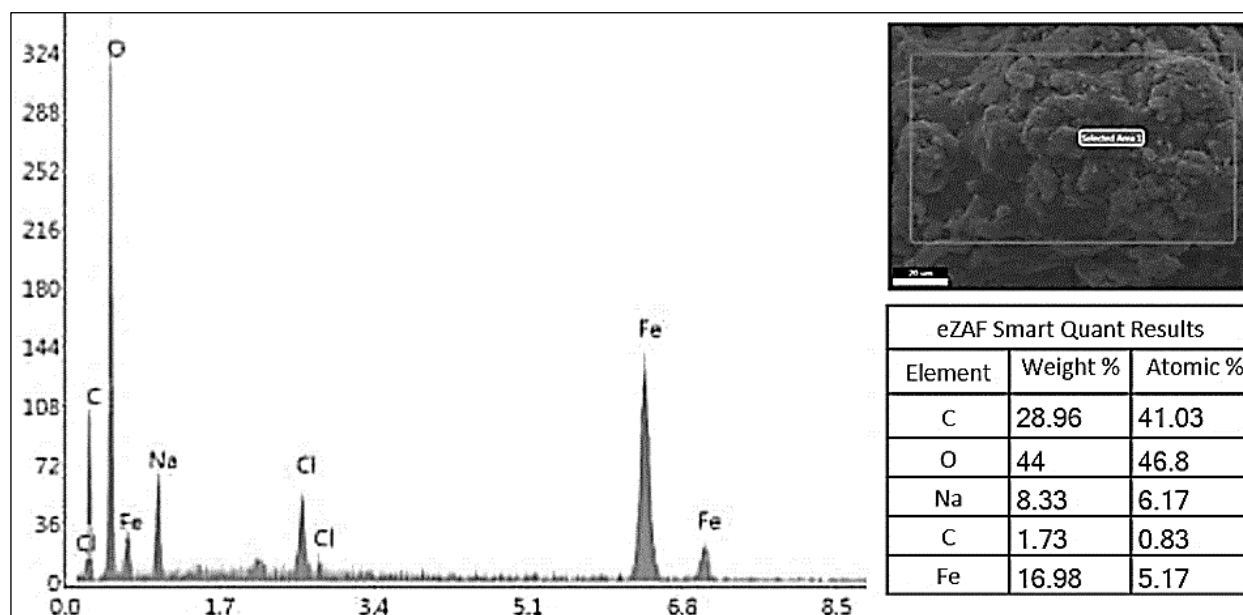
Fig.4. EDAX spectrum of iron oxide nanomaterials in the selected area and their characteristics.

The features of the molecular structure of iron oxide nanomaterials were explored in XRD data (Figure 5), the XRD pattern is $2\theta = 31.2°$, $44.3°$ and $45.1°$ and the XRD geometry data of the iron oxide nanomaterials corresponded well to rhombohedra geometry. The typical size of the synthesised nanomaterials was calculated in nanometers from the XRD peaks using the Scherrer equation. The range of the peak received by X-ray diffraction is based on the apparatus and crystallite size (Jahja *et al.,* 2018). The small particle below 100 nm in size broadening from the apparatus is negligible. Scherrer's method permits the calculation of the crystal size: DRX= 0.9 lambda/Δ cosθ, where 0.9 is a dimension constant of the equipment, lambda is the wavelength of the radiation corresponding to the peaks, and θ is the Bragg's angle. Hence, the grain of the particle is 80-90nm.

The infra-red spectra (IR) of the synthesised iron oxide nanomaterials were acquired by an FTIR spectrometer (Figure 4); they were used to find the possible biomolecules accountable for the reduction and stabilisation of the nanomaterials, and the IR spectra were collected between 400 and 4000cm^{-1}. The IR spectrum of iron oxide nanomaterials displayed prominent absorption bands at 705, 845, 1115, 1295, 1480, 1650, 1960 and 3650 cm^{-1} and would have resulted from (O-H) stretching vibration. The IR portion of the electromagnetic spectrum has been separated into 3 regions, viz. near, middle and far infrared, named for the visible spectrum (1980 – 2450cm^{-1}). The C = O stretching has also been observed in the IR spectrum.

3.3 Phytochemical analysis of three date palm varieties

Among the phytochemicals, terpenoids and phenols were produced by all three varieties of date palms, whereas cardioglycans were found only in one variety i. e. Ambera. None of the varieties produced flavonoids, saponins, tannins and alkaloids (Table 2).
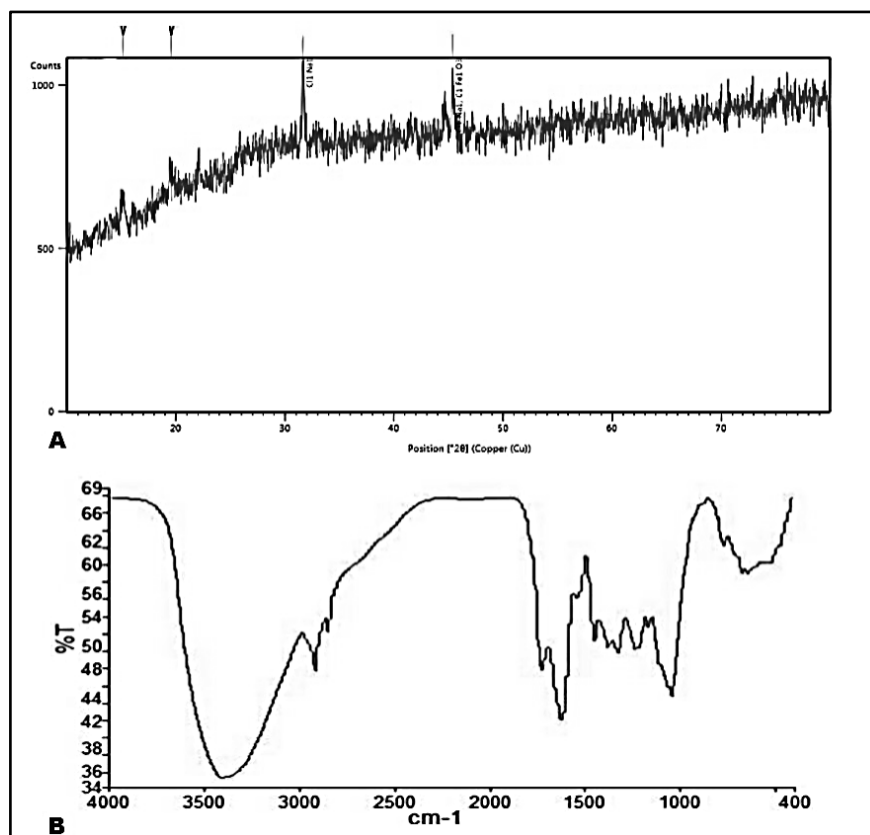
Fig. 5. A- XRD pattern of the iron oxide nanomaterials and
B. FTIR spectrum of the iron oxide nanomaterials

Table 2 Phytochemical constituents of three varieties of Date palms

Dates varieties	Terpenoids	Flavonoids	Phenols	Saponins	Cardioglycans	Tannins	Alkaloids
Ambera	++	-	+++	-	+++	-	-
Sukhri	+++	-	++	-	-	-	-
Khudri	+++	-	++	-	-	-	-

-not detected, ++moderate quantities, +++ high quantities

3.4 Determination of the antimicrobial activity of synthesised iron oxide nanomaterials

The antimicrobial property of the synthesised iron oxide nanomaterials revealed that they have high antimicrobial activity against *Staphylococcus* when compared with the standard antibiotic, ampicillin (Table 3). In contrast, moderate antimicrobial activity was observed against *Bacillus*. Synthesised iron oxide nanomaterials have equal antimicrobial activity compared to date palm fruit extract. Moreover, results reveal that the more susceptible bacteria were *Staphylococcus* and the more resistant were *Bacillus*. The iron oxide nanomaterials were naturally stabilised and has more surface area that could be used for various applications.

Table 3. Turbidity readings are taken at 600nm (*Staphylococcus* sp. and *Bacillus* sp.)

Extracts	Growth inhibition (absorbance at 600nm)					
	Staphylococcus sp.			*Bacillus* sp.		
	100 µl	250 µl	500 µl	100 µl	250 µl	500 µl
Ambera	0.09	0.12	0.07	0.61	0.72	0.94
Sukhri	0.11	0.10	0.09	0.82	0.08	0.68
Khudri	0.15	0.16	0.13	0.84	0.69	0.90
Fe NP	0.20	0.26	0.30	0.88	0.62	0.19
+ve Control		0.18			0.93	
-ve Control		0.25			0.90	

± Values are the mean of triplicates

3.5 Determination of the anticancer activity of synthesised iron oxide nanomaterials

The iron oxide nanomaterials were assessed for anticancer activity in human cancer cell lines exclusively, adeno carcinomic alveolar basal epithelial cell line (A 549) and breast cancer cell line (MDA – MB – 231) by the MTT assay method (Senthilraja & Kathiresan, 2015).

MTT assay of the synthesised iron oxide nanomaterials effectively against the cancer cell lines (Figure 5), and the half-maximal inhibitory concentration IC$_{50}$ can be a source to determine the cytotoxicity concentration for testing the behaviour of probable drug molecule under these experimental conditions. Therefore, the iron oxide nanomaterials obtained from Ambera, Sukhri and Khudri extracts were tested for repressive activities against the human adeno carcinomic alveolar basal epithelial cell line, A 549. The test sample concentration, 400 µg/ml of iron oxide nanomaterials, was used based on the value of IC50, 491.5 µg/ml. The assay exhibited that 44% of the lung cancer cells (A 549) had been obstructed by the iron oxide nanomaterials obtained from the Sukhri variety date palm extracts. The viability was thus reduced to 56%, making the iron oxide nanomaterials from date palms a green substitute for treating malignant cancer (Figure 5). Moreover, the iron oxide nanomaterials obtained from date palm extracts were also examined for inhibitory activity against the MDA-MB-231 cell line with the sample concentration as 400 µg/ml since the IC$_{50}$ value was 290 µg/ml. The results showed that 80% of the breast cancer cells (MDA - MB – 231) were inhibited, as the viability of the iron oxide nanomaterials obtained from date palms was 20%. The results reflect that the iron oxide nanomaterials from date palms effectively against cancer cells (Figure 5). The synthesised nanomaterials, their morphology, uniform distribution without any segregation, the FTIR spectroscopy findings to demonstrate physicochemical interaction between nanomaterial and moieties, X-ray diffraction analysis for the formation of nanostructures and its crystallinity are vital for the characterisation of nanoparticles (Farah *et al.,* 2021).
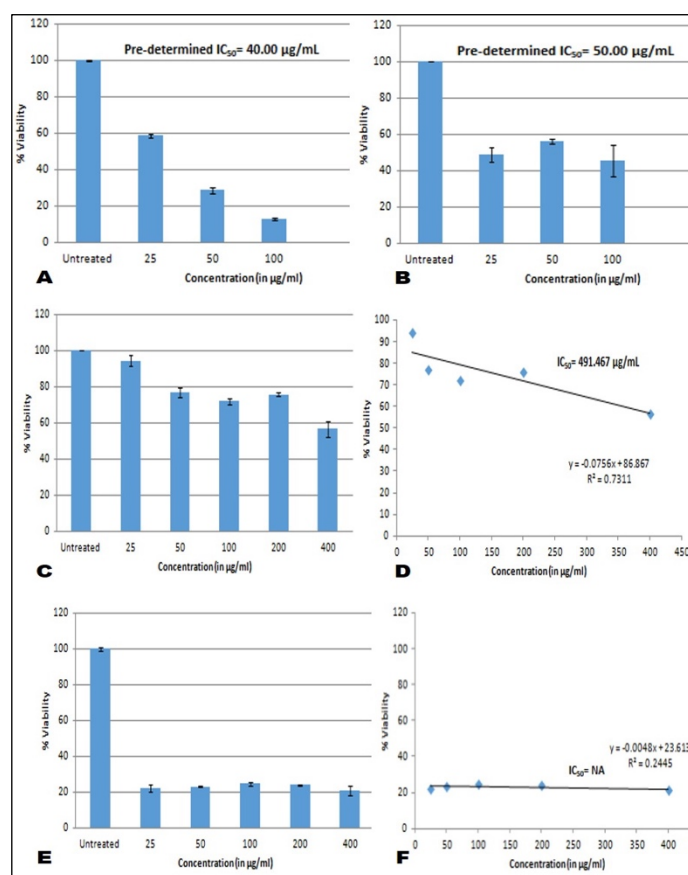
Fig. 6. MTT assay to test the anticancer effect of Fe NP and drugs on the breast (MDA MB 231) and lung cancer cell lines (A549). A. Effect of Cisplatin drug on the breast cancer cell line, B. Effect of Cisplatin drug on the lung cancer cell line, C. Effect of different concentration of Fe NP on lung cancer cell lines, D. IC$_{50}$ Concentration of Fe NP on A549, E. Effect of different concentration of Fe NP on the breast cancer cell line and F. IC$_{50}$ Concentration of Fe NP determined on the breast cancer cell line.

4.   Conclusion

Accomplished the eco-friendly synthesis method of iron oxide nanomaterials from three varieties of date palms, characterised the iron oxide nanomaterials using state-of-the-art techniques, and determined the sizes. The phytochemicals present in the extract of date palm fruits have served as capping and reducing agents and have stabilised the iron oxide nanomaterials. The iron oxide nanomaterials from the Sukhri date palm variety have shown substantial antibacterial and anticancer activity against human pathogens, *Bacillus* sp. and lung cancer cell lines (A 549). The yield of iron oxide nanomaterials obtained by the green synthesis method would be the most reasonable approach due to its nontoxic and eco-friendly nature. The major outcomes of the present study would form a basis for future research in iron oxide nanomaterials synthesis from dates and its therapeutic application studies.

References

Al-orf, S.M., Ahmed, M.H.M., Atwai, N.A., Al-Zaidi, H., Dchwah, A., Dchwah, S., *et al.* (2012) Review: Nutritional properties and benefits of the Date fruits (*Phoenix dactylifera* L.). Bulletin of National Nutritional Institution. The Arab Republic. Egypt. 97-129

Asiabani, N., Nabiyouni, G., Khaghani, S. & Ghanbari, D. (2017) Green synthesis of magnetic and photo-catalyst PbFe12O19-PbS nanocomposites by lemon extract: nano-sphere PbFe12O19 and star-like PbS. Journal of Materials Science and Materials Electronics, 28: 1101-1114. https://doi.org/10.1007/s10854-016-5635-6

Bouhlali, E., Dinc, T., Ramchoun, M., Alem, C., Ghafoor, K., Ennassir, J *et al.*, (2015) Functional composition and antioxidant activities of eight Moroccan date fruit varieties (*Phoenix dactylifera* L.). Journal of Saudi Society for Agricultural Sciences, 16: 257-264. https://doi.org/10.1016/j.jssas.2015.08.005

Breck, W. M. (2016) Nanotechnology. CBS Publishers and Distributors Pvt. Ltd., New Delhi**.** 2: 35

Das, Amlan Kumar, Avinash Marwal & Ruchi Verma. (2014) *Daturainoxia* leaf extract mediated one-step green synthesis and characterisation of magnetite (Fe_3O_4) nanoparticles. Research and Reviews: Journal of Pharmacy and Nanotechnology, 2(2). 21-24. https://doi.org/10.5923/j.nn.20120206.09

Das, R. K & Brar, S. K. (2013) Plant mediated green synthesis: modified approaches. Nanoscale, 5: 10155. https://doi.org/10.1039/c3nr02548a

Dash, S. S., Sikder, A. K., Bag, B. G &Bandyopadhyay, S. (2013) *Phoenix dactylifera* (Date palm) seed extract mediated green synthesis of gold nanoparticles and its application as a catalyst for the reduction of 4-nitrophenol to 4-aminophenol. International Journal of Nanomaterials and Biostructures, 3: 42-46

David, L., Moldovan, B., Vulcu, A., Olcnic, L., Perde-Schrepler, M., Fischer-Fodor, *et al.*, (2014) Green synthesis, characterisation and anti-inflammatory activity of silver nanoparticles using European black elderberry fruits extract. Colloids Surf. B Biointerfaces, 122: 767-777 https://doi.org/10.1016/j.colsurfb.2014.08.018

Farah Kanwal, Aisha Batool, Muniba Aslam, Fatima Aziz. (2021) Synthesis of coral-like silver chloride-polypyrrole nanocomposites derived from silver nanoparticles and studying their

structural, thermal, optical and electrical properties. Kuwait Journal of Science. 48 (**4**): 1-11. https://doi.org/10.48129/kjs.v48i4.9757

Gao, J., Liang, G., Zhang, B., Kuang, Y., Zhang, X & Xu, B. (2007) FePt@CoS2yolk-shell nanocrystals as a potent agent to kill HeLa cells. Journal of American Chemical Society, 129:1428-1433. https://doi.org/10.1021/ja067785c

Ghorbanpour, M. (2015) Major essential oil constituents, total phenolics and flavonoid content and antioxidant activity of *Salvia officinalis* plant in response to nano-titanium dioxide. Indian Journal of Plant Physiology, 20: 249-256. https://doi.org/10.1007/s40502-015-0170-7

Jahja Kokaj, Ali Shuaib, Yacoub Makdisi, Remya Nair & Joseph Mathew. (2018) Femtosecond laser-based deposition of nanoparticles on a thin film and its characterisation, Kuwait Journal of Science, 45 (**4**): 37 – 45.

Kajani, A. A., Bordbar, A. K., ZarkeshEsfahani, S. H &Razmjou, A. (2016) Gold nanoparticles as a potent anticancer agent: green synthesis, characterisation and in vitro study. RSC Advances, 6: 63973-63983. https://doi.org/10.1039/C6RA09050H

Karthik, R., Govindasamy, M., Chen, S.M., Mani, V., Lou, B.S., Devasenathipathy, R. *et al.*, (2016) Green synthesised gold nanoparticles decorated with graphene oxide for sensitive determination of chloramphenicol in milk, powdered milk, honey and eye drops. Journal of Colloid Interface Science, 475: 46-56 https://doi.org/10.1016/j.jcis.2016.04.044

Lebaschi, S., Hekmati, M & Veisi, H. (2017) Green synthesis of palladium nanoparticles mediated by black tea leaves (*Camellia sinensis*) extract: Catalytic activity in the reduction of 4-nitrophenol and Suzuki-Miyaura coupling reaction under ligand-free co. Journal of Colloid Interface Science, 485: 223-231. https://doi.org/10.1016/j.jcis.2016.09.027

Li Shikuo. (2007) Green synthesis of silver nanoparticles using *Capsicum annuum* L. Extract. Green Chemistry, 9 (**8**): 852-858. https://doi.org/10.1039/b615357g

Mahdavi, M., Namvar, F., Ahmad, M & Mohamad, R. (2013) Green biosynthesis and characterisation of magnetic iron oxide (Fe_3O_4) particles using seaweed (*Sargassum muticum*) aqueous extract. Molecules, 18: 5954-5964. https://doi.org/10.3390/molecules18055954

Muthu, K & Priya, S. (2017) Green synthesis, characterisation and catalytic activity of silver nanoparticles using *Cassia auriculata* flower extract separated fraction. Spectrochim. Acta – Part A Molecular and Biomolecular Spectroscopy, 179: 66-72. https://doi.org/10.1016/j.saa.2017.02.024

Nadagouda Mallikarjuna, N & Rajender S. Varma. (2008) Green synthesis of silver and palladium nanoparticles at room temperature using coffee and tea extract. Green chemistry, 10(**8**), 859-862.

Oladipo, I.C., Lateef, A., Azeez, M.A., Asafa, T.B., Yekeen, T.A., Akinboro, A., *et al.*, **(2017)** Recent advances in plant-mediated engineered gold nanoparticles and their application in a biological system. Journal of Trace Elements and Medical Biology, 40:10-23. https://doi.org/10.1016/j.jtemb.2016.11.012

Pansare, A.V., Kulal, D.K., Shedge, A.A & Patil, V.R. (2016) Green synthesis of anticancerous honeycomb Pt NPs clusters: their alteration effect on BSA andHsDNA using fluorescence probe. Journal of Photochemistry and Photobiology. B Biology, 162: 473-485. https://doi.org/10.1016/j.

Pattanayak Monalisa & Nayak, P.L. (2013) Green synthesis and characterisation of zero-valent iron nanoparticles from the leaf extract of *Azadirachta Indica* (Neem). World, 2(**1**), 06-09.

Philip Daizy. (2010) Green synthesises gold and silver nanoparticles using *Hibiscus rosa Sinensis*. Physica E: Low-dimensional Systems and Nanostructures, 42(**5**): 1417-1424

Rajan, A., Rajan, A.R & Philip, D. (2017) *Elettariacardamomum* seed-mediated rapid synthesis of gold nanoparticles and its biological activities. Open Nanotechnology, 2: 1-8. https://doi.org/10.1016/j.onano.2016.11.002

Ramya, M & Sylvia Subapriya, M. (2012) Green synthesis of silver nanoparticles. International Journal of Pharmacy, Medicine and Biological Sciences, 1(**1**): 54 – 61.

Raveendran Poovathinthodiyil, Jie Fu & Scott F. Wallen. (2003) Completely green synthesis and stabilisation of metal nanoparticles. Journal of American Chemical Society, 125 (**46**): 13940-13941. https://doi.org/10.1021/ja029267j

Rivera-Rangel, R.D., Gonzalez-Munoz, M.P., Avila Rodriguez, M., Razo Lazcano, T.A & Solans, C.A. (2018) Green synthesis of silver nanoparticles in oil-in-water microemulsions and nano-emulsions using *Geranium* leaf aqueous extract as a reducing agent. Colloids Surface. A. Physicochemical and Engineering Aspects, 536: 60-67. https://doi.org/10.1016/j.colsurfa.2017.07.051

Saafi, E.B., Louedi, M., Elfcki, A., Zakhama, A., Najjar, M.F., Hammami, M. *et al.*, **(2011)** Protective effect of Date palm fruit extract *(Phoenix dactylifera* L.) on dimethoate induced-

oxidative stress in rat liver. Experiments in Toxicology and Pathology, 63: 433-441. https://doi.org/10.1016/j.ctp.2010.03.002

Senthil, M & Ramesh, C. (2012) Biogenic synthesis of Fe₃O₄ nanoparticles using *Tridaxprocumbens* leaf extract & its antibacterial activity on *Pseudomonas aeruginosa*. Digest Journal of Nanomaterials and Biostructures, 7(**4**): 1665 – 1660.

Senthilraja, P & Kathiresan, K. (2015) In vitro cytotoxicity MTT assay in Vero HepG2 and MCF-7 cell lines study of marine yeast. Journal of Applied Pharmaceutical Sciences, 5: 80-84. https://doi.org/10.7324/JAPS.2015.50313

Song, J.Y., Kwon, E.Y & Kim, B.S. (2010) Biological synthesis of platinum nanoparticles using Diospyros kaki leaf extract. Bioprocess and biosystems Engineering, 33: 159-164. https://doi.org/10.1007/s00449-009-0373-2

Sudhama, V. N. & M. Ramakrishnan. (2019) phytochemical extractions, qualitative analysis, and evaluation of antimicrobial activity in the leaf and stem bark of Solanumpubescenswilld, Asian Journal of Pharmaceutical and Clinical Research, 12(**3**): 280-284.

Sudhama, V. N. & M. Ramakrishnan. (2020) Cytotoxicity studies of an ethnobotanically selected Solanumpubescenswilld. Against selected human cancer cell lines, International Journal of Pharmacy and Pharmaceutical Sciences 12(**1**): 31-35.

Yadav, R.S., Kuritka, I., Vilcakova, J., Urbanck, P., Machovsky, M., Masar, M. *et al.,* **(2017)** Structural, magnetic, optical, dielectric, electrical and modulus spectroscopic characteristics of ZnFe₂O₄-spinel ferrite nanoparticles synthesised via honey-mediated sol-gel combustion method. Journal of Physical Chemistry and Solids, 110: 87-99. https://doi.org/10.1016/j.jpcs.2017.05.029

Effect of *Trianthema triquetra* Rottl. ex Willed (Aizoaceae) on ethanol-induced gastric ulcers in experimental rats and assessment of various ulcer parameters

Hira Ijaz[1], Saiqa Ishtiaq[1, *], Faryal Rubab[1], Ans Munir[1], M. Sajid-ur-Rehman[1]

*[1]Punjab University College of Pharmacy, University of the Punjab,
Lahore-54000, Punjab, Pakistan
Corresponding author: saiqa.pharmacy@pu.edu.pk

Abstract

Trianthema triquetra Rottl. Ex. Willed (*T. triquetra*) is a medicinal plant that belongs to the family Aizoaceae. The plant has traditionally been used as fodder, a remedy for chronic ulcers, fever, and healing wounds**.** Therefore, the present study was intended to investigate the antiulcer ability of different fractions of *T. triquetra* to verify its folklore use in ulcer cure. Acute oral toxicity of all the fractions of *T. triquetra* was evaluated at 2 g/kg b.wt. The antiulcer potential of n-butanol (TTB), chloroform (TTC), ethyl acetate (TTEA), and aqueous (TTA) fraction of crude methanolic extract of *T. triquetra* was assessed by using ethanol-induced gastric ulcer model in rats. Omeprazole was used as the standard drug at a dose of 20 mg/kg b.wt. After 1 hour of administration of all the fractions of *T. triquetra*, at a dosage of 300 mg/kg b.wt. the gastric ulcer was induced in all animals by administering absolute ethanol (1mL/animal) orally except regular control group. After an hour, all the rats were sacrificed. Ulcer index, % age of ulcer inhibition, gastric pH, gastric volume, total acidity, gastric wall protein, gastric wall mucus, and histopathology of the stomach wall of rats were assessed. All fractions of *T. triquetra* showed a substantial decrease in ulcer index and improvement in percentage inhibition compared to the disease control group. In addition, there was a rise in gastric wall mucus content, total protein content, gastric pH, and a decrease in gastric volume and total acidity. Histopathological studies showed severe mucosal injury, leucocyte infiltration, and edema in the disease control group compared to omeprazole and plant fractions treated animal groups. The present work encourages the conventional use of *T. triquetra* to cure ulcers.

Keywords: Ethanol; gastric ulcer; NSAID's; omeprazole; *Trianthema triquetra.*

1. Introduction

Gastric ulcer (GU) and gastric hyperacidity are essential concerns for global health (Batista *et al*., 2013). These problems occur by a lack of balance between various mucosal defensive and harmful factors. The defensive factors include adequate mucous secretion and blood supply, intact mucous barrier, bicarbonate secretion, prostaglandins, phospholipids, antioxidants, and a sufficient nitric oxide level (NO). On the other hand, the harmful factors include gastric acids, ethanol, decreased blood flow to gastric mucosa, free radicals, misuse of NSAID's, and *Helicobacter pylori*. These factors contribute to gastric mucosal injury and ultimately lead to the development of gastric ulcers (Al-Rejai *et al*., 2012). The avoidance and cure of GU have become a global challenge. Antiulcer

medications which are commercially available have numerous side effects. The typical side effects of proton pump inhibitors (e.g., omeprazole) are diarrhea, nausea, stomach cramping, and constipation. H_2-receptor antagonists (e.g., cimetidine) can also have side effects such as galactorrhea and gynecomastia in females and males, respectively (Feldman & Burton, 1990). The shortfalls of current medicinal agents, their adverse effects, and their interactions with other drugs encourage the researchers to identify new therapeutic agents capable of scavenging reactive oxygen species (ROS) and providing protection against ulcer sores (Al-Rashdi et al., 2012). Nature presents a full reservoir of remedies to treat ailments of human beings. Medicinal plants or plant-derived products have been utilized for treatments and ailments of different diseases throughout the globe (Al-Naqeeb et al., 2003). Plants have medicinal value because of certain chemical compounds that have a specific physiological impact on the human body (Korcan et al., 2009). The therapeutic use of medicinal plants is increasing daily because of their lesser side effects and efficacy against antibiotic-resistant microorganisms (Samy et al., 1998). Genus "*Trianthema*" belongs to Aizoaceae, the ice plant family. This genus comprises 20 species, but only a few have been phytochemically reported (Geethalakshmi et al., 2010).

T. triquetra has been used traditionally as fodder for goats and cattle as a remedy for chronic ulcers, fever, and healing wounds (Wariss et al., 2014). Moreover, plant polyphenols have provided health benefits in several studies (Pandey et al., 2009). Preliminary phytochemical analysis of ethanolic root extract of *T. triquetra* has demonstrated the existence of multiple naturally occurring plant secondary metabolites such as saponins, tannins, alkaloids, flavonoids, phytosterols, and glycosides (Ghori & Humaira, 2016). The existence of various secondary metabolites can be responsible for the plant's gastroprotective impact. Hence, this study has been designed to confirm the traditional use of *T. triquetra* to cure GU disease.

2. Materials and methods

2.1 Plant material

The whole plant of *T. triquetra* was collected in July 2017 from Bahawalpur, Punjab, Pakistan. Expert plant taxonomist Dr. Zaheer-ud-din Khan at the Department of Botany, GC University, Lahore, Pakistan, authenticated the plant and issued voucher number GC.Herb.Bot.3445 (Salma & Saffan, 2003).

2.2 Drugs and chemicals

Omeprazole was kindly provided by Zafa Pharmaceuticals Laboratories Pvt. Ltd. Bovine Serum Albumin (BSA) was acquired from Bioshop (Canada). All other chemicals used in this study were of analytical grade and were obtained from Sigma-Aldrich (Germany).

2.3 Preparation of plant extract and its fractions

The collected plant material was washed with distilled water, shade dried, and pulverized using a mechanical mill. The plant powder (500 g) was subjected to maceration using methanol (2.5L) as solvent. After seven days, the extract was filtered through Whatman filter paper to get the filtrate.

The filtrate was then concentrated in a rotary evaporator at 40 ºC and dried in the oven. The dried crude methanolic extract (71.88 g) was then subjected to fractionation and partitioned with chloroform (250 mL), ethyl acetate (250 mL), n-butanol (250 mL), and water (250 mL). The different fractions of *T. triquetra*, such as n-butanol (TTB), chloroform (TTC), ethyl acetate (TTEA), and water (TTA), were dried and stored in the refrigerator.

2.4 Experimental animals

Male and female albino rats weighing (190-210 g) were utilized in the experiment. Animals were housed at room temperature of 22±2 °C, 12 hours of light and dark intervals, and 45-55% relative humidity (Liu *et al.,* 2018). The animals were randomly divided into seven groups containing six rats in different cages and acclimatized for one week under standard environmental conditions with food and water *ad libitum*. Food was withdrawn 24 hours before the experiment; however, rats had free access to water for about 2 hours before the commencement of the experiment (Okonkon *et al*., 2009). The assay was conducted with the permission of the Bio-Ethical Committee from the Department of Zoology, University of the Punjab, Lahore, Pakistan (Ethic No. 1593).

 2.5 Acute toxicity studies

Acute oral toxicity was conducted to determine the safe dose of different fractions of *T. triquetra*. Rats were randomly divided into 5 groups, and group 1 was orally administered with a vehicle (Distilled water, 5 mL/kg b.wt.). Group 2-5 was administered with plant fractions, TTC (2 g/kg b.wt.), TTB (2 g/kg b.wt.), TTEA (2 g/kg b.wt.), TTA (2 g/kg b.wt.) respectively. Rats were deprived of food for 24 hours before and 4 hours after. Animals were continuously observed for 4 hours after dosing for any behavioral or clinical abnormality. Mortality was recorded if any. The administered rats were followed up for 14 days. On the 15th day, blood samples were taken, and animals were sacrificed. The liver and kidney were taken for histopathological analysis (Goncalves *et al*., 2015).

2.6 Ethanol-induced acute gastric ulcer model

Group I (Normal group): Normal control group received distilled water (5 mL/kg b.wt.) orally (Al-harbi *et al*., 1994).

Group II (Negative control group): Negative or disease control group was orally given a vehicle (Distilled water, 5 mL/kg b.wt.).

Group III (Positive control group): The positive control group received an oral dose (20 mg/kg b.wt.) of omeprazole (Al-Wajeeh *et al*., 2016).

Group IV: TTC fraction was administered orally at 300 mg/kg b.wt.

Group V: TTB fraction was administered orally at a dose of 300 mg/kg b.wt.

Group VI: TTEA fraction was administered orally at a dose of 300 mg/kg b.wt.

Group VII: TTA fraction was administered orally at a dose of 300 mg/kg b.wt.

After 1 hour of the above treatment, absolute ethanol (1mL/animal) was orally administered to animals of all groups except the normal group (Madhuri *et al*., 2018). All animals were euthanized 1 hour after an overdose of xylazine and ketamine anesthetic drugs (Tayeby *et al*., 2017).

The stomach was isolated, and gastric contents were collected in centrifuge tubes. Then, the abdomen was opened with an incision along the broader curvature, washed with ice-cold normal saline, and placed on a soft white board for ulcer scoring (Abdulla *et al*., 2010).

2.6.1 Macroscopic and microscopic evaluation

The excised stomach tissues were observed under a magnifying glass and dissecting microscope to count lesions on the inner side of the stomachs (Dashputure & Naikwade, 2011).

2.6.2 Ulcer score

Ulcer Scores were assigned based on the severity of ulcers as follows:

No ulcer (0), Reddish mucosa (0.5), red spots (1), Hemorrhagic streak (1.5), Deep ulcer (2), and Perforations (3) (Khan *et al*., 2011).

2.6.3 Ulcer index (UI)

Ul was calculated using the following formula:

Ulcer index = (UN+US+UP) ×10^{-1}

UN=Average number of ulcers per animal

US=Average of severity score

UP=Percentage of animals with ulcer

2.6.4 Percentage of ulcer inhibition (PI)

The percentage formula determined the extent of the protection from ulcers (Njar *et al*., 1995).

$$\% \, Protection = \frac{UI(disease \, control) - UI(\, treated)}{UI(disease \, control)}$$

2.6.5 Determination of gastric juice volume, pH, and total acidity

Drained the gastric contents in falcon tubes (10 mL) followed by centrifugation for 10 minutes at 3000 rpm. The volume and pH of the supernatant were measured (Nwinyi & Kwanashie, 2013). Transparent supernatant (1mL) was titrated against freshly prepared 0.1N Sodium hydroxide (NaOH). Phenolphthalein was used as an indicator, and the endpoint was colorless to light pink. Total acidity was measured using the equation below (Dahputure & Naikwade, 2011).

$$Acidity = \frac{volume \, of \, NaOH \times normality \, of \, NaOH}{0.1} \times 100$$

Results were expressed in terms of the clinical units (mEq/L)

2.6.6 Determination of gastric wall protein

The total Protein content of glandular tissue homogenate was calculated by the Lowry *et al.* method (Lowry *et al.*, 1951).

2.6.7 Determination of gastric mucus content

Glandular segments from the stomachs were excised and weighed. These portions were soaked in 0.1% alcian blue dye (in 0.16 M sucrose buffered with 0.05 M sodium acetate adjusted to a pH=5). Excess dye was drained with 0.25 M sucrose solution by rinsing for 15 and 45 minutes. The dye complex with gastric wall mucus was extracted with 10 mL of 0.5 M magnesium chloride for 2 hours with consecutive shaking for 1 minute after 30 minutes intervals. 4 mL of this solution was shaken with an equal volume of diethyl ether. The resulting emulsion was centrifuged at 3000 rpm, and the absorbance of the aqueous layer was measured at 580 nm (Al-Batran *et al.,* 2013).

2.6.8 Histopathological evaluation

Samples of the gastric wall of rats of all groups were placed in a 10 % formalin solution. They were subsequently processed and firmly inserted into paraffin. Different portions of the stomach were sliced through microtome at a thickness of 5 μm. Staining has been achieved by eosin and hematoxylin. The slides were examined and photographed under a microscope (Al-Wajeeh *et al.*, 2017).

3. Statistical analysis

The results were statistically evaluated using one way analysis of variance (ANOVA) followed by Dunnet's test. All results have been presented as Mean ± SEM.

4. Results

Results of the current studies indicate that the Ulcer Index (UI) (Table 1**)** in the disease control group was (12.48), which is an indication of an ulcer. In contrast, the UI of the omeprazole-treated animal group was significantly reduced (5.13) and in the animal groups treated with fractions of *T. triquetra* as compared to the disease control group, which is a clear indication of antiulcer activity of *T. triquetra*. The UI of TTB, TTEA, TTC and TTA fractions are (7.22, 9.23, 10.95, and 11.28), respectively. The mean PI (Table 1**)** of the omeprazole treated group is 58.88%, whereas the mean PI of TTB, TTEA, TTC, and TTA is 42.20%, 26.04 %, 12.28%, and 9.61%, respectively. TTB has shown a maximum PI that is comparable with the standard drug omeprazole. It was observed that all four fractions of *T. triquetra* had raised the stomach pH and reduced gastric content volume (Table 2**)** compared to the disease control animal group. The gastric volume in the normal control group is 1.45±0.13 mL, and its pH is 3.6±0.06. The gastric volume in the disease control group is 10.88±0.33 mL, and the pH is 2.53±0.04. In the omeprazole-treated animal group, gastric volume and raised pH were reduced with p<0.001. Similar results have been observed in test samples of *T. triquetra*, in which TTB has shown a maximum decrease in gastric volume of 3.98±0.11 mL and increased pH of 5.62±0.04 among all the fractions of *T. triquetra*. Whereas TTEA has a gastric volume of 5.23±0.09 mL and pH is 5.1±0.06, TTC with 5.17±0.05 mL and pH

of 5.02±0.05 and gastric volume of TTA was 5.92±0.06 mL with pH 4.53±0.06. The total gastric acidity (Table 2) of disease control and omeprazole-treated groups was 94.5±3.28 mEq/L and 33 mEq/L, respectively. Similarly, all the fractions of *T. triquetra* reduced the stomach acidity compared to the disease control group. Values of gastric acidity of TTB, TTEA, TTC, and TTA were 41.67±4.94 mEq/L, 50±6.55 mEq/L, 51.5±7.94 mEq/L, and 56.5±7.63 mEq/L respectively and are mentioned in (Table 2). Total protein content in the disease control group was 281.83±15.30 µg/mL, whereas a significant increase in protein content was observed in omeprazole treated animal group, e.g., 450.25±54.48 µg/mL ($p<0.01$). At the same time, a substantial increase in gastric protein content (Table 3) in TTB was observed with 441.17±35.94 µg/mL ($p<0.01$) and TTEA with 431.58±28.81 µg/mL ($p<0.05$) has been observed. But in the case of TTC and TTA treated animal groups, a non-significant increase in protein content has been observed, e.g., 344.667±45.13 µg/mL and 341.42±5.31 µg/mL, respectively. The gastric wall mucus content (Table 3) in the normal group was 189.584 ±5.50 µg/g of glandular tissue ($p<0.05$), and in the disease control group, 114.92±12.64 µg/g of glandular tissue was determined. A non-significant increase in gastric mucus content has been observed in all *T. Triquetra* fractions treated animal groups. TTB, TTEA, TTC, and TTA have gastric mucus content values as follows; 172.67±30.91 µg/g of glandular tissue, 141.92±25.02 µg/g of glandular tissue, 136 ±9.44 µg/g of glandular tissue and 130.417±14.65 µg/g of glandular tissue respectively. In an acute oral toxicity study, oral administration of the plant's fractions (2g/kg b.wt.) treated rats showed no mortality or signs of toxicity during 14 days study period. Results of biochemical parameters (Bilirubin, SGPT, SGOT & ALT) of liver function and (Urea and Creatinine) of kidney function used in acute oral toxicity studies showed non-significant changes between the normal control and plant fractions treated rats (Table 4). Moreover, the vital organs of plant fractions treated rats, such as kidneys and liver, revealed no altered histology and signs of toxicity (Figure 3). Sheets of connective tissue divide the liver into small units called lobules. A lobule is hexagonal, with portal triads and a central vein. Normal histological structure of the central vein and surrounding hepatocytes was present. No fatty changes, necrosis, or necrobiosis were seen. Average-sized kidney and cellularity of glomeruli, normal tubules, endothelial lined vessel, and interstitium were present. No basement membrane thickening, deposits, necrosis, thrombosis, edema, and inflammatory changes were seen.

Table 1. Effect of *T.triquetra* fractions on gastric ulcer in experimental rats

Sr.	Groups	Ulcer number	Ulcer score	Incidence of ulcer (%)	Ulcer index (UI)	% Inhibition (PI)
1	Normal	0***	0***	0	0	-
2	Diseased	20.67±2.76	4.17±0.97	100	12.4833	0
3	Omeprazole	0.83±0.40***	0.5±0.26***	50	5.13333	58.8785
4	TTB	4±1.48***	1.5±0.48**	66.66	7.216	42.1949
5	TTEA	7±1.97***	2±0.68*	83.33	9.233	26.0374
6	TTC	8±0.52***	1.5±0.13**	100	10.95	12.283
7	TTA	10.67±0.84***	2.167±0.25*	100	11.2833	9.61282

All values are written as Mean±SEM. Significant at $p<0.05$*, $p<0.01$**, $p<0.001$***, ns=non-significant with respect to disease control group
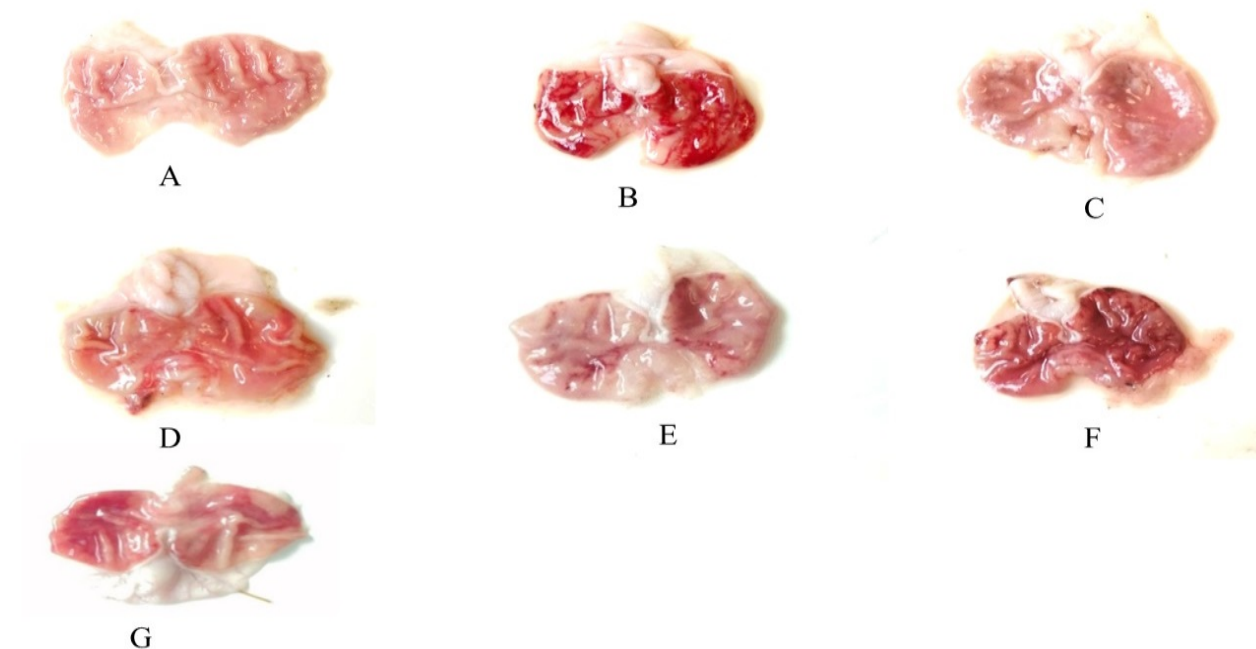
Table 2. Effect of *T.triquetra* fractions on gastric juice parameters

Sr.	Groups	Gastric volume (mL)	Gastric pH	Total acidity (mEq/L)
1	Normal	1.45±0.13***	3.6±0.06***	25±2.28***
2	Diseased	10.88±0.33	2.53±0.04	94.5±3.28
3	Omeprazole	2.417±0.09***	6.083±0.04***	33±2.577**
4	TTB	3.983±0.11***	5.617±0.04***	41.67±4.94***
5	TTEA	5.233±0.09***	5.1±0.06***	50±6.55***
6	TTC	5.167±0.05***	5.017±0.05***	51.5±7.94***
7	TTA	5.917±0.06***	4.533±0.06***	56.5±7.63***

All values are written as Mean±SEM. Significant at p<0.05*, p<0.01**, p<0.001***, ns=non-significant with respect to disease control group

Table 3. Effect of *T.triquetra* fractions on gastric wall protein and mucus content

Sr.	Groups	Protein content(μg/mL)	Mucus content (μg of alcian blue/g wet tissue)
1	Normal	474.67±17.80**	189.58±5.50*
2	Diseased	281.83±15.30	114.92±12.64
3	Omeprazole	450.25±54.48**	177.58±14.62[ns]
4	TTB	441.17±35.94**	172.67±30.91[ns]
5	TTEA	431.58±28.81*	141.92±25.02[ns]
6	TTC	344.67±45.13[ns]	136±9.44[ns]
7	TTA	341.92±5.21[ns]	130.417±14.65[ns]

All values are written as Mean ± SEM. Significant at p<0.05*, p<0.01**, p<0.001***, ns= non - significant with respect to disease control

Table 4. Effect of *T. triquetra* fractions on biochemical parameters in the acute oral toxicity study

		Biochemical Parameters					
Sr	Groups	Urea (mg/dl)	Creatinine (mg/dl)	Bilirubin (mg/dl)	SGPT (U/L)	SGOT (U/L)	ALP (U/L)
1	Normal	19.5±1.41	0.78±0.06	0.65±0.05	100.83±5.54	111.33±8.05	159±7.33
2	TTB	20.5±1.26[ns]	0.79±0.05[ns]	0.65±0.06[ns]	102.5±6.29[ns]	113±5.42[ns]	165.5±9.5[ns]
3	TTEA	21±0.97[ns]	0.75±0.05[ns]	0.64±0.07[ns]	108.33±9.46[ns]	116.33±8.59[ns]	163±10.05[ns]
4	TTC	19.67±1.23[ns]	0.80±0.05[ns]	0.61±0.05[ns]	110.83±8.60[ns]	114.67±7.80[ns]	161.83±7.94[ns]
5	TTA	18.67±1.02[ns]	0.75±0.04[ns]	0.63±0.06[ns]	105±8.47[ns]	119.67±4.05[ns]	158±10.54[ns]

All values are written as Mean ± SEM. Significant at p<0.05*, p<0.01**, p<0.001***, ns= non - significant with respect to normal control group

Fig. 1. Effect of *T.triquetra* fractions on the macroscopic appearance of the gastric mucosa in ethanol-induced gastric ulcer model in rats. (A) Normal control group, (B) Disease control group, (C) Omeprazole/Standard control group, and (D-G) were given *T.triquetra* fractions such as TTB, TTEA, TTC, and TTA, respectively
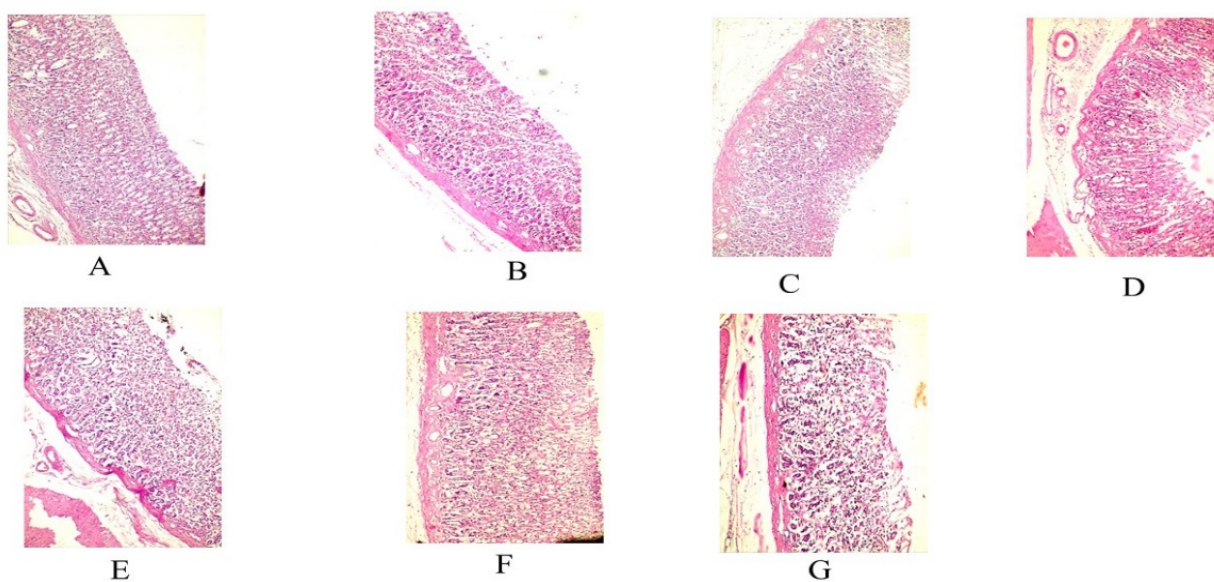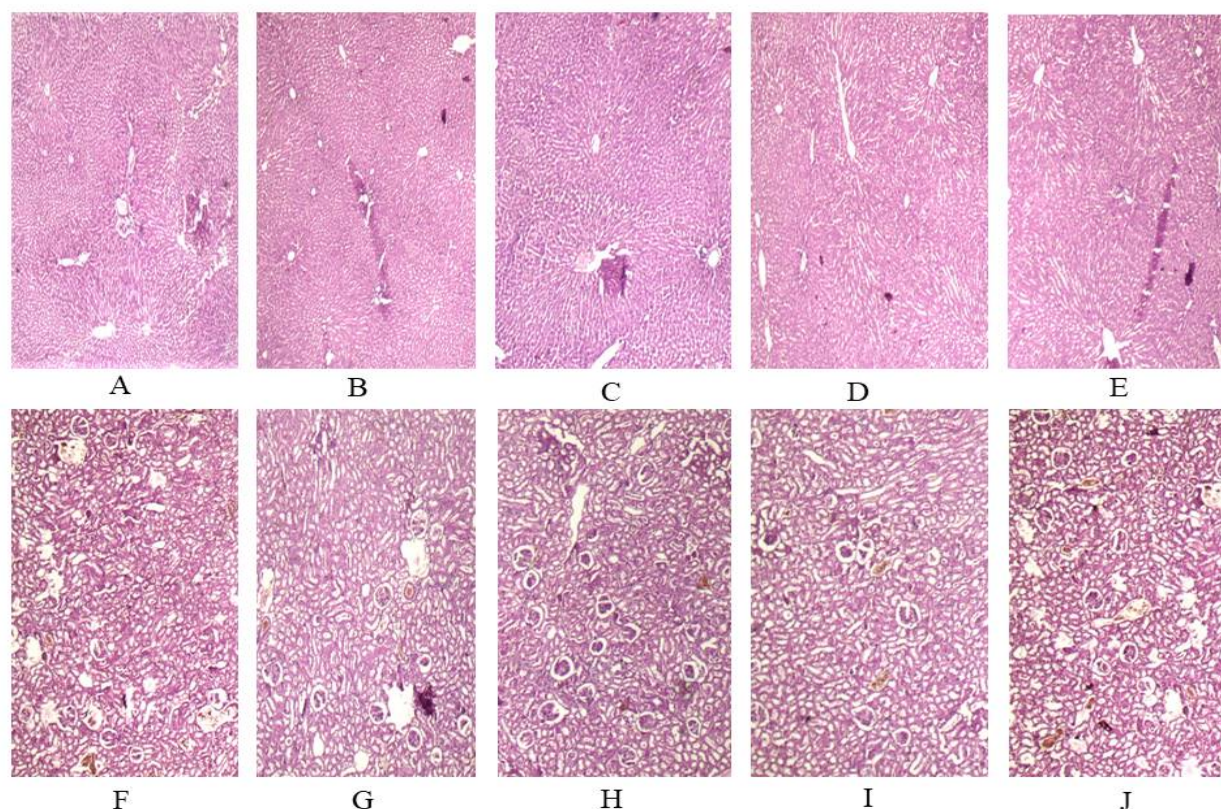

Fig. 2. Effect of *T.triquetra* fractions on the histology of stomach of rats in ethanol-induced gastric ulcer model. (A) Normal control group, (B) Disease control group, (C) Omeprazole/Standard control group, and (D-G) were given *T.triquetra* fractions such as TTB, TTEA, TTC, and TTA, respectively

Fig. 3. Histopathology of the liver (A, B, C, D, E) and Kidney (F, G, H, I, J) of normal control and *T. triquetra* fractions treated rats in acute toxicity study for 14 days. A and F: normal control; B and G: TTC 2g/kg b.wt; C and H: TTB 2g/kg b.wt; D and I: TTEA 2g/kg b.wt; E and J: TTA 2g/kg b.wt

5. Discussion

An acute oral toxicity study was carried out on different fractions of *T. triquetra* at 2 g/kg b.wt. After 15 days of administration of plant fractions, all animals were found healthy and alive. No significant differences in kidney and liver function biochemical parameters between normal, and plant fractions treated groups. No histological changes in the liver and kidney of the treated rats were observed. So it may be concluded that all the fractions of *T. triquetra* have a lethal dose LD_{50} above 2 g/kg b.wt. Thus the present dose regimen (300 mg/kg b.wt.) was chosen for the current study. *T. triquetra* has traditionally been used in treating chronic ulcers (Ketuly *et al*., 2011). Recent research has been conducted to evaluate the antiulcer potential of different fractions of *T. triquetra* using an ethanol-induced ulcer model in rats. Ethanol damages the gastric mucosa and results in gastric hemorrhage and tissue necrosis. Alcohol penetrates speedily into the mucus secretion lining of the stomach. It induces damage to the plasma membrane leading to cell death due to the increased accessibility of sodium and water into the intracellular membrane (Gupta *et al*., 2012). These effects are due to the lipid peroxidation and generation of free radicals before cell injury and death (Sannomiya *et al*., 2005). Omeprazole is used to cure disorders related to gastric acidity and protects against mucosal damage. Omeprazole specifically binds and inactivates

the enzyme H^+, K^+- ATPase (Ode & Asuzu, 2011). It is a proven fact that stomach acid secretions have an essential role in GU (Dokmeci *et al.,* 2005). All fractions of *T. triquetra* induced a substantial increase in pH of the stomach and decreased the volume of gastric content and gastric acidity compared to the disease control group indicating an antisecretory mechanism that can be a result of blockade of the H^+, K^+- ATPase enzyme (Bhajoni *et al*., 2016). Moreover, UI and PI are other parameters used for determining gastro-protective effects. All the fractions of *T. triquetra* have shown a significant decline in the UI and improved PI compared to the disease control group. This indicates the gastroprotective effects of *T. triquetra*. The stomach histology of rats of the normal control group has shown no histological changes. No gastric lesions and intact gastric mucosa were observed. Normal gastric glands were seen with rounded nuclei. In the disease control group, a deep ulcer was observed. Severe disruption of the surface epithelium with hyperplastic gastric glands was seen. Histological evaluation of the standard drug omeprazole treated animal group revealed mild disruption of the gastric mucosa. The histological studies of the TTB-treated animal group were similar to the common drug omeprazole-treated animal group. Histological evaluation demonstrated that in the TTB-treated animal group's case, optimum gastric mucosa safety was observed with moderate mucosal epithelium disruption with normal lamina propria. The histological studies of other groups had shown less destruction of gastric mucosa relative to the disease control group. No severe ulcer has been found, and shallow, superficial erosions accompanied by mild leucocyte infiltration and edema in the lamina propria were seen (Figure 2). Total protein content was also evaluated; a decline in the total protein content is a valuable tool for identifying cellular dysfunction. In our research, however, plant fraction treated groups caused an increase in protein synthesis, which was considered self-mechanism leading to a regeneration process (Sharma & Shukla, 2011). Treatment of rats with *T. triquetra* fractions has improved the quantity of mucus in the gastric mucosa suggesting that the plant has antiulcer potential. Although the exact mechanism is unknown, the gastroprotective effect might be due to the protection of the mucus in the stomach wall. Mucus consists of the mucin-type glycoproteins that can be detected by alcian blue dye (Wong *et al*., 2013). The gastroprotective effect may be due to the development of defensive complexes between *T. triquetra* fractions and mucus, serving as an obstacle to ethanol-induced damaging factors in the stomach. Past experiments have shown that the ethanolic root extract of *T. triquetra* holds ROS scavenging activity which might be responsible for its gastroprotective action (Chitra & Nithyanandhi, 2007).

6. Conclusion

The current study's findings underpin the conventional usage of *T. triquetra* as an antiulcerogenic agent. *T. triquetra* plant can be a novel drug candidate for the cure of ulcers. The TTB fraction of *T. triquetra* has shown the most prominent antiulcer activity among all the other fractions of the plant. Previous studies reported that the plant contains alkaloids, flavonoids, phytosterols, tannins, glycosides, and saponins. The presence of antioxidants like phenols, flavonoids, and tannins may also contribute to ulcer cure. Further experiments are advised to establish the mode of action and active compounds responsible for the antiulcer potential.

References

Abdulla, M.A., Al-Bayaty, F.H., Younis, L.T. & Abu Hassan, M.I. (2010). Antiulcer activity of *Centella Asiatica* leaf extract against ethanol-induced gastric mucosal injury in rats. Journal of Medicinal Plants Research, **4**(13): 1253-1259.

Al-Batran, R., Al-Bayaty, F., Al-Obaid, M.M.J., Abdualkader, A.M., Hadi, H.A., Ali, H.M. & Abdulla, M.A. (2013). In vivo antioxidant and antiulcer activity of *Parkia spicosa* ethanolic leaf extract against an ethanol-induced gastric ulcer in rats. *PLoS. One*. **8**(5): e64751.

Al-harbi, M.M., Qureshi, S., Raza, M., Ahmed, M.M., Afzal. & Shah, A.H. (1994). Evaluation of *Caralluma tuberculata* pretreatment for the protection of rat gastric mucosa against toxic damage. Toxicology and applied pharmacology, **128**(1), 1-8.

Al-Naqeeb M.A., Thomson, M., Al-Qattan, K., Kamel, F., Mustafa, T. & Ali, M. (2003). Biochemical and histopathological toxicity of an aqueous extract of ginger in female rats. Kuwait Journal of Science and Engineering, **30**(2): 35-48.

Al-Rashdi, A.S., Salman, S.M., Alkiyami, S.S., Abdulla, M.A., Hadi, A.H.A., Abdelwahab, S.I., Taha, M.M., Hussaini, J. & Asykin, N. (2012). Mechanisms of gastroprotective effects of ethanolic leaf extract of *Jasmium sambac* against HCl/Ethanol-induced gastric mucosal injury in Rats. Evidence-Based Complementary & Alternative Medicines, **2012**: 1-15.

Al-Rejaie, S.S., Abuohashish, H.M, Ahmed, M.M., Aleisa, A.M. & Alkhamees, O. (2012). Possible biochemical effects following inhibition of ethanol-induced gastric mucosa damage by *Gymnema Sylvestre* in male Wistar albino rats. Pharmaceutical Biology, **50**(12): 1542-1550.

Al-Wajeeh, N.S., Hajerezaie, M., Noor, S.M., Halabi, M.F., Al-Henhena, N., Azizan, A.H.S. & Ali, H.M. (2016). The gastroprotective effects of *Cibotium barometz* hair on ethanol-induced gastric ulcer in Sprague-Dawley rats. BMC Veterinary Research, **13(**1): 1-12.

Al-Wajeeh, N.S., Hajrezaie, M., Al-Henhena, N., Kamran, S., Bagheri., E., Zahedifard, M., Saremi, K., Noor, S.M., Ali, H.M. & Abdulla, M.A. (2017). The antiulcer effect of *Cibotium barometz* leaves in rats with experimentally induced acute gastric ulcer. Drug Design, Development, and Therapy, **11**: 995-1009.

Batista, L.M., Almeida, A.N.B., Lima, G.R.M., Falcao, H.S., Ferreira, A.L., Magri, L.P., Coelho, R.G., Calvo, T.R., Vileges, W. & Brito,A.R.M.S. (2013). Gastroprotective effect of the ethanolic extract and fractions obtained from *Syngoanthus bisulcatus.* Rul. Records of Natural Products, **7**: 35-44.

Bhajoni, P.S., Meshram, G.G. & Lahkar, M. (2016). Evaluation of the antiulcer activity of the leaves of *Azadirachta indica*. An experimental study. Integrative Medicines International, **3**:10-16.

Chitra, M. & Nithyanandhi, K. (2007). Radical scavenging activity of *Trianthema triquetra* in male albino rats intoxicated with CCl$_4$. Journal of Environmental Biology, **28**(2): 283-285.

Dashputra, N.L. & Naikwade, N.S. (2011). Evaluation of Antiulcer activity of methanolic extract of *Abutilon Indicum* Linn. Leaves in experimental rats. International Journal of Pharmaceutical Sciences and Drug Research, **3**(2): 97-100.

Dokmeci, D., Akpolat, M., Aydogdu, N., Dogany, L. & Turan, F.N. (2005). L-carnitine inhibits ethanol-induced gastric mucosal injury in rats. Pharmacology Reports, **57**(4): 481-488.

Feldman, M. & Burton, M.E. (1990). H$_2$-receptor antagonists: Standard therapy for acid-peptic diseases. New England Journal of Medicine, **323**: 1672-1680.

Geetalakshami, R., Sarada, D.V.L. & Ramasamy, K. (2010). *Trianthema decandra* L: a review on its phytochemical and pharmacological profile. International Journal of Engineering Science and Technology, **2**(5): 976-979.

Ghori, S.S. & Humaira, T. (2016). Evaluation of ethanolic extract of roots of *Trianthema triquetra* for antiulcer activity in albino rats. World Journal of Pharmaceutical and Life Sciences, **2**(5): 385-392.

Goncalves, N., Lino Junior, R.d.S., Rodrigues, C.R., Rodrigues, A.R., & Cunha, L.C.d. (2015). Acute oral toxicity of *Celtis iguanaea* (Jacq.) Sargent leaf extract (Ulmaceae) in rats and mice. Revista Brasileira de Plantas Medicinais, **17**(4), 1118-1124.

Gupta, J., Kumar, D. & Gupta, A. (2012). *Cayratia trifolia* in experimental animals. Asian Pacific Journal of Tropical Diseases, **2**(2): 99-102.

Ketuly, K.A., Abdulla, M.A., Hadi, H.A., Mariod, A.A. & Abdel-Wahab, S.I. **(2011).** Antiulcer activity of the 9 alpha-Bromo analogues of Beclomethasone dipropionate against ethanol-induced gastric mucosal injury in rats. Journal of Medicinal Plant Research. **5**(4): 514-520.

Khan, M.S.A., Hussain, S.A., Jais, A.M.M., Zakaria, Z.A. & Khan, M. (2011). Antiulcer activity of *Ficus religiosa* stems bark ethanolic etract in rats. Journal of Medicinal Plant Research, **5**(3): 354-359.

Korcan, S. E., Cigerci, I.H., Dilek, M., Kargioglu, M., Cenkci, S. & Konuk, M. (2009). Antimicrobial activity of endemic species, Thermopsis turcica, Turkey. Kuwait Journal of Science and Engineering, **35**(1A): 101-112.

Liu, W., Yang, M., Chen, X., Li, L., Zhou, A., Chen, S., You, P. & Liu, Y. (2018). Mechanism of the antiulcer effect of an active ingredient group of modified Xiao Chaihu decoction. Evidence-Based Complementary and Alternative Medicines, **2018:** 1-10.

Lowry, O.H., Rosebrough, N.J., Farr, A.L. & Randall, R.J. (1951). Protein estimation by Lowry's method. Journal of Biological Chemistry. **193**: 265.

Madhuri, Y., Narendra Babu, A., Kumar, E. & Yanadaiah, P. (2018). Antiulcer activity of *Hibiscus sabdariffa* on albino rats. International Journal of Pharmaceutics, **11**(3): 13-26.

Njar, V., Adesanwo, J. & Raji, Y. (1995). Methyl Angolenate: Antiulcer agent from the stem bark of *Entandrophragma angolense*. Planta Medica, **61**: 91-91.

Nwinyi, F.C. & Kwanashie, H.O. (2013). Comparative effects of *Sorghym bicolor* leaf base extract on tissue isolated from some body systems of experimental animals. Research Journal of Medicinal Plants, **7**(41): 3041-3051.

Ode, O.J. & Asuzu, O.V. (2011). In rats, investigate *Cassia singueana* leaf extract for antiulcer effects using ethanol-induced gastric ulcer models. International Journal of Plant, Animal and Environmental Sciences, **1**(1): 1-7.

Okokon, J., Antia, B. & Umoh, E. (2009). The antiulcerogenic activity of ethanolic leaf extract of *Lasianthera Africana*. African Journal of Traditional, Complementary and Alternative Medicines, **6**(2): 150-154.

Pandey, K.B., Mishra, N. & Rizvi, S.I. (2009). Myricetin can mitigate altered redox status in type 2 diabetic erythrocytes. Kuwait Journal of Science and Engineering, **36**(2A): 115-124.

Salma, H.M.H. & Saffan, S.E.S. (2003). Triterpenoids and flavonoids from the air-dried aerial parts of Plantago amplexicaulis. Kuwait Journal of Science and Engineering, **30**(2): 109-118.

Samy, R.P., Ignacimuthu, S. & Sen, A. (1998). Screening of 34 Indian medicinal plants for antibacterial properties. Journal of Ethnopharmacology, **62**(2): 173-181.

Sannomiya, M., Fonseca, V.B., Silva, M.A., Rocha, L.R.M., Santos, L.C., Hiruma- Lima, C.A., Brito, A.R.M.S. & Vilegas, W. (2005). Flavonoids and antiulcerogenic activity from *Byrosonima crassa* leave extracts. Journal of Ethnopharmacology, **97**(1): 1-6.

Sharma, N. & Shukla, S. (2011). Hepatoprotective potential of aqueous extract of *Butea monosperma* against CCl$_4$ induced damage in rats. Experimental and Toxicologic Pathology, 63(6-7): 671-676.

Tayeby, F., Salman, A.A.A., Kamran, S., Khaing, S.L., Salehen, N.B. & Mohan, G.M.A.D. (2017). Ulcer prevention effect of 3, 4, 5, Trihydroxy-NO-[(2-Methyl-1H-Indol-3yl) Methylidene] Benzohydrazine in HCl/Ethanol-induced gastric mucosal damage in rats. International Journal of Medical Sciences, **14**(13): 1317-1326.

Wariss, H.M., Ahmad, S., Anjum, S. & Alam, K. (2014). Ethnobotanical studies of dicotyledonous plants of Lal Suhanra National Park, Bahawalpur, Pakistan. International Journal of Science and Research, **3**(6): 2452-2460.

Wong, J.Y., Abdulla, M.A., Raman, J., Phan, C.W., Kuppusamy, U.R., Golbabapour, S. & Sabaratnam, V. (**2013**). Gastroprotective effects of Lion's Mane mushroom *Hericiumerinaceus* (Bull.: Fr.) Pers. (Aphyllophoromycetideae) extract against an ethanol-induced ulcer in rats. Evidence-Based Complementary and Alternative Medicines, **2013**: 1-9.

High-performance liquid chromatography-based characterization of fengycin produced by *Bacillus amyloliquefaciens* against *Fusarium graminearum* and *Rhizoctonia solani*

Muddasir Khan[1,*], Muhammad Salman[1], Abdullah[1]

[1]*Dept. of Health and Biological Sciences, Abasyn University Peshawar,*
Khyber Pakhtunkhwa, Pakistan
* Corresponding author: mk03025678947@gmail.com

Abstract

A substantial loss of crop production worldwide is attributed to fungal phytopathogens. The most important economic pathogens among these fungal phytopathogens are *Fusarium graminearum* and *Rhizoctonia solani*, which cause a wide range of plant diseases. In the present study, *Bacillus amyloliquefaciens* secondary metabolite fengycin was identified by High-performance liquid chromatography (HPLC) and in vitro screened against the *Fusarium graminearum* and *Rhizoctonia solani.* Based on the HPLC result, fengycin was identified at 215nm wavelength, a retention time of 5-7 minutes, and a peak area of 3.914. The obtained results indicated that fengycin (1, 1/2, 1/4, and 1/8) concentrations have a significant effect ($p<0.005$) on the growth of *F. graminearum* and *R. solani*. The current study concluded that *B. amyloliquefaciens* secondary metabolites fengycin have a high potential to inhibit the growth of *F. graminearum* and *R. solani.*

Keywords: Bacillus amyloliquefaciens; biopesticides; fengycin; phytopathogens; Secondary metabolite.

1. Introduction

Bacillus species produce various volatile agents that encourage the Plant's defense mechanism. Due to its pivotal bio-control activity, most bacterial and fungal phytopathogens have been controlled via bio-agents which play a significant role in phytopathology, the antimicrobial substances produced by *Bacillus* spp. Includes; subtilin, bacilysin, mycobacillin, bacillomycin, mycosubtilin, iturin, fengycin, and surfactin, having both antifungal and antibacterial activity (Ntushelo *et al.,* 2019).

Bacillus is used as an ideal biocontrol bacterium because it produces various types of environment-friendly antimicrobial agents. *B. amyloliquefaciens*, has been recognized as a safe bacterial spp. With outstanding excellent in-plant colonization capacities (Cao *et al.,* 2011; Liu *et al.,* 2017) and have a greater ability to protect plants from pathogenic microorganisms (Ongena & Jacques, 2008). Studies revealed that *B. amyloliquefaciens* could directly suppress pathogenic entities by secondary metabolites production, including polyketides, nucleic acids, proteins produced by microbes, amino acids, and lipopeptides (Ongena & Jacques, 2008; Chen *et al.,* 2015; Yan *et al.,* 2018). Lipopeptides with lower- molecular weight are the most common antimicrobial agents (Koumoutsi *et al.,* 2004). Fengycin, surfactin, and Iturin are the 3 significant families of

cyclic peptides with unique chemical and physical characteristics (Khan *et al.,* 2021; Santoyo *et al.,* 2012; Caulier *et al.,* 2019).

Fengycin is a cyclic lipodecapeptide made of a β-hydroxy fatty acid and a side chain of 16-19 carbon atoms (Steller *et al.,* 2000). According to previous studies, fengycin is produced mainly by *B. amyloliquefaciens* and *B. subtilis* (Hanif *et al.,* 2019; Geetha *et al.,* 2010)*.* These metabolites are reported to inhibit the growth of filamentous fungi and fungal enzymes such as aromatase and phospholipase A2 (Deleu *et al.,* 2005). Furthermore, studies revealed that fengycin is effective against various types of fungi, including *Magnaporthe grisea*, *Plasmodiophora brassicae*, *Botryosphaeria dothidea, C. gloeosporiodes, F. verticillioides, F. solani, F. solani f. sp. radicicola, F. oxysporum, F. oxysporum f. sp. spinaciae, F. verticillioides* and *F. graminearum* (Zhang & Sun., 2018; Li *et al.,* 2014; Fan *et al.,* 2017; Kim *et al.,* 2010; Li *et al.,* 2012)*.* In addition, Fengycins inhibit *F. graminearum*'s production by disrupting cell membrane permeability, and inhibition depends upon the concentration of fengycin (Liu *et al.,* 2019).

Worldwide, major loss of crop production is due to fungal phytopathogens (Ntushelo *et al.,* 2019). Among these fungal phytopathogens, the most significant and economic pathogens are *F. graminearum* and *R. solani,* which cause an extensive range of plant diseases (Kant *et al.,* 2011; Ajayi & Bradleyb, 2018). To control these fungal phytopathogens, chemical fertilizers, pesticides, and fungicides cause severe environmental issues (Khan *et al.,* 2021; Shafi *et al.,* 2017; Din *et al.,* 2019). Therefore, solving these issues requires an alternative approach for these fungal phytopathogens in a controlled environment.

Therefore, the study aimed to characterize *B. amyloliquefaciens* secondary metabolites, further analyzed through the high-performance liquid chromatography (HPLC) technique and screened against phytopathogens *F. graminearum* and *R. solani.*

2. Material and Methods

2.1 Study design

100 samples were collected from the rhizosphere of cereal crops to isolate *B. amyloliquefaciens* from places in Peshawar, Pakistan. To isolate *F. graminearum* and *R. solani*, the samples were collected from the diseased cereal crops in Peshawar, Pakistan.

2.2 Characterization of *B. amyloliquefaciens*

Soil samples were then processed through the serial dilution method. After the serial dilution with distilled water, the samples were streaked on nutrient agar media and incubated at 28ºC to 30ºC for 2-3 days. After incubation, the suspected colonies were examined through Gram's staining method. Gram-positive, rod-shaped, and spore-forming bacteria were selected for further Identification. *B. amyloliquefaciens* were identified through biochemical tests including citrate hydrolysis, catalase, indole production, nitrate reduction, Voges-Proskauer (VP), motility, H_2S production, and crystal formation (Amin *et al.,* 2015).

2.3 Production of secondary metabolites from *B. amyloliquefaciens*

B. amyloliquefaciens colonies were inoculated into a shaking flask containing a nutrient broth medium. After inoculation, the flasks were incubated at 30°C with a constant 200rpm at a shaking incubator for 16hours. Subsequently, 1ml of culture was transferred into an Erlenmeyer flask containing 99ml of Tryptic soy Broth (TSB) media and incubated at 30°C at a constant 200rpm on a shaker incubator overnight. The optical density (OD) of the growth curve of *B. amyloliquefaciens* was measured at 600nm using a spectrophotometer. Afterwards, the culture was removed and centrifuged for 30 minutes at 5590rpm. Finally, the supernatant was filtered at a sterile 0.22μm filter (Mater *et al.,* 2009).

2.4 High-performance liquid chromatography (HPLC) analysis

The supernatant was adjusted with concentrated HCL to pH 2 and centrifuged for 10 minutes at 894rpm and 20°C. The residue was dissolved in pH 8, methanol and water (50:50, v/v) solution and again filtered through a 0.22 μm membrane filter. The sample was treated three times with 20ml chloroform for purification. The lower layer was collected, and chloroform was evaporated through heat. The residue was dissolved in methanol. The secondary metabolites from the extract were identified by injecting 50μm of the extract in Shimadzu 20A UV-Vis HPLC at a wavelength range of 200–250nm. The isocratic HPLC method and 4.6×150mm C-18 normal phase column were used (Mater *et al.,* 2009). Acetonitrile was used as a mobile phase for the HPLC experiment. The obtained peak was compared to previously published data, and secondary metabolites were identified (Meena *et al.,* 2014).

2.5 Characterization of *F. graminearum* and *R. solani*

The infected part of the Plant was sliced by around 5mm, and 5% silver chloride was sterilized and washed with purified water 3 times. After sterilization, potato dextrose agar (PDA) was placed on the specimens and incubated for 3-4 days at 28°C (Uddin *et al.,* 2019). After incubation, the *F. graminearum* and *R. solani* were identified based on their colony colour, dense mycelia, and morphological characteristics on the microscope (John *et al.,* 2006).

2.6 Screening of secondary metabolites

The secondary metabolite was screened against *F. graminearum* and *R. solani*. Four wells of 5mm were made by using a sterile cork borer on potato dextrose agar (PDA). Various concentrations (1, 1/2, 1/4, and 1/8) of secondary metabolites were taken, and the zone of inhibition was measured in millimetres (mm) (Mater *et al.,* 2009).

2.7 Statistical Analysis

The data collected was analyzed and organized using the Statistical Package for Social Sciences (SPSS) version 23.0 software using a single ANOVA test.

3. Results

3.1 Characterization and cultivation of *B. amyloliquefaciens*

Among the 100 soil samples, *B. amyloliquefaciens was* isolated or found in 08 samples, which were confirmed based on colony morphology, gram staining, and biochemical tests (Figure 1). *B. amyloliquefaciens* was cultivated to produce secondary metabolites, and the growth curve's optical density (OD) was determined (Figure 2).

Bacillus amyloliquefaciens							
Circular, rough, opaque, fuzzy white or slightly yellow colonies							
Gram Staining	Shape	Motility	Catalase	Indole production	Citrate utilization	H2S production	Crystals formation
Gram Positive	Rod shaped	Positive	Positive	Negative	Positive	Negative	Negative

Fig. 1. Morphological and Biochemical characteristics of *B. amyloliquefaciens.*
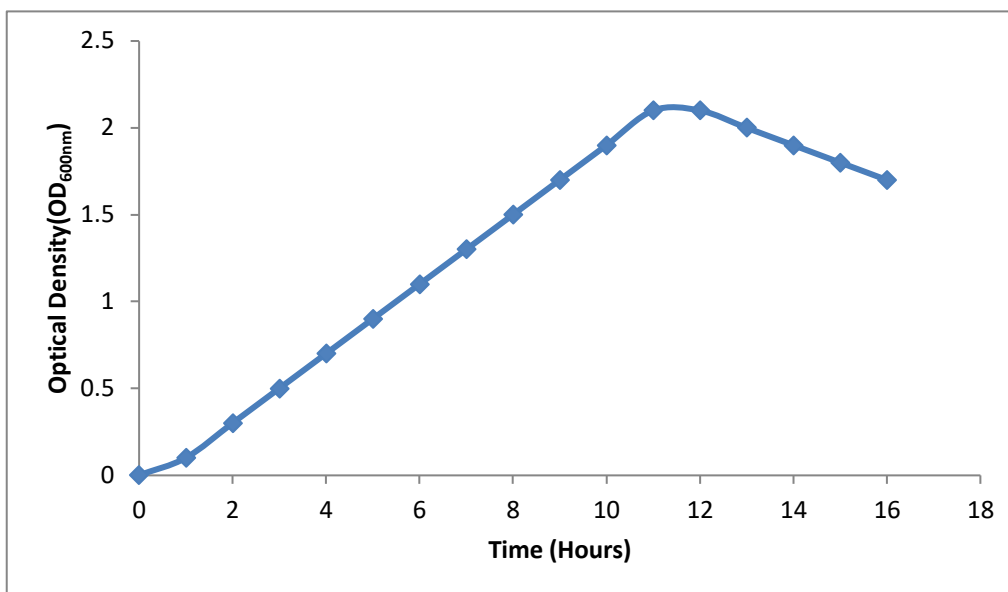
Fig. 2. Optical density (OD) of the growth curve of *B. amyloliquefaciens* at 600 nm wavelength

3.2 HPLC analysis of *B. amyloliquefaciens* secondary metabolites.

B. amyloliquefaciens purified secondary metabolites were analyzed using acetonitrile as the mobile phase. At 215nm and a retention time of 5-7minutes, the obtained peaks are similar to those obtained previously in literature data on fengycin (Figure 3). So, the secondary metabolite was confirmed as fengycin of *B. amyloliquefaciens* (Table 1).
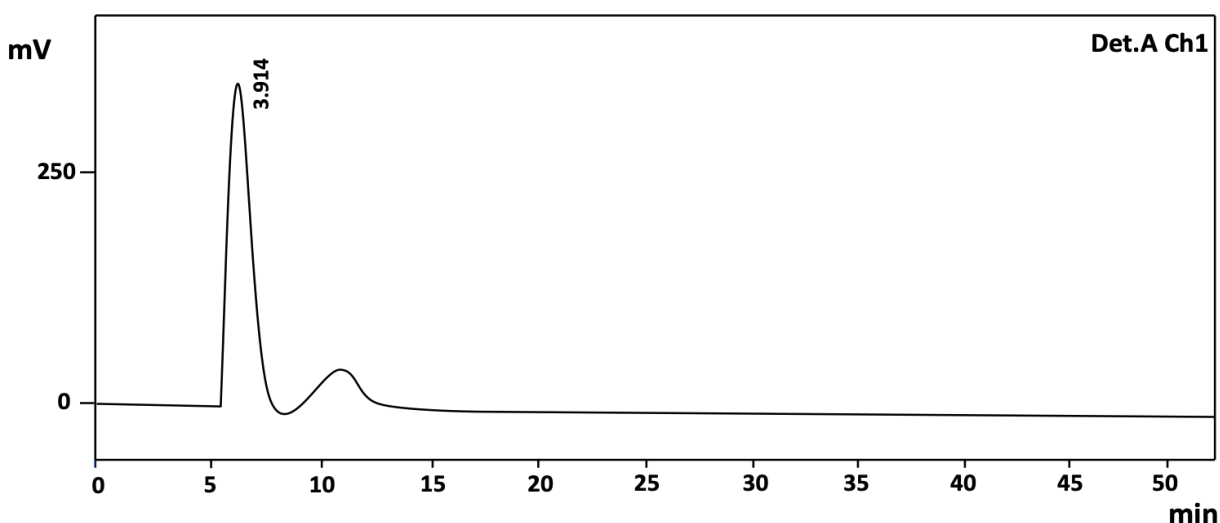
Fig. 3. HPLC Chromatogram of *B. amyloliquefaciens* secondary metabolites fengycin obtained at 215nm and retention time between 5-7 minutes.

Table 1. HPLC analysis results of secondary metabolites produced by *B. amyloliquefaciens*

Bacillus Strains	Wavelength (nm)	Retention time (minutes)	Peak area (Volts-minute)	Secondary metabolites
Bacillus amyloliquefaciens	215	5-7	3.914	Fengycin

3.3 Characterization of fungal species from infected Plant

F. graminearum was isolated from infected maize plants and identified based on their colony morphology, white to the pinkish and microscopic examination of hyaline septate hyphae, two to multi-celled and sickle-shaped. *R. solani* was also isolated from infected maize plants and identified based on their white to brown colony morphology and on microscopic examination of the long tube and septa or partition inside (Figure 4).

S.No.	Colony Morphology	Microscopic examination	Fungal species
1.	White to pinkish	Hyaline septate hyphae, two to multi-celled and sickle-shaped	*Fusarium graminearum*
2.	White to brown	Long tube and septa or partition inside	*Rhizoctonia solani*

Fig. 4. *F. graminearum* and *R. solani* results of colony morphology and microscopic examination.

3.4 Screening of *B. amyloliquefaciens* secondary metabolites against fungal species

B. amyloliquefaciens secondary metabolites fengycin were screened at (1, 1/2, 1/4, and 1/8) concentrations against the *F. graminearum* and *R. solani.* The zones of inhibition were calculated (Figure 5 & Table 2).

❖ Fengycin having significantly effect on the production of *F. graminearum* and *R. solani* (p<0.005)
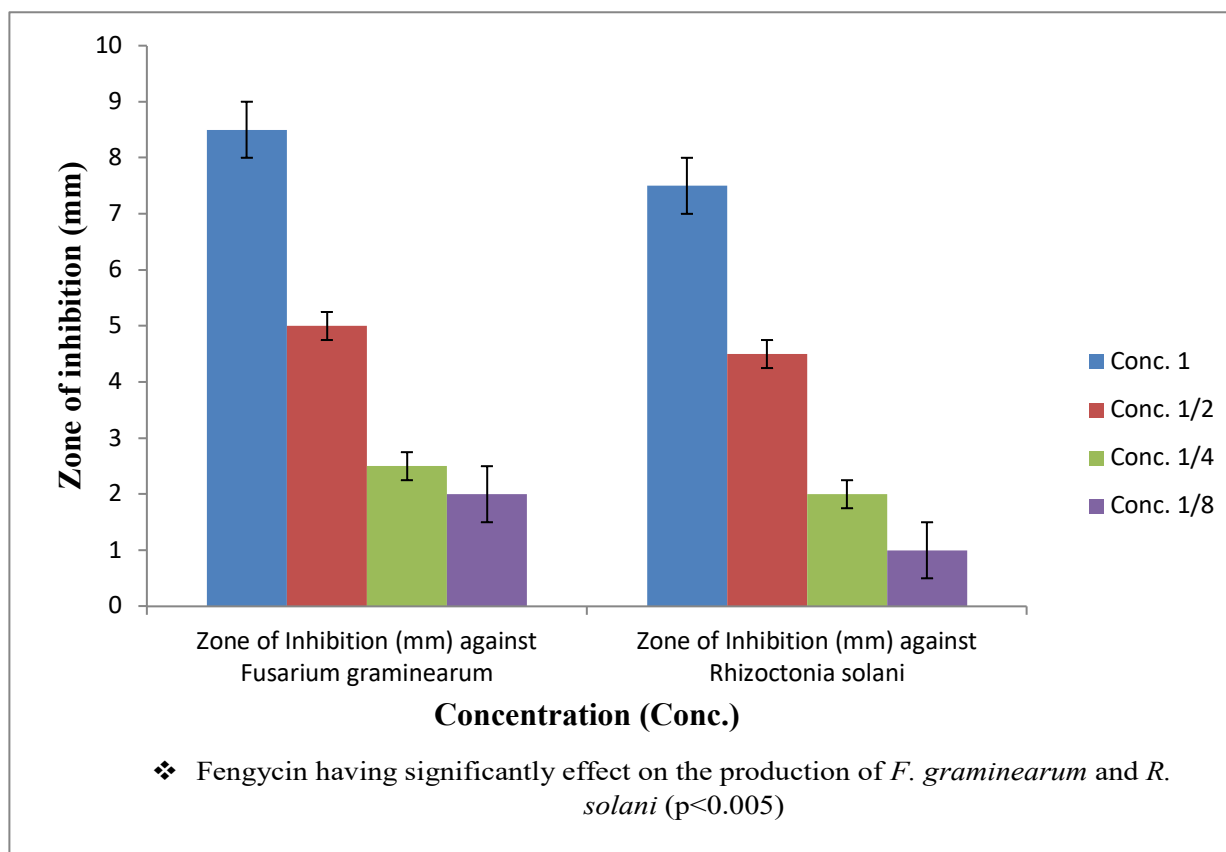
Fig. 5. *B. amyloliquefaciens* secondary metabolites fengycin zone of inhibition against *F. graminearum* and *R. solani*

Table 2. *B. amyloliquefaciens* secondary metabolites fengycin zone of inhibition against *F. graminearum* and *R. solani*

Bacillus Strain	Secondary metabolites	Concentration	Zone of Inhibition (mm) against *Fusarium graminearum*	Zone of Inhibition (mm) against *Rhizoctonia solani*
Bacillus amyloliquefaciens	Fengycin	1	8.5	7.5
		1 /2	5	4.5
		1 /4	2.5	2
		1 /8	2	1

❖ Fengycin has a significant effect on the production of *F. graminearum* and *R. solani* (p<0.005)

4. Discussion

4.1 Biocontrol of *B. amyloliquefaciens*

For several decades, chemical fertilizers, pesticides, and fungicides have been used to defend crops from the attacks of rodents and fungal plant diseases. The use of certain additives and agents has contributed to severe environmental problems. In biocontrol agents, production, and their environment-friendly behaviour, Plant growth-promoting rhizobacteria (PGPR) provides an appeal to replace these chemicals and fertilizers with biological agents. PGPR species found in soil, in the field of biopesticides, play an essential role since they produce several antimicrobial agents, including lipopeptides, antibiotics, and enzymes that stimulate plant growth and prevent pathogenic microorganisms (Lahmyed *et al.,* 2021; Dashti *et al.,* 2021; Shafi *et al.,* 2017; Din *et al.,* 2019). Among these PGPR, *Bacillus* spp. Develops metabolites with antibiotic properties capable of limiting or suppressing the development of other microorganisms (Amin *et al.,* 2015). Subtilin, bacilysin, mycobacillin, bacillomycin, mycosubtilin, iturin, fengycin, and surfactin are the antimicrobial substances developed by *Bacillus* spp. with both antifungal and antibacterial activity (Ntushelo *et al.,* 2019). *B. amyloliquefaciens* is known for producing antimicrobial substances and displayed antimicrobial activities against various fungal phytopathogens, including *F. proliferatum*, *F. asiaticum*, *F. verticilloides,* and *F. graminearum*, and some other diseases causing phytopathogens like *R. solani*, *C. coccodes*, and *B. cinerea*. According to previous reports, various *B. amyloliquefaciens* strains were more effective against *P. oryzae*, *R. necatrix*, *R. solani*, and *F. graminearum* (Yoshida *et al.,* 2001; Gong *et al.,* 2015 & Yu *et al.,* 2002). In the current study, *B. amyloliquefaciens* was isolated from soil, cultivated for the production of secondary metabolites and their secondary metabolites, such as fengycin produced by *B. amyloliquefaciens,* were characterized by HPLC, and their screening was performed against phytopathogens *F. graminearum* and *R. solani.* According to previous studies, *Bacillus* spp. Containing *B. amyloliquefaciens* were cultivated, and their extracts were identified through HPLC as fengycin, iturin, surfactin, bacillomycin, and cyclo (L-Pro-D-Tyr) (Hanif *et al.,* 2019; Jamal *et al.,* 2019; Gu *et al.,* 2017; Meena *et al.,* 2014). The findings mentioned above of various studies agree with the present study. The current study claimed that secondary metabolites produced by *B. amyloliquefaciens* have a high potential to inhibit the growth of *F. graminearum* and *R. solani.*

4.2 Biocontrol mechanisms of *B. amyloliquefaciens*

Due to cyclic lipopeptides, fengycin *B. amyloliquefaciens* broadly show antimicrobial activities (Ongena & Jacques, 2008). Both *B. subtilis* and *B. amyloliquefaciens* produce these lipopeptides (Ongena & Jacques, 2008; Wang *et al.,* 2007; Yoshida *et al.,* 2001); other bacterial spp. *B. licheniformis* and *B. megaterium* could also display antimicrobial activities attributed to fengycin and iturin (Kong *et al.,* 2010; Dey *et al.,* 2015). Additionally, a strain of *B. amyloliquefaciens* DA12 produced some volatiles inhibiting both fungi and bacteria. In the current study, we could not explore the inhibition mechanism. Still, the previously reported research claimed that the 2-hepatanone could be toxic for antifungal phytopathogens, including *R. solani* and some *Fusarium*

species. In addition, these compounds stop fungi colonization and spore germination (Lee *et al.,* 2017).

4.3 Role of fengycin against Phytopathogens

Some *Bacillus* species, including *B. subsites*, and *B. amyololiquefaciens,* play a vital role against fungal plant pathogens. The impressive antibiotic ability is mainly owing to their genetic potential and non-ribosomal lipopeptides due to the biocontrol activity of *Bacillus* spp. Most bacterial and fungal phytopathogens have been controlled and effective against plant pathology (Ntushelo *et al.*, 2019). Iturin, Surfactin, and fengycin are secondary metabolites produced by *Bacillus* spp. Comprises antifungal activity against various phytopathogens. According to previous studies, iturin, surfactin, and fengycin produced by *B. amyloliquefaciens, B. subtilis,* and *B. thuringiensis* were identified through thin layer chromatography (TLC) and HPLC having antifungal potential against *Aspergillus nigar, F. oxysporum,* and *F. graminearum* (Meena *et al.*, 2014; Hanif *et al.,* 2019) *F. culmorum, F. solani* (Harba *et al.,* 2020), *R. solani, F. solani* (Madhi *et al.,* 2020; Fadhal *et al.,* 2019; Margani *et al.,* 2018), *F. graminearum* (Hanif *et al.,* 2019; Jamal *et al.,* 2019), *Helminthosporium oryzae, Curvularia lunata,* and *F. semitectum* (Saechow *et al.,* 2018). The current study's findings also claimed and correlated to the previous studies. In the present study, *B. amyloliquefaciens* secondary metabolites fengycin was analyzed through HPLC and successfully inhibited the growth of *F. graminearum* and *R. solani* at various concentrations. *F. graminearum* produces mycotoxin such as deoxynivalenol (DON), trichothecenes nivalenol (NIV), its derivatives 3-and 15- acetyldeoxynivalenol (3-ADON, 15-ADON), which cause diseases in plants, animals, and humans. *R. solani* indicators on varied hosts comprise crown rot, root rot, seed rot, hypocotyl rot, limb rot, stem rot, stem canker, pod rot, pre- & post-emergence damping-off, black scurf, and seedling blight (Ajayi & Bradleyb, 2018). According to previous studies, *B. amyloliquefaciens* inhibit mycotoxin biosynthesis of *F. graminearum* due to fengycin (Hanif *et al.,* 2019). The current finding is in agreement with previously reported studies, which claimed that *B. amyloliquefaciens* metabolites fengycin inhibits *F. graminearum* propagation and inhibits biosynthesis of their mycotoxins, besides these; also prevents the mycelial development of *R. solani.*

Furthermore, we analyzed the extracted secondary metabolites against both phytopathogens at various concentrations, but 100% (1) of secondary metabolites were highly effective against *F. graminearum* and *R. solani,* then 1 /2, 1 /4 and 1 /8 concentrations. Fengycin at various concentrations significantly affects the production of *F. graminearum* and *R. solani* ($p<0.005$). Our findings correlate with the previously reported study by Jamal *et al.,* the various concentrations of *Bacillus* spp. Secondary metabolites were a significant ($p<0.005$) effect on the phytopathogens growth (Jamal *et al.,* 2019).

5. Conclusions

Bacillus species is an excellent candidate to use as a biocontrol agent against fungal phytopathogens because they produce various antimicrobial substances and their environmentally

friendly behaviour. In addition, *Bacillus* will eliminate many of the existing commonly used control agents, such as fungicides, and cultural activities that harm health and the ecosystem in controlling phytopathogens. The current study concluded that *B. amyloliquefaciens* secondary metabolites fengycin have a high potential to inhibit the growth of *F. graminearum* and *R. solani.*

References

Ajayi-Oyetundea, O.O., & Bradleyb, C.A. (2018). Rhizoctonia solani: taxonomy, population biology and management of Rhizoctonia seedling disease of soybean. Plant Pathology, **67**, 3–17.

Amin, M., Rakhisi, Z., & Ahmady, A. Z. (2015). Isolation and Identification of *Bacillus* Species from soil and evaluation of their antibacterial properties. Avicenna Journal of Clinical Microbiology and Infection, **2**(1), e2323.

Cao, Y., Zhang, Z.H., Ling, N., Yuan, Y.J., Zheng, X.Y., Shen, B. *et al.* (2011). *Bacillus subtilis* SQR 9 Can Control Fusarium Wilt in Cucumber by Colonizing Plant Roots. Biology and Fertilit of Soils, **47**(5), 495–506.

Caulier, S., Nannan, C., Gillis, A., Licciardi, F., Bragard, C., & Mahillon, J. (2019). Overview of the Antimicrobial Compounds Produced by Members of the *Bacillus subtilis* Group. Frontier in Microbiology, **10**.

Chen, Z., Huang, J., Zhao, J., Wang, C.B., & Liang, H. (2015). Research Advances on Antibacterial Mechanism of Bacillus Amyloliquefaciens. Biotechnology Bullitin, 31 (6), 37–41.

Deleu, M., Paquot, M., & Nylander, T. (2005). Fengycin interaction with lipid monolayers at the air-aqueous interface-implications for the effect of fengycin on biological membranes. Journal of Colloid and Interface Science, **283**, 358–365.

Dashti, N.H., Al-Sarraf, A.Y.N., Cherian, V.M., & Montasser, M.S. (2021). Isolation and characterization of novel plant growth-promoting rhizobacteria (PGPR) isolate from tomato (*Solanum Lycopersicum* L.) rhizospherical soil: A novel IAA producing bacteria. Kuwait Journal of Science, **48**(2), 1-17.

Dey, G., Bharti, R., Dhanarajan, G., Das, S., Dey, K.K., Prashanth Kumar, B. N., Sen, R., & Mandal, M. (2015). Marine lipopeptide iturin A inhibits Akt-mediated GSK3b and FoxO3a signalling, triggering apoptosis in breast cancer. Science Reports, **5**, 10316.

Din, M., Nelofer, R., Salman, M., Khan, F.H., Khan, A., Ahmad, M., & Khan, M. (2019). Production of nitrogen-fixing *Azotobacter* (SR-4) and phosphorus solubilizing *Aspergillus niger* and their evaluation on *Lagenaria siceraria* and *Abelmoschus esculentus*. Biotechnology Reports, **22**, e00323.

Fadhal, A., Al-Fadhal., Aqeel, N., AL-Abedy., Duaa, A., & Alkhafije. (2019). Isolation and molecular Identification of *Rhizoctonia solani* and *Fusarium solani* isolated from cucumber (*Cucumis sativus L.)* and their control feasibility by *Pseudomonas fluorescens* and *Bacillus subtilis*. Journal of Biological Pest Control, **29**, 47.

Fan, H., Ru, J., Zhang, Y., Wang, Q., & Li, Y. (2017). Fengycin produced by *Bacillus subtilis* 9407 plays a major role in apple ring rot disease biocontrol. Microbiology and Resistance, **199**, 89–97.

Geetha, L., Manonmani, A.M., & Paily, K.P. (2010). Identification and characterization of a mosquito pupicidal metabolite of *Bacillus subtilis* sub sp. *Subtilis* strain. Applied Microbiology and Biotechnology, **86**, 1737–1744.

Gong, A.D., Li, H.P., Yuan, Q.S., Song, X.S., Yao, W., He, W.J., Zhang, J.B., & Liao, Y.C. (2015). Antagonistic mechanism of iturin A and plipastatin A from *Bacillus amyloliquefaciens* S76-3 from wheat spikes against *Fusarium graminearum*. PLoS One, **10**, e0116871.

Gu, Q., Yang, Y., Yuan, Q., Shi, G., Wu, L., Lou, Z., Huo, R., Wu, H., Borriss, R., & Gaoa, X. (2017). Bacillomycin D produced by *Bacillus amyloliquefaciens* is involved in the antagonistic interaction with the plant-pathogenic fungus *Fusarium graminearum.* Applied and Environmental Microbiology, **83**(19), e01075-17.

Hanif, A., Zhang, F., Li, P., Li, C., Xu, Y., Zubair, M., *et al.* (2019). Fengycin produced by *Bacillus amyloliquefaciens* FZB42 inhibits *Fusarium graminearum* growth and mycotoxins biosynthesis. Toxins, **11**, 295.

Harba, M., Jawhar, M., & Arabi, M.I.E. (2020). In Vitro Antagonistic Activity of Diverse *Bacillus* Species against *Fusarium culmorum* and *F. solani* Pathogens. The Open Agriculture Journal, **14**, 1874-3315/20.

Jamal Q., Monkhung, S., Munir, S., Cho, J.Y., Moon, J.H., Khattak, B.U., *et al.* (2019). Identifying cyclo(L-Pro-D-Tyr) from *Bacillus amyloliquefaciens* Y1 exhibiting antifungal activity against *Fusarium graminearum* to control crown rot in wheat. Applied ecology and environmental research, **17**(3), 6299-6314.

John, F., Leslie, Brett, A., & Summerell. (2006). The *Fusarium* laboratory manual. First edition, Blackwell publishing.

Kant, P., Reinprecht, Y., Martin, C.J., Islam, R., & Pauls, K.P. (2011). Disease resistance / Pathology / *Fusarium*. Elsevier, 00263-4.

Khan, M., Salman, M., Jan, S.A., & Shinwari, Z.K. (2021). Biological control of fungal phytopathogens: A comprehensive review based on *Bacillus* species. MOJ Biology Medicine, **6**(2), 90–92.

Kim, P.I., Ryu, J., Kim, Y.H., & Chi, Y.T. (2010). Production of biosurfactant lipopeptides iturin A, fengycin and surfactin from *Bacillus subtilis* CMB32 for control of *Colletotrichum gloeosporides.* Journal of Microbiology and Biotechnology, **20**, 138–145.

Kong, H. G., Kim, J.C., Choi, G.J., Lee, K.Y., Kim, H.J., Hwang, E.C., Moon, B.J., & Lee, S.W. (2010). Production of surfactin and iturin by *Bacillus licheniformis* N1 is responsible for plant disease control activity. Plant Pathology Journal, **26**, 170- 177.

Koumoutsi, A., Chen, X.H., Henne, A., Liesegang, H., Hitzeroth, G., Franke, P. *et al*. (2004). Structural and Functional Characterization of Gene Clusters Directing Nonribosomal Synthesis of Bioactive Cyclic Lipopeptides in *Bacillus Amyloliquefaciens* Strain FZB42. Journal of Bacteriology, **186**, 1084–1096.

Lahmyed, H., Bouharroud, R., Qessaoui, R., Ajerrar, A., Amarraque, A., Aboulhassan, M.A., & Chebli, B. (2021). Actinomycete as biocontrol agents against tomato grey mold disease caused by *Botrytis cinerea.* Kuwait Journal of Science, **48**(3), (1-8)

Lee, T., Park, D., Kim, K., Lim, S.M., Yu, N.H., Kim, S., & Kim, J. C. (2017). Characterization of *Bacillus amyloliquefaciens* DA12 showing potent antifungal activity against mycotoxigenic *Fusarium* species. The plant pathology journal, **33**(5), 499.

Li, X.Y., Yang, J.J., Mao, Z.C., Ho, H.H., Wu, Y.X., & He, Y.Q. (2014). Enhancement of biocontrol activities and cyclic lipopeptides production by chemical mutagenesis of *Bacillus subtilis* XF-1, a biocontrol agent of *Plasmodiophora brassicae* and *Fusarium solani*. Indian Journal of Microbiology, **54**, 476–479.

Li, L., Ma, M., Huang, R., Qu, Q., Li, G., Zhou, J., Zhang, K., Lu, K., Niu, X., & Luo, J. (2012). Induction of chlamydospore formation in Fusarium by cyclic lipopeptide antibiotics from *Bacillus subtilis* C2. Journal of Chemistry and Ecology, **38**, 966–974.

Liu, H., Carvalhais, L., Crawford, M., Singh, E., Dennis, P., Pieterse, C. *et al*. (2017). Inner Plant Values: Diversity, Colonization and Benefits from Endophytic Bacteria. Frontier in Microbiology, **8**, 2552.

Liu, Y., Lu, J., Sun, J., Bie, X., & Lu, Z. (2019). Membrane disruption and DNA binding of *Fusarium graminearum* cell induced by C16-Fengycin A produced by *Bacillus amyloliquefaciens*. Food Control, **102**, 206–213.

Madhi, Q.H., & Jumaah, A.M. (2020). Affectivity evaluation of *Bacillus subtilis* in controlling eggplant root rot caused by *Rhizoctonia solani* and *Fusarium solani*, IOP Conf. Series: Earth and Environmental Science, **553**(2020), 012026.

Margani, R., Hadiwiyono, & Widadi, S. (2018). Utilizing *Bacillus* to inhibit the growth and infection by sheath blight pathogen *Rhizoctonia solani* in rice. IOP Conf. Series: Earth and Environmental Science, **142**(2018), 012070.

Mater, S.M., El-Kazzaz, S.A., Waigh, E.E., El-Diwany, A.I., Moustafa, H.E., Abo-Zaid, G.A., Abid Elsalam, H.E., & Hafez, E.E. (2009). Antagonistic and inhibitory effect of *Bacillus subtilis* against specific Plant pathogenic fungi. Biotechnology, **8**(1), 53-61.

Meena, K.R., Saha, D., & Kumar, R. (2014). Isolation and partial characterization of iturin-like lipopeptides (a bio-control agent) from a *Bacillus subtilis* strain. International Journal of Current Microbiology and Applied Sciences, **3**(10), 121-126.

Ntushelo, K., Ledwaba, L.K., Rauwane, M.E., Adebo, O. A., & Njobeh, P.B. (2019). The mode of action of *Bacillus* Species against *Fusarium graminearum*, Tools for investigation and prospects. Toxins, **11**, 606.

Ongena, M., & Jacques, P. (2008). *Bacillus* Lipopeptides: Versatile Weapons for Plant Disease Biocontrol. Trends in Microbiology, **16**(3), 115–125.

Saechow, S., Thammasittirong, A., Kittakoop, P., Prachya, S., & Thammasittirong, N.S. (2018). Antagonistic activity against dirty panicle rice fungal pathogens and plant growth promoting activity of *Bacillus amyloliquefaciens* BAS23. Journal of Microbiology and Biotechnology, **28**(9), 1527–1535.

Santoyo, G., Orozco-Mosqueda, M.D.C., & Govindappa, M. (2012). Mechanisms of Biocontrol and Plant Growth-Promoting Activity in Soil Bacterial Species of *Bacillus* and *Pseudomonas*: A Review. Biocontrol Science and Technology, **22**(8), 855–872.

Shafi, J., Tian, H., & Ji, M. (2017). *Bacillus* species as versatile weapons for plant pathogens: a review. Biotechnology & Biotechnological equipment, **31**(3), 446–459.

Steller, S., & Vater, J. (2000). Purification of the fengycin synthetase multienzyme system from *Bacillus subtilis* b213. Journal of Chromatography B: Biomedical Sciences and Applications, **737**, 267–275.

Uddin, M.N., Nasrullah, & Khan, M. (2019). Isolation and Identification of fungal pathogens associated with diseases of onion crop in district Swat, Pakistan. Abasyn Journal of Life Sciences, **2**(2), 91-99.

Wang, J., Liu, J., Chen, H., & Yao, J. (2007). Characterization of *Fusarium graminearum* inhibitory lipopeptide from *Bacillus subtilis* IB. Applied Microbiology and Biotechnology, **76**, 889-894.

Yan, W.R., Xiao, M., Chen, Y., Fu, M.Y., & Zhao Z.X. (2018). Research Progress in Antimicrobial Lipopeptides of *Bacillus Amyloliquefaciens*. Northwest Horticultural, **07**, 162–167.

Yoshida, S., Hiradate, S., Tsukamoto, T., Hatakeda, K., & Shirata, A. (2001). Antimicrobial activity of culture filtrate of *Bacillus amyloliquefaciens* RC-2 isolated from mulberry leaves. Phytopathology, **91**, 181-187.

Yu, G.Y., Sinclair, J.B., Hartman, G.L., & Bertagnolli, B.L. (2002). Production of iturin A by *Bacillus amyloliquefaciens* suppressing *Rhizoctonia solani*. Soil Biology and Biochemistry, **34**, 955- 963.

Zhang, L., & Sun, C. (2018). Fengycins, cyclic lipopeptides from marine *Bacillus subtilis* strains, kill the plant-pathogenic fungus Magnaporthe grisea by inducing reactive oxygen species production and chromatin condensation. Applied and Environmental Microbiology, **84**, e00445-18.

Investigation of the effect of selected edible and medicinal plants on *in-vitro* blood coagulation profile

Hoda M. Fathy*, Rahma SR. Mahrous, Rasha M.Abu EL-Khair,
Abdallah A. Omar, Reham S. Ibrahim

Dept. of Pharmacognosy, Faculty of Pharmacy, Alexandria University
Alexandria, Egypt.
*Corresponding author: hodasherif@hotmail.com

Abstract

Anticoagulation therapy represents a mainstay of treatment and prevention of cardiovascular diseases, which are the leading causes of mortality worldwide. In addition, several case reports of spontaneous bleeding occurred, linking the consumption of many dietary supplements during treatment with anticoagulants or in postoperative patients. This prompted our study, which was conducted on eleven well-known Egyptian medicinal plants, to highlight their effect on blood coagulation profile using Prothrombin time (PT) and activated partial thromboplastin time (aPTT) tests. Some of these plants showed exciting results that need a more in-depth evaluation of their anticoagulant activity as *Hibiscus sabdarifa* calyx, for its effect on PT. In addition, extracts of *Trifolium alexandrinum* aerial parts and *Pimpinella anismum* fruit were proved to affect aPTT. Therefore, postoperative or cardiovascular patients using herbal supplements should be cautioned about food-drug or herb-drug interactions and adjust their herbal medication regimen before surgery.

Keywords: Activated partial thromboplastin time**;** coagulation; Egyptian medicinal plants; *Hibiscus sabdarifa*; prothrombin time.

1. Introduction

Thromboembolic disorders, including pulmonary emboli and myocardial infarction, are the leading causes of mortality and morbidity (Moses, 2015). Many plants were recognized in folk medicine for their use in blood-related disorders; to prevent clot formation as anticoagulants or antiplatelets, but the mechanism of action and efficacy of most of them were not thoroughly studied (Cordier & Steenkamp, 2012). The well-known oral anticoagulant; warfarin was developed based on the molecular structure of dicoumarol in spoiled sweet clover (Moualla & Garcia, 2011; Stahmann *et al*., 1941).

Many plants have been reported to contain several potential antiplatelet and anticoagulant compounds. Some of these active plants are well-known edible ones, for example, onion and garlic (Liakopoulou-Kyriakides *et al*., 1985). Besides, clinically significant drug interactions were reported when certain herbal supplements were concomitantly used during warfarin therapy (Nutescu *et al*., 2006). As an example, ginkgo and ginseng present in many dietary supplements

showed several case reports of spontaneous bleeding during their use with warfarin because of their effects on platelets and coagulation (Vaes & Chyka, 2001).

The process of developing a novel anticoagulant drug is costly. Meanwhile, there is a pressing need for an oral cheaper yet more effective alternative. Currently, scientific evidence demonstrates that the intake of phytochemicals or dietary supplements with anticoagulant properties can minimize the risks of thromboembolic disorders. The *in-vitro* screening methods to evaluate newly developed anticoagulants obtained from natural and synthetic sources include the Prothrombin time (PT) and the activated partial thromboplastin time (aPTT). These two assays are currently employed within most laboratory testing for monitoring anticoagulant medication (Brace, 2001; Favaloro *et al.*, 2011).

Two integrated procoagulant pathways are triggered upon vascular wall injury, namely, primary and secondary haemostasis. The direct pathway involves platelets activating a significant role in haemostasis and thrombosis (Gresele, 2013). The secondary path is represented by "blood coagulation", which is based on the properties of blood components; procoagulant proteins "coagulation factors"(Moore *et al.*, 2016). This secondary hemostatic pathway comprises the (intrinsic) coagulation pathway initiated through vascular wall injury via the tissue factor (extrinsic) pathway (Favaloro *et al.*, 2011). The two *in-vitro* assays used in our study represent these two pathways of secondary haemostasis.

The prothrombin time (PT) test estimates the extrinsic coagulation mechanism. It detects effects on coagulation factors II, V, VII and X. It is primarily used to monitor vitamin K antagonists (VKA) therapy that acts on three of these five factors and is the most commonly used anticoagulant medication. For this reason, this *in-vitro* test is the major haemostasis test performed in laboratories. Besides, most reagents in this assay contain a heparin neutralizing agent to increase specificity for VKA therapy and prevent the detection of heparin activity. The activated partial thromboplastin time (aPTT) *in vitro* test model acts on the components of the intrinsic and common pathways, including factors II, V, VIII, IX, FX, XI and XII (Osoniyi & Onajobi, 2003). This test is used mainly to monitor patients receiving unfractionated heparin (UH) and as a screening test for haemophilia A and B.

Egyptian flora has a wide molecular diversity of bioactive compounds. In the present study, eleven Egyptian medicinal plants previously reported affecting bleeding confirmed by *in-vitro* or *in-vivo* experiments were in vitro screened for their coagulation profile using (PT) and (aPTT) testing.

2. Materials and methods

2.1.Preparation of sample solutions:

Roots of *Glycyrrhiza glabra,* leaves of *Olea europaea*, aerial parts of *Trifolium alexandrinum* and *Medicago sativa* were collected from Alexandria, Egypt (table1). *Ammi visnaga, Ammi majus, Hibiscus sabdariffa, Linum usitatissimum, Matricaria recutita*, *Pimpinella anisum* and *Trigonella foenum-graecum* were purchased from a well-reputed herb store (Madi, Alexandria) in 2018 they are originated in Alexandria, Egypt. Still, the exact time of collection is not available. Plant samples

were kindly identified by Professor Dr Selim Zidan Heneidy, professor of Applied Ecology, Faculty of Science, Alexandria University. Voucher specimens; (GG106, OE107, TA108, MS109) have been deposited in the Pharmacognosy Department, Faculty of Pharmacy, Alexandria University. Each of the eleven plants was treated as follows; 15 g of dried powdered plant material was separately extracted with 70% ethanol three times, each with 150 ml using sonication at room temperature for 30 min. The combined filtrates were concentrated to dryness under vacuum. Dried plant extracts were dissolved in 10% DMSO in PBS, filtered using a 0.45 µ syringe filter and used in 2 concentrations (3 & 10 mg/ml).

Table 1. Site and date of collection of some plants

Plant	Site of collection	Date
Roots of *Glycyrrhiza glabra*	Smouha, Alexandria	from November to December 2018
leaves of *Olea europaea*	Borg-El-Arab, Alexandria	from October to November 2018
aerial parts of *Trifolium alexandrinum*	El-Awayed- Alexandria	from November 2018 to March 2019
Medicago sativa	Borg-el-Arab, Alexandria	December 2018

2.1. *In-vitro* prothrombin time (PT) and activated partial thromboplastin time (aPTT) testing

Prothrombin time (PT) and activated partial thromboplastin time (aPTT) were measured according to the procedure described in previous literature (Brown, 1988). All the experiments were carried out identically. EDTA at 10 mg/ml concentration was used as a positive control. The effect of the samples on bleeding was expressed as clotting times in seconds. Prothrombin time (PT) Platelet poor plasma was prepared by centrifuging citrated blood for 15 min at 4000 g. Samples were prepared by adding 0.5 ml of the prepared plant extract to 1 ml of platelet-poor plasma and then incubated for 5 min. at 37°C (extract- plasma mixture). 200 µl of Thromboplastin calcium reagent (Hemostat thromboplastin-SI, Human, Diagnostica Stagio) after reconstitution and pre-warming was added to 100 µl of (extract- plasma mixture) while simultaneously starting a timer. Then gently shaken until the formation of a clot and clotting time are recorded. For the negative control, 10% DMSO in PBS was mixed with platelet-poor plasma and used instead of the sample extract.

2.1.1. Activated partial thromboplastin time (aPTT)

The (extract-plasma mixture) prepared as in the PT test was mixed with the prewarmed aPTT reagent (aPPT-EL, Human, Diagnostica Stagio) in an equal amount (100 µl). Then, incubation at 37°C for 3 min. I was followed by the addition of 100 µl of the prewarmed calcium chloride solution (0.02 M) while, at the same time, starting a timer. Next, the tube was gently shaken while still in the water bath every 5 s. after 20 s, it was removed and gently shaken until a clot was observed and the time recorded. The negative control used is 10% DMSO in PBS.

2.2. Statistical analysis

The statistical analysis was performed using Graphpad Prism® (V. 6.01) software. All the experiments were carried out identically, and the measured data are expressed as the means ±

standard deviation. In addition, an unpaired student t-test was used to determine the statistical significance between the control and treatment groups.

2.3. Ethical review

The study received ethical approval from the Ethics Committee of the faculty of pharmacy because of the very small volume of blood used; only oral consent of blood donors was obtained after explaining the aim of the study.

3. Results

The standard clotting time is 12.5 to13.7 s for the PT test and between 31 and 39 s for aPTT. Values deviated from these standard times indicate an effect on the coagulation either as an anticoagulant; with prolonged clotting times, or as a coagulant, with rapid clot formation (Cordier *et al.*, 2012). The eleven plants proved their anticoagulant effects as concluded from the differences in their clotting times compared to the control in the PT and aPTT *in-vitro* testing (Table 2). It was observed that almost all the tested plants showed a significant effect in aPTT testing rather than PT test at the two concentrations used: (3& 10 mg/ml)

Table 2. Effect of ethanolic plant extracts on PT and aPTT clotting times

Sample	Concentration (mg/ml)	PT (Seconds)#	aPTT (Seconds)#
Normal plasma	-	12.80	26.58
NegativeControl (10%DMSO)	-	14.65± 0.07	56.1±1.06
Positive control (EDTA)	10	23.25± 0.35	506.4±0.74
Ammi majus[b]	3	14.60±0.14	31.5±0.42**
(AM)	10	19.2±0.14**	35.2±1.41**
Ammi visnaga	3	18.25±0.78	49.1±0.14*
(AV)	10	18.75±0.21*	57.6±0.42
Glycyrrhiza glabra[b]	3	16.6±0.28	35.3±1.48**
(GG)	10	16.65±0.21*	30.1±0.85**
Hibiscus sabdariffaa[b]	3	20.35±0.07***	41.10±0.14**
(HS)	10	no clotting*	44.8±0.99**
Linum usitatissimum[b]	3	18.95±0.64	80.35±0.78**
(LU)	10	15.90±0.14*	111.6±0.85***
Matricaria recutita[b]	3	20.65±0.07***	75.6±0.07**
(MC)	10	17.35±0.64	67.8±0.57**
Medicago sativa[a]	3	11.20±0.14**	15.1±1.2***
(MS)	10	21.55±0.07***	55.2±2.55
Olea Europae[a]	3	16.00±0*	32.4±0.42***
(OE)	10	16.65±0.21*	53.7±1.84
Pimpinella anisum[b]	3	13.80±0.28	75.85±1.48**
(PA)	10	13.45±0.07**	91.25 ±2.19**
Trifolium alexandrinum[b]	3	15.55±0.35	76.40±1.41**
(TA)	10	15.65±0.64	116.6±1.84***
Trigonella foenum-graecum[b]	3	14.10±0.42	36.1±0.42**
(TF)	10	19.50±0.42*	89.4±2.26**

#Values are expressed as the means of 2 replicates ± SD, values statistically significant when compared to negative control using unpaired t-test: *$p \leq 0.05$; **$p \leq 0.01$, ***$p \leq 0.001$

plants with significant effects on PT. [b] plants with substantial impacts on aPTT

3.1. Prothrombin time (PT) testing

In PT testing, only three plants (*Olea europaea*, *Hibiscus sabdariffa* and *Medicago sativa*) showed significant effects on the clotting times compared to control when tested at two concentrations suggesting dose-dependent activity (Figure 1). Additionally, seven plants gave substantial observed impacts for one of the two concentrations (Table 2). These effects mainly prolonged clotting times except for *Pimpinella anisum*, which significantly showed shorter clotting times compared to control (13.45 s) at concentration10 mg/ml.

The highest effect was manifested by *H. sabdariffa* extract as it showed prolongation of the clotting time at a concentration of 10 mg/ml where the blood did not clot.

M. sativa extract also increased the PT at the higher concentration tested as it gave a bleeding time of 21.55 s, while at a lower concentration, bleeding time (11.20 s) wasn't affected but was lower than the time measured for normal plasma (12.80 s).

Change in clotting times for *O. europaea* extract showed minimal difference in increasing the concentration used.

T. foenum-graecum, A. majus, A. visnaga, G. glabra and L. usitatissimum showed significant prolongation of clotting times (19.50 s, 19.20 s, 18.75 s, 16.65 s and 15.90 s, respectively) at the highest concentration used). On the contrary, *M. Recutita* is the sole extract that gave longer times when tested at 3mg/ml *(*20.65 s).

3.2. Activated partial thromboplastin time (aPTT) testing

All the tested plant extracts showed statistically significant differences in their clotting times compared to the control in aPTT test (Figure 2, Table 2). In addition, eight of the examined plant extracts had effects in the two concentrations used, while the remaining three plants observed significant effects for one concentration only.

T. alexandrinum, L. usitatissimum, P. anisum, and T. foenum-graecum extracts showed the highest effects in prolongation of the clotting times (116.60 s, 111.60 s, 91.25 s and 89.40 s, respectively) at the highest concentration tested. *M. Recutita* extract at 3 mg/ml also prolonged aPTT significantly (75.6 s), while higher concentration at 10 mg/ml showed shorter times. On the other hand**,** *G. glabra, H. sabdariffa* and *A. majus* extracts showed shorter clotting times than the control used (56.10 s). Besides, shorter clotting times were observed for the three plants: *Olea europaea*, *Ammi visnaga* and *Medicago sativa.* These clotting times were significant at the lower concentration, 3 mg/ml being 32.40 s, 49.10 s and 15.10 s, respectively.
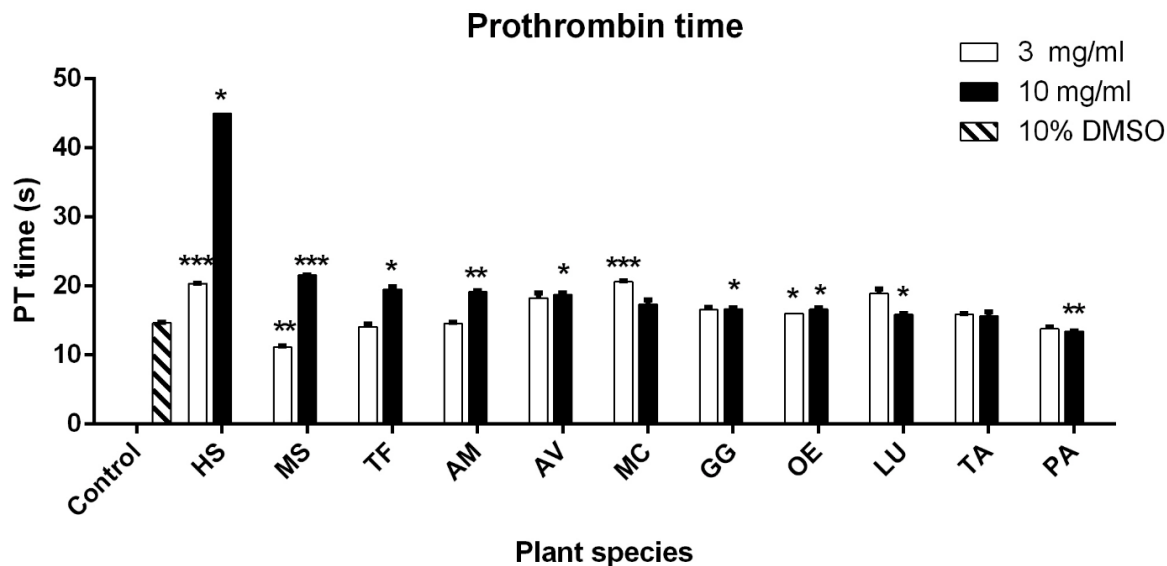
Fig. 1. Effect of plants ethanolic extracts on PT *in-vitro*. *$p< 0.05$, **$p < 0.01$ and ***$p< 0.001$ compared to negative control (10%DMSO).
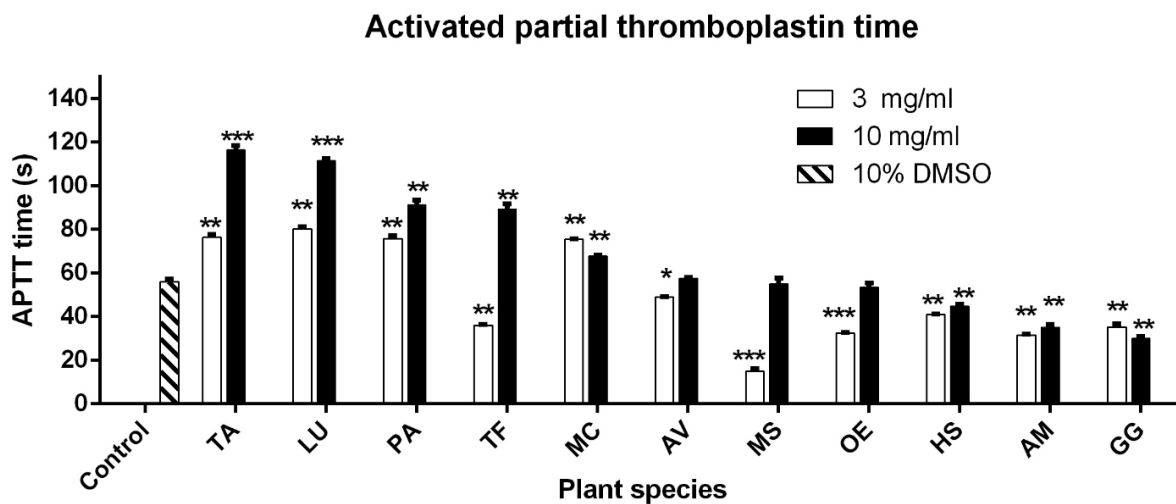Bars without symbols refer to non-significant results

Fig. 2. Effect of plants ethanolic extracts on aPTT *in-vitro*. *$p<0.05$, **$p< 0.01$ and ***$p< 0.001$ compared to negative control (10% DMSO).
Bars without symbols refer to the non-significant result

4. Discussion

The results indicated that some of the tested plant extracts affected different coagulation factors through their effects on PT and aPTT compared to the control. Our findings agreed with some plants' previously reported anticoagulant activities, as in the case of *O. Europea,* where a previous study showed that oral supplementation of the plant leaves extract possessed a significant prolongation of PT with no effect on aPTT (Dub & Dugani, 2013).

Anticoagulant effects of *G. glabra* are well known, and their impact on PT and aPTT has been reported in many studies (Braun and Cohen, 2015; Nakagawa *et al*., 2008). Some used it as a positive control with other plant extracts (Aalikhani Pour *et al*., 2016). In our study, clotting time found for *G. glabra* was very close to the previously reported times for PT test *in-vitro (*17.30 s) (Aalikhani Pour *et al*., 2016). However, the aPTT time was shorter than the values reported in the literature (82.66 s at a concentration of 0.1 mg/ml). Hence, further examination of the effect of *G. glabra* extract on aPTT using a wider concentration range is highly recommended.

T. alexandrinum extract showed strong activity towards aPTT even at concentrations as low as 3 mg/ml, with no effect on PT. The obtained aPTT activity, as opposed to the previously obtained results, suggested that the plant did not affect the coagulation times (TT, PT or aPTT) (Kolodziejczyk-Czepas *et al*., 2018). Differences in the sample preparation could be one of the reasons for the differences in the results. In our study, we used the total ethanolic extract in *vitro* testing; compared to phenolic fractions in the mentioned study.

The prolongation of PT observed for *H. sabdariffa* dried calyx extract is an interesting finding that needs a further examination of the exact mechanism and phytoconstituents responsible for this activity. Previous studies reported *in-vivo* antiplatelet effects for dried Hibiscus calyx extract (Ali *et al*., 2016).

Previous studies showed that *M. Recutita* extract; (especially the aqueous one) exhibited significant *in-vitro* antiplatelet aggregation (Memariani *et al*., 2018). This antiplatelet activity was induced by polysaccharide–polyphenolic conjugates present in the dry flowering parts of the plant (Bijak *et al*., 2013). luteolin, a flavone presents in chamomile, inhibited thrombin (factor II) and FXa activity. It also prolonged aPTT and PT, reaching 81.0 s and 16.2 s, respectively, when tested at a concentration of 10 μg. This could explain the anticoagulant activity observed in our study for *M. Recutita* extract, as the aPTT was more affected by the plant extract than PT (Choi *et al*., 2015). Our findings revealed that *M. Recutita* extract is an effective anticoagulant using these two *in-vitro* tests, especially at low concentrations (3 mg/ml).

The majority of the results on flaxseed showed that its ingestion or its oil does not influence platelet aggregation (Rodriguez-Leyva *et al*., 2010). Only a few studies have shown that the oil inhibited platelet aggregation induced by thrombin and fibrinogen (Prasad, 2009). Recent *in-vitro* studies indicated that a phenolic extract of the seed has moderate activity on both coagulation pathways, as indicated by PT and aPTT testing (Boukeria *et al*., 2020). Moreover, flax seed proteins were evaluated for their effects on coagulation disorders. The results showed that this protein preparation prolonged the clot formation process of only aPTT but not PT at 0.1 mg (Nandish *et al*., 2018). Our findings confirmed these results regarding the aPTT activity.

A literature survey regarding *T. foenum-graecum* showed that the plant extract inhibited platelet aggregation in *an in-vivo* rat model (Ulbricht *et al*., 2008). Moreover, the 5% aqueous fenugreek extract inhibited the coagulation process *in-vitro* and prolonged PT in a dose-dependent manner, reaching 23.60 s when 75 µl was used (Taj Eldin *et al*., 2013). Our findings came from these studies as the plant extract showed significant prolonged PT (19.50 s) at 10 mg/ml. Moreover, significantly longer clotting times were observed in our study in aPTT test. Thus, our results partly explain the increased bleeding risk reported for concomitant use of fenugreek preparations with warfarin (Lambert & Cormier, 2001).

The results obtained for *M. sativa* came from earlier studies where the plant aqueous and methanolic extracts had aPTT clotting times of 50.40 s and 51.20 s, respectively, in previous studies (Cordier *et al*., 2012).

A. visnaga, A. majus and P. anisum are three plants belonging to the family Apiaceae famous for their content of coumarins, well-known anticoagulants (Arora & Mathur, 1963). Previous studies showed that *A. visnaga* improves blood supply to coronary smooth muscles (Khalil *et al*., 2020).To our knowledge, anticoagulant and antiplatelet activity of *A.visnaga* and *A. majus* haven't been previously evaluated. Our findings revealed the significant anticoagulant activity of *P. anismum* demonstrated by the prolonged aPTT. In contrast, *A. majus* extract showed shorter clotting times observed in aPTT, indicating coagulating activity. The same extract showed anticoagulant properties in PT manifested by longer clotting time (19.20 s) at a concentration of 10 mg/ml. *A. visnaga* is the only plant that didn't show significant effects in both *in-vitro* anticoagulant models.

5. Conclusion

Our *in-vitro* anticoagulant study gave further evidence on the activity of some medicinal plants known for blood clot management. Some of these plants showed exciting results that need a more in-depth evaluation of their anticoagulant activity as *H. sabdarifa* calyx extract, for its effect on PT. In addition, extracts of *T. alexandrinum* aerial parts and *P. anismum* fruit were proved to affect aPTT.

It should be noted that plants containing coumarins that didn't show anticoagulant effects in our study will need further investigations using *in-vivo* models for coagulation since they exert their anticoagulant properties by inhibiting the vitamin K epoxide reductase complex, which can be monitored *in-vivo* (Hildebrandt and Suttie, 1982; Kasperkiewicz *et al*., 2020).

In general, plant extracts suppressing the extent of coagulation in PT are suggested to have an effect on one or more of the coagulation factors involved in the extrinsic pathway. Plants prolonging the aPTT are considered to act on coagulation factors VIII, IX, XI and XII of the endogenous coagulation (Giddens, 2015).

References

Aalikhani Pour, M., Sardari, S., Eslamifar, A., Rezvani, M., Azhar, A. & Nazari, M. (2016) Evaluating the anticoagulant effect of medicinal plants in vitro by cheminformatics methods. Journal of Herbal Medicine, 6(**3**)**,** 128-136. https://doi.org/10.1016/j.hermed.2016.05.002.

Ali, A. H., Abdul-Azeez, L., Humood, J., Ali, Z., Helal, Z. & Wahab, F. (2016) The effect of ethanolic extract of Hibiscus sabdariffa on some physiological and antioxidant parameters in female rabbits. Journal of Animal Health and Production, 4**,** 37-41.

Arora, R. B. & Mathur, C. N. (1963) Relationship between structure and anticoagulant activity of coumarin derivatives. British journal of pharmacology and chemotherapy, 20(**1**)**,** 29-35. 10.1111/j.1476-5381.1963.tb01294.x.

Bijak, M., Saluk, J., Tsirigotis-Maniecka, M., Komorowska, H., Wachowicz, B., Zaczyńska, E., Czarny, A., Czechowski, F., Nowak, P. & Pawlaczyk, I. (2013) The influence of conjugates isolated from Matricaria chamomilla L. on platelets activity and cytotoxicity. International Journal of Biological Macromolecules, 61**,** 218-229. https://doi.org/10.1016/j.ijbiomac.2013.06.046.

Boukeria, S., Mnasri, S. R., Kadi, K., Benbott, A., Bougueria, H., Biri, K. & Lazbbache, W. (2020) Evaluation Of The Antibacterial And Anticoagulant Activity Of Phenolic Extracts Of Linum Usitatissimum L. Journal of Fundamental and Applied Sciences, 12**,** 667-682.

Brace, L. D. (2001) Current Status of the International Normalized Ratio. Laboratory Medicine, 32(**7**)**,** 390-392. 10.1309/2rn7-44hb-wp2r-q6b3.

Braun, L. & Cohen, M. (2015) Herbs and Natural Supplements, Volume **2**: An Evidence-Based Guide. Elsevier Health Sciences.

Brown, B. A. (1988) Hematology: principles and procedures. In: 5th ed. ed. Philadelphia: Lea & Febiger.

Choi, J.-H., Kim, Y.-S., Shin, C.-H., Lee, H.-J. & Kim, S. (2015) Antithrombotic Activities of Luteolin In Vitro and In Vivo. Journal of Biochemical and Molecular Toxicology, 29(**12**)**,** 552-558. 10.1002/jbt.21726.

Cordier, W., Cromarty, A. D., Botha, E. & Steenkamp, V. (2012) Effects of selected South African plant extracts on haemolysis and coagulation. Human & experimental toxicology, 31(**3**)**,** 250-257. 10.1177/0960327111398675.

Cordier, W. & Steenkamp, V. (2012) Herbal remedies affecting coagulation: a review. Pharmaceutical biology, 50(**4**)**,** 443-452. 10.3109/13880209.2011.611145.

Dub, A. M. & Dugani, A. M. (2013) Antithrombotic effect of repeated doses of the ethanolic extract of local olive (Olea europaea L.) leaves in rabbits. Libyan J Med, 8**,** 20947. 10.3402/ljm.v8i0.20947.

Favaloro, E. J., Lippi, G. & Koutts, J. (2011) Laboratory testing of anticoagulants: the present and the future. Pathology, 43(**7**)**,** 682-692. https://doi.org/10.1097/PAT.0b013e32834bf5f4.

Giddens, J. F. (2015) Homeostasis and regulation. In: Concepts for Nursing Practice - E-Book. Elsevier Health Sciences.

Gresele, P. (2013) Antiplatelet agents in clinical practice and their haemorrhagic risk. Blood transfusion = Trasfusione del sangue, 11(**3**)**,** 349-356. 10.2450/2013.0248-12.

Hildebrandt, E. F. & Suttie, J. W. (1982) Mechanism of coumarin action: sensitivity of vitamin K metabolizing enzymes of normal and warfarin-resistant rat liver. Biochemistry, 21(**10**)**,** 2406-2411. 10.1021/bi00539a020.

Kasperkiewicz, K., Ponczek, M. B., Owczarek, J., Guga, P. & Budzisz, E. (2020) Antagonists of Vitamin K-Popular Coumarin Drugs and New Synthetic and Natural Coumarin Derivatives. Molecules (Basel, Switzerland), 25(**6**). Available at: https://doi.org/10.3390/molecules25061465.

Khalil, N., Bishr, M., Desouky, S. & Salama, O. (2020) Ammi Visnaga L., a Potential Medicinal Plant: A Review. Molecules, 25(**2**)**,** 301.

Kolodziejczyk-Czepas, J., Sieradzka, M., Moniuszko-Szajwaj, B., Nowak, P., Oleszek, W. & Stochmal, A. (2018) Phenolic fractions from nine Trifolium species modulate the coagulant properties of blood plasma in vitro without cytotoxicity towards blood cells. Journal of Pharmacy and Pharmacology, 70(**3**)**,** 413-425. 10.1111/jphp.12872.

Lambert, J.-P. & Cormier, J. (2001) Potential Interaction between Warfarin and Boldo-Fenugreek. Pharmacotherapy: The Journal of Human Pharmacology and Drug Therapy, 21(**4**)**,** 509-512. 10.1592/phco.21.5.509.34492.

Liakopoulou-Kyriakides, M., Sinakos, Z. & Kyriakidis, D. A. (1985) Identification of alliin, a constituent of Allium cepa with an inhibitory effect on platelet aggregation. Phytochemistry, 24(**3**)**,** 600-601. https://doi.org/10.1016/S0031-9422(00)80777-3.

Memariani, Z., Moeini, R., Hamedi, S. S., Gorji, N. & Mozaffarpur, S. A. (2018) Medicinal plants with antithrombotic property in Persian medicine: a mechanistic review. Journal of Thrombosis and Thrombolysis, 45(**1**)**,** 158-179. 10.1007/s11239-017-1580-3.

Moore, G., Knight, G. & Blann, A. D. (2016) Haemostasis in Health and Disease. In: Haematology. Oxford University Press.

Moses, D. (2015) A survey of data mining algorithms used in cardiovascular disease diagnosis from multi-lead ECG data. Kuwait Journal of Science, 42(**2**).

Moualla, H. & Garcia, D. (2011) Vitamin K antagonists--current concepts and challenges. Thrombosis Research, 128(**3**)**,** 210-215. 10.1016/j.thromres.2011.04.011.

Nakagawa, K., Kitano, M., Kishida, H., Hidaka, T., Nabae, K., Kawabe, M. & Hosoe, K. (2008) 90-Day repeated-dose toxicity study of licorice flavonoid oil (LFO) in rats. Food and Chemical Toxicology, 46(**7**)**,** 2349-2357. https://doi.org/10.1016/j.fct.2008.03.015.

Nandish, S. M., Kengaiah, J., Ramachandraiah, C., Shivaiah, A., Chandramma, Girish, K., Kemparaju, K. & Sannaningaiah, D. (2018) Anticoagulant, antiplatelet and fibrin clot hydrolyzing activities of flax seed buffer extract. Pharmacognosy Magazine, 14**,** 175.

Nutescu, E. A., Shapiro, N. L., Ibrahim, S. & West, P. (2006) Warfarin and its interactions with foods, herbs and other dietary supplements. Expert Opin Drug Saf, 5(**3**)**,** 433-51. 10.1517/14740338.5.3.433.

Osoniyi, O. & Onajobi, F. (2003) Coagulant and anticoagulant activities in Jatropha curcas latex. Journal of Ethnopharmacology, 89(**1**)**,** 101-105. https://doi.org/10.1016/S0378-8741(03)00263-0.

Prasad, K. (2009) Flaxseed and cardiovascular health. Journal of cardiovascular pharmacology, 54(**5**)**,** 369-377. 10.1097/fjc.0b013e3181af04e5.

Rodriguez-Leyva, D., Bassett, C. M. C., McCullough, R. & Pierce, G. N. (2010) The cardiovascular effects of flaxseed and its omega-3 fatty acid, alpha-linolenic acid. Canadian Journal of Cardiology, 26(**9**)**,** 489-496. https://doi.org/10.1016/S0828-282X(10)70455-4.

Stahmann, M. A., Huebner, C. F. & Link, K. P. (1941) Studies On The Hemorrhagic Sweet Clover Disease: V. Identification And Synthesis Of The Hemorrhagic Agent. Journal of Biological Chemistry, 138(**2**)**,** 513-527.

Taj Eldin, I. M., Abdalmutalab, M. M. & Bikir, H. E. (2013) An in vitro anticoagulant effect of Fenugreek (Trigonella foenum-graecum) in blood samples of normal Sudanese individuals. Sudanese journal of paediatrics, 13(**2**), 52-56.

Ulbricht, C., Basch, E., Burke, D., Cheung, L., Ernst, E., Giese, N., Foppa, I., Hammerness, P., Hashmi, S., Kuo, G., Miranda, M., Mukherjee, S., Smith, M., Sollars, D., Tanguay-Colucci, S., Vijayan, N. & Weissner, W. (2008) Fenugreek (Trigonella foenum-graecum L. Leguminosae): An Evidence-Based Systematic Review by the Natural Standard Research Collaboration. Journal of Herbal Pharmacotherapy, 7(**3-4**), 143-177. 10.1080/15228940802142852.

Vaes, L. P. & Chyka, P. A. (2001) Interactions of warfarin with garlic, ginger, ginkgo, or ginseng: nature of the evidence. Ann Pharmacother, 34(**12**), 1478-82. 10.1345/aph.10031.

Production, optimization, purification, kinetic analysis, and applications of alkaline proteases produced from *Bacillus subtilis* through solid-state fermentation of agricultural byproducts

Roheena Abdullah[1,*], Maham Asim [1], Muhammad Nadeem[2], Kinza Nisar[1], Afshan Kaleem[1], Mehwish Iqtedar[1]

[1]Dept. of Biotechnology Lahore College for Women University, Lahore, Pakistan
[2]Food and Biotechnology Research Centre, PCSIR Labs. Complex, Lahore-54600, Pakistan
*Corresponding author: roheena_abdullah@yahoo.com

Abstract

Proteases have gained commercial value due to multiple applications in different industrial sectors. The current research aimed to use cheaper agricultural waste for optimal protease production. The maximum level of protease production was achieved at 37 °C, an incubation period of 24 h, pH 9.0, inoculum size 3%, 1.5 g sucrose as a carbon source, and 30% moisture content by using solid-state fermentation. Ammonium nitrate and yeast extract tremendously increased protease production among the various inorganic and organic nitrogen sources. Ca^{2+} ions and Tween 40 showed optimal protease production among the tested metal ions and surfactants. Protease purification was carried out by ammonium sulphate precipitation followed by Sephadex G-100 gel filtration chromatography. The purification resulted in 1.3-fold of purified protease with 51.5U/mg specific activity and a total yield of 37.5 %. The molecular weight of purified protease was confirmed upon SDS-PAGE with a single band of ~36 kDa. The protease was stable over a temperature range of 35-45 °C and pH 7-9, with maximal activity at 40 °C and pH 9. The kinetic parameters Vmax (maximum rate) and Km (Michaelis-Menten constant) were calculated as 0.307 U/g and 11.2 mg/mL, respectively. The alkaline protease significantly dehair the goat skin and successfully removed the animal blood stain from cotton cloth.

Keywords: *Bacillus*; chromatography; protease; Sephadex G-100; soya bean meal.

1. Introduction

Proteases are the hydrolytic group of enzymes that cleave proteins by degrading peptide bonds (Niyonzima & More, 2015). Proteases are commercially important enzymes and have gained more attention among all the hydrolytic enzymes because of their wide range of industrial, environmental, and biotechnological applications. They play a vital role in the food, pharmaceutical, detergent, chemical, silk, and leather industries. Microbial sources are more widely exploited than any other source due to their simple production method (Das & Prasad, 2010). Proteases are produced by various major bacterial genera, including *Aeromonas, Arthrobacter, Alcaligenes, Bacillus, Halomonas, Serratia,* and *Pseudomonas*. *Bacillus* species are the chief source that secretes different extracellular soluble enzymes (Selvam *et al*., 2016). Solid state fermentation (SSF) has acquired economic interest due to its ability to utilize cheap raw materials. SSF is a process that involves a solid matrix and occurs without

free water. The substrate must contain adequate moisture to support the organism's metabolism and growth (Pandey, 2003). SSF has gained more interest over submerged fermentation because of reduced production costs by utilizing moderately processed or unprocessed raw materials (Adelere & Lateef, 2016; Çakmak & Aydoğdu, 2021). Additional advantages of SSF are superior productivity and improved recovery of products (Pandey *et al*., 2000). Production of the enzyme is generally influenced by media components, cultural factors such as time, pH, temperature, and nutritional factors, especially nitrogen and carbon sources, surfactants, and metal ions. Several studies used municipal solid wastes (MSW) as cheap raw materials to produce enzymes (Hasan *et al*., 2017; Iqbal *et al*., 2018; Hakim *et al*., 2018). The MSW comprises 65- 75-% of organic material, including carbohydrates, peptides, proteins, fatty acids, and their esters. These organic waste materials can be used as raw material in fermentation processes to produce pure and commercially essential products, reducing environmental pollution and other health hazards (Iqbal *et al*., 2015; Hasan *et al*., 2017; Iqbal *et al*., 2018;). However, very few studies have been done to produce enzymes with agricultural byproducts.

Thermo stability is one of the industrial enzymes major and unique properties, and it is beneficial because it reduces microbial contaminants. Purification overall involves the recovery of protein with a high degree of purity. Furthermore, the specific activity of enzymes is also increased by the purification process, making them more specific for different industrial applications.

The present work focused on the production, optimization of significant parameters, purification, kinetic analysis, and applications of alkaline proteases by *Bacillus subtilis* NCIMB-10144. This may satisfy the future need for alkaline proteases and open up the path for industrial applications.

2. Materials and methods

2.1 Microorganism

The strain of *Bacillus subtilis* NCIMB-10144 was taken from Industrial Biotechnology Laboratory, Food, and Biotechnology Research center, PCSIR.

2.2 Preparation of Inoculum

A loopful of *Bacillus subtilis* strain was aseptically transferred into the 50ml sterilized nutrient broth.   The inoculated broth was placed in a shaker at 37ºC, 150 rpm for 24 hours. The obtained vegetative cells after 24 h of incubation were used as inoculum.

2.3 Fermentation process

20 g of sterilized solid substrate moistened with 15 ml of sterilized mineral salt medium (g/100ml): $CaCl_2$, 0.5, NaCl 0.05, K_2HPO_4 0.5, $MgSO_4$, 0.05, Sucrose 1.5, Yeast extract 2, Ammonium nitrate 0.5 was inoculated with vegetative inoculum (1.0 mL) of *Bacillus subtilis* and incubated for 48h at 37 °C (Imtiaz *et al.,* 2013). After a fixed time interval, 50 ml of phosphate buffer (0.25M, pH 9.0) was added to each flask and placed for 30 min in a shaker

at 150 rpm. The enzyme solution was centrifuged at 6,000 rpm for 15 min and used for the estimation of enzyme activity (Shivasharana & Naik, 2012).

2.4 Proximate analysis

The physiochemical value of soya bean meal (i.e., moisture, fat, ash, and protein contents were evaluated according to AOAC (2000).

2.5 Protease assay and total protein content determination

The enzyme assay was measured by following the Anson (1938) method. One unit of protease activity is represented as "the amount of enzyme required to release 1μmol of tyrosine per minute from casein under standard assay conditions" (Bajaj *et al.,* 2009). At the same time, total protein was estimated by following the Lowry *et al*. (1951) method.

2.6 Enzyme purification

Three steps were used to purify the protease enzyme. Initially, the crude extract was precipitated to its saturation level by adding ammonium sulfate 50 -80% (w/v). The precipitated fraction was then recovered by centrifugation at 7000 rpm for 15 min (4 °C). After centrifugation, the obtained pellet was re-suspended in 0.05 M Tris-HCl buffer (pH 9.0) and finally dialyzed in dialyzing tubing (12,000 Da) against the same buffer overnight with two or three changes.

The dialyzed sample was subjected to a Sephadex column (G 100, Pharmacia; 1.5 cm x 30 cm) by using the FPLC system (Bio-Rad, Biologic LP, USA), which was pre-equilibrated with (pH 9.0, 0.05 M) Tris-HCl buffer. At the flow rate of 60 mL/h, the active fractions of 2 mL were collected with the same buffer. All the active fractions that showed the maximum protease activity were collected carefully and stored at −20 °C for further analysis.

2.7 Molecular weight determination

Molecular weight was determined according to the suggested method by Laemmli (1970).

2.8 Protease characterization

2.8.1 Effect of different temperatures, pH, and metal ions

To determine protease activity, the purified enzyme was incubated within the temperature range of 30-50°C for 10 min. Its stability was assessed between 30-50°C for 2 hours. However, the effect of different initial pH ranges (4-11) on protease activity was also evaluated. The optimal enzyme activity was investigated by using the following buffers (0.05 M) Citrate buffer (pH 4-5), potassium Phosphate buffer (pH 6-7), and Tris-HCl buffer (pH 8.0, 9.0, and 10.0). The residual activity of the protease enzyme was studied within a pH range of (4-11) for 2 hours. The impact of several metal ions (5 mM) on the protease activity was also tested for 30 min in different ionic solutions.

2.9 Applications of alkaline Protease

2.9.1 De-staining property of protease

A white cotton cloth (4cm x 4cm) was stained with animal blood. Afterwards, 1.0 mL of enzyme solution for the de-staining process was prepared as defined by Adinarayana *et al.* (2003) and applied for 50 minutes.

2.9.2 Dehairing agent

To perform the leather Dehairing process, the goat skin was cut into $4.5 \times 4.5\,cm^2$ size, washed, and dried. First, the hairy side of the goat hide was completely soaked into the mixture containing protease enzyme along with 14 % Sodium sulphide and lime. Later the piece was incubated at 37º C for different periods (3-18 h). However, goat hide treated only with distilled water without the addition of protease enzyme was used as a control. Each treatment's softness and hair loss were observed (Mukhtar & Haq, 2008; Nadeem *et al.,* 2010).

2.10 Statistical analysis

All the data were expressed as the average of three replicates in each experiment. The SPSS 22.0 version was used for all the statistical analyses.

3. Results and discussion

3.1 Screening of agro-residues as substrates for the production of protease

The current study conducted the protease production through SSF by *Bacillus subtilis* NCIMB-10144. SSF is an environment friendly technique and is greatly influenced by the nature of solid substrates. In addition, this solid material plays a dual role in fermentation by supplying nutrients to the microbial culture and anchorages the growth cells. In the present study various solid substrates (soya bean meal, wheat bran, and chickpea) were tested for the protease production. Figure 1a revealed that among all the substrates, the use of soybean meal significantly increased the enzyme activity in contrast to other substrates. This could be due to the reason that soya bean is a good source of proteinaceous nitrogen, carbohydrates, and other nutritious substances essential for the growth of bacteria. In continuation, different concentrations ranging from 5-30 g of soybean meal (SBM) were also tested for protease production. Figure 1b showed that the soybean meal at 5g gave maximal protease productivity a greater or lesser concentration of SBM than the optimal value resulting in less production. Present results agreed with Su *et al.* (2018), who reported a positive effect of soya bean meal on the protease production by *Clostridium butyricum*. Moreover, proximate analysis of the soya bean meal was also carried out. In Figure 2 high percentage of protein contents were observed in the soya bean meal compared to the crude fiber (CF), fat, moisture, and ash content.
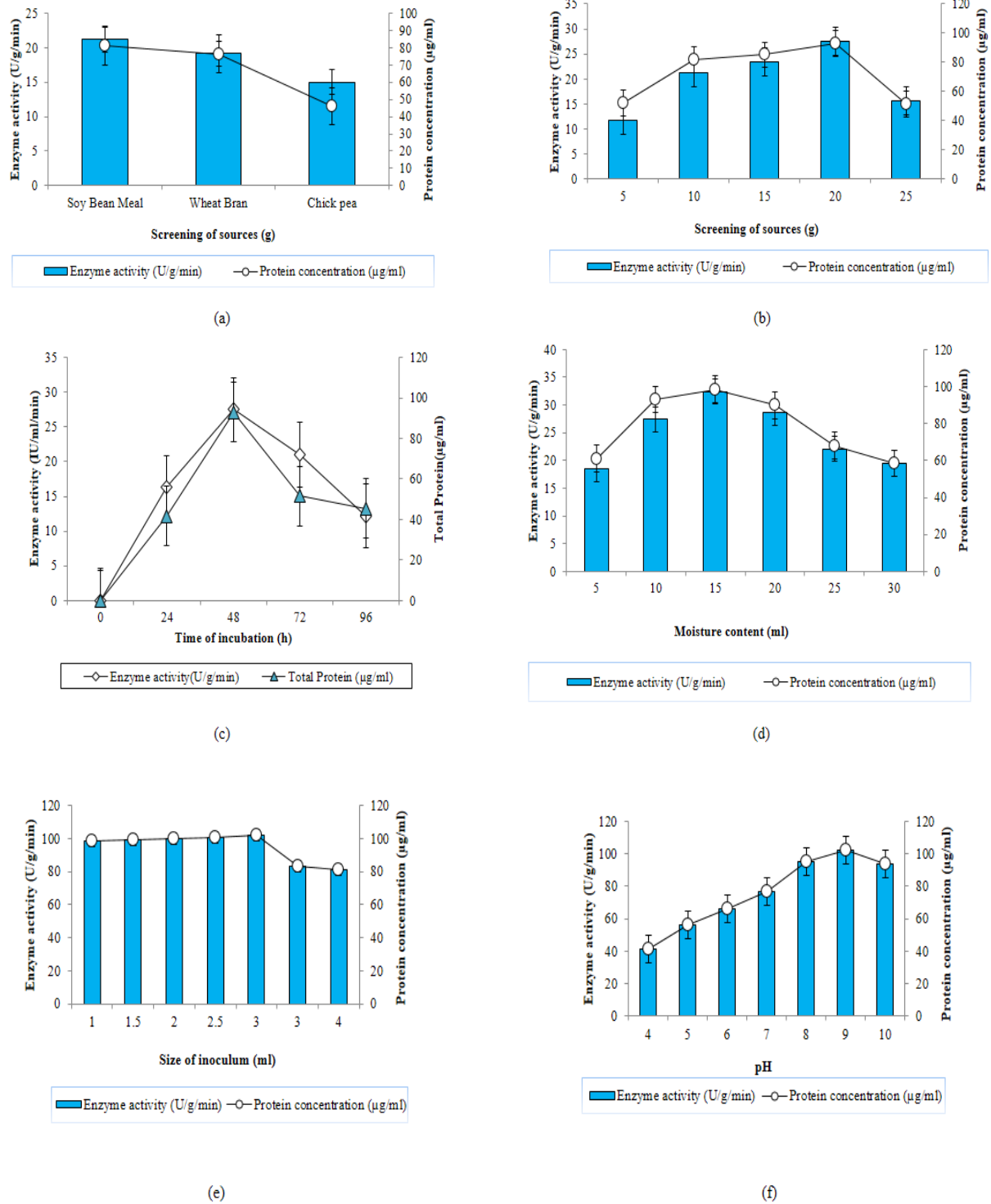
Fig. 1. Impact of various physical factors on the protease production by *Bacillus subtilis* NCIMB-10144 (a) Different substrates (b) Soya bean meal conc. (c) Time of incubation (d) Moisture contents (e) Size of inoculum (f) pH
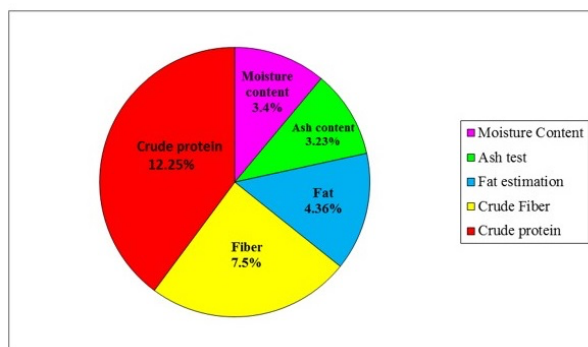
Fig. 2. Proximate analysis of soybean meal

3.2 Influence of incubation time and moisture content

Figure 1c depicted the impact of incubation time (0-96h) on enzyme production. Results revealed that the protease production gradually increased after 24 hours of incubation and reached a maximum at 48 hours. The decline in protease activity was noticed before and after the optimal incubation time. It could be due to the decomposition or denaturation of protease due to interaction with other compounds in the fermentation medium (Uyar & Baysal, 2004). *Bacillus* species generally produce optimum proteases in stationary or post-expression phases (Sharipova *et al*., 2000). However, depending upon the medium composition and other factors, it may produce maximum production in an exponential phase. Current results disagreed with George-Okafor and Mike-Anosike (2012), who reported maximum protease production after 72 h incubation.

In a solid state fermentation (SSF) water content of substrate is greatly influenced by the substrate's absorbing capacity and capillary forces. Moreover, moisture level significantly affects the substrate's physical properties, which makes it different from submerged fermentation. Figure 1d shows the impact of moisture content (5-30%) on protease production. Among all the levels, higher titers of protease enzyme were achieved at 15%. However, less production was observed with a further rise or drop in moisture content than 15%. It was believed that the increased amount of moisture content reduces the porosity of the substrate; thereby limiting the oxygen supply; on the other hand, lower moisture content causes sub-optimal growth and lowers the swelling of the substrate, which ultimately decreases protease production. The current study contradicts Akcan and Uyer (2011), who reported 30% moisture content for protease production.

3.3 Influence of different inoculum sizes and pH

Inoculum size is one of the main biological factors in enzyme production. Figure 1e depicted the impact of various inoculum sizes (1-4 %) on protease production. Among all the tested inoculum sizes, the maximum production was witnessed with 3.0 % of inoculum. Above or below the optimal level inoculum size influence the enzyme yield. A similar observation reported optimal protease production with 3 ml of inoculum (Muthulakshmi *et al*. 2011).

The pH of the fermentation medium helps in the enzymatic processes and the transportation of different components through the cell membrane. Figure 1f shows the effect of initial pH (4-11) on protease production. Results indicated a gradual increase in enzyme activity from pH 4 to 7; optimum production was noticed at pH 9. Current work agreed with Akcan and Uyer (2011), who reported maximum protease production at pH 9.

3.4 Effect of different carbon and inorganic-organic nitrogen sources

Nutrient sources were also found to be an important factor in protease production. Carbon is one of the primary nutrients for bacteria. The effect of carbon sources (sucrose, starch, maltose, fructose, and lactose) on the protease activity was also investigated. Figures 3a & b show that the maximal protease activity was achieved when sucrose served as the carbon source at 1%. Current work contradicts with Asha and Palaniswamy (2018), who reported lactose as the best carbon source for protease production. Nitrogen also serves as an important nutrient source next to carbon for protease production. The effect of inorganic nitrogen sources (ammonium nitrate, ammonium chloride, and ammonium acetate) and organic nitrogen sources (yeast extract, urea, tryptone, nutrient broth, and peptone) on protease production were studied. Among all the inorganic (Figures 3c &d) and organic nitrogen sources (Figures 3e & f), the maximum protease production was obtained with ammonium nitrate and Yeast extract at 0.5% and 2 %, respectively. Present results are in accordance with Badhe *et al*. (2016), who mentioned maximum protease production with yeast extract.
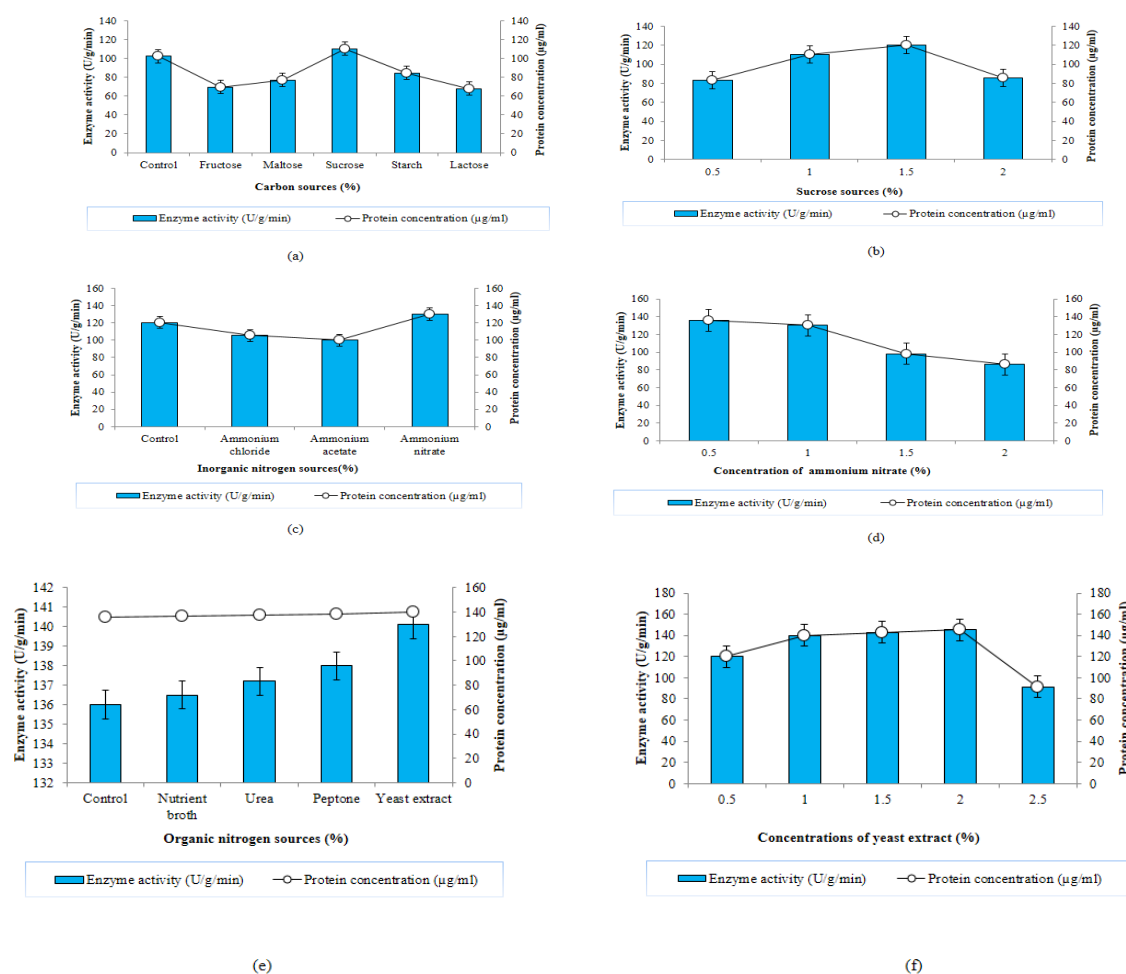

Fig. 3. Impact of various nutritional parameters on the protease production by *Bacillus subtilis* NCIMB-10144 (a) Carbon sources (b) Sucrose conc. (c) Inorganic nitrogen sources (d) Ammonium nitrate conc. (e) Organic nitrogen sources (f) Yeast extract conc.

3.5 Impact of various metal ions and surfactants

Metal ions play an important role in enzyme action and their structural modification. The influence of supplementation of metal ions ($CaCl_2$, KCl, $ZnCl_2$, and $MgSO_4$) and surfactants (Tween 80, Tween 20, Tween 40, and SDS) for protease production were also studied (Figures 4a & b). The results showed that adding of Ca^{2+} ions to the medium resulted in high protease activity. The use of surfactants significantly affected the extracellular enzyme production by bacteria, including *Bacillus* species (Nascimento & Martins, 2006). Figure 4c depicted that enzyme production was higher in the presence of Tween 40. Current research differs from Ananthan (2014), who reported the positive effect of Tween 80 by *Vibrio* sp.
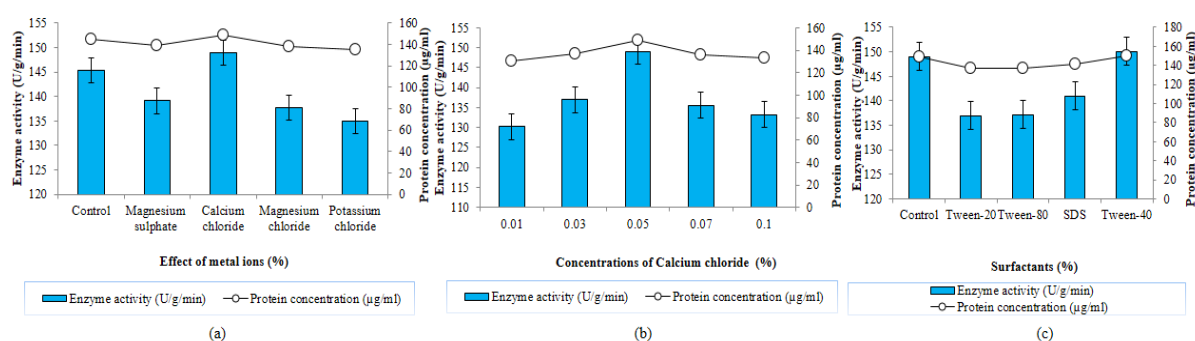
Fig. 4. Impact of metal ions and surfactant on the protease production by *Bacillus subtilis* NCIMB-10144 (a) Different metal ions (b) Calcium chloride conc. (c) Surfactants

3.6 Purification of protease

The purification scheme of protease by *Bacillus subtilis* NCIMB-10144 was presented in Table 1. Initially, the crude extract was precipitated with 80% ammonium sulfate. A 1.9-fold purification with 66.6 % yield purification along with 73.68 U/mg specific activity was obtained. Then, the concentrated active fractions were further purified using Sephadex-G 100 (Pharmacia) column (1.5 cm x 30 cm). Figure 5a shows the elution profile of the protease enzyme. The active fractions of the single peak indicated 1.3-fold purification with a purification yield of 37.5% and 51.5 U/mg of a specific activity. Current results are in accordance with Ravindran *et al*. (2011), who reported protease purification by Sephadex column (G-100). The purity of the protease enzyme was confirmed by a single band of ~36 kDa molecular weight (Figure 5b). Similar results were presented by Vijayaraghavan *et al*. (2016).

Table 1. Stepwise purification of protease enzyme

Sr #	Steps of Partial purification	Volume of enzyme (ml)	The specific activity of the protein (U/mg)	Total protein contents (mg)	Total activity of protease (IU)	Fold Purification	Yield percentage (%)
1	Crude enzyme	50 ml	38.3	99.5	103.4	1	100
2	$(NH_4)_2SO_4$ Precipitation	25.8	40.5	65.14	74.03	1.0	71.5
3	Dialysis	5	73.68	34.6	68.9	1.9	66.6
4	Sephadex-G 100	2	51.5	27.57	38.72	1.3	37.5

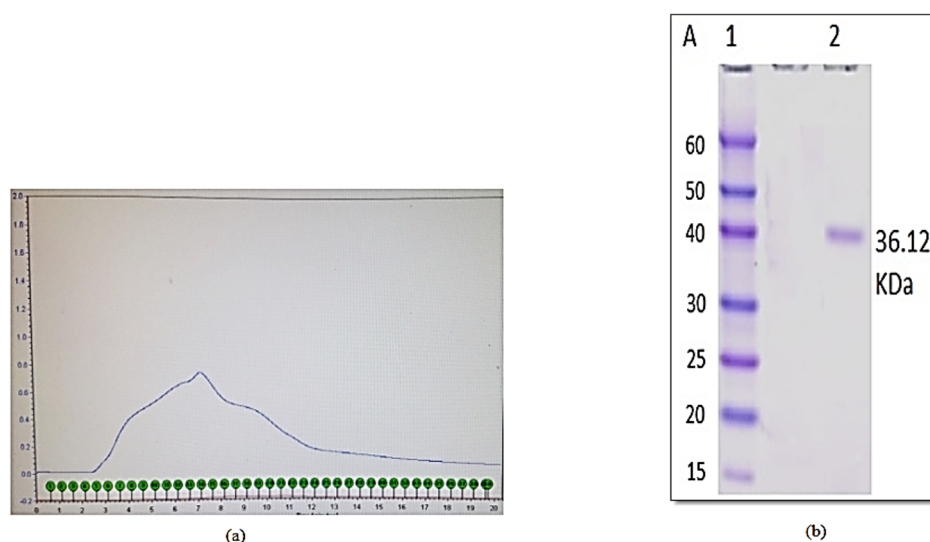(a)   (b)

Fig. 5. Purified alkaline protease (a) Elution profile on Sephadex-G 100
(b) Molecular weight on SDS PAGE

3.7 Characterization of protease

The maximum activity of purified protease was recorded at 40°C; it gradually decreased above 40 °C and gave minimum activity at 50°C. The protease retained 100% residual activity for 2 h of incubation at 40 °C (Figure 6a).

Usually, the commercially produced microbial proteases by *Bacillus* sp. have an alkaline pH range between 8 to 12 (Rao *et al*., 1998). In the current study, purified protease from *Bacillus subtilis*, NCIMB-10144, exhibited maximum activity at pH 9. It retained 97% activity at pH 9 and 50% at pH 11 (Figure 6b). In response to various metal ions, the Ca^{2+} ion positively regulates the optimal protease activity and stability (Figure 6c). These results follow the observations of Shivakumar *et al*. (2012). They reported maximum protease activity by Ca^{2+} ion.
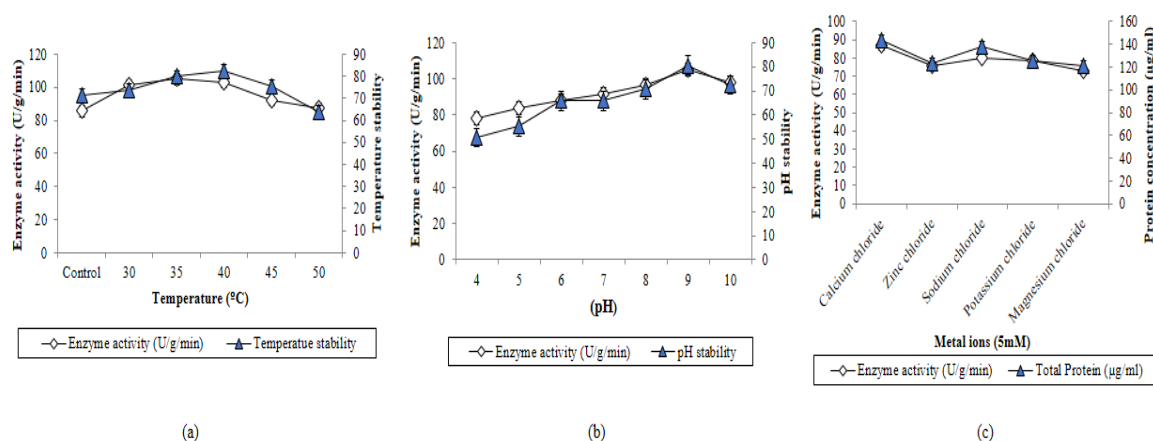

(a)   (b)   (c)

Fig. 6. Impact of protease activity and stability of purified protease by *Bacillus* s*ubtilis*
NCIMB-10144 (a) Temperature (b) pH (c) Metal ions

3.8 Kinetic analysis

The Lineweaver-Burk (LB) plot for the proteolytic reaction of casein revealed that the Vmax of the reaction was 0.307 U/g. The Michaelis-Menten constant (Km) was 11.2 mg/mL (Figure 7).
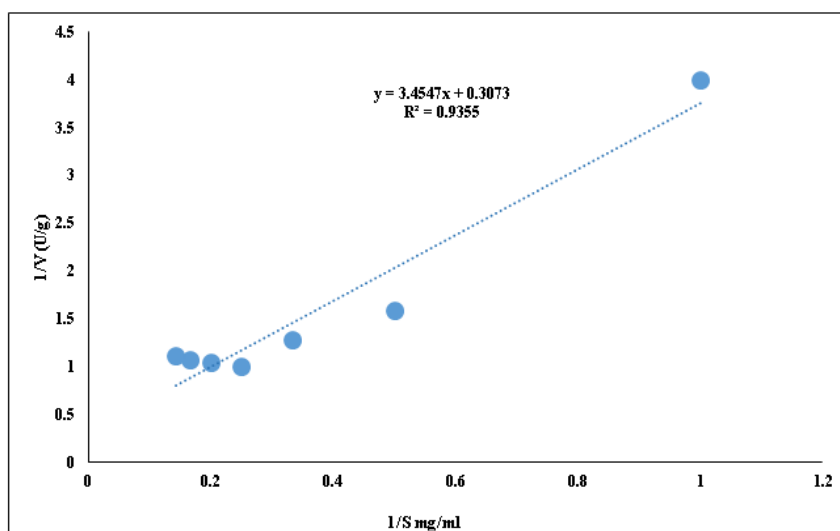

Fig. 7. Michaelis–Menten for protease activity

3.9 De-staining of blood

In the blood stain removal experiment, the compatibility of the protease enzyme was determined with the detergent. In the experiment, slight disappearance of blood stain was observed on the cotton cloth, which was washed only with the detergent, while no blood stain was removed from the cloth, which was soaked in the enzyme solution only. Contrary to this, blood stain was fully removed from the cotton cloth when dipped in 1 mL of the enzyme along with 1 ml (8 mg/mL) of detergent for 50 min (Figure 8). The experiment shows the cleaning effect of alkaline protease on white cotton cloth. It might be the reason that the protease enzyme enhances the stain removal property when used as an additive (Chimbekujwo & Moses, 2020). The present work was in accordance to Roshni *et al*. (2016), who used protease to remove animal blood stains from white cotton cloth.
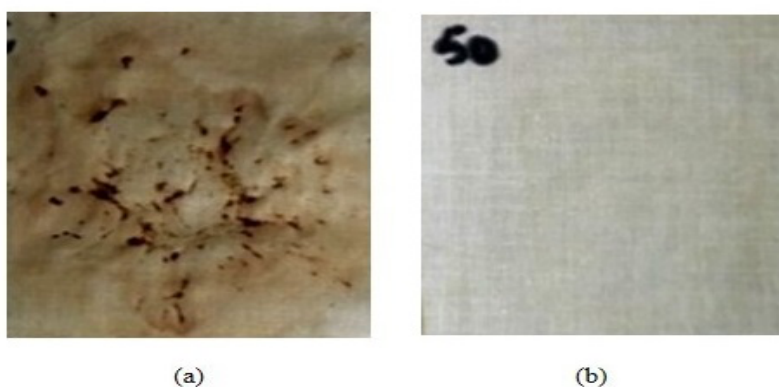

Fig. 8. Removal of blood stain (a) Control (b) Enzyme and detergent

3.10 The Dehairing of goat skin

Proteases produced from *Bacillus* sp. are proven efficient in leather processing (Zambare *et al*., 2007). In the current study, the Dehairing experiment successfully used protease on goat hide by removing the maximum amount of fine hairs. The protease enzyme can digest the collagen, so the Dehairing must be controlled to maintain the quality and avoid damage to the leather. Thus, the present results showed that the protease could be used in the Dehairing application. Figure 9b indicates that the complete dehairing of goat's hide was achieved after 15 h of incubation when treated with alkaline protease and sodium sulfate along with the lime; contrary to this, the skin that was treated only with distilled water (control) remained unaffected (Figure 9a). It was observed that the addition of the sodium sulphide de-haired the goat hide by removing all the hair above the epidermis due to which the leather did not become smooth and silky (Figure 9b). However, the protease enzyme attacked the hair below the epidermis and maintained the quality of the leather (Figure 9c) (Hakim *et al.,* 2018). A similar experiment was conducted by Hamza (2017), who used alkaline proteases on goat hide.
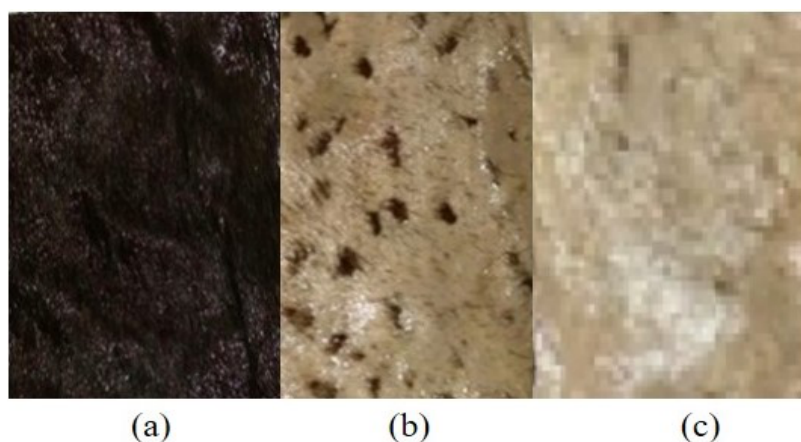

Fig. 9. Effect of protease on dehairing of goat hide(a) Control (b) partial hair removal from the goat hide (C) Full hair removal from the goat hide

4. Conclusion

In the current study, various physicochemical parameters were optimized for protease production. Considering as a cheap source soya bean meal was used as an ideal substrate for enzyme bioprocess. Furthermore, purified protease showed its stability and activity at high pH and temperature ranges. The practical application of blood stain removal from white cotton cloth and the Dehairing of goat hide indicates the potential use of alkaline protease in detergent and the leather industry.

References

Adelere, I. A. & Lateef, A. (2016). Keratinases: emerging trends in production and applications as novel multifunctional biocatalysts. Kuwait Journal of Science, **43**(3): 118-127.

Adinarayana, K., Ellaiah, P. & Prasad, D.S. (2003). Purification and partial characterization of thermostable serine alkaline protease from a newly isolated *Bacillus subtilis* PE-11. American Association of Pharmaceutical Scientists, **4**(4): 440-448.

Akcan, N. & Uyar, F. (2011). Production of extracellular alkaline protease from *Bacillus subtilis* RSKK96 with solid state fermentation. Eurasian Journal of Biosciences, **5**: 64-72.

Ananthan, G. (2014). Optimization of novel protease production through submerged fermentation by ascidian associated *Vibrio* sp. GA CAS2. World Journal of Pharmacy and Pharmaceutical Sciences, **3**(12): 756-770.

Anson, M.L. (1938). The estimation of pepsin, trypsin, papain, and cathepsin with hemoglobin. The Journal of General Physiology, **22**(1): 79-89.

AOAC. (2005). Official Methods of Analysis, Association of Officials. Analytical Chemists Washington DC, USA,

Asha, B. & Palaniswamy, M. (2018). Optimization of alkaline protease production by *Bacillus cereus* FT-1 isolated from soil. Journal of Applied Pharmaceutical Science, **8**(2): 119-127.

Badhe, P., Joshi, M. & Adivarekar, R. (2016). Optimized production of extracellular proteases by *Bacillus subtilis* from degraded abattoir waste. Journal of Bioscience and Biotechnology, **5**(1): 29-36.

Bajaj, B. K., Pangotra, H., Wani, M. A., Sharma, A. & Sharma, P. (2009). Partial purification and characterization of a highly thermostable and pH stable endoglucanase from a newly isolated *Bacillus* strain M-9. Indian Journal of Chemical Technology, **16**(5): 382-387.

Çakmak, M. & Aydoğdu, H. (2021). Screening of microfungi for lipolytic activity and optimization of process parameters in lipase production by solid substrate fermentation using selected microfungi (*Penicillium aurantiogriseum*). Kuwait Journal of Science, **48**(1): 98-105.

Chimbekujwo, K. I. & Moses, A. O. (2020). Purification, characterization, and optimization of protease produced by *Aspergillus brasiliensis* strain BCW2. Scientific African, **8**(2020): e00398.

Das, G. & Prasad, M. P. (2010). Isolation, purification, and mass production of protease enzyme from *Bacillus subtilis*. International Research Journal of Microbiology, **1**(2): 26–31.

George-Okafor, U. O. & Mike-Anosike, E. E. (2012). Screening and optimal protease production by *Bacillus* sp. SW-2 using a low-cost substrate medium. Research Journal of Microbiology, **7**(7): 327-336.

Hakim, A., Bhuiyan, F. R., Iqbal, A., Emon, T. H., Ahmed, J. & Azad, A. K. (2018). Production and partial characterization of dehairing alkaline protease from *Bacillus subtilis* AKAL7 and *Exiguobacterium Indicum* AKAL11 using organic municipal solid wastes. Heliyon, **4**(6): e00646.

Hamza, T. A. (2017). Studies on animal skin dehairing by alkaline protease produced from bacteria isolated from soil. International Journal of Scientific and Technology Research, **6**(8): 34-39.

Hasan, M. M., Marzan, L. W., Hosna, A., Hakim, A. & Azad, A. K. (2017). Optimization of some fermentation conditions for the production of extracellular amylases by using Chryseobacterium and Bacillus isolates from organic kitchen wastes. Journal of Genetic Engineering and Biotechnology, **15**(1): 59-68.

Imtiaz, S., Mukhtar, H. & Haq, I. (2013). Production of alkaline protease by *Bacillus subtilis* using solid-state fermentation. African Journal of Microbiology Research, **7**(16): 1558:1568.

Iqbal, A., Hakim, A., Hossain, M. S., Rahman, M. R., Islam, K., Azim, M. F. & Azad, A. K. (2018). Partial purification and characterization of serine protease produced through fermentation of organic municipal solid wastes by *Serratia marcescens* A3 and *Pseudomonas putida* A2. Journal of Genetic Engineering and Biotechnology, **16**(1): 29-37.

Iqbal, M. K., Nadeem, A., Sherazi, F. & Khan, R. A. (2015). Optimization of process parameters for kitchen waste composting by response surface methodology. International Journal of Environmental Science and Technology, **12**(5): 1759-1768.

Laemmli, U. K. (1970). Cleavage of structural proteins during the assembly of the head of bacteriophage T4. Nature, **227**(5259): 680-685.

Lowry, O. H., Rosebrough, N. J., Farr, A. L. & Randall, R. J. (1951). Protein measurement with the Folin phenol reagent. Journal of Biological Chemistry, **193**(1): 265-275.

Mukhtar, H. & Haq, I. (2008). Production of alkaline protease by *Bacillus subtilis* and its application as a depilating agent in leather processing. Pakistan Journal of Botany, **40**(4):1673- 1679.

Muthulakshmi, C., Gomathi, D. & Kumar, D. G. (2011). Production, purification, and characterization of protease by *Aspergillus flavus* under solid state fermentation. Jordan Journal of Biological Sciences, **4**(3): 137-148.

Nadeem, M., Qazi, J. I. & Baig, S. (2010). Enhanced alkaline protease production by a mutant of *Bacillus licheniformis* N-2 for dehairing. Brazilian Archives of Biology and Technology, **53**(5): 1015-1025.

Nascimento, W. C. A. D. 7 Martins, M. L. L. (2006). Studies on the stability of protease from *Bacillus sp*. And its compatibility with commercial detergent. Brazilian Journal of Microbiology, **37**(3): 307-311.

Niyonzima, F. N. & More, S. S. (2015). Purification and characterization of detergent-compatible protease from *Aspergillus terreus* GR. 3 Biotech, **5**(1): 61-70.

Pandey, A. (2003). Solid-state fermentation. Biochemical Engineering Journal, **13**(2-3): 81-84.

Pandey, A., Soccol, C. R., Nigan, P., Brand, D., Mohan, R., Mohan, R. & Roussos, S. (2000) Biotechnological potential of coffee pulp and coffee husk for bioprocesses. Biochemical Engineering Journal, **6**(2): 153-162.

Rao, M. B., Tanksale, A. M., Ghatge, M. S. & Deshpande, V.V. (1998). Molecular and Biotechnological Aspects of Microbial proteases. Microbiology and Molecular Biology Reviews, **62**(3): 597635.

Ravindran, B., Kumar, A. G., Bhavani, P. A. & Sekaran, G. (2011). Solid-state fermentation for alkaline protease production by *Bacillus cereus* 1173900 using proteinaceous tannery solid waste. Current Science, **100**(5): 726-730.

Roshni, C., Ram, K. V., Ravi, P. M. & Pooja, S. (2016). Study on isolation, optimization, and immobilization of alkaline protease produced by *Aspergillus flavus*. Research Journal of Biology, **4**(2): 19-25.

Selvam, K., Selvankumar, T., Rajiniganth, R., Srinivasan, P., Sudhakar, C., Senthilkumar, B. & Govarthanan, M. (2016). Enhanced production of amylase from *Bacillus sp*. Using groundnut shell and cassava waste as a substrate under process optimization: Waste to wealth approach. Biocatalysis and Agricultural Biotechnology, **7**(2016): 250-256.

Sharipova, M. R., Shakirov, E. V., Gabdrakhmanova, L. A., Balaban, N. P., Kalachewa, N. V., Rudenskaya, G. N. & Leshchinskaya, I. B., (2000). Factors influencing the cellular location of proteolytic enzymes of *Bacillus intermedius*. Medical Science Monitor, **6**(1): BR8-BR12.

Shivakumar, S. (2012). Production and characterization of an acid protease from a local *Aspergillus* sp. by solid substrate fermentation. Archives of Applied Science Research, **4**(1): 188-199.

Shivasharana, C. T. and Naik, G. R. (2012). Production of alkaline protease from a thermoalkalophilic *Bacillus specie* JB-99 under solid state fermentation. International Journal of Pharmaceutical and Biological Sciences, **3**(4): 571 - 587.

Su, L. W., Cheng, Y. H., Hsiao, F. S. H., Han, J. C. & Yu, Y. H. (2018). Optimization of mixed solid-state fermentation of soybean meal by *Lactobacillus* species and *Clostridium butyricum*. Polish Journal of Microbiology, **67**(3): 297-305.

Uyar, F. & Baysal, Z. (2004). Production and optimization of process parameters for alkaline protease production by a newly isolated *Bacillus sp*. Under solid state fermentation. Process Biochemistry, **39(**12): 1893-1898.

Vijayaraghavan, P., Arun, A., Al-Dhabi, N.A., Vincent, S. G. P., Arasu, M. V. & Choi, K. C. (2016). Novel *Bacillus subtilis* IND19 cell factory for the simultaneous production of carboxy methyl cellulase and protease using cow dung substrate in solid-substrate fermentation. Biotechnology for Biofuels, **9**(1): 63-73.

Zambare, V. P., Nilegaonkar, S. S. & Kanekar, P. P. (2007). Production of an alkaline protease by *Bacillus cereus* MCM B-326 and its application as a dehairing agent. World Journal of Microbiology and Biotechnology, **23**(11): 1569.1574.

Climate change and food security: Assessing the prospect for Kuwait using an economy-wide model

Ayele U. Gelan[1,*], Giles Atkinson[2]

[1]*Techno-economic Division, Kuwait Institute for Scientific Research (KISR), Kuwait*
[2]*Dept. of Geography & Environment, London School of Economics,London, UK*
*Corresponding author: augelana@gmail.com

Abstract

This study is concerned with food security effects of global warming in Kuwait. The Intergovernmental Panel on Climate Change (IPCC) approach to monitor impacts of human activities on climate change has essentially remained top-down. Hence, it fallen out of favour among end user communities. In this procedure, the needs of policymakers at national scale have been peripheral. Kuwait's food security is a good illustration of this. The study is implemented by applying a recursive dynamic computable general equilibrium model for Kuwait. The model was calibrated on Kuwaiti data to examine food security impacts of the five Shared Socio-economic Pathways. The simulation results indicate asymmetrical impacts on Kuwait's agriculture and food processing industries. Arid countries would benefit by enhancing national capacities to assess food security implications of global warming scenarios.

Keywords: Arid agriculture; food prices; food security; global warming scenarios; integrated assessment models.

1. Introduction

This study is concerned with food security effects of global warming in Kuwait. Kuwait's food security provides a useful focus to explore the IPCCs global scenarios. Indeed, Kuwaiti authorities would benefit from knowing impacts of exogenous shocks on the status of Kuwait's food security. In the context of global warming scenarios, food security effects are often assessed in terms of global warming either helping or hindering food production depending on biophysical conditions and agro-ecological zones of the country in question (FAO *et al*., 2018). Regional and national targets are often indirectly drawn using assessments by the IAV modelling communities. These often work with high resolution remote sensing and geographical information systems to draw food production implications of global targets set according to IAM projections (Phetheet *et al*., 2021; Uchiyama & Stevenson, *et al*., 2020, Nebie *et al*.,2021).

Food security in arid countries is often affected by what happens elsewhere. That is, production conditions in food exporting countries and how those changes affect demand and supply relationships for food products and hence food prices in the world market. Integrated Assessment models (IAMs) often work with exceedingly coarse regional groupings, lumping extremely heterogeneous regions into one group (Moss *et al*., 2008). For instance, in some IAM models, the MAF region lumps together the Middle East and Africa (Gütschow, *et al.,* 2020, Happman *et al*., 2019).

The current study is implemented by applying a recursive dynamic CGE model for Kuwait. It examined food security impacts of five IPCC Shared Socio-economic Pathways (SSP). A world food price index (WPI) was constructed and used as an exogenous variable to shock the Kuwaiti national model through its influence on food imports prices.

The remainder of this paper is organized as follows. Section 2 highlights the global scenarios and socio-economic pathways. Section 3 provides an overview of the Kuwaiti recursive dynamic CGE mode. Section 4 discusses simulation results. Section 5 presents concluding remarks.

2. Global climate change scenarios

The IPCC approaches to developing its global climate change scenario have undergone two rounds of revisions. These are briefly discussed in this section.

2.1 The Special Report on Emissions Scenarios (SRES)

The procedure for monitoring GHG emission in scenarios was initially formalized in the Special Report on Emissions Scenarios (SRES) (Nakicenovic *et al.,* 2000). This took a sequential approach, which begins with specifications of scenarios for major drivers and associated CO2 emissions (left hand side of Figure 1). At an early stage, the IPCC was closely coordinating and leading efforts by IAM communities. Population, GDP, and technology assumptions developed in stage 1 and the associated CO2 emissions cascaded down to stage 2, radiative forcing, which denotes increases in temperature and global warming effects.

In stage 3, outputs of stages 1 and 2 are fed into climate change models to undertake projection by global scenarios. The IAV implications of the climate changes are assessed in the final stage of the sequential approach (stage 4).
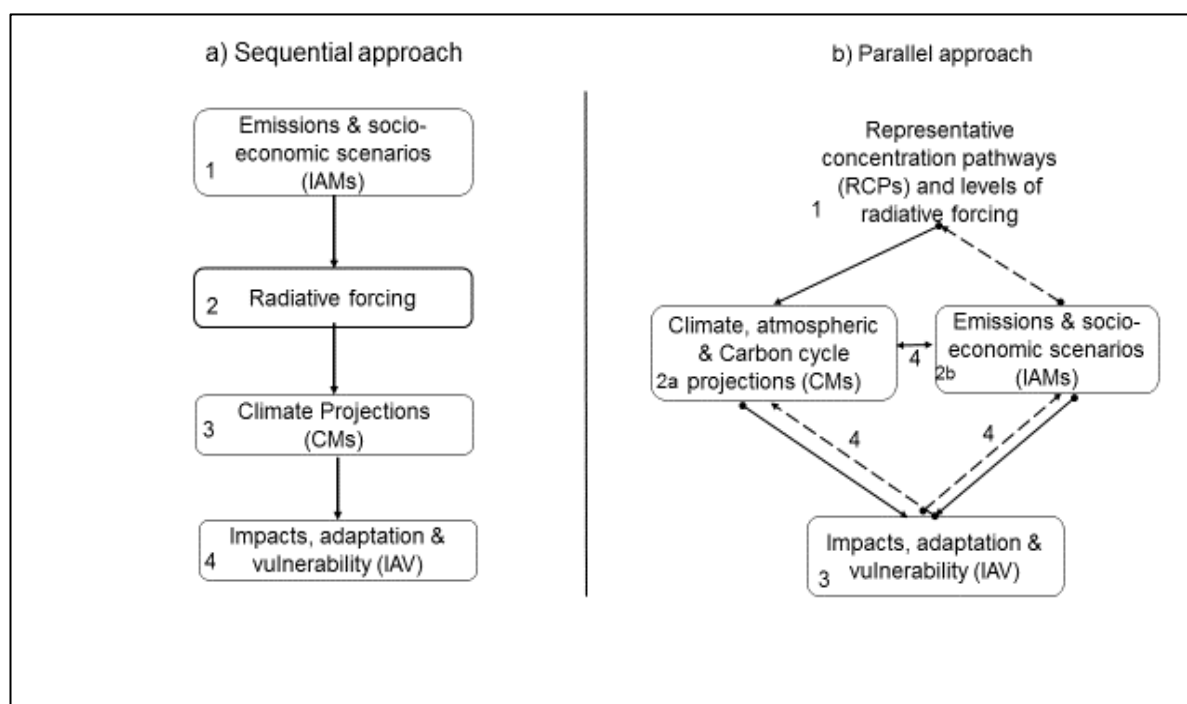

Fig. 1. Approaches to developments of global scenarios. Source: Moss *et al*. (2008**)**.

The sequential approach fell out of favor among many end user communities (in climate change and IAV modelling). Moss *et al.* (2008) discusses the circumstances surrounding a shift to the parallel approach (the right-hand side of Figure 1). Climate modelers were not supposed to start their activities until outputs from the IAMs were released. The IAV communities had to wait for releases from climate change models (CM) results. This led to a shift to the parallel approach, which created room for different end user communities to operate independently (Moss *et al.,* 2008).

While the concerns of the modeling community as one end user group seems to have been addressed through a move to the parallel approach, it seems concerns of policy practitioners have remained unaddressed, subjecting the IAM models to serious criticisms regarding their top-down approach (Gambhir *et al.* 2019, Kebede *et al.* 2018).

2.2   Shared socioeconomic pathways (SSP)

SRES was replaced by a new set of scenarios referred to as Shared Socio-economic Pathways (SSP) (O'Neill *et al.,* 2014). The change was made to recognize the fact that human activities or anthropogenic factors are responsible for not only driving climate change but also facilitating or hindering policy response measures such as mitigation and adaptation strategies (Huppmann *et al.* 2019; IPCC 2019, Riahi *et al.,* 2017; Kristie *et al.,* 2014).

Five distinct SSPs were identified. The ranges in global warming scenarios (expressed in terms of Representative GHGs Concentration Pathways (RCPs) were pretty much as specified in the previous global scenarios (SRES). However, each SSP was separately mapped to the RCPs in different ways. Riahi *et al.* (2017) presents a concise description of the SSP narratives.

- SSP1: Sustainability – taking the green road (low challenges to mitigation and adaptation)
- SSP2: Middle of the road – medium challenges to mitigation and adaptation
- SSP3: Regional rivalry – a rocky road (high challenges to mitigation and adaptation)
- SSP4: Inequality – a road divided (low challenges to mitigation, high challenges to adaptation)
- SSP5: Fossil-fuelled development – taking the highway and economic growth first (high challenges to mitigation, low challenges to adaptation)

The latest IPCC report focused on "greenhouse gas (GHG) fluxes in land-based ecosystems, land use and sustainable land management in relation to climate change adaptation and mitigation, desertification, land degradation and food security" (IPCC, 2019, p. 6).

Kuwait's agricultural activity trends are assumed to follow patterns reflected in the IAM projections for the MAF region to which Kuwait belongs. Since imports constitute the bulk of the country's food supply, Kuwait's food security is greatly influenced by what happens to food prices in the world market. Changes in these food prices depend critically on excess demand for food: balance of changes between demand and supply (production).

3. The Kuwaiti National Model

The global scenarios described in the preceding section were evaluated using an economy-wide national model developed for Kuwait. The model was calibrated on Kuwait's comprehensive socioeconomic database, a Social Accounting Matrix (SAM), which was constructed with 2013 as its base year (Gelan, 2018).

The Kuwaiti model was reformulated to suit the SSP scenarios on Kuwait's food security. Given the SSP scenarios long-term projections, the impacts can be evaluated using a recursive dynamic CGE model that corresponds to IPPC SSP scenarios run from 2010 to 2100. The shock applied to the model was related to long-term food price scenarios in the world market corresponding to each SSP.

The food price effects of imbalances between demand and production were captured by altering relationships in the food import functions in the model, specifically the relationships between food prices in domestic and world markets.

$$PM_{C,T} = pwm_{C,T}(1 + tm_{C,T}) * EXR_T + \sum_{CT} PQ_{CT,T} \, icm_{CT,C,T} \tag{1}$$

Where
Subscripts:
C, CT: commodities and trade services respectively
T: time
Parameters:
tm: import tariffs
pwm: world market price of imports
icm: trade margins
Variables
PM: domestic prices of imports
EXR: exchange rate
PQ: composite price of commodities

Equation 1 represents import price formation, whereby domestic sales price of imported food products are given as a function of world market price, import tariffs, exchange rate, and domestic trade margins.

The standard import function displayed in Equation 1 was reformulated to suit the purpose of this study:

$$PM_{C,S,T} = pwm_{C,S,T} WPI_{C,S,T} * (1 + tm_{C,S,T}) * EXR_{S,T} + \sum_{CT} PQ_{CT,S,T} \, icm_{CT,C,S,T} \tag{2}$$

Equation 2 differs from equation 1 in two respects. First, the introduction of an additional subscript, S denoting scenarios, and the world price index (WPI), which is multiplied by the world market price (pwm). If the value of WPI is greater than 1, then the value of PM will increase: i.e. domestic sales prices of imported food will rise, and vice versa.

Increases in prices of imported food items affect the relationships between demand for domestic products and imported products. The expected change in this relationship is given in equation 3.

$$\frac{QM_{C,T}}{QD_{C,T}} = \left(\frac{PD_{C,T}}{PM_{C,T}} \frac{\delta q_{C,T}}{(1-\delta q_{C,T})} \right)^{\frac{1}{1+\rho q_C}}$$ (3)

Where
Parameter
δq: share of domestic products in total demand
$\rho q = (1/\sigma q) - 1$: where σq is elasticity of substitution in the commodity demand function
Variables
QD, PD: quantity and price of domestic products
QM, PM: quantity and price of imports

When WPI > 1, then the value of PM increases in equation 2. This enters the import demand function in equation 3. If PM increases, then PD/PM falls, and hence QM/QD falls too. If SSP scenarios cause world market prices to rise, this is bound to encourage local primary production, but discourages local food processing.

4. Simulation experiments

4.1 Constructing the long term World food Price Index (WPI)

IPCC's IAM have not yet produced price projections by SSPs. Hence, it was necessary to derive world market price indices (WPI) using indirect methods from food demand and production relationships presented in the long-term projection by SSPs on crop production and demand relationships, separately for World and the MAF region. The projections were obtained from the SSP database (Riahi *et al.,* 2017). The SSP projections were made from 2005 to 2100. Given the base year of the Kuwaiti SAM was 2013, it was necessary to drop 2005 and adopt 2010 as a base year, which is closer to 2013. In order to show the position of the Middle East and Africa region relative the world average, the projected figures were converted to indices as changes from the 2010 baseline year scenario.

The most relevant factor in determining world market price trends is imbalance between demand and supply. Table 1 presents gaps between demand for crops and supply of crops at global scales. Having decided demand and supply imbalance as a suitable variable to serve as proxy to calculate WPI, then we turn our attention to describing methods used to calculate the indices by SSPs. This is derived by using the following relationship:

$$WPI0_{C,S,T} = \frac{Log(D_{C,S,T})}{Log(P_{C,S,T})}$$ (4)

Where
Subscripts
C: Food products
S: scenarios, SSP1... SSP
T: denotes decades, 2010, 2020,...,2100.
Variables
WPI0: World price index derived from excess demand function
D: Demand for crops

P: Production of crops

Two food product categories were considered. The first was primary agricultural products. In the baseline database, agricultural activities are aggregated into a single industry producing a composite agricultural product: "primary agricultural product". The second was processed food, which comes from the food-processing branch of manufacturing. Food security is affected by what happens to production conditions of these two branches of Kuwait's domestic food sectors, which in turn are firmly linked to food prices in the world market.

Table 1. World market price indices (WPI) by SSP (2010 = 100)

	2010	2020	2030	2040	2050	2060	2070	2080	2090	2100
SSP1	1.0000	0.8595	0.9646	1.0016	1.0518	1.1173	1.1826	1.2568	1.3363	1.4214
SSP2	1.0000	0.8609	0.9773	1.0378	1.0947	1.1616	1.2319	1.3047	1.3834	1.4670
SSP3	1.0000	0.8624	0.9687	1.0031	1.0748	1.1452	1.2181	1.2943	1.3727	1.4561
SSP4	1.0000	0.8597	0.9708	1.0569	1.1224	1.1893	1.2642	1.3425	1.4239	1.5090
SSP5	1.0000	0.8607	0.9748	1.0756	1.1501	1.2188	1.2945	1.3745	1.4612	1.5539

Source: Derived by the authors based on information obtained from Riahi *et al.* (2017); FAO (2018).

The world market food price indices (WPI0) were derived from SSP projections of excess demands for crop. However, the indices may not necessarily reflect the level of price changes. For this reason, WPI0 would need to be adjusted so that the indices come closer to prices changes reported in the literature. First, price changes compiled from various studies varied from 3% to 84%, but the extent of price changes implied by WPI0 fell short of these figures. Second, in its publication entitled "The future of food and agriculture – Alternative pathways to 2050", FAO (2018) reported price increase scenarios. The FAO projections were used to adjust and upscale the WPI0. The adjusted figures are reported in Table 1.

The simulation experiments were conducted by running a recursive dynamic model 50 times (S x T), five scenarios (SSP1 to SSP5) and years in decades (2010 to 2100). It is important to note WPI takes a value of unity for the "base" for 2010.

4.2 Results and discussion

4.2.1 Domestic prices of food products

The SSP projections discussed below typically undertake long-term scenario analysis. Accordingly, Figure 2 displays imported food prices on the vertical axis and years in decades on the horizontal axis. This indicated drops in food prices in the near term, up to 2030, implying excess supply over demand and hence declines in prices of crops in the world market. However, supply will fall short of demand beyond 2030 and the gaps would get wider for the subsequent decades.

In Figure 2 SSP5 depicted the highest of all the scenarios for the period beyond 2030. In Equation 2, WPI entered the import price function, multiplying the exogenous world prices of imported food products (pwm). The differences in prices of imported food products reflects the

WPI value reported in Table 1 and the translations of those values to domestic import prices of food displayed in equation 2. All SSP scenarios show sharp increases in prices of imported food products. SSP5 projects a nearly 4.5-fold increase from the 2010 level while in the SSP1, the sustainability scenario is expected to lead to nearly 2.5-fold increase in imported food prices. The other scenarios fall in between these extremes.
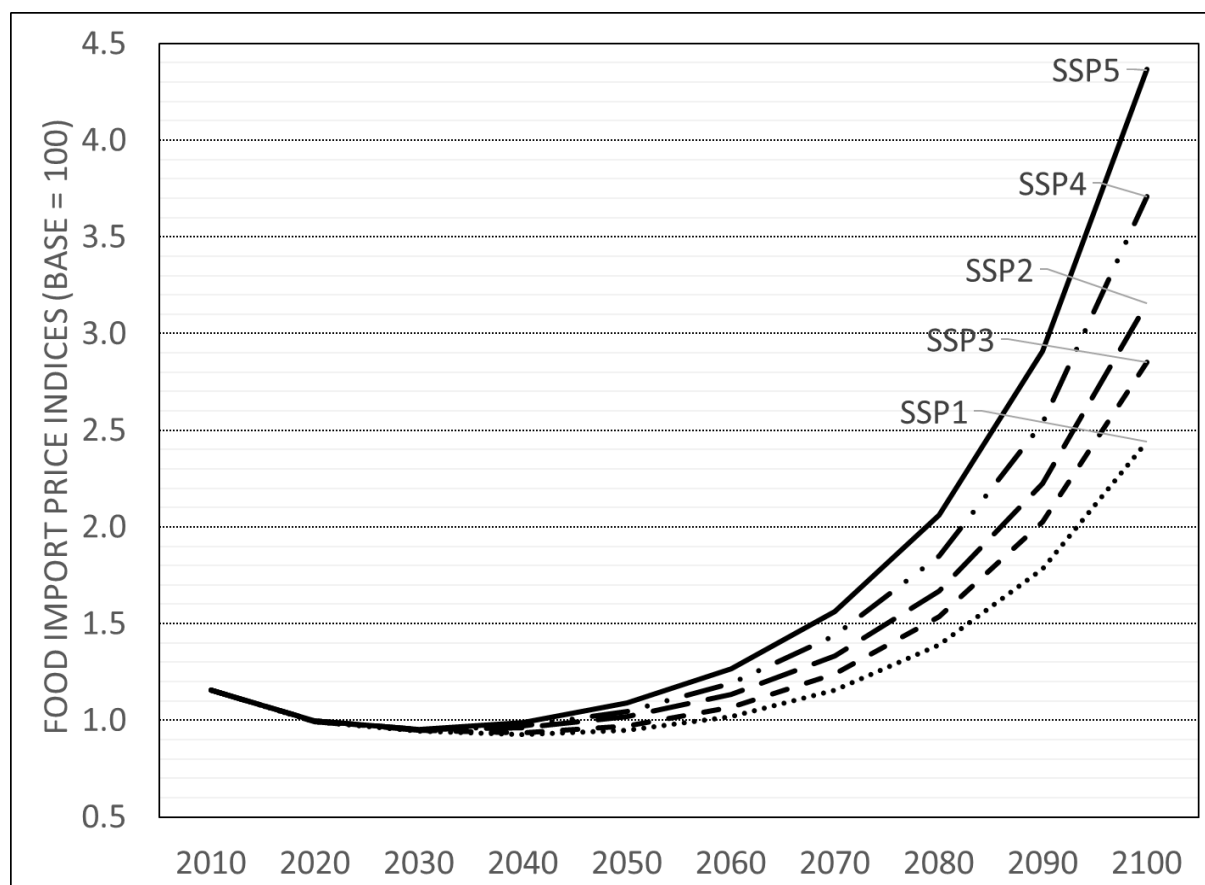

Fig. 2. Import price effects

The differences in import price scenarios reflect underlying assumptions adopted in constructing the SSP scenarios. SSP1 and SSP5 portray two sharply contrasting features. The world population growth assumptions for SSP1 and SSP5 are similar, but GDP growth scenarios do sharply contrast. SSP5 (economic growth first scenario) projects global GDP nearly three times to that reported under SSP1 (sustainability scenario). SSP5 is characterized by high material intensity and waste both in production and consumption, while the opposite is true with SSP1.

4.3   Aggregate food production effects

The domestic output index reported in Figure 3 is the weighted average of primary and processed food products. The differently shaded SSP5 comes closest to what would be Kuwait's status quo scenario: i.e. fossil fuel-based growth, the current trajectory.
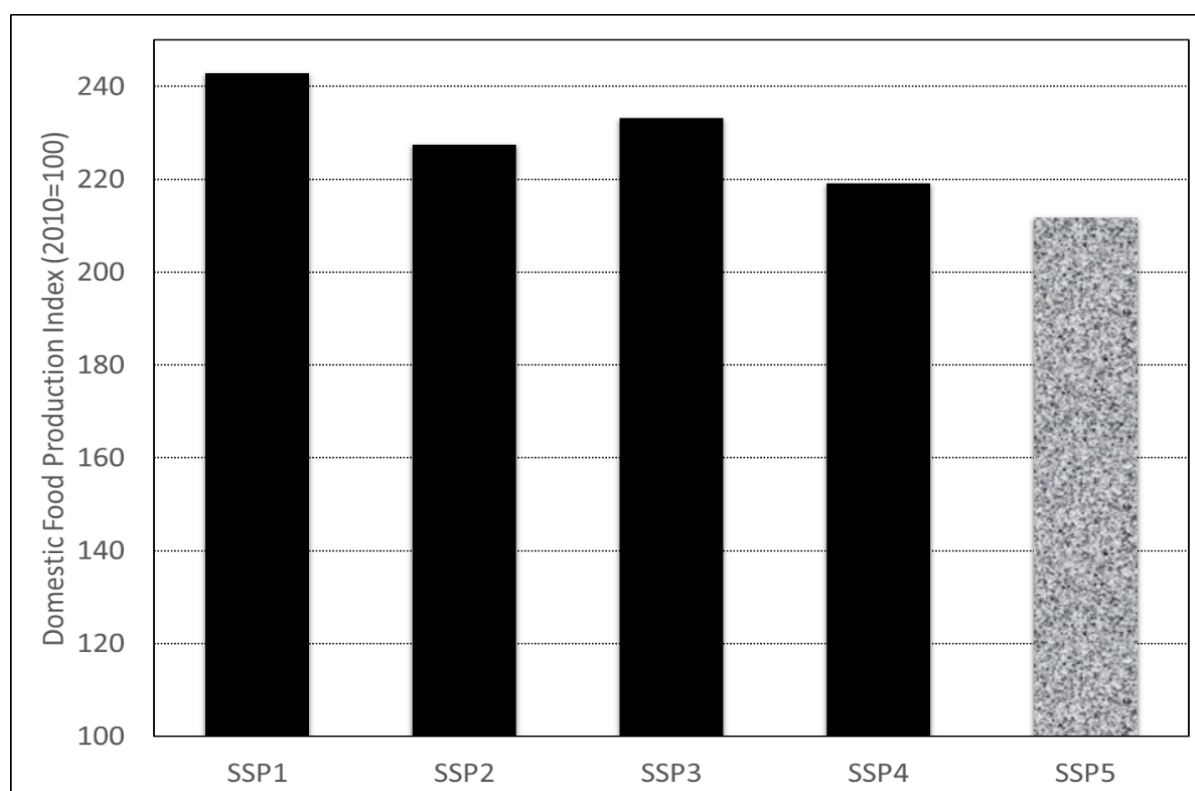
Fig. 3. Aggregate domestic food production effects

Domestic food production effects contrast with changes in prices of food products in the world market. The possibility of expanding Kuwait's primary agricultural production is severely constrained by biophysical conditions. However, within the limits set by the country's arid natural environment, there have been expansions of farming activities, historically, aided by substantial government support. Therefore, the model was specified considering these realities.

SSP5 has the highest import price increases and hence it yields the lowest domestic food output increase. The output of processed or manufactured food has much larger weight in Kuwait's domestic food production. Increases in imported food prices hurt food processing, since the bulk of Kuwait's food processors import inputs. This gives the lowest domestic food production level in the SSP5 scenario. Given it yielded the lowest price increase, SSP1 caused the largest increase in processed food production, because it offers cheaper imported inputs for the domestic industries. Kuwait's domestic food production is likely to be higher in SSP5 than all other SSPs. Under all conditions of global warming and related socioeconomic pathways, Kuwait is likely to increase domestic food production, mostly domestic food processing relying on imported inputs.

4.3.1 Disaggregated food production effects

Figure 4 disaggregates the domestic food production effects already reported in Figure 3 into primary and processed food counterparts. Given its greater weight in the composition of domestic food production, the pattern of changes across the scenarios for the processed food remained much as in Figure 3, the highest increase in SSP1 and the lowest in SSP5.

Disaggregation highlights interesting insights for the primary agricultural production effects. Importantly, it reveals contrasting fortunes for primary and secondary food production systems. Higher import prices have contractionary effects on food processing resulting in an increase in the cost of production, given the bulk of intermediate inputs are imported (e.g. cereals for flour-mills, even powder milk for dairy processing plants, etc.).

An increase in world market prices for primary farm products means domestic production of primary products become more competitive. This creates favorable conditions for primary agricultural production; a positive influence on Kuwait's food production system. Given we considered SSP5 to be closer to the status quo, the global warming and socioeconomic pathways means limited prospects to expand Kuwait's primary agricultural production.
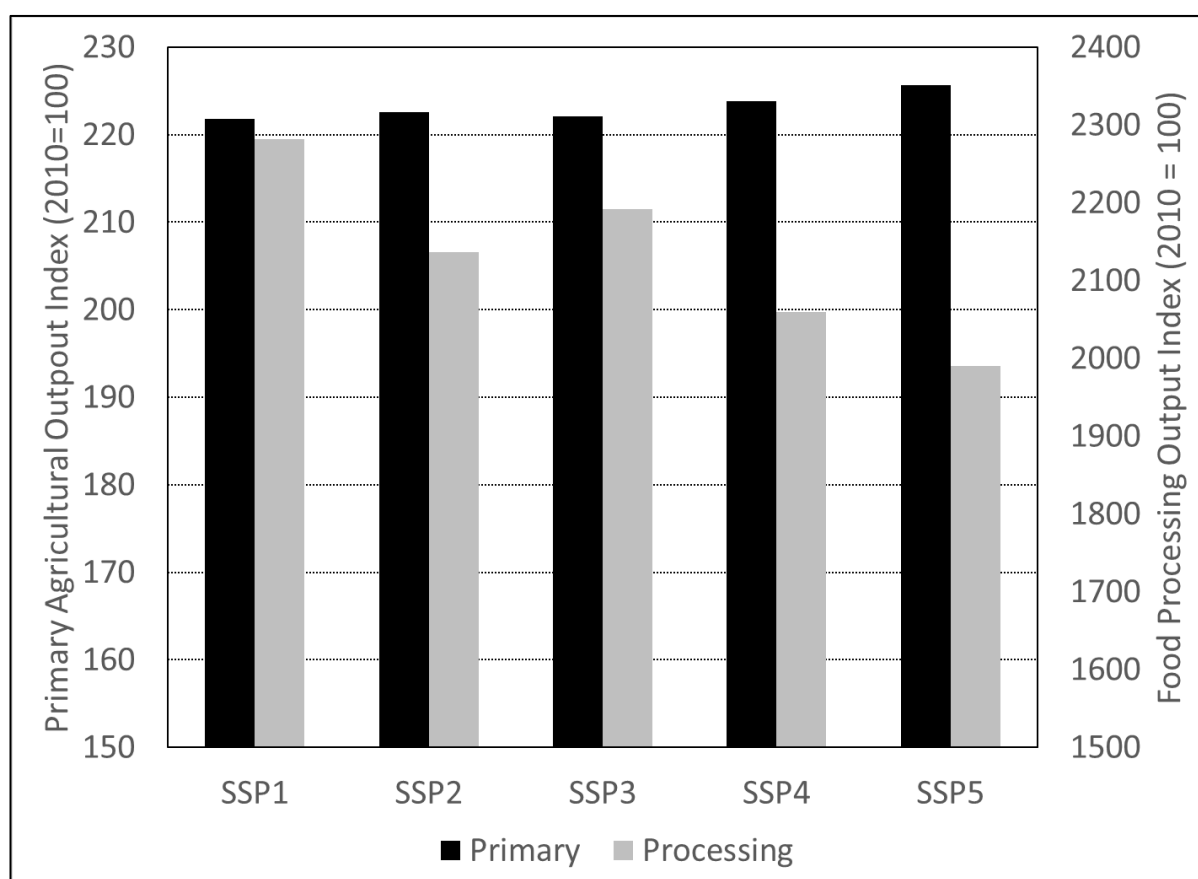

Fig. 4. Primary and processed food production effects

Broadening the scope of analysis is likely to reveal constrained outcomes for primary food production in Kuwait. First, it is likely that existing generous government subsidies are not sustained, particularly due to falling oil revenues and government budget constraints. Second, increasing GHG emission controls means the Kuwaiti farms will not be allowed to utilize energy at the current rate. Finally, water scarcity is likely to worsen. The simulation results displayed in Figure 3 regarding primary agricultural output are thus likely to represent a conservative estimate. Primary agricultural output is unlikely to increase even at the rate displayed in SSP1.

4.3.2 Food import effects

The food production results discussed in the preceding sections were presented with domestic food production and its long-term dynamics. However, overall food supply consists of domestic production and imports. Except for differences across the SSP scenarios with regard to domestic food production (primary plus processed), ultimately Kuwait is bound to rely on imports to feed its rapidly growing population.
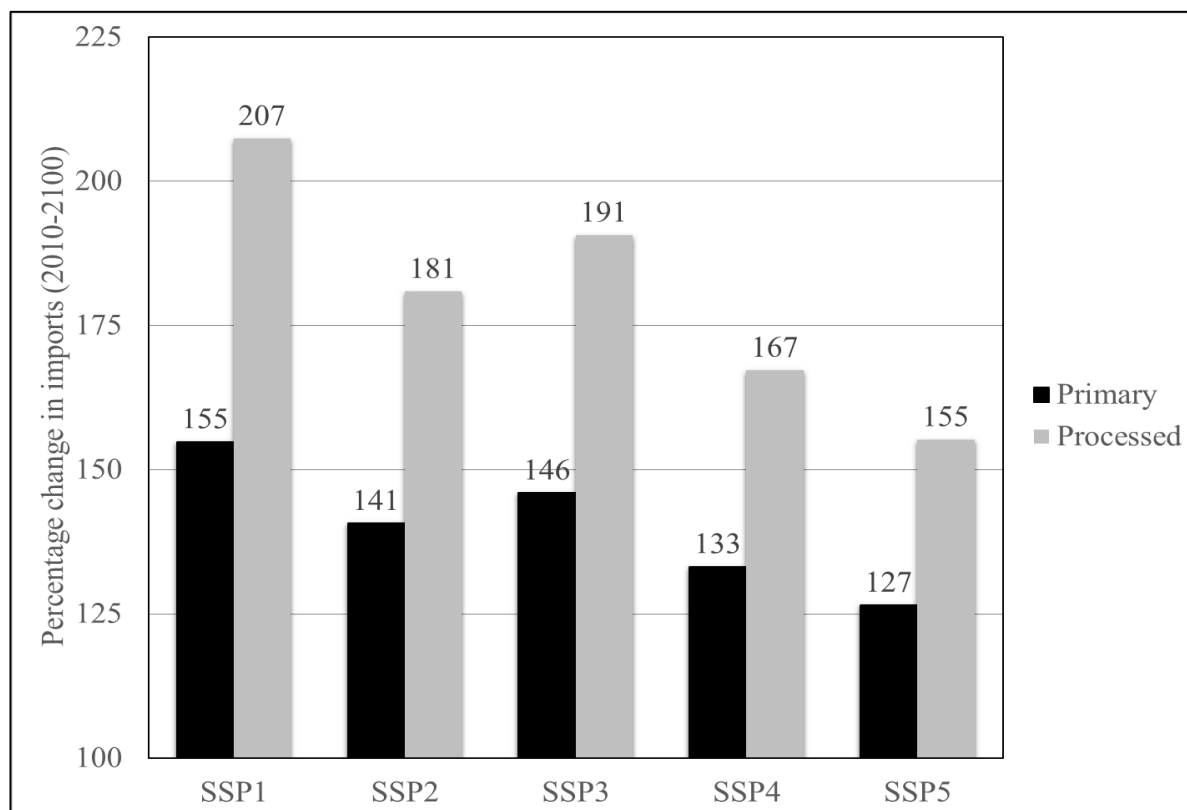

Fig. 5. Primary and processed food import effects

Figure 5 presents percentage changes in the level of food imports between the initial and final periods, 2010 and 2100. A rise in primary food imports is projected from 127% (SSP5) to 155% (SSP1). The corresponding percentage increases for processed food would be 155% and 207% respectively. These results are likely to represent conservative estimate of Kuwait's future food imports. The results reported in this study hinge on projected world market prices. If food prices increase by larger proportions, causing food import increases to be much higher than the results reported.

5. Conclusions

Food price variability in the world market have always been a major source of concern for Kuwaiti policymakers. Securing its food supply hinges on production conditions in food exporting countries. Adverse exogenous shocks at global scale can cause deterioration in Kuwait's food security. Sudden shocks like COVID-19 have disrupted global trade in a relatively short span of time. Climate change is a different category of adverse shock. Here

changes occur slowly but steadily over a long-term horizon. While ad hoc and one-off shocks like COVID-19 can be reversed, long-term shocks would prove to be long-lasting and not easily reversible.

In this simulation experiment, WPI increases varied from over 4.5 and 2.5 times in SSP5 and SSP1, respectively. In the IPCC scenario, SSP5 is associated with "economic growth first", fossil fuel and material intensity in both production and consumption. However, SSP1 was associated with "green growth", most favorable to sustainability. This implies the worst scenario would be the projection of WPI in the business as usual scenario. In other words, Kuwait would expect to pay less for food imports with alternative SSP scenarios than if the current trend continued in the long-term.

The experiments were conducted by classifying domestic food production into primary agricultural production and food processing manufacturing sectors. In aggregate, Kuwait is expected to produce more food domestically with the alternative sustainability scenario. However, the increase in domestic production is expected to come more from food processing and adding value to the food value chain. SSP1 offered a relatively cheaper food import scenario, with cheaper intermediate inputs of primary food products. Cheaper primary agricultural products mean less favorable conditions for local primary producers. SSP5 has already been favoring local agricultural production, which survived by not only large subsidies but also rising food prices in the world market. SSP5 simply projects the current situation into the longer time horizon.

Inevitably, Kuwait will continue to import food, both primary and secondary. The food import-value index rose by just over 200, double the current level. These results are likely to represent conservative estimates of Kuwait's future food imports. The results reported depend on projected world market prices, and results reported are likely to be conservative especially if food prices increase by larger proportions. Sensitivity analysis of the results obtained to the key parameters was not conducted in this study. This emanates from the relatively wide scope of the study ranged from simulation experiments to report. The above drawback will be addressed in subsequent research.

ACKNOWLEDGMENTS

References

FAO (2018) The future of food and agriculture – Alternative pathways to 2050. Retrieved from Rome. http://www.fao.org/global-perspectives-studies/resources/detail/en/c/1157074/.

Gambhir A., Butnar, I., Li, P., Smith, P., Strachan, N. (2019) A Review of Criticisms of Integrated Assessment Models and Proposed Approaches to Address These, through the Lens of BECCS. Energies, 12(**3**): 1-21.

Gelan, A. (2018) Kuwait's energy subsidy reduction: examining economic and CO_2 emission effects with or without compensation. Energy Economics, 71: 186-200.

Gütschow, J., Jeffery, M. L., Günther, A., and Meinshausen, M. (2020) Country resolved combined emission and socio-economic pathways based on the RCP and SSP scenarios. Earth system science data. https://essd.copernicus.org/preprints/essd-2020-101/essd-2020-101.pdf

Huppmann, D., Kriegler, E., Krey, V. Riahi, K., Rogelj, J., Calvin, Zhang, R., *et al.* **(2019)** *IAMC 1.5°C Scenario Explorer and Data hosted by IIASA.* Integrated Assessment Modeling Consortium & International Institute for Applied Systems Analysis, 2019. doi: 10.5281/zenodo.3363345.

IPCC (2019) IPCC Special report on climate change, desertification, land degradation, sustainable land management, food security, and greenhouse gas fluxes in terrestrial ecosystems. Summary for Policymakers, Retrieved from https://www.ipcc.ch/srccl/chapter/summary-for-policymakers/

Kebede A. S., Nicholls, R. J., Allan, A., *et al.* **(2018)** Applying the global RCP–SSP–SPA scenario framework at sub-national scale: A multi-scale and participatory scenario approach. Science of the Total Environment, 635: 659-672.

Kristie, E., Hallegatte, S., Kram, T., *et al.* **(2014)** A new scenario framework for climate change research: background, process, and future directions. Climatic Change, 122(3): 363-372.

Moss, R., Babiker, M., Brinkman, S., *et al.* **(2008)**. Towards New Scenarios for Analysis of Emissions, Climate Change, Impacts, and Response Strategies: Technical Summary. Intergovernmental Panel on Climate Change, Geneva, 2007. https://archive.ipcc.ch/pdf/supporting-material/expert-meeting-report-scenarios.pdf

Nakicenovic, N., Alcamo, J., Davis, G., de Vries, B., Fenhann, J., Gaffin, S., Dadi, Z., *et al.* **(2000)**. Special report on emissions scenarios, a special report of working group III of the intergovernmental panel on climate change, intergovernmental panel on climate change. Retrieved from https://www.ipcc.ch/site/assets/uploads/2018/03/sres-en.pdf.

Nebie, E. K. I., Ba, D. & Giannini. A. (2021) Food security and climate shocks in Senegal: Who and where are the most vulnerable households? Global Food Security, 29, 100513.

O'Neill, B.C., Kriegler, E., Riahi, K., *et al.* **(2014).** A new scenario framework for climate change research: the concept of shared socioeconomic pathways. Climate Change, 122: 387–400.

Phetheet, J., Hill, M. C., Barron, R. W., Gray, B. J., Wu, H., Amanor-Boadu, V., Rossi, M. W, *et al.* **(2021)** Relating agriculture, energy, and water decisions to farm incomes and climate projections using two freeware programs, FEWCalc and DSSAT. Agricultural Systems, 193, 103222.

Riahi, K., van Vuuren, D. P., Kriegler, E., Edmonds, J., O'Neill, B. C., Tavoni, M., *et al.* **(2017)** The shared socioeconomic pathways and their energy, land use, and greenhouse gas emissions implications: An overview. Global Environmental Change, 42:153-168

Uchiyama, C., Stevenson, L. A., Tandoko, E. (2020) Climate change research in Asia: A knowledge synthesis of Asia-Pacific network for global change research (2013–2018). Environmental Research, 188, 109635.

Delineating weak zones in limestone based on borehole drilling and electrical resistivity tomography

Muhammad Jahangir Khan[1], Siddique Akhtar Ehsan[2, *], Umair Bin Nisar[3],
Syed Shahrukh Ali[1], Mubarik Ali[1], Hummad Habib Qazi[4], Saif-ur-Rehman [5], Sarfraz Khan[6]

*[1]Dept. of Earth & Environmental Sciences, Bahria University,
Karachi Campus, Pakistan*
[2] Dept. of Physics, COMSATS University Islamabad, Lahore Campus, Pakistan
[3] Centre for Climate Research and Development, COMSATS University Islamabad,Pakistan
[4]Innovative Eng. Research Alliance, University Teknologi Malaya, Johar, Malaysia
*[5]Key laboratory of Continental Collision and Plateau Uplift,
Institute of Tibetan Plateau Research, Chinese Academy of Sciences, Beijing, China*
[6]National Center for Excellence in Geology, University of Peshawar, KPK, Pakistan
* Corresponding author: siddiquemir1@gmail.com

Abstract

This study is focused on imaging weak zones in the subsurface using borehole and geophysical datasets. These weak zones are present within the Jhill limestone of the Miocene age across northern Karachi. A total of forty-nine core samples were collected from eleven boreholes about 30 m deep within the study area. The core analysis reveals the presence of cavities in fractured limestone at shallow and deep levels. The lateral extension and thickness of these weak zones are well imaged by the electrical resistivity tomography (ERT) dataset. The 2D tomographs of the six profiles show variability in the ground resistivity response. The ERT profiles are interpreted using on-hand samples collected from boreholes. These tomographs reveal relatively high resistivity values interpreted as intercalation of dry clay and marl beds within the limestone. The medium resistivity values suggest the presence of clay and sand in highly fractured limestone or surficial dry features. The low resistivity values are interpreted to be originated from the weak zones filled with lithologies having high moisture content within the limestone. The collected core samples were analysed for geotechnical parameters. The integration of borehole and ERT datasets delineated weak zones in the northern and central regions, which should be well-cemented to avoid any geohazard.

Keywords: Borehole data; electrical resistivity tomography; limestone; resistivity; weak zones.

1. Introduction

Under the influence of rapid urban developments of towns and cities, it is pertinent to locate safe ground for construction to avoid any potential geohazard. The potential geohazards for civil structures may include earthquakes, volcanic activity, tsunamis, landslides, floods, and the presence of weak zones in the subsurface. Although the massive beds of limestone are recognized

as a stable platform, however dissolution character of the carbonate rocks in the presence of the acidic groundwater may cause voids, cavities/weak zones, sinkholes, and caverns which are considered sensitive zone for mega-construction projects (Zhu *et al.,* 2011; Cueto *et al.,* 2018; Butchibabu *et al.,* 2019).

The most common procedures for assessing ground stability conditions include drilling boreholes, geophysical measurements, and geotechnical studies (Khan & Ali, 2020). Besides the wide spectrum of geophysical studies, the electrical resistivity tomography (ERT) helps investigate such anomalies in the subsurface (Hussian *et al.,* 2017; André *et al.,* 2016; Li *et al.,* 2020). The ERT method reveals horizontal and vertical discontinuities in terms of the electrical properties of the shallow subsurface (Alle *et al.,* 2018; Ewusi *et al.,* 2009). Although the identification of the dissolution features in the subsurface is a real challenge, ERT delineations produce better results to address the influence of anisotropic medium, heterogeneity in physical properties, and derivatives of dimensions in shallow subsurface ((Zhu *et al.,* 2011; Redhaounia *et al.,* 2016; Kearey *et al.,* 2002). The main advantage of the ERT and drilling data combination is the calibration of the electrical resistivity measurements in shallow environments.

The geotechnical estimation of core samples provides local ground stability conditions at a centimeter scale (Tao *et al.,* 2018b; Khalil & Hanafay, 2016). The geotechnical parameters that include natural moisture content, dry density, bulk density, and specific gravity are usually considered to determine subsurface rock conditions which contribute to the safe foundation design of buildings, bridges, and mega infrastructures (Régnier *et al.,* 2016). The geotechnical analysis of core samples may be coupled with the ERT results to reveal anomalous zones and substrate conditions at high resolution (Khalil & Hanafay, 2016; Rasul *et al., 2018*). In this study, we have focused on the identification of voids/weak zones in the shallow subsurface across the Jhill limestone.

2. Study area

Karachi city is expanding in its outskirts. There are aforementioned concerns of the surveyors and town developers regarding safe constructions and the identification of anomalous pockets in the subsurface. The current study is carried out across Jhill limestone outcrops located about 55 km northeast of Karachi (Figure 1a). The study area spreads over 34706 m^2 (8.58 Acres), and it is covered by moderate hilly sedimentary rocks about 600 m above the mean sea level (Figure 1b). Thereby sedimentary outcrops mainly consist of limestone interbedded with shale, siltstone, and sandstone of the Gaj Formation of the Miocene age in the Karachi region (Shah, 2009). The Jhill limestone is a thick carbonate deposit of the Gaj Formation, which was deposited in the shallow marine environment and is partly recrystallized (Figure 2).
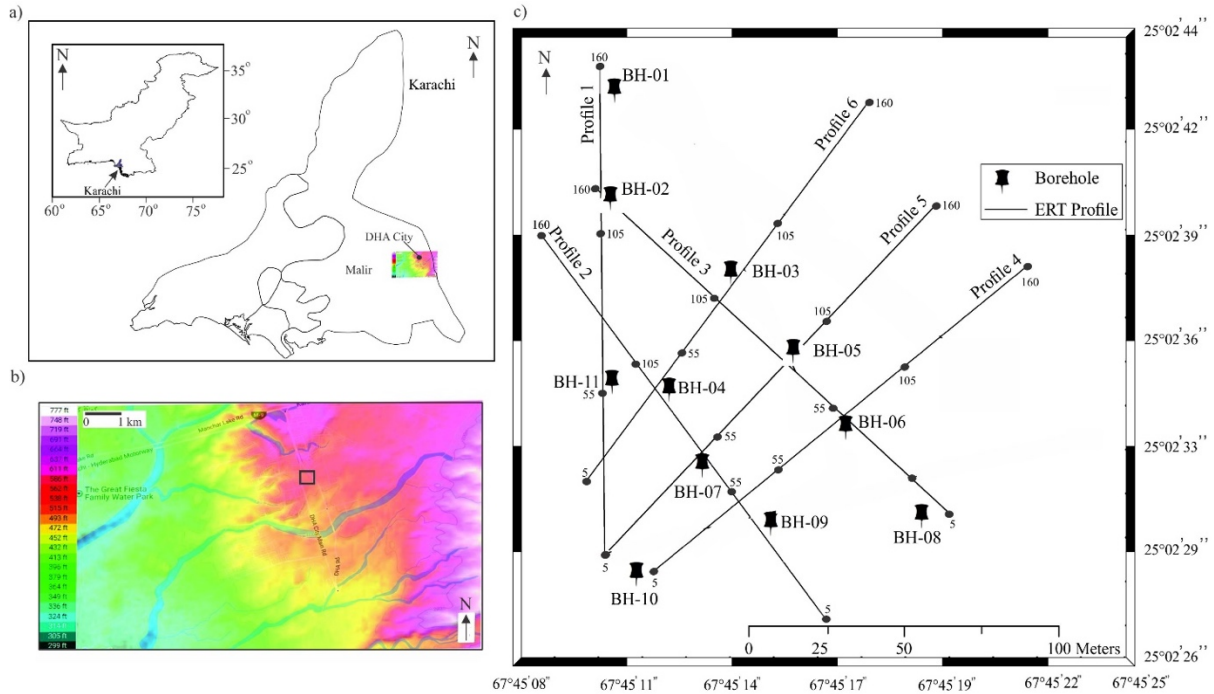
Muhammad Jahangir Khan, Siddique Akhtar Ehsan, Umair Bin Nisar, Syed Shahrukh Ali, Mubarik Ali, Hummad Habib Qazi, Saif-ur-Rehman, Sarfraz Khan

Fig. 1. a) Geographical map of Pakistan. Karachi is highlighted on the onset of the map, b) the Topographic map of the study area and its surroundings, and c) Basemap of electrical resistivity profiles and boreholes in the study area.
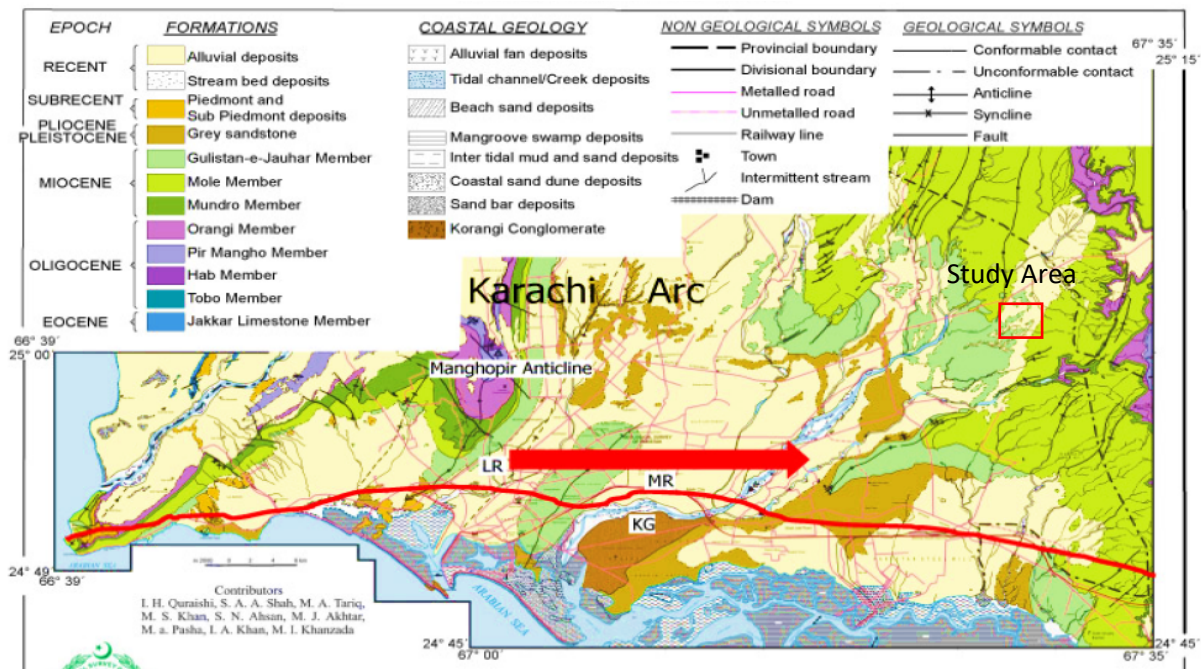

Fig. 2. Geological map of Karachi City and its surroundings. The red rectangle shows the location of the study area (Modified after Quraishi *et al.*, 2001).

3. Data acquisition and processing

3.1 Borehole data

A total of eleven boreholes of about 10 cm diameter were drilled, ranging in depth from 25 m to 45 m (Figure 1c). The boreholes were drilled with a straight rotary rig having an HQ double tube core barrel. This technique produced continuous soil and rock cores samples. About forty-nine core samples were preserved in the core boxes for laboratory examination of the natural moisture content, dry density, bulk density, and specific gravity. The presence of cavities was evident during the drilling operation.

3.2. Geophysical data

The ERT survey was carried out using a composite Wenner-Schlumberger configuration across the study area (Figures 3a and 3b). The six ERT profiles (Profile-1 to Profile-6) run in a grid manner across a reworked flat soil cover in the vicinity of undulating limestone beds (Figure 1c). 2D ERT data acquisition was conducted using POLARES 2.0, in which thirty-two electrodes were connected at 5 m intervals to a profile of cover 160 m. The electrodes inserted in the ground are connected through a wire to the link boxes and the recording system. The link boxes were connected to the main instrument through box to box cables. After completing the first test, the next profile was acquired utilizing the same acquisition parameters. The acquired 2D ERT data were pre-processed with the help of POLARES utility software. The noises were removed from the raw ERT data. The ERT data were imported to inversion software "RES2DINV" for further iterative processing. The ERT profiles show subsurface resistivity contrast, which helps analyze the heterogeneities.
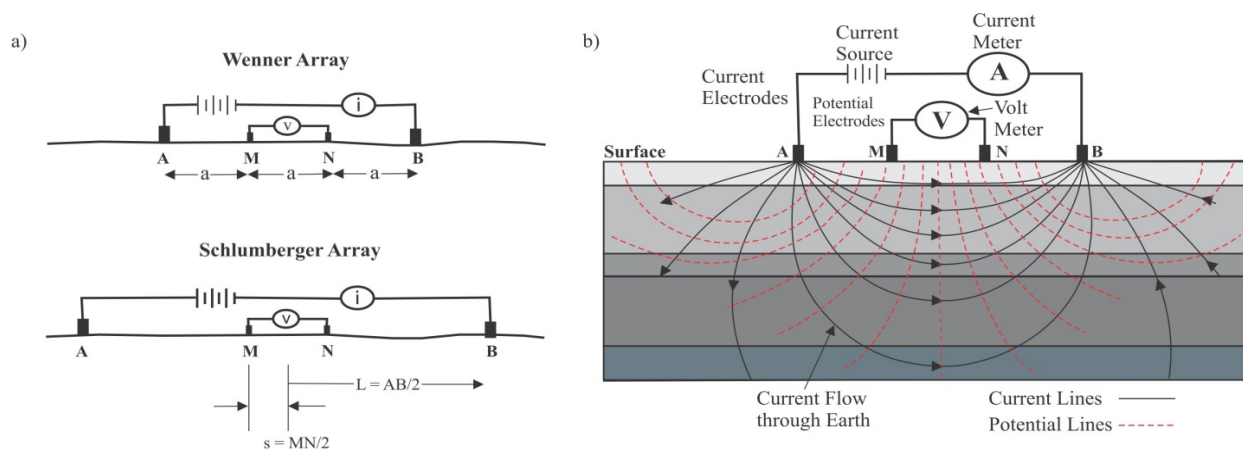

Fig. 3. a) Schematic illustration of the electrode configurations Wenner (Top) and Schlumberger (Bottom). AB represents the spacing between current electrodes, and MN represents the spacing between potential electrodes. b) Schematic illustration of the basic measurements using the electrical resistivity method. Solid black lines represent current flow through the layered subsurface structure and dashed red lines contour electrical potential. (Modified after Robinson & Coruh, 1988).

a)

b)

Fig. 4. a) Preserved core samples of drilled boreholes in the study area.
b) a single core sample.

4. Results and discussion

4.1 Geological analysis

This borehole data is utilized to constrain the subsurface lithologies, presence of voids, and tying with ERT profiles interpretation across the study area. Based on eleven boreholes (BH-01 to BH-11), three cross-sections (A-A', B-B,' C-C') are prepared (Figures 5a, 5b, and 5c). The cross-section A-A' was generated from boreholes BH-08, 06, 05, and 03 to reveal the extent of limestone and minor lithologies. The cross-section A-A' reveals that the top layer consists of yellowish-brown fine to coarse grain sand with gravel. This layer varies in thickness from about 2.5 m in the northwest to 1 m in the southeast. These are the recent depositions associated with the stream fluctuations. The prominent layer encountered during drilling is fractured limestone, about 27 m thick (Figure 5a). The presence of thick limestone is evident across the A-A'; however, intercalation of thin claystone layer is encountered at about 17 m depth and 28 m in BH-06 and 08, respectively. The boreholes (BH-03 and 05) drilled in the central part of the study area which shows the presence of cavities at about 12 m depth. The boreholes (BH-06 and 08) drilled in the south show no sign of voids/weak zones in the limestone. The ERT Profiles-6, 5, and 4 run cross-sections A-A' from north to south (Figure 5a).
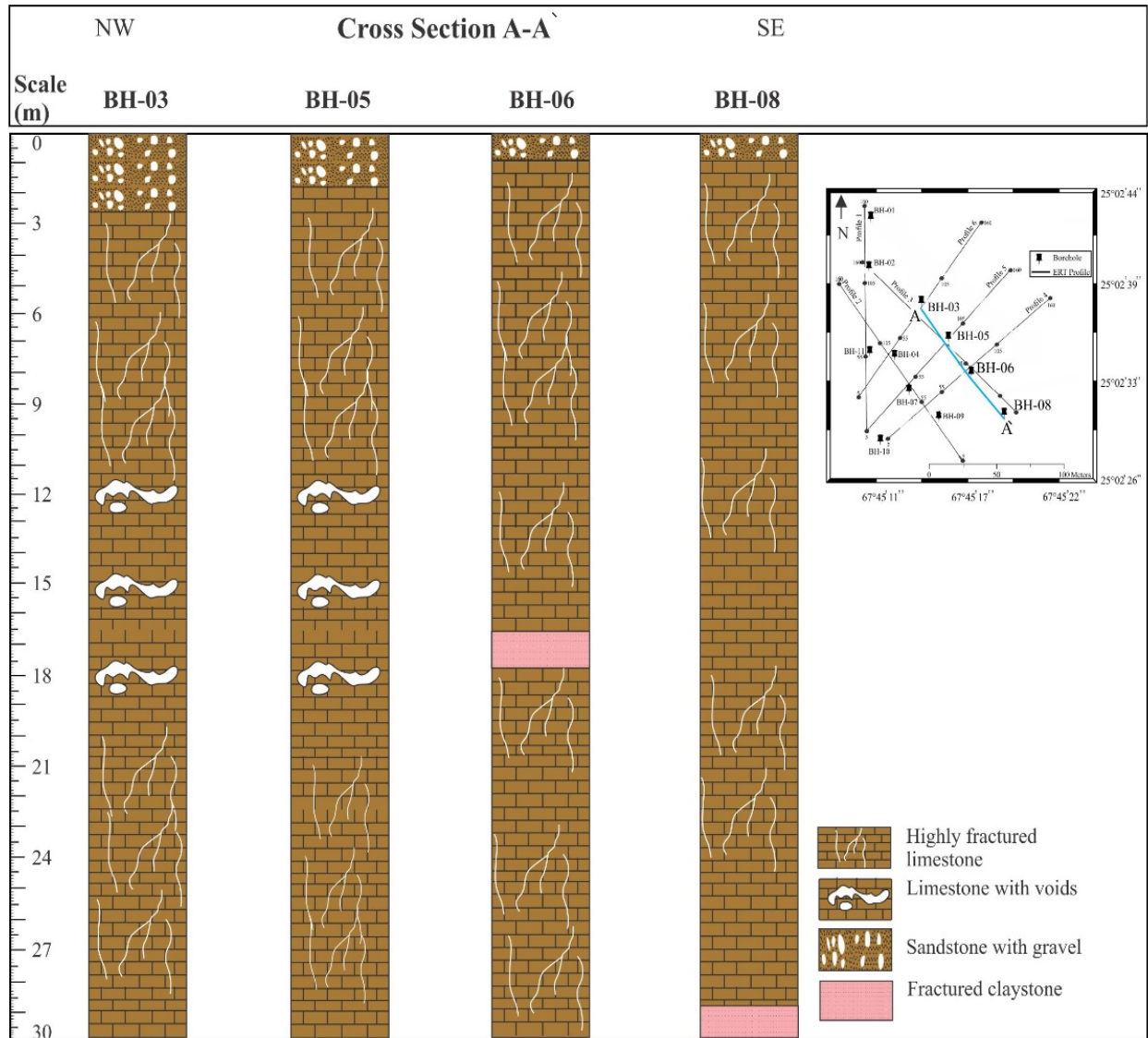
Fig. 5. a) Cross Section A-A' shows a correlation between four boreholes. The location of the Cross Section A-A' is highlighted in the onset of the map with a blue line.

The cross-section B-B' consists of three boreholes (BH-04, 07, and 09) and reveals a fractured and weathered massive limestone layer having a total thickness of 29 m. The presence of voids in limestone is only evident in BH-04 from a depth ranging from 10 m to 14.5 m in the northwest. The intercalation of the thin claystone layer in fractured limestone is evident in the southeast at about 2 m and 17 m depths. These lithological variations correspond to stream fluctuation due to subaerial exposure of deposited limestone. The boreholes (BH-07 and 09) drilled in the southwest shows no sign of voids/weak zones in the limestone. The ERT Profiles-2, 5, and 4 runs across cross-sections B-B' (Figure 5b).
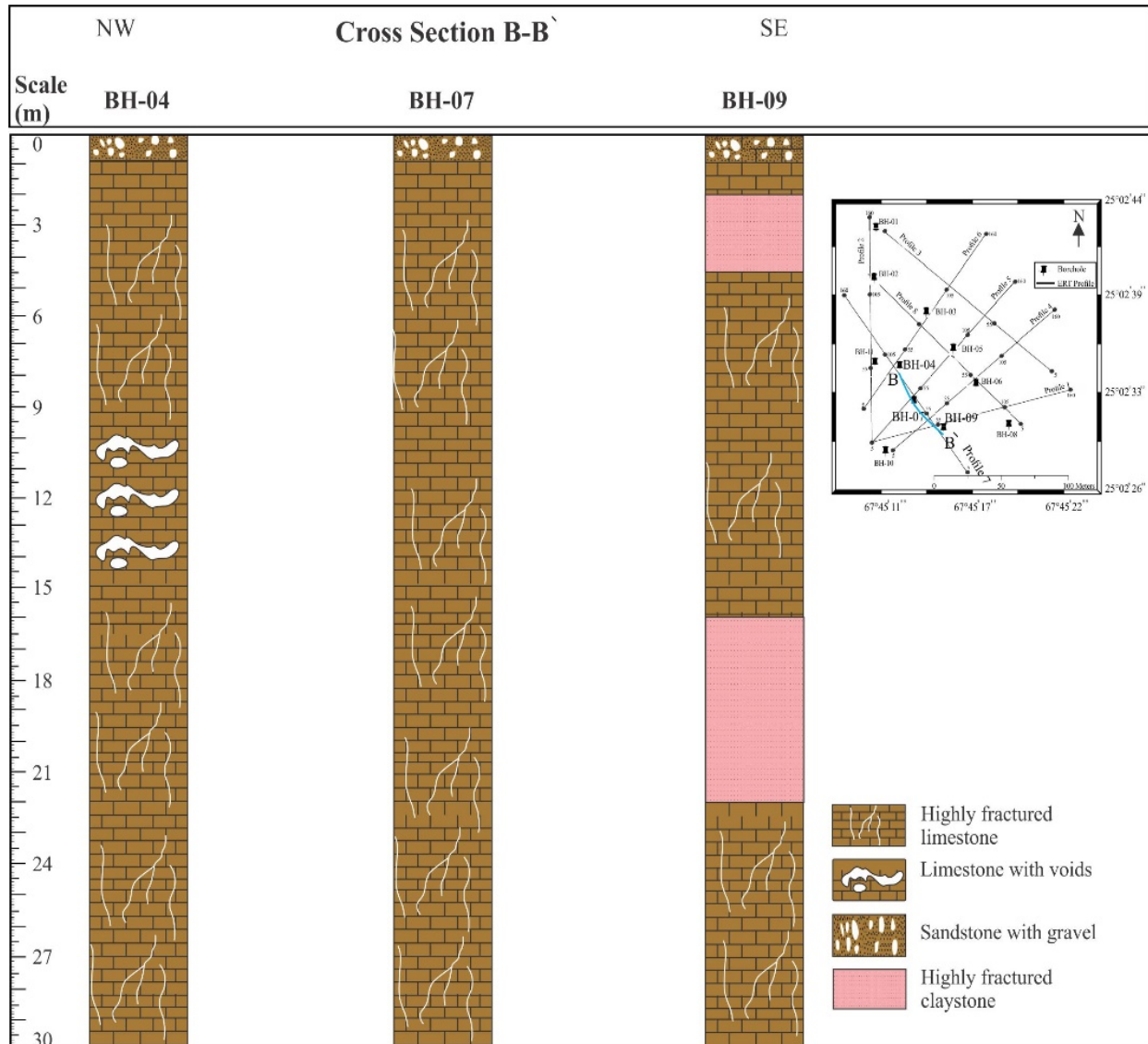
Muhammad Jahangir Khan, Siddique Akhtar Ehsan, Umair Bin Nisar, Syed Shahrukh Ali, Mubarik Ali, Hummad Habib Qazi, Saif-ur-Rehman, Sarfraz Khan

Fig. 5. b) Cross Section B-B' shows a correlation between three boreholes. Location of the Cross Section B-B' is highlighted in the onset of the map with a blue line.

The cross-section C-C' was generated from boreholes (BH-01, 02, 11, and 10) and reveals the presence of variable lithologies (Figure 5c). A remarkable limestone layer about 20 m thick and highly fractured in the south is evident across C-C'. The presence of filled voids, depths ranging from 3 m down to 16 m, is evident from BH-01 in the north. The BH-02 shows the presence of unfilled voids at a similar depth; however, intercalation of thin clays and marls is also evident. The BH-11 and 10 reveal no sign of voids to the south. Two alternative layers of claystone interbedded with sand and sandstone interbedded with clay about 5 m in thick are presence with limestone layers. The ERT Profile-1, 6, and 5 runs across the cross-section C-C' from north to south (Figure 5c).
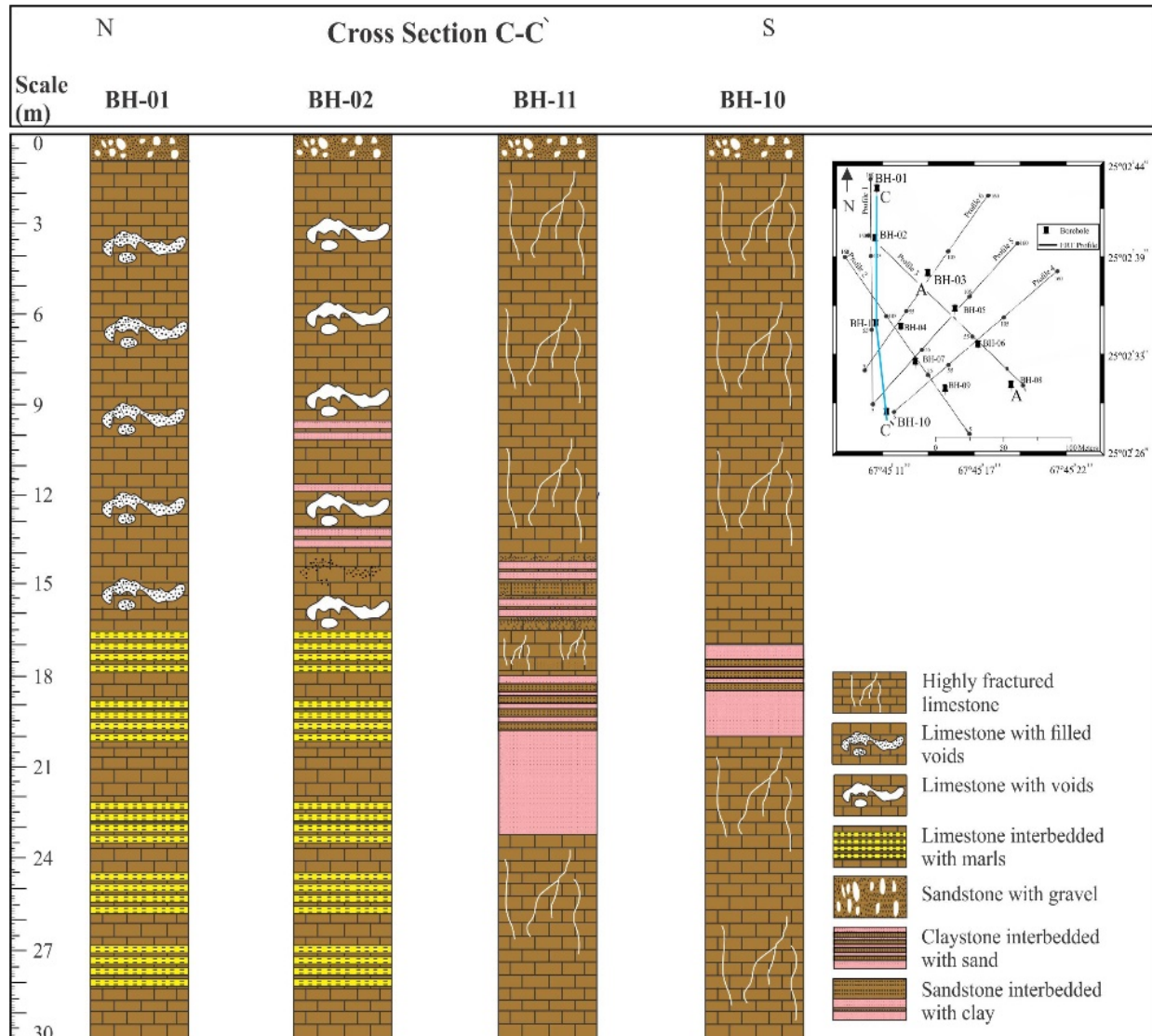
Fig. 5. c) Cross Section C-C' shows correlation between four boreholes
(BH-01, BH-02, BH-11, and BH-10). Location of the Cross Section C-C' is highlighted in the
onset map.

4.2. Electrical Resistivity Tomographs

The ERT results were interpreted by considering the lithological information obtained from the borehole data. For instance, if a direct measurement of lithology from drilling indicates the presence of a lithology with certain properties from the surface up to 10 m in-depth and in the same depth range, the ERT is showing a resistive body; therefore, it is logical to make the association of lithology and resistivity. This association is applied to different lithologies encountered across all the boreholes. However, the lithologies may vary due to subsurface weathering intensity; as it increases, the resistivity values decrease.

The ERT Profiles-1 to 6 show a range of resistivity values which are subdivided into three sections attributing to variations in lithologies (Table 1). In particular, the ERT profiles are interpreted through analysis of lithologies encountered in the boreholes and resistivity classification of respective lithology.

Table 1. Resistivity values assigned to sedimentary packages based on the VES results.

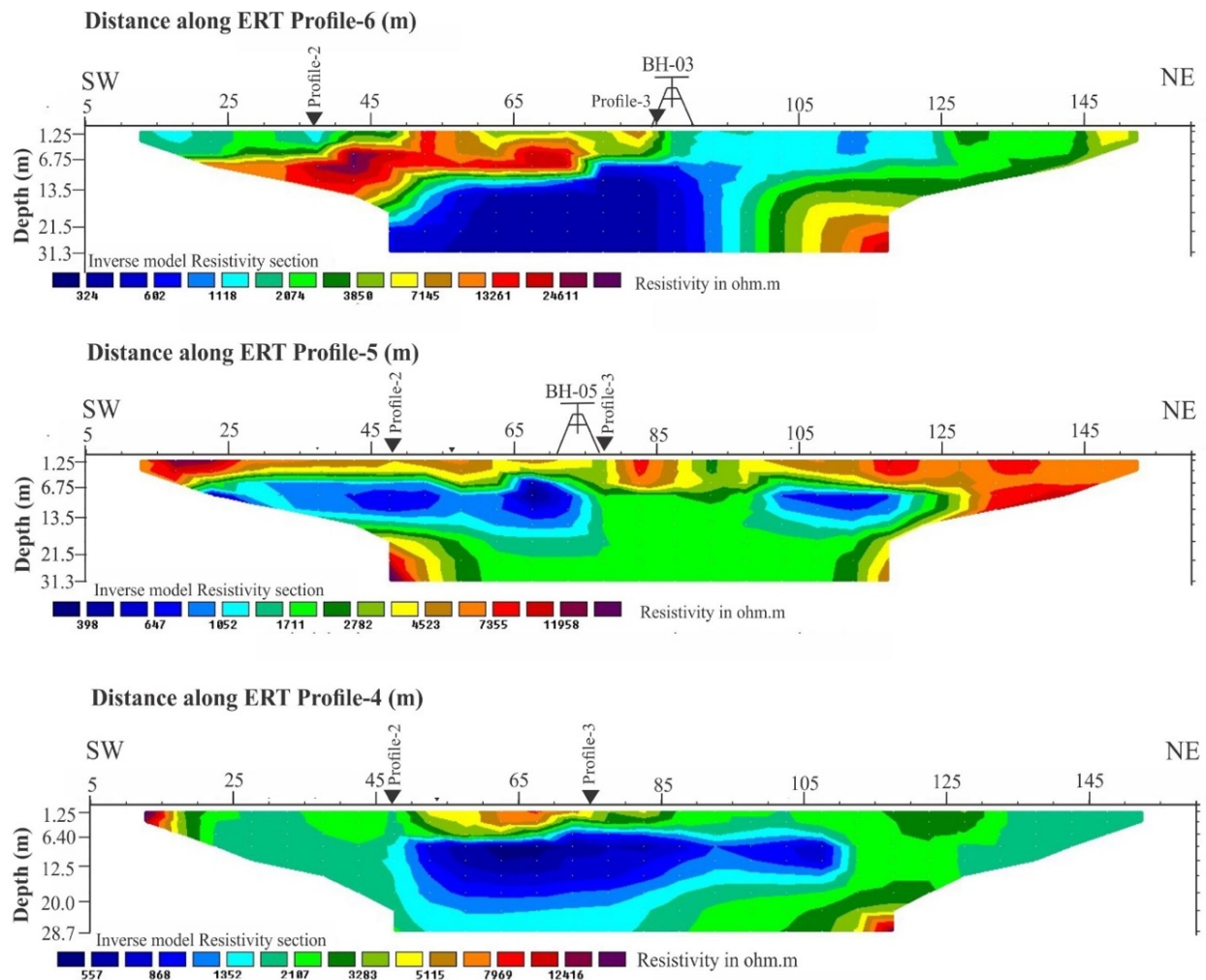| Lithology	Resistivity (Ωm)
Filled voids in limestone with moisture content	250-1000
Fractured limestone	1000-3000
Dry limestone	3000

Fig. 6. a) The Electrical Resistivity Tomographs (ERT) were acquired across the study area. The locations of the drilled boreholes are also highlighted on the profiles.

The ERT Profiles-4, 5, and 6 run northeast to southwest (Figures 1c, and 7a). The ERT Profile-6 reveals resistivity values ranging from 300 Ωm to 25000 Ωm. A high resistive zone, values ranging from 7000 Ωm to 25000 Ωm, between distances 20 m to 70 m at about 8 m depth. This zone is interpreted as the intercalation of marl in the fractured limestone. A medium resistivity zone (1600 Ωm to 4000 Ωm) between distances 95 m to 145 m is attributed to dry clay-filled into the fractured limestone down to 32 m depth. The borehole (BH-03) drilled across Profile-6 reveals the presence of voids at about 10 m depth. A loss of about 100-liter drilling fluid was observed while the drilling operation of the BH-03, which may also be due to fractured limestone. A low resistive zone (250 Ωm to 1000 Ωm) between distances 45 m to 90 m and at about 10 m depth is present at the location of voids encountered in the BH-03. However, the water loss during drilling of BH-03 along this void was not observed below 18 m depth. This may suggest filling of this particular voids at a depth greater than 18 m. This low resistive zone present in the Profile-6 and two other parallel profiles (Profile-5 and Profile-4) may represent its extension as a major void in the subsurface.

The ERT Profile-5 shows resistivity values ranging from 350 Ωm to 12000 Ωm, subdivided into three distinct zones (Figure 6a). The borehole (BH-05) drilled in the center of the Profile-5 indicates the presence of dry sand and gravel deposits. A shallow high resistive zone (4000 Ωm to 12000 Ωm) spreads throughout the profile, constrain the presence of surficial dry sand and gravel deposits also indicated by the lithologies in BH-05. An intermediate resistivity zone, between distances of 45 m to 125 m at about 7 m depth, is characterized as fractured limestone interbedded with silt and clay. The image reveals the presence of two low resistive zones, values ranging between 300 to 1050 Ωm, between distances 30 m to 75 m and 100 m to 120 m at about 10 m depth. These low resistive zones can be classified as voids within limestone filled with saturated clay, which are ascertained with BH-05. This may also indicate extension and bifurcation of major voids encountered in Profile-6 from northwest to southeast. The ERT Profile-4 reveals two remarkable resistivity zones, such as between distances 25 m to 130 m at shallow and deeper levels are identified as fractured limestone and between distances 50 m to 110 m at about 7 m depth. This zone represents the subsurface voids within limestone filled with saturated clay.

The ERT Profile-1 runs north-south, and it is located on the western side of the study area (Figure 1c). Three boreholes (BH-01, 02, 11) were drilled across Profile-1. The tomograph of the Profile-1 shows resistivity values ranging from 500 Ωm to 8000 Ωm (Figure 6b). The high resistive zones are interpreted between 100 m to 115 m and 125 m to 140 m at shallow depths, which may be attributed to fractured limestone filled with sand and dry clayey silt in the fractures. The medium resistive zones between distances 30 m to 50 m, 65 to 90 m, and 115 m to 125 m are interpreted to be limestone with high fractured density interbedded with claystone. The BH-01 and 02 identified voids at about 3 m depths (Figure 6c). A low resistive zone between distances of 90 m and 125 m at about 3 m depth constrains the presence of a major voids of about 17 m as identified in BH-01 and 02 (Figure 6b).

The ERT Profiles-2 and 3 run northwest to southeast and parallel to each other (Figure 1c). The tomograph of the ERT Profile-2 image is about 29 m deep and reveals four main features

Muhammad Jahangir Khan, Siddique Akhtar Ehsan, Umair Bin Nisar, Syed Shahrukh Ali, Mubarik Ali, Hummad Habib Qazi, Saif-ur-Rehman, Sarfraz Khan

based on the resistivity values (Figure 6a). A high resistive zone is imaged between distances of 40 m and 75 m, starting at shallow depth and extending down to 16 m depth is interpreted to be intercalations of clay and marl with fractured limestone. Similar, high resistivity values are also observed between distances of 78 m to 128 m at shallow levels, which is interpreted as surficial dry clay. A medium resistive zone is present between distances 70 m to 115 m at about 18 m depth which is attributed as fractured limestone. The BH-04 identified the presence of voids at about 9 m deep. Two low resistive zones are present between 75 m and 90 m and 104 m to 124 m at about 9 m depth. These zones are interpreted as voids in the subsurface.
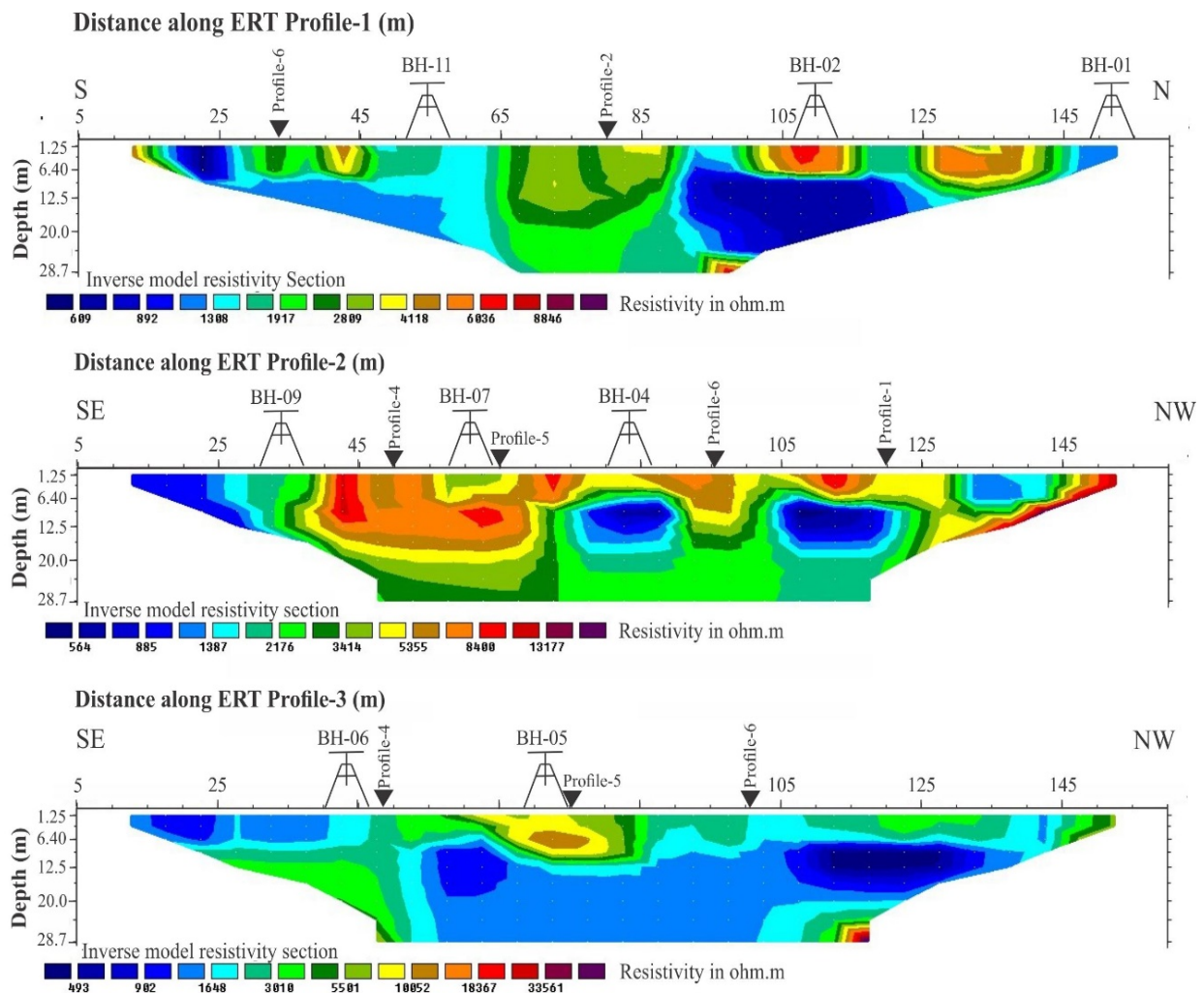

Fig. 6. b) The Electrical Resistivity Tomographs (ERT) were acquired across the study area. The color variations show the resistivity contrast of the subsurface across the profiles. The locations of the drilled boreholes are also highlighted on the profiles.

The ERT Profile-3 (Figure 6b) shows a high resistive zone between distances of 60 m to 75 m at shallow levels. This high resistive zone is located at BH-05 and is attributed to be surficial dry clay. Profile-8 reveals at least three medium resistive zones, values ranging from 2000 to 5500, between distances 45 m to 60 m, 75 m to 100 m, and 108 m to 137 m at shallow levels. These medium resistive zones are interpreted as fracture limestone. The BH-05 encountered voids at about 12 m depth. A low zone resistive zone between distances 55 m to 130 m at about 12 m depth is interpreted as a weak zone in limestone. This is a major zone imaged across the Profile-3. This zone has a lateral extension of about 70 m and goes down to 29 m depth. The Profile-8 also shows two relatively low resistive zones located between distances of 10 m to 45 m at a shallow level. The BH-06 is located between distances of 40 m to 45 m (Figure 6b) and encountered a thickly bedded limestone with intercalation of saturated marls. These low resistive zones constrain the presence of limestone with intercalation of marl from surface to 20 m depth.

4.3. Integration between ERT delineations and geotechnical parameters

The lithology encountered in the eleven boreholes, BH-01 to BH-11, is dominantly limestone with intercalations of marls, clay, silt, sand, and gravel. A reasonable correlation is carried out between the ERT dataset and geotechnical parameters, including moisture content, dry density, bulk density, and specific gravity estimated from the core samples at variable depths (Table 2). The geotechnical parameters are correlated with resistivity values to provide a better understanding of the behavior of different parameters with depth (Table 2). The bulk density shows higher values, 2.15 g/cm^3 to 2.13 g/cm^3, at a shallow level and low values, 2.1 g/cm^3, within the voids zone. The specific gravity shows comparatively higher values for shallow levels, 2.682 to 2.684, and low values, 2.671, for the voids zone. Below the voids, zone-specific gravity reveals the highest value of 2.697 (Table 2). These values suggest a close relationship between geotechnical parameters and electrical resistivity. An inverse relationship between the moisture content and electrical resistivity is observed. At a shallow level, high electrical resistivity and comparatively high values of geotechnical parameters are present. This may indicate the presence of surficial dry clay within fractured limestone at shallow levels. The decrease of resistivity values and geotechnical parameters for depths greater than 7 m suggest filling identified voids with saturated clay or sand. The increase in resistivity and geotechnical parameters for depths greater than 18 m may indicate compaction of the fractured limestone. A similar relationship between geotechnical parameters and electrical resistivity values is present for the remaining four boreholes (BH-02 to BH-05), in which voids have been identified (Table 2).

Table 2. Geotechnical parameters estimated from core samples taken from boreholes

Borehole No.	Sample Depth (m)	Moisture Content (%)	Dry Density (gr/cm³)	Bulk Density (gr/cm³)	Specific Gravity
BH-01	3.31	4.07	2.07	2.15	2.682
	6.9	3.74	2.05	2.13	2.684
	12.73	3.73	2.03	2.1	2.671
	24.84	5.6	2.13	2.25	2.697
BH-02	1.6	0.98	2.17	2.19	2.664
	3.12	0.99	2.28	2.3	2.671
	9.5	1.02	1.89	1.91	2.682
	12.3	1.66	2.1	2.13	2.684
	15.9	0.69	2.3	2.32	2.674
	16.9	2.02	1.97	2.01	2.691
	24.91	2.53	2.09	2.14	2.691
BH-03	1.5	3.52	1.74	1.81	-
	6.2	0.95	2.07	2.09	2.661
	18.2	7.48	2.18	2.34	2.741
	21.35	1.25	2.05	2.07	2.674
	25.9	0.92	2.09	2.1	2.67
	27.25	0.85	2.13	2.15	2.672
	33.4	1.78	2.11	2.15	2.68
BH-04	14.4	1.01	2.18	2.2	2.697
	17.1	2.93	2.2	2.26	2.732
	24.15	5.12	2.45	2.57	2.74
	29.23	4.92	2.06	2.16	2.694
BH-05	13.7	5.23	2.04	2.15	2.674
	18.3	6.11	2.07	2.15	2.734
	45	3.13	2.01	2.07	2.724
BH-06	1.9	7.74	2.11	2.27	2.727
	6.5	5.5	2.05	2.16	2.684
	16.7	0.6	2.23	2.25	2.715
	29.1	4.3	2.14	2.24	2.684
BH-07	3.3	5.38	2.03	2.14	2.684
	22.7	4.68	2.04	2.14	2.695
	29.5	6.5	2.33	2.48	2.734
BH-08	4.65	4.32	2.16	2.25	-
	15.3	5.41	2.13	2.24	-
	22.5	5.44	2.1	2.21	-
	27	3.81	2.01	2.09	2.672
BH-09	1.2	0.98	2.01	2.03	2.67
	15.4	3.48	2	2.07	2.741
	28.7	2.69	2.1	2.16	2.674
BH-10	3.5	5.09	2.04	2.14	-
	12.7	5.36	2.1	2.21	-
	18	10.2	2.21	2.44	-
	20.22	8.4	2.06	2.23	2.746
	26.1	2.94	2.11	2.17	2.671
BH-11	1.1	2.2	2.5	2.56	2.675
	16.7	3.79	2.18	2.27	-
	19.5	7.81	1.87	2.02	-
	26.1	1.59	2.38	2.42	-
	28.5	1.25	2.46	2.49	-

The integration of datasets of ERT profiles and boreholes is shown in Figure 7. The interpreted weak zones in the limestone bed are shown on the base map of the study area. It is visualized that the weak zones are concentrated in the north, northwest, and central regions. The region containing weak zones is highlighted with a polygon outlined with dashed lines (Figure 7). The voids in the north and northwest are relatively shallow than in the central region (Table 2 and Figure 7).
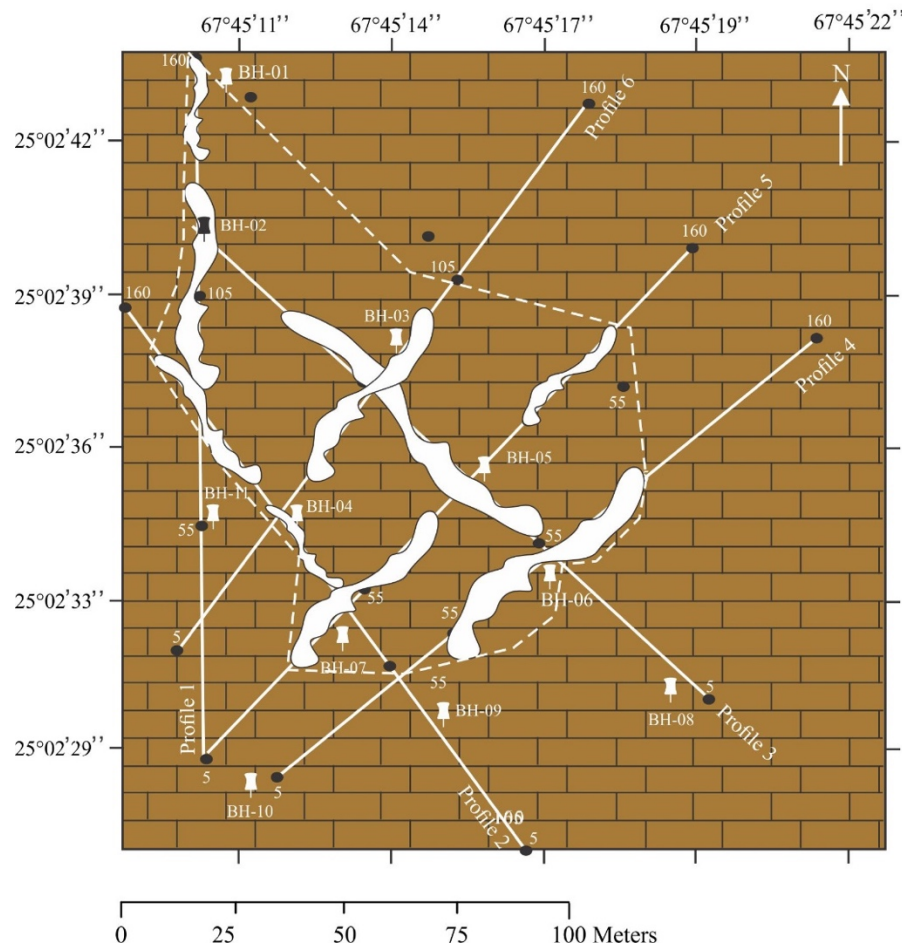

Fig. 7. The voids in limestone delineated using boreholes and ERT datasets are presented on location map of the study area.

5. Conclusion

The ERT Profiles were well-constrained with the borehole dataset and geotechnical analysis of the core samples to map subsurface weak zones. The voids identified by borehole and ERT datasets are relatively shallower in the northwestern region than in the northern and central regions of the study area. In the central region, the voids are relatively large in size, and their thickness may range from about 8-12 m. These weak zones may cause ground instability and hazard to future construction and development projects of mega infrastructure.

References

Alle, I. C., Descloitres, M., Vouillamoz, J. M., Yalo, N., Lawson, F. M. A., & Adihou, A. C. (2018). Why 1D electrical resistivity techniques can result in inaccurate siting of boreholes in hard rock aquifers and why electrical resistivity tomography must be preferred: the example of Benin, West Africa. Journal of African Earth Sciences, 139: 341-353

André, L., E.Lamya, E., P.Lutz, P., Pernier, M., Lespinard, O., Pauss, A., & Ribeiro, T. (2016). Electrical resistivity tomography to quantify in situ liquid content in a full-scale dry anaerobic digestion reactor. Bioresource Technology, 201: 89-96

Butchibabu, B., Khan, P. K., & Jha, P. C. (2019). Foundation evaluation of underground metro rail station using geophysical and geotechnical investigations. Engineering Geology, 248: 140-154

Cueto, M., Olona, J., Fernández-Viejo, G., Pando, L., & López-Fernández, C. (2018). Karst-induced sinkhole detection using an integrated geophysical survey: a case study along the Riyadh Metro Line 3 (Saudi Arabia). Near Surface Geophysics, 16(**3**): 270-281

Ewusi, A., Kuma, S. J., & Voigt, H. J. (2009). Utility of the 2-D Multi-Electrode Resistivity Imaging Technique in Groundwater Exploration in the Voltaian Sedimentary Basin, Northern Ghana. Natural Resources Research, 18(**4**): 267-275

Hussain, Y., Ullah, S. F., Akhter, G., & Aslam, A. Q. (2017). Groundwater quality evaluation by electrical resistivity method for optimized tubewell site selection in an ago-stressed Thal Doab Aquifer in Pakistan. Modeling Earth Systems and Environment, 3(**1**): 7-15

Kearey, P., Michael B., & Ian H., (2002). An introduction to Geophysical Exploration Chapter No. 08, Electrical surveying, pp. 183

Khalil, M. H., & Hanafy, S. (2016). Geotechnical Parameters from Seismic Measurements: Two Field Examples from Egypt and Saudi Arabia. Journal of Environmental and Engineering Geophysics, 21(**1**): 13-28

Khan, M. J., & Ali S., (2020). Delineation of Uncertainties in Anisotropic Shallow Subsurface by Integrated Geophysical and Geotechnical Examination. Pakistan Journal of Science, 72 (**1**): 61-67

Li, Z. T., Ming, Q. Li, & Hong Z., (2020). Integrated physical detection technology in complicated surface subsidence area of mining area. Kuwait Journal of Sciences, 47(**1**): 86-96.

Quraishi, I. H., Shah, S. A. A., Tariq, M. A., Khan, M. S., Ahsan, S.N., & Khanzada, M.L. (2001). Geological map of Karachi area, Sindh Pakistan: Geological Survey of Pakistan, 3

Rasul, H., Zou, L., & Olofsson, B. (2018). Monitoring of moisture and salinity content in an operational road structure by electrical resistivity tomography. Near Surface Geophysics, 16(**4**), 423-444

Redhaounia, B., Bédir, M., Gabtni, H., Batobo, O. I., Dhaoui, M., Chabaane, A., & Khomsi, S. (2016). Hydro-geophysical characterization for groundwater resources potential of fractured limestone reservoirs in Amdoun Monts (North-western Tunisia). Journal of Applied Geophysics, 128: 150-162

Régnier, J., Cadet, H., & Bard, P. Y. (2016). Empirical quantification of the impact of nonlinear soil behavior on site response. Bulletin of the Seismological Society of America, 106(**4**): 1710-1719

Robinson, E.S., & Coruh, C. (1988). Basic Exploration Geophysics. John Wiley & Sons, New York, **Pp.** 462

Shah, M. I. (2009). Stratigraphy of Pakistan, GSP Memoirs, 22: **Pp.** 5-6

Tao, Z., Li, M., Zhu, C., He, M., Zheng, X., & Yu, S. (2018b). Analysis of the Critical Safety Thickness for Pretreatment of Mined-Out Areas Underlying the Final Slopes of Open-Pit Mines and the Effects of Treatment. Shock and Vibration, 18: 1-8

Zhu, J. C., Currens, J., & Dinger, J. S. (2011). Challenges of using electrical resistivity method to locate karst conduits-a field case in the inner Bluegrass region, Kentucky. Journal of applied Geophysics, 75 (**3**): 523-530

, Mona Lisa , Muyyassar Hussain Zah, Syed A. Ahmed Zah ZahidKn,hMdoLsZuLZ

myznbnlner

dZ gwIdBZyUS,LZ

myznbnlnerd

The Pab Formation of Zamzama block, lying in the
prominent gas-producing sand reservoir. The optimized
encroachment surrounding the gas-producing wells, thus
facies from the remainder of the wet sands and shales for
is adopted based on the relation between petrophysical a
prospect locations. Petro-elastic models (PEMs) for th
distinguish lithologies in their elastic ranges. Several ela
(11,600-12,100 m/s*g/cc), s-impedance (7,000-7,330 m
were calculated from the simultaneous prestack sei
identification of gas sands in the field. The inverted elas
were incorporated into the Bayesian framework to eva
determine the reservoir quality, bulk volumes of PHIE
volumes trained on well logs by employing Probabili
effectively handles heterogeneity effects. The results s
passing through the existing well locations exhibited
effective porosities of 9%, confirming the reservoir's g
widely implemented in producing fields to completely a
production with minimal risks.,

cdzFuUMakBayesianclassification; elastic attributes; petro-elastic models (PEMs);,

aneous prestack seismic inversion (SPSI). gw

zama gas field covers the western portion of Kirthar Foredeep (Figure 1a), a part of the
Fold and Thrust Belt (Khan Zhndus Basin among
Zamzama anticlinal structure resulted due to the
plates resulting in a significant N-S directed thrust
nd Gas-Water-Contact (GWC) measurements from

ZahidZU.Kn,aZKMa,ZooUZ.aZL,suU,yZrHZrZ,nZa,s.dLM,.K,SZe.aAZK,AmUuTnm,.KPdUAdM,dLZaA.b,
ZAAU.iTAda,Zaa.aAdM,F.Am,Stt,ZooUuf.rZA.uK,us,odAUuomza.bZL,oUuodUA.da,

,

the initial discovery well at Zamzama-01-ST1 verified a 300m gas column with 3Tscf in the Pab Formation (Jackson *et al*., 2004).

The Zamzama gas field produced 1.7Tscf gas; however, lateral ramps connecting the hanging and footwall caused differential water encroachment and pressure depletions in the gas producing wells. GWC is still found deeper in the crestal portions, and new wells can be drilled (Zafar *et al*., 2018). Accurate mapping of gas-bearing sand facies may be considered risky for using conventional methods. Consequently, seismic reflection interpretation is linked with wells to generate petro-elastic relationships that quantitatively discriminate gas and wet sands (Al-Sulaimi & Al-Ruwaih, 2004). The advanced techniques such as SPSI produce reservoir elastic properties that effectively highlight hydrocarbons in the active fields, such as Niger delta Sandfish (Adesanya *et al*., 2021), Lower Wilcox lowstand sand deposits along the Texas Gulf Coastal Plain (Zhang *et al*., 2020), etc.
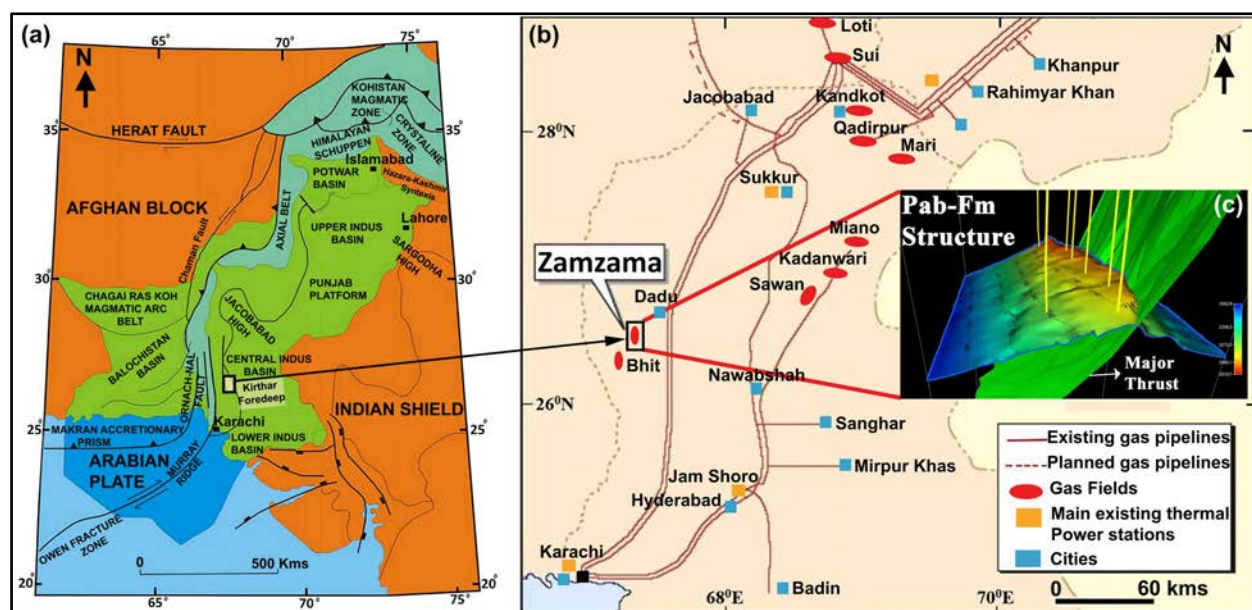

Fig. 1. (a) The regional map highlighting Zamzama field location and demarcating main structural features, (b) The Zamzama region is surrounded by major gas fields, and (c) The anticline of the Pab Formation is cut by a major thrust fault, and wells penetrate it.

Before the seismic inversion, the elastic values of gas-bearing sand facies are analyzed from hard constraint well data. The PEMs combine geology and reservoir parameters to determine elastic responses that differentiate facies and assist in quantitative interpretation (Miraj *et al*., 2021). For petrophysical distributions (porosity and clay), PNN was used to better manage shales inside sands (Durrani *et al*., 2020). The main aims included de-risking of new drilling points and improved reserve scheming through integrated geophysical exploration techniques (Li *et al.,* 2020).

2. Methods and techniques

The basic dataset is a 3D seismic cube with seven wells (Zamzama-02, Zamzama-03, Zamzama-04, Zamzama-05, Zamzama-06, Zamzama-07, and Zamzama-08-ST02), produced from the Pab Formation (Figure 2a). Well data included well tops, raw logs, mineralogy, and reservoir in-situ properties. All wells were used in the SPSI process and PNN approximation, while the gas-sands probability was assessed without Zamzama-04 and Zamzama-07 to confirm the high probability in gas-producing locations. Figure 2b delineates a petro-elastic relation in estimating pay probability and PNN approximation of petrophysical properties for Pab gas-sands characterization.
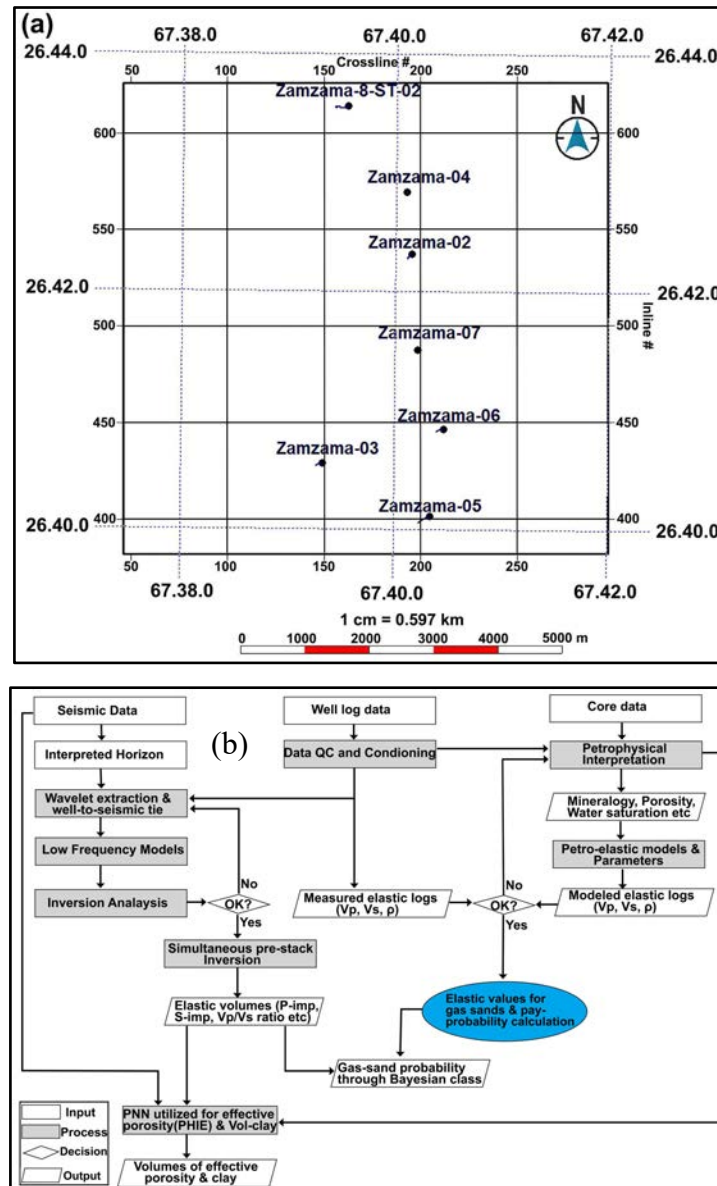

Fig. 2. (a) Base map showing wells and 3D seismic, (b) Workflow with a petro-elastic relation for discriminating gas sands based on estimated pay-probabilities and petrophysical properties.

Lithological identifications are made using cut-off values on petrophysical logs (Table 1). These lithofacies (shale, wet, and gas sands) among reservoir properties were used in PEMs to model consistent elastic logs.

Table 1. Identified lithofacies based on petrophysical cut-off values.

Litho-facies	Cut-off Values
Shale	Clay Volume >0.30
Wet Sands	Clay volume ≤ 0.30, Sw ≥0.45
Gas Sands	Clay volume ≤ 0.30, Sw < 0.45

The SPSI method includes the interpreted horizons, accurate well-to-seismic tie, strata models of low frequencies (LFMs), and inversion analysis. The output inverted elastic volumes can be calibrated for gas-sands appraisal following the value ranges of modeled elastic logs. Furthermore, the modeled logs relate to the inverted elastic properties in the Bayesian framework for litho-cubes probability estimate. To predict petrophysical volumes, the seismic and inverted volumes were integrated and trained on petrophysical logs using PNN.

2.1 Petro-elastic models (PEMs)

The logs encountered a variety of errors, including poor borehole conditions, washouts, and the invasion of mud filtrates (Zeb & Murrell, 2015). The reliable PEMs, developed using HampsonRussells software, overcame the errors and hence delineated the facies according to their elastic ranges.

PEMs signified elastic responses from petrophysical parameters (lithologies, Sw, porosities), reservoir in-situ conditions (salinity, pressure, temperature), and their association with seismic data (Singha & Chatterjee, 2017). Individual PEMs for the identified facies were created by combining the rock matrix bounds of Voigt (1928) with the reservoir-fluid properties of Batzle & Wang ,1992 substituted by the Gassmann (1951) relation.

The mineral volumes with bulk and shear moduli were selected according to Avseth *et al.* (2005). For K_{dry} calculation, the concept of pore-space stiffness compressibility worked well to manage a limited number of reservoir input parameters (Babasafari *et al.*, 2020). The selected granular model considered porosities between zero and a critical value, i.e., 20% for Pab Formation (Han *et al.*, 1986), and separated the load-bearing sands from grains and fluid suspension.

Figure 3 reveals the petrophysical evaluation of Zamzama-03 for key properties, such as volumetrics, lithologies, porosities, saturations, etc., whereas Table 2 summarizes the parameters used in PEMs.
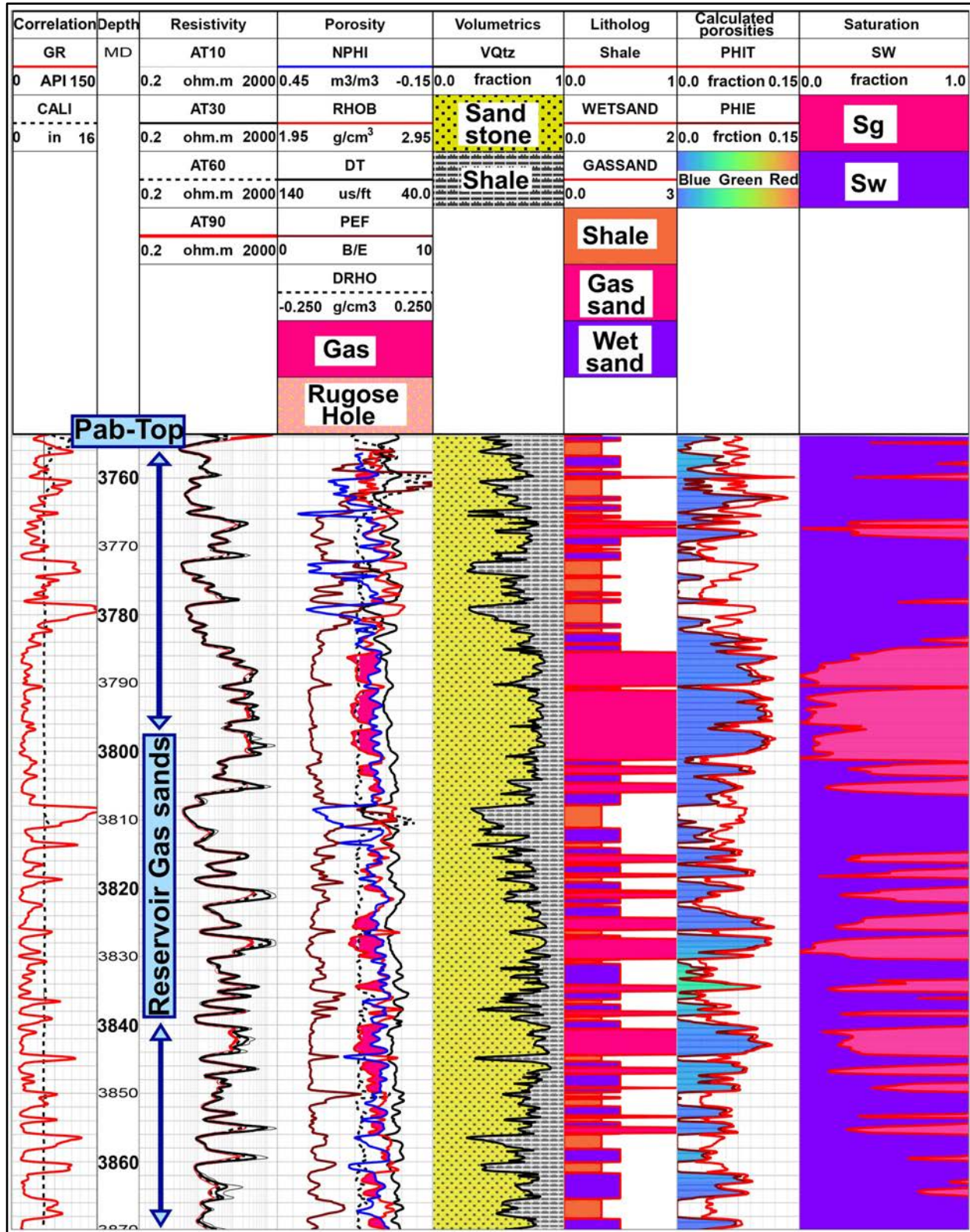
Fig.3. The petrophysical analysis for reservoir Pab Formation (3750-3870m) showing volumetrics, lithologies, calculated porosities, and saturations in their respective tracks.

Table 2. Reservoir petrophysical and elastic properties are utilized in PEMs.

Reservoir Parameters	Avg. Porosity	Avg. Shale	Avg. Water (Sw)	Pressure (PSI)	Temp °C	Salinity (g/l)	Gas gravity
Values	10%	25%	45%	3400	130	0.15	0.689

Elastic Parameters	Bulk Modulus (GPA)				Shear Modulus (GPA)				Density (g/cm3)			
	Quartz	Clay	Sw	Gas	Quartz	Clay	Sw	Gas	Quartz	Clay	Sw	Gas
Values	37	15	2.38	0.02	44	7	0	0	2.65	2.6	1.0	0.1

The modeled elastic logs show consistency with measured logs, i.e., Vp, Vs, and density in the identified lithologies within Pab Formation (Figure 4a). Additional QC was performed in quantitative QC plots of measured vs modeled logs (Figure 4b). The prediction quality (PQ) is 0.94, 0.86, and 0.84 in the cross plots of Vp, Vs, and density, respectively. The correlation coefficient (CC) quantified log values ranging from -1 (anticorrelation) to 1 (perfect correlation) and denoted 0.88, 0.74, and 0.70 in respective cross plots. Similarly, normalized root mean square error (NRMSE) dealt with the degree of difference, with 0 for identical curves and 2 for the greatest difference, indicating 0.07, 0.13, and 0.03 respectively. The log value range was represented by a histogram and the data point size showed its density. This analysis provides confidence in the selected PEMs because all the QC plot values were within reasonable ranges.
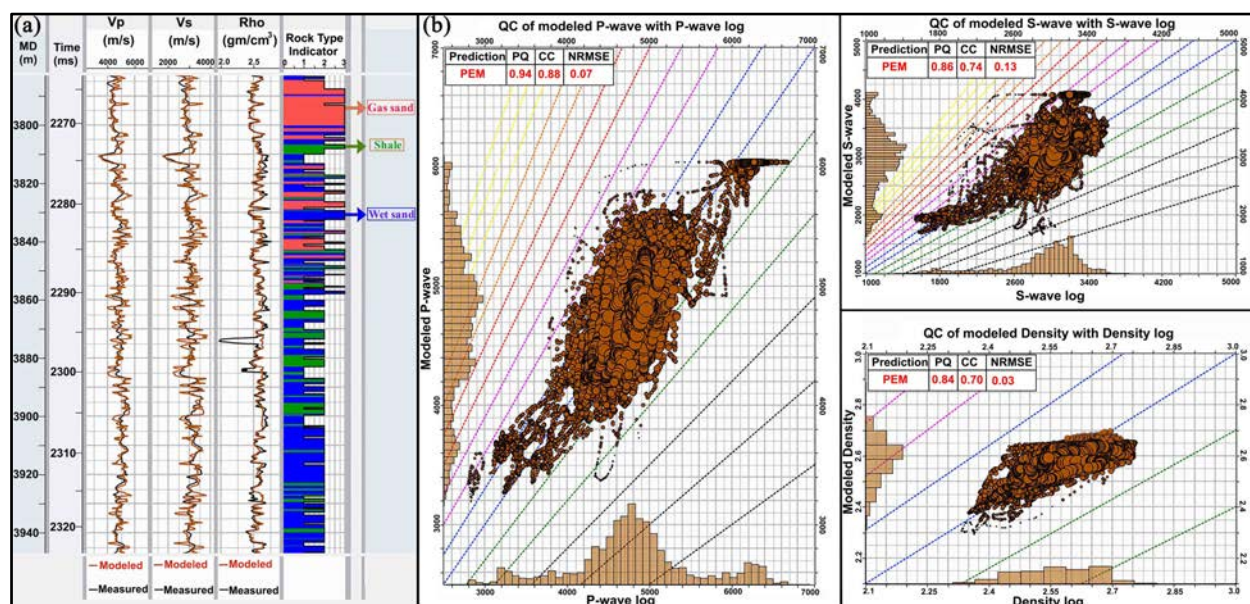

Fig. 4. (a) Modeled logs are overlaid on measured logs with a good fit of trends, (b) The coherence of selected PEMs is demonstrated by the in-range values of quantitative QC plots of real and modeled Vp, Vs, and density.

2.2 Strata Model

The Strata Model, created using HampsonRussells strata module (version 10.6), is a geologic model that uses interpreted horizons, stratigraphic pattern interpolation, and well logs. The seismic data is lacking in low frequencies due to its band-limited nature (Figure 5a). The models incorporate the missing low frequencies from well logs, calculated using the kriging interpolation method, to obtain the absolute elastic properties of seismic (Sams & Saussus, 2013). LFMs (8Hz) acted as background information and were updated with high frequencies in the inversion algorithm (Sams & Carter, 2017). LFMs showed a reliable correlation with low-pass filtered well logs (Figure 5b).
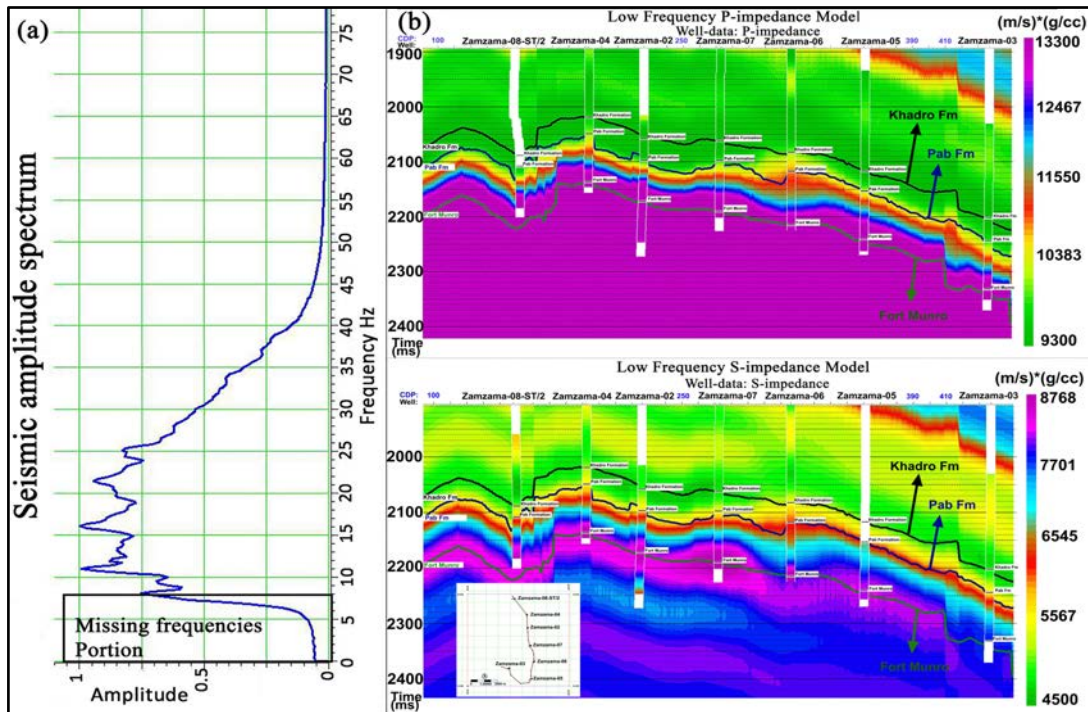

Fig. 5. (a) Seismic spectrum delineating missing low frequencies, (b) LFMs of P and S-impedances with low-pass filtered well logs provided background trend and updated with high frequencies in the inversion process.

2.3 Simultaneous prestack seismic inversion (SPSI)

The LFMs were incorporated into the prior model in SPSI inversion to outline the background trend in inversion analysis. Inversion analysis is a key process that detects discrepancies between inverted and measured logs as errors at well locations.

A reliable comparison of LFMs, well logs, and inverted logs are displayed in the Zp, Zs, and Vp/Vs ratio tracks (Figure 6). The inverted logs were utilized to generate synthetic by convolving an extracted angle gathers wavelet and for comparison with seismic data. A good correlation of 0.93 between synthetic and seismic angle gather was achieved with a residual error of 0.3654.
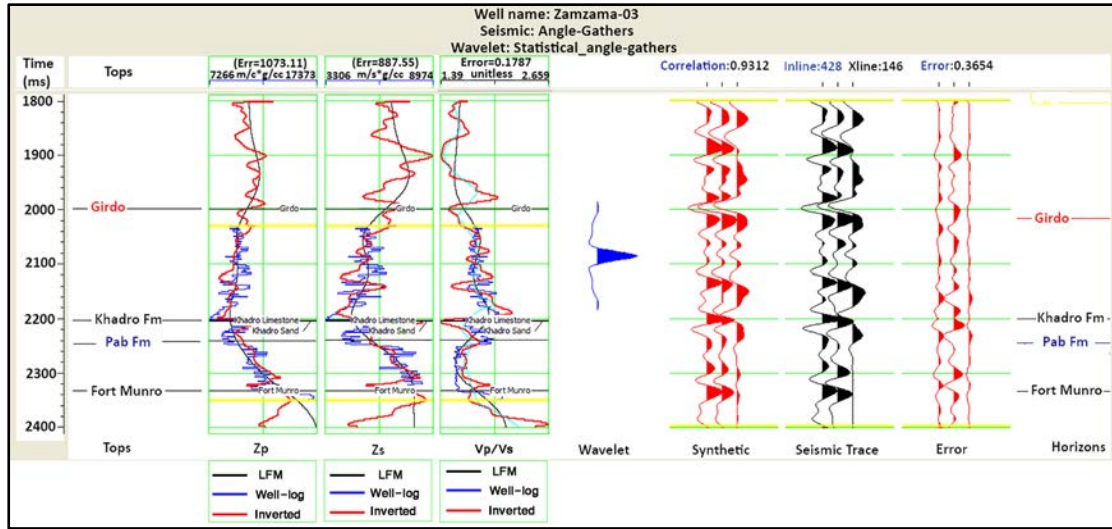
Fig. 6. LFMs are used as background trends in wells and inverted logs comparison. Synthetics (red) and seismic (black) traces provide a correlation of 0.9312 with an error of 0.3654.

The seismic inversion consists of modeling the seismic traces by a 1D convolutional model, utilizing a recursive equation (Russell & Hampson, 1991). For prestack seismic data with different incident angles (θ), an updated version is used in SPSI defined by Fatti *et al.* (1994). The process suggests a constant Vp/Vs ratio with the density estimation using Gardner *et al.* (1974) relation. Hampson *et al.* (2005) incorporated the clastic rocks as background trends (LFMs) in Fatti's equation along with establishing a linear relationship between different logarithms of elastic properties. The linear models fitted to the values of the background trend used p-impedance (Zp), s-impedance (ZS), and density (ρ) to calculate the change in the s-impedance (ΔLs) and density (ΔLD) that indicated the hydrocarbon presence (Cataldo & Leite, 2018). Figures 7a & b demonstrate ΔLs and ΔLD for Zamzama wells indicating gas presence.
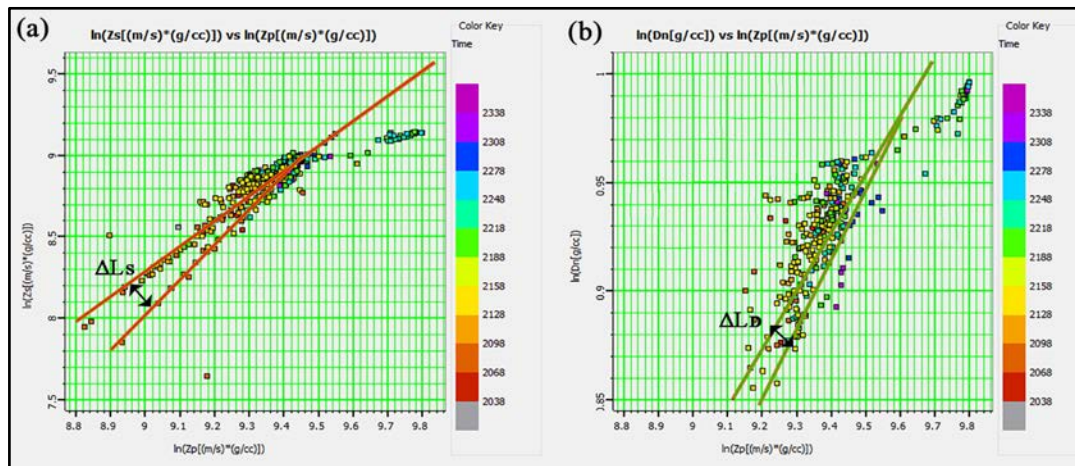

Fig. 7. (a) ΔL_S derived from ln(Z_S) vs. ln(Zp), (b) ΔL_D derived from ln(Dn) vs. ln(Zp). The deviations ΔL_S and ΔL_D from the background trend indicated the presence of gas anomalies in the field.

Finally, the seismic angle gathers inverted through matrix inversion technique $[L_P \quad \Delta L_S \quad \Delta L_D]^T = [\ln (Z_{Pn}) \quad 0 \quad 0]^T$, in which Z_{P0} represented initial impedance and afterward iterated to get solution by the conjugate gradient method (Hampson *et al*., 2005). For QC, the inverted p-impedance (Zp) and s-impedance (Zs) were compared to the corresponding well logs, indicating a good correlation within Pab Formation (Figures 8a & b).
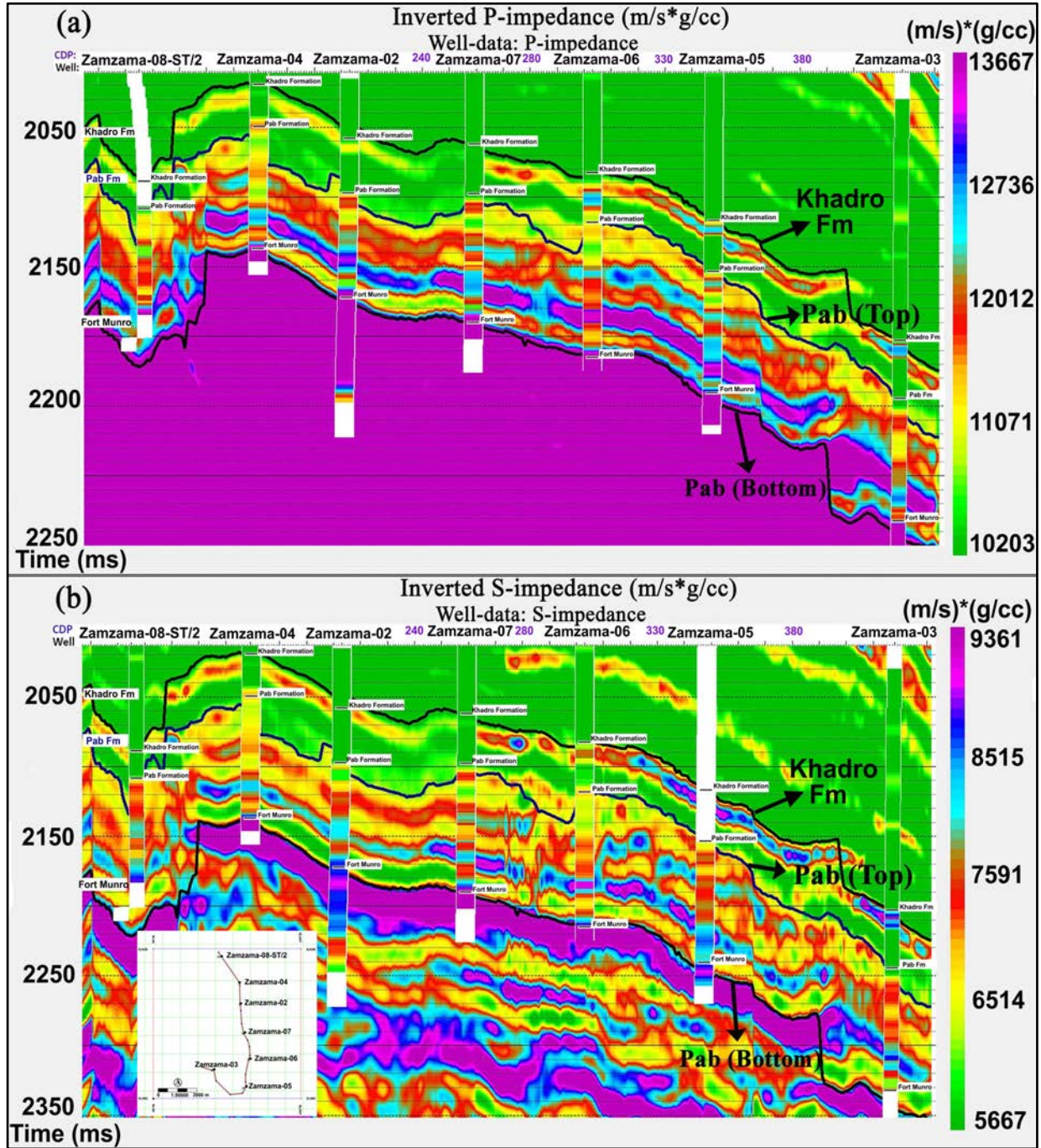

Fig. 8. (a) Inverted p-impedance, (b) Inverted s-impedance, depicting decent correlation with well logs, while the arbitrary line passes through all wells (index map).

2.4 Bayesian probability estimation

Several forms of information, such as petrophysics, seismic characteristics, and subsurface geological knowledge, are combined into the Bayesian framework to obtain reliable pay probability information. Equation (1) is the mathematical expression of the Bayes theorem.

$$p(c_i|X) = \frac{[p(X|c_i) * p(c_i)]}{p(X)} \qquad (1)$$

The c represents the class (gas sands), X signifies the inverted elastic properties (Zp and Vp/Vs ratio) (Figure 9a), and $p(c)$ reflects the prior probability of class as identified from wells (Figure 9b). For multiple distributions, probability density functions (pdfs) are computed on the Zp and Vp/Vs ratio cross plot using the kernel density estimation approach in the Bayes inference (Figure 9c). The mathematical measure for overlapping and the degree of separation of pdfs between the classes is cross-validated through a confidence matrix that provides classifier-success information. The confidence matrix reveals the probability of obtaining the target facies, i.e., gas sands (89.5%) from upscaled logs. The upscaled lithofacies logs, which resulted from the pdfs computation on a 2D cross plot, showed an acceptable correlation with the lithologies of the well (Figure 9d). In this process, five wells were utilized, while two operational wells Zamzama-04 and Zamzama-07 were tested for gas-bearing sand facies without incorporating them in this procedure. The output gas-sand probability within the Pab Formation was extracted through all available wells having GR logs depicting potential zones at the gas-producing well locations (Figure 9e).
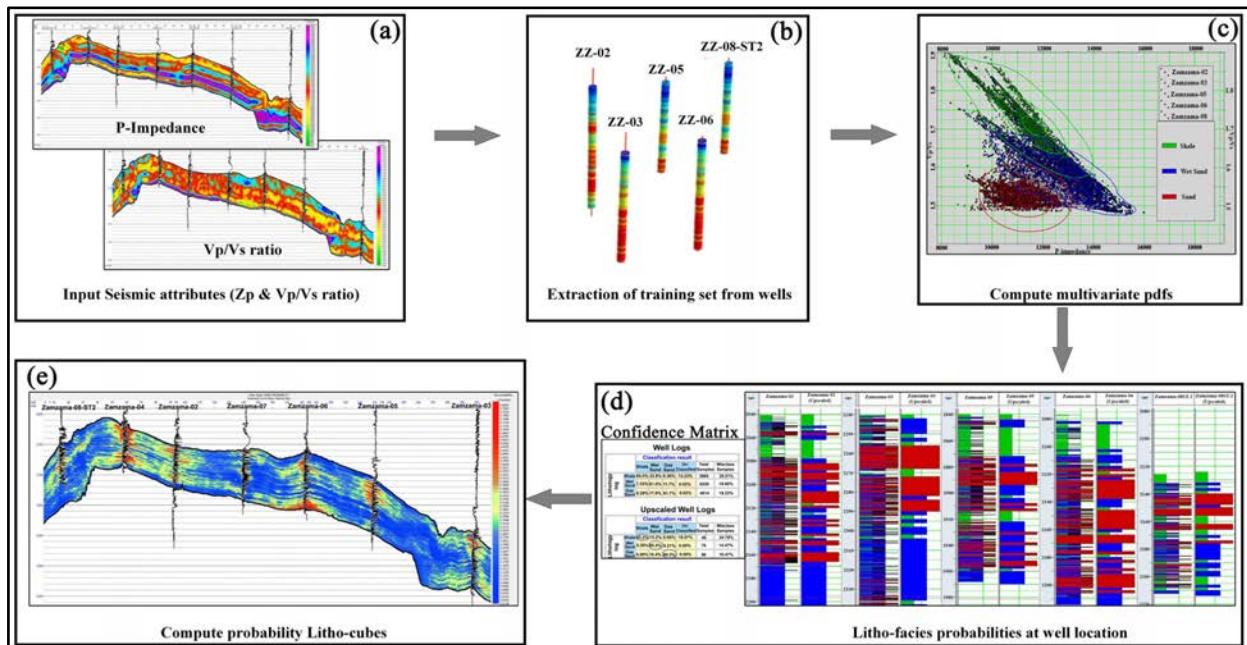

Fig. 9. (a) Inverted p-impedance and Vp/Vs ratio within Pab Formation, (b) Well-based facies and logs utilized as training set, (c) PDFs of identified facies, (d) Upscaled lithologies of pdfs and confusion matrix, and (e) Estimated gas-probability passing all the wells.

3. Probabilistic neural networking (PNN) approximation

The accurate estimation of reservoir properties away from well is one of the critical aspects of reservoir characterization. The linear and multi-linear regression analyses were adopted for the relation between petrophysical and elastic properties (Lorenzen, 2018). However, their reliability can be limited due to variations in the reservoir properties. The advancement in computational technology suggests non-linear relations for solving complex problems even for shale plays without any prior information (Durrani *et al.*, 2020). The PNN is a non-linear interpolation mathematical procedure explained in detail by Sinaga *et al.* (2019), which trains the input petrophysical logs with internal (sample-based seismic volume) and external attributes (impedances and Vp/Vs ratio). The internal attributes are generated by mathematical transforms on seismic amplitudes, including trace envelope, amplitude weighted cosine phase, amplitude weighted frequency, and instantaneous phase, while external attributes include inverted elastic properties or AVO attributes.

The clay volume is trained at well locations within Pab Formation using PNN (Figure 10a). A good agreement of predicted and actual logs could be observed having a correlation coefficient of 0.9161 with an error of 0.0489. The cross plot confirms the match of trends by setting a regression line (Figure 10b). The estimated clay volume is passing through all wells, filled with colored clay logs for the QC of the estimated volume (Figure 10c).
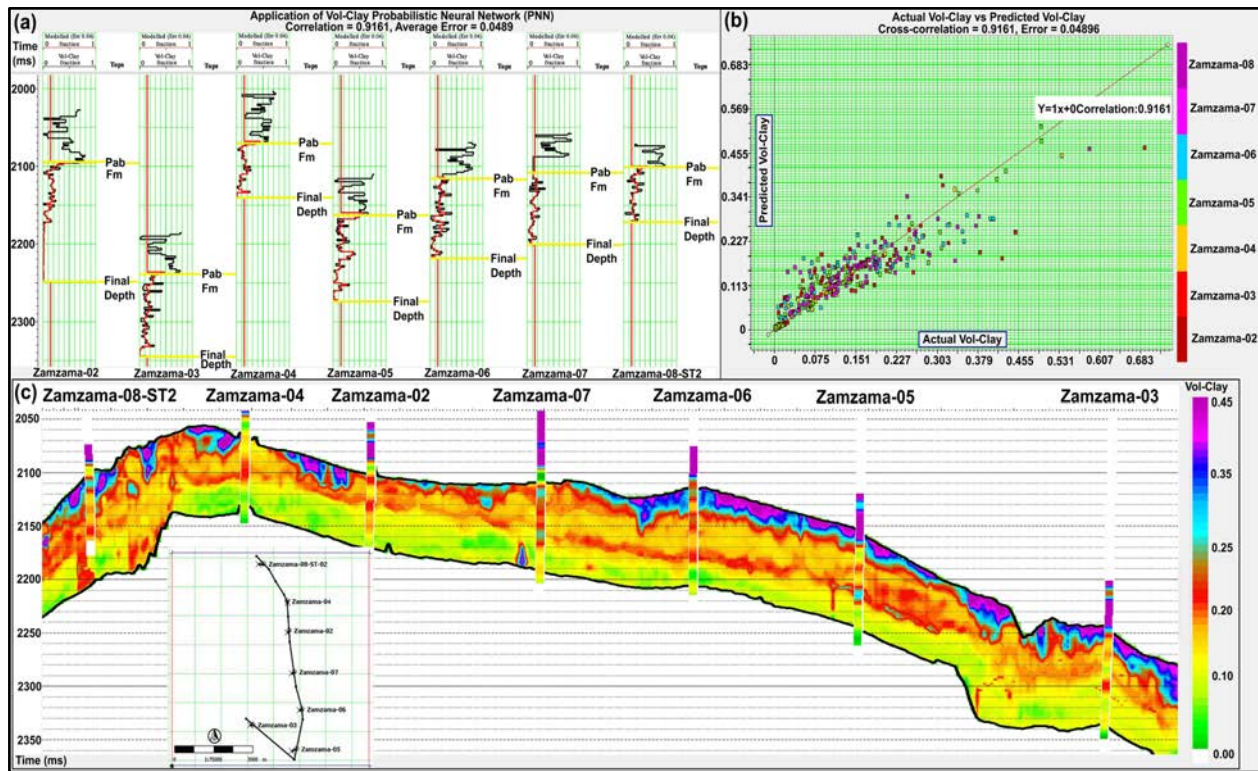

Fig. 10. (a) At the well sites, clay volume is trained using PNN, (b) Regression line showing correlation of 0.9161, and (c) Estimated clay volume depicts precise match with clay logs.

A similar process was adopted for effective porosity (PHIE) prediction, starting at the well points (Figure 11a). The correlation coefficient of 0.9326 between actual and predicted logs was observed with an error of 0.0118 (Figures 11b). The cross-section of effective porosity volume confirmed decent accordance with PHIE logs (Figure 11c).
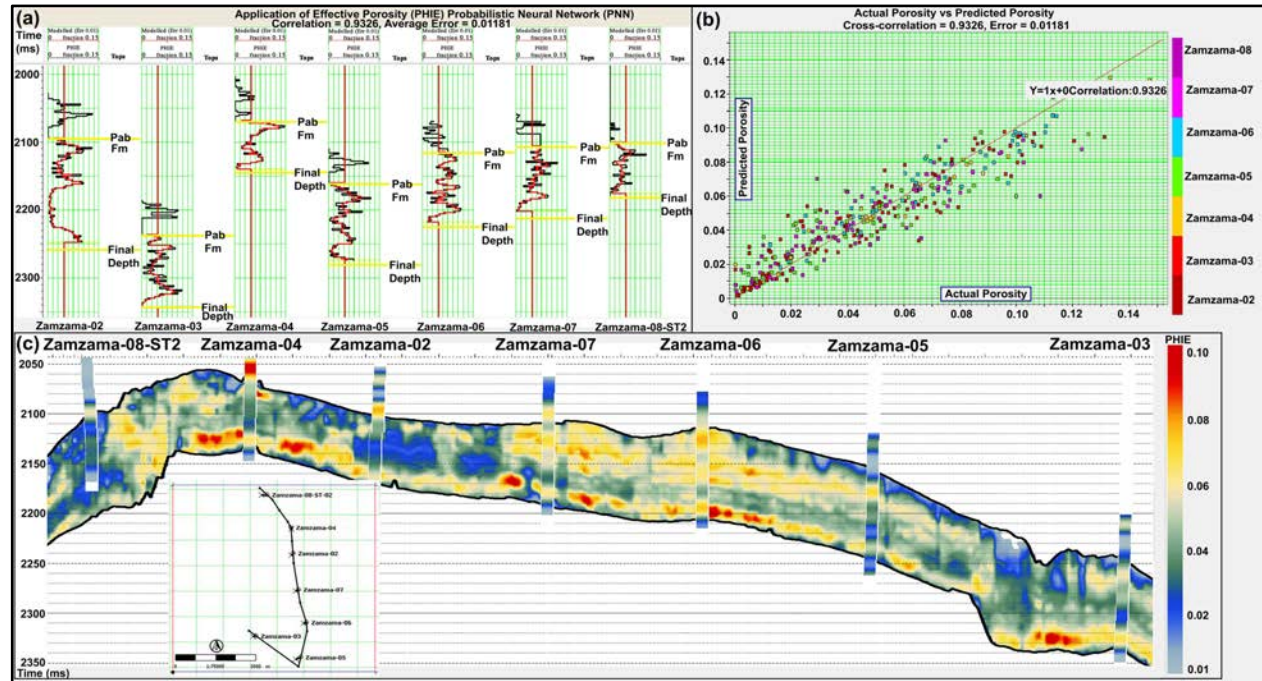
Fig. 11. (a) PNN training of PHIE at wells, (b) Regression line showing correlation of 0.9326, and (c) PHIE volume reveals appropriate match with PHIE logs.

4. Results and discussion

Typically, geologic facies hold a range of elastic values that help in their discrimination (Naeini & Exley, 2017). Certain factors, such as recording tool limitations for managing reservoir heterogeneity, may cause these ranges to overlap as seen in the Zamzam-03 well, where shales, wet, and gas sands are not distinguished (p-impedance versus Vp/Vs ratio) (Figure 12a). In the modeled elastic logs, the elastic values of identified lithofacies are more consistent. Figure 12b shows a good match between the modeled (blue) and measured (red) logs while correcting the outrange density log at 2295m. Figure 12c shows facies separation and the Rock Physics Template (RPT) delineates an acceptable gas quantity of 8-12% of porosities with an inverse relationship to p-impedance (Al-Ruwaih, 1998).
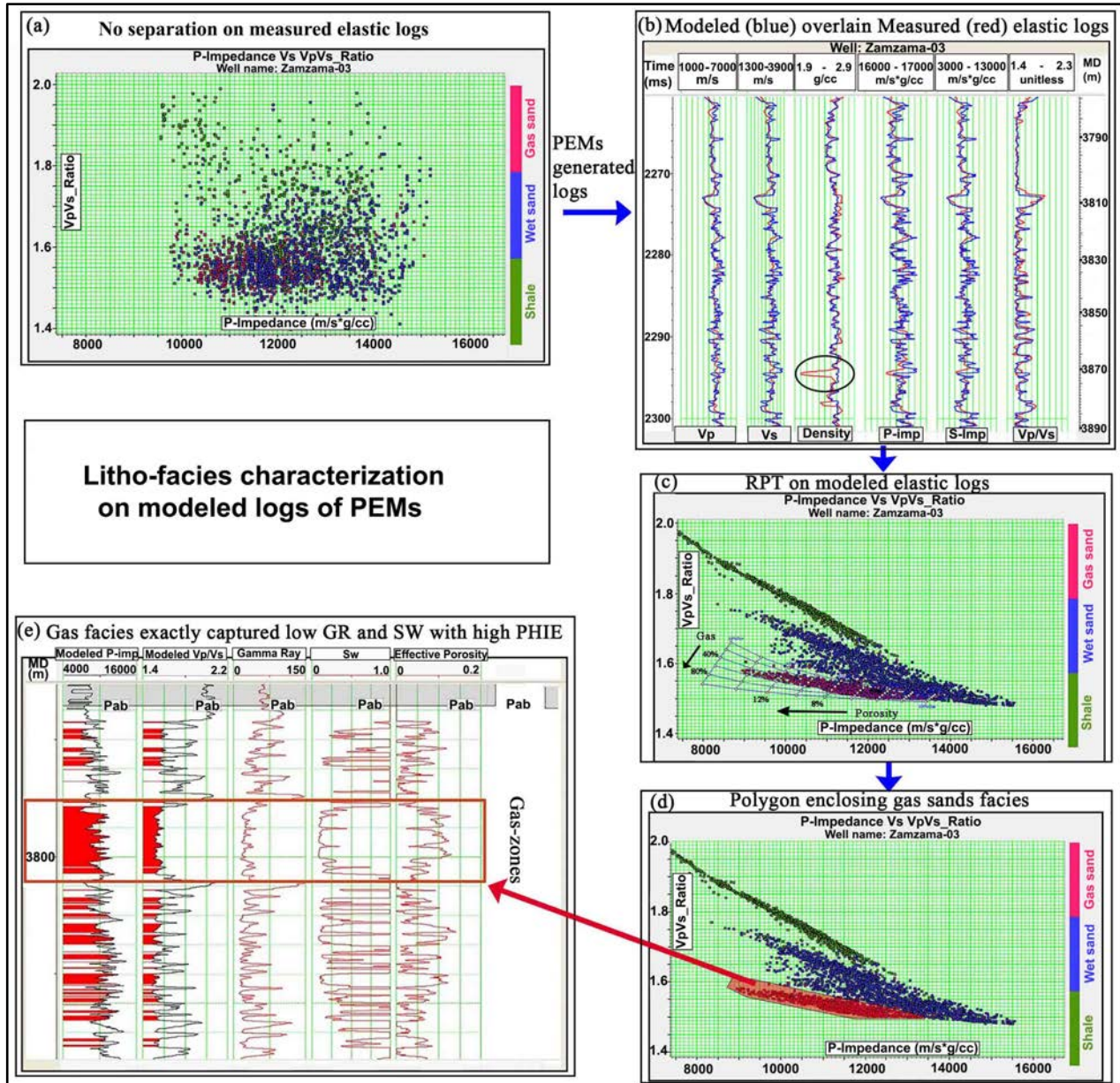
Fig. 12. (a) Mixed lithofacies in measured logs, (b) Modeled logs exhibit trend consistency with measured logs and corrected outrange values, such as the encircled density log at 2295m, (c) RPT captured a significant amount of gas at 8-12% PHIE, (d) Polygon bounding the gas-sands, and (e) Projection of gas sands show low GR, Sw, and high PHIE.

The cross plot provides value ranges of p-impedance (9,000-13,000 m/s*g/cc) and Vp/Vs ratio (1.5-1.62) that aided in the location of gas sands on SPSI inverted volumes. The gas facies are encircled and projected in the well-bore to investigate elastic and petrophysical relationships (Figures 12d). The gas intervals matched the perforation history, evident by low GR and Sw with good effective porosities (Figure 12e).

The stratigraphic maps are generated by averaging the elastic properties (Zp, Zs, and Vp/Vs ratio) within the Pab Formation. The P-impedance map, which shows values ranging from 11,600 to 12,100 (m/s)*(g/cc) for all gas-producing well locations, can help to identify prospects in these ranges (Figure 13a). The S-impedance values range from 7,000 to 7,330 (m/s)*(g/cc), suggesting gas sands at the well sites (Figure 13b). The Vp/Vs ratio is significant as several field examples have demonstrated its effectiveness in identifying the fluid types (Hamada, 2004). The Vp/Vs ratio suggests gas-sand facies with values ranging from 1.57 to 162 and it passes through all the producing wells, confirming the fairway of the channelized gas-sand body (Figure 13c).
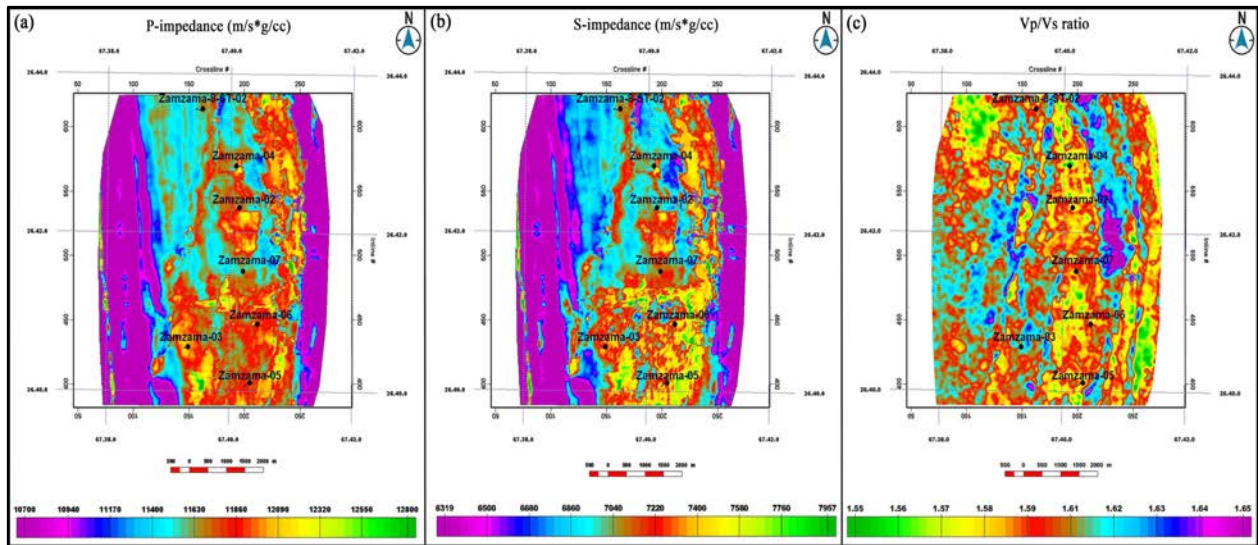
Fig. 13. (a) P-impedance ranges from 11,600 to 12,100 m/s*g/cc at the productive well locations, (b) S-impedance range between 7,000 to 7,330 m/s*g/cc indicates gas-filled sands, and (c) Vp/Vs ratio is less than 1.62 in producing wells, suggesting channelized sands.

The pay-probability map, developed by extracting maximum values inside the Pab Formation, verifies the channelized gas sands at well positions (Figure 14a). The polygons constructed over the high probability zones demarcate channelized gas sands, enclosing zones (north of the Zamzama-03 well) that can be used to assess additional prospect locations. The average valued clay map reflects the cleanliness of the Pab Formation, with a minor clay concentration of about 30% in the major producing crestal section of the anticline structure (Figure 14b). The effective porosity map depicted 9% effective porosities surrounding the operational well locations (Figure 14c). Overall, the Pab Formation comprises majorly of sandstone with low clay volumetrics and fair effective porosities.

Fig. 14. (a) High probability channelized gas-sand facies encircled by polygons passing through all wells, (b) Clay map confirms good quality of sands having minor clay content, and (c) The 9% effective porosities are present along the operational wells. (The 3D views 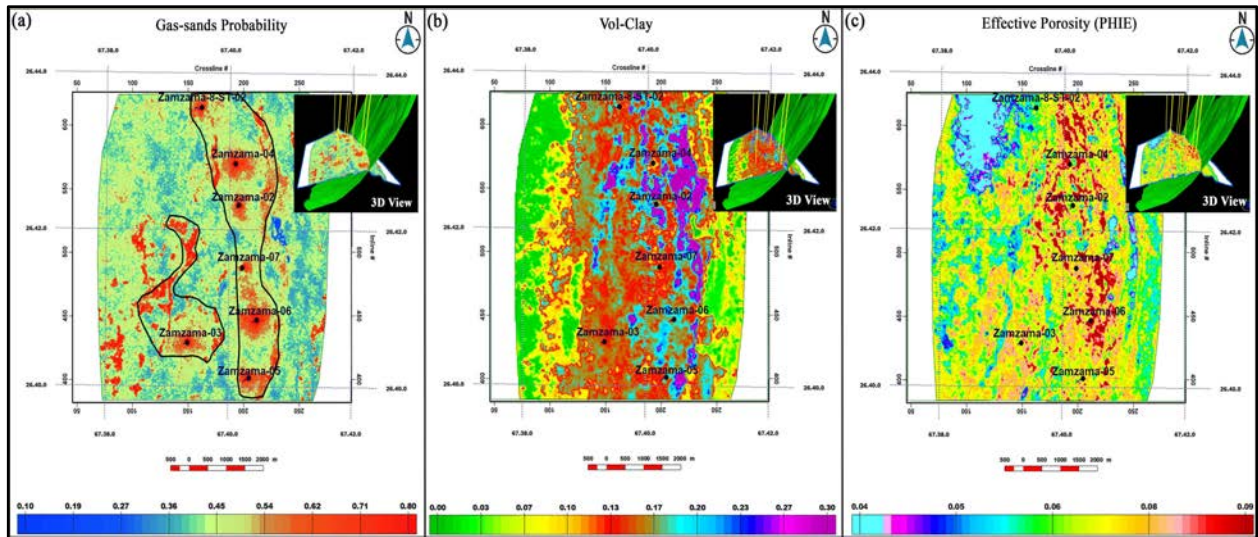illustrate the corresponding property distribution with wells penetrating the anticline's crestal zone and a large thrust bisecting the structure).

5. Conclusion

The approach used here included an integrated petro-elastic relation, which resulted in reliable gas-sands prediction with minimum uncertainties. PEMs were used to quantify the gas-sand facies, which were traced on inverted elastic volumes and confirmed by high pay probabilities. The gas-probability map revealed channelized gas sands and highlighted new prospect locations. The prospect areas indicate reduced clay volumetric with maximum effective porosities of 9%, supporting a good sand quality. Such information integration efficiently characterizes the producing facies, allowing the optimal site location for new wells with the lowest risk.

References

Adesanya, O.Y., Adeoti, L., Oyedele, K.F., Afinotan, I.P., Oyeniran, T. & Alli, S. (2021) Hydrocarbon reservoir delineation using simultaneous and elastic impedance inversion in a Niger Delta field. Journal of Petroleum Exploration and Production Technology, 11(**7**): 2891-2904.

Al-Ruwaih, F. M. (1998) Numerical modeling of Umm-Gudair well field, Kuwait. Kuwait Journal of Science and Engineering, 25, 231-248.

Al-Sulaimi, J.S. & Al-Ruwaih, F.M. (2004) Geological, structural, and geochemical aspects of the main aquifer system in Kuwait. Kuwait Journal of Science and Engineering, 32(**1**): 149-174.

Avseth, P., Mukerji, T. & Mavko, G. (2005) Quantitative seismic interpretation: Applying rock physics tools to reduce interpretation risk. Cambridge University Press.

Babasafari, A.A., Ghosh, D.P., Salim, A.M.A. & Kordi, M. (2020) Integrating petro-elastic modeling, stochastic seismic inversion, and Bayesian probability classification to reduce the uncertainty of hydrocarbon prediction: Example from Malay Basin. Interpretation, 8(**3**): SM65-SM82. https://doi.org/10.1190/INT-2019-0077.1

Batzle, M. & Wang, Z. (1992) Seismic properties of pore fluids. Geophysics, 57(**11**): 1396-1408. https://doi.org/10.1190/1.1443207

Cataldo, R.A. & Leite, E.P. (2018) Simultaneous prestack seismic inversion in a carbonate reservoir. REM-International Engineering Journal, 71(**1**): 45-51.

Durrani, M.Z.A., Talib, M., Ali, A., Sarosh, B. & Naseem, N. (2020) Characterization and probabilistic estimation of tight carbonate reservoir properties using the quantitative geophysical approach: A case study from a mature gas field in the Middle Indus Basin of Pakistan. Journal of Petroleum Exploration and Production Technology, 10(**7**): 2785-2804.

Ehsan, M., Gu, H., Akhtar, M.M., Abbasi, S.S. & Ehsan, U. (2018) A geological study of reservoir formations and exploratory well depths statistical analysis in Sindh Province, Southern Lower Indus Basin, Pakistan. Kuwait Journal of Science, 45(**2**): 84-93.

Fatti, J.L., Smith, G.C., Vail, P.J., Strauss, P.J. & Levitt, P.R. (1994) Detection of gas in sandstone reservoirs using AVO analysis: A 3D Seismic Case History Using the Geostack Technique. Geophysics, 59(**9**): 1362-1376. http://dx.doi.org/10.1190/1.1443695

Gardner G.H.F., Gardner L.W. & Gregory A.R. (1974) Formation velocity and density—the diagnostic basics for stratigraphic traps. Geophysics, 39(**6**): 770-780. https://doi.org/10.1190/1.1440465

Gassmann, F. (1951) Elastic waves through a packing of spheres. Geophysics, 16(**4**): 673-685.

Hamada, G.M. (2004) Reservoir Fluids Identification Using Vp/Vs Ratio. Oil & Gas Science and Technology, 59(**6**): 649-654. https://doi.org/10.2516/ogst:2004046

Hampson, D., Russell, B.H. & Bankhead, B. (2005) Simultaneous inversion of pre-stack seismic data. SEG Annual Meeting, Houston, 2015, Abstracts No. 21, Pp. 1633-1637. https://doi.org/10.1190/1.2148008

Han, D.H., Nur, A. & Morgan, D. (1986) Effects of porosity and clay content on wave velocities in sandstones. Geophysics, 51(**11**): 2093-2107.

Jackson, M.A., Hill, R., Roberson, P., Woodall, M.A., Wormald, G. & Jafri, N. (2004) Zamzama Gas Field – Balancing Risk and Value. Proceedings of SPE Asia Pacific Oil and Gas Conference and Exhibition, Perth, 18th to 20th October 2004.

Li, Z., LI, Q. & Zhang, H. (2020) Integrated physical detection technology in complicated surface subsidence area of mining area. Kuwait Journal of Science, 47(**1**): 86-96.

Lorenzen, R. (2018) Multivariate linear regression of sonic logs on petrophysical logs for detailed reservoir characterization in producing fields. Interpretation, 6(**3**): T543-T553. https://doi.org/10.1190/INT-2018-0030.1

Miraj, M.A.F., Ali, A., Javaid, H., Rathore, P.W.S., Ahsan, N., Saleem, R.F., Afgan. & S., Malik, M.B. (2021) An integrated approach to evaluate the hydrocarbon potential of Jurassic Samana Suk Formation in Middle Indus Basin, Pakistan. Kuwait Journal of Science, 48(**4**): 1-11.

Naeini, E.Z. & Exley, R. (2017) Quantitative interpretation using facies-based seismic inversion. SEG, 5(**3**): SL1-SL8. http://dx.doi.org/10.1190/INT-2016-0178.1

Russell, B. & Hampson, D. (1991) Comparison of Poststack Seismic Inversion Methods. SEG Technical Program, Abstracts No. 10, Pp. 876-878. https://doi.org/10.1190/1.1888870

Sams, M. & Carter, D. (2017) Stuck between a rock and a reflection: A tutorial on low-frequency models for seismic inversion. Interpretation, 5(**2**): B17-B27.

Sams, M. & Saussus, D. (2013) Practical implications of low-frequency model selection on quantitative interpretation results. SEG Technical Program Expanded Abstracts 2013, Pp. 3118-3122. https://doi.org/10.1190/segam2013-0660.1

Sinaga, T.M., Rosid, M.S. & Haidar, M.W. (2019) Porosity Prediction Using Neural Network Based on Seismic Inversion and Seismic Attributes. The 4th International Conference on Energy, Environment, Epidemiology, and Information System (ICENIS 2019), E3S Web of Conferences 125, article no. 15006, Pp. 1-5. https://doi.org/10.1051/e3sconf/201912515006

Singha, D.K. & Chatterjee, R. (2017) Rock physics modeling in the sand reservoir through well log analysis, Krishna-Godavari basin, India. Geomechanics and Engineering, 13(**1**): 99-117. https://doi.org/10.12989/gae.2017.13.1.099

Voigt, W. (1928) Lehrbuch Der Kristallphysik. Teubner, Leipzig. ISBN: 978-3-663-15884-4, Pp. 962.

Zafar, Z.A., Shoaib, K., Afsar, F., Raja, Z.A., Tanveer, A. & Burley, S.D. (2018) A RADICAL SEISMIC INTERPRETATION RE-THINK RESOLVES THE STRUCTURAL COMPLEXITIES OF THE ZAMZAMA FIELD, KIRTHAR FOREDEEP, PAKISTAN. PAPG/SPE Annual Technical Conference, Islamabad, 11-12 December 2018.

Zeb, J. & Murrell, R. (2015) Evaluation of Rock Properties from Logs Affected by Deep Invasion-A Case Study. The 3rd International Workshop on Rock Physics, Perth, 13th to 17th April 2015.

Zhang, T., Lin, Y., Liu, K.H. & Gao, S.S. (2020) Pre-stack simultaneous inversion for delineation of the Lower Wilcox erosional remnant sandstone beneath the Texas Gulf Coastal Plain: A case study. Interpretation, 8(**4**): T991-T1005. https://doi.org/10.1190/INT-2019-0178.1

Radiation dose risk variability and its implication in industrial and mining regions, NW Nigeria

Ologe Oluwatoyin[1, *], Joseph Aisabokhae[2]

Dept. of Applied Geophysics, Federal University Birnin Kebbi,
Birnin Kebbi, Kebbi State, Nigeria.
*Corresponding author: oluwatoyin.ologe@fubk.edu.ng

Abstract

The study area in the southern part of Kebbi State, Northwestern Nigeria, has witnessed intense mining activities and upscale industrialization in recent years. These events have necessitated deeper and insightful studies into radiological hazard evaluation to mitigate associated adverse consequences and enforce environmental protective measures. A total of 45 sampled locations each were taken for industrial and mining sites in Northwestern Nigeria to determine the concentration of Potassium-40, Thorium-232 and Uranium-238 radionuclides as applied to radiological hazard analysis. The mean value of the absorbed dose in the industrial site was 90 nGy/h, whereas the mining site recorded a mean value of 210 nGy/h. Other radiological indices such as radium equivalent factor, external risk assessment, internal index and representative gamma index recorded mean values of 187.68, 0.507, 0.547 and 0.768 respectively, whereas the same hazard indices presented higher values of 412.58, 1.114, 1.231 and 1.675 respectively in the mining site. The variability studies showed that the dose risk ratio of the industrial region to the mining region is 1:2. The mining site presented radiological hazard indices higher than the acceptable global threshold, hence should be classified as a restricted zone to forestall health-related crises which may manifest among local dwellers.

Keywords: Dose risk; industrial site; mining site; Northwestern Nigeria; radiological hazards.

1. Introduction

The study area lies between latitude 11°24' to 11°30' north and longitude 5°8' to 5°16' East as shown in Figure 1. The region is dominated by plutonic emplacements which have given clues to mineral exploration and also provided raw materials for construction and industrialization (Aisabokhae & Oresajo, 2019; Aisabokhae & Tampul, 2020). The environment is continually threatened by natural and anthropogenic causes which can affect the environment's safety for human habitation (Horasan & Arik, 2019; Ozturk & Arici, 2021). Various characteristics of in-situ elements in rocks or soils make them useful to the environment. However, a major characteristic of concern is the natural radioactivity potential of elements in rocks and soils.

Natural radionuclides can be categorized into cosmogonic, primordial and anthropogenic (UNSCEAR, 2000). Primordial and cosmogonic radionuclides like potassium (^{40}K) and the nuclides from thorium (^{232}Th) and uranium (^{238}U) series, and their decay products exist in all ground formations at the trace level. Their ubiquitous nature in the environment makes them a major source of radiation for the human population. ^{40}K, ^{232}Th and ^{238}U are the three major radionuclides whose radioactive concentrations are often monitored in the environment to

control or mitigate the adverse effects which their enrichment may portend to human population. The knowledge of the rate of exposure of man to radiation is important in determining the degree of threat to human life which the environment poses.

In this study, a comparative analysis is being presented to inform the research community of the contrast between the radiological significance of measured radiation doses in mining and in industrial sites. The consequences of continuous human exposure to background ionizing radiation can result in major health challenges including stunted growth, skin diseases and cancer (Kumari *et al*., 2017). As such, geological and geographical locations with sizeable population density such as the mining and industrial sites studied in this work must be assessed for their environmental radioactivity indices.

2. Geological setting of the study area

The Precambrian basement complex (Figure. 1) in Northern Nigeria is a mobile belt which is dominated by Neoproterozoic rocks due to the ubiquitous nature of the Pan-African event that occurred around 600 Ma (Kogbe, 1979). The region is primarily dominated by migmatite gneiss of granodiorite-to-granite composition (Ramadan & Abdel Fattah, 2010).
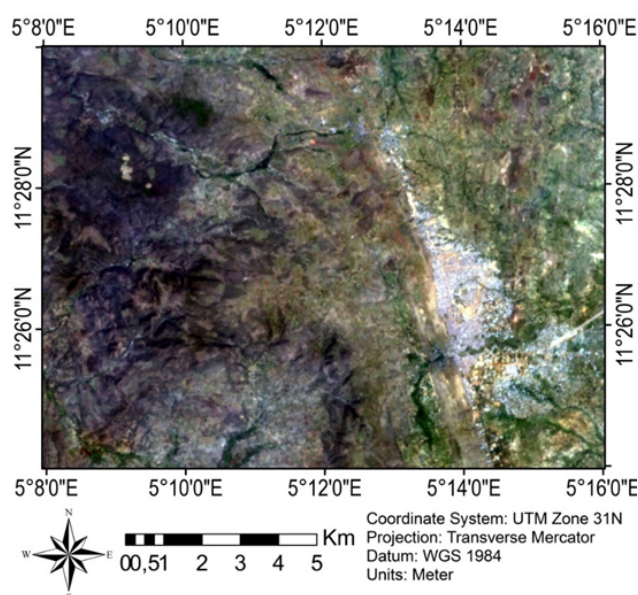
Fig. 1. Landsat-8 false colour image of the study region showing lineation trend and the exposed basement rock emplaced in the area (USGS, 2015).

3. Materials and methods

3.1 Data acquisition

In the area under study, 377 sites were earmarked for radioactivity concentration measurement encompassing mining and industrial sites. 23 more sites are expected to be delineated from satellite images depicted as alteration zones for potential future mining activities using ERDAS imaging software, thus bringing the total proposed sample site to 400 throughout the region.

The Scintrex GAD-6 model portable gamma-ray spectrometer was used to conduct ground surface spectrometric survey. The four-channel digital spectrometer is designed with

Scintrex gamma-ray sensors (KEL, 1978). The measurement of radioelement concentration can be effectively performed by using a portable detector placed on a rock surface to detect radiation from approximately 0.15 m depth and 1.0 m radius with minimal contribution from deep sources (McCay *et al*., 2014; Lovborg, 1984). The energy peaks were given as 1.76 MeV from 214Bi (uranium) and 2.61 MeV from 208Ti (thorium) while potassium measurement was directly from 1.46 MeV emitted from ^{40}K. The spectrometer used in this study was calibrated using laboratory-grade concrete calibration pads of plain potassium, thorium and uranium of the Canadian model (Killeen & Conaway, 1978). The measurements were taken five (5) times in each sample point with the geographical coordinate, elevation and site number properly recorded from the GPS device. While recording the measured data, the prevalent geographic features and geologic imprints of the area were observed.

3.2 Data processing

The measured primordial radioactive concentration data were computed for the statistical mean, standard deviation and covalence of variance and then used as input data to calculate the following parameters:

Radium equivalent radiological factor (Ra_{eq})

This radiological activity refers to the central factor in comparing the radionuclides in any material. In the study area, the concentration of the radioelement emanating from the surface can be examined using the radium equivalent factor. For each of the radioelements that produce gamma dose, equation (1) (Joel *et al.,* 2020) will estimate the radiological factor as follows:

$$Ra_{eq} = C_U + 1.43\ C_{Th} + 0.077\ C_K \hspace{4cm} (1)$$

External risk assessment (H_{ex})

The external risk assessment (H_{ex}) activity associated with gamma radiation emanating from the earth's surface can be examined using equation (2) (Joel *et al*., 2020) thus:

$$H_{ex} = C_U/370 + C_{Th}/259 + C_K/4810 \hspace{4cm} (2)$$

C_K, C_{Th}, and C_U are the activity concentration in Bq/kg.

Internal hazard index (H_{in})

The determination of the internal hazard represented by H_{in} can be examined using equation (3) (Joel *et al*., 2020) thus:

$$H_{in} = (C_U/185) + (C_{Th}/259) + (C_K/4810) \hspace{3cm} (3)$$

Such that C_U, C_{Th}, and C_K are activity concentrations of 238-U, 232-Th, and 40-K, respectively.

Representative gamma index ($I\gamma$)

Representative gamma index represents the hazard associated with occurring primordial radioactive concentration in an area under investigation. The representative index ($I\gamma$) activity is estimated by the use of equation (4) (Joel *et al*., 2020) thus:

$$I\gamma = C_U/300 \ (Bqkg^{-1}) + C_{Th}/200 \ (Bqkg^{-1}) + C_K/3000 \ (Bqkg^{-1}) \tag{4}$$

Representative alpha index (Iα)

Representative alpha index (Iα) is an important radiological index activity that can examine the measure of protection for the human population subjected to radiation exposure due to proximity to gamma-ray sources. The evaluation of Iα is performed using equation (5) (Joel *et al*., 2020) thus:

$$I\alpha = C_U/200 \ (Bqkg^{-1}) \tag{5}$$

Annual effective dose (AED)

The AED for the measured locations can be assessed by applying equation (6) (Joel *et al*., 2020).

$$AED = (0.49C_U + 0.76C_{Th} + 0.048C_K) \times 87.6 \times 10^{-2} \tag{6}$$

Excess lifetime cancer risk (ELCR)

A major radiological parameter to be calculated in this study is the excess lifetime cancer risk (ELCR), which can be calculated using equation (7) (Taskin *et al*., 2009).

$$ELCR = AED \times LD \times RF \tag{7}$$

Given that AED is the annual effective dose, Life Duration (LD) is estimated at 70 years, and the risk factor is determined as 0.05 Svy^{-1} (Taskin *et al*., 2009).

Dose risk

The computation for dose risk is given by equation (8) (Durham, 2007; Martin, 2011).

$$G = fHP \tag{8}$$

Such that G represents the number of potential casualties likely to die from radiation-related complications. F is the dose risk conversion factor (DRCF) of 5% per Sievert (ICRP, 1991). H is the estimated annual effective dose, whereas P is the total number of dwellers in the sampling area.

4. Results and discussion

Radioactive concentration measurement from 45 locations each in both the mining and industrial sites were collected to serve as input data for this study. The absorbed dose activity computed in the industrial and mining sites is presented in Table 1. In the industrial site, the absorbed dose ranged from 71 to 125 nGy/h with an estimated average of 96 nGy/h. In the mining site, the gamma absorbed dose values ranged from 152 to 249 nGy/h with an estimated mean value of 210 nGy/h.

Some radiological hazard indices such as radium equivalent factor, external risk assessment, internal hazard index and representative gamma index estimated within the industrial site and mining site are shown in Table 2. The radium equivalent factor, which compares the radionuclide content present in a material, ranged from 140 to 247 with a mean value of 187 in the industrial site, whereas the radium equivalent factor in the mining site

ranged from 301 to 496 with an average of 412 in the area. For building materials to be considered acceptable, the value of Ra_{eq} must be below unity for the induced radiation from natural radioactivity. This corresponds to 370 Bq/kg (Samwell, 2010).

Table 1. Absorbed dose computation.

Site No	Absorbed Dose D (nGy/h)							
	Industrial Site				Mining site			
	0.0414 K	0.621 Th	0.462 U	Total	0.0414 K	0.621 Th	0.462 U	Total
1	70.415	11.638	4.399	86.452	122.338	20.362	12.604	155.304
2	67.538	10.436	5.512	83.485	117.129	27.156	12.992	157.278
3	76.233	12.601	5.215	94.049	118.490	28.268	11.999	158.757
4	61.409	12.637	6.510	80.556	138.679	41.901	12.256	192.835
5	62.420	12.939	7.269	82.628	150.458	37.068	11.491	199.017
6	68.380	14.275	6.242	88.898	173.173	27.056	13.928	214.157
7	72.579	12.957	7.503	93.039	142.786	33.820	16.392	192.999
8	77.918	11.194	7.880	96.992	157.040	23.243	12.490	192.774
9	74.885	12.377	6.624	93.887	176.400	37.068	12.233	225.701
10	53.297	12.430	7.081	72.808	167.381	27.076	11.491	205.948
11	65.193	12.400	5.717	83.309	129.245	28.278	15.999	173.522
12	52.001	14.969	6.316	73.286	167.226	40.370	16.084	223.680
13	53.271	12.614	8.633	74.518	168.897	36.087	15.822	220.806
14	51.968	14.291	5.244	71.522	182.27	27.012	12.604	221.887
15	65.983	13.085	5.129	84.198	182.439	28.248	13.329	224.015
16	66.864	11.754	4.656	83.274	172.590	51.819	15.805	240.215
17	71.179	11.820	10.395	93.395	173.199	46.938	10.949	231.087
18	64.817	12.369	4.587	81.774	176.841	43.870	11.092	231.802
19	80.224	12.503	5.135	97.862	169.380	62.101	9.323	240.814
20	92.133	12.389	5.592	110.114	170.323	47.427	28.449	246.199
21	82.207	15.468	4.650	102.325	153.969	41.888	23.582	219.439
22	79.758	16.537	5.575	101.869	168.470	29.068	26.155	223.692
23	85.770	15.455	9.191	110.418	143.020	37.080	27.889	207.989
24	80.185	17.639	9.813	107.638	169.027	37.852	27.918	234.796
25	88.906	16.794	10.966	116.667	167.783	56.020	25.670	249.473
26	72.747	15.887	3.857	92.491	125.811	51.711	20.649	198.171
27	77.490	16.164	4.639	98.293	162.496	41.964	20.472	224.932
28	72.565	16.797	5.021	94.384	182.957	36.231	21.202	240.390
29	79.421	21.794	5.169	106.384	173.264	46.550	20.204	240.018
30	79.537	19.431	5.226	104.195	116.663	25.513	21.619	163.794
31	86.418	23.740	5.689	115.847	170.776	24.302	22.766	217.844
32	84.397	20.513	5.763	110.673	139.651	28.286	24.848	192.785
33	84.228	10.584	6.065	100.878	149.913	15.740	25.778	191.432
34	82.997	11.134	6.225	100.356	176.517	23.455	27.564	227.536
35	80.639	15.581	8.365	104.585	155.291	29.544	25.168	210.003
36	80.211	15.554	5.780	101.545	154.086	22.747	28.432	205.264
37	84.099	15.707	5.215	105.021	165.204	38.096	29.293	232.593
38	53.556	16.966	15.999	86.521	175.104	41.976	23.958	241.039
39	58.182	20.084	12.233	90.500	170.958	49.760	22.743	243.460
40	54.411	19.237	9.928	83.577	162.405	28.783	25.967	217.155
41	61.318	23.047	12.627	96.992	147.322	47.009	26.298	220.628
42	92.146	22.616	10.949	125.710	103.808	25.263	23.439	152.510
43	79.537	24.320	5.831	109.689	127.431	25.127	21.562	174.120
44	84.397	19.454	6.356	110.207	118.153	33.820	28.603	180.576
45	96.344	18.151	5.831	120.326	128.766	40.355	28.466	197.587
Mean	73.560	15.563	6.947	96.070	154.781	35.407	19.946	210.134

Table 2. Deduced radium equivalent, external and internal risk indices, and gamma index.

Site	Industrial site				Mining site			
	Ra_{eq}	H_{ex}	H_{in}	I_y	Ra_{eq}	H_{ex}	H_{in}	I_y
1	167.286	0.452	0.477	0.692	301.706	0.815	0.888	1.240
2	161.574	0.436	0.468	0.668	308.504	0.833	0.909	1.255
3	182.092	0.492	0.522	0.753	311.446	0.841	0.911	1.268
4	157.405	0.425	0.463	0.643	380.944	1.029	1.100	1.542
5	161.624	0.436	0.478	0.660	390.067	1.053	1.120	1.593
6	173.564	0.469	0.505	0.711	414.534	1.119	1.201	1.713
7	181.065	0.489	0.533	0.743	378.929	1.023	1.120	1.540
8	187.751	0.507	0.553	0.774	372.638	1.006	1.080	1.542
9	182.119	0.491	0.531	0.750	439.922	1.188	1.259	1.807
10	143.076	0.386	0.427	0.580	398.534	1.076	1.143	1.649
11	162.180	0.438	0.471	0.666	340.130	0.918	1.012	1.384
12	144.857	0.391	0.428	0.585	438.801	1.185	1.279	1.788
13	146.811	0.396	0.447	0.593	431.478	1.165	1.257	1.765
14	140.950	0.381	0.411	0.571	428.489	1.157	1.230	1.776
15	163.957	0.443	0.472	0.674	433.216	1.170	1.248	1.793
16	161.506	0.436	0.463	0.667	474.538	1.281	1.374	1.921
17	182.106	0.492	0.552	0.743	453.921	1.226	1.290	1.851
18	158.965	0.429	0.456	0.655	453.935	1.226	1.291	1.857
19	189.116	0.511	0.541	0.784	478.231	1.291	1.346	1.931
20	211.991	0.572	0.605	0.882	487.573	1.317	1.483	1.958
21	198.580	0.536	0.563	0.820	433.868	1.172	1.309	1.747
22	198.489	0.536	0.569	0.816	436.884	1.180	1.333	1.779
23	215.013	0.581	0.635	0.881	411.756	1.112	1.275	1.651
24	210.997	0.570	0.628	0.858	461.965	1.247	1.411	1.867
25	227.767	0.615	0.678	0.930	496.622	1.341	1.491	1.987
26	180.234	0.487	0.509	0.741	397.769	1.074	1.196	1.578
27	191.386	0.517	0.543	0.788	443.170	1.197	1.317	1.794
28	184.512	0.498	0.527	0.756	469.604	1.268	1.392	1.918
29	209.090	0.565	0.595	0.852	473.178	1.277	1.395	1.916
30	203.990	0.551	0.581	0.835	322.524	0.871	1.000	1.301
31	227.710	0.615	0.649	0.928	422.866	1.142	1.275	1.735
32	216.680	0.585	0.619	0.886	378.656	1.023	1.168	1.531
33	194.157	0.524	0.560	0.807	370.867	1.001	1.153	1.520
34	193.479	0.522	0.559	0.803	441.978	1.194	1.355	1.809
35	203.966	0.551	0.600	0.835	411.335	1.111	1.258	1.670
36	197.512	0.533	0.568	0.813	400.505	1.082	1.248	1.629
37	203.874	0.550	0.581	0.841	458.394	1.238	1.409	1.848
38	173.306	0.468	0.561	0.683	474.196	1.280	1.420	1.921
39	180.941	0.489	0.560	0.718	481.775	1.301	1.434	1.941
40	166.988	0.451	0.509	0.665	424.542	1.146	1.299	1.727
41	194.447	0.525	0.601	0.770	439.174	1.186	1.339	1.754
42	247.130	0.667	0.732	1.003	301.981	0.815	0.952	1.208
43	216.557	0.585	0.618	0.878	341.540	0.922	1.048	1.384
44	215.525	0.582	0.619	0.882	359.542	0.971	1.138	1.430
45	233.609	0.631	0.665	0.964	394.033	1.064	1.231	1.567
Mean	187.687	0.507	0.547	0.768	412.584	1.114	1.231	1.675

The internal hazard index estimated in the industrial site ranged from 0.411 to 0.678 with a mean value of 0.547, whereas the values recorded in the mining site ranged from 0.888 to 1.491 with an average estimate of 1.231. The representative gamma index estimated in the industrial site ranged from 0.571 to 1.003 with an estimated average of 0.768, whereas the gamma index estimated in the mining site ranged from 1.208 to 1.987 with an average value of 1.675.

Table 3. Deduced alpha index, annual effective dose and excess cancer lifetime risk indices.

Site	Industrial site			Mining site		
	I_α	AED	ELCR	I_α	AED	ELCR
1	0.048	0.106	0.372	0.136	0.190	0.667
2	0.060	0.102	0.358	0.141	0.193	0.675
3	0.056	0.115	0.404	0.130	0.195	0.681
4	0.070	0.099	0.346	0.133	0.236	0.828
5	0.079	0.101	0.355	0.124	0.244	0.854
6	0.068	0.109	0.382	0.151	0.263	0.919
7	0.081	0.114	0.400	0.177	0.237	0.828
8	0.085	0.119	0.416	0.135	0.236	0.827
9	0.072	0.115	0.403	0.132	0.277	0.969
10	0.077	0.089	0.313	0.124	0.253	0.884
11	0.062	0.102	0.358	0.173	0.213	0.745
12	0.068	0.090	0.315	0.174	0.274	0.960
13	0.093	0.091	0.320	0.171	0.271	0.948
14	0.057	0.088	0.307	0.136	0.272	0.952
15	0.056	0.103	0.361	0.144	0.275	0.962
16	0.050	0.102	0.357	0.171	0.295	1.031
17	0.113	0.115	0.401	0.119	0.283	0.992
18	0.050	0.100	0.351	0.120	0.284	0.995
19	0.056	0.120	0.420	0.101	0.295	1.034
20	0.061	0.135	0.473	0.308	0.302	1.057
21	0.050	0.125	0.439	0.255	0.269	0.942
22	0.060	0.125	0.437	0.283	0.274	0.960
23	0.099	0.135	0.474	0.302	0.255	0.893
24	0.106	0.132	0.462	0.302	0.288	1.008
25	0.119	0.143	0.501	0.278	0.306	1.071
26	0.042	0.113	0.397	0.223	0.243	0.851
27	0.050	0.121	0.422	0.222	0.276	0.965
28	0.054	0.116	0.405	0.229	0.295	1.032
29	0.056	0.130	0.457	0.219	0.294	1.030
30	0.057	0.128	0.447	0.234	0.201	0.703
31	0.062	0.142	0.497	0.246	0.267	0.935
32	0.062	0.136	0.475	0.269	0.236	0.828
33	0.066	0.124	0.433	0.279	0.235	0.822
34	0.067	0.123	0.431	0.298	0.279	0.977
35	0.091	0.128	0.449	0.272	0.258	0.901
36	0.063	0.125	0.436	0.308	0.252	0.881
37	0.056	0.129	0.451	0.317	0.285	0.998
38	0.173	0.106	0.371	0.259	0.296	1.035
39	0.132	0.111	0.388	0.246	0.299	1.045
40	0.107	0.102	0.359	0.281	0.266	0.932
41	0.136	0.119	0.416	0.285	0.271	0.947
42	0.118	0.154	0.540	0.254	0.187	0.655
43	0.063	0.135	0.471	0.233	0.214	0.747
44	0.069	0.135	0.473	0.310	0.221	0.775
45	0.063	0.148	0.516	0.308	0.242	0.848
Mean	0.075	0.118	0.412	0.216	0.258	0.902

Other hazard indices comprising alpha index, annual effective dose and excess cancer lifetime risk indices have been computed in Table 3. Within the industrial site, the alpha index showed varying indices ranging from 0.042 to 0.173 with a mean value of 0.075, whereas a range of values from 0.101 to 0.317 and a mean value of 0.216 was recorded in the mining site. The annual effective dose in the industrial site presented values ranging from 0.088 to 0.154 with

an average of 0.118, whereas the mining site showed values ranging from 0.187 to 0.306 and had an average of 0.258 in the area. The excess cancer lifetime risk indices produced in the area reflected varying indices for the industrial and mining sites. ELCR indices in the industrial site ranged from 0.307 to 0.540 with an average of 0.412, whereas in the mining site, it ranged from 0.655 to 1.071 with an average of 0.902. The ELCR values in both industrial and mining sites are below the recommended safe limit of 3.75 X 10^{-3} (UNSCEAR, 2000). The result of ELCR in the industrial site is comparable to the values obtained in soil samples collected at Covenant University, Ota, Nigeria (Joel *et al*., 2020). More so, the results of some radiological hazards deduced in the mining site are similar to those obtained in a kaolin mining field in Ifonyintedo, Nigeria (Adagunodo *et al*., 2018).

The estimated dose risk from primordial radiation sources was deduced for industrial and mining sites in the region. The dose risk indices may be suitable for estimating possible adverse implications due to gamma-ray exposures. The AED disparity between the industrial site and mining site is displayed in Figure 2. All AED estimations in the mining site are numerically higher than those obtained in the industrial site. In Figure 3, the ELCR activity in the mining site also appears to be higher than in the industrial site.
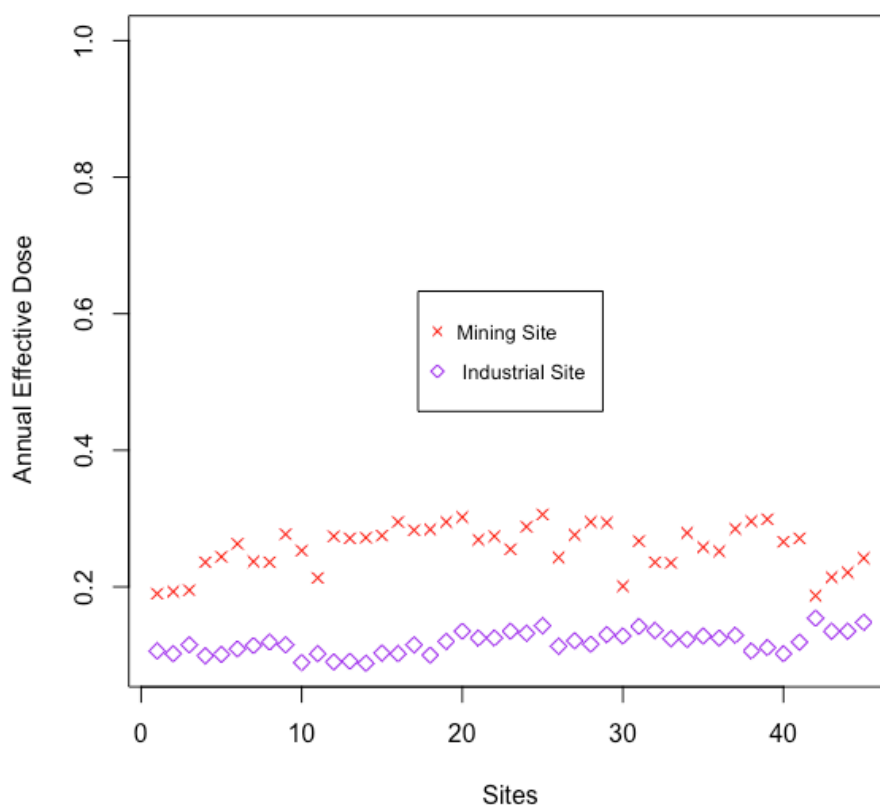

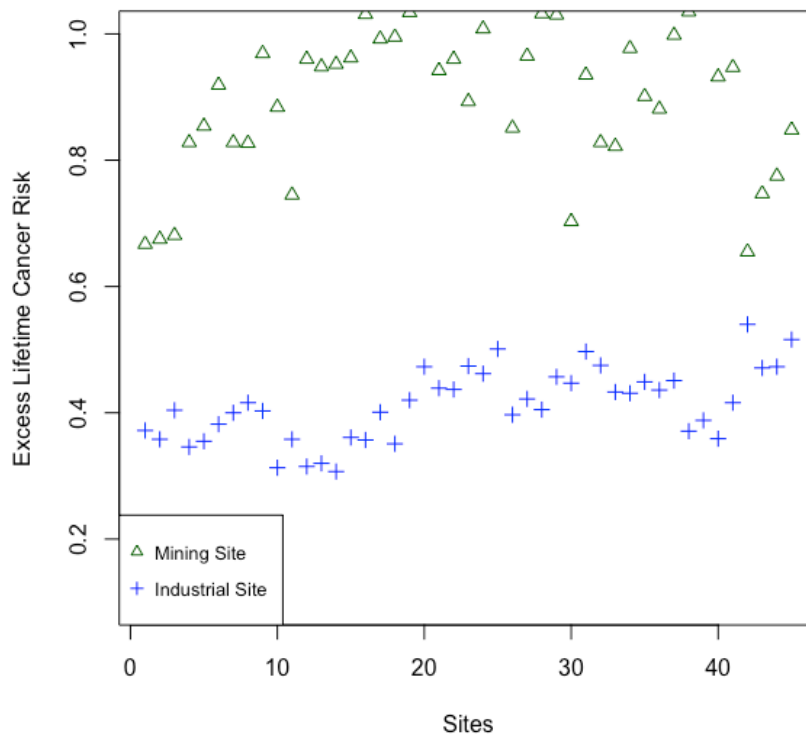**Fig. 2.** Plot of AED variability in industrial and mining sites.

Fig. 3. Plot of ELCR variability between industrial and mining sites.

    With an estimated population of 14,272 dwellers in the industrial area, and a dwindling 3,414 inhabitants in the mining area (NBS, 2016), a credible dose risk analysis may provide information about the possibility of fatal cancer occurrence in the area. Table 4 provides a comparative analysis of the dose risk in the industrial and mining sites.

Table 4. Dose risk computation

Site	AED (mean)	DRCF (5% Sv^{-1})	Dose risk per year
Industrial	0.118	0.05	84
Mining	0.258	0.05	44

Predictions from the comparative analysis suggest that 84 people (0.6%) of the entire population living in the industrial sites may die due to exposure to gamma-ray radiation, whereas 44 people (1.3%) are in danger of becoming casualties of exposure to gamma-ray radiation in the mining site (Table 4). Regarding DRCF indices, certain parameters such as age, gender, personal habits, diet, etc., may influence the degree of intensity.

5. Conclusion

The results of the predicted radiation dose risk in the study area were presented based on the measurements of primordial radioactive concentrations. Some conclusions drawn from the study are listed.

i. The Ra_{eq} activity estimated in the industrial site is averaged at 187.68 Bq/kg. It is well below the recommended limit of 370 Bq/kg as stated by UNSCEAR (2000), whereas in the mining site, the Ra_{eq} presented an average of 412 Bq/kg which is well above the recommended limit.

ii. The mean annual effective dose in the industrial site showed 0.118 mSv/y, whereas the mean value obtained from the mining site was 0.258 mSv/y. The AED activity in both sites was below the global limit of 0.70 mSv/y (UNSCEAR, 2000).

It is recommended that the mining site be restricted from residual inhabitation for health safety purposes.

ACKNOWLEDGEMENTS

References

Adagunodo, T.A., George, A.I., Ojoawo, I.A., Ojesanmi K., & Ravsankar, R. (2018). Radioactivity and radiological hazards from a Kaolin field in Ifonyintedo, Nigeria. MethodX, **5**: 362-314.

Aisabokhae, J.E., & Oresajo B. (2019). The magnetic response of hydrothermal alteration in iron-oxide basement complex, NW Nigeria. Geology, Geophysics and Environment, **45**(2): 145–156. http://dx.doi.org/10.7494/geol.2019.45.2.145.

Aisabokhae, J., & Tampul H. (2020). Statistical variability of radiation exposures from Precambrian basement rocks, NW Nigeria: Implication on radiogenic heat production. Scientific African, **10**: 1-11. https://doi.org/10.1016/j.sciaf.2020.e00577

Durham, J. (2007). Concepts, quantities, and dose limits in radiation protection dosimetry. Radiation Measurement, **41**:28-35.

Horasan, B.Y., & Arık, F. (2019). Assessing Heavy Metal Pollution in the surface soils of Central Anatolia Region of Turkey, Carpathian Journal of Earth and Environmental Sciences, **14**(1): 107–118.

ICRP (1991). Annual limits on intake of radionuclides by workers based on 1990 recommendations. International Commission of Radiological Protection. Annals of the ICRP 21, Publication 4.

Joel, E.S., Omeje, D.K, Adewoyin, O., Olawole, O.C., Akinwumi, A., Erubami, S., & Adeyemi, G.A. (2020). Assessment of background radionuclide and gamma dose rate distribution in urban-setting and its radiological significance. Sci. Afri. **8**:1-8.

Kelvin Energy Limited (1978). Report on airborne electromagnetic, magnetometer and radiometric survey. Kettle River Area, British Columbia. Appendix III, gad-6 and gsa-42 specifications.

Killeen, P.G., & Conaway, J.G. (1978). New facilities for calibrating gamma-ray spectrometric logging and surface exploration equipment. CIM Bull **71**:84–87.

Kogbe, C. (1979). Geology of the south-eastern sector of the Iullemmeden Basin. Bulletin of Department of Geology, Ahmadu Bello University, Zaria, **2**(1):34–78.

Kumari, R., Kant, K., & Garg, M. (2017). Natural radioactivity in rock samples of Aravali hills in India. Int. J. Radiat. Res. **15**:91-398.

Lovborg, L. (1984). The calibration of portable and airborne gamma-ray spectrometers theory, problems, and facilities. Rise Natl. Lab 2456. pp. 3–207

Martin, M. M. (2011). Measurements of the elemental and radionuclide concentrations of environmental and geological samples from selected areas of Kibwezi District, Kenya. Msc. Thesis (Physics), Kenyatta University, Kenya.

McCay, A.T., Harley, T.L., Younger, P.L., Sanderson, D.C., & Cresswell, A.J. (2014). Gamma-ray spectrometry in geothermal exploration: state of the art techniques. Energies **7**:4757–4780. https://doi.org/10.3390/en7084757

Nigeria Bureau of Statistics (2016). National population estimates. Population forecast publication.

Ozturk, A., & Arici, O.K. (2021). Carcinogenic-potential ecological risk assessment of soils and wheat in the eastern region of Konya (Turkey). Environ Sci Pollut Research, **28**:15471–15484.

Ramadan T.M., & Abdel Fattah M.F. (2010). Characteristics of gold mineralization in Garin Hawal area, Kebbi State, NW Nigeria, using remote sensing. The Egyptian Journal of Remote Sensing and Space Science, **13**:153–163. https://doi.org/10.1016/j.ejrs.2009.08.001.

Samwell, O. (2010). Radiometric survey and estimation of radiation exposure from Archean rocks: A case study of Migori gold belt company, Kenya. M.Sc. Dissertation, School of Pure and Applied Sciences, Kenyatta University, Kenya.

Taskin, H., Karavus, M., Ay, P. *et al.* (2009). Radionuclide concentrations in soils and life time cancer risk due to gamma radioactivity in Kirklareli, Turkey. J. of Environ. Radioat. **100**:49-53. https://doi:10.1016/j.jenvrad.2008.10.012

United States Geological Survey (2015). Landsat-8 (L8) data user handbook. Version 1.0

UNSCEAR (2000). Sources and effects of ionizing radiation. Report of the United Nations Scientific Committee on the Effects of Ionizing Radiation to the General Assembly. United Nations, New York.

Sedimentary and mineralogy characteristics of late quaternary sediments, Garmian area, Kurdistan Region, NE Iraq

Barween O. Qader[1, *], Sabah A. Majeed[2]

[1]Dept. of Geology, College of science, University of Sulaimani, Kurdistan, Iraq
[2]Dept. of Civil Engineering, University of Garmian, Kurdistan, Iraq
[*]Corresponding author: parween.qader@univsul.edu.iq

Abstract

The quaternary sediments have been studied in four sections; Garmian area, Kurdistan Region, North East Iraq, which are multi-features, multi-sources, and variable lithological compositional characteristics. The grain size granulometry was used and identified, gravel, sand and mud. Gravel-sized particles are partially producing a greater amount than sand and mud size in both sections (Sar-Qallah-1 and Salih-Agha). Statistical parameters such as (mean, mode, sorting, skewness and kurtosis), have shown that the sediments are very poorly sorted, very fine skewed and platykurtic. Petrographic studies of sediments under polarized microscope investigated that these sediments are predominately consisting of (chert and carbonate rock fragments), with the existence of few amounts of igneous and metamorphic rock fragments, feldspar and monocrystalline quartz. These fragments types are an indication of multiple source rocks originate from Ophiolites and thrust sheets from the Penjween area (North Iraq). Various types of heavy minerals are identified; opaque (hematite and pyrite), and nonopaque minerals (pyroxene, amphibole, epidote and zircon). X-ray diffraction technique is used to interpret clay mineralogy which indicates that chlorite and palygorskite are the main clay mineral with the presence of non-clay minerals such as quartz and calcite.

Keywords: Clay; minerals; quaternary; rock fragments; source rocks.

1. Introduction

The quaternary period is globally characterized by a series of glaciers interspersed with relatively warm periods (Elias & Mock, 2013). The marine oxygen isotope record investigations of stratigraphical position of quaternary found four major glaciation periods north hemisphere (Raymo, 1997), long core studies revealed the climatic developments and delta structures later time in the same area (Krenmayr, 1996 in Van Husen, 2004). Worldwide quaternary deposits have glacial sedimentary characteristics (Péwé,1975a; Krenmayr, 1996 in Van Husen, 2004), rarely with glacial characteristics have been found in the Middle East, Iraq, and the region, most of which are fluvial and alluvial clastic sediments. Most of the Iraqi territory is covered by quaternary deposits that incorporate various environments fluvial, delta, lacustrine, and Aeolian in the Mesopotamia plains and Foothill Zone. Recently Abdula *et al*., (2020) recorded the indicators of Pleistocene in High Folded Zone-North Iraq that show the existence of the glacial period. The characteristics of quaternary sediments in north Iraq indicated sandy, and silty dominant grains, rich heavy minerals, and high presence of light minerals (muscovite) (Al-Kaaby & Albadran, 2020). However, clay-silt particles dominant has been recorded in Bahr Al-Najaf depression with unstable heavy minerals

(amphibole and pyroxene) (Benni *et al*., 2012). The Garmian region, as a plain terrain covered by multi-origin sediments that occurs valleys fill, river bed deposits (Figure 1). These sediments are composed of gravel, sand and mud, which are resulted from weathering and erosion of older rocks. This study aims highlighting the sedimentary features of quaternary deposits such as sedimentary texture, properties of minerals and source of rocks.
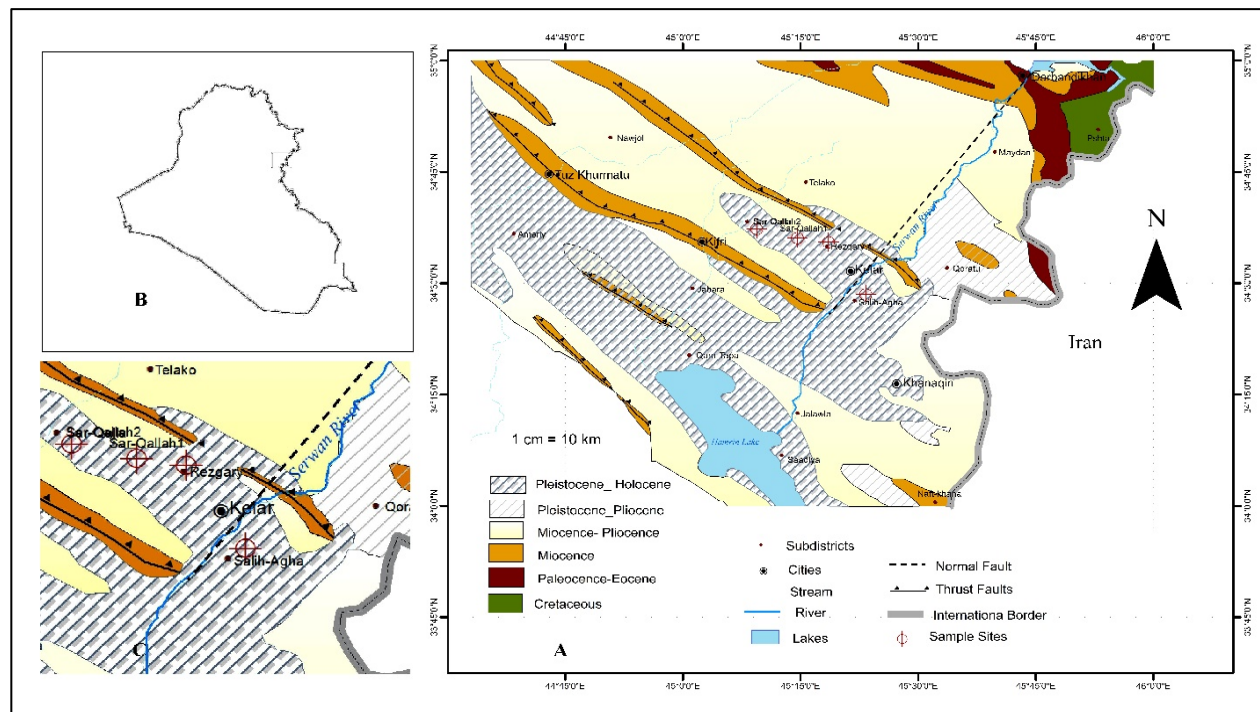

Fig. 1. Geological map of the Garmian area, Kurdistan region, North East of Iraq

(after Iraq Geological Survey, 1986).

2. Geological Setting

The Garmian area, located in the northern portion of Iraq, about 80 Km South of Sulaymaniyah city, and represent a part of Zagros Low Folded Thrust Zone (Lawa *et al.,*2013; Omar *et al.,* 2015) (Figure 1).

The Quaternary deposit in the study area forms a discontinuous sheet above the pre-quaternary deposits. The later represent either by Miocene–Pliocene fluvial siliciclastic sediments involving Bai Hassan and Mukdadiya formations or by the Miocene deltaic clastic deposits of Injana Formation which underlain by mixed lagoonal facies of the Fatha Formation (Lawa & Ghafur, 2015). Accordingly, the Neogene deposit shows rapid shallowing upwards associated with the last phase of Alpine tectonic activity (Omar *et al.,*2015). Tectonically, the area is a part of the Foothill Zone, Chamchamal-Hamrin subzone within Arabian Plate (Jassim & Goff, 2006), and bordered by the High Folded Zone from the northern side, and stable shelf from the Arabian plate. The area is including one of the main normal faults adjacent to Sirwan River starting from the Darbandikhan Lake basin in the north ending at the north of the Hamrin Lake basin in the South (Lawa, 2004). Kent (2010) suggested the studied area tectonically part of simply folded zone or is part of the Low Folded Thrust zone (Lawa *et al*., 2013). Intensive uplifting and folding of sedimentary complex sequence are the result of a few alpine orogenic phases. Consequently, numerous large anticlines

and synclines have been formed. In the studied area Quaternary sediments with the rock of Miocene Pliocene age cutting by the Sirwan River flows (Sissakian & Al-Jiburi, 2014).

3. Methods

The two main methods have been done in the studied area: firstly, field work which included, 27 samples were collected from unlithified sediment in the Garmian area. Secondly, granulometric analysis was carried out by the conventional method and approximately 50Kg weight of each sample was sieved were taken in each location (Table 1). The statistical parameters of graphic like median (Md), mean (Mz), sorting (σ_1), skewness (SK_1), and kurtosis (KG_1) were determined using the equation of (Folk, 1980) (Table 2). While we prepared (15) thin sections from collected samples for petrographic analysis by polarizing microscope. Separation heavy minerals from light minerals have been done by using bromoform liquid ($CHBr_3$) with a specific gravity (2.89) (Carver, 1971). This study also used X-Ray diffraction technique was done in Laboratory Ministry of Science and Technology, Baghdad- Iraq for analysis and identified the clay mineral composition for the Sar-Qallah-2 section.

Table 1. Grain size distribution in Salih-Agha and Sar-Qallah-1 sections, (Wentworth, 1922; Folk *et al.*,1970)

	Salih-Agha			Sar-Qallah-1			
Sieves (mm)	Weights (Kg)	%	Accumulative ratio	Weights (Kg)	%	Accumulative ratio	Particles
> 64	8.6	16.93	16.93	6	19.99	19.99	Cobble
31.5	5.75	11.32	28.25	2	6.66	26.65	Pebble
22.4	4.32	8.5	36.75	1.8	6	32.64	
16	3.6	7.09	43.84	1.8	6	38.64	
11.2	4.75	9.35	53.19	2	6.66	45.3	
8	3.32	6.54	59.72	2.98	9.93	55.23	
5.6	2.5	4.92	64.65	2.2	7.33	62.56	
4	2.2	4.33	68.98	1.52	5.06	67.62	
2	3.43	6.75	75.73	2.24	7.46	75.08	Granule
1	3.16	6.22	81.95	1.54	5.13	80.21	Sand
0.56	3.65	7.19	89.13	2.92	9.73	89.94	
0.256	2.76	5.43	94.57	1.9	6.33	96.27	
0.125	1.51	2.97	97.54	0.8	2.66	98.93	
0.063	0.92	1.81	99.35	0.2	0.67	99.6	
< 0.0063	0.33	0.65	100	0.12	0.4	100	Silt + Clay
	50.8	100		30.02	100		

Table 2. Results of Statistical parameters of (Salih-Agha and Sar-Qallah-1) sections.

Sections\Phi ϕ	95	84	75	50	25	16	5
Salih-Agha	2.1	0.2	-1.1	-3.5	-5.4	-6	-6
Sar-Qallah-1	1.8	0.4	-1	-3.2	-5.5	-6	-6

		Salih-Agha	Description	Sar-Qallah-1	Description		
Statistical	Mean	-3.1	Coarse	-2.93	Coarse		
	Sorting	2.77	VPS	2.78	VPS		
	Skewness	0.28	VFS	0.2	VFS		
	Kurtosis	0.77	Platykurtic	0.71	Platykurtic		

4. Lithology

Sissakian & Saeed (2012) mentioned that most of the Iraqi territories are covered by sedimentary rocks and quaternary deposits, and they classified them into 18 types depending on their lithological units. The lithology of quaternary deposits studied in four different locations (Figure 2). The column stratigraphy of the sediments was taken only in Rzgari which penetrated all vertical thickness in this subsurface section, while the three other sections have studied on the surface. In general, quaternary deposits in the Garmian area are rich in coarse grain particles (boulder and gravel dominant characteristic) (Table 1), except in the mud layers that appeared in Sar-Qallah-2, and the lower part of the Rzgari location. The accurate lithological characteristics of each section showed as the following:

Sar-Qallah-1 Section: These quaternary deposits are about 6m thick and consist of a mixture of friable gravel, sand, and mud that are exposed along the major valley that runs towards the Sirwan River. The coarse clastic, which is comprised of polymictic boulders, cobbles, pebbles, and gravels represent the majority and is more than 75%, while the sand ratio is about 24.52%, and less than 2% silt and clays.

Sar-Qallah-2 Section: This section is located on one of the seasonally flooded tributaries of Sirwan River from the right flank and it's about 20m thick, consist mainly of light reddish color mud, occasionally shows variation from clay to silty clay and siltstone. The mud bed contains some vertical cracks and small clusters of bedding layers (Figure 3A).

Salih-Agha Section: It is located on the left bank of the Sirwan River, about 5m in thickness and composed of a mixture of gravel and sands with a few lenses of mud, this is somewhat similar to the Sar-Qallah-1 section and as well as many of mixed sequences pebbles (Figure 2). Due to the weathering and erosion processes and the nature of the river environment, there is no united lithology appearing in the Rzgari and Sar-Qallah-2 sections.

Rzgari borehole: This subsurface section is about 120m thick and penetrated the quaternary column sediments within Rzgari borehole, which is drilled for water supply for domestic purposes (Figure 3B). The lithological component in this borehole mostly reflects an alternation between the Sirwan River terraces and flood plain deposits due to the meandering of the river course.

The coarse grain clastic intervals consist of cobble, pebble and gravels of multi-origin (sedimentary, igneous and metamorphic) rocks, most probably derived from the weathered and eroded parts of Penjween Ophiolites and Zagros Fold Thrust Belt (Stevanovic & Markovic, 2003). Occasionally, lensoidal sandy bodes are cutting across the coarse clastic. The fine clastic intervals represent by pinkish-red to reddish-brown mud and are about 20m thick in the lowermost part of the well.
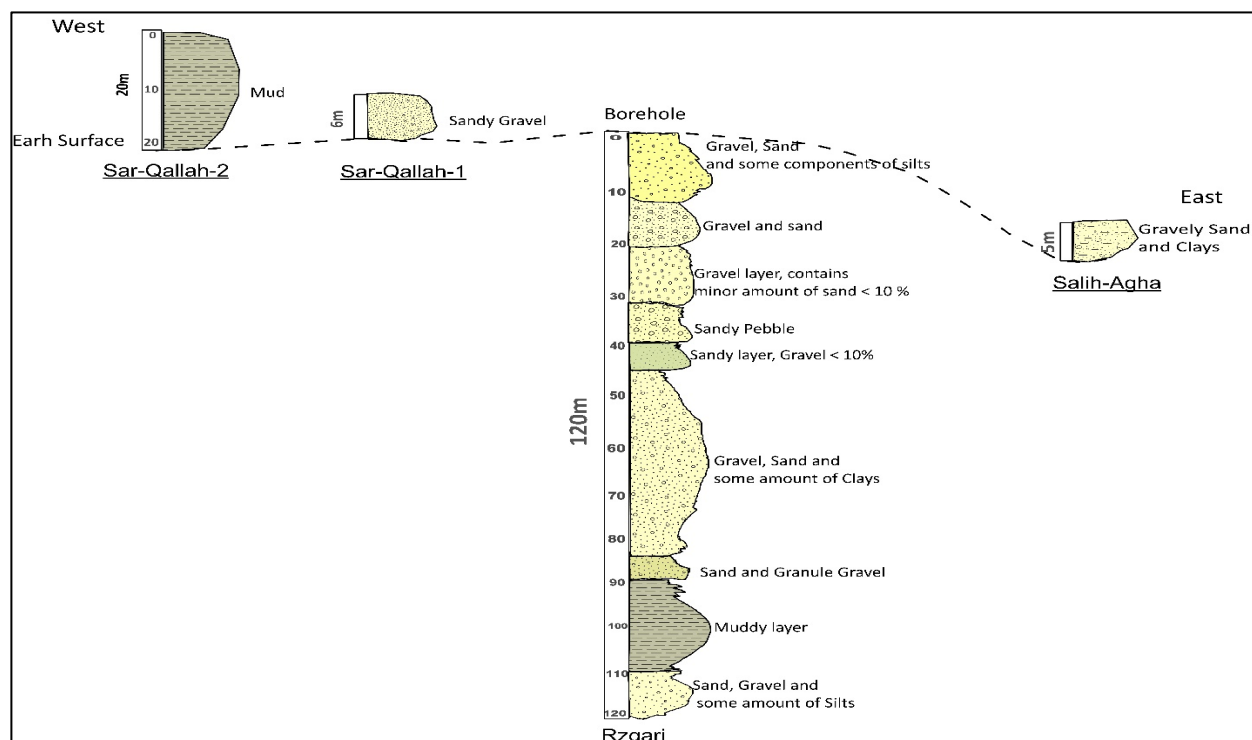

Fig. 2. Stratigraphic column of lithological unites in the Quaternary deposits in the studied area.
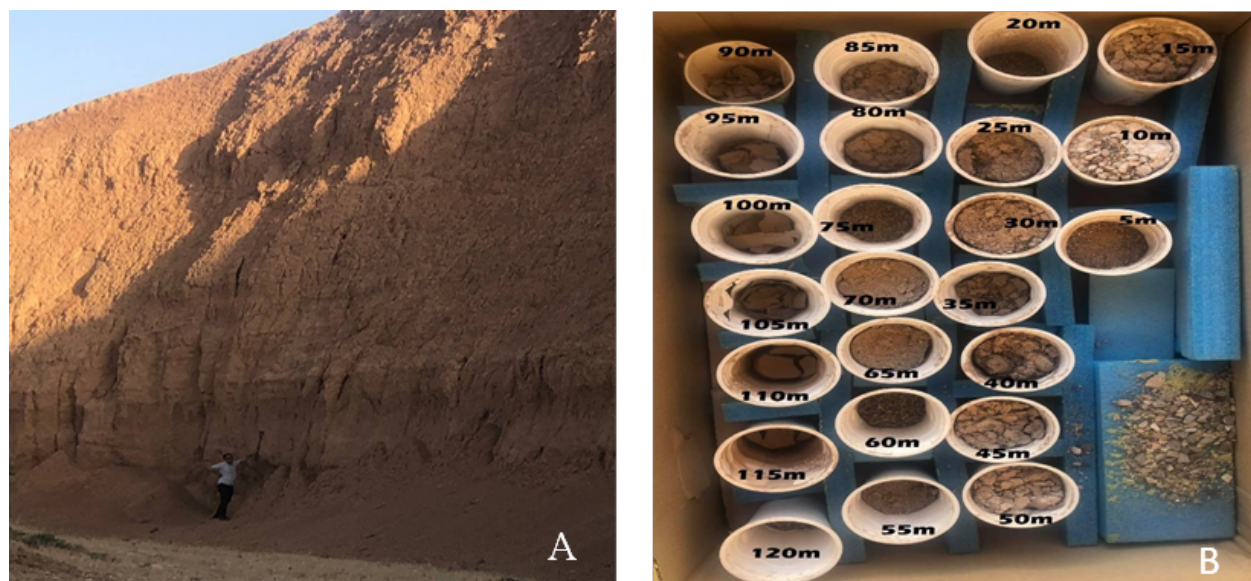
Fig. 3. (A) Sar-Qallah-2 section showing the pure mud layer alternated with thin silty layers, (B) Rzgari section, the samples were taken during well drilling, in cooperation with the Directorate of Groundwater Exploration in Garmian (10/02/2021).

5. Results

5.1 Grain size analysis

The scales (Wentworth 1922; Folk *et al.*, 1970) are considered the main scales that are widely practically used to describe and analyze grain size particles of sedimentary rocks. Three major types of fractions have been recognized, gravel, sand, and mud (Table 1). Sedimentary analysis for the quaternary deposits in the Garmian area is based on two sites, which are reflecting the variations of the sedimentation. They are analyzed by the sieve method. The gravel-sized partial is the largest part, composed approximately (75%) of the sediment in both (Salih-Agha and Sar-Qallah-1) sections of different sizes including Cobble, Pebble, and Granule. Particle's form is elongated and plated, most of gravel-sized particles are low sphericity (blades and rods), and are sub-rounded to sub-angular (Power, 1953). The majority of the particles have a frosted and polished surface (Ture 4). Sand, silt, and clay-sized particles are about (25%). The range of sands is (22-23%) distributed between VC (very coarse sand), (5-6%), C (coarse sand), (7-9%), M (medium sand), (5-6%), F (fine sand), (2-3%), and VF (very fine sand), (1-2%). In addition, the silt and clay portion are less than (1%).

The studied samples have been analyzed by statistical parameters. The results are shown in (Table 2). In general, the sediments in both sections (Salih-Agha and Sar-Qallah-1) are very poorly sorted (VPS), very fine skewed (VFS), and Platykurtic. According to (Figure 4 and Table 2), the large size of the particles indicates the high flow and the strong current energy, and then carrying fewer coarse grains in the sediments mentions turbidity phenomena during sedimentation. The sorting value is acquiring from the standard deviation value. The high value of standard deviation is an indicator of poorly sorted. The sorting value of (Salih-Agha and Sar-Qallah-1) sections is very high, which versus very poorly sorted. This is a sign of high current energy and velocity. The skewness value of the samples ranged between (0.20-0.28), which implies a dominance of coarse grain size. The positive skewness of the sediments is a reflection of high transportation energy during the sedimentation. Kurtosis is a measurement of curve peakedness. The significance of kurtosis is to measure the extreme values of tails. The samples were showed that the type of Platykurtic in both locations is (0.77- 0.71).
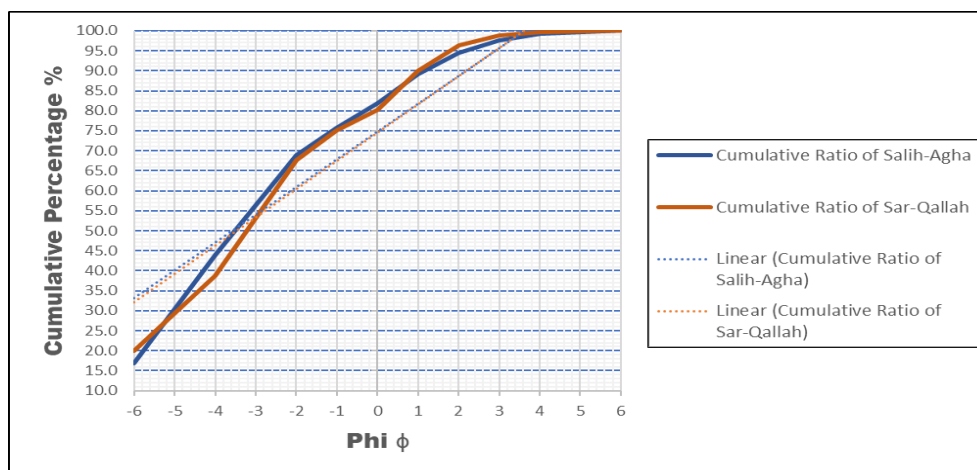

Fig. 4. Relationship between grain size (*phi*) and cumulative percentage of (Salih-Agha and Sar-Qallah-1) sections.

5.2 Petrography and mineralogy

The mineralogical composition of the studied samples was identified under a polarized microscope to determine their lithology and studying the parent rocks.

The petrographic study can be referred to lithic rock fragments, these are the predominant constituents of the quaternary deposits include sedimentary, igneous, and metamorphic rock fragments which are existing in different amounts. Lithic sedimentary fragments are the majority constituent of more than (%95) of quaternary deposits and represent by chert, radiolarian chert, and carbonate rock fragments. Here are brief characteristics of each component:

• The chert rock fragments occur as angular to subangular in shape, and they are more common than another type of sedimentary rock fragments that observed from all studied sections (Rzgari, Sar- Qallah-1, and Salih- Agha) (Figure 5a). Chert is hard, composed of microcrystalline or cryptocrystalline quartz (silica) (Knauth, 1979). Chert is of biological origin (organic, radiolarian), also may occur inorganically as a diagenetic replacement or a chemical precipitate (Bates & Jackson 1984). These fragments may be derived from the radiolarian chert beds of Qulqula Group which exposed in the thrust zone and far for 70-80 km from the studied area (Buday & Jassim, 1987). (Jassim & Goff, 2006) mention that radiolarian chert is the common composition of Qulqula Group and exceed 2000 meters in thickness.

• Carbonate lithics are the main constituent within the studied samples that occur as subangular to subrounded, mostly represented by micritic crystalline calcite, ferroginous detrital limestone, and detrital limestone (Figure 5b). The different types of carbonate rock fragments are indicated carbonate source rocks (Al-Juboury, 1994). The coexistence of these detrital is derived from Avroman Formation appear in northeastern Iraq. The fragments of chert and carbonate are very common in the study samples with an average (%92).

• Radiolarian chert rock fragments that occur as angular to subrounded and about (%3) was identified. A homogeneous sedimentary rock that is predominately composed of microscopic radiolarian organisms (Figure 5c). This fragment is derived from radiolarian chert beds and which are considered as a weathering product of the Cretaceous Qulqula Radiolarites series, NE Iraq that is adjacent to the Sanandaj- Sirjan Zone of Iran (Al- Juboury *et al*., 2009).

• Occurrence of igneous rock fragment as subangular is usually rare, with a value (%2) (Figure 5d). The existence of this fragment is indicating Penjween Ophiolites Complexes parent rocks from Thrust Zone.

• Metamorphic rock fragment is represented by minor constituents of serpentine fragments about (%1). The source of these fragments is from Ophiolites Complexes, which are exposed in the Nappe Zone (thrust and folded) cover the area of northern and northeastern Iraq.

• Monocrystalline quartz is less abundant in the studied samples with a value (%1). It is subangular with medium grain sizes (Figure 5e). It is composed of single crystal, non-undulatory (uniform extinction), and derived from volcanic igneous rocks.

• The feldspar grain is (plagioclase) less abundant accounting only (%1). Feldspar grain is elongated shape as a fresh (Figure 4f). The shape of fresh grains of feldspar is indicating the relatively short distance of transportation and might be a sign of rapid erosion in the source area (Boggs, 2006).
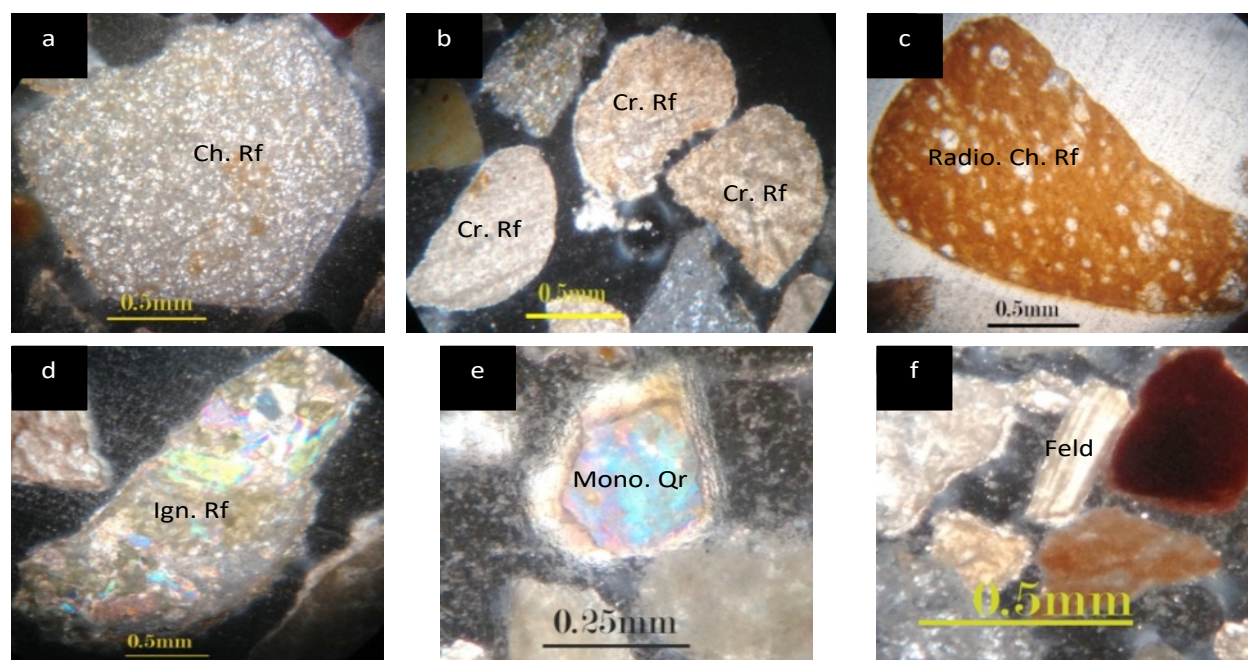
Fig. 5. (a) Chert rock fragment (Ch. Rf), Salih- Agha, XP, (b) Carbonate rock fragments (Cr. Rf), Sar-Qallah-1, XP (c) Radiolarian chert fragment (Radio. Ch. Rf), Rzgari, XP, (d) Igneous rock fragment (Ign. Rf), Rzgari, XP, (e) Monocrystalline quartz (Mono. Qr), Sar-Qallah-1, XP, (f) Feldspar grain (Feld), Salih- Agha, XP.

The mineral composition of the studied samples indicated that the area is exposed to deformation, which is caused to uplifting and erosion by orogenic (Alpine orogeny) in northeastern Iraq. The coexistence of different types of fragments indicated various rock types from the Thrusted Zone. Boggs, (2006) mentioned that the parent rocks are more reliable than individual minerals, where they could be derived from different source rocks.

5.3 Heavy minerals

Individual of heavy mineral is separated from unlithified sediments, after light grains have been removed by floatation on heavy liquids (Bromoform). The heavy minerals analysis is very important, it can give some useful indications of events in the source area and their provenance. Huang, *et al.,* (2018) mention that petrography, heavy mineral assemblages and geochemistry composition are a powerful and useful tool for detecting provenance in difficult situations. Webster *et al.,* (2003) documented that the identified heavy minerals are not affected by mineralogical composition only, it is affected also by other factors that occurring during sedimentation.

More than (20 grains) were used for identification. These minerals were identified by using a polarized microscope. The results are showing opaque minerals (hematite and pyrite), and nonopaque minerals (pyroxene, amphibole, epidotes and zircon) (Figure 6). Pyroxene and amphibole minerals are common types of heavy minerals that occur in the studied samples with an average (%95). These minerals grains as occur angular to subrounded. Aziz & Sadiq (2020) stated that the presence of opaque grains, pyroxene, amphibole and, epidotes that derived from mafic to ultramafic igneous rocks and zircon grains are indicator of derivation from metamorphic and earlier

igneous source. The variety of heavy minerals in quaternary sediment reflects the multiple sources of rock types, represented by the igneous, metamorphic and sedimentary rocks.

5.4 Clay minerals

Using the X-Ray diffraction technique for interpretation and determining clay mineral composition. The mineralogical composition of clay samples in (Sar-Qallah-2) were identified and interpreted by X-Ray analysis that represented by non-clay minerals (quartz and calcite). The percentage ratio of the minerals was calculated by the semi-quantitive method. X-ray chart shows that quartz minerals have the highest percentage about (%45.8) than calcite minerals (%39.0) (Figure 7). In addition, the clay minerals represented by chlorite and palygorskite that having different values. Chlorite minerals have the highest percentage with an average (%60.55) than palygorskite (%39.44) (Figure 8). The origin of chlorite mineral is derived from erosion of igneous and metamorphic rocks which are rich the ferromagnesian minerals that contain high Fe and Mg (Velde, 1992). The second mineral ratio in the study samples is palygorskite, it is formed from erosion of mafic volcanic igneous rocks and also it appeared in the semi-arid and arid climate (Grim, 1968).

Clay minerals that formed by weathering and erosion processes took place in source rocks caused some minerals alteration to clay minerals (Grim, 1968; Millot, 1970). The difference in clay minerals assemblage probability is caused by changes in climate or sediment source (Al-Jaberi, 2017). The non-presence of kaolinite mineral in the studied clay samples indicated that the occurrence of a low amount of acidic igneous rocks and arid climate in the source area because kaolinite is formed from the weathering of acidic igneous rocks in a moisturizing climate (Millot, 1970).
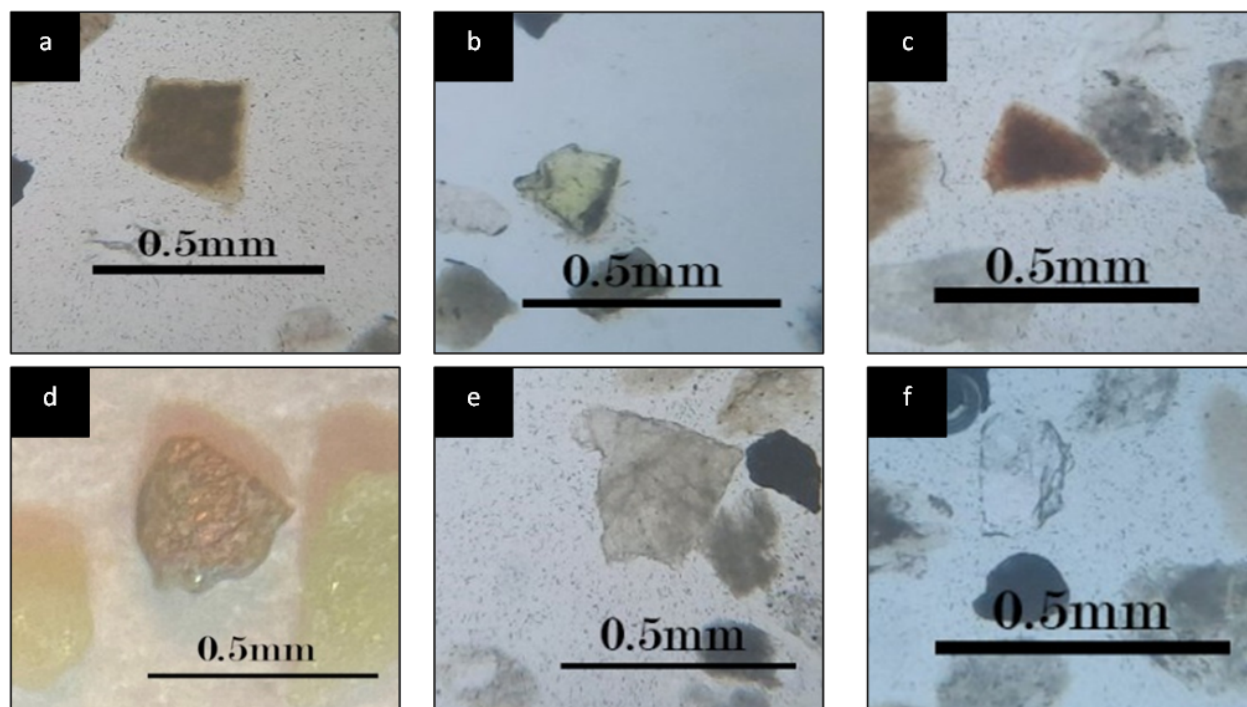

Fig. 6. (a) Amphibole, Sar-Qallah-1, ppl, (b) Epidote, Salih- Agha, ppl, (c) Hematite, Sar- Qallah-1, ppl, (d) Pyrite, Salih- Agha, ppl, (e) Pyroxene, Sar-Qallah-1, ppl, (f) Zircon, Salih- Agha, ppl.
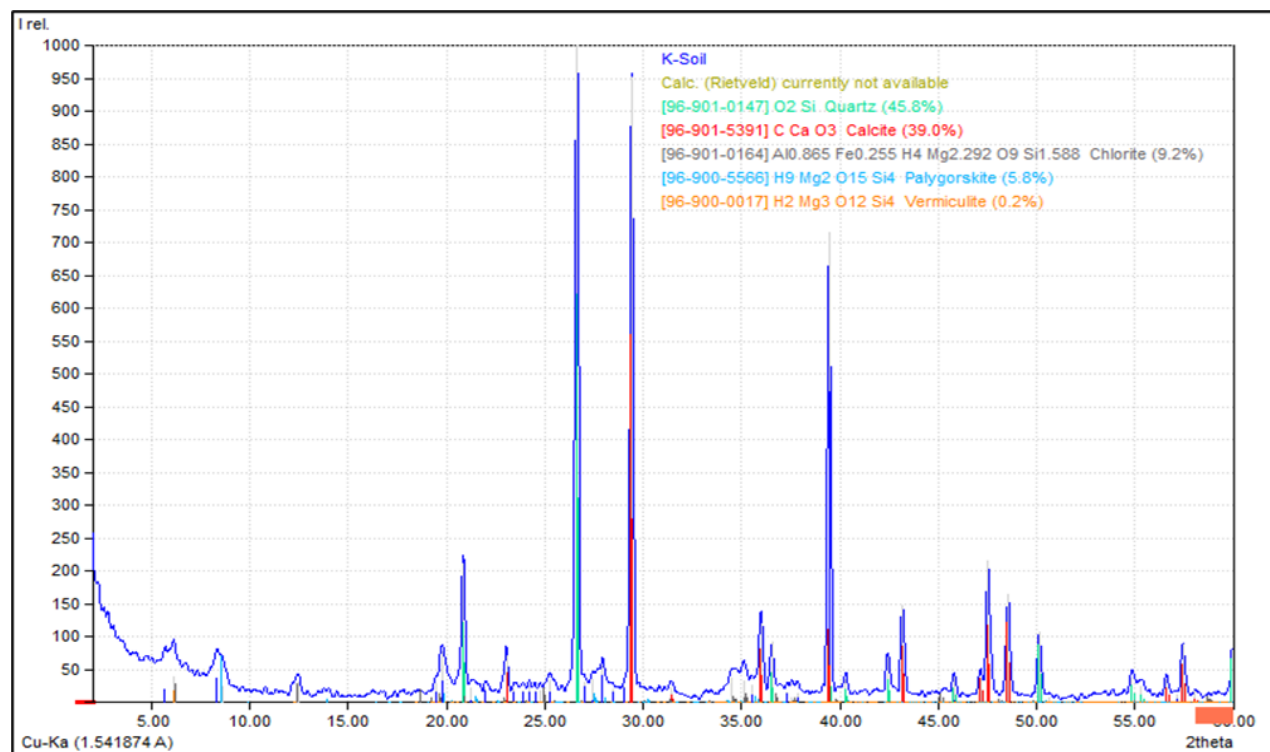
Fig. 7. X-Ray diffractograms of clays mineral samples of (Sar-Qallah-2) section.
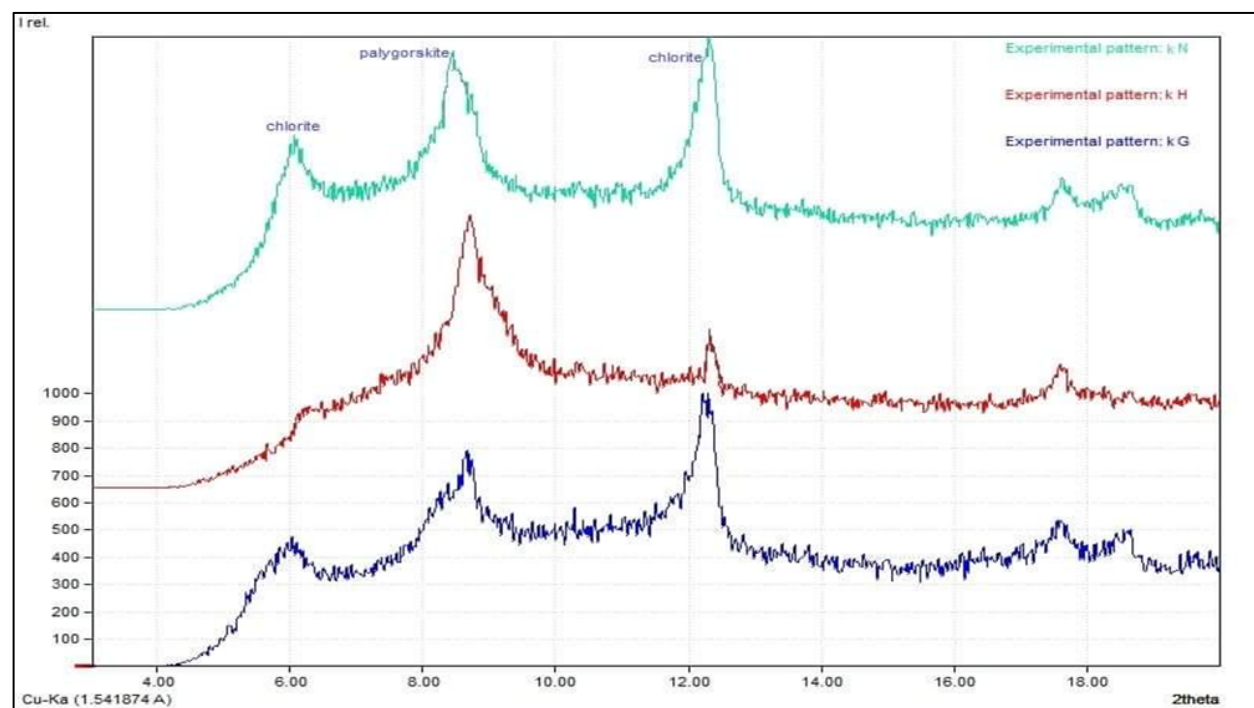

Fig. 8. X-Ray diffractograms of clay minerals samples of (Sar-Qallah-2) section.

5. Conclusions

Some significant points have been concluded as following:

1. The grain size analysis of the studied samples was identified, the gravel size partially is greater amount than sand and mud size in both sections (Sar-Qallah-1 and Salih-Agha). Based on statistical parameters such as (mean, sorting, skewness and kurtosis), it is obvious that the results of the sediments are very poorly sorted, very fine skewed and platykurtic.

2. The petrographic study of Quaternary sediments shows different compositional types of lithic rock fragments and represented essentially by sedimentary rocks (mainly carbonate and chert) followed by radiolarian chert and then by, igneous, and metamorphic rock fragments.

3. The huge distribution of chert and carbonate rock fragments within quaternary deposited indicated closeness to the source area.

4. The predominant opaque heavy minerals such as hematite and pyrite with nonopaque minerals are like pyroxene, amphibole, epidote and zircon, almost reflect different source rock types.

5. The clay minerals are represented by chlorite and palygorskite types, the quartz and calcite are the common in non-clay minerals.

6. The clay minerals are derived from erosion of igneous and metamorphic rocks in the semi-arid and arid climate.

References

Abdula, R. A., Khailany, R. N., Rasheed M. J. & Abdi, B. S. (2020) Glacial Activity Signs During The Pleistocene Epoch in Rawanduz River Valley, Kurdistan Regin, Northeast Iraq. Iraqi Bulletin of Geology and Mining, 16(**2**):75-93.

Al- Juboury, A. I. (1994) Petrology and provenance of the Upper Fars Formation (Upper Miocene), Northern Iraq. Acta Geologica Universities Comenianae Bratislava, 50:45- 53.

Al- Juboury, A. I., McCann, T. & Ghazal, M. M. (2009) Provenance of Miocene sandstones in northern Iraq: constrains from framework petrography, bulk-rock geochemistry and mineral chemistry. Russian Geology and Geophysics, 50:517-534.

Al-Jaberi, M.H. (2017) Clay mineral variation in Quaternary sediments of Basrah City-Iraq. Earth Science Research, 6 (**2**): 41-55.

Al-Kaaby, L. F. & Albadran, B.N. (2020) Minerals and Sedimentary characteristics of quaternary sediments of different regions in Southern Iraq. Iraqi Geological Journal. Vol.53: 68-89.

Aziz, N.R.H. & Sadiq, D.M. (2020) U-P Zircon dating of upper cretaceous siliciclastic rocks from the Tanjero Flysch, NE Iraq: New constraints on their provenance and tectonic evolution. Kuwait J. Sci. 47(**4**): 106-117.

Bates, R. L. & Jackson, J. (eds) (1984) Dictionary of geology terms, 3rd ed. American Geological Institute, Doubleday.

Benni, T.J., Al-Tawash, B. S. & Al-Mukhtar, L.A. (2012) The study of Late Quaternary sediments using grain size analysis and heavy minerals in Bahr Al-Najaf depression, Central Iraq. Iraqi Geological Survey and Mining Journal. 8 (**2**): 1-18.

Boggs, S. J. (2006) Principles of sedimentology and stratigraphy. 4th Edition.

Buday, T. & Jassim, S. Z. (1987) The regional geology of Iraq. Tectonism, magmatism and metamorphism. V.2, D.G. of geology survery and mineral investigation Baghdad, Iraq. Pp.352.

Carver, R. E. (1971) Procedures in sedimentology petrology, wiley- interscince, New York. Pp.653.

Elias A. S. & Mock J. C. (2013) Encyclopedia Of Quaternary Science (Vol. II). Amsterdam, Netherlands: Elsevier.

Folk, R. L. (1980) Petrology of Sedimentary Rocks. Austin (Texas): Hemphil Company.

Folk, R.L., Andrews, P.B. & Lewis, D.W. (1970) Detrital Sedimentary Rock Classification and Nomenclature for Use in New Zealand: New Zealand Journal of Geology and Geophysics. 13: 937–968.

Grim, R. E. (1968) Clay Mineralogy, 2nd; Mc. Graw-Hill, New York. Pp.596.

Huang, Y., Yao, G. & Zhou, F. (2018) Provenance analysis for submarine fan sandstone of Huangliu Formation, Dongfang 13 gas field in Yinggehai Basin, South China Sea. Kuwait J. Sci. 45(**3**): 72-92.

Jassim, S. Z. & Goff, J. C. (2006) Geology of Iraq, (1rd ed.) Dolin, Prague and Moravian Museum, Brno, Czech Republic. Pp.345.

Kent, W. (2010) Structures of the Kirkuk Embayment, northern Iraq: Foreland structures or Zagros Fold Belt structures? Geo Arabia. 15: 147-188.

Knauth, L. P. (1979) A model for the origin of chert in limestone. Geology. 7(**6**):274-277.

Krenmayr, H G 1996. Sedimentologie der letzintergla-zialen lim nischen Deltasedimente von Mondsee als Basisfur die palaoklimatologische Interpretation. DEUQUA '96' Alpine Gebirge im Quartar p. 26, Hannover

Lawa, F. A. A. (2004) Sequence stratigraphic analysis of the Middle Paleocene-Middle Eocene in the Sulaimani District (Kurdistan Region), Ph.D. Thesis. Sulaimani University.

Lawa, F. A.A. & Ghafur, A.A. (2015) Sequence stratigraphy and biostratigraphy of the prolific late Eocene, Oligocene and early Miocene carbonate from Zagros fold-thrust belt in Kurdistan region. Arab. J. Geosci. http://dx.doi.org/10.1007/s12517-015-1817-4.

Lawa, F.A. A., Koyi, H. & Ibrahim, A. (2013) Tectono-stratigraphic evolution of the NW segment of the Zagros fold-thrust Belt, Kurdistan, NE Iraq. Journal Pet Geol. 36(**1**):75–96.

Millot, G. (1970) Geology of Clays, Springer-Verlag. New York. Hedelberg. Berlin. Pp.429.

Omar, A. A., Lawa F.A. & Sulaiman S.H. (2015) Tectonostratigraphic and structural imprints from balanced sections across the north-western Zagros fold-thrust belt, Kurdistan region, NE Iraq, Arab J. Geosciences. 8(**10**): 8107–8129.

Péwé, T. L. (1975a) Quaternary geology of Alaska: U.S. Geological Survey Professional Paper 835, 145 p.

Powers, M. C. (1953) A new roundness scale for sedimentary particles. Journal of Sedimentary Petrology. 23(**2**): 117-119.

Raymo, M.E. (1997) The Timing of Major Climatic Terminations. Paleoceanography, 12: 577-585.

Sissakian, V. K. & Saeed, Z. B.(2012) Lithological Map of Iraq, compiled using GIS Techniques. Iraqi Bulletin of Geology and Mining. 8(**3**):1-13

Sissakian, V.K. & Al-Jiburi, B.S.M. (2014) Stratigraphy of the high folded zone. Iraqi Bull. Geol. Min., 6:73−161.

Stevanovitic, Z., Markovitic, M.Y. & Adrian, M. (2003) Geology and hydrogeology of Sulaimani and Kirkuk area, FAO (UN) report. Sulaimaniyah office. 52 maps: Pp.176.

Van Husen, D. (2004) Quaternary glaciations in Austria. In: Ehlers, J., Gibbard, P.L. (Eds.), Quaternary Glaciations—Extent and Chronology, Part I, pp. 1–13.

Velde, B. (1992) Introduction to clay minerals, chemistry, Origin, used and environmental significance. Chapman and Hall, London, 1989.

Webster, J.R.R., Kight, R.P., Winburn, R.S. & Cool, C.A. (2003) Heavy mineral analysis of sandstone by rietveld analysis, international center for diffraction data, advances in x-ray analysis. 46: 198- 203.

Wentworth, C.K. (1922) A Scale of Grade and Class Terms for Clastic Sediments: Journal of Geology. 30: 377–392.

The impact of land use and land cover change on hydrological processes in Brantas watershed, East Java, Indonesia

Mohamad Wawan Sujarwo[1], Indarto Indarto[*,1], Marga Mandala[1]
*[1]Dept. of Natural Resources and Environmental Management,
Post-Graduate Faculty, University of Jember, Indonesia
Jl. Kalimantan No. 37 Kampus Tegalboto Jember 68121,
Jawa Timur, Indonesia*
Corresponding author: indarto.ftp@unej.ac.id

Abstract

Assessing the impact of land use and land cover change (LULCC) on hydrology is essential for water resource management. The Brantas watershed contributes about 30% of the water supply of the East Java region. The present rapid pace of land occupation for agriculture and settlements is expected to continue to alter flow processes within the watershed. This study aims to simulate LULCC and its impact on the hydrological processes of the watershed. The long-term impact of LULCC is evaluated using the Soil and Water Assessment Tool (SWAT). The analysis model is calibrated using monthly data series from 1996 to 2005 and then validated using data series from 2006 to 2015. Two editions of maps (2001 and 2015) are then used to calculate the LULCC that took place across this period. The impacts of LULCC on hydrological processes at the sub-basin level are also evaluated. The results show that the variability of rainfall patterns from 2001 to 2015 strongly affected flow variability. The LULCC from agricultural land to other uses (irrigated rice fields, settlements, and forests/plantations) is most evident in three sub-basins (sub-basins 2, 9, and 17). However, each sub-basin may respond differently with respect to the LULCC taking place. The increase in the area occupied by each class of land use and cover use (LULC) is not always linear to the observed flow, and widely differing LULC classes may display similar flow responses while classes with similar characteristics may have differing impacts on flows within a sub-basin. In other words, the hydrological processes are too complex to be simplified at the sub basin level.

Keywords: Climate change; LULC; monthly flow; sub-basin; SWAT.

1. Introduction

Climate change (CC) and land use and land cover change (LULCC) may generate complex hydro environmental problems at both global and local levels. Both CC and LULCC may represent changes propagated by human-induced activities (IPCC, 2007; Parece & Campbell, 2015). When both affect the same area, the impact of the two phenomena (CC and LULCC) may propagate severe hydro-meteorological disasters such as flash floods and landslides (as detailed in the works of Spruce *et al.*, 2018; Lamichhane & Shakya, 2019).

There are many possible drivers of LULCC. It may be caused by aspects of rapid development of urbanization, such as urban sprawl, peri-urban migration, and conversion of agricultural land to pavemented areas. Furthermore, industrial sites, transportation networks, education, cultural facilities, agricultural sites, and tourism activities may all contribute to change. However, actual change may be caused by a combination of types of development (Al-Jiboori *et al*., 2020; Ahmed & Alla, 2019).

Researchers usually study LULCC by investigating two or more maps produced at different times, for example, the work of Ptak & Ławniczak, 2012; Marie *et al.,* 2019). Conventional maps and satellite images can be interpreted to study the causal effects of LULCCs and their implications for society and the environment (Kang *et al.*, 2019). The use of Landsat imagery to study LULCC is a widely known method and has been published in research reports worldwide (e.g., Lamichhane & Shakya, 2019; Marie Mireille *et al.*, 2019; Li *et al.*, 2019; Al-Jiboori *et al.*, 2020). LULCC may have positive or negative impacts on hydrological processes. However, human activities tend to change the natural landscape into human-influenced landscapes that have the potential to disturb natural processes.

Other research has investigated LULCC related to CC processes and the various impacts caused. Ermoshin *et al*., (2013) studied the long-term land-use change in the transboundary Amur river basin. Nikitin *et al.,* (2019) have evaluated the possible impact of LULCC in the central part of the East European plain on regional meteorological conditions using the regional COSMO model. CC and LULCC are the main drivers of streamflow change and play predominant roles both upstream and downstream (Liu *et al.*, 2020). The effects of CC and LULCC on hydrological processes have been discussed extensively by Kang *et al.*, 2019 and Liu *et al.*, 2020. The impacts of LULCC on hydrological processes are usually elaborated using a hydrological model. For example, Liu *et al.,* (2020) use the Distributed Hydrology Soil Vegetation Model (DHSVM) to study the Beichuan river basin in the northeast Tibetan plateau.

The SWAT (Soil & Water Assessment Tool) is frequently used to simulate the impact of LULCC on hydrological processes (Neitsch *et al.*, 2012). SWAT can analyze the impacts of climate, soil, vegetation, and agricultural activities on river flow, and researchers worldwide have used it to study the impact of LULCC and CC on hydrological processes, for example, the work carried out by Lamichhane & Shakya (2019) in Nepal. A similar study has been conducted by Marie *et al.,* (2019) in Kenya, and Kang *et al.,* (2019) have applied SWAT and statistical methods to evaluate the effects of climate and land-use change on surface hydrology in the Loess Plateau hilly-gully region of China.

Recently, Li *et al.,* (2019) have applied the SWAT model to analyze LULCC and CC impacts. They state that a decrease in forest, grass, and wetland areas has reduced water balance and baseflow, but that annual evapotranspiration has increased. Finally, Rafiei *et al.* (2020) have used SWAT to identify soil erosion hotspots through simulating hydrological processes, soil erosion, and sediment transport. The SWAT model is based on the concept of the hydrological response unit (HRU) used to calculate spatially distributed hydrological processes (Neitsch *et al.*, 2012). The HRU approach dynamically analyses and models the hydrology of various structures into

homogeneous structures based on their soil type, geology, and cover-crop interactions. Each HRU will produce one hydrological value distributed to other HRUs based on land cover, soil, and slope (Pignotti *et al.*, 2017). The hydrological processes identified influence vegetation growth and determine nutrient, pesticide, and sediment movements within the watershed. The vertical components of water balance are calculated for each HRU, and the runoff, sediments, and nutrients are accumulated from the HRUs to each sub-basin. The horizontal movement of water, nutrients, and sediments from each sub-basin to the watershed outlet is then calculated using the transfer function (Neitsch *et al.*, 2012).

This research aims to use the SWAT model to simulate LULCC during two ten-year periods between 1996 and 2015 and to elaborate on their impact on hydrological processes as modeled at the monthly level. The study is conducted in the Brantas watershed in East Java Province, Indonesia.

2. Materials and methods

2.1 Study area

Brantas watershed (Figure 1) covers an area of 14,103 km^2, equivalent to 30% of East Java Province's total area (47,075.35 km^2). The length of the main channel of the Brantas river is 320 km. The Brantas watershed area includes the administrative districts and cities of Malang, Kediri, Blitar, Nganjuk, Batu, Blitar, Tulungangung, Trenggalek, Jombang, Mojokerto, Sidoardjo and Surabaya (Table 1). This study focuses on the upstream and middle regions of the watershed (8,842.76 km^2). The watershed area is populated by more than 8 million inhabitants (> 30% of the population of East Java) (BPS Jatim, 2017) and is the most urbanized area in the region (Table 1). The land is occupied for residential use, agricultural land, urban and city facilities, road networks, tourism sites, plantations, industry, and other social-cultural economic activities.

About 60% of the agricultural produce of the province comes from areas served by tributaries of the Brantas. Major reservoirs for collecting water have been constructed on these tributaries: D1 (Sengguruh), D2 (Sutami), D3 (Lahor), D4 (Selorejo), D5 (Lodoyo), D6 (Wlingi), D7 (Wonrorejo), D8 (Waru Turi), D9 (Menturus), D10 (Gunungsari), D11 (Gubeng), and D12 (Jagir Dams) (Figure 1).

The population of East Java increased from 34 million in 2000 to more than 39 million in 2019, an increase of 16.76% (more than 5.6 million people). Thus, the watershed plays a vital role in shaping the limits and capacity of the environment to support this region's sustainable development.

The rapid development of population, urbanization, industrial sites, food services, energy, and tourism has significantly converted natural landscapes into human-influenced ones over the last two decades. This has led to changes in the hydrological regime of the river.

These changes will likely exacerbate the risk of erosion, sedimentation, and landslides in the coming years. Land cover changes in the Brantas watershed have already had an impact on erosion and flooding, with about 70% of the eroded area being categorised as having suffered severe erosion and being prone to flooding (DLH Jatim, 2017).

Table 1. District and city administrative areas in the Brantas watershed
(Source: BPS Jatim, 2017)

| District/city	Area (Km²)	Population (in 1000s)		Population (%)
		2000	2015	
Batu	189.54	168	200	19.0
Blitar District	1,299.74	1,065	1,145	7.5
Blitar City	33.35	119	137	15.1
Bojonegoro	2.13	1,165	1,236	6.1
Jombang	276.4	1,127	1,241	10.1
Kediri District	1,485.79	1,408	1,547	9.9
Kediri City	69.14	245	280	14.3
Lamongan	0.03	1,182	1,188	0.5
Lumajang	3.79	965	1,030	6.7
Madiun	127.85	640	676	5.6
Malang District	2,257.5	2,244	2,544	13.4
Malang City	109.95	757	851	12.4
Mojokerto	0.82	908	1,080	18.9
Nganjuk	1284.3	973	1,042	7.1
Pasuruan	6.1	1,367	1,582	15.7
Ponorogo	71.08	841	867	3.1
Probolinggo	0.13	1,005	1,140	13.4
Trenggalek	643.96	650	689	6.0
Tulungagung	981.12	930	1,021	9.8
Total population	8,842.76	17,759	19,496	194.6
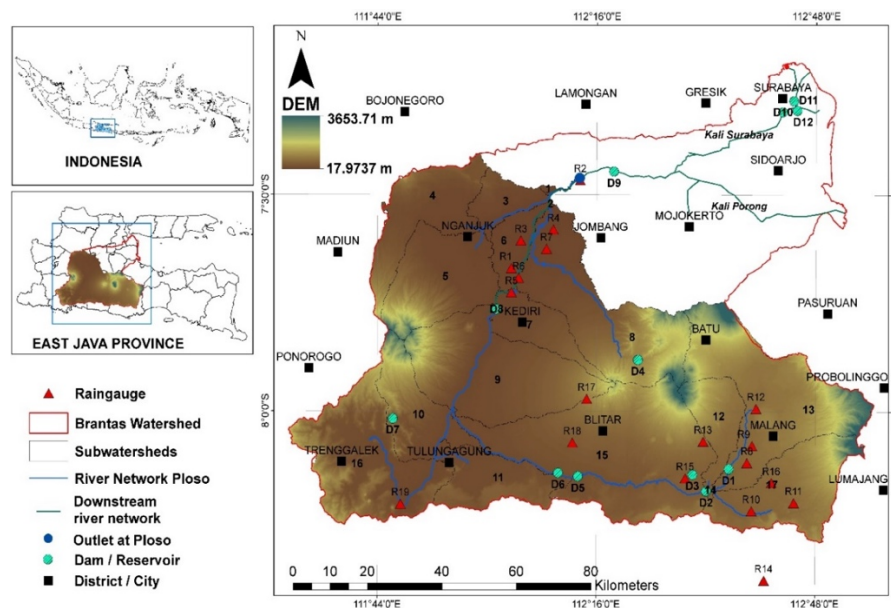
Fig. 1. Study area

Other water resource management problems in the watershed include a lack of water availability for irrigation and water supply, below standard water quality, domestic waste in the river body and irrigation channels, rapid erosion, and sedimentation processes. The risk of flood and drought events has also increased (Anwar & Kusumawati,2015; Indarto *et al.*, 2020).

2.2 Input data

This study used flow measurements located in Ploso. Then, the sub-watershed boundary was delineated using Ploso as an outlet. The sub-watershed area covers an area of 8,844.26 km^2 (Figure 1).

The inputs to SWAT are digital elevation model (DEM) data, land cover, soil characteristics, climate variables (rainfall, temperature, solar radiation, relative wind speed, and humidity), and land management practices. All input spatial data are formatted in a raster graphic (Table 2). In this study, ArcSWAT (2012) is used as the primary tool for hydrological analysis, while GIS software visualizes the maps.

Table 2. Description of model inputs

Data type	Source	Description
DEM (digital elevation model)	Geospatial Information Agency of Indonesia (BIG, 2019)	Resolution 8.3 m
Digital soil layer	Soil Research Institute, 1998, Bogor, Indonesia	Scale 1:250,000
Land use land cover layer	Rupa Bumi, Indonesia https://tanahair.indonesia.go.id/) Intepretation of Landsat 8	Scale 1:250,000 (satellite image)
Climate/ Meteorological data series	Meteorology and Climatology Geophysical Agency of Banyuwangi	1996–2015 (20 years)
Daily rainfall data	19 measurement sites (R1 to R19, as in Figure.1)	1996–2015 (20 years)

2.3 Procedure

The general modeling procedure consists of four steps, as illustrated in Figure 2: (1) watershed delineation and development of HRU; (2) modeling with SWAT, including table creation, climate data input, and model output into SWAT; (3) calibration and validation; (4) simulation of the impact of LULCC on hydrology.
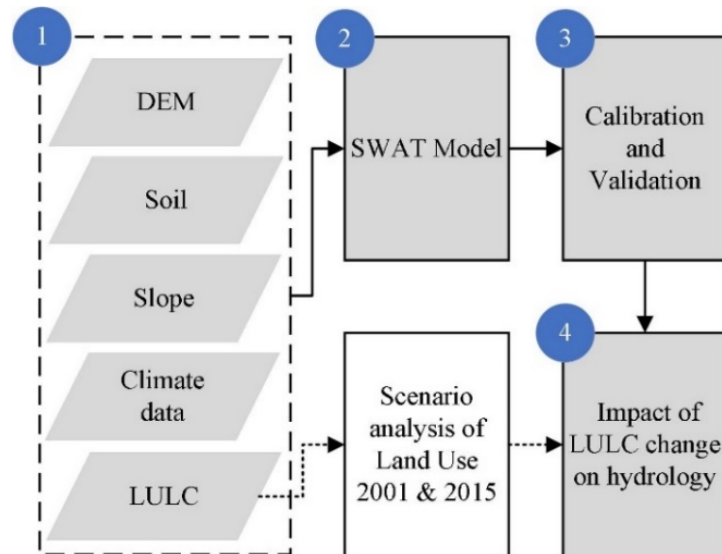
Fig. 2. Procedure

1. Watershed delineation and HRU processing: The ArcSWAT module fills sinks to determine the input DEM flow direction and accumulation (BIG, 2019). The result is then used to create the stream network, outlet, and sub-basins. ArcSWAT will delineate the boundary of the watershed and produce the HRUs. HRUs are constructed from three layers: LULC maps, soil-type maps, and slope classes. Finally, each HRU is determined using a 10% threshold.

2. In the SWAT model, the SWAT weather database (Weather Generator) calculates 14 necessary parameters. Seven parameters depend on rainfall data, and the other seven are adjusted for climate data (Table 2). The parameters are then used for updating the SWAT database (SWAT Output).

3. Calibration is set for the ten-year period 1996 to 2005, while validation is for the period 2006 to 2015. The model is tested for the two periods using the SWAT graphical user interface (GUI). Simulation results are then read through the SWAT output menu. The SWAT CUP module is used to evaluate model performance. In this case, SUFI-2 (Sequential Uncertainty Fitting) is explored to fit the parameter values during calibration and validation. Calibration and validation follow the procedure as published by Abbaspour (2015). Water balance is calculated at monthly and annual intervals. Sensitivity analysis is then conducted following procedures used in previous publications (Arnold *et al.*, 2012; Moreira *et al.*, 2018; Brighenti *et al.*, 2019). About 33 parameters are selected for sensitivity analysis, and then 500 iterations are run in the model. In this case, the *r* (multiples) and *v* (replace) procedures are used to find optimal parameter values (Abbaspour, 2015). Two statistical tests are used to evaluate model performance: the Nash-Sutcliffe Efficiency (NSE) test and the coefficient of determination (R^2) (Moriasi *et al.*, 2007).

4. Water balance, water, and sediment yield are then calculated during the simulation periods to study the impact of LULCC on hydrology.

3. Results and discussion

3.1 Land use/land cover change (LULCC)

This study covers the period from 1996 to 2015. Two map editions of land use (LU) and land cover (LC) are used for this study (Figure 3).
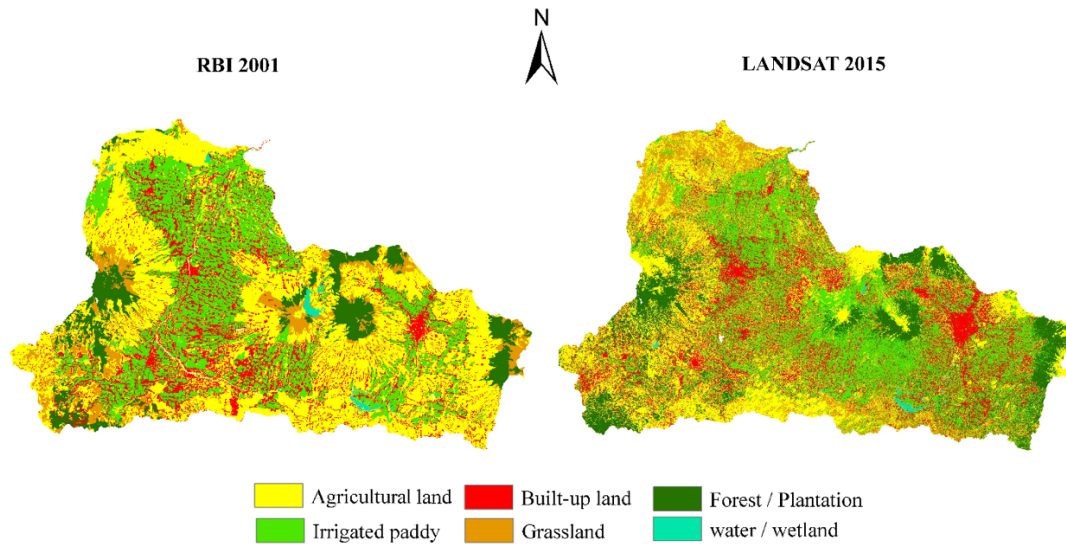

Fig. 3. LULC maps for 2001 and 2015.

The first is an LULC map clip from RBI digital maps (BIG, 2019). The RBI map was produced during the year 2000–2001. The second map clip is from classified Landsat-8 images. The available time-series data are divided into periods 1 (1996–2005) and 2 (2006–2015), and the model was run for these periods. The RBI data represents LULC for the first period, while Landsat data represents LULC for the second period (Figure 3).

LULCC in the Brantas watershed from 2001 to 2015 is significant. The change is marked by increasing irrigated paddy (+ 8.4%) and forest/plantation areas (+ 4.7%). The land occupied by built-up regions also increased by + 6.5%. These increases are compensated for by a 20.6% decrease in agricultural land (non-irrigated areas) (Table 3).

Table 3. LULC in the Brantas watershed

LULC	Area (%)		Change (%)
	2001	2015	
Irrigated paddy	24.7	33.1	8.4
Agricultural land	43.4	22.8	-20.6
Built-up land	16.4	22.9	6.5
Grassland	6.7	7.8	1.0
Forest/plantation	8.2	12.9	4.7
water/wetland	0.5	0.6	0.1

Reducing vegetation coverage will increase water flow and cause curve values to increase. Canopy and plant root systems influence the hydrological function of the watershed, especially with runoff and baseflow.

3.2 Calibration and validation

As listed in Table 4, parameter values are evaluated through iteration processes on the SWAT CUP module. Table 4 shows the best-fitted results for parameter values. The *t*-stat value indicates the sensitivity of the parameter, with the *t*-stat value of 0 indicating the most sensitive parameter.

Furthermore, the *P*-value of a parameter visualizes how its strength contributes to the flow calculation. *P*-value close to 1 signifies the most strongly determinant parameter, and therefore the change in calculated flow is made more significant by changing or manipulating this parameter's value (Abbaspour, 2015).

Finally, Table 4 presents the fitted values of the nine parameters most sensitive to producing runoff for the Ploso. Data in Table 4 is obtained after 10 x simulation processes and is treated with 500 iterations for each simulation (Brighenti *et al*., 2019).

Figure 5 then presents the observed and calculated hydrograph of monthly flow for calibration periods from 1996 to 2005. The calibration processes produce NSE = 0.66 and R² = 0.67. The calculated flow pattern follows the fluctuation of observed flow and rainfall events. The validation processes then produce NSE and R² of 0.55 and 0.56, respectively.

Table 4. The fitted value of each parameter

| Rank	Parameter name	Definition	*t*-stat	*P*-value	Fit
1	V__GW_REVAP.gw	Groundwater revap coefficient	0.16	0.87	0.06
2	V__ESCO.hru	Plant uptake compensation factor	-0.19	0.85	0.13
3	V__SMFMX.bsn	Maximum melt rate for snow during the year (occurs on the summer solstice)	-0.26	0.80	15.09
4	R__SOL_AWC.sol	Available water capacity of the soil layer (mm H_2O/mm soil)	-0.26	0.79	1.03
5	R__SLSUBBSN.hru	Average slope length (m)	-0.27	0.79	22.25
6	R__CH_N1.sub	Manning's *n* value for the tributary channels	0.35	0.73	1.31
7	V__GW_DELAY.gw	Groundwater delay (days)	-0.37	0.72	0.57
8	R__CH_L1.sub	The longest tributary channel length in the sub-basin	0.38	0.70	87.93
9	V__REVAPMN.gw	Threshold depth of water in the shallow aquifer for revamp to occur (mm)	-0.43	0.67	66.90
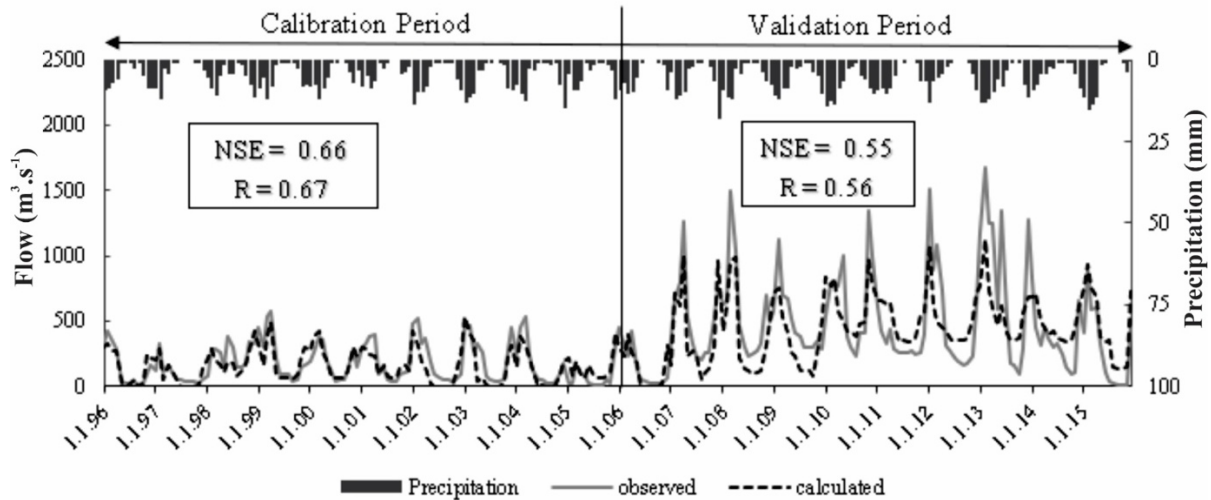
Fig. 4. Monthly calculated and observed flow (1996–2015).

3.3 Water yield

Figure 5 presents the LULC of the watershed produced from clips from RBI (2001) and Landsat (2015).
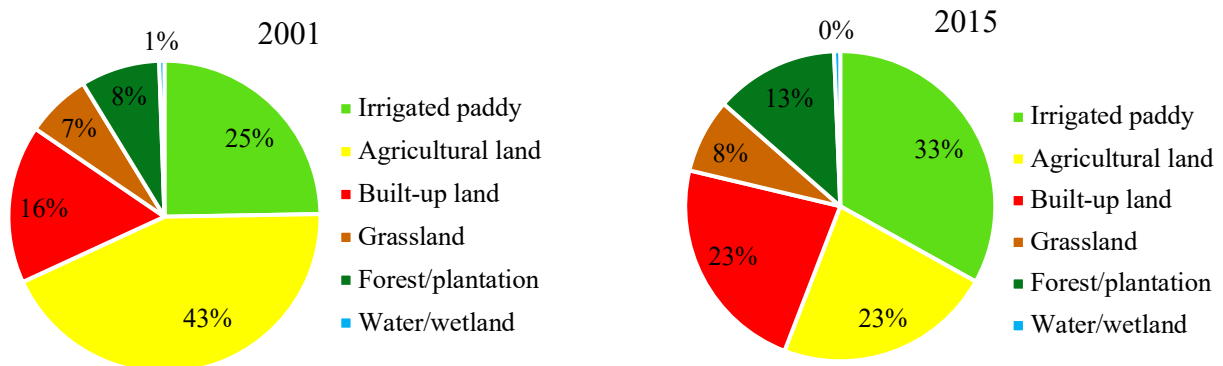

Fig. 5. LULC 2001 and 2015

A significant change has occurred in four classes of land use: agricultural land, irrigated paddy, built-up land, and forest. These four classes cover about 92% of the total area. In 2001, 43% of the watershed area was occupied by agricultural land (Figure 5: top image), which produced 65% of the total water yield in the same year (Figure 6: top image).
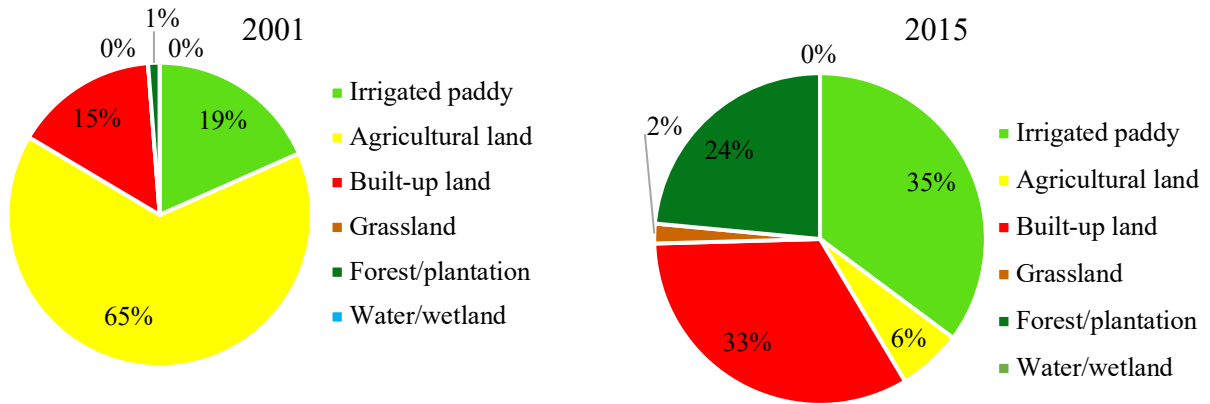
Fig. 6. Water yield 2001 and 2015.

It can be seen that 43% of the watershed area is cultivated for various agricultural products such as corn, carrots, and many types of legumes. A further area ($\pm$ 25% of the total) is used for irrigated paddy.

The water yields shown in Figure 6 are calculated for each LULC class. Agricultural practices, when they become dominant as land occupations, will produce more and more runoff. Therefore, 43% of agricultural land made 65% of the total water yield in 2001. Usually, agricultural land is cultivated from the late wet season (monsoon) until the dry season. The crops typically have low coverage compared to grassland, and their roots occupy only the soil's upper layer. Figure 7 presents a view of a typical seasonal crop cultivated around annual trees. The bare soil in the photo represents crop replacement after harvesting.

Fig. 7. Example of agricultural practice in the steepest hilly terrain.

Moreover, most crops are cultivated in hilly areas with the steepest slopes in the terrain. As a result, less water will be saved in the soil layer, producing more runoff when precipitation falls (Figure 7). In the year 2015, LULC changed significantly. More agricultural land has been

converted to irrigated paddy. This change results from an increased available water supply for irrigation and a new irrigation network (Fitri *et al.*, 2017; Valiant *et al.*, 2021).

The percentage of the land occupied by built-up areas and forest/plantations is also more significant in 2015 than in 2001. Therefore, the water yield in 2015 is more marked in irrigated paddy, built-up areas, and forest/plantation areas. The impact of LULCC on water yield is determined by the proportion of LULC classes in watershed areas. However, this process results from many sub-processes and is moderated by the type of LULC, soil, topography, and climate change.

3.4 Overall watershed area

Table 5 shows the annual water balance components of the whole area of the watershed: precipitation (P), water storage in the soil profile (SW), actual evapotranspiration (ET), potential evapotranspiration (PET), water yield (WY), and sediment yield (SY). The water balance is calculated using two LULC scenarios: the LULC map for 2001 calculates the water balance using data from 1996 to 2005, while the LULC map for 2015 uses data for 2006 to 2015.

In general, all hydrological components increased in the second period (2006 to 2015): P increased to 16.6%, SW increased to 296.7%, PET to 2.4%, WY to 26.2%, and SY to 68.7%. At the same time, the ET component decreased to 29.6%. The decrease in ET reflects that the vegetation coverage was less in the second period than in the first period (1996 to 2005).

However, the annual water yield (WY) and sediment yield (SY) values varied yearly. For example, in the first period of 1996 to 2005, in wet years (years with high rainfall events such as 1998 - 2001), the annual WY and SY values are more important than in dry years (such as 1996 - 1997). The period 1996–1997 was an intense El Nino period, in which the East Java area was the driest. It is shown that rainfall, as an element of CC, still more strongly influences hydrological processes than the LULCC.

Table 5. Comparison of annual hydrologic features

Scenario of land use 2001						Scenario of land use 2015					
Year	P	SW	ET	PET	WY	SY	Year	P	SW	ET	PET	WY	SY
1996	1,570.7	7.5	502.0	1,952.1	1,141.6	946.1	2006	1,237.2	54.3	256.6	1,852.1	953.6	368.9
1997	1,158.7	8.1	426.7	2,194.3	724.7	385.1	2007	1,905.3	86.0	354.5	2,027.5	1,431.2	727.8
1998	3,990.6	20.9	606.8	1,881.4	3,344.4	1,959.0	2008	1,714.3	76.7	335.8	2,007.1	1,388.1	597.0
1999	3,736.6	19.4	513.0	1,797.1	3,198.0	1,794.8	2009	1,945.3	84.0	405.7	2,151.7	1,486.8	573.0
2000	3,923.1	10.9	548.7	1,751.2	3,361.4	2,202.4	2010	4,267.5	63.5	403.7	1,787.3	3,818.3	3,238.1
2001	3,680.1	13.3	535.5	1,925.7	3,120.8	1,998.9	2011	3,789.1	62.4	334.8	1,875.4	3,445.9	3,789.2
2002	1,632.5	22.5	554.6	2,156.3	1,067.3	1,115.3	2012	3,778.8	62.9	327.4	1,775.2	3,414.7	3,734.5
2003	1,825.3	31.5	494.4	1,953.7	1,322.8	1,066.8	2013	4,145.1	61.9	379.1	1,941.3	3,738.8	3,665.3
2004	879.3	12.5	282.6	2,036.6	616.5	588.4	2014	3,726.8	61.7	359.1	2,111.1	3,345.9	3,765.6
2005	3,741.6	23.7	522.9	1,920.6	3,186.3	2,534.1	2015	3,970.5	62.1	354.3	2,508.3	3,579.1	4,149.6
Avg	2,613.9	17.0	498.7	1,956.9	2,108.4	1,459.1	Avg	3,048.0	67.6	351.1	2,003.7	2,660.2	2,460.9

P = precipitation (mm), SW = water storage in soil profile (mm), ET = actual evapotranspiration (mm), PET = potential evapotranspiration (mm), WY = water yield (mm), SY= sediment yield (ton/ha), Avg = average.

3.5 Impact at sub-watershed scale

The three sub-basins (2, 9, and 17) detailed in Table 6 were selected to track the impact of LULC and flow changes. In sub-basin 2, an increase in grassland and a decrease in irrigated paddy and agricultural land areas contributed to the rise in SW by 57.9 mm. In contrast, ET was reduced to 221.1 mm. Consequently, WY increased to 1,832.9 mm (+ 768.3 mm from 2001 to 2015). In sub-basin 9, a decrease in irrigated paddy, agriculture, and grassland and an increase in forest/plantation and built-up land led to a reduction in ET by 131.7 mm and a contrasting impact on an increase in SW and WY of 69.6 and 508 mm, respectively.

Table 6. Comparison of annual hydrologic features on sub-basin

Sub basin	2		9		17	
LULC	2001	2015	2001	2015	2001	2015
Area km^2	2.2	2.2	978.9	978.9	596.9	596.9
Irrigated paddy %	64.4	41.2	34.2	29.5	11.1	35.3
Agricultural land %	24.4	21.4	34.7	27.8	64.8	16.4
Built-up land %	10.4	15.7	19.8	27.4	12.7	21.2
Grassland %	0.0	9.3	5.9	3.4	3.0	6.2
Forest/plantation %	0.0	0.0	5.0	11.6	8.5	20.7
Water/wetland %	0.0	12.2	0.0	0.2	0.2	0.1
P mm	1,596.7	2,239.8	1,435.9	1,862.6	36,243.9	36,142.4
PET mm	1,904.6	2,496.3	1,917.3	2,502.9	1,934.3	2,484.1
ET mm	527.0	305.9	504.8	373.1	1,510.0	897.7
SW mm	3.1	61.5	10.5	80.1	62.1	89.0
WY mm	1,064.3	1,832.9	919.7	1,427.7	34,423.0	35,190.1

Moreover, in sub-basin 17, an increase in built-up land, irrigated paddy, forest/plantation, and agricultural land impacted the rise in SW and PET, producing a decrease in ET. The change in LULC class areas is not purely linear to the change in hydrological response. Different LULC combinations can have similar hydrological effects, while similar LULC combinations can yield different hydrological responses. Many factors may contribute to the processes detailed above, such as intensity and distribution of rainfall and topography (Lu *et al.*, 2015). In reality, the hydrological response observed in the sub-basin level and the whole watershed areas is more determined by the simultaneous and combined effect of changes (CC and LULC).

4. Conclusion

This study concludes that changes in LULC from 2001 to 2015 included the transformation of agricultural land into irrigated rice fields, settlements, and forests/plantations. These changes reflect increased socio-economic development (irrigation water services, population, and plantation potential) in the East Java region. Three types of LC contributed most to water yield (WY), namely 35% from irrigated rice fields, 33% from settlements, and 24% from forest/plantations. The expansion of irrigated paddy, forests/plantations, and built-up areas from 2001 to 2015 decreased the ET component and slightly increased the PET component. The SW component also increased due to the expansion of irrigated paddy. Also, rainfall significantly affected hydrological conditions in the Brantas watershed.

References

Abbaspour, K. (2015). SWAT-CUP Calibration and uncertainty programs. In *User Manual*. Eawag Aquatic Research. Doi: 10.1007/s00402-009-1032-4.

Ahmed, I. M., & Alla, E. M. A. (2019). Landuse impact on the environment of Tuti Island, Sudan. Geography, Environment, Sustainability. Lomonosov Moscow State University, **12**(3), pp. 27–33. doi: 10.24057/2071-9388-2018-13.

Al-Jiboori, M. H., Abu-Alshaeer, M. J., & Ahmed, M. M. (2020). Impact of land surface changes on air temperatures in Baghdad, Kuwait J. Sci. **47** (4), pp. 118 -126, 2020. Available at: http://earthexplorer.usgs.gov/ (Accessed: 12 February 2021).

Anwar, N., & Kusumawati, S. (2015). Water Allocation Optimisation for Combined Users of Energy Generation and Irrigation Demand At the Upstream Brantas River Reach Using Mixed Integer Linear Programming Method. in International commission on irrigation and drainage. Surabaya, pp. 4–7.

Arnold, J. G., Moriasi, D. N., Gassman, P.W., Abbaspour, K. C., White, M. J., Srinivasan, R., Santhi, C., Harmel, R. D., Van Griensven, A., Liew, M.W., Van Kannan, N., Jha, M K., Harmel, D., Member, A., Liew, M.W., Arnold, V., Jef-Frey G. (2012). Swat: Model Use, Calibration, and Validation. American Society of Agricultural and Biological Engineers. **55**(4), pp. 1491–1508.

BIG (2019). Indonesia Geospatial Portal. Available at: http://tanahair.indonesia.go.id/portal-web (Accessed: 15 December 2019).

BPS Jatim(2017). Provinsi Jawa Timur dalam Angka. Jawa Timur Province in Figures 2017. Badan Pusat Statistik Provinsi Jawa Timur. Available at: https://jatim.bps.go.id/4dm!n/pdf%7B_%7Dpublikasi/Provinsi-Jawa-Timur-Dalam-Angka-2017.pdf (Accessed: 3 April 2020).

Brighenti, T.M., Bonumá, N.B., Grison, F., Mota, A., Kobiyama, M., & Chaffe, P. (2019). Two calibration methods for modeling streamflow and suspended sediment with the swat model. Ecological Engineering, **127**(May 2018), pp. 103–113. doi: 10.1016/j.ecoleng.2018.11.007.

DLH Jatim (2017). Dokumen Infmrasi Kinerja Pengelolaan Lingkungan Hidup Daerah Jawa Timur. Surabaya.

Ermoshin, V., Ganzey, S., & Shiraiva, T. (2013). Land-use change in the transboundary Amur river basin in the 20th century. GEOGRAPHY, ENVIRONMENT, SUSTAINABILITY. 6(2), pp. 4–19. doi: 10.24057/2071-9388-2013-6-2-4-19.

Fitri, M., Wardoyo, W., & Theresia, S.T. (2017). Improvement Strategy of Porong Kanal Irrigation Network Performance in Delta Brantas Irrigation Area with Swot Analysis (Strength, Weakness, Opportunities, and Threats). in The 2nd International Conference on Civil Engineering Research (ICCER) 2016 "Contribution of Civil Engineering toward Building Sustainable City." Surabaya, pp. 19–26. doi: 10.12962/j23546026.y2017i1.2186.

Indarto, I., Andiananta Pradana, H.,Wahyuningsih, S., & Umam, M.K..(2020). Assessment of hydrological alteration from 1996 to 2017 in Brantas watershed, East Java, Indonesia. Journal of Water and Land Development. **46(46)**, pp. 121–130. doi: 10.24425/jwld.2020.134204

IPCC (2007). AR4 Climate Change 2007: The Physical Science Basis — IPCC, Contribution of Working Group I to the Fourth Assessment Report of the Intergovernmental Panel on Climate Change. Available at: https://www.ipcc.ch/report/ar4/wg1/ (Accessed: 13 October 2020).

IPCC (2007). Climate Change 2007: The Physical Science Basis. Contribution of Working Group I to the Fourth Assessment

Kang, Y., Gao, J., Shao, H., Zhang, Y. (2019). Quantitative Analysis of Hydrological Responses to Climate Variability and Land-Use Change in the Hilly-Gully Region of the Loess Plateau, China. Water. MDPI AG, 12(1), p. 82. Doi: 10.3390/w12010082.

Lamichhane, S., & Shakya, N. (2019). Integrated Assessment of Climate Change and Land Use Change Impacts on Hydrology in the Kathmandu Valley Watershed, Central Nepal', Water. MDPI AG, 11(10), p. 2059. doi: 10.3390/w11102059.

Li, F., Alewell, C., Borrelli, P., Meusburger, K., & Panagos, P. (2019). Land-use change impacts hydrology in the Nenjiang River Basin, Northeast China. *Forests.* 10(6), pp. 1–18. doi: 10.3390/f10060476.

Li, Y., Chang, J., Luo, L., Wang, Y., Guo, A., Ma, F., Fan, J. (2019). Spatiotemporal impacts of land use land cover changes on hydrology from the mechanism perspective using SWAT model with time-varying parameters. Hydrology Research. IWA Publishing, 50(1), pp. 244–261. Doi: 10.2166/nh.2018.006.

Liu, Z., Cuo, L., Li, Q., Liu, X., Ma, X., Liang, L., & Ding, J. (2020). Impacts of Climate Change and Land Use/Cover Change on Streamflow in Beichuan River Basin in Qinghai Province, China. Water, 12(4), p. 1198. doi: 10.3390/w12041198.

Lu, Z., Zou, S., Qin, Z., Yang, Y., Xiao, H., Wei, Y., Zhang, K., & Xie, J. (2015). Hydrologic Responses to Land Use Change in the Loess Plateau: Case Study in the Upper Fenhe River Watershed. Advances in Meteorology. Doi: 10.1155/2015/676030.

Marie Mireille, N., M. Mwangi, H., K. Mwangi, J., Mwangi Gathenya, J. (2019). Analysis of Land Use Change and Its Impact on the Hydrology of Kakia and Esamburmbur Sub-Watersheds of Narok County, Kenya. Hydrology. MDPI AG, 6(4), p. 86. doi: 10.3390/hydrology6040086.

Moreira, L. L., Schwamback, D. & Rigo, D. (2018). 'Sensitivity analysis of the Soil and Water Assessment Tools (SWAT) model in streamflow modeling in a rural river basin', Revista Ambiente e Agua, 13(6), pp. 1–12. doi: 10.4136/1980-993X.

Moriasi, D.N., Arnold, J.G., Liew, M.W., Van-Bingner, R. L., Harmel, R.D., & Veith, T. L. (2007). Model Evaluation Guidelines For Systematic Quantification Of Accuracy In Watershed Simulations. 50(3), pp. 885–900.

Nikitin, M. A., Tatarinovich, E.V., Rozinkina, I.A., & Andrei E. (2019). Effects of deforestation and aforestation in the central part of the East European plain on regional weather conditions. Geography, Environment, Sustainability. Lomonosov Moscow State University. 12(2), pp. 259–272. doi: 10.24057/2071-9388-2019-12.

Parece, T. E., & Campbell, J. B. (2015). Land Use/Land Cover Monitoring and Geospatial Technologies: An Overview. pp. 1–32. doi: 10.1007/978-3-319-14212-8_1.

Pignotti, G., Rathjens, H., Cibin, R., Chaubey, I., & Crawford, M. (2017). Comparative analysis of HRU and grid-based SWAT models. Water *(Switzerland)*, **9**(4), p. 272. doi: 10.3390/w9040272.

Ptak, M., & Ławniczak, A. E. (2012). Changes in land use in the buffer zone of lake of the Mała Wełna catchment. Limnological Review. Berlin: Sciendo, 12(1), pp. 35–44. doi: https://doi.org/10.2478/v10194-011-0043-z.

Rafiei, V., Ghahramani, A., An-Vo, D., & Mushtaq, S. (2020). Modelling Hydrological Processes and Identifying Soil Erosion Sources in a Tropical Catchment of the Great Barrier Reef Using SWAT. Water. 12(8), p. 2179. doi: 10.3390/w12082179.

S.L. Neitsch, J.G. Arnold, J.R. Kiniry, J. R. W. (2012). *Soil and Water Assessment Tool Theoretical Documentation Version 2009*. Texas: Blackland Research Center ○ Texas Agricultural Experiment Station.

Spruce, J., Bolten, J., Srinivasan, R., Lakshmi, V. (2018). Developing Land Use Land Cover Maps for the Lower Mekong Basin to Aid Hydrologic Modeling and Basin Planning. Remote Sensing. MDPI AG. 10(12), p. 1910. doi: 10.3390/rs10121910.

Valiant, R., Nugroho, W., Bisri, M., Utomo, W. (2021). Water productivity simulation for irrigated farmlands in the Brantas River Basin. Journal of Degraded and Mining Lands Management. **8**(2), pp. 2577–2585. doi: 10.15243/jdmlm.2021.082.2577.

Using artificial intelligence methods for shear travel time prediction: A case study of Facha member, Sirte basin, Libya

Bahia M. Ben Ghawar[*], Moncef Zairi, Samir Bouaziz

Ecole Nationale d'Ingénieurs de Sfax, University of Sfax, Tunisia
[*]*Corresponding author: gloriamuftah@yahoo.com*

Abstract

Shear wave travel time logs are major acoustic logs used for direct estimation of the mechanical properties of rocks. They are also important for prediction of critical drawdown pressure of the reservoir. However, core samples are sometimes not available for direct laboratory measurements, and the time-consuming dipole shear imager tool is generally not used. Hence, there is a need for simple indirect techniques that can be used reliably. In this study, cross-plots between the available measured shear travel time and compressional travel time from three oil wells were used, and three artificial intelligence tools (fuzzy logic, multiple linear regression and neural networks) were applied to predict the shear travel time of Facha member (Gir Formation, Lower Eocene) in Sirte Basin, Libya. The predicted times were compared to those obtained by the equation of Brocher. The basic wireline data (gamma ray, neutron porosity, bulk density and compression travel time) of five oil wells were used. Based on principle component analysis, two wireline data sets were chosen to build intelligent models for the prediction of shear travel time. Limestone, dolomite, dolomitic limestone and anhydrite are the main lithofacies in the Facha member, with an average thickness of about 66 m. The simple equation gave 87% goodness of fit, which is considered comparable to the measured shear travel time logs. The Brocher equation yielded adequate results, of which the most accurate was for the Facha member in the eastern part of the Sirte basin. On the other hand, the three intelligent tools' predictions of shear travel time conformed with the measured log, except in the eastern area of the basin.

Keywords: Carbonate Rock; intelligent tools; Libya; shear travel time; sirte basin.

1. Introduction

The dipole shear imaging logging tool measures both compressional ($\Delta Tc = 1/Vp$) and shear ($\Delta Ts = 1/Vs$) travel time waves to estimate the mechanical properties of rocks (Liu, 2017; Bateman, 2012). However, when ΔTs is not measured (*i.e.*, in old wells) or cannot be measured (*i.e.*, in soft formations or poor cement jobs), synthetic shear travel times are computed using other petrophysical data. Therefore, many empirical relations for estimating shear velocity (Vs) from compressional velocity (Vp) have been published, but most of them are established for clastic rocks, carbonate rocks and coal. For example, the Greenberg & Castagna ,(1992) relation is easily applied and commonly used, but it is unsuitable for anhydrite rock, such as at the site described in the current study.

Therefore, methods based on rock physics are being developed. Miraj *et al*., (2021) used seismic line and wireline log data to define the structural features and hydrocarbon potential of rock. Also, Tao *et al.,* 2020 applied high-density resistivity and shallow seismic reflection methods in a mine in Shandong, China to define the cause of subsidence. Different techniques were applied on a reduced-to-magnetic equator (RTE) anomaly map to define geologic features and their geometry, which included solid minerals emplacement in the Igbeti-Moro area of southwestern Nigeria (Olasunkanmi *et al.,* 2020). Singh & Kanli, (2015) applied a back-propagation artificial Neural Network (ANN) based on neutron porosity, density, true resistivity, compressional wave velocity and gamma ray logs as input data. They demonstrated good correlation between shear velocity estimated by the ANN and an empirical equation. In another context, Amiri *et al.,* (2018) used NN to predict precipitation in two provinces in Iran.

Furthermore, Khamehchi *et al.,* (2014) estimated critical total drawdown as an index of sand production onset from the data of 23 problematic wells in the North Adriatic Sea. The authors started with simple linear regression, MLR and genetic algorithm evolved MLR to estimate critical total drawdown. They then developed two ANN with back propagation and particle swarm optimization algorithms. The study demonstrated the performance and accuracy of the artificial neural networks in predicting sanding onset. Also, well logging data at the BD Madura gas field were used to calculate drilling geological and mechanical parameters. The results were used to estimate drilling risk probability distributions as a function of pore pressure and equivalent circulation fluid density (ECD) as uncertainty analysis (Guan *et al.,* 2018).

Carbonate rocks are common reservoir rocks in the western part of Sirte Basin (Zallah Trough), and petrophysics studies generally focus on reservoir evaluation. However, most exploration wells do not have ΔTs logs and lack some of the basic wireline data such as neutron porosity and litho-density logs. Therefore, prediction of ΔTs of the Facha reservoir requires the development of a geomechanical model in order to minimize drilling problems and instability in newly developed wells. Loss of circulation was recognized in two wells located in Dahab and Ghani oil fields in the lower part of the Facha member, and was attributed to a change of rock type from porous dolomite to limestone. Different intelligent tools can be used to predict ΔTs in carbonate lithofacies, and these predictions can be compared with both simple cross-plot regression and the results of the Brocher, (2005) equation. Here, the intelligent tools, the Brocher equation and the simple cross-plots of measured travel times were applied to data from five oil wells in the Ghani oil field, El Nagah field, Mabrouk area, and Sarir trough in Libya to find a suitable prediction tool for generating synthetic ΔTs logs.

2. Geological background

The Sirte Basin is one of the main hydrocarbon provinces of Libya with clastic (pre-Tertiary) and carbonate (Tertiary) reservoirs. Platforms and troughs are the main structural features of the basin in the northwest to southeast trend (figure. 1).

The structural setting of this basin was postulated based on continental rifting (extensional) related to evidence of Cretaceous–Tertiary events (Hallett & El Ghoul, 1996; Gras, 1996; Guiraud, 1998; Tawadros, 2001; Ahlbrandt, 2001). Abdunaser & McCaffrey, (2014) interpreted the structural configuration of Sirte basin as related to the African plate motion. Accordingly, Sirte Arm, Tibesti Arm and Sarir Arm are the three main rifting arms

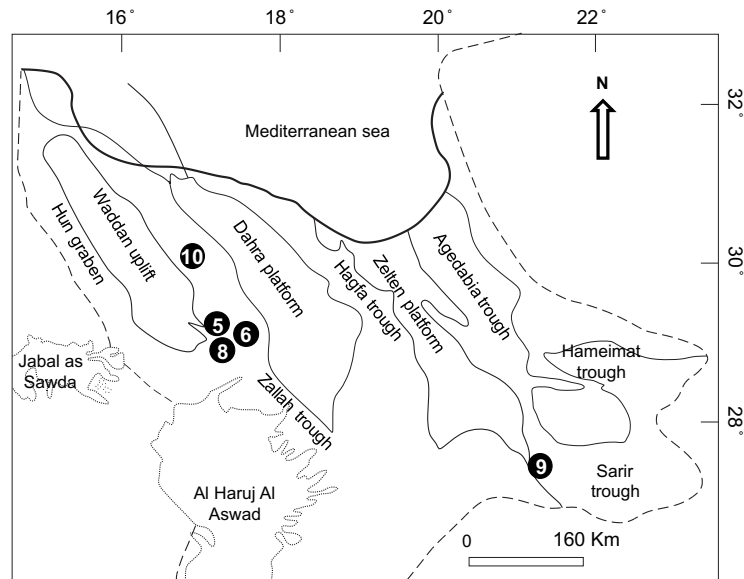formed in early Cretaceous and early Tertiary (Harding, 1984; Gras & Thusu, 1998; Ambrose, 2000).

Fig. 1. Study area and wells location

Three troughs (Dur al Abd, Zallah and Abu Tumayam) have a northwest-southeast direction in the western part of the Sirte Basin. These troughs are asymmetric from the north to the south trend, with the northeast tilting towards Ajdabiya (Hallett & Lowes, 2017). The formations of Gir, Beda, Dahra, Zelten and Farrud are the major reservoir rocks in the western Sirte Basin. The Gir Formation of Lower Eocene (Mijalkovice, 1977; Banerjee, 1980) has a thickness of about 610 meters (Barr & Weeger, 1972). Also, Facha member, Hon Evaporite member and Mesdar Limestone member are parts of the Gir Formation with different lithofacies (figure 2).

Age		Stratigraphic unit Fm. Mbr.		Lithology	Description
Tertiary	Lower Eocene	Gir	Mesder		Limestone and anhydrite interbedding
			Hon Evaporite		Salt and dolomite interbedding within thick anhydrite beds
			Facha		Dolomite with anhydrite and shaly limestone

Fig. 2. Generalized stratigraphic section of the Gir Formation.

The variety of lithofacies is due to three depositional environments: deep marine outer shelf, shallow marine inner shelf and restricted shelf. The restricted condition, which includes lagoon, tidal flats, sabkhas, bays, ponds and subbasins (Abugares, 1996), is prevalent in the Zallah trough. Therefore, the rock types of the Facha member are limestone, dolomite, dolomitic limestone and anhydrite, with the dolomite being predominant. Lashhab & West, (1996) and Elag , (1996) demonstrated an early and late diagenetic dolomitization phases and classified the dolomite into microsparitic crystalline, fine-to-medium crystalline, and coarse-grained dolomite.

3. Methodology for predicting ΔTs

The major basic wireline data recorded in wells 5, 6, 8, 9 and 10 are GR, ΔTc, ΔTs, Øn, ρb, photoelectrical factor (PEF), caliper (CAL), and electrical resistivity (induction, laterolog or array). Figure 3 illustrates the workflow for the processing track of these data to define a suitable prediction model for the shear travel time of the Facha member.
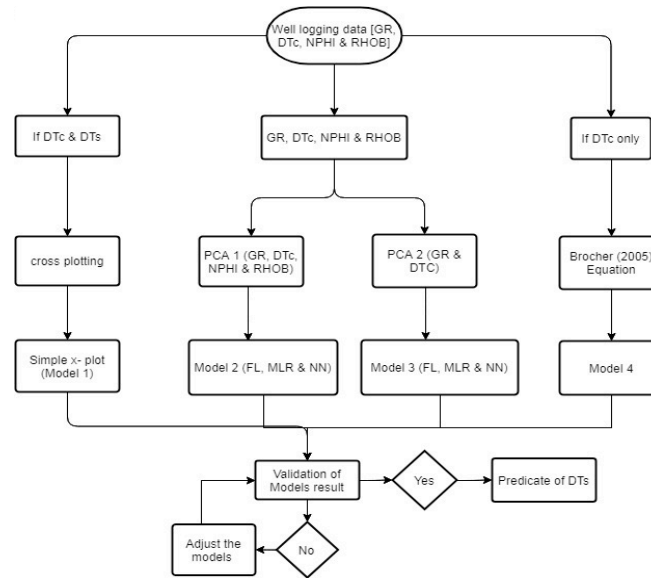

Fig. 3. Workflow of a process for shear travel time prediction

Data from wells 5, 6 and 8 were used to construct simple or direct cross-plots between measured interval travel times, and models were built by using intelligent tools. Wells 10 and 9 were used for models validation. The Øn, ρb and PEF logs were used to discriminate the Facha lithofacies by cross-plots of ρb–Øn and ρb–PEF. Data of the measured shear and compressional interval travel time (DSI logs) of wells 5, 6 and 8 were used to construct simple cross-plots of the Facha member.

Interactive Petrophysics (version 4.2) was used for principal component analysis (PCA), FL, MLR and NN tools to construct the best model for ΔTs prediction. Different sets of basic measured wireline data (GR, ΔTc, Øn and ρb) were used as input. Equation 1 (Brocher, 2005), which is dependent on log (Vp = 1/ΔTc), was used for different lithologies with primary velocities (Vp) between 1.5 km/sec and 8.5 km/s (Maleki *et al.*, 2014).

$$V_S = 0.7858 - 1.2344\,V_P + 0.7949\,V_P^2 - 0.1238\,V_P^3 + 0.006\,V_P^4 \qquad (1)$$

where Vp = sonic velocity (compressional velocity = 1/ΔTc, km/s), Vs = sonic velocity (shear velocity = 1/ ΔTs, km/s), ΔTs = shear travel time (μsec/ft), and ΔTc = compressional travel time (μsec/ft).

The PCA is used to reduce multidimensional data sets to lower dimensions for analysis. The PCA curves can be used for multi-well tops correlation and regression analysis. The FL curve prediction module uses FL as described by Cuddy, (1997), which allows the prediction of a result curve from a number of input curves. In fuzzy estimation, the number of bins was set to 10 for training divided data. Thus, the two statistics parameters μ and σ are calculated of

each data bin and used to compute the FL average probability. Whereas the MLR allows the prediction of a result curve from a number of input curves, the least squares regression routine is intended to find the best fit to the input data.

The same well-logging input data of the PCA, FL and MLR were used in the NN tool with one input layer, one hidden layer and one output layer. The trial zones were selected in front of input data curves at different depths of the Facha member. Training passes, epoch per pass and cross-validation percentage are three training settings of the NN technique. The training passes specify how many times the NN will be trained each time, and in this case, it was 3. The epoch per pass shows how many times the training data will be taken, and in this case, it was 100. The cross-validation percentage of the input data defines how much of the training data cross-check to process, and this was 5%. Epochs trained, the epoch of best cost and raw sensitivity are four outputs of the training settings. Therefore, after training the tool many times, it was used to build the NN model.

4. Results and discussion

Figure 4 shows a plot of bulk density (ρb) versus neutron porosity ($\emptyset$n) in four wells, illustrating the average matrix density (ρma) lines of different lithology; Sandstone = 2.65 g/cm^3, Limestone = 2.71 g/cm^3, Dolomite = 2.87 g/cm^3 and Anhydrite = 2.98 g/cm^3. Most of the plotting points fall between the average matrix density lines of limestone rock (2.71 g/cm^3) and anhydrite rock (2.98 g/cm^3). The shifting of the plotted points of wells 5, 6 and 8 from the dolomite line towards the anhydrite line is attributed to the existence of the anhydrite as a cement material, while the plotting points of well 9 fall on the average matrix density of the dolomite line with high values of neutron porosity ($\emptyset$n). The cluster points in the lower part of the plot close to zero neutron porosity and less than 2.8 g/cm^3 of bulk density demonstrate anhydrite lithofacies. Also, anhydrite strips are clearly present within the Facha member at different depths: 3990, 4215 and 4240 ft in well 8 (figure 6). It worth mentioning that well 10 was excluded because no neutron and litho-density logs are available. Therefore, dolomite is the most common rock type in the Facha member, along with limestone, dolomitic limestone and anhydrite.
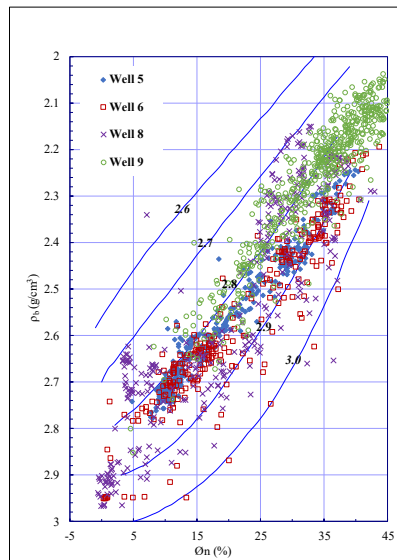

Fig. 4. Cross-plot of bulk density (ρ_b) versus neutron porosity ($\emptyset$n)

The PCA on models run with the first input data set (GR, ΔTc, Øn and ρb) of wells 5, 6 and 8 has a variability of 64.7%, 23.2%, 7.9% and 4.2%, respectively. PCA of the second input set has a variability of 58.6% and 41.3 % for GR and ΔTc, respectively. These two sets of basic well logging data were used to build an intelligent model of ΔTs. The second set of logs enabled the prediction of synthetic ΔTs for wells that had no basic wireline logs, such as well 10, which has neither a Øn nor a ρb log. Wells 9 and 10 were used to validate different ΔTs models. Figure 5 shows a simple plot between measured ΔTs and ΔTc for wells 5, 6 and 8 using 787 data points. A simple regression equation was generated (Equation 2, $R^2 = 0.87$). The model built on MLR used 787 data points from the first and second input data sets from the same wells, and Equations 3 and 4 were extracted with a regression coefficient $R^2 = 0.91$ and 0.89, respectively.

$$\Delta Ts = 3.32 + (1.6 * \Delta Tc) \tag{2}$$
$$\Delta Ts = 122.7 - (0.3 * GR) + (1.3 * \Delta Tc) - (26.7 * Øn) - (33.6 * ρb) \tag{3}$$
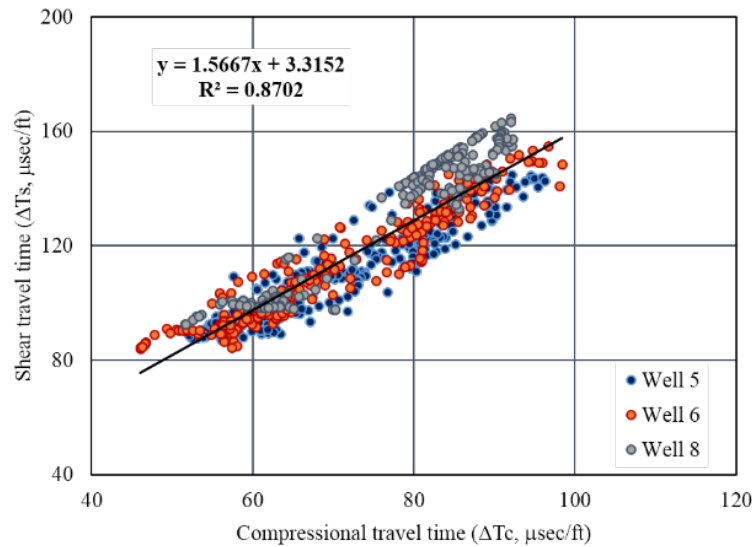$$\Delta Ts = 14.9 - (0.3 * GR) + (1.5 * \Delta Tc) \tag{4}$$

Fig. 5. Plot of log data of measured ΔTs and ΔTc

One stage of training was performed on the NN tool, with the epoch of best cost equal to 65 as the second and third training passes did not improve the first pass. Also, the minimum error of the best cost was equal to 1.4E-314, where a lower value is better.

MLR, NN, simple plot and the Brocher (2005) equation (Equation 1) yielded ΔTs values that generally agreed with the measured values. In wells 5 and 6, ΔTs values derived from the simple cross-plot equation were higher than the measured values in porous dolomite lithofacies. On the other hand, in wells 8, 9 and 10 it was less than the measured log in dolomitic limestone and anhydrite lithofacies. In less porous dolomite lithofacies, ΔTs calculated from simple plots was similar to the measured values (figures 6 and 7). Well 9 is located at the Sarir Trough (southern shelf), and the depositional environment is the shallow carbonate-inner shelf in the Eocene time (Hallett & Lowes, 2017). However, in this well, the simple plot and intelligent

models yielded lower estimations of ΔTs, whereas the Brocher (2005) equation yielded the most accurate estimate (figure 8).

Figure 9 compares the ΔTs of well 10 showing clear agreement between the predicted and measured values, except below the depth of 3430 feet due to the increase of GR. The NN tool gave the best prediction of ΔTs in this well throughout the Facha member.
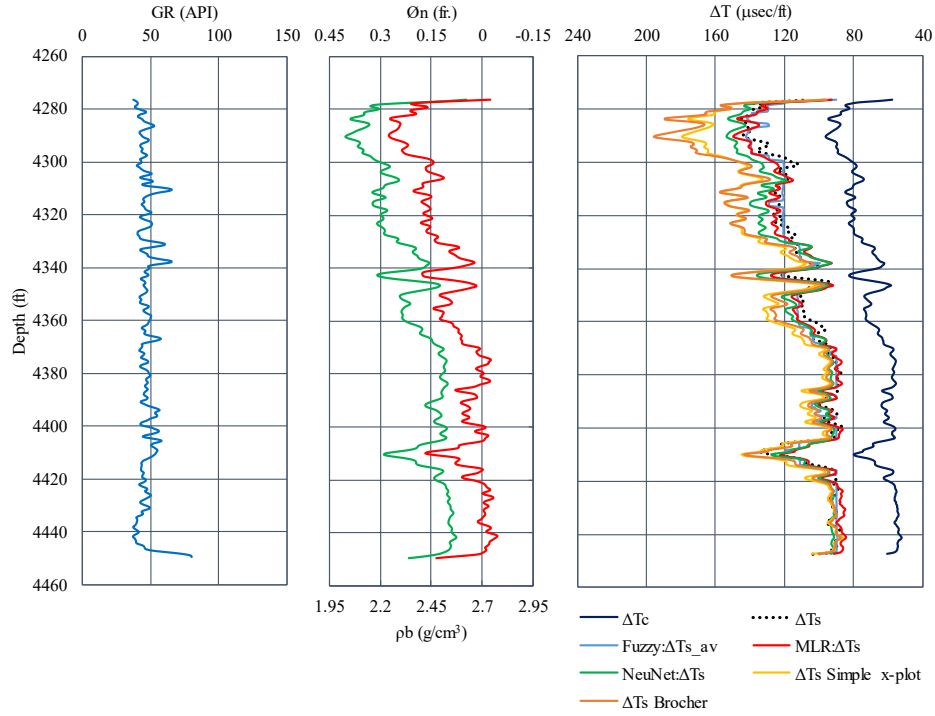

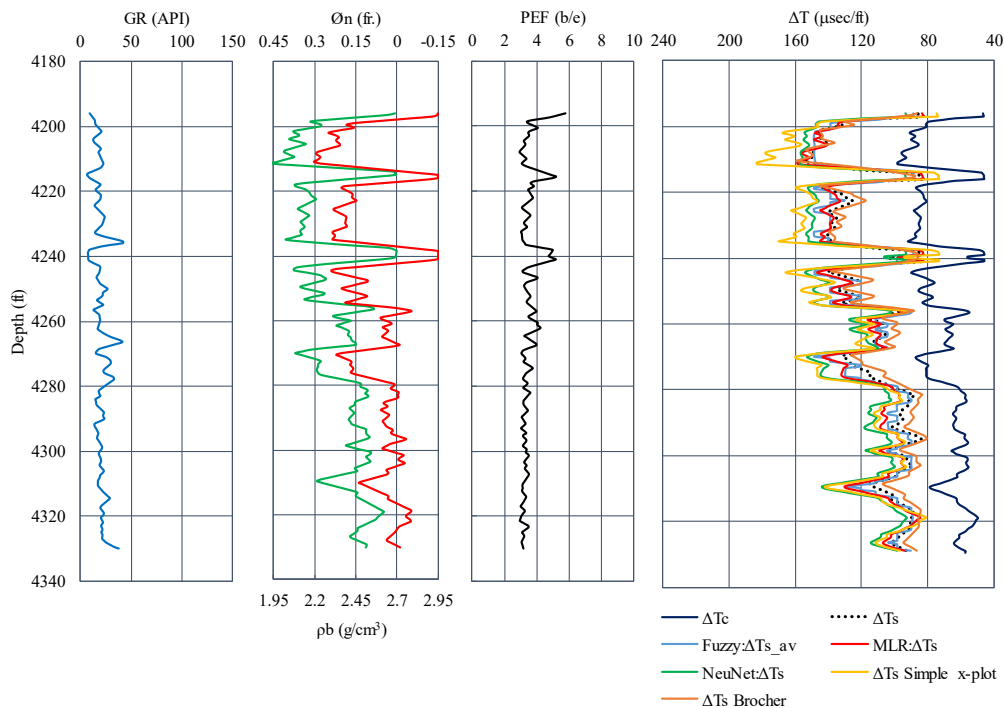**Fig. 6.** Measured and predicted ΔTs and basic wireline data of well 5

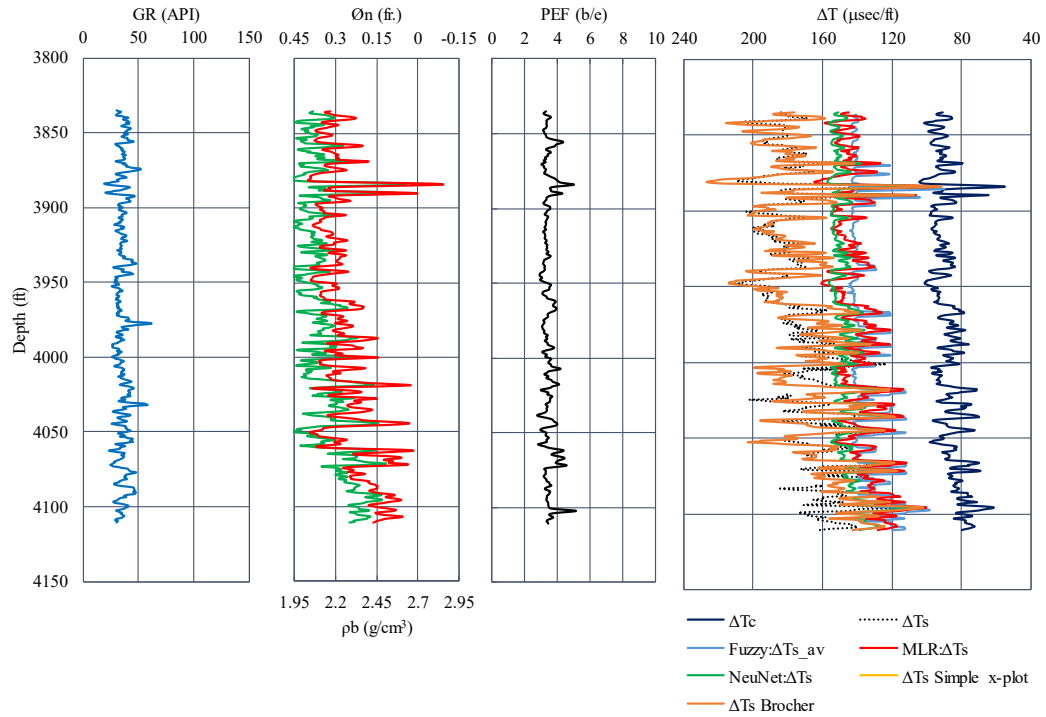**Fig. 7.** Measured and predicted ΔTs and basic wireline data of well 6.

Fig. 8. Measured and predicted ΔTs from basic wireline data of well 9
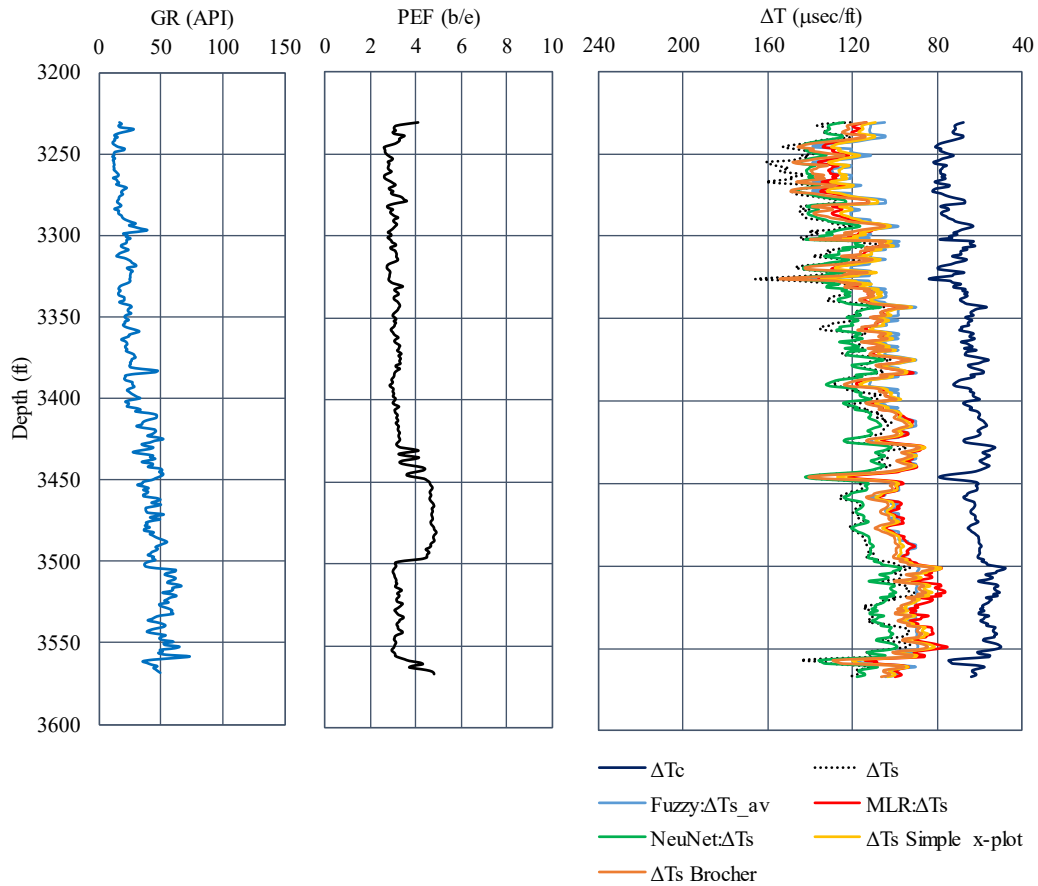

Fig. 9. Measured and predicted ΔTs of well 10, GR and PEF

The statistical analysis tools, IHS Kingdom and IBM SPSS Statistics 20, were applied by Ehsan *et al.,* (2018) to well logs and seismic data to classify reservoir and source rocks depth at Sindh province in the Southern Lower Indus Basin of Pakistan. Hence, the Table 1 summarizes the statistical of error measurements and performance of the models. It includes the average difference between measured and predicted values of ∆Ts (∆TsM – ∆TsP), standard error (SE), and goodness of fit (R^2). The differences between the measured and predicted values of ∆Ts for the first and second input data sets were 5-15 μsec/ft and 4-17 μsec/ft, respectively. The SE of the predicted shear travel time, calculated by using Equation 5, reached up to 19 μsec/ft.

$$SE = \sqrt{\frac{(\Delta TsM - \Delta TsP)^2}{n-2}} \tag{5}$$

∆TsM: measured shear travel time (μsec/ft); ∆TsP: shear travel time (μsec/ft) predicted by the different techniques; n = number of data points; SE: standard error.

The Correlation between ∆TsM and ∆TsP for the first input data set for wells 6 and 9 are shown in figure 10. The assessment of the intelligent tools in predicting shear travel time in the Zallah and Sarir Troughs were with the R^2 equal to 0.9 and 0.6, respectively. On the other hand, cross-plots and the Brocher equation were more suitable for the Facha member at different locations in the Sirte Basin, with 90% goodness of fit. The lower R^2 in well 9 could be attributed to dolomitic limestone lithofacies and higher shale content. Similar results have been reported by Akhundi *et al.,* 2014, who applied artificial NN, the Castagna empirical equation and MLR to estimate ∆Ts. They found that ∆Ts prediction by the ANN was acceptable in relation to the measured values. Also, the MLR yielded predictions with 92% fit, but it cannot be used for generalization across different lithologies. However, the Castagna empirical equation had a correlation coefficient (R^2) of 0.72 and was considered acceptable for use in wells with incomplete well logging data.
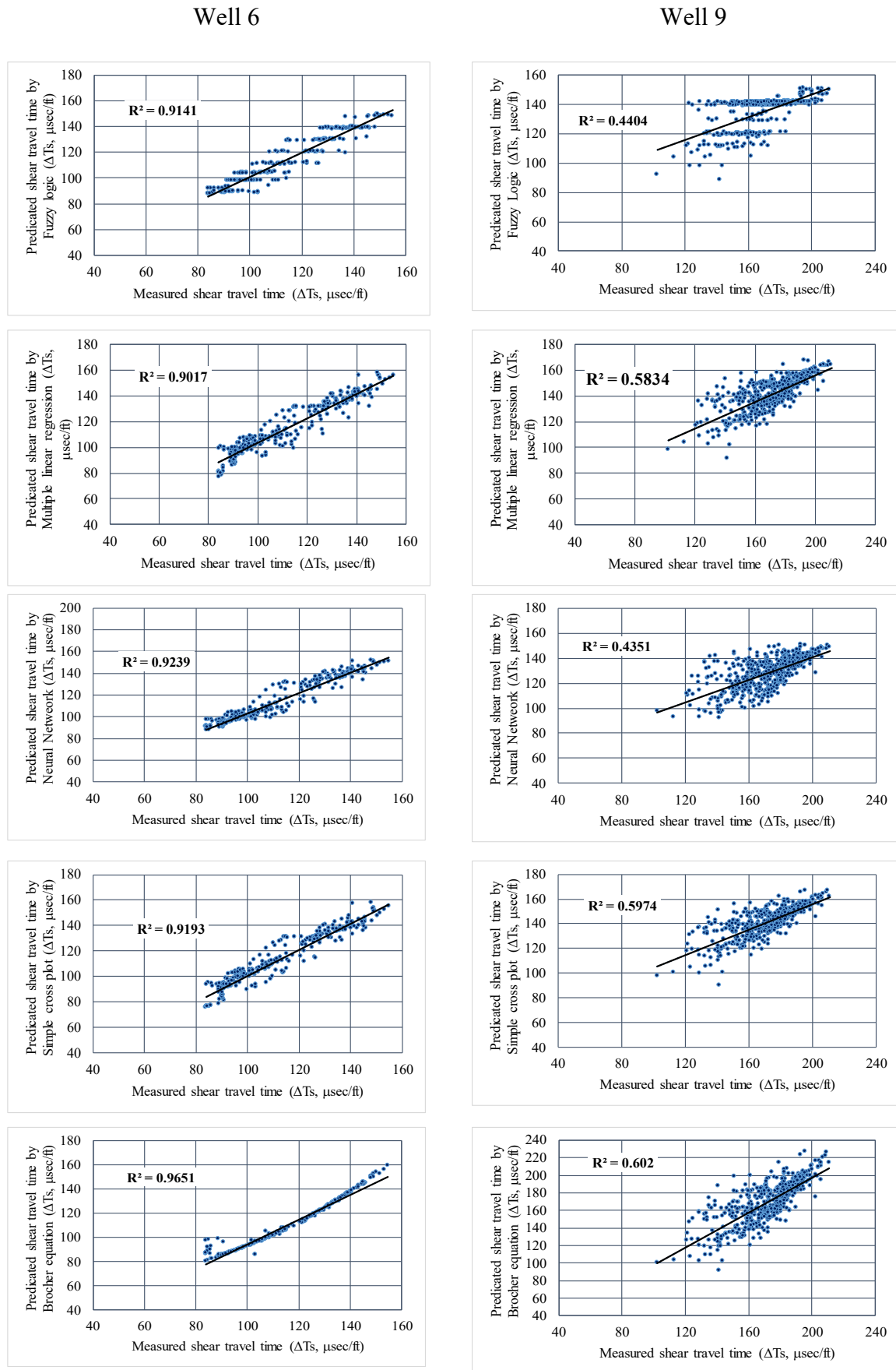
Well 6   Well 9

Fig. 10. Correlation between measured and predictions ΔTs by different models in wells 6 and 9 by using the first set of data

5. Conclusions

In general, prediction of ΔTs on the basis of GR, ΔTc, $\varnothing n$, and ρb is important in old wells or wells with borehole problems, such as collapse or caving. Predicted ΔTs is useful for understanding the mechanical behavior of rocks and helpful in dealing with well instability. However, though this approach is applicable to clastic and carbonate rocks, it is not applicable to situations where limestone, dolomite, dolomitic limestone and anhydrite are present, and the use of any empirical equation could be ruled out.

Table 1. Goodness of fit, average difference and standard error of the input data set

Well	Model	1st PCA input data			2nd PCA input data		
		R^2	Difference	SE	R^2	Difference	SE
5	Fuzzy logic	0.83	7.1	10.66	0.89	4.1	5.6
	Multiple linear regression	0.86	4.6	6.25	0.88	4.9	6.3
	Neural Network	0.85	5.4	7.58	0.86	6.8	8.7
	Simple cross plot	0.89	14.1	17.70	-	-	-
	Brocher (2005) equation	0.88	13.4	18.40	-	-	-
6	Fuzzy logic	0.91	4.7	8.06	0.93	4.7	6.2
	Multiple linear regression	0.90	5.8	9.00	0.93	5.2	6.6
	Neural Network	0.92	4.9	8.20	0.92	12.2	13.8
	Simple cross plot	0.91	4.9	8.30	-	-	-
	Brocher (2005) equation	0.96	6.5	8.56	-	-	-
8	Fuzzy logic	0.92	6.9	9.05	0.93	7.7	8.9
	Multiple linear regression	0.89	6.9	8.99	0.94	7.5	8.7
	Neural Network	0.93	8.6	12.2	0.95	4.8	6.7
	Simple cross plot	0.89	11.0	16.3	-	-	-
	Brocher (2005) equation	0.89	11.9	19.2	-	-	-
9	Fuzzy logic	0.44	36.2	38.54	0.45	36.9	39.4
	Multiple linear regression	0.58	30.7	32.68	0.58	32.7	34.8
	Neural Network	0.43	44.2	46.38	0.55	26.3	28.8
	Simple cross plot	0.60	31.0	33.00	-	-	-
	Brocher (2005) equation	0.60	12.3	15.29	-	-	-
10	Fuzzy logic	-	-	-	0.88	16.6	17.7
	Multiple linear regression	-	-	-	0.89	15.4	16.3
	Neural Network	-	-	-	0.85	4.1	5.4
	Simple cross plot	0.92	15.4	16.4	-	-	-
	Brocher (2005) equation	0.91	10.5	11.5	-	-	-

The measured basic wireline data were used as input data to predict ΔTs by using intelligent tools. These tools predicted ΔTs with a good of fit (about 90%). In addition, simple cross-plots of measured versus predicted ΔTs in the wells show that ΔTs is overestimated at dolomite lithofacies due to increasing neutron porosity. Both the simple plots and MLR models show estimated values of ΔTs lower than measured values in the dolomitic limestone and limestone lithofacies. The Brocher, (2005) equation results fit well with the measured ΔTs at dolomite and dolomitic limestone lithofacies, but the predicted ΔTs were shorter than the measured time due to the reduced porosity and the changes to the limestone lithofacies. For the anhydrite lithofacies, the intelligent tools and the Brocher equation yielded predictions of ΔTs equivalent to the measured values, but the simple plot equation provided less accurate predictions. According to that, the simple cross-plot and the Brocher equation could be used for the dolomite and dolomitic limestone lithofacies in the Facha member, particularly if no intelligent tools are available. MLR yielded results closer to the measured shear travel time than the NN results in dolomite lithofacies, but NN is more suitable for dolomitic limestone. Generally, the second PCA input data set gave better results than the first PCA input data set for the ΔTs estimated by the intelligent tools.

ACKNOWLEDGMENTS

References

Abdunaser, K. & McCaffrey, K. (2014). Rift architecture and evolution: The Sirt Basin, Libya: The influence of basement fabrics and oblique tectonics. *Journal of African Earth Sciences*, (**100**):203-226.

Abugares, Y.I. (1996). Sedimentology and hydrocarbon potential of the Gir Formation. Sirt Basin. Libya. First Symposium on the Sedimentary Basins of Libya, Geology of the Sirt Basin, vol. 2. (Eds. M. J. Salem, A. S. El Hawat, A.M. Sbeta). Amsterdam, Netherlands.

Akhundi, H., Ghafoori, M. & Lashkaripour, G.R. (2014). Prediction of shear wave velocity using artificial neural network technique, multiple regression and petrophysical data: A case study in Asmari reservoir (SW Iran). *Open Journal of Geology*, (**4**):303-313.

Ahlbrandt, T.S. (2001). The Sirte basin province of Libya: Sirte-Zelten total petroleum system: US Department of the Interior, US Geological Survey. 29p.

Ambrose, G. (2000). The geology and hydrocarbon habitat of the Sarir Sandstone, SE Sirt Basin, Libya. *Journal of Petroleum Geology*, 23(**2**):165-192.

Amiri, M.A., Conoscenti, C., & Mesgari, M.S. (2018). Improving the accuracy of rainfall prediction using a regionalization approach and neural networks. *Kuwait Journal of Science,* **45**(4):66-75.

Banerjee, S. (1980). Stratigraphic lexicon of Libya. Department of geological researches & mining. Bulletin (**13**).

Barr, F. & Weeger, A. (1972). Stratigraphic nomenclature of the Sirte Basin, Libya: Petroleum Exploration Society Libya, Tripoli. 179p.

Bateman, M.R. (2012). Openhole Log Analysis and Formation Evaluation. Society of Petroleum Engineers, United States of America. 653p.

Brocher, T.M. (2005). Empirical relations between elastic wave speeds and density in the Earth's crust. *Bulletin of the seismological Society of America*, 95(**6**), 2081-2092.

Cuddy, S. (1997). The application of the mathematics of fuzzy logic to petrophysics. Paper presented at the SPWLA 38th annual logging symposium.

Ehsan, M., Gu, H., Akhtar, M.M., Abbasi, S.S. & Ehsan, U. (2018). A geological study of reservoir formations and exploratory well depths statistical analysis in Sindh Province, Southern Lower Indus Basin, Pakistan. *Kuwait Journal of Science,* **45**(2):84-93.

Elag, M. O. (1996). Sedimentological study of the Facha Member in the southwest Sirt Basin, Libya. Paper presented at The First Symposium on the Sedimentary Basins of Libya, Geology of the Sirt Basin. Amsterdam, Netherlands.

Gras, R. (1996). Structural style of the southern margin of the Messlah High. The geology of the Sirt Basin. Amsterdam, Elsevier, (**3**):201-210.

Gras, R. & Thusu, B. (1998). Trap architecture of the Early Cretaceous Sarir sandstone in the eastern Sirt Basin, Libya. Geological Society, London, Special Publications, 132(**1**):317-334.

Greenberg, M.L. & Castagna, J.P. (1992). Shear-Wave Velocity Estimation in Porous Rocks: Theoretical Formulation, Preliminary Verification and Applications. Geophysical Prospecting, (**40**):195-209.

Guiraud, R. (1998). Mesozoic rifting and basin inversion along the northern African Tethyan margin, an overview. Geological Society, London, Special Publications, 132(**1**):217-229. Guan, Z., Sheng, Y., Luo, M., Xu, Y., Zhang, B. & Wang, Q. (2018). A new quantitative evaluation method for drilling risk based on uncertainty analysis. *Kuwait Journal of Science,* **45**(3):105-113.

Hallett, D. & Clark-Lowes, D. (2017). Petroleum geology of Libya. Elsevier, Netherlands. 393p.

Hallett, D. & El Ghoul, A. (1996). Oil and gas potential of the deep trough areas in the Sirt Basin, Libya. In Salem, M.J., El-Hawat, A.S., and Sbeta, A.M., eds., The geology of Sirt Basin: Amsterdam, Netherlands.

Harding, T. (1984). Graben hydrocarbon occurrences and structural style. AAPG Bulletin, 68(**3**):333-362.

Khamehchi, E., Kivi, I.R. & Akbari M. (2014). A novel approach to sand production prediction using artificial intelligence. *Journal of Petroleum Science and Engineering,* (**123**): 147-154.

Lashhab, M.I. & West, I.M. (1996). Dolomitization of the Jir and Rawaghah Formations in Jabal al Jir and the western Sirt Basin**.** First Symposium on the Sedimentary Basins of Libya. Geology of the Sirt Basin, vol. 2. (Eds. M.J. Salem. A.S. El-Hawat and A.M. Sbeta). Elsevier, Amsterdam, Netherlands.

Liu, H. (2017). Principles and Applications of Well Logging. In: Sonic Logs, Pp. 59-114. **Springer, China.**

Maleki, S., Moradzadeh, A., Riabi, R.G., Gholami, R. & Sadeghzadeh, F. (2014). Prediction of shear wave velocity using empirical correlations and artificial intelligence methods. *NRIAG Journal of Astronomy and Geophysics*, (**3**):70-81.

Mijalkovic, N. (1977). Geological Map of Libya, Al Qaddahiyah (NH33-3). Explanatory Booklet. Industrial Research Centre, SPL AJ. Tripoli.

Miraj, A. F. M., Ali, A., Javaid, H., Rathore, P.S., Ahsan, N., Saleem., R., Afgan, S. & Malik, B.M. (2021). An integrated approach to evaluate the hydrocarbon potential of Jurassic Samana Suk Formation in Middle Indus Basin, Pakistan. *Kuwait Journal of Science*, 48(**4**):1-11.

Olasunkanmi, N., Sunmonu, L.A. & Adabanija, M.A. (2020). Geophysical investigation for mineral prospect in Igbeti-Moro area, southwestern Nigeria. *Kuwait Journal of Science,* **47**(3):2-14.

Singh, S., Kanli, A.I. (2015). Estimating shear wave velocities in oil fields: a neural network approach. *Geosciences Journal*, DOI 10.1007/s12303-015-0036-z.

Tao, L.Z., Ming, L.Q. & Hong, Z. (2020). Integrated physical detection technology in complicated surface subsidence area of mining area. *Kuwait Journal of Science,* **47**(1):86-96.Tawadros, E. (2001). Geology of Egypt and Libya. Balkema-Rotterdam**,** Netherlands. 468p.